ADAM MICKIEWICZ
UNIVERSITY
POZNAŃ

Exploring the photoresponse of Orange Carotenoid Protein: a subpicosecond to minute time-resolved absorption studies

PhD Thesis by

Stanisław Niziński

Supervisor:

Prof. dr hab. Gotard Burdziński

Assistant supervisor:

CNRS Research Director Michel Sliwa

Poznań 2023

Acknowledgements

Firstly, I would like to thank both my supervisors, prof. dr hab. Gotard Burdziński (Quantum Electronics Laboratory, Faculty of Physics, Adam Mickiewicz University, Poznań, Poland) and CNRS Research Director Michel Sliwa (Laboratoire de Spectroscopie pour les Interactions, la Réactivité et l'Environnement, Lille, France) for all the support and patience during the time of my PhD studies. Their guidance made it possible to complete this thesis.

Moreover, I would like to express my gratitude to our collaborators, Emeritus CNRS Director Diana Kirilovsky (Institute for Integrative Biology of the Cell, Gif-sur-Yvette, France), CNRS Research Director Jacques-Philippe Colletier (Institut de Biologie Structurale, Grenoble, France) and prof. Ilme Schlichting (Max-Planck-Institut für medizinische Forschung, Heidelberg, Germany) for the support during the project, all discussions and making OCP samples available. I am also thankful to dr Adjéle Wilson for preparing the majority of samples used in the project.

I would like to thank dr Sabina Brazevič for extensive corrections of my thesis, constructive conversations and all the help with all the administrative issues which were very hard to solve for me. I am also thankful to dr Lucas Martinez Uriarte for all the kindness and help during my stay in LASIRE, Lille. I would like to thank all colleagues from ZEK and LASIRE, for being a good company for all this time.

A special thanks to my parents, for their continuous support and patience during the endless time of my PhD studies.

This work was performed with financial support from the Polish National Science Centre (NCN) project Preludium 2018/31/N/ST4/03983 and the French National Research Agency (grant ANR-18-CE11-0005). My stay in LASIRE laboratory was financed by Lille University and Uniwersytet Jutra project.

Abstract

The object of the research conducted within this thesis is the Orange Carotenoid Protein (OCP). It contains a carotenoid chromophore within the protein structure, between N-terminal and C-terminal domains, which results in an orange (OCP^O) or red (OCP^R) color. The OCP performs a photoprotective function in cyanobacteria, providing a defense mechanism against harsh irradiation conditions. The OCP is a photoactive protein, it has the ability to dynamically react to changes in sunlight intensity, and activate dissipative mechanisms only when they are required. In low irradiation conditions, the defense mechanism remains disabled in order to avoid spoiling the photosynthesis efficiency. After being illuminated by strong green or blue light, the dark-adapted OCP^O form undergoes complex structural rearrangements, finally being converted into the red, active OCP^R form. The OCP^R can attach itself to the phycobilisomes, which are antenna complexes of the cyanobacteria, responsible for light harvesting. Then it quenches their excited states, providing a dissipative channel, that allows to dispose of the excess of the harvested energy into the environment, protecting the delicate photosystems from damage. The process of photoconversion to the OCP^R form is fully reversible *in vitro,* while *in vivo* it requires the assistance of Fluorescence Recovery Protein (FRP), so eventually the OCP^R form can relax to the non-quenching OCP^O form, finishing the photocycle and allowing cyanobacteria to regain full photosynthesis capability.

Despite staggering progress in OCP research in recent years, only the structure of dark-adapted OCP^O and metastable OCP^R forms are currently quite well understood. OCP^O is structured as a two-domain protein, the carotenoid chromophore is embedded at their interface. The mechanism of the photoresponse and intermediate species that control the $OCP^O \rightarrow OCP^R$ photoconversion quantum yield are still obscured. Phenomena occurring during conversion to the OCP^R form are not trivial to investigate, due to the very low quantum yield of the OCP^R formation (0.1% order of magnitude), involvement of at least 4 excited states (decaying at the picosecond timescale) and sequentially populated 6 intermediate forms (spanning from nanosecond to second time scale). After absorption of a photon, the carotenoid located within the OCP is promoted to the second excited state S_2. The relaxation through Intramolecular Charge Transfer (ICT) state, S_1 and S* states takes place within tens of picoseconds and leads to the P_1 form, where the carotenoid is back in the electronic ground state, but its interaction with the protein scaffold is altered. Afterward, a complex sequence of the protein and carotenoid rearrangements occurs, the carotenoid is translocated to the N-terminal domain and finally both OCP domains dissociate. This sequence consists of several intermediates (P_1, P_2, P_2', P_N, P_M, P_X), which quantum yield is different depending on the selected variant of the OCP.

Most of the work done within this thesis has been focused on the characterization of the OCP photoconversion process using various time-resolved absorption spectroscopy techniques, covering time regime from hundreds of femtoseconds up to minutes. Information retrieved this way is directly related with the carotenoid, however, the protein rearrangements influence the carotenoid properties. Due to the high molar absorption coefficient of the carotenoid, it is possible

to track even very minor OCP populations formed after the photoexcitation. The most important accomplishments described in this thesis are:

1. The relaxation of the ICT, S_1 and S* states ending with a formation of the P_1 form was observed using femtosecond transient absorption spectroscopy in the function of excitation wavelength and pulse energy. OCPs from *Planktothrix* (the fastest photo-activation reported in the literature) and *Synechocystis* cyanobacteria have been investigated, moreover, C-tagged and N-tagged variants containing echinenone and canthaxanthin carotenoids were compared. It is proposed that the first intermediate form - P_1, is a result of the carotenoid S_1 state relaxation, not S* as it has been claimed before. A similar quantum yield of the P_1 form has been found ($\Phi_{P1} \approx 0.5\%$) regardless of the OCP variant.
2. OCP variants containing canthaxanthin or echinenone were investigated using nanosecond transient absorption spectroscopy. It allowed to describe the evolution of the protein intermediate forms in the time window up to one second. These results opened a way to characterize the consecutive steps for each OCP variant, determine the quantum yield for each intermediate form and propose a new, complete photoconversion scheme. It was observed, that N-tagged OCP from *Planktothrix* functionalized with a canthaxanthin chromophore has the highest photoconversion efficiency among all investigated OCP variants. The data suggest that carotenoid translocation is more efficient for OCP from *Synechocystis* compared to OCP from *Planktothrix*. Furthermore, domain separation is more efficient for canthaxanthin-functionalized OCP compared to echinenone-functionalized OCP.
3. Experiments in the function of temperature and protein concentration were carried out for the so-called "monomeric mutant" and its wild-type equivalent. Collective analysis of these data coupled with Wide Angle X-ray Scattering (WAXS) results acquired by French collaborators allowed to describe the photoconversion process of the OCP dimers. It was found that excitation with a nanosecond pulse does not seem to result in OCP^R formation. Based on all results, it was proposed, that a single pulse excitation of the OCP^O dimer leads to the P_3/OCP^O dimer, which relaxes back to the OCP^O/OCP^O dimer.
4. It was proposed that the OCP^R formation requires consecutive absorption of two photons in the C-tagged OCP from *Synechocystis* containing echinenone. In other OCP types, this kind of process may coexist with a single-photon photoconversion pathway. The existence of a two-photon process is interesting from the biological point of view because it means that the OCP activity may depend on a square, not a linear function of the light intensity. Therefore the OCP can adapt to the dynamic changes of the ambient light much better than it has been expected before.

These results were published in 4 articles. The investigations were done within an International funded project (DynOCP) that involves the team of prof. dr hab. Gotard Burdziński (Quantum Electronics Laboratory, Faculty of Physics, Adam Mickiewicz University, Poznań, Poland), CNRS Research Director Michel Sliwa (LAboratoire de Spectroscopie pour les

Interactions, la Réactivité et l'Environnement, Univ. Lille, CNRS, Lille, France), Emeritus CNRS Director Diana Kirilovsky (Institute for Integrative Biology of the Cell, CEA, Univ. Paris Saclay, CNRS, Gif-sur-Yvette, France), CNRS Research Director Jacques-Philippe Colletier (Institut de Biologie Structurale, Univ. Grenoble Alpes, CEA, CNRS, Grenoble, France) and prof. Ilme Schlichting (Department of Biosciences, Physics and Astronomy, Univ. Heidelberg, Max Planck-Institut für medizinische Forschung, Heidelberg, Germany).

Abstrakt w języku polskim

Przedmiotem badań przeprowadzonych w ramach przedstawionej pracy doktorskiej był kompleks karotenoidowo-białkowy - OCP (ang. Orange Carotenoid Protein). OCP jest fotoaktywnym białkiem zawierającym karotenoid, nadający mu pomarańczową lub czerwoną barwę. Dzięki OCP sinice są w stanie dostosowywać się dynamicznie do warunków oświetleniowych. OCP na bieżąco reaguje na zmiany nasłonecznienia i aktywuje mechanizmy ochronne jedynie wtedy, kiedy są one niezbędne, natomiast w innych przypadkach dezaktywuje je aby nie sabotować procesów fotosyntezy. Po naświetleniu zielono-niebieskim światłem OCP ulega złożonym przemianom konformacyjnym i przechodzi w czerwoną, aktywną formę (OCP^R), która ma zdolność przyczepiania się do fikobilisomów (kompleksów odpowiadających za zbieranie światła w sinicach). OCP^R potrafi rozpraszać w postaci ciepła energię stanów wzbudzonych, pozyskaną dzięki absorpcji światła przez fikobilisomy, co chroni delikatny system fotosyntetyczny. Proces fotokonwersji do formy OCP^R jest odwracalny *in vitro*, natomiast *in vivo* wymagana jest obecność dodatkowego białka - FRP (ang. Fluorescence Recovery Protein), które katalizuje zanik formy OCP^R do nieaktywnej formy OCP^O, pozwalając tym samym na odzyskanie przez sinice pełnej zdolności do fotosyntezy.

Pomimo znacznego postępu w badaniach nad OCP przeprowadzonych w ostatnich latach, jedynie struktury ciemnej formy OCP^O oraz metastabilnej formy OCP^R są dobrze poznane. OCP^O składa się z dwóch domen, oraz znajdującego się między nimi karotenoidu. Mechanizm i stany pośrednie determinujące kwantową wydajność fotokonwersji $OCP^O \rightarrow OCP^R$ są wciąż obiektem kontrowersji. Badania zjawisk zachodzących w trakcie fotokonwersji do formy OCP^R są trudne, ze względu na niską kwantową wydajność tworzenia formy OCP^R, obecność co najmniej 4 elektronowych stanów wzbudzonych (zanikających w skali pikosekund) oraz 6 kaskadowo relaksujących stanów pośrednich (w skali od nanosekund do sekund). W wyniku absorpcji fotonu, karotenoid znajdujący się w białku przechodzi do stanu wzbudzonego S_2. Relaksacja następuje w skali czasu dziesiątek pikosekund poprzez stan wzbudzony z wewnątrzcząsteczkowym przeniesieniem ładunku ICT (ang. Intramolecular Charge Transfer), stan wzbudzony S_1, oraz stan S*. W rezultacie powstaje forma P_1, w której karotenoid znajduje się ponownie w stanie podstawowym, jednak oddziaływania z otoczeniem białkowym są zaburzone. W dalszej kolejności następuje złożona sekwencja zmian w strukturze białka oraz karotenoidu, karotenoid ulega translokacji do N-zakończonej domeny, następnie C- i N-zakończone domeny ulegają separacji. Ta sekwencja została opisana serią stanów pośrednich (P_1, P_2, P_2', P_N, P_M, P_X), tworzonych z wydajnością zależną od badanego wariantu OCP.

Większość badań opisanych w przedstawionej rozprawie polegało na charakteryzacji procesu fotokonwersji OCP za pomocą różnych technik czasowo-rozdzielczej spektroskopii absorpcyjnej, pokrywających skale czasu od setek femtosekund do minut. Informacja pozyskiwana w ten sposób jest bezpośrednio związana z zachowaniem karotenoidu, które z kolei jest modulowane przez geometrię białka. Ponieważ karotenoidy posiadają bardzo wysoki molowy współczynnik absorpcji, możliwe jest śledzenie nawet bardzo niewielkich populacji OCP

przekonwertowanych do nierównowagowego stanu przez absorpcję promieniowania. W ramach przeprowadzonych badań udało się uzyskać następujące wyniki:

1. Za pomocą femtosekundowej absorpcji przejściowej zaobserwowano relaksację stanów ICT, S_1 oraz S* zakończoną utworzeniem formy P_1. Pomiary wykonano w funkcji energii i długości fali wzbudzenia. Porównano różne warianty OCP, tagowane na C-końcu i N-końcu, pochodzące zarówno z sinic *Planktothrix* jak również *Synechocystis*, zawierające karotenoidy kantaksantynę lub echinenon. Zaproponowano, że pierwsza forma pośrednia białka – P_1, jest wynikiem relaksacji stanu S_1, a nie stanu S* jak wcześniej sądzono. Wszystkie zbadane warianty OCP posiadają zbliżoną kwantową wydajność tworzenia formy P_1 ($\Phi_{P1} \approx 0{,}5\%$).
2. Kolejne eksperymenty zrealizowano z wykorzystaniem nanosekundowej absorpcji przejściowej. W ten sposób rozszerzono zakres czasowy eksperymentu, aż do jednej sekundy po impulsie wzbudzającym. Dzięki temu możliwa była charakteryzacja stanów pośrednich dla każdego wariantu OCP, wyznaczenie ich kwantowej wydajności tworzenia i zaproponowanie nowego schematu opisującego proces fotokonwesji OCP. Dla OCP pochodzącego z sinic *Planktothrix* funkcjonalizowanych kantaksantyną, ze znacznikiem polihistydynowym na N-końcu zaobserwowano najwyższą kwantową wydajność fotokonwersji wśród przebadanych wariantów OCP. Wyniki sugerują, że proces translokacji karotenoidu zachodzi wydajniej dla OCP z sinic *Synechocystis* w porównaniu do sinic *Planktothrix*. Proces separacji domen białka okazał się bardziej wydajny dla OCP funkcjonalizowanych kantaksanytną niż echinenonem.
3. Przebadano również wariant OCP posiadający mutację uniemożliwiającą mu tworzenie dimerów, wykonując pomiary w funkcji temperatury i stężenia. Dane uzyskane dzięki spektroskopii absorpcyjnej w zakresie widzialnym zostały zinterpretowane wspólnie z wynikami szerokokątnej dyfrakcji rentgenowskiej w ramach współpracy międzynarodowej. Dzięki temu uzyskano opis procesu fotokonwersji z uwzględnieniem dimeryzacji. Zauważono, że wzbudzenie nanosekundowym impulsem nie skutkuje pojawieniem się długożyjącego sygnału związanego z populacją OCP^R. Na podstawie zbiorczej analizy danych w obu ośrodkach naukowych zaproponowano, że wzbudzenie dimeru OCP^O pojedynczym impulsem światła powoduje powstanie heterodimera P_3/OCP^O, który relaksuje do homodimera OCP^O/OCP^O.
4. Zaproponowano hipotezę, wedle której aby utworzyć formę OCP^R, konieczna jest absorpcja kolejnych dwóch fotonów. Dane zebrane dla OCP z sinic *Synechocystis* zawierające echinenon, posiadające znacznik polihistydynowy na C-końcu wskazują na istnienie takiego mechanizmu. W przypadku OCP ze znacznikiem na N-końcu, bardziej prawdopodobne jest że istnieje zarówno dwufotonowa jak i jednofotonowa ścieżka tworzenia się formy OCP^R. Proces dwufotonowy jest interesujący z biologicznego punktu widzenia, ponieważ oznacza że aktywność OCP może przyrastać w sposób nieliniowy z intensywnością światła. Jeśli ta hipoteza jest prawdziwa, oznacza to że OCP pozwala zaadaptować się sinicom do warunków oświetleniowych znacznie lepiej niż dotychczas sądzono.

Wyniki badań zostały opublikowane w 4 artykułach. Finansowanie uzyskane z grantu NCN Preludium umożliwiło nam wykonanie kompleksowych pomiarów spektroskopii optycznej, która jest specjalnością naszego laboratorium. Ponadto badania były wykonane w ramach międzynarodowego projektu (DynOCP), w kolaboracji między zespołami prof. dra hab. Gotarda Burdzińskiego (Zakład Elektroniki Kwantowej, Wydział Fizyki, Uniwersytet Adama Mickiewicza w Poznaniu), CNRS Research Directora Michela Sliwy (LAboratoire de Spectroscopie pour les Interactions, la Réactivité et l'Environnement, Univ. Lille, CNRS, Lille, Francja), Emeritus CNRS Director Diany Kirilovsky (Institute for Integrative Biology of the Cell, CEA, Univ. Paris Saclay, CNRS, Gif-sur-Yvette, Francja), CNRS Research Directora Jacquesa-Philippe Colletiera (Institut de Biologie Structurale, Univ. Grenoble Alpes, CEA, CNRS, Grenoble, Francja), prof. Ilme Schlichting (Department of Biosciences, Physics and Astronomy, Univ. Heidelberg, Max Planck-Institut für medizinische Forschung, Heidelberg, Niemcy).

List of Articles Constituting the Thesis

- Nizinski, S.; Wilson, A.; Uriarte, L. M.; Ruckebusch, C.; Andreeva, E. A.; Schlichting, I.; Colletier, J. P.; Kirilovsky, D.; Burdzinski, G.; Sliwa, M. A unifying perspective of the ultrafast photo-dynamics of Orange Carotenoid Proteins from Synechocystis: Peril of high-power excitation, existence of different S* states and influence of tagging. *JACS Au* **2022,** 2 (5), 1084–1095.
- Wilson, A.; Andreeva, E. A.; Nizinski, S. J.; Talbot, L.; Hartmann, E.; Schlichting, I.; Burdzinski, G.; Sliwa, M.; Kirilovsky, D.; Colletier, J. P. Structure-function-dynamics relationships in the peculiar Planktothrix PCC7805 OCP1: Impact of his-tagging and carotenoid type. *Biochim. Biophys. Acta Bioenerg.* **2022**, 1863 (7), 148584.
- Andreeva, E. A.; Nizinski, S.; Wilson, A.; Levantino, M.; De Zitter, E.; Munro, R.; Muzzopappa, F.; Thureau, A.; Zala, N.; Burdzinski, G.; Sliwa, M.; Kirilovsky, D.; Schirò, G.; Colletier, J. P. Oligomerization processes limit photoactivation and recovery of the Orange Carotenoid Protein. *Biophys J.* **2022**, 121 (15), 2849-2872.
- Niziński, S.; Schlichting, I.; Colletier, J. P.; Kirilovsky, D.; Burdziński, G.; Sliwa, M. Is Orange Carotenoid Protein photoactivation a single-photon process? *Biophys. Rep.* **2022**, 2 (3), 100072.

Grants

- Polish National Science Centre (NCN) PRELUDIUM grant "Investigating mechanism of orange carotenoid protein (OCP) photoactivation using time-resolved optical spectroscopy methods", project number 2018/31/N/ST4/03983.

List of Other Articles Submitted Before PhD Thesis

- Wendel, M.; Nizinski, S.; Tuwalska, D.; Starzak, K.; Szot, D.; Prukala, D.; Sikorski, M.; Wybraniec, S.; Burdzinski, G. Time-resolved spectroscopy of the singlet excited state of betanin in aqueous and alcoholic solutions. *Phys. Chem. Chem. Phys.* **2015**, 17 (27), 18152-18158.
- Wendel, M.; Nizinski, S.; Gierszewski, M.; Prukala, D.; Sikorski, M.; Starzak, K.; Wybraniec, S.; Burdzinski, G. Chemical quenching of singlet oxygen by betanin. *Photochem. Photobiol. Sci.* **2016**, 15 (7), 872-878.
- Wendel, M.; Nizinski, S.; Prukala, D.; Sikorski, M.; Wybraniec, S.; Burdzinski, G.; Ultrafast internal conversion in neobetanin in comparison to betacyanins. *J. Photochem. Photobiol. A: Chem.* **2017**, 332, 602-610.
- Nizinski, S.; Wendel, M.; Rode, M. F.; Prukala, D.; Sikorski, M.; Wybraniec, S.; Burdzinski, G. Photophysical properties of betaxanthins: miraxanthin V – insight into the excited-state deactivation mechanism from experiment and computations. *RSC Adv.* **2017**, 7 (11), 6411-6421.

List of Other Articles Submitted During PhD Thesis

- März, M.; Kohout, M.; Neveselý, T.; Chudoba, J.; Prukała, D.; Niziński, S.; Sikorski, M.; Burdziński, G.; Cibulka, R. Azodicarboxylate-free esterification with triphenylphosphine mediated by flavin and visible light: method development and stereoselectivity control. *Org. Biomol. Chem.* **2018**, 16 (36) 6809-6817.
- Brazevic, S.; Nizinski, S.; Szabla, R.; Rode, M. F.; Burdziński, G. Photochromic reaction in 3H-naphthopyrans studied by vibrational spectroscopy and quantum chemical calculations. *Phys. Chem. Chem. Phys.* **2019**, 21 (22), 11861-11870.
- Nizinski, S.; Popenda, L.; Rode, M.; Kumorkiewicz, A.; Fojud, Z.; Paluch-Lubawa, E.; Wybraniec, S.; Burdzinski, G. Structural studies on stereoisomerism of a natural dye miraxanthin I. *New J. Chem.* **2019**, 43 (46), 18165-18174.
- Tran, T.; Rabah, J.; Ha-Thi, M.; Allard, E.; Nizinski, S.; Burdzinski, G.; Aloise, S.; Fensterbank, H.; Baczko, K.; Nasrallah, H.; Vallée, A.; Clavier, G.; Miomandre, F.; Pino, T.; Meallet-Renault, R. Photoinduced electron transfer and energy transfer processes in a flexible BODIPY-C_{60} dyad. *J. Phys. Chem. B* **2020**, 124 (42), 9396-9410.
- Brazevic, S.; Nizinski, S.; Sliwa, M.; Abe, J.; Rode, M.; Burdzinski, G. Control of the photo-isomerization mechanism in 3H-naphthopyrans to prevent formation of unwanted long-lived photoproduct. *Int. J. Mol. Sci.* **2020**, 21 (21), 7825.
- Uriarte, L. M.; Vitale, R.; Niziński, S.; Hadjidemetriou, K.; Zala, N.; Lukacs, A.; Greetham, G. M.; Sazanovich, I. V.; Weik, M.; Ruckebusch, C.; Meech, S. R.; Sliwa, M. Structural information about the *trans*-to-*cis* isomerization mechanism of the photoswitchable fluorescent protein rsEGFP2 revealed by multiscale infrared transient absorption. *J. Phys. Chem. Lett.* **2022**, 13 (5), 1194–1202.

Abbreviations

- ADP - adenosine diphosphate
- A_g, A_u, B_u, B_g – irreducible representations of the symmetry group C_{2h}
- APC – allophycocyanin
- apo-OCP – OCP deprived of the carotenoid chromophore
- apo-RCP - RCP deprived of the carotenoid chromophore
- Arg – arginine
- ATP - adenosine triphosphate
- BS – beamsplitter
- CAN – canthaxanthin
- COCP – C-terminal OCP-related Carotenoid Protein
- CrtO – monoketolase enzyme causing synthesis of echinenone from β-carotene
- CrtW – diketolase enzyme causing synthesis of canthaxanthin from β-carotene
- CT – charge transfer
- CTD – C-terminal domain
- CTT – C-terminal tail
- Cyt b_6f – cytochrome b_6f
- DAS – decay associated spectra
- DMSO - dimethyl sulfoxide
- EAS – evolution associated spectra
- ECN – echinenone
- ESA – excited state absorption
- FWHM – full width at half maximum
- FRET - Förster resonance energy transfer
- FRP – fluorescence recovery protein
- FT-IR – Fourier-transform infrared spectroscopy
- Glu – glutamic acid
- GSB – ground state bleach
- GVD - group velocity dispersion
- H^+ - proton
- HCP – helical carotenoid protein
- hECN – hydroxyechinenone
- His – histidine
- hν – equivalent of the one photon energy
- HOMO – highest occupied molecular orbital
- ICT/S_1 – mixed ICT and S_1 state with a predominance of ICT character
- ICT – intramolecular charge transfer
- IPTG - isopropyl β-D-1-thiogalactopyranoside
- IRF – instrument response function
- K-matrix – a matrix built properly from rate constants
- LED – light emitting diode

- Leu – leucine
- LHC – light-harvesting complex
- LH1 – light-harvesting complex 1
- LH2 – light-harvesting complex 2
- LUMO – lowest unoccupied molecular orbital
- ^{3}MLCT - metal to ligand charge transfer triplet state
- MCR-ALS - multivariate curve resolution - alternating least squares
- NADPH - reduced nicotinamide adenine dinucleotide phosphate
- $NADP^+$ - nicotinamide adenine dinucleotide phosphate
- Nd:YAG - neodymium-doped yttrium aluminum garnet
- Nd:YLF - neodymium-doped yttrium lithium fluoride
- NIR – near infrared light
- NPQ – nonphotochemical quenching
- NTD – N-terminal domain
- NTE – N-terminal extension
- NTF2 - nuclear transport factor 2
- $^1O_2$ – singlet oxygen
- OCP – orange carotenoid protein
- OCP1 – orange carotenoid protein 1 *viz.* orange carotenoid protein
- OCP2 – orange carotenoid protein 2
- OCP^O - orange carotenoid protein in dark-adapted (orange) form
- OCP^R - orange carotenoid protein in photoactive (red) form
- OPA – optical parametric amplification
- OPO – optical parametric oscillator
- pAC-Beta – plasmid used to produce the β-carotene
- pBAD-crtO – plasmid used to produce the CrtO enzyme
- PBS – phycobilisome
- PC – phycocyanin hexamer
- pCDF-OCP – plasmid used to produce the OCP
- PD – photodiode
- PE – phycoerythrin
- PEC – phycoerythrocyanin
- P_i – phosphate
- PMT – photomultiplier
- PPFD - photosynthetic photon flux density
- PSI – photosystem I
- PSII – photosystem II
- PQ – plastoquinone
- PQH_2 – plastoquinol
- QM/MM – hybrid quantum mechanics and molecular mechanics approach
- RCP – red carotenoid protein

- ROS – reactive oxygen species
- S_0 – electronic singlet ground state
- S_1, S_2, S_3 … - electronic singlet excited states (numbered by increasing energy)
- S_1/ICT – mixed S_1 and ICT state with a predominance of S_1 character
- SAS – species associated spectra
- SE – stimulated emission
- SFX - serial femtosecond crystallography
- S/N – signal to noise ratio
- SRA – stimulated Raman amplification
- SVD – singular value decomposition
- T_1, T_2, T_3 … - electronic triplet excited states (numbered by increasing energy)
- TPA – two-photon absorption
- Trp – tryptophan
- Tyr – tyrosine
- UV – ultraviolet light
- VAZ – violaxanthin to zeaxanthin
- VERA – vibrational energy relaxation approach
- vis – visible light
- WLG – white light generation
- XPM – cross-phase modulation
- YAG - yttrium aluminum garnet
- ZEA – zeaxanthin

Table of Contents

1. Introduction

Light – essential energy source and a potential threat

No life can exist without the light, however, sometimes it can turn into a destructive force. Strong irradiation conditions, especially ultraviolet light can possess a serious threat to living organisms. Therefore, photosynthetic organisms evolved a vast set of mechanisms, which allow them to survive even in the most harsh light conditions, that can be encountered on Earth. The following thesis describes the photoconversion dynamics of the Orange Carotenoid Protein (OCP), which performs an important role in the photoprotection of cyanobacteria. In this chapter, the photoprotective mechanism performed by the OCP in cyanobacteria is presented in order to emphasize the place of OCP in the photosynthetic machinery.

Light harvesting in cyanobacteria

Photosynthesis makes it possible to transform the sunlight into chemical energy in plants, algae and cyanobacteria.[2] During this process, carbon dioxide and water are transformed into oxygen and carbohydrates. In the first step, the light is captured by the antenna complexes, where the pigment molecules are promoted to the excited state. This way, the energy of the photon is converted into an electronic excitation. Obtained electronic excitations can be passed to other pigments, in the process known as Förster resonant energy transfer. This way electronic energy is funneled to the reaction centers located in two types of photosystems in the thylakoid membrane of the chloroplast (Figure 1). Here, NADPH and ATP molecules are prepared, which power the Calvin-Benson-Bassham cycle, where the carbohydrate molecules are produced.[2]

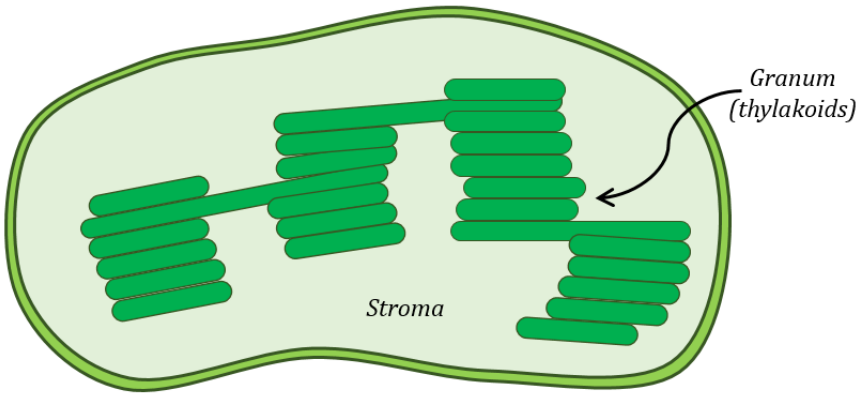

Figure 1. Schematic representation of the chloroplast. Stroma, which is an internal space of the chloroplast, contains stacked thylakoids, called grana.

Cyanobacteria are responsible for a significant part of global photosynthesis. Moreover, they are probably at the origin of primary oxygen in the Earth's atmosphere which emerged in so-called "Great oxidation event" about 2.3 billion years ago.[3]

Similarly to other photosynthetic organisms, cyanobacteria possess two photosystems (PSII and PSI) utilized to convert electronic excitation energy into chemical energy.[4-6] Both photosystems, together with cytochrome b_6f complex (Cyt b_6f) and ATP synthase reside in the thylakoid membrane (Figure 2).

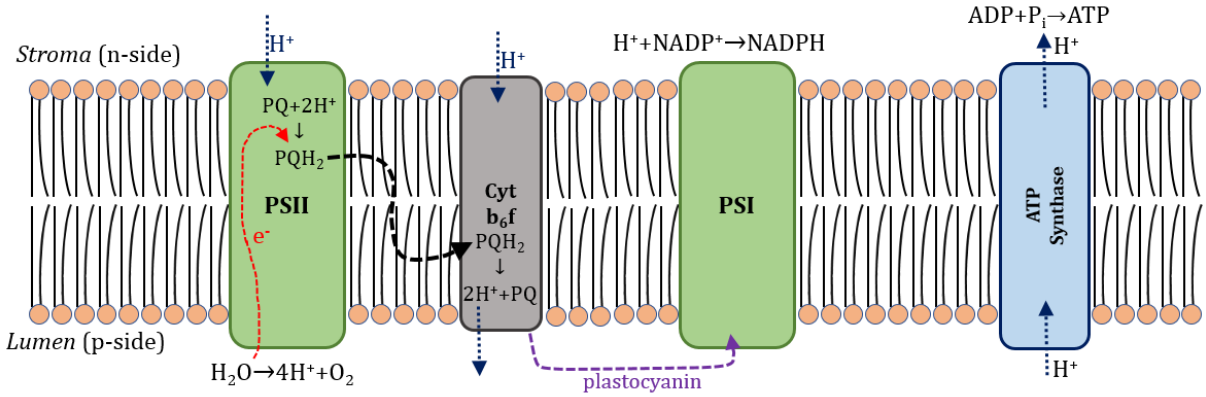

Figure 2. Schematic representation of the thylakoid membrane.[5-6] PSII generates protons on the p-side of the membrane, while electrons are transported from PSII across Cyt b_6f to the PSI. As a result, proton gradient across the membrane is built and NADPH molecules are generated at PSI.[5-6]

Both photosystems are capable of harvesting light energy themselves, as well as accepting electronic excitations from external antenna complexes. The thylakoid membrane separates *Lumen*, the internal space of the thylakoid, from *Stroma*, the outside space. In each photosystem, the electronic excitation energy flows to the reaction center, where charge separation takes place. In the PSII, water molecules on the lumenal side of the membrane are oxidized and split into the O_2 and H^+, whereas a plastoquinone (PQ) molecule is reduced to a plastoquinol (PQH_2) in the membrane. PQ molecules are supplied from within the membrane. In the Cyt b_6f, PQH_2 is oxidized back to the PQ and the electron is transported by plastocyanin on the lumenal side of the membrane towards the PSI. In PSI the $NADP^+$ is reduced to the NADPH. Reactions taking place in the PSI and PSII are energetically uphill and require electronic excitations to power them up. As a result, the protons are accumulated on the lumenal side of the membrane and electrons are transported over the membrane from the PSII to the PSI. Potential difference across the thylakoid membrane is induced, positive on the lumenal side (p-side) and negative on the stromal (n-side). This potential, as well as the proton motive force (surplus of H^+ on the luminal/p-side generated by PSII), is used by the ATP synthase to form ATP (adenosine triphosphate) molecules. The product of the PSI activity (NADPH) as well as ATPs are used in Calvin-Benson-Bassham cycle, where carbon dioxide is reduced to carbohydrate.[4-6]

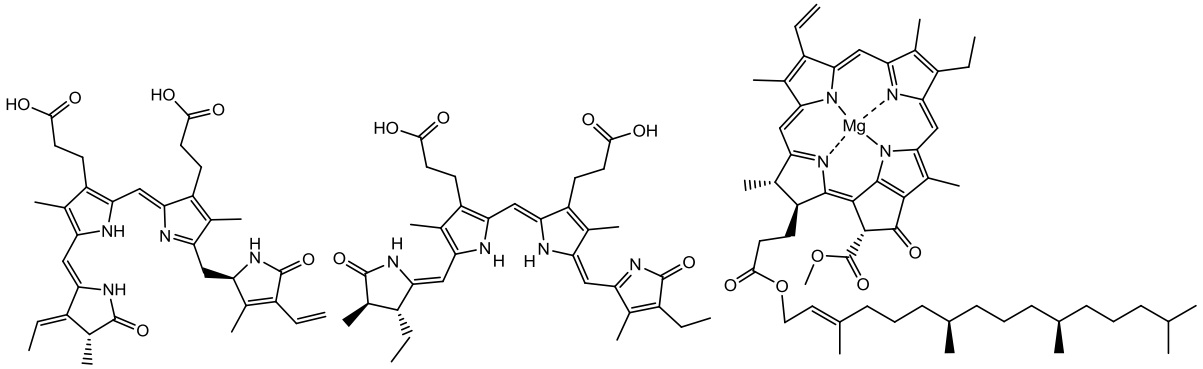

Figure 3. Exemplary phycobilins, which can be found in cyanobacterial phycobilisomes, compared to chlorophyll *a*.

Photosystems, especially PSII, contain a limited number of chlorophyll *a* molecules (structure in Figure 3), which can't harvest enough of the electronic excitations required to fully power up the reaction centers.[4-9] Instead, dedicated light-harvesting complexes are used to collect the majority of light energy and pass it to the reaction centers, increasing their absorption cross-section even by 1000 fold. Cyanobacteria possess a specific external light-harvesting complex, the phycobilisome (PBS), which is extrinsic to the thylakoid membrane (resides in Stroma, see Figure 4).

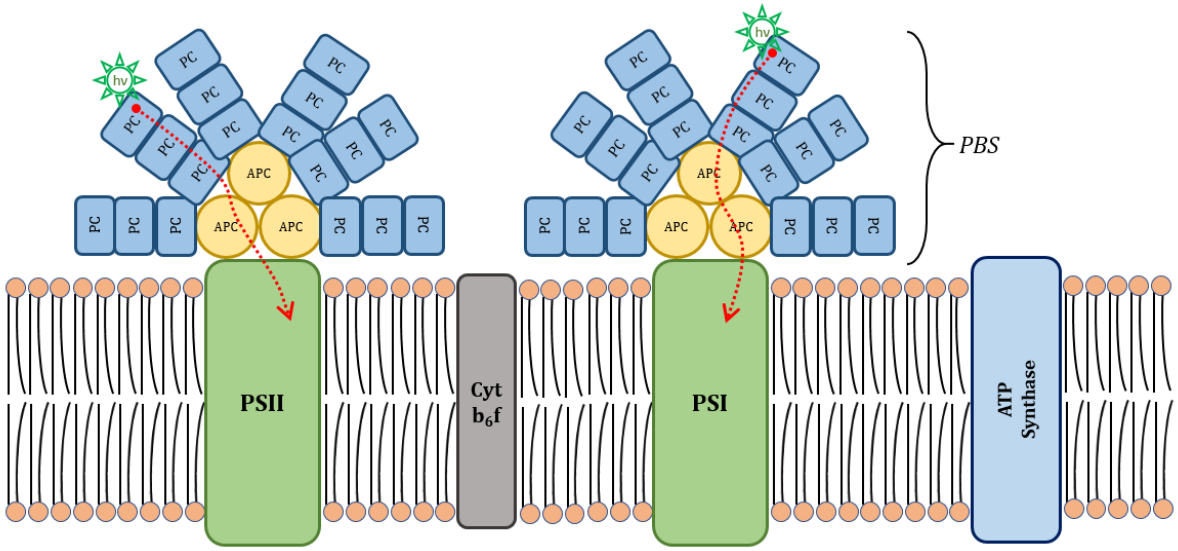

Figure 4. Phycobilisome (PBS) antenna complexes attached to the photosystems I and II in the thylakoid membrane. PBS can attach to photosystems to supply them with energy. Pictured PBS consist of rods constructed from three phycocyanin hexamers (PC) each and a core constructed from three cylinders of allophycocyanin (APC).

PBS allows cyanobacteria to capture a wide range of sunlight wavelengths (490 nm - 650 nm), especially the green part of the sunlight spectrum, which is not absorbed by chlorophyll molecules. PBS supplies the electronic excitations to the chlorophylls located in photosystems via energy transfer. It can move along the thylakoid membrane and attach to any photosystem. The PBS can be built from phycoerythrins (PE), phycocyanins (PC), phycoerythrocyanins (PEC) and allophycocyanins (APC). They contain phycobilins as chromophores (Figure 3). The core of PBS is constructed mostly from the APCs. The PBS core is surrounded by rods, constructed from PC, and optionally also from PEC and PE. Electronic excitations harvested by the PBS attached to the photosystem travel from the rods, through the core to the chlorophylls *a* in the photosystem, and finally to the reaction center. Usually, the S_1 energy levels of the chromophores which transfer the electronic excitation to the reaction center are subsequently decreasing along the energy transfer pathway. It is manifested in a fluorescence redshift. The electronic excitation travels energetically downhill.[4-9]

Photoprotective mechanisms are required in cyanobacteria

Compared to the short excited state lifetime in carotenoids, chlorophyll molecules have a relatively long living S_1 excited state (nanosecond order of magnitude[10]), which allows them to perform charge separation.[4, 11-12] However, chlorophyll molecules also have a not negligible

probability of intersystem crossing to a triplet state. Triplet states can be also formed during charge recombination reactions. Chlorophyll in the triplet state can interact with molecular oxygen, forming reactive oxygen species (ROS), especially singlet oxygen ($^1O_2$), but also hydrogen peroxide (H_2O_2), superoxide ($O_2^{\bullet -}$), or hydroxyl radical ($OH^{\bullet}$). If not promptly scavenged, these generated species can subsequently react with other elements of the photosynthetic machinery, causing their degradation and consequently, photoinhibition. The PSII reaction centers are exposed to these effects the most because they produce an abundance of singlet oxygen. Photosynthetic machinery is at least partially protected by carotenes, which can effectively quench chlorophyll triplet states.[4, 11-12]

Photosynthetic organisms developed a variety of photoprotective mechanisms to cope with excessive electronic excitations.[4-6, 8-9] A photoprotective reaction may be triggered by excessive sunlight, but also by stress conditions different than an increase in illumination intensity. A similar reaction may be triggered in response to different kinds of stressors, that reduce the plant's capability to perform photosynthesis (even if irradiation intensity is unchanged), therefore less of electronic excitations can be utilized. These conditions may be intermittent freezing, drought, nutrient starvation, low CO_2 conditions, etc.[4-5, 8-9] Controlling so many variables requires existence of an extensive number of mechanisms to fine-tune performance of the process, maximize the efficiency and minimize the damage. Some of these mechanisms work in the long term (synthesis of the photoprotective pigments, regulation of the proper genes expression, alteration of the total number of antenna complexes), or in the short term (decoupling of the external antenna from the photosystems, state transitions, thermal energy dissipation via non-photochemical processes).[4-6, 8-9]

In case of the rapid emergence of excessive light conditions, photosynthetic organisms can employ so-called non-photochemical quenching (NPQ).[6, 8-9, 13-14] This mechanism can be switched on to dissipate excessive energy into the surrounding. This regulated process is manifested by the decrease in PBS fluorescence. Machinery of this process is not the same in all photosynthetic organisms. Without NPQ, the high irradiation conditions would lead to the production of reactive oxygen species (ROS), like singlet oxygen, which may damage the photosynthetic apparatus. Because in cyanobacteria, a large part of the light-harvesting is done by the PBS, there is also a special mechanism suited to modulate the PBS function. It is performed by the Orange Carotenoid Protein (OCP), which is a photoactive protein, that can react dynamically to the changing light conditions.[15-16] When the light intensity is very high, OCP is reversibly photoconverted to the OCP^R form, which can attach itself to the PBS and quench the electronic excitations, disabling their flow towards the reaction centers (Figure 5).[15, 17]

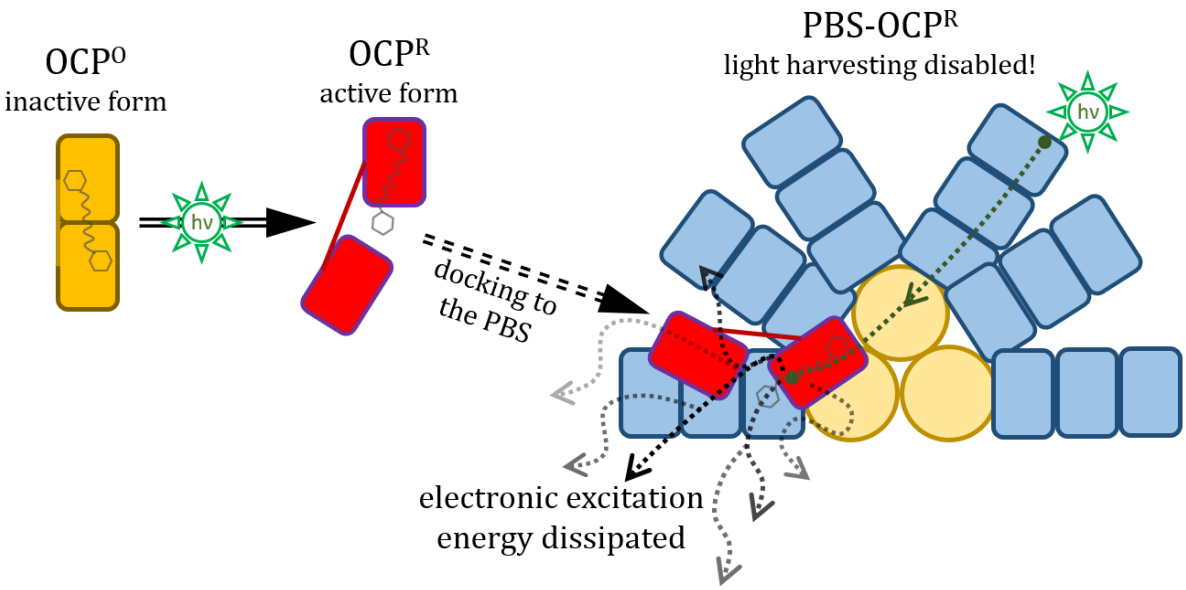

Figure 5. Simplified scheme of the OCP photoactivation in the presence of PBS. OCP^R can attach to the core of the PBS, quench harvested electronic excitations and dissipate their energy into the environment as heat.

This mechanism allows cyanobacteria to tune the activity of their most important antenna complex, the PBS.[15-16, 18] OCP owes her name to the orange color, possessed in the dark-adapted form. This form, usually abbreviated as OCP^O, undergoes photoconversion into red-colored OCP^R form upon blue/green irradiation. The OCP^R form is metastable, and undergoes back-conversion in the darkness *in vitro*, while *in vivo* its back-conversion is supported by Fluorescence Recovery Protein (FRP).[18] The mechanisms underlying these processes have been intensively debated recently[19-33] (including the last moments before submitting this thesis[34-37]), however, no definitive answers have been reached yet.

Motivation, goals and outline of the thesis

The OCP-induced NPQ mechanism is crucial for cyanobacteria to dynamically manage variations in the illumination conditions. Therefore, understanding the OCP photoconversion process is of great interest from the fundamental knowledge point of view. Moreover, OCP can potentially be utilized as the light uptake regulator in artificial photosynthetic systems. It was also proposed that the OCP can serve as an optogenetic tool.[38] The OCP already has interesting features: it acts as a photoswitch triggered by blue/green light, where the effector domain dissociates from the sensor domain upon absorption of a photon (Figure 5).[39-42] However, low photoconversion quantum yield (below 0.2% [15, 43-45]) limits eventual usage of the OCP in optogenetic applications. In order to engineer the OCP for any specific application, the details of its functionality/mechanics must be revealed. Understanding the bottlenecks limiting the photoconversion efficiency is the most important issue, which is deeply explored in this work. Unfortunately, very little is known about the machinery of the OCP photocycle. Especially, how the photon energy absorbed by the carotenoid triggers the photoconversion of the OCP has been actively debated in recent years.[21, 23-24, 28] Indeed photoconversion dynamics involves at least 4 excited states (decaying at the picosecond timescale) and sequentially populated 6 intermediate

forms (spanning from nanosecond to second timescale). After absorption of a photon, the carotenoid located within the OCP is promoted to the second excited state S_2. The relaxation through Intramolecular Charge Transfer (ICT) state, S_1 and S* states takes place within tens of picoseconds and leads to the P_1 form, where the carotenoid is back in the electronic ground state, but its interaction with the protein scaffold is altered. Afterward, a complex sequence of the protein and carotenoid rearrangements occurs, the carotenoid is translocated to the N-terminal domain and finally, both OCP domains dissociate. This sequence consists of several intermediates (P_1, P_2, P_2', P_N, P_M, P_X), which quantum yield is different depending on the selected variant of the OCP.

Due to the very high molar absorption coefficient of the carotenoid, the transient-absorption vis-NIR spectroscopy technique is perfectly suited to trace very small populations involved in the low-quantum yield OCP photoconversion process. By observation of the absorbance change induced by the excitation pulse (ΔA), one can track the OCP's photodynamics, estimate the contribution of individual intermediate states and determine their quantum yields. Based on the structural knowledge about the OCP, one can attempt to identify the physical processes which are hiding behind the time constants determined using time-resolved techniques. Therefore, time-resolved optical spectroscopy combined with structural crystallography has the potential to build a complete picture of the processes taking place during the conversion of the OCP^O into the OCP^R. Nevertheless, this thesis covers only optical spectroscopy measurements.

The following chapter describes technical aspects of the experiments performed within this thesis and details of the data analysis, which allowed to obtain novel results and interpret them. In chapter 3, basic properties of the carotenoids in the solution phase are introduced based on the available literature, including the symmetry and environment effect on the carotenoid photophysics and the nature of observed electronic states. In chapter 4, a history of the OCP research is briefly presented, the structure of the OCP and carotenoid enclosed within OCP is described. Chapter 5 summarizes current literature knowledge about the OCP photoconversion in order to present the background for articles included in this thesis. In chapter 6, results obtained for each publication are summarized in a short abstract with emphasis on the results obtained by the author of this thesis.

2. *Methodology*

Most of the measurements within this work were done using time-resolved optical spectroscopy methods. Femtosecond transient absorption spectroscopy allowed to characterize the relaxation of the carotenoid excited states, as well as the formation of initial intermediate states of the protein formed within 1 ns. Nanosecond transient absorption (or "nanosecond flash photolysis", which is a legacy designation) is a similar technique, which extends the experiment's temporal window up to single seconds, allowing to track both dynamics of rapid protein movements finished within microseconds up to a large scale rearrangements exceeding tens of milliseconds. Stationary UV-vis absorption can track the accumulation of the active form - OCP^R. All these techniques have one thing in common, they probe directly the carotenoid embedded within the protein. The information about the protein dynamics stems exclusively from the fact that the carotenoid spectroscopic properties are actively modulated by the protein (and *vice versa*). The carotenoid-protein interactions and the constraints imposed on the carotenoid are reflected in its photophysics. Therefore, one can think of the carotenoid as a probe, being in the center of all the phenomena occurring within the OCP. It has to be emphasized that not all protein rearrangements must be reflected in the carotenoid state, therefore the information provided by techniques introduced below is by no means complete. Other methods, like X-ray crystallography or time-resolved vibrational spectroscopy are required to obtain a holistic view of the OCP photoconversion processes. However, due to a very rich knowledge about carotenoid photophysics in various environments, accumulated over a long period of research (reviewed in the next chapter), one can extrapolate it to the OCP case. Due to the very high molar absorption coefficient of the carotenoids, one can obtain very accurate information by focusing at the carotenoid itself.

The techniques used to obtain the results presented within this thesis are summarized in the following chapter. Firstly (section 2.1), experimental details and data analysis of femtosecond transient absorption spectroscopy are described. This technique covers the time regime from hundreds of femtoseconds up to a few nanoseconds, allowing to observe decay of the carotenoid excited states and formation of the first photoproduct – P_1, where the carotenoid is in its electronic ground state, but the interactions with the protein structure are altered. Subsequently, the global analysis is introduced. It allows to interpret time-resolved data in terms of some specific scheme, which consists of the ensemble of intermediate states connected by relaxation pathways. This approach can be used to model pulse-induced evolution in any timescale. In section 2.2, nanosecond transient absorption is described. It covers the time regime from tens of nanoseconds to single seconds, where the protein rearrangements occur. Later, after data analysis of the nanosecond transient absorption data, an application of comparative actinometry to determine quantum yields of the intermediate products is explained. In section 2.3, the stationary absorption measurements done upon continuous irradiation are described. Since this experiment has a potential to reflect the natural irradiation conditions in which OCP functions, these conditions are also defined. Numerical simulations applied to model the behavior of the OCP upon continuous

irradiation are also described. At the end (section 2.4), the production of OCP samples is briefly outlined.

2.1 *Femtosecond transient absorption spectroscopy*

*Experi*mental details

Femtosecond transient absorption spectroscopy covers the temporal window from hundreds of femtoseconds up to single nanoseconds, where the relaxation of the excited states takes place. It is a pump-probe technique, meaning that firstly a strong pump pulse (duration of about 100 fs) excites the sample, and then at some specific delay after the pump, a weak broadband probe pulse (duration of about 100 fs) arrives and probes the sample. Transient information about the sample absorbance is imprinted on the probe spectrum. This experimental sequence must be repeated for numerous pump-probe delays in order to obtain complete information on photo-triggered sample evolution. The experimental setup (Helios, *Ultrafast Systems*) exploited in this work is drawn in Figure 6 and pictured in Figure 7.

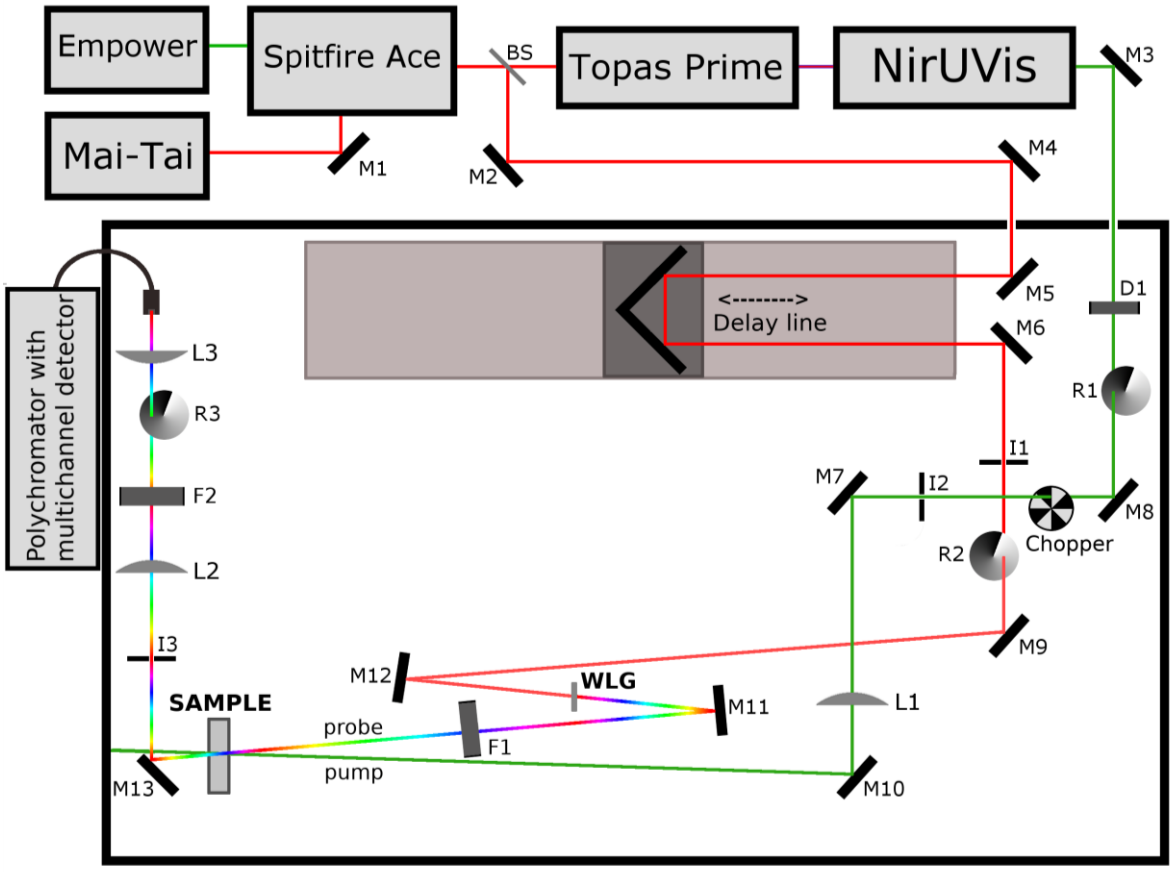

Figure 6. Scheme of the transient absorption UV-vis-NIR spectroscopy setup. Abbreviations of the optical elements are explained in the text.

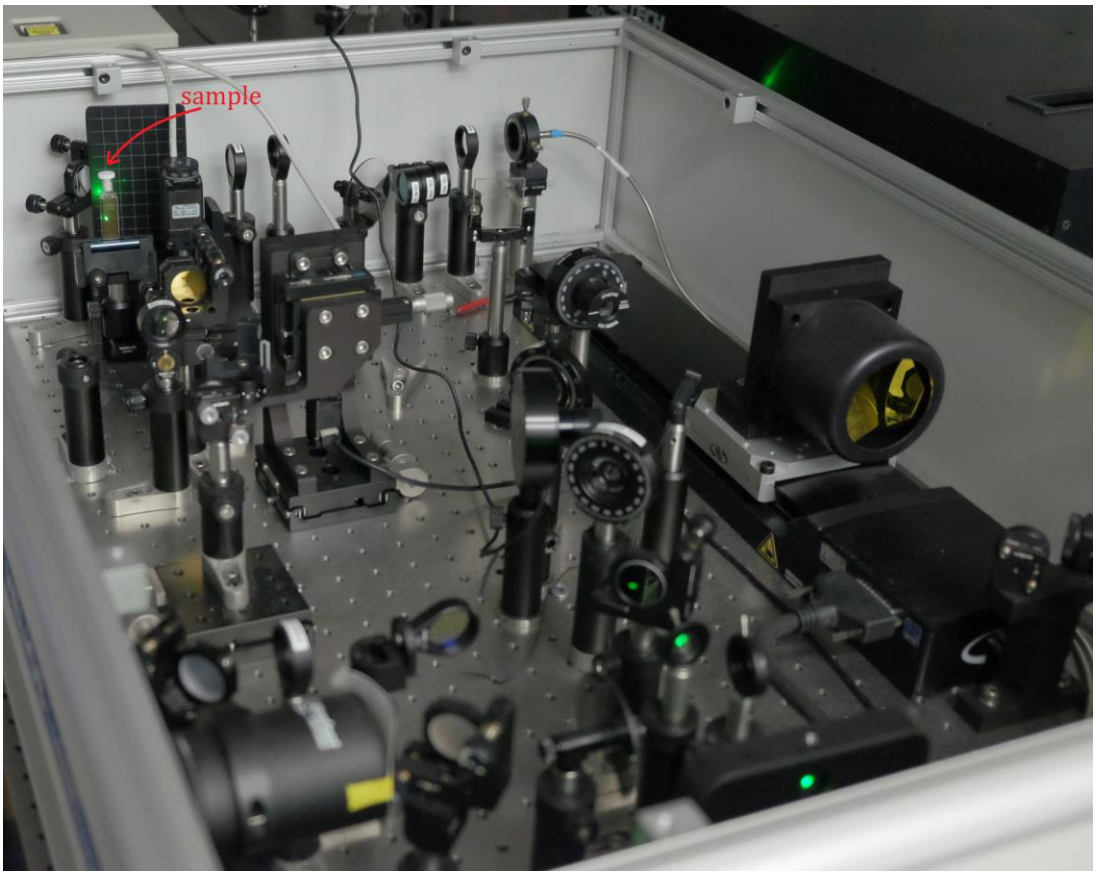

Figure 7. Picture of the transient absorption UV-vis-NIR spectroscopy setup.

In order to perform the experiment, one must prepare proper pump and probe beams. The journey of the laser pulse starts in the Mai-Tai (*Spectra Physics*). It is Ti:Sapphire oscillator, which is capable of producing 800 nm pulses, with a temporal width of about 70 fs (FWHM) and 84 MHz repetition frequency. These pulses are much too weak (nJ order of magnitude), and their repetition is too high to be used in the transient absorption experiment. Spitfire Ace (*Spectra Physics*) regenerative amplifier is used to amplify them and reduce their repetition frequency down to 1 kHz. Spitfire Ace is pumped by the Empower Nd:YLF laser (*Spectra Physics*), which delivers 5W of 527 nm beam of approximately 100 ns long pulses at 1 kHz repetition. Seed pulses from the Mai-Tai oscillator enter the Spitfire Ace regenerative amplifier, which selects one pulse every 1 ms. Firstly, the pulse is stretched by delaying its spectral components in a regular way, so the delay is a function of wavelength. The power density of the stretched pulse is greatly reduced, so this pulse can be amplified. It is done by passing it multiple times through a Ti:Sapphire cavity, while the long pumping pulse from Empower ensures that the crystal is in the population inversion state. Stretched seed pulse is gradually amplified each time it passes through the crystal, due to the stimulated emission process. After a specific number of round trips, the amplified pulse is ejected from the Ti:Sapphire cavity and compressed back in the temporal domain. Hereafter, the pulse regains its temporal width (≈ 100 fs, FWHM), however now it possesses much higher energy (millijoules of energy per pulse) compared to the seed pulse, and the repetition rate is decreased to 1 kHz. Pulse amplification is necessary to enable various nonlinear processes, necessary to generate pump and probe pulses, as well as to excite a significant amount of the

sample (usually a few percent in solution) and induce a transient absorption signal. Only pulses with a sufficient power density can accomplish these tasks.

In order to generate pump pulses, the amplified beam from Spitfire Ace is directed into the Topas Prime (*Light Conversion*) and NirUVis (*Light Conversion*) units (see Figure 6), which together can produce any wavelength tuned in the 240 nm to 800 nm range, with temporal width close to 150 fs (FWHM). Topas Prime is a colinear optical parametric amplifier, while NirUVis is a frequency mixer, both are computer-controlled units. Subsequently, the pump beam passes through the depolarizer D1, variable neutral density filter R1 and synchronized chopper which removes every second pulse, decreasing repetition frequency from 1 kHz down to 500 Hz. The I2 iris is used to block any peripheral parts of the beam, which do not pass through the chopper properly. The pump pulses are focused in the sample by the L1 lens (f = 500 mm).

The fundamental beam obtained from Spitfire Ace is also split by beamsplitter BS (see Figure 6) so that a small fraction is reflected towards the delay line (*Newport*). A retroreflector mounted on a long translational stage reflects the beam parallelly to the incident beam (in fact the beam is passed through the delay stage twice, to extend available time window, it is not depicted in the scheme for the sake of simplicity). The motorized delay line controls the Δt delay between pump and probe pulses. After the delay line, the beam is trimmed by I1 iris, the power is adjusted by the R2 variable neutral density filter, and concave mirror M12 is used to focus the beam in the medium for white light generation (WLG). Type of the material used to perform WLG is selected based on probing wavelength requirements (see Figure 8). A white light probe generated this way is reflected by the concave mirror M11, which refocuses the beam in the sample. The F1 filter is used accordingly (for example BG 38), to remove fundamental beam leftovers (800 nm) from the white light. After traveling through the sample, the probe is reflected by the M13 mirror towards the optical fiber leading to the polychromator equipped with the multichannel detector, which registers the spectrum of each probe pulse (at 1kHz repetition rate). The I3 iris is used to block scattered pump light, while L2 (f = 250 mm) and L3 (f = 50 mm) lenses recollimate and focus the probing beam in the optical fiber. The F2 filter and R3 variable neutral density filter are optional and used to avoid

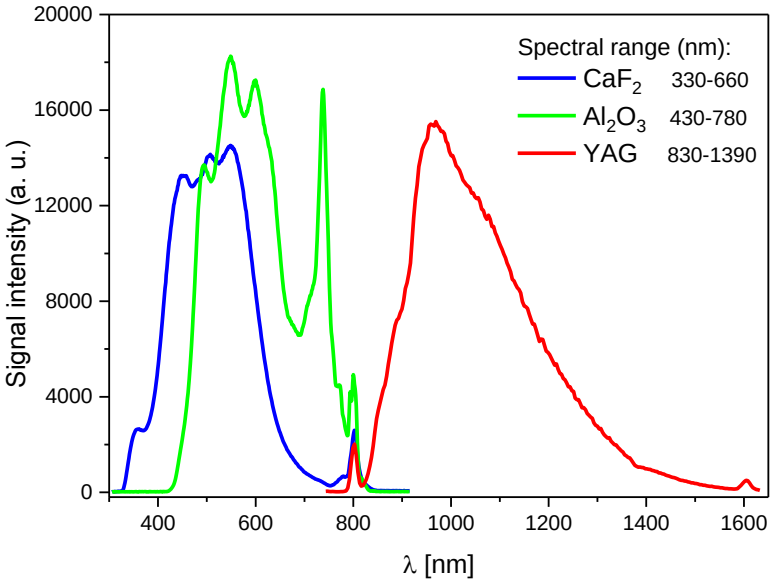

Figure 8. Exemplary spectra of the generated white light pulses.[1]

saturation of the detector. When NIR light is being measured, the F2 filter is used to cut off the visible part of the probe spectrum and residual 800 nm. When the visible part of the probe is measured, F2 is a notch filter, which reduces the scattered pump light in the detector.

The sequence of the experiment is the following. The retroreflector is moved to adjust the delay Δt (a time between the arrival of the pump pulse and probe pulse in the sample, see Figure 9). In order to calculate the transient absorption spectrum, two measurements must be done. Firstly the probe pulse travels through the sample not excited by the pump pulse (which is blocked by the chopper), and the spectrum $I_{probe}^{without\ pump}(\lambda)$ reflecting the unperturbed state of the sample is measured. Then the $I_{probe}^{with\ pump}(\lambda, \Delta t)$ spectrum is measured, in which case the probe pulse arrives at the sample after the pump (not blocked by the chopper). Both types of spectra are measured in an alternating way, so that 500 pairs are registered per second. For each delay Δt, both spectra types are integrated over 1-2 s and averaged, then the transient absorption spectrum is calculated (eq. 1). Delay line is used to scan over the selected range of delays Δt. Based on accumulated spectra, two dimensional $\Delta A(\lambda, \Delta t)$ transient absorption map is constructed. Due to the iterative nature of this experiment, the noise associated with ΔA along the spectral dimension is structured and correlated (due to the specific spectrum of the probe pulse), but along the temporal dimension it is independent and identically distributed.[46]

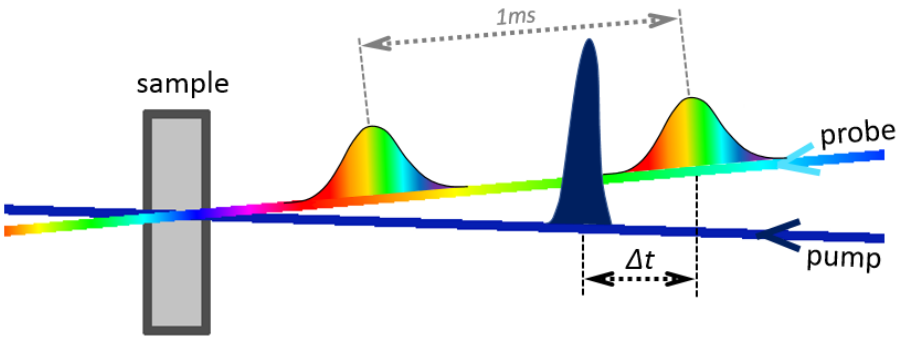

Figure 9. Experimental sequence of probe and pump laser pulses (simplified view).

$$\Delta A(\lambda, \Delta t) = -log\left(\frac{I_{probe}^{with\ pump}(\lambda, \Delta t)}{I_{probe}^{without\ pump}(\lambda)}\right) \quad (1)$$

The pump pulse energy is usually between 0.2 μJ and 1 μJ. Typically, the pump energy is tuned, so only a few percent of the sample is excited. In the case of OCP, the pump energy has to be possibly high, in order to maximize the formation of the low-yield P_1 form. On the other hand, the pump energy must be in the linear regime, where no multiphoton absorption occurs. The optimal energy for 540 nm excitation is 0.8 μJ per pump pulse, which equals $3 \cdot 10^{15}$ incident photons per cm^2 or 12 μJ per mm^2 at the center of the pulse. The optimal energy for 470 nm excitation is 0.4 μJ per pump pulse, which equals $1.4 \cdot 10^{15}$ incident photons per cm^2 or 6 μJ per mm^2 at the center of the pulse. These are the maximum values for which unwanted species formation is avoided (in the OCP case). Above these values, there is the nonlinear regime and multiphoton effects become significant. The probe pulse is much weaker (approximately 10 nJ),

to avoid pumping the sample for the second time, but strong enough to register its spectrum. Spatial cross-section of the focused pump beam is much larger compared to the probe beam, approximately 250 μm (FWHM). The probe beam must be overlapped with the central part of the pump beam. The sample located within a 2 mm thick quartz cell is continuously mixed using a thin magnetic stirrer, to reduce the effect of reexcitation and uniformly scatter the damaged molecules over the whole cuvette volume. The absorbance of the sample at the excitation wavelength is usually close to 0.7 (between 0.5 and 1).

Femtosecond transient absorption data analysis

In order to analyze the data, they need to be firstly preprocessed.[47] The measurement usually consists of a few scans, the delays are scanned in forward and backward directions. After the measurement, the obtained surfaces are averaged and the background spectrum is subtracted from all the registered spectra. The background spectrum is obtained by averaging of a few spectra registered for negative Δ*t* delays (meaning that the pump pulse arrived after the probe). Background spectrum contains scattering of the pump, the sample fluorescence, or minor contribution of the long-lived millisecond photoproducts. Usually, these signals contribute almost uniformly to all delays. After the background subtraction, the wavelengths affected by the pump scattering are removed (if the F2 notch filter is used, this region contains electronic noise only). Another effect, which must be compensated for is a group velocity dispersion (GVD). The white light of the probe pulse travels through dispersive materials like cuvette quartz or BK7 glass usually utilized in optical filters. Therefore, red components of the probe reach the sample before blue ones, this phenomenon is called normal dispersion. It results in uneven growth of registered kinetics, as time zero (Δt=0 delay between pump and probe) depends on the wavelength (see Figure 10A).

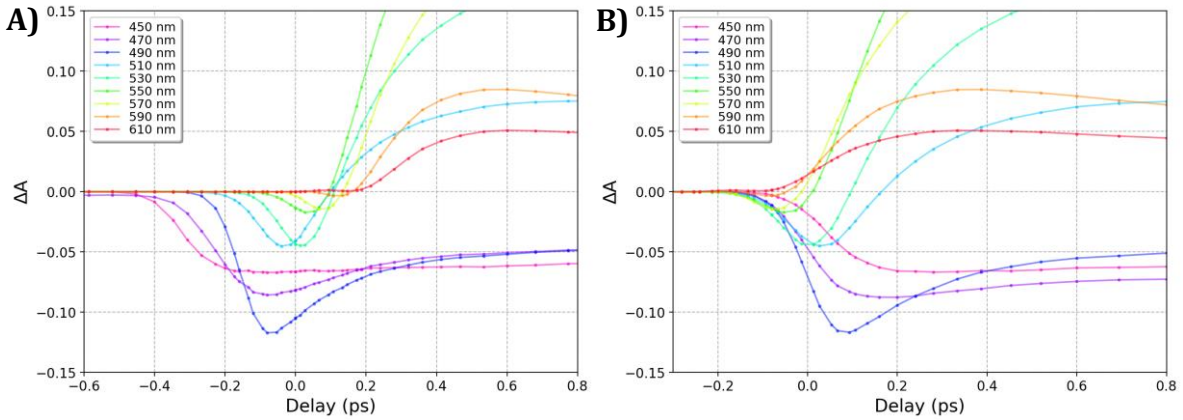

Figure 10. Example of raw kinetics obtained using transient absorption spectroscopy for β-carotene in *n*-hexane, A) before GVD correction, B) after GVD correction.

This effect can be described by the Sellmeier-Helmholtz equation:

$$n^2(\lambda) = A + \frac{B}{\lambda^2 - C} - D\lambda^2 \qquad (2)$$

where A, B, C, D are material-dependent parameters, while n is an index of refraction. Because the parameters are known for all common materials (BK7 glass, water, CaF_2, sapphire), the GVD effect can be corrected by calculating a delay of each wavelength for a specified amount of each material. For each probe wavelength, the kinetics is shifted by a given delay with respect to other wavelengths. The amount of materials is adjusted to reach the pump-probe temporal overlap for all probe wavelengths, *i. e.* to obtain uniform growth of all the transient spectra in the temporal domain (like in Figure 10B). A final step of the data preprocessing is a projection of the data onto a new grid of wavelengths and Δt delays. Usually, 5 nm wavelength spacing is used, which allows to reduce the noise and the size of the data, without significant loss of the resolution.

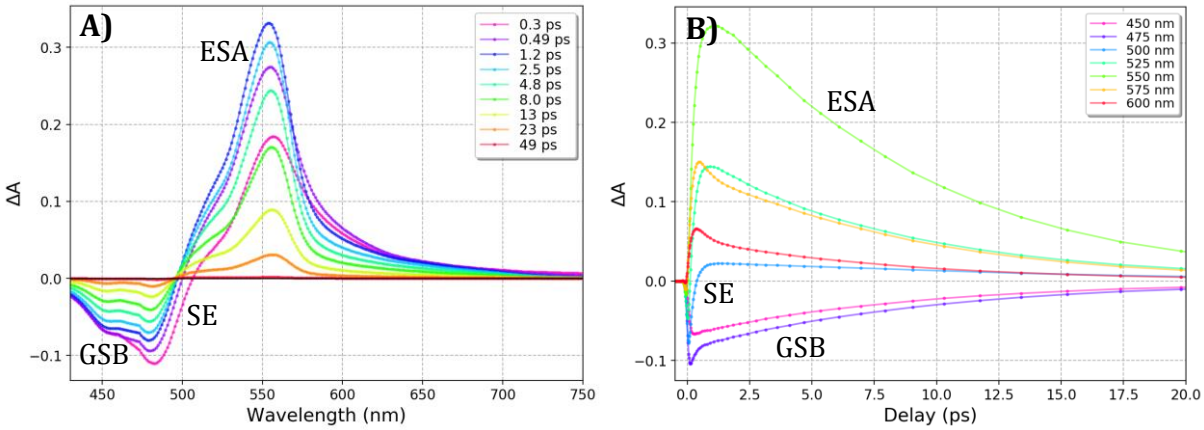

Figure 11. Preprocessed exemplary transient absorption dataset registered for the β-carotene in *n*-hexane sample excited at 470 nm (0.4 μJ). Ground state bleaching band (400 - 500 nm) shows up almost instantly after the excitation, while excited state absorption (500 – 600 nm) grows slower within the first picosecond.

Figure 11 presents preprocessed transient spectra and kinetics recorded for a β-carotene, which will serve as an example. One can observe basic types of bands commonly encountered in transient absorption spectroscopy. Ground state bleach (GSB) is a negative band located in the same spectral area where the ground state absorption band is located (in the stationary absorption band). The negative value of the GSB is a result of the decrease of absorbance, due to the depletion of the S_0 ground state population, caused by the laser pulse which promotes molecules to an excited state (see Figure 12).

Decay of the GSB indicates relaxation of the excited state population towards the electronic ground state population (its repopulation). Excited state absorption (ESA) is a positive band(s), characteristic of the newly populated states, associated with transition to some even higher excited states (for example $S_1 \rightarrow S_3$). The third type of contribution is a stimulated emission band (SE), which is negative and redshifted with respect to the GSB band. In Figure 11, one can see a very weak emission from the S_2 state located at about 500 nm, which decays within hundreds of femtoseconds. All discussed bands may be spectrally overlapped, allowing the negative (GSB and SE) and positive (ESA) bands to compensate, which poses an analytical challenge to separate them from each other.

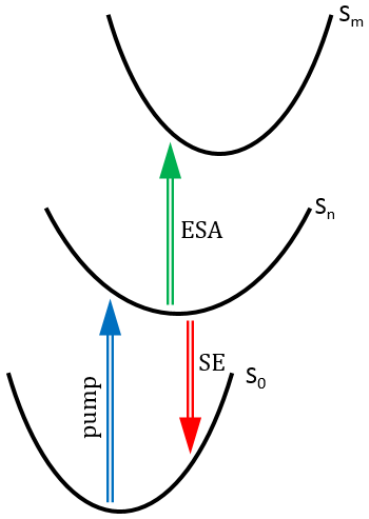

Figure 12. Origin of the excited state absorption (ESA) and stimulated emission (SE) bands, explained using exemplary scheme of electronic states.

Global and target analysis

In order to start the analysis of an unknown sample, it is important to evaluate the complexity of the data in the first place. The number of required exponential components (which are adequate if all the processes are first-order type) depends on the nature of the investigated system. In the most simple case, one can imagine a system that is excited to the first electronic excited state S_1, which subsequently decays back to the ground state S_0. In this case, only one exponential term may be sufficient to model the data. However, in a general case there may be at least a few additional processes, for example, i) additional electronic states engaged in the relaxation, ii) external vibrational relaxation (cooling), iii) internal vibrational redistribution, iv) relaxation of the solvation shell, v) relaxation of the molecule geometry in the excited state, vi) presence of the long-living products, for example, a triplet state etc. These factors increase the complexity of the registered data. The simplest formula to describe a dataset is to use a multiexponential function:

$$\Delta A(\lambda, t) = a_1(\lambda) \exp\left(-\frac{t}{\tau_1}\right) + a_2(\lambda) \exp\left(-\frac{t}{\tau_2}\right) + \cdots \qquad (3)$$

Application of this formula leads to the decomposition of the $\Delta A(\lambda, t)$ surface into so-called decay associated spectra (DAS) $a_1(\lambda)$, $a_2(\lambda)$, $a_3(\lambda)$ ... and time constants τ_1, τ_2, τ_3 ... which can be perceived as some specific representation of a given dataset. Guessing the correct number of exponential components is by no means an easy task. It may require some understanding of the investigated system *a priori*, however, one can utilize techniques such as singular value decomposition (SVD) in order to estimate the minimal number of components required to describe the data well. For a more general description of the analysis methods, please check these reviews.[48-51]

It must be emphasized, that not all processes can be described in terms of an exponential function. For example, association of two species into one is not an exponential process in principle. Even if all the observed processes are exponential, still it does not mean that any sum of exponential terms can retrieve a physical meaning of the observed phenomena. In order to obtain a meaningful decomposition of the dataset, the number of exponential processes must be correctly guessed.

The goal of the transient absorption data analysis is to understand i) what the species involved in the relaxation are, and ii) what are the pathways between them, *i. e.* what are the consecutive steps of the observed relaxation process occurring after the excitation? In principle, one can describe such a reaction in terms of the rate equations. The most simple case is when there is only one decaying population. It can be described by the following differential equation:

$$\frac{d[P]}{dt} = -k \quad [P] \tag{4}$$

This first order differential equation has also a very simple solution:

$$[P] = [P]_{t=0} \exp(-kt) \tag{5}$$

where k is a rate constant (a reciprocal of the time constant τ). $[P]$ represents a molar concentration of some population *P*, which decays with a time constant τ. Equation 4 describes a physical process, where the probability of a decay within population *P* per time unit ($d[P]/dt$) is proportional to $[P]$, *i. e.* each molecule in the metastable *P* population is equally likely to decay in any moment of its lifetime. Concentration $[P]$ and absorbance are related by Beer-Lambert law:

$$A = l\, \varepsilon\, [P] \tag{6}$$

where ε is a molar absorption coefficient defined for the specific probe wavelength, l is an optical path over which the absorbance is measured. If there is more than one species, the total absorbance is the sum of all contributing absorbances. In the transient absorption experiment, the measured quantity is ΔA, which represents a change of the absorbance with respect to the stationary ground state (GS):

$$\Delta A(\lambda, \Delta t) = A_{\Delta t} - A_{without\ pump} = l\, (\varepsilon_P \ - \varepsilon_{GS})\, [P]_{\Delta t} \tag{7}$$

where $[P]_{\Delta t}$ is concentration of the species removed from the ground state at delay Δt, ε_P is the molar absorption coefficient associated with newly populated species *P*, ε_{GS} is the molar absorption coefficient associated with the ground state GS. Therefore, a monoexponentially decaying ΔA means that a certain metastable state relaxes completely to the stationary ground state. But not always things are so simple because other metastable states can be also populated.

Let's consider an exemplary case where a metastable state *A* decays to the ground state *C* through an intermediate state *B*.

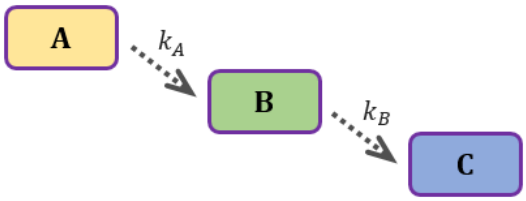

Figure 13. Graphical representation of the sequentially decaying model.

$$\begin{cases} \frac{d[A]}{dt} = -k_A\,[A] \\ \frac{d[B]}{dt} = k_A\,[A] - k_B\,[B] \\ \frac{d[C]}{dt} = k_B\,[B] \end{cases} \tag{8}$$

The set of equations presented above describes a more complex relaxation scheme, where the population $[A]$ decays to the population $[B]$, and then population $[B]$ decays to the population $[C]$ and stays there forever. Note that $k_A\,[A]$ term figures in two places, once with a negative sign (to indicate depletion of the $[A]$ population) and once with a positive sign (to indicate a flow of decaying $[A]$ species into the $[B]$ population). Also note that the total concentration of all the species is constant ($[A] + [B] + [C] = const.$), so nothing leaks "outside of the equation". Equation set 8 has an analytic solution, which provides an explicit formula for all $[A]$, $[B]$, $[C]$ concentrations:

$$\begin{cases} [A] = \exp(-k_A t) \\ [B] = \frac{k_A}{k_B - k_A}\exp(-k_A t) - \frac{k_A}{k_B - k_A}\exp(-k_B t) \\ [C] = \frac{-k_B}{k_B - k_A}\exp(-k_A t) + \frac{k_A}{k_B - k_A}\exp(-k_B t) + 1 \end{cases} \tag{9}$$

Figure 14 shows the concentration profiles calculated for each population. Lifetimes $1/k_A = 1\text{s}$ and $1/k_B = 2\text{s}$ and initial conditions $[A]_{t=0} = 1$, $[B]_{t=0} = 0$, $[C]_{t=0} = 0$ were assumed.

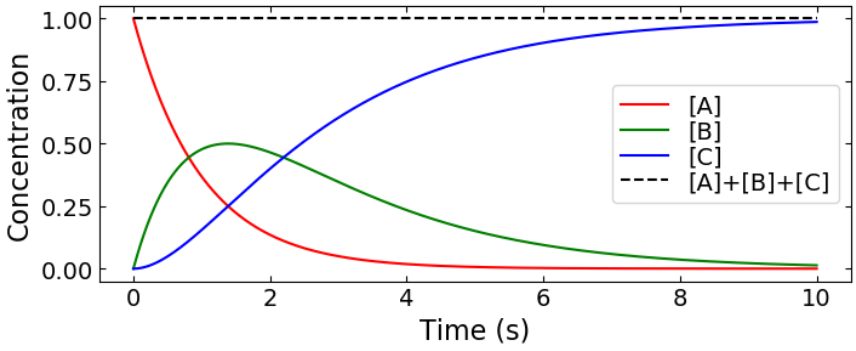

Figure 14. Concentration profiles based on equations 9.

At this point, it is clear, that the sum of the exponential terms introduced in eq. 3 will not provide physical interpretation in the general case. In order to understand better this issue, it is useful to consider a case of β-carotene. Figure 15 presents two kinds of decomposition, performed on a β-carotene dataset.

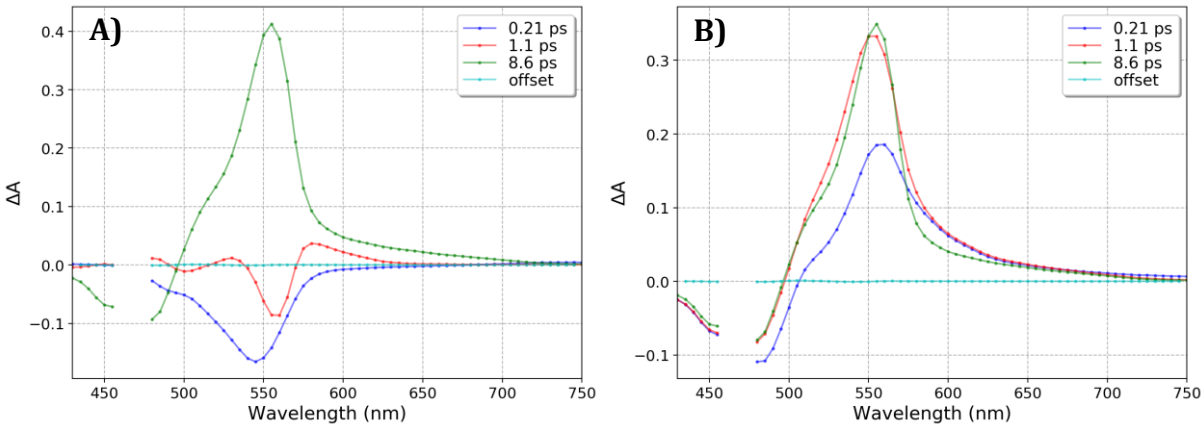

Figure 15. A) DAS, B) EAS decomposition of the β-carotene transient absorption spectrum.

DAS decomposition is obtained using eq. 3, where each spectrum is one of $a_1(\lambda)$, $a_2(\lambda)$, $a_3(\lambda)$, $a_4(\lambda)$ preexponential factors associated with one of 4 decay time constants used to describe the data (the last time constant is an infinity *i. e.* offset). Do they describe species engaged in the relaxation process properly? The answer is not straightforward. One can imagine a relaxation scheme like in Figure 16, where a mixture of different compounds (or different forms of some compound) is excited, so that each compound is promoted to his own excited state. Then, they relax in an independent fashion, parallelly. In this case, one can write a set of independent terms as in eq. 4, which can be solved and yield a sum of exponentials like in eq. 3. If such a picture is true, then DAS will represent the difference spectra of the excited states relaxing this way. Unfortunately, it is not the way the β-carotene relaxes. In this case, a scheme similar to the one described in Figure 13 is much more helpful. In this scheme, the populations form a cascade (A→B→C), where the first populated species evolves into the next one, which subsequently goes into another one. In fact, β-carotene relaxation resembles this type of scheme, where the initially populated S_2 state undergoes sequential S_2→hot S_1→S_1→S_0 relaxation. To describe this type of mechanism, one cannot just take a preexponential terms (DAS). In this case, the so-called evolution associated spectra (EAS) have to be resolved. They are presented in Figure 15B.

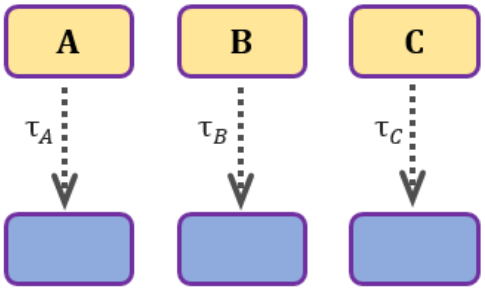

Figure 16. Graphical representation of the parallelly decaying populations. DAS decomposition provides the description of such decay scheme.

In order to solve any relaxation scheme (not only sequential or parallel relaxation cases), one has to take a more general approach. The case described by the eq. 8 can be rewritten in the matrix form:

$$\frac{d}{dt}\begin{bmatrix} A \\ B \\ C \end{bmatrix} = \begin{bmatrix} -k_A & 0 & 0 \\ k_A & -k_B & 0 \\ 0 & k_B & 0 \end{bmatrix}\begin{bmatrix} A \\ B \\ C \end{bmatrix} \tag{10}$$

Note that this is exactly equivalent representation (square brackets around A, B, C indicating concentrations are skipped for clarity). In fact, any set of equations with any number of species can be formulated this way. So let's rewrite it again in a general form:

$$\frac{d}{dt}\boldsymbol{C} = \boldsymbol{KC} \tag{11}$$

where **C** is a vector of concentrations of all the n species taking part in the relaxation scheme. **K** is a n×n matrix of rate constants, which define the relaxation scheme. The target is to obtain the explicit formula describing the evolution of all concentrations (**C** vector), such as these in the eq. 9. It is clear that in any case, it will be a combination of exponential terms with some factors preceding them and some time constants within them. All these values can be calculated from the **K**-matrix and initial conditions. Then, concentration profiles can be calculated using some specific set of rate constants. So the optimization routine can be implemented, where the rate constants are varied and the concentration profiles are fitted to the data.

Equation 11 describes the general case, which is a set of mutually dependent differential equations. It is possible to simplify this problem. If one can find a way to diagonalize the **K**-matrix, then the equations produced by the eq. 11 will be independent, *i.e.* $d[A]/dt$ will depend exclusively on the A concentration, not B or C or D. Then each equation can be solved separately, and even better, the solution will be just one exponential term, like in eq. 5, so the problem will be reduced to the case similar to the DAS decomposition. Fortunately, such a simplification can be achieved by finding the eigenvalues and eigenvectors for the **K**-matrix. Algorithms to perform this task are well known (for example refer to *numpy.linalg.eig* function in Python environment). Solution of the eigenproblem for **K**-matrix yields λ_1, … , λ_n eigenvalues and corresponding $\boldsymbol{v_1}, \ldots, \boldsymbol{v_n}$ eigenvectors. One can build the n×n transformation matrix $\boldsymbol{P}$, where values in the columns are the same as in the eigenvectors:

$$\boldsymbol{P} = \begin{bmatrix} \boldsymbol{v_1} & \ldots & \boldsymbol{v_n} \end{bmatrix} \tag{12}$$

The diagonal matrix $\boldsymbol{D}$ has eigenvalues located at the diagonal, while all nondiagonal values are zero:

$$\boldsymbol{D} = \begin{bmatrix} \lambda_1 & \cdots & 0 \\ \vdots & \ddots & \vdots \\ 0 & \cdots & \lambda_n \end{bmatrix} \tag{13}$$

The matrices defined this way are very useful because one can use them to decompose the **K**-matrix in the following way:

$$\boldsymbol{K} = \boldsymbol{PDP}^{-1} \tag{14}$$

At this point it is possible to apply this construct and solve the eq. 11.

$$\frac{d}{dt}\boldsymbol{C} = \boldsymbol{P}\boldsymbol{D}\boldsymbol{P}^{-1}\boldsymbol{C} \tag{15}$$

Note that $\boldsymbol{P}^{-1}\boldsymbol{P}$ is just an identity matrix ($\boldsymbol{I}$), so one can multiply both sides by $\boldsymbol{P}^{-1}$ and obtain:

$$\frac{d}{dt}\boldsymbol{P}^{-1}\boldsymbol{C} = \boldsymbol{D}\boldsymbol{P}^{-1}\boldsymbol{C} \tag{16}$$

Let's substitute $\boldsymbol{P}^{-1}\boldsymbol{C}$ with a new vector, $\boldsymbol{X}$. Now we have an equation in the same form as in the eq. 11, but **K**-matrix is replaced with diagonal $\boldsymbol{D}$ matrix, and $\boldsymbol{C}$ vector of concentrations is replaced with a new vector $\boldsymbol{X}$.

$$\frac{d}{dt}\boldsymbol{X} = \boldsymbol{D}\boldsymbol{X} \tag{17}$$

Since $\boldsymbol{D}$ is a diagonal matrix, the formula above generates a set of independent differential equations, which can be easily solved. Moreover, we know how to calculate $\boldsymbol{D}$ matrix and how to build the matrix $\boldsymbol{P}$ required to swap between $\boldsymbol{C}$ vector and $\boldsymbol{X}$ vector. It requires a solution of the eigenproblem for **K**-matrix only. It may be surprising that we can actually exchange the eq. 11 into diagonal eq. 17 so smoothly, without losing the generality of the problem. One can try to visualize this operation as a rotation of the vector in the n-dimensional space. The $\boldsymbol{P}$ matrix, is a unitary transformation matrix, which transforms the $\boldsymbol{C}$ vector to a different coordinate system that is aligned with $\boldsymbol{v_1}, \dots, \boldsymbol{v_n}$ eigenvectors. In this system, the $\boldsymbol{K}$ matrix has a simple, diagonal form. So we are just exploiting this remarkable property, solving the problem in the transformed coordinate system, and then we only need to perform a reverse transformation, in order to re-complexify the solution. Eq. 17 can be rewritten explicitly as:

$$\begin{cases} \frac{d[X_1]}{dt} = \lambda_1\,[X_1] \\ \qquad\dots \\ \frac{d[X_n]}{dt} = \lambda_n\,[X_n] \end{cases} \tag{18}$$

This set of equations is trivial to solve, just like in eq. 5 we can write:

$$\begin{cases} [X_1] = [X_1]_{t=0}\,\exp(\lambda_1 t) \\ \qquad\dots \\ [X_n] = [X_n]_{t=0}\,\exp(\lambda_n t) \end{cases} \tag{19}$$

Because eigenvalues are known, it is only necessary to determine the $[X_1]_{t=0}, \dots, [X_n]_{t=0}$ constants. Note, that at $t = 0$ the exponential functions reduce to unity, therefore the $\boldsymbol{X}$ vector consists of $[X_1]_{t=0}, \dots, [X_n]_{t=0}$ constants only. Using the $\boldsymbol{C} = \boldsymbol{P}\boldsymbol{X}$ back transformation, we have:

$$\begin{bmatrix} C_1 \\ \dots \\ C_n \end{bmatrix}_{t=0} = \begin{bmatrix} P_{1,1} & \cdots & P_{1,n} \\ \vdots & \ddots & \vdots \\ P_{n,1} & \cdots & P_{n,n} \end{bmatrix} \begin{bmatrix} X_1 \\ \dots \\ X_n \end{bmatrix}_{t=0} \tag{20}$$

The solution of this linear equation system is simple, if the initial concentrations $\boldsymbol{C}_{t=0}$ are specified and $\boldsymbol{P}$ matrix is known. $\boldsymbol{C}_{t=0}$ vector describes the population of all the species at the moment when the pump pulse excites the sample. In many cases unity can be assumed for one population (for example the excited state directly populated by the pump pulse), and zero for the remaining ones. To solve the eq. 20 algorithmically, the *numpy.linalg.solve* function from the Python environment can be utilized. At this point, the $\boldsymbol{X}$ vector is completely resolved, and one can obtain the final, analytic solution of the eq. 11. It is similar to eq. 9, however, this time the solution is general.

$$\boldsymbol{C} = \boldsymbol{P} \begin{bmatrix} [X_1]_{t=0} \exp(\lambda_1 t) \\ \dots \\ [X_n]_{t=0} \exp(\lambda_n t) \end{bmatrix} \tag{21}$$

All the required parameters can be calculated from the $\boldsymbol{K}$ matrix and the $\boldsymbol{C}_{t=0}$ initial conditions. In any case, the result is a linear combination of n exponential terms. This formalism can be applied to model any reaction which involves first-order reactions. In the case of transient absorption spectroscopy, fitted data are ΔA values defined on the two-dimensional temporal and spectral grid. In order to calculate the $\Delta A(\lambda, t)$ from the $\boldsymbol{C}$ vector, the Beer-Lambert law needs to be utilized (eq. 6). In most cases, it is more practical to multiply a concentration of each species with the corresponding spectrum, which is usually denoted as species associated spectrum (SAS):

$$\Delta A(\lambda, t) = \sum_{i=1}^{n} SAS(\lambda)_i \, C_i(t) \tag{22}$$

This equation completes the pathway from any general first-order relaxation scheme to a description of the registered dataset. Described formalism was used to develop a package, which can fit transient absorption datasets using a graphically represented scheme. By defining the number of species in the reaction, the relaxation channels between them and initial conditions (which species are populated by the excitation), the program can fit the dataset and recover the rate constants ($\boldsymbol{K}$-matrix) as well as SAS spectra. Users can define which variables should be varied, and which ones must stay constant.[52]

The approach described above is often referred to as “hard modeling”, as opposed to the “soft modeling” methods, like MCR-ALS (Multivariate Curve Resolution - Alternating Least Squares). A significant disadvantage of the hard modeling methods is that one has to put forward some specific model in order to obtain some information. It is not always possible to discriminate between different relaxation schemes (especially complex ones). As we demonstrated in Figure 15, one can decompose the dataset into a DAS (parallel decaying species) or EAS (sequentially decaying species), so different sets of spectra are obtained with a different meaning. In fact, one can fit the data with various decay schemes, and differentiation can only be done by analysis of the SAS spectra. Then one can judge, if obtained spectra seem valid, for example using comparison with similar molecular systems or by extending the dataset with more experiments

performed in various conditions. Finally, it may still be impossible to determine which decay scheme is a valid one. Soft modeling methods utilize a different approach, where data are decomposed without such straight assumptions done *a priori*. In this case, one gives up on the indecent desire to know all the details of the system, in order to understand only its general characteristics. The system may be willing to return the favor, by revealing some hidden information.

The last important aspect of the femtosecond data analysis is the initial evolution around $t = 0$. When the pump and probe pulses overlap, the signal gradually grows. The initial moments of the evolution are described by the convolution of the instrument response function (IRF) and the exponential terms describing the decay. In transient absorption experiments, the IRF is usually expressed by a Gaussian distribution:

$$IRF(t) = \frac{1}{\sigma\sqrt{2\pi}} \exp\left(-\frac{t^2}{2\sigma^2}\right) \tag{23}$$

After the convolution with an exponential term $\exp(-kt)$, one can obtain the following formula:

$$\Delta A(t) = \frac{1}{2}\left[1 + \mathrm{erf}\left(\frac{t - \sigma^2 k}{\sigma\sqrt{2}}\right)\right] \exp\left(-kt + \frac{1}{2}\sigma^2 k^2\right) \tag{24}$$

The full width at half maximum of the Gaussian pulse is related to σ as FWHM $= 2\sigma\sqrt{2ln2}$. It defines the temporal resolution of the experiment and depends on multiple factors such as probing wavelength, pump and probe pulse durations, length of the optical path over which they interact in the sample, refractive properties of the sample, etc. Gauss error function (erf) is a result of the integration of $\exp(-t^2)$ function, which is necessary during convolution calculation. In order to model the ΔA surface around $\Delta t = 0$, one has to exchange all the exponential terms with a formula in eq. 24.

Another important issues are artifacts encountered at $\Delta t = 0$, when the pump and probe pulses temporally overlap. Usually, two-photon absorption (TPA), stimulated Raman amplification (SRA) and cross-phase modulation (XPM) are encountered. These effects distort Gaussian growth of the signal, complicating the analysis.[53]

2.2 *Nanosecond transient absorption spectroscopy*

*Experi*mental details

Nanosecond transient absorption spectroscopy typically utilizes the excitation of the Nd:YAG laser, which usually has temporal pulse width of around 10 ns and 10 Hz repetition frequency.[47] It allows to probe the evolution of the OCP intermediate forms, when the carotenoid is already back in the electronic ground state. In this technique, a monochromatic continuous light is used as a probe, therefore in one record a whole kinetics is collected at the selected wavelength. To probe at different wavelengths, one has to repeat the experiment. The repetition rate of this experiment is much slower compared to femtosecond transient absorption spectroscopy, because the probing time window of the experiment is much longer. A nanosecond excitation pulse has

much higher energy than the femtosecond pulse (typically milijoules vs microjoules). The repetition rate should be slow enough to allow the sample to recover completely. On the other hand, a temporal length of the nanosecond pulse results in a much lower power density than the femtosecond pulse. Therefore nonlinear effects like two-photon absorption are usually avoided. Because excited states of the carotenoid decay much faster than a nanosecond pulse (≈ 10 ps, around 1000 times longer), one molecule can be reexcited several times during one nanosecond pulse. However, the excitation pulse power density is much lower than in the femtosecond transient absorption experiment, so the nonlinear effects (like multiphoton excitation) are avoided.

The 532 nm excitation beam can be generated by a frequency-doubled Nd:YAG laser (Continuum Surelite II, *Continuum*). In order to generate different excitation wavelengths, the Optical Parametric Oscillator (*Continuum*) is used. An OPO employs the optical parametric amplification process. The third harmonic of the Nd:YAG laser (355 nm) pumps the nonlinear crystal in the OPO, which results in the generation of signal and idler beams. Their wavelengths can be tuned by changing the tilt angle of the crystal. The scheme of the nanosecond transient absorption setup is presented in Figure 17.

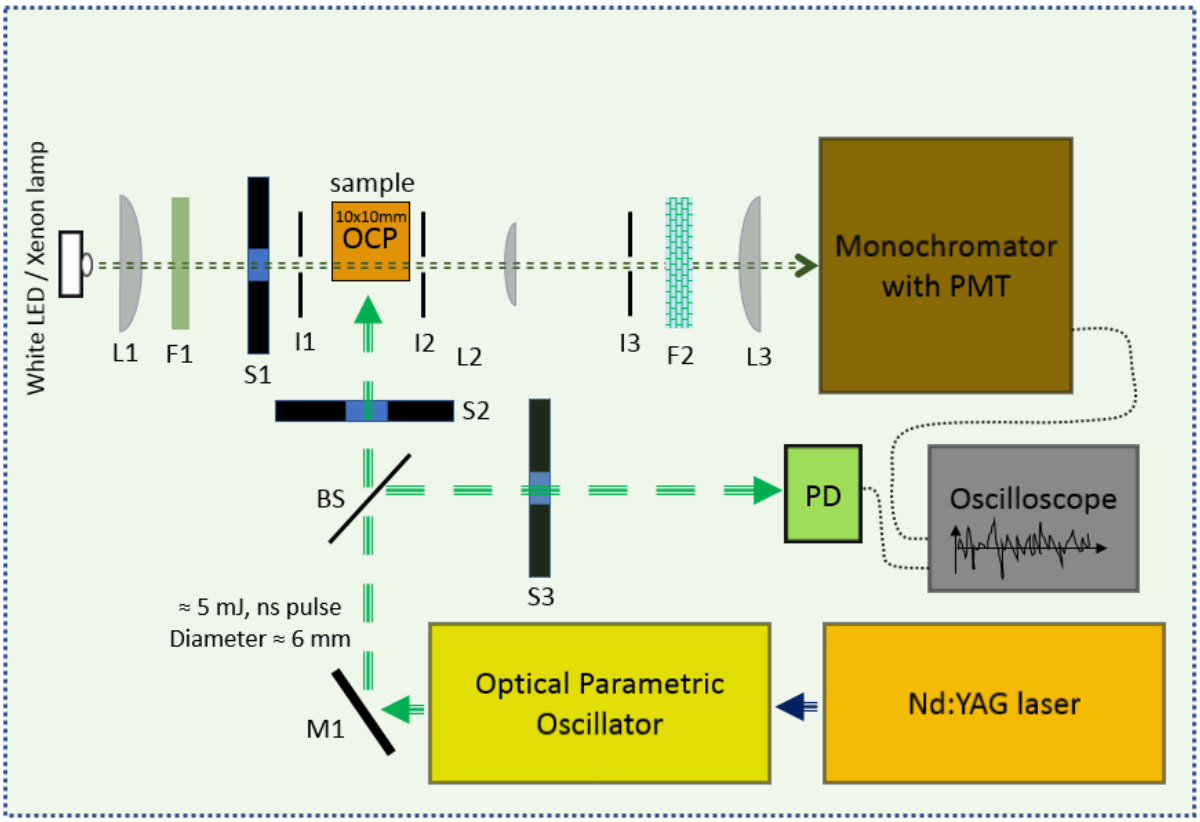

Figure 17. Outline of the nanosecond transient absorption spectrometer in the right-angle configuration.

Nd:YAG laser is driven by a 10 Hz pulse train, which is necessary for synchronization. To obtain the triggering signal for the oscilloscope, there is an additional photodiode PD (S1722-02 from *Hamamatsu*), which allows for triggering with nanosecond precision. Depending on the repetition frequency, the S2 shutter selects the excitation pulse from the 10 Hz pulse train,. For

the OCP the usual repetition of the experiment was 20 s between consecutive excitation pulses. In this case, the S1 and S3 shutters are opened simultaneously every 10 s. Therefore, the sample is repeatedly probed with and without an excitation pulse in an alternating fashion. Each time the S1 and S3 shutters open, the sample is probed and the photodiode PD triggers the oscilloscope.

Xenon lamp (*Applied Photophysics*) is a probing beam source, however, it can be replaced with the LED (custom-built module with standard 3W *Cree* emitter). Xenon lamp light is delivered through a thick optical fiber bundle. The L1 lens collimates the probing light, slightly focusing it in the sample cell (see Figure 18). The F1 bandpass filter is selected to transmit a quasi-monochromatic beam (to avoid the undesirable effect of the sample irradiation by the probing beam). The S1 shutter opens for a short period, when the data are being collected (so the sample is kept in the dark most of the time). I1 and I2 apertures are set to ensure that only the irradiated sample volume is being probed, close to the side from which the irradiation laser pulse strikes. The diameter of these apertures is smaller (≈ 2 mm) than the diameter of the excitation beam. The L2 lens recollimates the light transmitted by the sample, the F2 notch filter removes the scattered irradiation light, while the I3 iris blocks the light leaking around the F2 filter. Finally, the L3 lens focuses the probing beam in the monochromator (SpectraPro-300i from *Acton Research*). The monochromator is coupled with an R928 PMT from *Hamamatsu*, where 5 dynodes are used. It possesses approximately 2 ns temporal resolution. *Tektronix* TDS 680 C oscilloscope triggered by the PD photodiode collects the signal from the PMT. The bias voltage of the PMT is usually within the 500-700 V range. The maximum sampling frequency is 5 GS/s, and 15 000 samples per kinetics

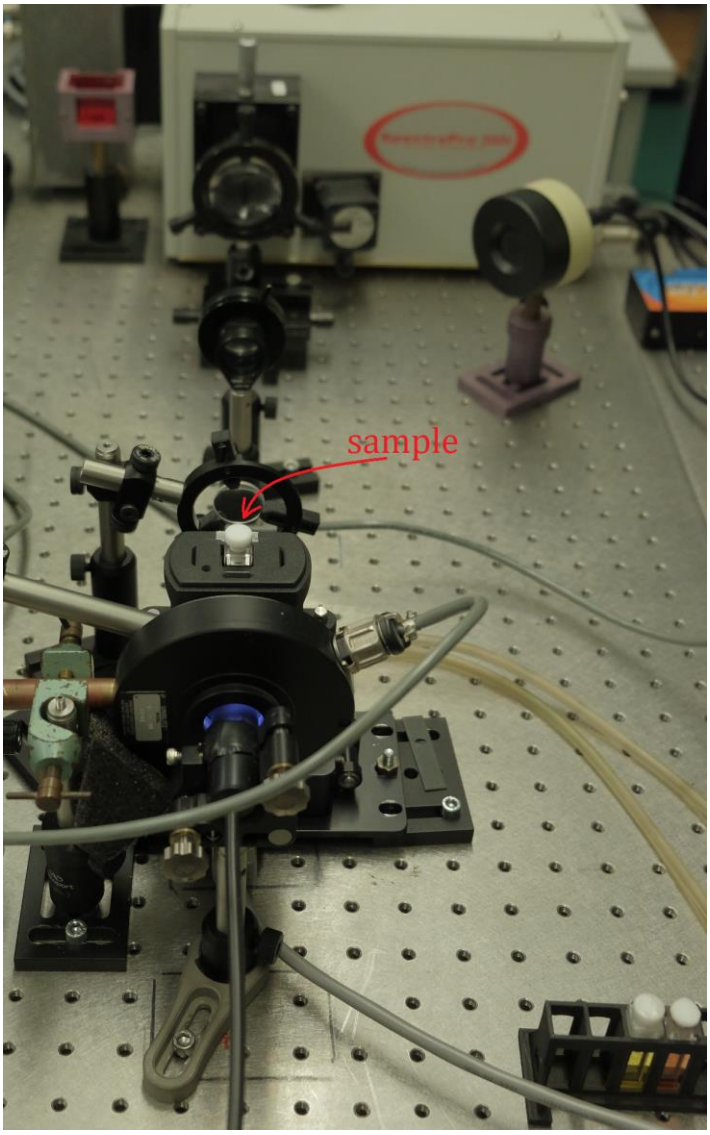

Figure 18. The path of the probing beam in the nanosecond transient absorption experiment. The excitation pulse strikes from the right side (in right-angle configuration).

can be collected at once. In order to cover a wide temporal resolution, one has to repeat the measurements with various sampling rates.

The advantage of the xenon lamp is high luminance, wide spectral range, and ability to boost the light intensity by order of magnitude for a short moment of time (so-called "pulsing mode"). For the short temporal window of the experiment, there is a considerable contribution of the shot noise. It stems from the Poissonian distribution of a low number of photons per sample collected by the oscilloscope. The number of photons per sample drops, when one increases the sampling frequency of the oscilloscope. To counteract this effect, the Xenon lamp power can be boosted for a short period of time, approximately 500 μs. For the longer time regimes, it is more convenient to use LED as a probing light source, which exhibits much better long-term stability. When working without boosting the Xenon lamp intensity, the oscilloscope input impedance must be increased from 50 Ω, usually to 5 kΩ. It increases detection sensitivity, but degrades temporal resolution.

The experimental sequence is thefollowing: each time the kinetics is measured, the S1 and S3 shutters are opened. Shutter S2 opens every second time the S1 is opened. Therefore kinetics with and without excitation are collected alternatingly. For the samples like OCP, a large number of kinetics must be averaged in order to obtain a high quality $\Delta A(\Delta t)$ trace. Usually, the $I_{probe}^{with\ exc}(\Delta t)$ and $I_{probe}^{without\ exc}(\Delta t)$ kinetics are measured 100 times, and subsequently averaged so the $\Delta A(\Delta t)$ is calculated according to the equation below.

$$\Delta A(\Delta t) = -log\left(\frac{I_{probe}^{with\ exc}(\Delta t)}{I_{probe}^{without\ exc}(\Delta t)}\right) \tag{25}$$

For the concentrated samples, the experimental configuration has to be modified. The collinear variant of the experiment is presented in Figure 19 (only the altered part of the setup). Reduction of the probing path to 2 mm is necessary to keep the sample transparent for the probing light, however for very high concentrations even 0.5 mm cuvettes were applied. The disadvantage of collinear configuration is an increase in the irradiation pulse scattering (which is also partially reflected from the cuvette towards the monochromator).

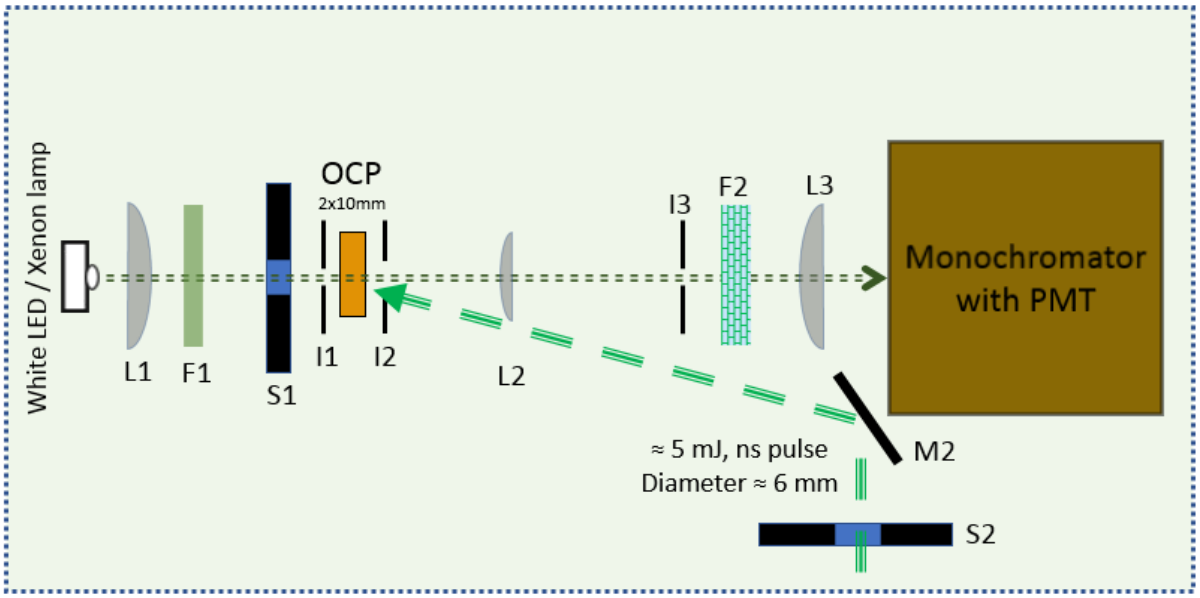

Figure 19. Collinear variant of the nanosecond transient absorption spectrometer.

Nanosecond transient absorption data analysis

The analysis of the nanosecond transient absorption data is similar to femtosecond transient absorption, the main difference is a preprocessing procedure. In the case of OCP, usually only kinetics for one or two probing wavelengths have been collected. It is due to ultralow signals (≈ 1 mOD), the requirement to cover a wide temporal range and keep the probing light intensity and repetition rate low. Measurement of only one kinetics with sufficient S/N ratio is a very challenging and time-consuming task.

Because the number of samples collected per kinetics is limited (15 000), the experiment must be repeated a few times for each probing wavelength, to cover a temporal range from tens of ns to single seconds. Moreover, technical requirements are different for the ns-µs regime, where xenon lamp with pulser is used, and for the ms-s regime where LED probing light is more adequate. Therefore, usually one kinetics is built from 3-5 raw ones. The algorithm for data reduction is the following: i) Background signal (before laser irradiation pulse) is subtracted. ii) Negative delays and first tens of ns are removed (due to high laser scattering). iii) All raw kinetics are superimposed and rescaled to overlap perfectly to compensate for differences in the excitation energy (an exemplary dataset is shown in Figure 20). iv) A new logarithmic grid of times is generated, which covers all the time regimes of the interest. v) All the raw data are projected onto the logarithmic grid, with averaging if possible. Usually, logarithmic grid with about one hundred points is sufficient to preserve the important kinetic information while keeping the data clear. These data can be fitted using the sum of exponential decays, without the convolution (eq. 3).

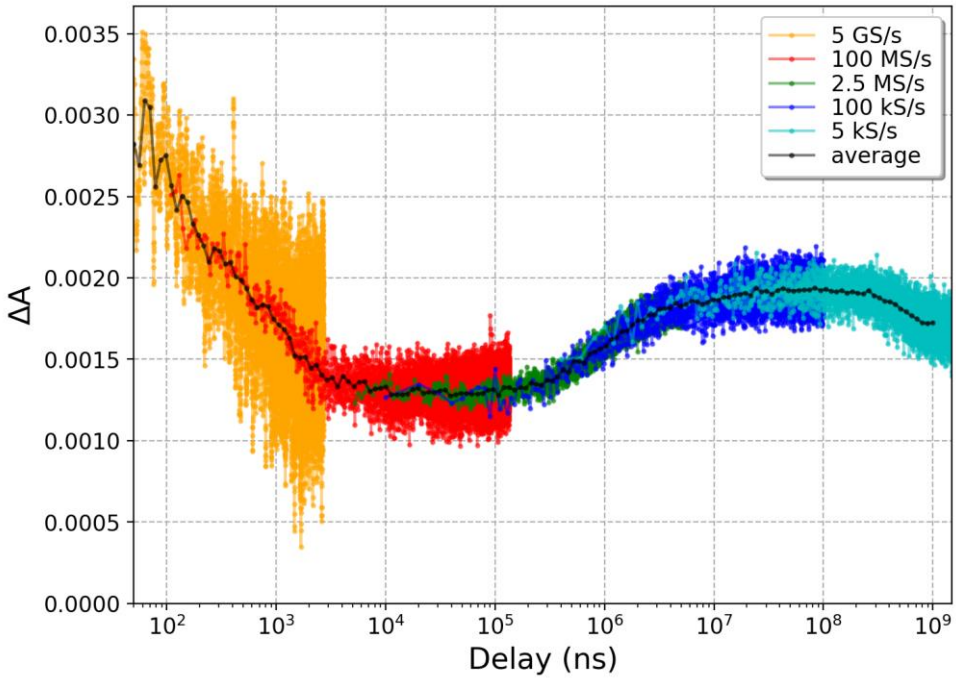

Figure 20. Raw superimposed nanosecond transient absorption kinetics before averaging and merging. Each color represents a measurement done in a different time window, with a specific sampling frequency expressed as number of samples per second.

Determination of photoproduct quantum yield with comparative actinometry

In order to calculate a quantum yield for some state observed in a transient absorption experiment, it is useful or even necessary to perform additional measurement with a reference compound. In this thesis, tris(bipyridine)ruthenium(II) has been applied as a reference (it will be abbreviated as "ruthenium"). Ruthenium solution in water possesses significant stationary absorption of green, blue and UV light. After the excitation, it undergoes efficient intersystem crossing to the metal-to-ligand charge transfer state (^{3}MLCT). It decays with about 600 ns lifetime, making it visible in the picoseconds-nanoseconds time regime.[54] Since the formation quantum yield of the ^{3}MLCT state is known and equal to unity, and triplet spectral properties are well characterized in literature[54-56], tris(bipyridine)ruthenium(II) can be used as a reference to determine quantum yields of the other states. In order to obtain an accurate result, the absorbance of the reference solution at the excitation wavelength should be approximately the same as the absorbance of the measured sample of interest (OCP). The reference measurement should be done with exactly the same experimental geometry and excitation pulse energy. One can use the following equation, to determine a quantum yield of some specific state:

$$\Phi = \frac{\left(1 - 10^{-A^{exc}_{ruthenium}}\right) \Delta A^{probe}_{OCP} \, \Delta\epsilon^{452nm}_{ruthenium}}{\left(1 - 10^{-A^{exc}_{OCP}}\right) \Delta A^{452nm}_{ruthenium} \, \Delta\epsilon^{probe}_{OCP}} \tag{26}$$

where $A^{exc}_{ruthenium}$ and A^{exc}_{OCP} are absorbances of the ruthenium and OCP solutions at the excitation wavelength, respectively. ΔA^{probe}_{OCP} is a difference absorbance observed for the state of interest at the probing wavelength. $\Delta A^{452nm}_{ruthenium}$ is a difference absorbance observed mainly for the bleached

ruthenium ground state population at 452 nm. $\Delta\epsilon_{ruthenium}^{452nm}$ is a difference molar absorption coefficient of the ruthenium ^{3}MLCT state at 452 nm. It is equal to -11 000 M^{-1} cm^{-1}.[54] $\Delta\epsilon_{OCP}^{probe}$ is a difference molar absorption coefficient of the OCP state of interest at the probing wavelength. We assumed that the molar absorption coefficient of the OCP at 490 nm is equal to 63 000 M^{-1} cm^{-1}.[57] It can be used to calculate $\Delta\epsilon_{OCP}^{probe}$ at the GSB band of the given state ($\Delta\epsilon^{\lambda} = \epsilon_{state-of-interest}^{\lambda} - \epsilon_{stationary}^{\lambda}$). Because the shape of the ESA band may be unknown, some assumptions may be required. In the OCP, excited states absorb at the red side of the stationary OCP absorption band, so the blue-shifted probing wavelengths reflect mainly the OCP bleach population (ESA contribution is minor).

2.3 Absorption change measurements upon continuous irradiation

*Experi*mental details

The most simple approach to observe the photoconversion process is to track the accumulation of the long-living OCP^R species upon steady-state irradiation conditions. For this purpose, a stationary UV-vis absorption spectrophotometer can be used. Due to the presence of the continuous reference beam, this technique can track minor changes in absorption, much below 1 mOD. It can be used to calculate the quantum yield of the OCP^R, based on the slope of its growing absorption kinetics. It can also answer some questions about the photoconversion mechanism without using pulsed irradiation. If the data are collected in the function of light intensity, temperature, concentration, irradiation wavelength, etc., one can model the OCP^R accumulation process and verify, if the multivariate dataset can be described by the proposed model. In this case, precise knowledge about all experimental conditions is required. This technique allows to accumulate enough OCP^R, to observe its decay after the irradiation is switched off (which is hard after pulsed irradiation, due to low OCP^R quantum yield).

Jasco V-550 spectrophotometer uses a very weak, monochromatic probing beam generated by the deuterium (190 – 350 nm) or halogen lamp (330 – 900 nm). The beam travels through the monochromator, and then the chopper alternately reflects it or allows it to pass. This way it is effectively split into two beams: one that scans the sample and the second one which works as a reference. Both beams are slightly astigmatic, with the most narrow waist in the middle of the measurement chamber. The beam intensities are measured by a PMT, and the absorbance is calculated according to the following formula:

$$A(\lambda, t) = -log\left(\frac{I_{sample}(\lambda, t)}{I_{ref}(\lambda, t)}\right) \tag{27}$$

Figure 21 presents the layout of the experiment. In order to obtain a sufficient time resolution, only one wavelength has been scanned during one experiment. The 2×10 mm cuvette has been used with sample volume V_s=0.3 mL. The advantage of this geometry is a short irradiation path (so the photons are absorbed uniformly over the whole cuvette volume and sample stirring can be omitted), and a long probing path, which increases observed absorbance changes. I1 and I2 irises are used to ensure that the probing beam travels through the sample

solution only, not through the cuvette glass. Usually, 450 nm LED irradiation has been used, focused with the L1 lens. The F1 filter blocks the scattering of the irradiation beam before it enters the PMT. The sample was located in the temperature-stabilized holder. The reference beam is covered to avoid interference from the irradiation light.

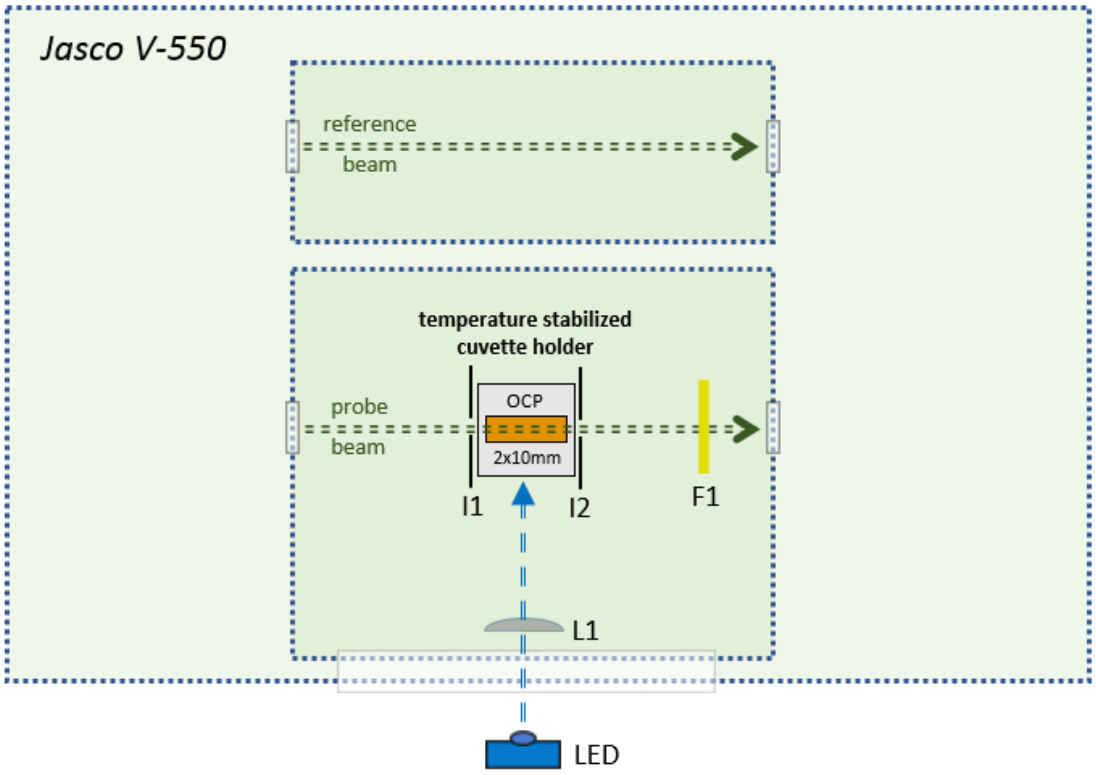

Figure 21. Configuration of the experiment based on Jasco V-550 spectrophotometer operating in a kinetic mode.

The typical experimental procedure is the following. Firstly, the cuvette with a solvent is placed in the holder, and the absorbance value is zeroed (so all measured values will be given with respect to the solvent). Then cuvette with the OCP sample is placed, and the measurement of the kinetics is started (in the dark). After 10 seconds, the irradiation is switched on, and the OCP^R accumulation starts (Figure 22). Exactly after the predefined time, the irradiation light is switched off and the OCP^R decay is observed. Absorbance is measured with a time step of 1s. One recorded kinetics consists of hundreds of points. The experiment can be repeated multiple times, with different experimental parameters such as LED irradiation intensity.

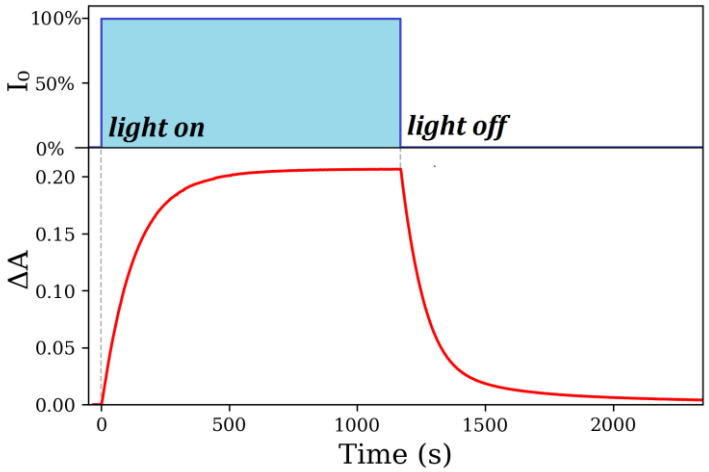

Figure 22. Exemplary kinetics probed at 580 nm. OCP is irradiated with 452 nm LED light, which is switched on at t = 0s and switched off at t = 1200 s.

The irradiation LED is calibrated before the experiment in order to determine the relation between LED current and photon flux density in the sample. It can be done using a power meter or an actinometer. The actinometer method is more accurate, because it takes into account the geometry of the cuvette, and the photon flux density is determined "from the perspective of the sample". Usually, it is sufficient to measure the photon flux density for a few currents of the LED and then use the interpolated values.

Determination of photon flux density with potassium ferrioxalate actinometer

In order to determine the photon flux density of the blue LED light entering the sample, the potassium ferrioxalate actinometer is very adequate.[58-60] It can be obtained by potassium oxalate and iron (III) chloride reaction. To obtain the proper purity, recrystallization is usually sufficient (eventually repeated to obtain nice, big crystals). Crystals need to be stored in complete darkness. The first required solution is 0.012 M of potassium ferrioxalate in 0.05 M of H_2SO_4. The second solution is 0.1% of phenanthroline in 1.65 M of sodium acetate and 0.5 M of H_2SO_4. Firstly, the potassium ferrioxalate solution is prepared in the 10×10 mm cuvette, with the same volume V_s as the measured sample (usually V_s=1.5 mL). This cuvette is kept in the dark (a red light is acceptable), and placed in the sample holder. Then, the irradiation source is switched on for an accurately defined period of time, t_{irr}. After irradiation, the phenanthroline solution is added in quantity equal to 1/8 of the used ferrioxalate solution (usually 0.25 mL). The solution should take on a raspberry color, and the A_{510} absorbance at 510 nm is measured. If obtained absorbance is very large (>1) or very small (<0.2), the measurement needs to be repeated with a shorter or longer t_{irr} irradiation time, respectively. At the end of the experimental session, it is also useful to perform a "reference" measurement for a non-irradiated actinometer. By subtracting its absorbance, one can obtain the value ΔA_{510} compensated for any accidental exposure of the potassium ferrioxalate solution to the background light. One can calculate moles of photons per second and per sample volume:

$$I_0 = \frac{10^{-3}\, V_c\, \Delta A_{510}}{\Phi_\lambda\, t_{irr}\, l_{irr}\, \varepsilon_{510} V_s\, (1 - 10^{-A_{irr}})} \tag{28}$$

where V_c is a volume after mixing the phenanthroline and potassium ferrioxalate solutions (usually 1.75 mL). l_{irr} is the irradiation path length expressed in cm. A_{irr} is an absorbance of the potassium ferrioxalate solution before irradiation at the irradiation wavelength. ε_{510} is a molar extinction coefficient of the complexed ferrous ions generated during irradiation (11100 M^{-1} cm^{-1}). Φ_λ is a quantum yield of ferrous ions production (1.1 value has been used for the irradiation at 450 nm).[58-60]

Irradiation conditions

At this point, it is important to define the maximum light intensity of the Sun, which can be encountered at the surface of the Earth, as this is a limit point for all living organisms. Photosynthetic Photon Flux Density (PPFD) equals around 2200 µmol m^{-2} s^{-1} for noon at the equator at equinox.[61] It represents the number of mols of photons arriving per second and per square meter of the surface area. The PPFD value is adjusted for the wavelength range of 400 - 700 nm, which is relevant for photosynthesis. However, the OCP protein studied in this work absorbs mostly between 420 nm and 550 nm wavelengths, therefore sun-equivalent photon flux density should be below 1000 µmol m^{-2} s^{-1}, if narrowband laboratory irradiation light source is being used. One must note, that these conditions correspond to the most harsh ones, which any organism can encounter on Earth. Conditions like clouds, Sun not being at the zenith, being covered by other organisms or underneath front layers of the water, etc. may cause that given organism will never encounter PPFD conditions (2200 µmol m^{-2} s^{-1}).

Modeling the system upon continuous irradiation

In order to fit the absorbance evolution upon continuous irradiation, one cannot use the same approach that is exploited for the relaxation processes in transient absorption spectroscopy. In the general case, the differential equations are no longer analytically solvable if the irradiation light continuously interacts with the sample. Therefore it is much more convenient to solve them numerically.

The principles of building the differential equations are the same as in the previously discussed cases. One can take into account not only first-order decay processes (exponential), but also higher orders (like association processes). For example, a dimerization of the A species can be incorporated by adding $-k_d\,[A]^2$ term. The formula describing light-dependent photoconversion is more complicated. Let's consider a simple case:

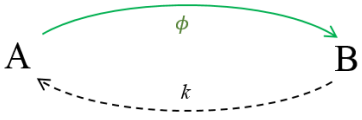

$$\begin{cases} \dfrac{d[A]}{dt} = -\phi\, I_0\, F\, [A]\, \epsilon_A\, l_{irr} + k[B] \\ \dfrac{d[B]}{dt} = \phi\, I_0\, F\, [A]\, \epsilon_A\, l_{irr} - k[B] \end{cases} \tag{29}$$

Figure 23. Single-photon model

The equation system presented above describes a simple system, where A species can be photoconverted to the B species, and thermal relaxation proceeds in an opposite way. Moreover,

the absorption of light by the B species does not cause $B \rightarrow A$ photoconversion. ϕ is a quantum yield of the light induced $A \rightarrow B$ transition, defined as a fraction of the photons absorbed by A population, which cause the transition to the B population. I_0 is a photon flux density expressed as moles of photons per second and per liter of the sample. ϵ_A is a molar absorption coefficient of the A species at the wavelength of irradiation. l_{irr} is an optical path length of the irradiation light. F is a photokinetic factor, defined as:

$$F = (1 - 10^{-A_{irr}})/A_{irr} \tag{30}$$

where A_{irr} is a total absorbance of the sample (of both A and B species) at the irradiation wavelength. Note that $[A]\,\epsilon_A\,l_{irr}$ term is an absorbance of the A species, according to the Beer-Lambert law. $1\text{-}10^{-A_{irr}}$ term is a fraction of the incident light absorbed by the sample. Therefore, $F[A]\,\epsilon_A\,l_{irr}$ represents a fraction of the incident light absorbed exclusively by A species. After multiplying by $\phi\,I_0$, one obtains a complete term describing the moles per liter of the A species transformed into the B species per second.[62]

Equations 29 require numerical integration to be solved. If one is very determined to find an analytical solution, it is possible to neglect the evolution of the photokinetic factor F by fixing it, then the numerical approach can be avoided. The assumption that F is constant is justified only if the sample is irradiated at the isosbestic point, where all the species have the same molar absorption coefficient.

Going further, one can build much more sophisticated schemes. For example, the one presented below describes a system where the sequential absorption of two photons is required to populate the C form.

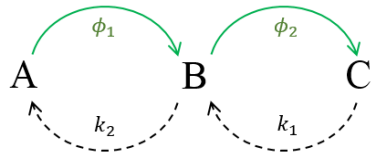

$$\begin{cases} \dfrac{d[A]}{dt} = -\phi_1\,I_0\,F\,[A]\,\epsilon_A\,l_{irr} + k_2\,[B] \\ \dfrac{d[B]}{dt} = \phi_1\,I_0\,F\,[A]\,\epsilon_A\,l_{irr} - \phi_2\,I_0\,F\,[B]\,\epsilon_B\,l_{irr} + k_1\,[C] - k_2\,[B] \\ \dfrac{d[C]}{dt} = \phi_2\,I_0\,F\,[B]\,\epsilon_B\,l_{irr} - k_1\,[C] \end{cases} \tag{31}$$

Figure 24. Two-photon model

Using this method, one can simulate very complex models, by solving the differential equations. It can be done using *scipy.integrate.odeint* procedure available in the Python environment. In this work a custom package has been developed, which allows to solve such schemes directly (a program can be used to generate a proper set of equations from the diagram and solve it).[63]

2.4 OCP sample preparation

All the proteins used in this work were produced, prepared and made available to the author of this thesis by the Emeritus CNRS Director Diana Kirilovsky's team (Institute for Integrative Biology of the Cell, CEA Paris-Saclay), prof. Ilme Schlichting's team (Max Planck Institute for Meducal Research, Heidelberg) and CNRS Research Director Jacques-Philippe

Colletier's team (Institut de Biologie Structurale, Grenoble, France). The proteins were extracted directly from the cyanobacterial cells (*Synechocystis* binding hECN carotenoid) or expressed in *E. coli* (in this case OCP binds ECN or CAN carotenoids). Production of the OCP directly within *Synechocystis* cells is very inefficient. In this case, the cyanobacteria are grown in large Erlenmeyer flasks in a rotary shaker, under the light intensity of approximately 100 μmol m^{-2} s^{-1}. Before purification, the cells dissolved in tris-HCl buffer (at pH 8.0) are prepared, and broken with a French Press. The supernatant separated from the pelleted membranes is loaded into the Nickel-chelating resin column. It has a high affinity to proteins containing polyhistidine tag (6xHis sequence added to the N-terminus or C-terminus). The OCPs bound to the column resin are eluted later and finally purified using ion-exchange chromatography.[15, 17, 64-65]

To produce a large amount of the OCP, the *E. coli* cells were used. The cells with 3 plasmids were prepared. The pAC-Beta plasmid carried genes responsible for β-carotene synthesis, pBAD-crtO plasmid carried genes responsible for CrtO enzyme production (which converts β-carotene into ECN), pCDF-OCP plasmid carried the *ocp* gene. If the CrtO enzyme (monoketolase) is replaced with CrtW (diketolase), the CAN carotenoids are produced instead of the ECN. The transcription of the *crtO*/*crtW* genes and *ocp* gene were controlled by special promoters, which are triggered by the presence of arabinose or IPTG (isopropyl β-D-1-thiogalactopyranoside). It allows to induce sequential expression of the contributing genes. This way a high concentration of the proper carotenoids is ensured before the OCP synthesis starts. This method allowed to obtain cells with high OCP concentration and low percentage of apo-OCP (possessing no carotenoid).[64]

Samples are stored in a freezer for a long term (ideally at -80 °C), and in the fridge for a short term (between experiments, maximum of a few days). Repeated freezing/unfreezing damages OCP samples, therefore they are divided into aliquots, and each aliquot is never freezed/defreezed more than 3 times (preferably only once). After the unfreezing, samples are centrifuged to remove any floating solids, which are a result of protein degradation. If necessary, samples are diluted with 40 mM tris HCl pH 8.0 buffer.

3. Photophysics of carotenoids

Most of the experiments performed within this thesis are based on direct spectroscopic observation of the carotenoid, not the protein itself. The protein creates an environment, which modulates the properties of the carotenoid, so conclusions for the protein dynamics are usually drawn indirectly. Therefore is crucial to understand the nature of carotenoids first and build simple analogs, which later can help in understanding of the whole system.

In this chapter, the photophysical properties of carotenoids are introduced. Firstly, in section 3.1 the roles performed by carotenoids in living organisms are promptly described. Then, in section 3.2 polyene molecule will be discussed. Carotenoids inherit a lot of their properties from polyenes, therefore it is a good starting point before looking directly at carotenoids. The symmetry of the polyene molecules is a very important aspect, determining its electronic structure and optical spectroscopic properties. It results in a forbidden $S_0 \rightarrow S_1$ transition, which is not a usual property among pigments. Carotenoids inherit this property, despite violating the polyene symmetry. However, violation of the symmetry may result in the presence of Intramolecular Charge Transfer State (ICT). In section 3.3, the effect of environment and structure on carotenoids is discussed based on available knowledge. Due to the abundance of carotenoid molecules, as well as various possible environments (solution phase, various proteins), the general properties of the carotenoids will be emphasized. Some generalizations are necessary in order to draw conclusions relevant to the OCP. Unfortunately, most of the studies present in the literature were performed for carotenoids other than ECN, CAN and hECN, which are significant for the OCP. Therefore, this chapter is an attempt to review the literature concerning the photophysical properties of the carotenoids, especially the ones important for the OCP function, such as the nature of the S_1, ICT and S* states.

3.1 Carotenoids in light harvesting and photoprotection

Interestingly, carotenoids perform a variety of functions the photosynthetic organisms, apart from being the chromophore in the OCP. Carbonyl carotenoids are very common accessory pigments in solar light harvesting.[66-68] They are capable of transferring electronic excitation to chlorophylls with very a high efficiency, despite short excited state lifetime.[66-68] Since the absorption band of carotenoids can be tuned by the length of the conjugated double bond system, they can be optimized to harvest various light wavelengths.[69-70] β-carotene can be found in photosynthetic reaction centers, lutein and neoxanthin in light-harvesting antennae, violaxanthin, zeaxanthin and other carotenoids in lipid membranes, where they are synthetized.[71] Carotenoids are effective antioxidants. They effectively quench triplet state chlorophyll and Reactive Oxygen Species (ROS), such as singlet oxygen.[66-68, 72] ROS are toxic products of photosynthesis, however recent studies also point to their signaling function associated with acclimatory responses and role in programmed cell death.[71, 73] Carotenoids scattered across photosynthetic apparatus take place in the ROS metabolism, and can neutralize ROS before the damage is done.[71] Physical $^1O_2$ quenching allows to safely dissipate the excited state energy and neutralize harmful ROS species. Alternatively, chemical $^1O_2$ quenching leads to various carotenoid oxidation products, like cyclic

endoperoxides, which are known markers of oxidative stress in plants.[71] Interestingly, different carotenoid isomers are selected for different biological functions.[74] It was shown that 15-*cis* isomers (bent in the middle) are present in the reaction centers, while all-*trans* isomers (straight) can be found in the light-harvesting complexes. It seems that *cis* isomers are better suited to quench the chlorophyll triplet states.[74]

An interesting example of elaborate photoprotective activity is a xanthophyll cycle, for example, VAZ cycle (violaxanthin → zeaxanthin), present in plants and algae.[4-5, 75-78] Upon strong irradiation, zeaxanthin molecules are enzymatically formed by removal of the epoxy group in violaxanthin. This process is reversed in the dark. Zeaxanthin presence enhances NPQ, affects the thylakoid membrane fluidity and modifies the organization of the light-harvesting complex.[4-5, 75-78]

3.2 Polyenes – simplified carotenoid molecules

The simplest model approximating the carotenoid molecule is the potential well model. After removing the terminal rings of carotenoid and side methyl groups, one usually ends with a polyene molecule, which is built from carbon chain of alternating single and double bonds. Because π electrons in the polyene are delocalized and can move along the whole chain of the molecule, one can use a simple potential well model to have a glimpse of their simplified wavefunctions (neglecting repulsion between electrons and other crucial effects). Solutions of Schrödinger's equation for potential well can be found in any introduction to quantum mechanics[79], wavefunction of 3 lowest energy "orbitals" are plotted in Figure 25. n is a number of the orbital, x is a coordinate along the polyene of L length, h is the Planck constant, m is a weight of the electron. Hexatriene, which we use as an example, has 6 π electrons, delocalized along 5 carbon-carbon conjugated bonds. **x** coordinate is scaled, unity is equivalent of one bond length so $L = 5$. Each wavefunction is occupied by two electrons with antiparallel spins. Therefore HOMO has $n = 3$ (and 2 nodes) and LUMO $n = 4$ (and 3 nodes).

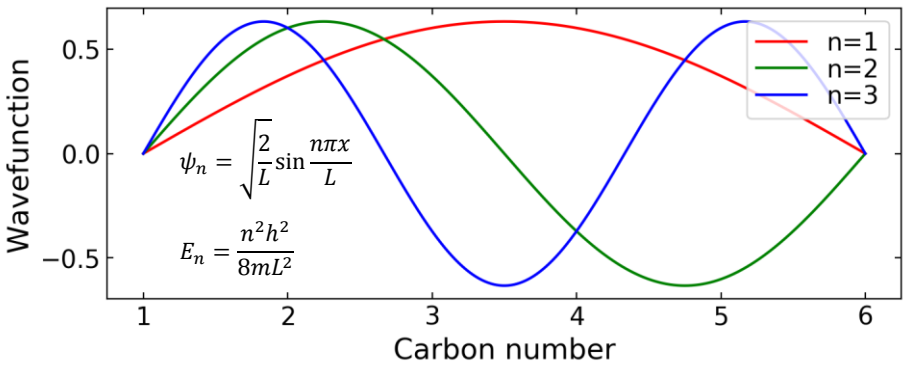

Figure 25. Wavefunctions from potential well equation as a trivial model of π electrons in polyenes.

Using such a trivial approach, it can be rationalized why longer polyenes (and carotenoids) experience redshift of the ground state UV-vis absorption band, when conjugated chain length increases. For hexatriene approximated by potential well, the energy gap between HOMO and

LUMO is $\Delta E = E_4 - E_3 = \frac{4^2h^2}{8m\,5^2} - \frac{3^2h^2}{8m\,5^2} = \frac{7h^2}{200m} = 0.035\frac{h^2}{m}$. If one extends this structure with an additional C=C-C unit (obtaining octatetraene), the length will be increased from $L = 5$ to $L = 7$, and additional pair of π electrons will be added. So in this case $\Delta E = E_5 - E_4 = \frac{5^2h^2}{8m\,7^2} - \frac{4^2h^2}{8m\,7^2} = \frac{9h^2}{392m} = 0.023\frac{h^2}{m}$. This energy gap is clearly smaller than for shorter hexatriene, indicating a redshift of the stationary UV-vis absorption band. Qualitatively the same effect can be derived from Hückel method[80], which is a more formal and complicated approach. Note that in reality π electron density is located on both sides of the conjugated polyene plane and no electron can be found directly on this plane.

It is a general rule, that for longer polyenes/carotenoids, the S_0 - S_2 and S_0 - S_1 energy gaps are decreasing (S_0 - S_1 decreases faster, so S_1 – S_2 increases when longer polyenes are considered[81-82]). The same trend can be observed in the excited state lifetimes τ_{S_1}, which settle when the conjugated bond length reaches a certain limit.[83]

Symmetry of polyene molecule

Many simple carotenoids can be described in terms of **C_{2h}** symmetry point group. It contains the following symmetry operations: i) **E** identity operation, ii) **C_2** a twofold symmetry axis, iii) **i** center of inversion, iv) **σ_h** a horizontal mirror plane (see Figure 26). This symmetry becomes much more evident, when we consider the polyene molecule, which is a carotenoid deprived of the terminal rings and side methyl groups. Indeed, various properties of polyenes are inherited by carotenoids, therefore it is useful to discuss them first due to their simplicity. Especially the electronic properties of the carotenoids are derived from polyene conjugated bond backbone, and modulated by the terminal rings and additional functional groups.

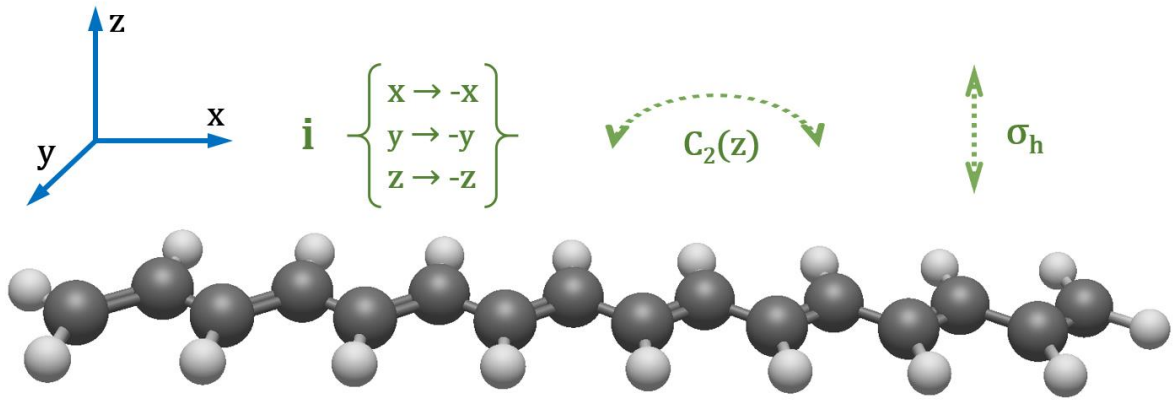

Figure 26. Polyene molecule and symmetry operations

The presence of any molecular symmetry usually implies, that some electronic transitions may be forbidden due to zeroing of the transition dipole moment. Table 1 shows all irreducible representations of the **C_{2h}** point group.[84] Each electronic state of the molecule must be assigned to one of the four possible representations, and its wavefunction must belong to the basis functions of the representation. Columns on the right of the table show basis functions. Characters (1 or -1) determine, if the given function changes sign after a given symmetry operation. For example, $f(x, y, z) = z$ will stay the same after **E** and **C_2(z)** operations, but change sign ($z \rightarrow -z$) after **i** and

$\boldsymbol{\sigma_h}$ operations.[84] In order to understand polyene photophysics, it is useful to consider possible electronic transitions between the states of $\mathbf{A_g}$ and $\mathbf{B_u}$ symmetries. The transition dipole moment of $S_0 \rightarrow S_n$ transition along **x** axis can be calculated as $\mu_x = \int \psi_{S_0}^* \hat{\mu}_x \psi_{S_n} dr$. The electric dipole moment operator $\hat{\mu}_x$ has $\mathbf{B_u}$ symmetry ($\hat{\mu}_x = \sum_i q_i x_i$, check linear basis functions of $\mathbf{B_u}$ group in Table 1). Multiplication of two functions yields a function with characters that are products of characters associated with functions being multiplied. One can consider a transition between two states of $\mathbf{A_g}$ symmetry. In this case function under μ_x integral is the product of $\mathbf{A_g} \cdot \mathbf{B_u} \cdot \mathbf{A_g}$ symmetries. By multiplying characters from Table 1, one can see that the resulting characters are +1, -1, -1,+1, so the function in the integral has $\mathbf{B_u}$ symmetry. It implies that $\mathbf{A_g} \rightarrow \mathbf{A_g}$ transition dipole moment along **x** axis must be zero, because none of the characters can be -1 in order to have a nonzero integral. For example, it is clear that when the integrated function is odd and changes the sign upon inversion (which is indicated by -1 character for **i** operation), the integral is zero. The analogic rule follows for other symmetry operations. To have a nonzero integral value (allowed transition), the function under the integral must be fully symmetric ($\mathbf{A_g}$, where all characters equal +1). These considerations lead to the conclusion, that for light polarized along **x** axis (and **y**, because this is an analogic case) $\mathbf{A_g} \rightarrow \mathbf{A_g}$ transition must be forbidden. A similar calculation can predict, that for light polarized along **z** axis, $\mathbf{A_g} \rightarrow \mathbf{A_g}$ transition is also forbidden ($\mathbf{A_g} \cdot \mathbf{A_u} \cdot \mathbf{A_g}$ symmetry functions under the integral results in $\mathbf{A_u}$ symmetry, which possess -1 characters). So electronic transitions between any two states of $\mathbf{A_g}$ symmetries in polyenes must be forbidden, and this result is critical for further considerations. One can easily verify, that transitions between any two $\mathbf{B_u}$ states are also forbidden. What are the implications for transitions between $\mathbf{A_g}$ and $\mathbf{B_u}$ symmetry states? For the **x** and **y** polarized light, the symmetries under the integral are $\mathbf{A_g} \cdot \mathbf{B_u} \cdot \mathbf{B_u}$, so after multiplication the characters are +1,+1,+1,+1. Therefore $\mathbf{A_g} \rightarrow \mathbf{B_u}$ transitions are not forbidden by symmetry. However, the integral for **z** axis is also zero, which implies that the transition dipole moment of the polyene must be located at the XY plane.

Table 1. Character table for point group C_{2h}.[84] Rows describe irreducible representations, u and g subscripts indicate orbitals change upon inversion, B and A indicate change upon rotation. Therefore in B_u representation, the wavefunction sign is changed upon both inversion and rotation, which can be inferred from the -1 characters in $C_2(z)$ and i column.

C_{2h}	E	$C_2(z)$	i	σ_h	linear functions, rotations	quadratic functions
A_g	+1	+1	+1	+1	R_z	x^2, y^2, z^2, xy
B_g	+1	-1	+1	-1	R_x, R_y	xz, yz
A_u	+1	+1	-1	-1	z	-
B_u	+1	-1	-1	+1	x, y	-

It has been determined, that the polyene ground electronic state has **1** $^1\mathbf{A_g}^-$ symmetry (meaning that it is the first lowest energy singlet state of $\mathbf{A_g}$ symmetry, **-** sign will be explained later).[85] S_1 state has **2** $^1A_g^-$ symmetry, the same as S_0. S_2 state has **1** $^1\mathbf{B_u}^+$ symmetry. Therefore transition between S_0 and S_1 states is forbidden, because they possess the same $\mathbf{A_g}$ symmetry. A

stationary polyene absorption band in the visible range represents $S_0 \rightarrow S_2$ transition, which is symmetry-allowed. $S_0 \rightarrow S_2$ transition dipole moment is parallel to the conjugated bond chain.[85]

Limitations of trivial polyene picture

Atomic 2p orbitals change their sign under reflection in their symmetry plane (-1 characters for $\boldsymbol{\sigma_h}$ operation in Table 1), therefore π orbitals must belong to $\mathbf{A_u}$ or $\mathbf{B_g}$ symmetry classes.[85] π-electron orbitals ordered with respect to increasing energy are expected to alternate between $\mathbf{A_u}$ or $\mathbf{B_g}$ symmetries, which can be rationalized by wavefunctions in Figure 25 (n=1 is even upon inversion, n=2 is odd, etc.). Since polyenes possess 2n π-electrons, the wavefunction of polyene electronic state will have symmetry determined by the product of the characters of the occupied spinorbitals.[85] It can result only in an $\mathbf{A_g}$ or $\mathbf{B_u}$ symmetry. If all the orbitals are doubly occupied (for example in the ground state), the resulting symmetry must be $\mathbf{A_g}$ (the result of the character multiplication will be always +1,+1,+1,+1, check Table 1). It is usual for the electronic ground state to possess $\mathbf{A_g}$ symmetry. If one electron is excited to the orbital with changed symmetry (for example after HOMO→LUMO transition), the symmetry of such state must be $\mathbf{B_u}$. Using the same logic, HOMO→LUMO+1 transition should produce an $\mathbf{A_g}$ symmetry state, because the symmetry of LUMO+1 is expected to be the same as that of HOMO. Note that the σ-electron core is usually fixed and doubly occupied, therefore not affecting the overall symmetry.[85] This idyllic picture totally neglects effects of electron correlation (electrons are treated independently, there is no Columbic repulsion), therefore it miserably fails to describe the experimental picture, where the first excited state has $\mathbf{A_g}$, not $\mathbf{B_u}$ symmetry.[85]

Moreover, bonds between carbon molecules are not ideally conjugated, which is manifested in bond length alteration.[83] C=C bonds are slightly shorter than C-C bonds, which means that π electrons are not perfectly delocalized. This effect decreases with the increase in polyene length, and disappears for the infinite polyenes, where carbon-carbon bonds have perfectly conjugated character (like in benzene molecule).[83]

It has been established experimentally, that the first singlet excited state is located below symmetry allowed $\mathbf{1}\ {}^1\boldsymbol{B_u}^+$ state and has the same $\mathbf{A_g}$ symmetry as the ground state.[86-94] As already discussed, $\mathbf{1}\ {}^1\boldsymbol{A_g}^- \rightarrow \mathbf{2}\ {}^1\boldsymbol{A_g}^-$ symmetry transition is symmetry forbidden, so its contribution to the ground state UV-vis absorption spectrum is negligible, and this property is general for polyenes and carotenoids as well.[86, 88, 95-97] Despite one photon transition from the ground state to the first singlet excited state is forbidden, two-photon $S_0 \rightarrow S_1$ transition is allowed.[98]

S_2 state has $\mathbf{B_u}$ symmetry, which allows $S_0 \rightarrow S_2$ transition.[95, 97, 99-100] To reproduce these energy levels correctly, complex quantum chemistry calculations are required, for example, Configuration Interaction (CI) methods taking into account both double-excited and single-excited configurations (or even triple and quadruple, for longer polyenes). Addition of proper configurations results in decreasing the energy of the first excited $\mathbf{A_g}$ symmetry state below the first excited $\mathbf{B_u}$ symmetry state, without significant alteration of the $\mathbf{1}\ {}^1\boldsymbol{A_g}^- \rightarrow \mathbf{1}\ {}^1\boldsymbol{B_u}^+$ transition energy itself.[95, 97, 99-100] Unfortunately, discussion of these issues greatly exceeds the scope of this work.

Distorted C_{2h} symmetry and alternacy symmetry

Carotenoids inherit the basic symmetry properties of the polyenes. However, it is important to mention, that some carotenoids encountered in the OCP (therefore relevant for this thesis), deviate significantly from the $\mathbf{C_{2h}}$ symmetry point group. Carotenoids like hydroxyechinenone possess two different terminal groups on both ends (hydroxyl and carbonyl). Even the symmetric carotenoids such as canthaxanthin are heavily bent in the carotenoid binding pocket, which breaks the inversion symmetry. Surprisingly, it causes no visible absorption indicating the presence of $S_0 \rightarrow S_1$ transition, there is no redshifted band in the stationary absorption spectra. With broken symmetry, and geometry bent due to interaction with the protein cavity, the $S_0 \rightarrow S_1$ transition is still forbidden. Even in highly asymmetrical peridinin, it was estimated that the $S_0 \rightarrow S_1$ transition is still 100 times less allowed than the $S_0 \rightarrow S_2$ transition.[101] It has been found that even isomerization at the centrally located double bonds do not affect the nature of this transition significantly![29] The reason is, there are different types of symmetries, which are preserved even if $\mathbf{C_{2h}}$ symmetry is heavily violated. Especially so-called "alternacy symmetry" is crucial, which applies to the systems of conjugated bonds.[29, 81-82, 102-105] It stems from the topological feature of alternant, unsaturated hydrocarbons, where carbon atoms can be divided into two disjunct and equivalent sets (=C- and -C= atoms). States are classified to **+** of ionic nature (called "charge transfer" excitations) or **-** of covalent nature (called "spin-wave" excitations). **+/-** sign indicates even/odd particle-hole symmetry in the conjugated bond chain. Transitions between states of the same sign are forbidden. Ionic **+** states are usually well described by singly excited configurations. Covalent **–** states require at least doubly excited configurations to construct highly correlated state. It is necessary to obtain flat, uniform electron distribution, and minimize electron-electron repulsion.[29, 81-82, 102-105]

In 2016, an attempt was made to explain the effect of forbidden $S_0 \rightarrow S_1$ transition with a different approach.[106] It has been proposed, that in carotenoids such as β-carotene the true symmetry is C_2, and $S_0 \rightarrow S_1$ transition is in fact symmetry allowed. But due to the highly different, nonplanar geometry of the S_1 state compared to S_0, it is unreachable directly from the ground state.[106]

Electronic structure of polyenes

As already mentioned, calculation of the excited state energies in polyenes requires many electron configurations to account correctly for the electron correlation energy.[81-82, 97] It is especially crucial for the S_1 ($\mathbf{2}\ ^1\boldsymbol{A_g^-}$) state, and correctly predicting its lower-than-S_2 state energy is a major computational challenge. S_1 state is characterized by collectively excited configurations of the π electrons spin degrees of freedom (triplet configurations).[81-82, 97] One can easily rationalize the requirement of taking into account electron correlation, by realizing that Hückel resonance interaction results in delocalization of the π electrons, which can move freely over the whole conjugated molecular backbone.[85] So they are expected to meet quite often at the same atomic sites, which however is affected by Coulomb repulsion. To account for this effect, the motion of the electrons must be correlated to avoid each other. Therefore, without taking electron correlation, no proper description of the system can be introduced.[85]

Quantum chemical calculations have demonstrated that **2** $^1A_g^-$ is not the only state, in which energy may drop below the optically allowed **1** $^1B_u^+$ state. When conjugation length increases, the energy of the **1** $^1B_u^-$ state may drop below the **1** $^1B_u^+$ state[81-82, 100] and affect the photophysics, especially by shortening the **1** $^1B_u^+$ state lifetime.[91, 107-114] If the conjugation length is even longer, the **3** $^1A_g^-$ state energy can also decrease below the **1** $^1B_u^+$ state, adding additional complexity to the system.[115] Some reports indeed identified short living state in various carotenoids mediating S_2 relaxation ($S_2 \rightarrow S_X \rightarrow S_1$), abbreviated as S_X.[112, 116-120] This state is presumably a manifestation of the **1** $^1B_u^-$ state.[112, 116-120]

These findings render the S_0, S_1, S_2... nomenclature problematic, meaning that the first optically allowed singlet state may be higher than S_2 in some longer polyenes/carotenoids. Nevertheless, for the sake of simplicity, the states will be denoted in the following order S_0 (**1** $^1A_g^-$), S_1 (**2** $^1A_g^-$), S_2 (**1** $^1B_u^+$). However, it is important to keep in mind, that this ordering may be altered in reality and affect the photophysics of the longer carotenoids (see Figure 27).

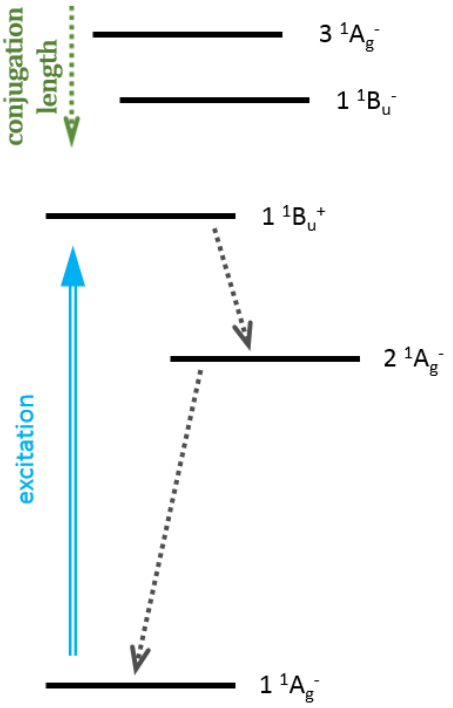

Figure 27. Excited states in polyenes. Increasing the conjugation length downshifts the energy of some higher electronic states.

Solvent polarizability shifts the $S_0 \rightarrow S_2$ absorption band to the red, due to dispersion interaction, as spectral shifts are proportional to $(n^2 - 1)/(n^2 + 2)$. $S_1 \rightarrow S_0$ fluorescence is much less affected by the solvent.[85] It is consistent with theory, where spectral shifts due to the dispersion interaction are proportional to the transition dipole moment, which is small for the S_1 state.[85] Vibrational structure in the polyenes absorption spectrum usually shows two important vibrational modes, single-bond C-C stretching about 1200 cm^{-1} and double-bond C=C stretching about 1600 cm^{-1}.[85] C=C stretching mode energy is significantly altered upon $S_0 \rightarrow S_1$ excitation, for example in β-carotene from 1521 cm^{-1} to 1777 cm^{-1}.[121] This vibrational mode plays an important role in **2** $^1A_g^- \rightarrow$ **1** $^1A_g^-$ internal conversion.[109]

3.3 Carotenoids

Nonpolar carotenoids

Carotenoids are more complex molecules than polyenes. For example, β-carotene is built from eight isoprene units arranged in a symmetrical way, so a long polyene chain structure is created, with additional side CH_3 groups, having 40 carbon atoms in total (Figure 28).[122] In some cases, terminal parts of the carotenoid forms a ring, which is the case of β-carotene (β indicates a β-ionine type of this ring).[122] All carotenoids, which are of importance for the OCP, are derivatives of β-carotene, and possess additional functional groups attached to the terminal rings.

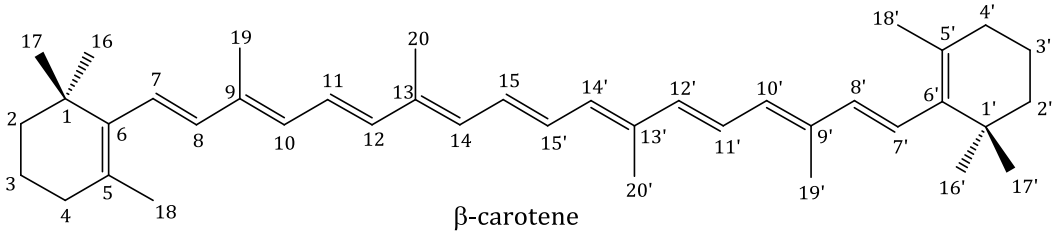

Figure 28. β-carotene structure

Carotenoid analogs of compounds like β-carotene (with terminal rings)[69] or spheroidene (without terminal rings)[70] with various polyene chain lengths have been extensively described in the literature. Their properties are quite general for all carotenoids without specific functional groups that might disturb the charge distribution in the molecule. They inherit the majority of their properties from simple linear polyenes. There is general dependence, that the lifetime of the S_1 state of carotenoids depends on polyene chain length, and each additional C=C bond shortens the lifetime by a factor of two.[69, 123] In nonpolar toluene, β-carotene has 8 ps τ_{S_1} lifetime.[124] Presence of any additional terminal groups does not affect the nature of the S_1 state, provided that a nonpolar solvent is used.[123] Carotenoids emit from both S_2 and S_1 state, violating the Kasha rule.[125] Absorption maxima of the S_0 state (in the stationary spectrum), as well as the S_1 state (in the transient spectrum) follow similar rule - an increase in conjugated bond system length redshifts these bands.[123] However, for very long carotenoids (longer than β-carotene), energy gap between S_1 and S_2 states increases so much, that $S_1 \rightarrow S_0$ internal conversion becomes very efficient (due to small S_1 - S_0 energy gap), and no fluorescence from S_1 state can be observed, leaving only fluorescence from S_2 state.[69-70, 126] S_2 state of the β-carotene has 180 fs decay time constant in *n*-hexane.[127]

For nonpolar carotenoids in nonpolar solvents, high polarizability of the solvent affects the $S_0 \rightarrow S_2$ transition, causing absorption band redshift, due to dispersion interaction between strong $S_0 \rightarrow S_2$ transition dipole moment and solvent polarizability (an effect known as Kundt's rule).[85, 128-131] If carotenoid or solvent are polar, this effect can be accompanied by other interactions.[85, 128-131] Analogically to polyenes, $S_1 \rightarrow S_0$ transition dipole moment is very small, therefore the effect of the solvent polarizability is negligible.[85] Internal conversion from S_1 to S_0 in β-carotene is coupled with in-phase C=C stretching mode.[109]

$S_2 \rightarrow S_1$ internal conversion of polyenes is accelerated, when the polyene chain is methyl-substituted (like in β-carotene), due to the increased density of vibronic states.[132] On the other hand, methyl substitution does not decrease $S_2 - S_1$ energy gap.[132] Repulsion between the methyl group located on β-ionylidene ring and the closest hydrogen on the polyene chain forces the ring out of the conjugated bonds plane, creating a distribution of conformers and introducing a broadening of the ground state absorption spectrum.[133] Therefore, due to presence of the β-ionylidene ring in the β-carotene, the effective conjugation length is shorter than could be expected.[133]

Carotenoids possess an interesting absorption band located usually between 300 nm and 350 nm, called "*cis*-peak".[134-136] It represents the transition between $A_g^- \rightarrow A_g^+$ symmetries, which is forbidden in symmetric all-*trans* conformation, but starts to appear when the symmetry is

violated by isomerization. The magnitude of this band, relatively to the main absorption band, is very small when *cis* isomerization is located in close proximity to the terminal rings, but grows significantly when it is located at the central part of the conjugated bond chain (15-*cis* isomer). The presence of this peak is a valuable indicator of isomerization in carotenoids.[134-136] All-*trans* isomers generally are the most stable compared to *cis*-isomers in solution.[137] S_1 lifetimes of the all-*trans*, 7-*cis*, 9-*cis*, 13-*cis* and 15-*cis* isomers are similar to each other. The isomerization process does not occur in the S_1 state.[74]

There are carotenoids, that break out from these general characteristics, like peridinin (Figure 29B), which are affected by the presence of a Charge Transfer (CT) state.[101, 138] In our case carbonyl carotenoids are of special interest, due to their relationship with OCP (see ECN and CAN structures in Figure 29B).

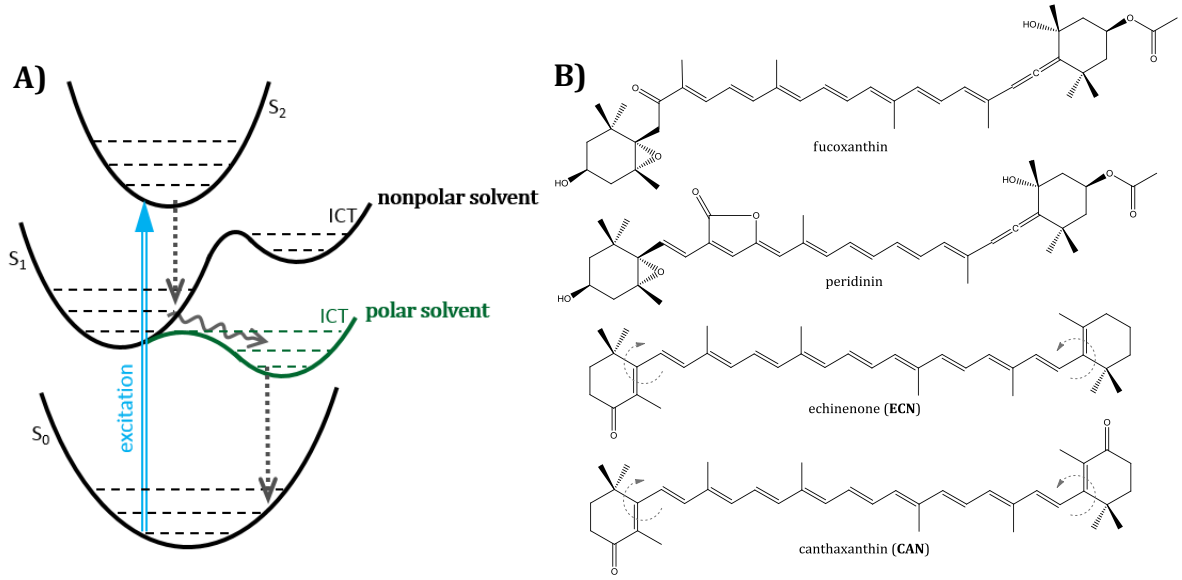

Figure 29. A) Carbonyl carotenoids with ICT state, which energy decreases with increase in the solvent polarity. B) Structures of commonly investigated carbonyl carotenoids.

Carbonyl carotenoids and ICT state

All carotenoids encountered in photoactive variants of OCP possess a carbonyl group.[139] Carotenoids possessing a carbonyl group coupled with polyene conjugated bond system may be sensitive to solvent polarity, in contrast to carotenoids lacking this group.[101] It is due to electron-withdrawing property of carbonyl group affecting charge distribution of the polyene chain.[101] To explain the effect of the polar solvents on the first excited state lifetime of the carbonyl carotenoids, presence of ICT (Intramolecular Charge Transfer) state has been postulated.[101, 138, 140-147]

Solvent polarity has a great stabilizing effect on the ICT state, decreasing its energy (Figure 29A).[101, 148] While the S_1 state usually absorbs above 550nm ($S_1 \rightarrow S_n$), the ICT state, which is exclusive for carbonyl carotenoids, absorbs above 600nm ($S_{ICT} \rightarrow S_{n'}$ where $S_{n'}$ has A_g^+ symmetry[149-150]). Photophysics mentioned above can be explained in the following way: ICT and S_1 states are strongly coupled, establishing a common potential energy surface (often referred to as mixed S_1/ICT state).[101, 148] When ICT energy drops below S_1 state energy, new minimum on the

potential energy surface is established.[101] It facilitates faster radiationless decay to the ground state (due to the energy gap law), causes a redshift of the fluorescence and blueshift of the $S_{ICT}\rightarrow S_{n'}$ absorption band. Moreover, it is accompanied by a decrease in $S_1\rightarrow S_n$ band magnitude and an increase in $S_{ICT}\rightarrow S_{n'}$ band magnitude in the transient absorption spectrum.[101]

After the excitation of carbonyl carotenoid, the S_2 state is populated, which usually has a lifetime below 100 fs.[140] It decays to the ICT/S_1 state, which is characterized by lifetime of a few ps or less.[140] Carbonyl carotenoids exhibit an anomalous behavior, showing significant decrease in the ICT/S_1 state lifetime when solvent polarity exceeds certain threshold.[101] This effect is not present, if two carbonyl groups are arranged symmetrically.[145, 151] Moreover, it has been demonstrated, that carbonyl group must be effectively conjugated with the central double bond system.[149] It has been proposed, that in symmetrical carbonyl carotenoids, ICT state is populated as well, but $S_{ICT}\rightarrow S_{n'}$ absorption band is not visible, because $S_{n'}$ has A_g^+ symmetry, so the transition is symmetry forbidden, but the ICT state is still there.[149] Some carotenoids, which possess carbonyl group at the terminal rings, which are decoupled from the central polyene chain due to *s-cis* conformation in solution phase, show no ICT character.[152] Strength of carbonyl group coupling is reflected in the time-resolved spectroscopy data, especially in the magnitude of the charge-transfer character, manifested especially in i) $S_{ICT}\rightarrow S_{n'}$ absorption band above 600 nm in the transient absorption spectrum and ii) fluorescence from the S_1/ICT state visible above 950 nm.[140] Conversely to dramatic polarity influence, no significant influence of solvent polarizability on S_1/ICT states has been observed.[138]

The S_2 lifetime in polar solvents is also shortened in carbonyl carotenoids compared to noncarbonyl ones, due to a narrower S_2 – S_1/ICT energy gap.[127, 140] It is because the presence of the carbonyl group decreases the energy level of the S_2 state, reducing the gap between the ICT/S_1 and S_2 states.[140, 153] However, the energy of the S_2 state is not influenced by solvent polarity, contrary to the ICT state.[140] A high degree of conjugation between the carbonyl group and the polyene chain (the carbonyl group must be in *s-trans* configuration and planarity must be preserved) strengthens the fluorescence from the S_1 state, compared to the S_2 state fluorescence.[154] In nonpolar solvents, one can only detect fluorescence from the S_1 state, located in the 600-800 nm region.[141] In polar solvents, the S_1 state fluorescence is overwhelmed by emission from the ICT state located in NIR around 1000 nm.[141]

The existence of a carbonyl group results in conformational disorder manifested in a spectral broadening of the ground state absorption band, which is especially pronounced in the polar environment.[101, 140, 148] In highly polar solvents the vibrational structure of the ground state absorption band disappears, due to strong interactions between the carbonyl group and polar solvent molecules.[101, 140, 148] It was also found that the presence of the carbonyl group accelerates vibrational relaxation in the excited states in the solution phase.[153]

Based on the case of peridinin (Figure 29B) and its analogs, it has been found that ICT state lifetime does not depend on conjugated chain length.[146] Moreover, analysis of transient absorption spectra suggest, that ICT and S_1 deactivate independently.[146] On the other side, for the series of analogs of fucoxanthin with varied polyene chain length, it was found that only short ones possess

ICT character.[155] It may be due to very low S_1 state energy obtained usually for a long conjugated chain lengths.[155]

The nature of the ICT state is still a matter of debate. There are numerous experimental studies, explaining the ICT state in different ways. Chatterjee et al. and Papagiannakis et al. concluded, based on peridinin and its analogs, that ICT and S_1 are different, but strongly coupled states separated by energy barrier, and they deactivate independently (Figure 30).[146, 156-158] Redeckas et al. study of fucoxanthin supported these findings, moreover they found that there is an equilibrium between ICT and S_1 states, which is restored with τ = 1.7 ps after ICT is depleted by stimulated emission.[159] On the other side, Durchan et al. investigated 8′-apo-β-carotenal and claim that the "ICT band" stems from the same S_1 state and its presence in polar solvents is caused by C_{2h} symmetry breaking, which enables the $S_1 \rightarrow S_3$ transition visible between 600 nm and 700 nm.[150] Shima et al. found, that S_1 state in peridinin (which possess carbonyl group) has much higher dipole moment (16 D in polar and nonpolar solvents) than the ground state (6 D in nonpolar solvents and 8 D in polar solvents).[160] No additional ICT state was found, suggesting that S_1 gains the ICT nature when carbonyl group is attached to the conjugated bond chain.[160] Kosumi et al. claim that ICT is a separate state, populated directly from the S_2.[144] Vaswani et al. calculated the energy of ICT state and found that it is close to S_2 state, but the presence of polar solvent can decrease its value below S_1.[161] Quantum chemistry calculations of Enriquez et al. found, that 2 ^1A_g-like and 1 ^1B_u-like states form a linear combination in the presence of a polar solvent, and the resulting mixed state has a very high dipole moment (above 25 D), which is a good candidate for ICT.[145, 162-163] In this state, charge is moved towards the carbonyl group, and it is accompanied by bond-order reversal in the central part of the polyene chain.[145, 162-163] Spezia et al. found that the presence of conjugated carbonyl group results in low lying nπ* state, which may be responsible for the ICT characteristics.[164]

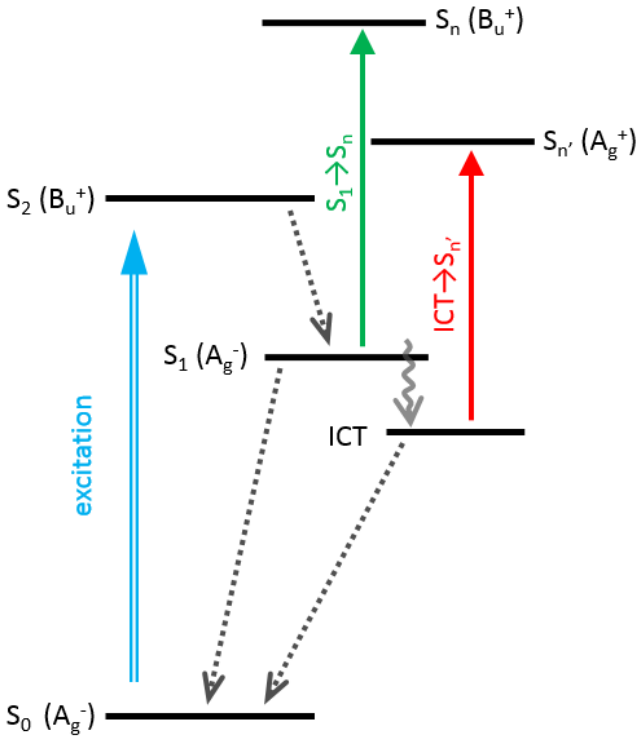

Figure 30. Carbonyl carotenoids excited states, assuming that ICT and S_1 are separate electronic excited states. Symmetry of the ICT state is hard to define due to asymmetrical nature of this state.

It has to be emphasized that there is a huge difference in carotenoids such as peridinin or fucoxanthin, where the carbonyl group is attached directly to the central polyene chain, and carotenoids such as canthaxanthin or echinenone, where carbonyl group is attached to the

terminal rings and can be decoupled by their rotation. Carbonyl carotenoids relevant for this study are canthaxanthin (CAN), hydroxyechinenone (hECN) and echinenone (ECN), their structures are presented later in Figure 46. Surprisingly, no ICT state has been observed in these carotenoids dissolved in polar solvents, despite they show other effects known for the carbonyl group, such as inhomogeneous broadening of the absorption band.[152, 165] It can be explained by the *s-cis* configuration of terminal rings, which decouples the carbonyl groups from the central double bond chain.[152, 165]

In toluene, CAN has a 5 ps lifetime of the S_1 state, compared to 8 ps of β-carotene.[124] In benzene, the S_1 state has a lifetime of 6.2 ps for ECN and 4.5 ps for CAN, compared to 9.3 ps observed for β-carotene.[152] The maximum of $S_1 \rightarrow S_n$ absorption band is located at 607 nm for ECN and at 620 nm for CAN, compared to 575 nm for β-carotene dissolved in benzene, with almost no contribution above 700 nm. S_2 state decays with a time constant faster than 100 fs for canthaxanthin and rhodoxanthin in benzene, and it is accompanied by $S_2 \rightarrow S_0$ stimulated emission at 500 nm.[152]

In search of the S state nature*

Various additional states involved in relaxation from the S_2 state have been proposed, which may be important, especially for the long carotenoids. One of these states, denoted as S*, is of special interest to us, due to its possible engagement in the OCP photoconversion.[28] Despite the results published within this thesis do not support a hypothesis that the S* state leads to the OCP^R form, it still affects the photophysics of the carotenoid in the OCP, so revealing its nature is essential.[166]

S_0* and S_1* states were firstly proposed to explain the relaxation of long homologs of β-carotene.[167] It was found, that after excitation to the S_2 state, it promptly relaxes to the S_1 state with an excess of vibrational energy (Figure 31). It results in an additional redshifted contribution to the S_1 ESA band, which decays faster (in a subpicosecond time scale) than the S_1 state, causing uneven evolution of the S_1 absorption band. This additional contribution was denoted as S_1*,

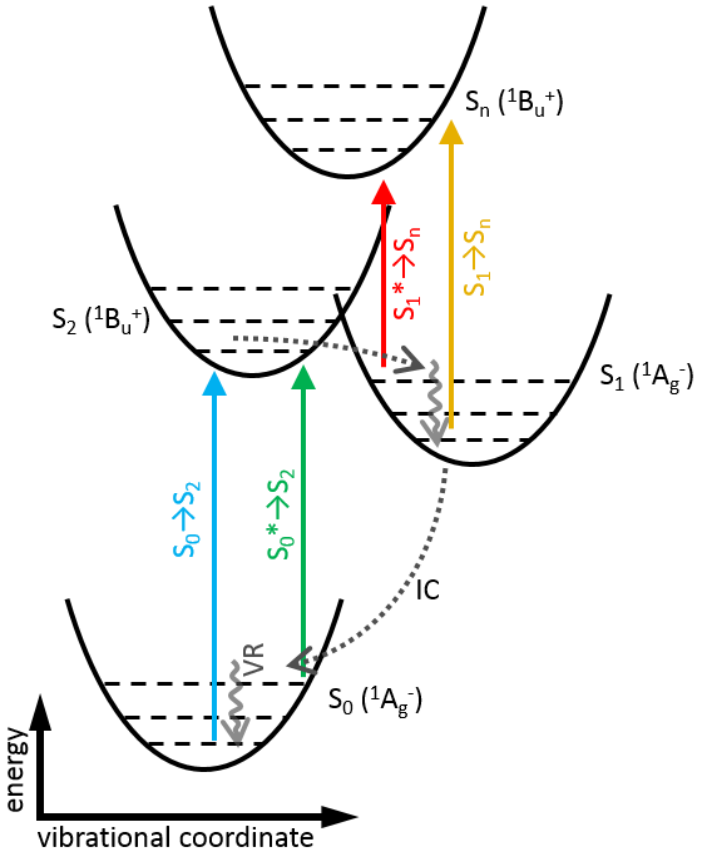

Figure 31. Vibrationally excited (hot) S_1 and S_0 states explain blue-shifted absorption bands with respect to species in thermal equilibrium.

underlining that this is a vibrationally and electronically excited state.[113, 167-168] Similar effect was observed after the decay of the S_1 state, which populates the S_0* state, a vibrationally excited S_0 state. Because the energetic gap between S_2 and S_0* states is smaller than between S_2 and S_0 (Figure 31), one can observe a positive S_0* band redshifted with respect to the ground state absorption of the S_0 state. This feature decays with a time constant on the order of magnitude of 10 ps.[167, 169] Vibrationally-excited origin of this state is also supported by time-resolved anti-stokes Raman scattering spectroscopy, which demonstrated the appearance of anti-Stokes bands (C=C and C-C stretching modes) growing after the excitation and decaying within tens of ps, which clearly indicate the presence of a hot ground state.[170] Through investigating the C=C and C-C vibrational stretching modes in spirilloxanthin by anti-Stokes resonance Raman spectroscopy, it has been found that after the deactivation of the S_1 state, the hot S_0 population indeed decays within a 50 ps time window.[170] Note that S_1 and S_0 states are strongly coupled via C=C stretching mode.[171] Therefore, vibrational energy in S_0* state is expected to be initially confined within this mode, and then redistributed among other modes, and dissipated to the solvent environment within S_0* state lifetime.[171]

The nature of the S* state is a matter of long debate, because in later studies it has been assigned as an electronically excited state serving as a precursor of triplet in spirilloxanthin of LH1 complex (*Rs. rubrum*), spheroidene of LH2 complex (*Rb. sphaeroides*) and other light-harvesting complexes.[172-174] The target analysis of the transient absorption data indicated that the S* may be populated directly from the S_2 state, and it has been proposed that it may be an excited state of covalent nature (**-** symmetry), for example, the $^1\mathbf{B_u}^-$ (this state has been shown to lie between **1** $^1\mathbf{B_u}^+$ and **2** $^1\mathbf{A_g}^-$ states in all-*trans*-spheroidene[108]).[114] As discussed in previous sections, the energy of states like **1** $^1\mathbf{B_u}^-$ and **3** $^1\mathbf{A_g}^-$ may be significantly lowered if the conjugation length is long enough. Moreover, these states have the potential to dissociate into two triplet states localized at separate areas of the long polyene chain if the carotenoid symmetry is distorted.[81] It has been also observed, that the S* state has a vibrationally well-resolved spectrum, the bleaching band suggests that this state emerged from some very specific geometry of the carotenoid.[172] In the presence of light-harvesting protein environment, the triplet excited state population is formed, causing a similar S_0 bleaching signature as the S*. Therefore it has been suggested, that the triplet state originates from S*, which then must also be an excited state of covalent nature (Figure 32). For spirilloxanthin in solution, no triplet state was found, but in the protein environment, where carotenoid symmetry is distorted, an excited triplet state population is formed.[172] So it was concluded, that the geometrical deformation caused by the protein environment, not the specificity of the carotenoid, tunes the S* state deactivation paths.[175]

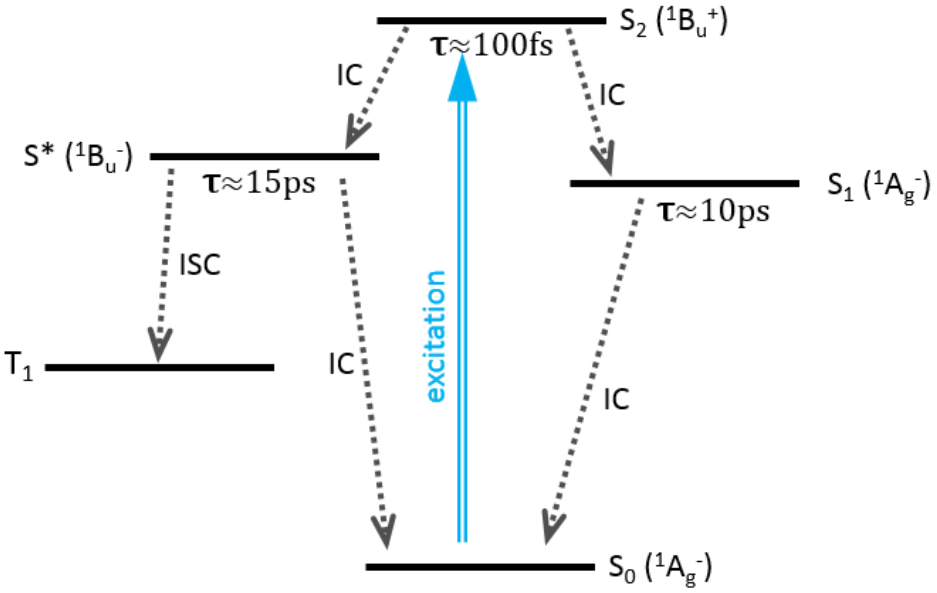

Figure 32. The S* state interpreted alternatively as a separate excited state in the protein environment, instead of invoking vibrational relaxation processes.

These observations have opened numerous questions. Especially, how do we know that all the states denoted as S* have the same nature in all the carotenoids and all types of environments? Latter pump-dump-probe absorption spectroscopy study with a series of β-carotene analogs in the solution phase resolved the nature of the S* as a vibrationally hot ground state.[176] Therefore, if S* is an electronically excited state in a protein environment, it must be a different state than the one in solution.[177] So it has been proposed, that "hot ground state" S* (S_0*) is populated both in solution and in light-harvesting proteins. To explain the presence of this state instantly after the excitation, it was proposed, that a spectrally broad femtosecond pump pulse, containing both stimulated Raman pump and red-shifted Stokes wavelengths, cause an efficient population of the S_0 excited vibrational modes.[177] Therefore S_0* can be populated both from S_1 relaxation (in general) and from S_2 by impulsive stimulated Raman scattering process (only after femtosecond pulse excitation). On the other hand, "electronically excited state" S* (which is in fact **1** $^1\mathbf{B_u^-}$ state, formed after the decay of S_2) is present only in the protein-distorted carotenoid, where it spectrally overlaps with much weaker S_0*. Accidentally, both states have completely different nature, but similar spectral signatures and lifetimes. Only the excited S* (**1** $^1\mathbf{B_u^-}$) state is considered as a precursor of the triplet excited state.[177]

This unified explanation has not been widely accepted, and both interpretations (hot ground state S* vs electronically excited S*) have their own caveats. For example, it was found that both S* and S_1 states are populated in relatively different proportions, upon the increase of pump pulse energy.[178] Therefore, a more complex scheme with additional pathways had to be proposed to uphold the hypothesis about the excited state nature of S*.[178] In terms of this observation, hot S* hypothesis seems to be more convincing due to its simplicity.[179]

Multiple recent reports support the assignment of S* as a manifestation of vibrational cooling (S_0*→S_0) in a solution phase. Ostrumov et al. interpreted femtosecond transient

absorption results in terms of lifetime density maps, and found that the hot S* state hypothesis fully explains their data.[180] Moreover, they pointed out that presumably some older studies have been done with excitation power density, which exceeded linear regime (details about the used pump pulse are not always provided).[180] It has been observed, that the S* signature matches well with the stationary UV-vis absorption spectrum of carotenoid in solution heated to high temperatures, where higher vibrational modes of the S_0 state are excited.[169, 181] Staleva et al. investigated the zeaxanthin analogs of various lengths in solution, and found that S* lifetime does not scale well with conjugated chain length in a way expected for the electronically excited state, as the S_1 does.[182] Khan et al. found that usage of an UV excitation, carrying excess energy compared to the visible excitation, results in a more pronounced S* feature, which strongly points to the hot ground state nature of S*.[183] Balevičius et al. directly modeled transient absorption data, in so-called Vibrational Energy Relaxation Approach (VERA), using a simple $S_2 \rightarrow S_1 \rightarrow S_0$ deactivation scheme with the addition of excited vibrational states of S_1 and S_0.[184] It allowed to explain all the results with vibrational properties of S_1 and S_0 states, without the need of an additional excited state. So the S* signal stems mostly from the hot S_1 state in shorter carotenoids, and the hot S_0 state in longer carotenoids.[184] Other reports also confirmed, that S* can be well explained by a vibrational cooling.[185-186] Similar conclusions as for carotenoids have been drawn for polymers with long conjugated double bond chains.[83]

There are also reports, which undermine the ground state nature of the S* state. Results of two-dimensional electronic spectroscopy experiments applied to β-carotene spoke in favor of the excited state nature of S*.[187] Femtosecond stimulated Raman spectroscopy studies found that C=C stretching frequency in the S* state is similar to the S_1 state.[188] Transient absorption experiment with a narrowband pump pulse questioned the presence of impulsive stimulated Raman scattering as an instantaneous source of S*.[189] Temperature and excitation wavelength dependent transient absorption spectroscopy study established that there is no pathway between S* and S_1, therefore they both must be independent excited states.[190] However, conversely to previous reports, they proposed that the T_1 state is formed from S_2, not S* state.[190] This observation is important because the presence of the $S^* \rightarrow T_1$ pathway had been one of the reasons to assign S* as an excited state at the very beginning.[172]

There are also various alternative hypotheses, not always fully consistent with each other. De Weerd et al. suggested, that the internal conversion from S_2 to the S_1 state may be accompanied by delicate polyene chain bond twisting, due to the weakening of β-carotene all-*trans* structure in the S_2 state.[191] Niedzwiedzki et al. extended this hypothesis and proposed that S* in solution may be electronically excited twisted state.[192-193] Another proposition is that the S* is, in fact, the S_1 state of different, higher energy carotenoid conformation.[194-195] It was proposed (Figure 33), that there are at least two conformations in the ground state, which have their own S_2, S_1 and S_0 states, but the difference is manifested mostly for the S_1 state.

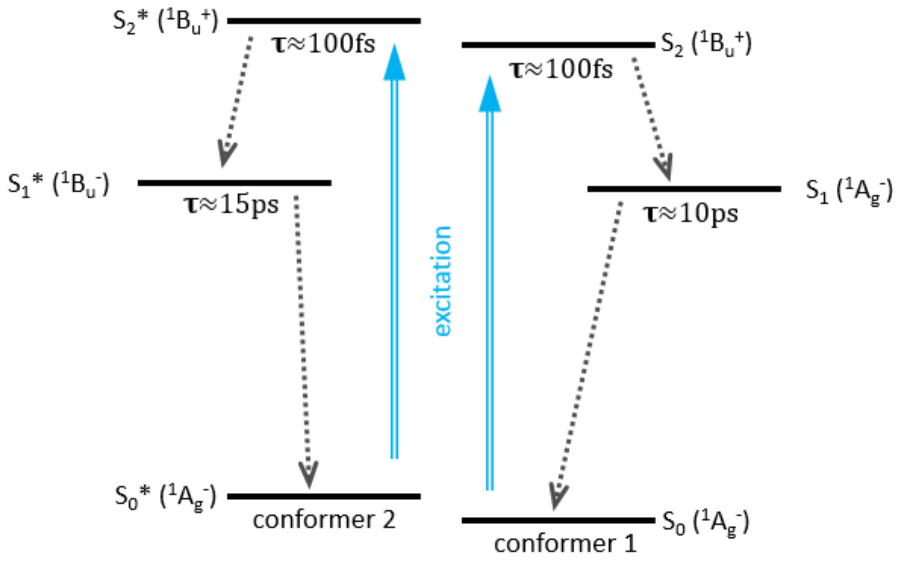

Figure 33. Inhomogeneous Ground State Model. It explains S* as an S_1 state of some specific carotenoid geometry, which can be "freezed out" in low temperature.

This hypothesis is supported by low temperature experiments, where it was found that one can decrease the contribution of the S* state by dropping temperature. Quantum chemical calculations indeed found a proper second minimum on the potential energy surface for β-carotene and spirilloxanthin, which have geometry slightly further from all-*s*-*trans*, explaining blue-shifted S* spectral feature, which in this case is interpreted as a S_1 state of the second carotenoid conformation.[194-195] Analysis of the S_0 bleaching band shows, that indeed S* state may arise from some specific, well defined subset of ground state conformers.[152] It is possible that planarity of the conjugated bond structure is favored.[152] However, the strong vibrational structure of the ground state bleach band may just stem from being overlapped with S* ESA, which is also very structured.[169] So the structured shape of the GSB does not necessarily have to be a result of some specific geometry of the S* origin population.[169] It was also demonstrated, that two-photon excitation utilized to populate directly the S_1 state results in much more pronounced S* feature.[196] It supports the hypothesis, that ground state population is inhomogeneous, and two-photon excitation presumably selects subpopulation which exhibits exceptionally strong S* character.[196] Excitation at higher vibronic levels of the S_2 state of spheroidene also results in more pronounced S* signal.[197] Niedzwiedzki et al. proposed, that the S* feature in LH2 (Light-Harvesting Complex 2) is a result of charge separation between carotenoid (neurosporene) and bacteriochlorophyll, which affects the local electric field and triggers an electrochromic response in neighboring carotenoids.[198] In LH1 (Light-Harvesting Complex 1) they concluded, that the S* feature can be explained by triplet-triplet annihilation following triplet states formation by a singlet fission mechanism.[199]

A final remark is that there is no direct dependence between S* lifetime and conjugation length, however, S* is more evident in longer carotenoids, especially where conjugation is extended to the end rings.[182, 192] Canthaxanthin, which is of importance for this study, shows significant involvement of the S* state in DMSO and benzene (while S_1 lifetime is about 9 ps).[152]

On the other hand, no evident S* was found in echinenone in these solvents. This is surprising, since S* is present in β-carotene, with the same lifetime as in canthaxanthin.[152]

At this point, one can fully appreciate the complexity of the debate about S* nature. The vibrationally excited origin of S* in the solution phase seems to be the most well-supported, simple and complete-enough hypothesis. Long carotenoids like β-carotene are effective light energy dissipators, with a short S_1 lifetime of about 10 ps, therefore it is not surprising that excess vibrational energy manifests itself so violently before ending in the solvation shell. However, one must remember that there are also other possible explanations, and the nature of S* in the protein environment may differ from that in the solution phase. A more detailed view on the nature of the mysterious S* state can be found in review articles.[119, 200-201]

Carotenoid triplet state

One of the roles performed by the carotenoid within the OCP is to quench reactive oxygen species (ROS). Carotenoids are effective quenchers of the singlet oxygen species ($^1O_2$) and acceptors of the potentially harmful triplet state energy in bacteriochlorophyll and other proteins.[66-68, 72] Resulting carotenoid triplet states subsequently decay to the ground state, harmlessly dissipating the energy. Quenching efficiency increases for longer chain carotenoids.[202-204] Recently it was found, that carotenoids like β-carotene cannot chemically quench $^1O_2$ species, only a physical quenching mechanism is possible.[205] Moreover, carotenoids in triplet state can react with $^3O_2$, forming carotenoid-endoperoxides, which later repopulate isomeric forms of initial carotenoid over a longer period of time.[205]

T_1 state energy of β-carotene is estimated to be slightly below singlet oxygen (approx. 7900 cm^{-1}).[133, 204] It has been found, that 15-*cis* β-carotene isomer in the T_1 state converts rapidly into all-*trans* isomer, both in solution and thylakoid membranes.[74, 206] Surprisingly, the remaining population of β-carotene isomers in the T_1 state retain their geometry.[74, 206] Other study of zeaxanthin found that the triplet state populated by UV excitation (266 nm) decays to the carotenoid radical.[207]

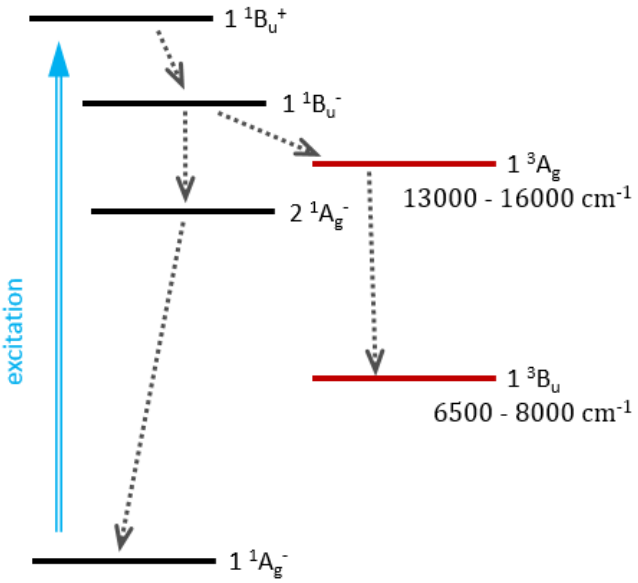

Figure 34. Triplet states in carotenoids.

Triplet states are populated directly from the singlet state in carotenoids (Figure 34) such as spirilloxanthin or spheroidene in light-harvesting complexes (LHCs).[172-174] These T_1 states show a band maximum at 575 nm (spirilloxanthin) or 530 nm (spheroidene) in transient absorption spectrum.[172-174] The triplet state formation efficiency is higher for carotenoids in proteins compared to carotenoids in solution.[175, 208] Moreover, the formation efficiency of the

carotenoid triplet state grows when the protein structure imposes larger geometrical deformation on the carotenoid.[175, 208]

In solution, excited triplet state has absorption band maximum of about 520 nm for β-carotene and 560 nm for canthaxanthin.[209-210] Increase in conjugation length redshifts maximum of the T_1 absorption band.[114] GSB band associated with the T_1 state in transient absorption spectra is vibrationally structured.[114] The T_1 state also has an absorption band in the NIR region, located around 1200 nm, however it is approximately 300 times weaker than its absorption band in the visible range.[211] It was proposed, that the T_2 state formation in solution proceeds from the S_2 state ($1\ ^1B_u^+$) via $1\ ^1B_u^-$ state, through the singlet fission mechanism with a very low yield Φ_T below 0.05 (see Figure 34).[114, 212] Then the T_2 (A_g symmetry) decays to the T_1 state (B_u symmetry) with time constant of about 10 ps.[114, 212] Another hypothesis state that triplet state origins from S* state, however in this case it was also proposed to be in fact $1\ ^1B_u^-$ state.[172] Triplet state formation quantum yield varies greatly among carotenoids, probably due to different $1\ ^1B_u^-$ state energy levels, which need to be well aligned with $1\ ^3A_g$ state energy to obtain efficient intersystem crossing.[114, 212] In zeaxanthin no triplet state formation after excitation to the S_2 state takes place.[207] The T_1 excited state lifetime is about 5 μs, regardless of conjugation length or exact solvent/protein environment.[213-214] T_1 state energy is usually located halfway between S_0 and S_1 states.[85, 114]

Carotenoid radical cation

Due to the presence of carotenoid radical cation species after the high energy excitation of the OCP, it is important to briefly summarize also their photophysical properties. Long carotenoids such as β-carotene, canthaxanthin or zeaxanthin can efficiently quench free radical species such as hydroxyl radical[215], phenoxyl radical[216] or nitrogen dioxide radical[217], which results in bleaching of the carotenoid ground state absorption band, formation of carotenoid radical cation or adduct. Carotenoid radical cation is characterized by the absorption band in the NIR region below 1000 nm.[215, 218] Carotenoid radical cation species have been widely observed in Light-Harvesting Complexes.[219-224] Carotenoids can also trap the radicals, which are added to the conjugated polyene system and stabilized by resonance, until a termination reaction with another radical species occurs to produce the final non-radical product.[225] It was also demonstrated, that the radical cation can be generated from the B_u symmetry state (**1** $\mathbf{B_u^-}$ or **1** $\mathbf{B_u^+}$), through an electron transfer to the solvent molecules.[226] Electrochemically induced cation radicals (bulk electrolysis) have absorption bands at about 900 nm (canthaxanthin) or 1000 nm (β-carotene). Their lifetime is over one hundred seconds in dichloromethane.[227-228] It has been found that the presence of carbonyl groups (or electron-withdrawing groups in general) in the carotenoid results in higher oxidation potential and stabilization of the carotenoid cation radical compared to dication (doubly oxidized carotenoid).[229-230] It has been found that cation radical species can lead to isomerization, populating various *cis* species.[228, 231] *Cis*/*trans* isomerization barrier, especially in the central part of the polyene chain, is much lower in the cation radical species compared to neutral carotenoids.[228, 231]

4. Structure and function of the OCP

Carotenoids can perform many important functions as chromophores embedded within the structure of various proteins. The properties of these carotenoids significantly differ from those in the solution phase. Protein structure constrains the carotenoid geometry, forcing some specific conformation. This effect results in different photophysical properties of the protein-bound carotenoids in comparison to the same carotenoids in solution.[201, 232]

In the following chapter, the structures of the OCP^O and OCP^R forms are described in detail. The first discoveries, which inaugurated the OCP research, are mentioned. Section 4.1 promptly describes a photoprotective mechanism performed by the OCP. Section 4.2 gathers the most important facts about the OCP^O structure. Section 4.3 introduces more details about the photoconversion process and the requirements, which must OCP must meet to be photoactive. Section 4.4 gives a more detailed description of the OCP^R structure.

Discovery of OCP

Orange Carotenoid Protein was firstly isolated from three different cyanobacteria in 1981 by Holt and Krogmann.[233] It has been found, that this 35 kDa water-soluble protein contains hydrophobic hydroxyechinenone (hECN) chromophore embedded inside. The OCP gene *slr1963* was later identified in the *Synechocystis* 6803 genome.[234] OCP from *Arthrospira maxima* was firstly crystallized in 1997.[235] When the obtained crystals are illuminated by a polarized light oriented with the long edge of the crystal (crystallographic *a* axis), the blue/green light is strongly absorbed.[235] If the orthogonal polarity is used, the crystals are transparent (see Figure 35).

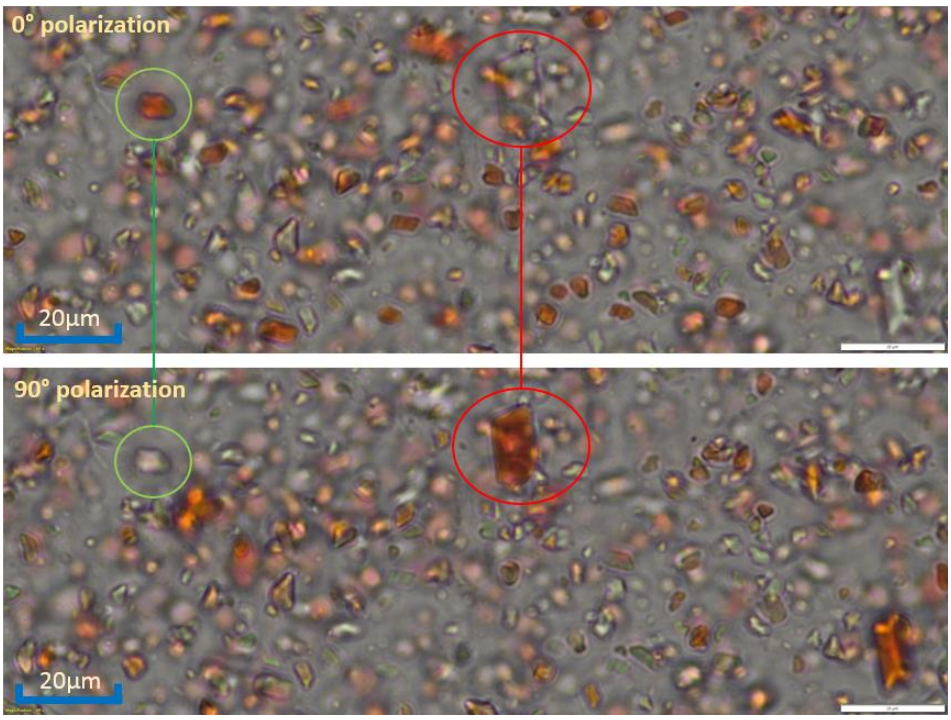

Figure 35. Microscope images of OCP crystals obtained using linearly polarized illumination. Different crystals are selected depending on polarization plane angle. Crystals were prepared by prof. Ilme Schlichting.

This remarkable property indicated, that all carotenoid molecules have well-defined position inside the protein and are oriented uniformly along one axis in the crystal.[235] The OCP structure from *Arthrospira maxima* containing hECN was resolved in 2003 (1M98 in the RCSB database, Figure 36).[236] The structure of OCP from *Synechocystis* containing ECN, which is of special concern for this work, was characterized later (3MG1 in the RCSB database, Figure 37).[237]

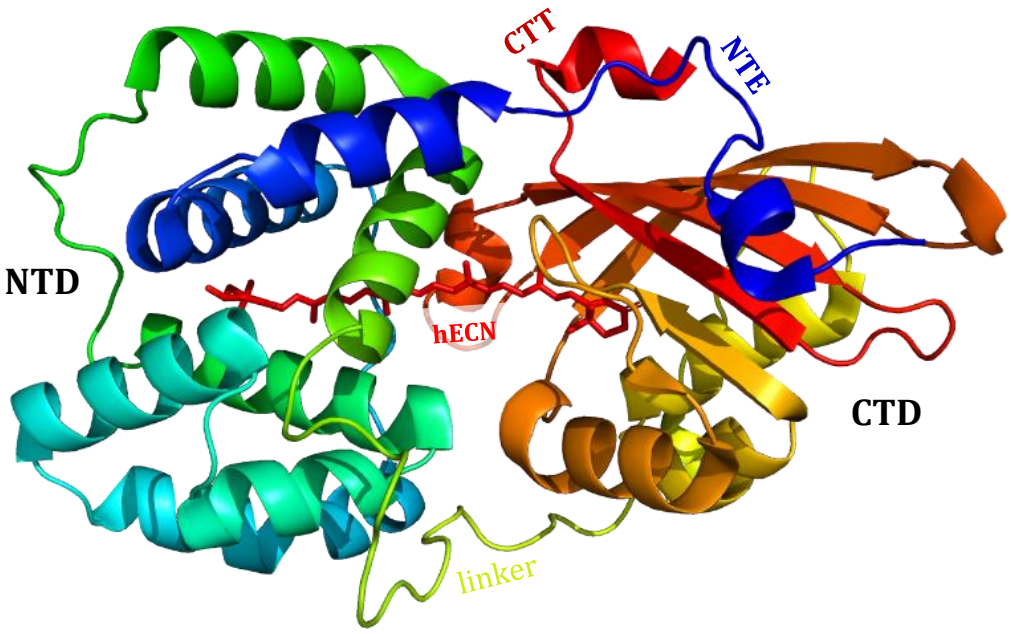

Figure 36. Crystal structure of Orange Carotenoid Protein from *Arthrospira maxima* (one monomer from 5UI2 dimeric structure from RCSB database)[236]. Carotenoid molecule spans both NTD (on the left) and CTD (on the right). Both domains are linked by an extended loop (yellow, at the bottom). All protein structures have been plotted using PyMOL package.

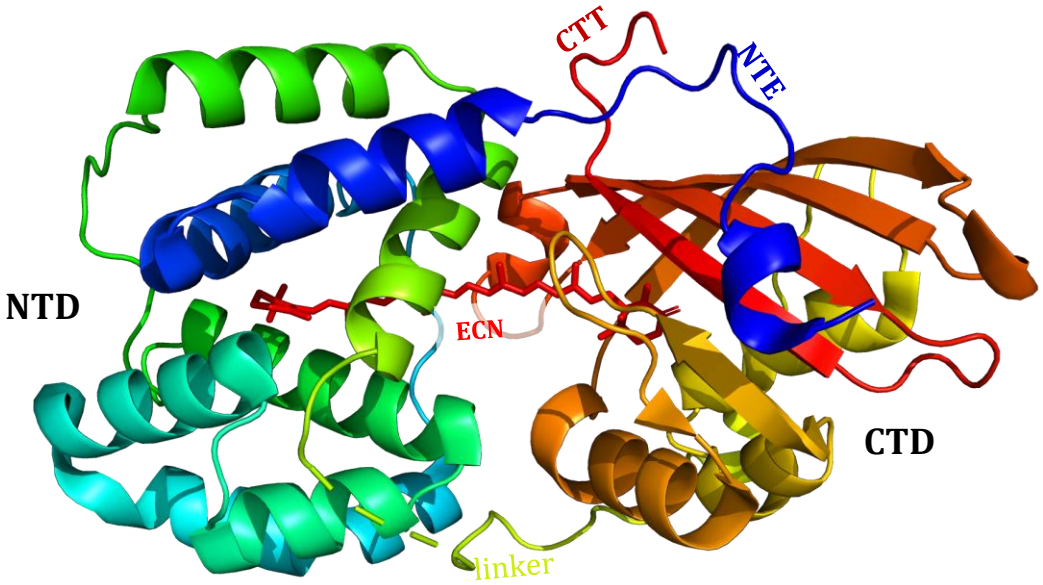

Figure 37. Crystal structure of Orange Carotenoid Protein from *Synechocystis* (one monomer from 3MG1 dimeric structure from RCSB database).[237]

Later, two new clades of OCPs named OCPx and OCP2 have been discovered in different cyanobacterial strains.[238-239] OCP1 (firstly discovered OCP in *Arthrospira maxima* and *Synechocystis*), OCP2 (found in *Tolypothrix* genome) and OCPx (found in *Scytonema* and *Gloebacter* genomes) differ in character and structure, but still perform the same photoprotective function. Within this thesis, only the OCP1 has been investigated.

4.1 Biological function

From the very beginning, it has been expected that the OCP is involved in photoprotection, because carotenoids are effective singlet oxygen quenchers. Moreover, it has been observed, that transcript levels of *slr1963* gene, which encodes the OCP, increase dramatically after short (15 min) exposure to strong irradiation light.[240-241] Therefore, it has been suggested that OCP may be responsible for singlet oxygen quenching, or carotenoid transport, shuttling them from the site of synthesis to various locations, like thylakoid membranes.[236, 242-243] In parallel it has been discovered that phycobilisome fluorescence in cyanobacteria decreases after being irradiated with blue-green or UV-B light.[244] The determined action spectrum suggested the engagement of a carotenoid molecule.[245] Finally, it was discovered that OCP is the protein responsible for this phycobilisome fluorescence quenching.[16, 246] Indeed, the action spectrum overlaps perfectly with the OCP absorption spectrum registered in the dark.[247] It has been clarified, that OCP is involved in two photoprotective mechanisms: quenching of singlet oxygen species and excitations harvested by phycobilisomes.[16] Expression of the *slr1963* gene can also be enhanced by salt stress or hyperosmotic stress, so that the OCP may be a part of a more general response to stress stimulus.[248]

Based on the PBS fluorescence measurements in the presence and absence of the OCP, it has been established, that OCP is necessary to induce an electronic excitation energy dissipation in the PBS, which is manifested by a decrease in the PBS fluorescence.[16] This type of process, leading to controlled dissipation of the excess of harvested light, is known as nonphotochemical quenching (NPQ). Upon strong blue/green light conditions, the OCP^O (inactive form) is converted into the OCP^R (active form), which is accompanied by a visual change from orange to red color (see Figure 38).

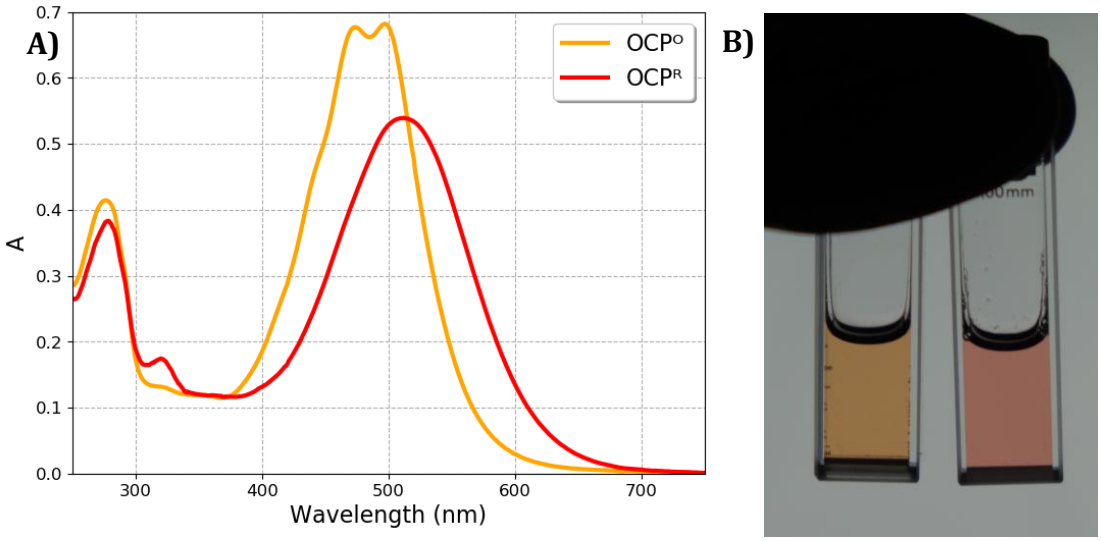

Figure 38. A) Stationary UV-vis absorption spectra of the OCP^O (dark-adapted) and OCP^R (active) forms from *Synechocystis* containing ECN (at 11 °C).[166] B) Picture of OCP^O (orange cuvettes) and OCP^R forms (red cuvette).

The relation between OCP^R concentration and electronic excitation quenching (NPQ) was confirmed in a variety of mutants.[15, 42, 249] An OCP^R attaches itself to the PBS core[40-42], induces quenching of the PBS electronic excitations, thus causing neutralization of the excessive light energy, that otherwise could result in some damage.[250-251] The NTD of the OCP^R attaches specifically to allophycocyanin core cylinders (emission located at λ_{max} = 660nm), and quenches around 80-90% electronic excitations harvested by the PBS, which are normally delivered to photosystem complexes (see Figure 39). A single OCP^R is sufficient to induce significant quenching in one PBS complex.[17, 250-257]

OCPs from various cyanobacteria have different affinity to the PBS.[258] Only a light-adapted OCP (OCP^R form) can attach to PBS, however, the process of attachment itself is not light-dependent.[17] Quantum yield of the quenching center formation *in vivo* is very small, 0.1% order of magnitude.[15, 43-45] Firstly it was proposed that one OCP is enough to quench one PBS.[17] In 2019, single-molecule fluorescence spectroscopy identified, that apart from the non-quenched state (no OCP attached), there are two quenched states of the PBS: Q_1 having 11% of the non-quenched state fluorescence intensity and Q_2 having 6% of the non-quenched state fluorescence intensity.[31] Because there are two symmetric OCP-binding sites on the PBS, it has been proposed that the Q_1 state corresponds to single bound OCP, and Q_2 state to doubly bound OCPs on the PBS, therefore producing stronger quenching.[31] Even more recent work demonstrated, that two OCP^R dimers are required to effectively quench single PBS.[19]

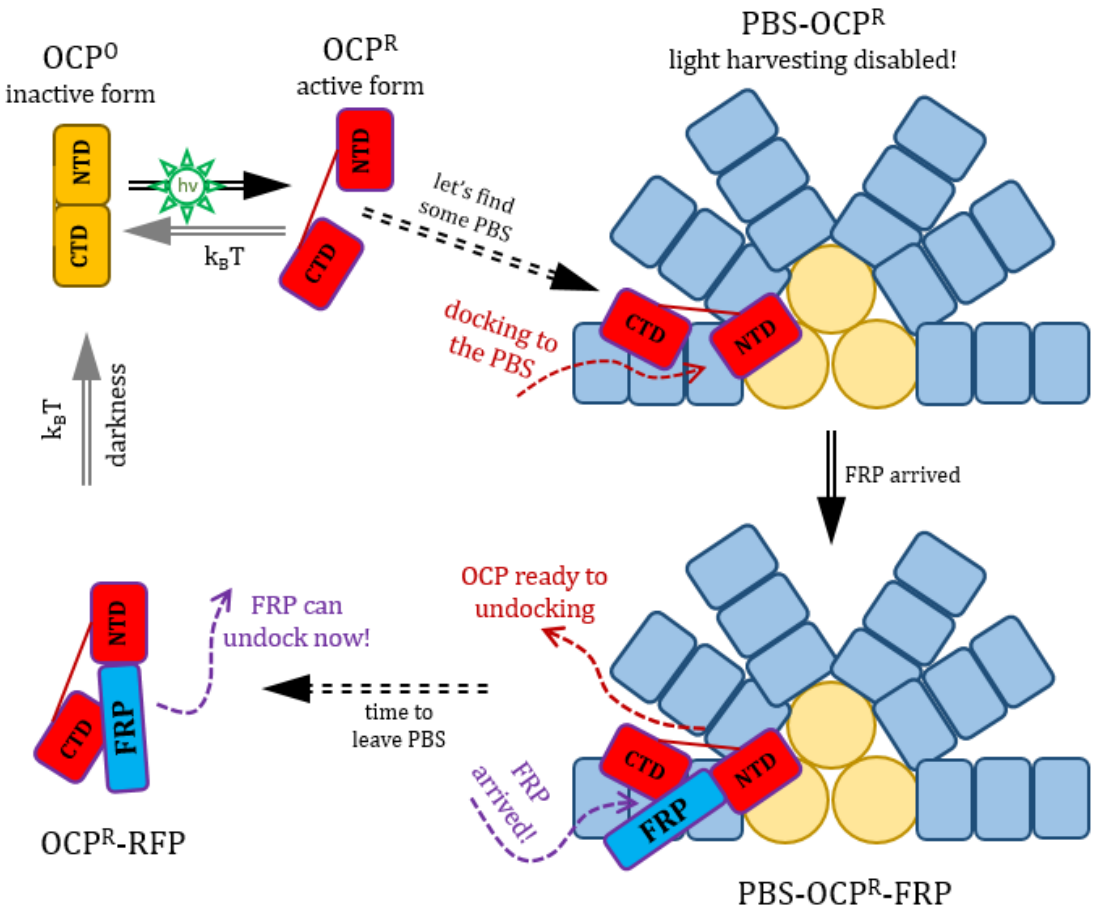

Figure 39. Scheme of the OCP photocycle including interaction with the PBS and FRP *in vivo*. OCP can attach to the PBS and regulate its function.

Provided that the light conditions returned to a safe regime, OCP function is no longer required. Fluorescence Recovery Protein (FRP) triggers detachment of the OCP^R from the PBS and facilitates back conversion to OCP^O, which allows the photosynthetic apparatus to fully recover its light-harvesting function in low light conditions.[17, 259] In order to perform this task, monomeric FRP interacts with the CTD domain of the OCP^R (Figure 39).[260] The FRP shares some similarities with the N-terminal extension (NTE) of the OCP.[27, 261] In the dark-adapted OCP^O form, α-helix present within the NTE is bound to the CTD domain, to keep both domains close to each other. However, in the OCP^R form, NTE is detached from the CTD, allowing the protein to open and expand.[27, 40-42, 261-262] It opens the opportunity for the FRP, which can attach in the same place as the NTE normally does in the OCP^O form.[263] When the FRP is bound to the CTD, it facilitates the back conversion to the OCP^O state.[263] FRP must be in the dimer form, to effectively bind to the OCP^R.[264] A high concentration of the FRP effectively prevents OCP from quenching PBS.[57] In 2023, it was proposed that FRP can prevent the OCP^O from opening, effectively disabling the $OCP^O \rightarrow OCP^R$ photoconversion process.[34]

It has been proposed, that the C-terminal tail (CTT), which normally points away from the protein in the OCP^O state (as shown in Figure 36), covers the carotenoid cavity in the CTD in the

OCP^R form, when the carotenoid itself is translocated into the NTD.[265] Despite that, it has been found that CTT facilitates carotenoid uptake by the CTD.[265]

As already discussed, carotenoids are effective singlet oxygen quenchers.[68] The quenching rate constant for hECN-containing OCP from *Synechocystis* in D_2O is 7.6×10^8 M^{-1} s^{-1}, compared to 2×10^{10} M^{-1} s^{-1} for hECN in chloroform.[266] Canthaxanthin and echinenone in acetonitrile have quenching rate constants of 1.9×10^{10} $M^{-1}s^{-1}$ and 1.6×10^{10} $M^{-1}s^{-1}$, respectively.[266] Note, that RCP has a higher quenching constant compared to OCP, *i. e.* 4.5×10^9 M^{-1} s^{-1}, due to more solvent-exposed carotenoid.[236] However, more recent studies have shown, that dark-adapted OCP has much better singlet oxygen quenching properties compared to RCP (Red Carotenoid Protein).[267] Therefore, it can perform its photoprotective function even in low light conditions.[267]

More detailed information about the photoprotective OCP's function can be found in review articles.[9, 18, 238, 268-270]

It has been proposed, that OCP exhibits functional modularity, where isolated NTD is equal to the RCP.[41] Without the CTD, the NTD retains carotenoid, and quenches the PBS like an OCP^R, regardless of irradiation conditions. Therefore CTD performs a regulatory function, and unregulated NTD (≈RCP) is quenching the PBS even in the darkness. The CTD and NTD are sensor and effector domains, sharing the same carotenoid. CTD does not interact with carotenoid, when it is in OCP^R form. CTD is not required to achieve binding to the PBS or quenching.[41]

4.2 OCP^O structure

Crystal structure of dark-adapted OCP

OCP crystallizes as a homodimer, where both carotenoids are parallel to each other, which explains already mentioned dichroism.[236] Each monomer consists of two parts, C terminal domain (CTD) and N terminal domain (NTD).[236] NTD consists of two similar α-helix bundles (four helices per bundle), with the hydroxyl group of hECN chromophore between them. NTD is unique to OCP.[236] Conversely, CTD resembles the NTF2 domain (Nuclear Transport Factor 2),[236] which can be found in various proteins responsible for nuclear import and export (comparison in Figure 40).

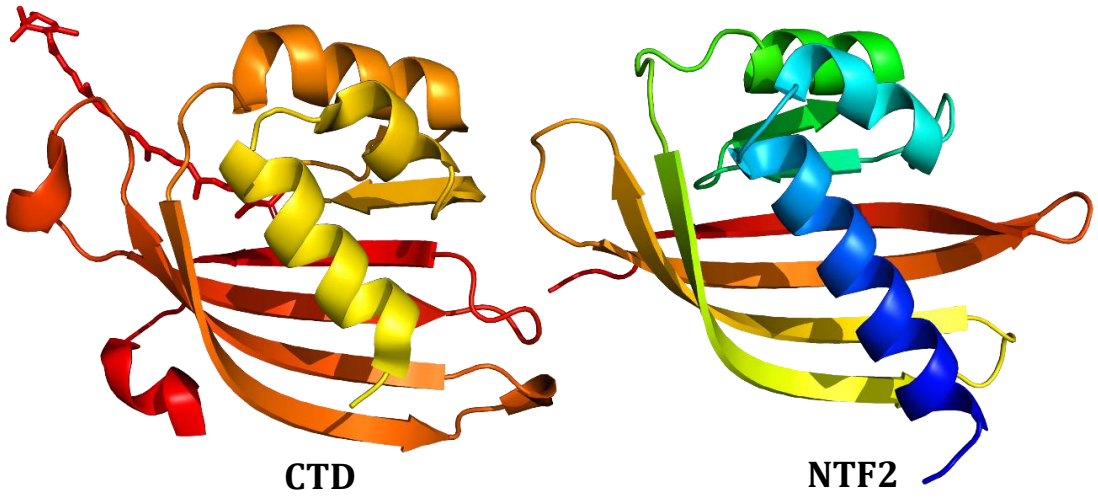

Figure 40. Crystal structure of CTD (from 5UI2)[236] compared to NTF2 monomer (from 1OUN).[271]

These proteins have been shown to bind small molecules and facilitate transport through Nuclear Pore Complexes located at the membranes of the nucleus.[271-273] OCP monomer is pictured in Figure 36. CTD consists of four α-helices and one β-sheet bent around the hydrophobic pocket, which encloses the carbonyl group and β1 ring of hECN.[236] The carotenoid spans both domains of OCP, moreover, it is almost completely separated from the solvent (almost fully covered by the protein, only 3.4% of the hECN surface is exposed to the solvent).[236] Oxygen in the carbonyl group of hECN is bound to Tryptophan and Tyrosine residues in the hydrophobic pocket of CTD: Trp-290 (2.8 Å hydrogen bond length) and Tyr-203 (2.7 Å hydrogen bond length).[65, 236] Note that residue numbering may slightly differ for other OCP variants. The numbering introduced here will be also used for these variants (indicated as equivalent numbering), to avoid confusion. All hydrogen bonds formed between the hECN molecule and protein residues (and one water molecule) are shown in Figure 41.

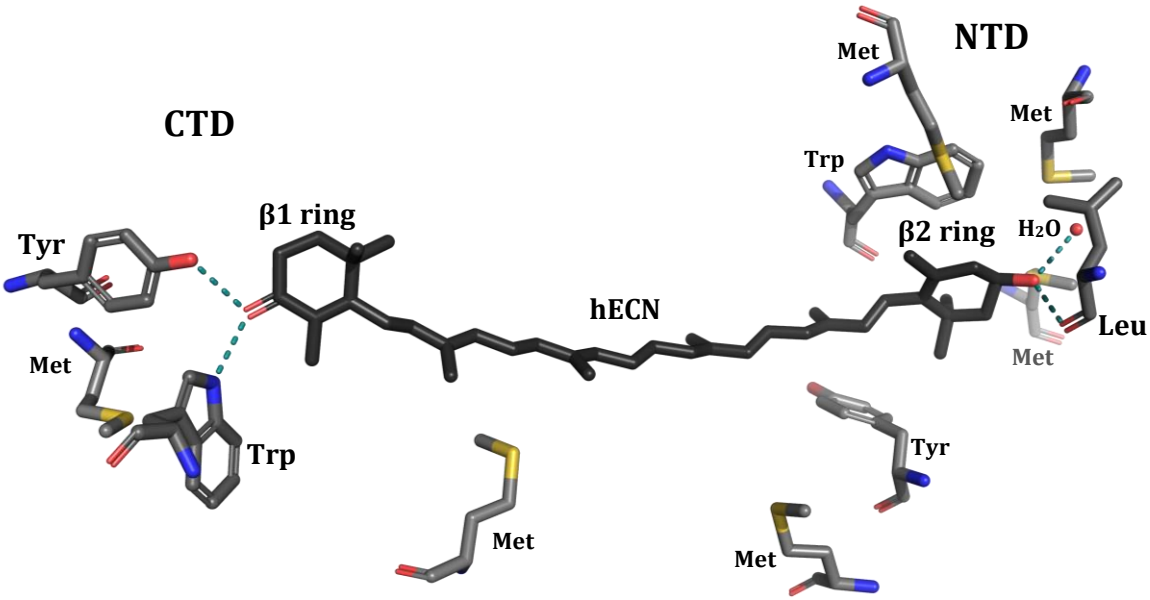

Figure 41. Hydroxyechinenone and the hydrogen bonds with protein residues (from 5UI2 structure[236]). Hydrogen atoms are not resolved.

Carotenoid β2 ring located in the NTD interacts with Tyr-44 and Trp-110 residues.[65, 237] There are 6 methionine residues in close proximity to the hECN, with their side chains directed toward the hECN, which provide a hydrophobic environment for hECN.[236] Such an abundance of methionine is not typically encountered in proteins. Thioether (Me-S-) groups of methionine are highly polarizable, which presumably affects the photophysical properties of the carotenoid.[236]

Positively charged Arg-155 residue in NTD and Glu-244 in CTD are located at the central interface between both domains and form a salt bridge, which is important for OCP^O stabilization (see Figure 42).[42]

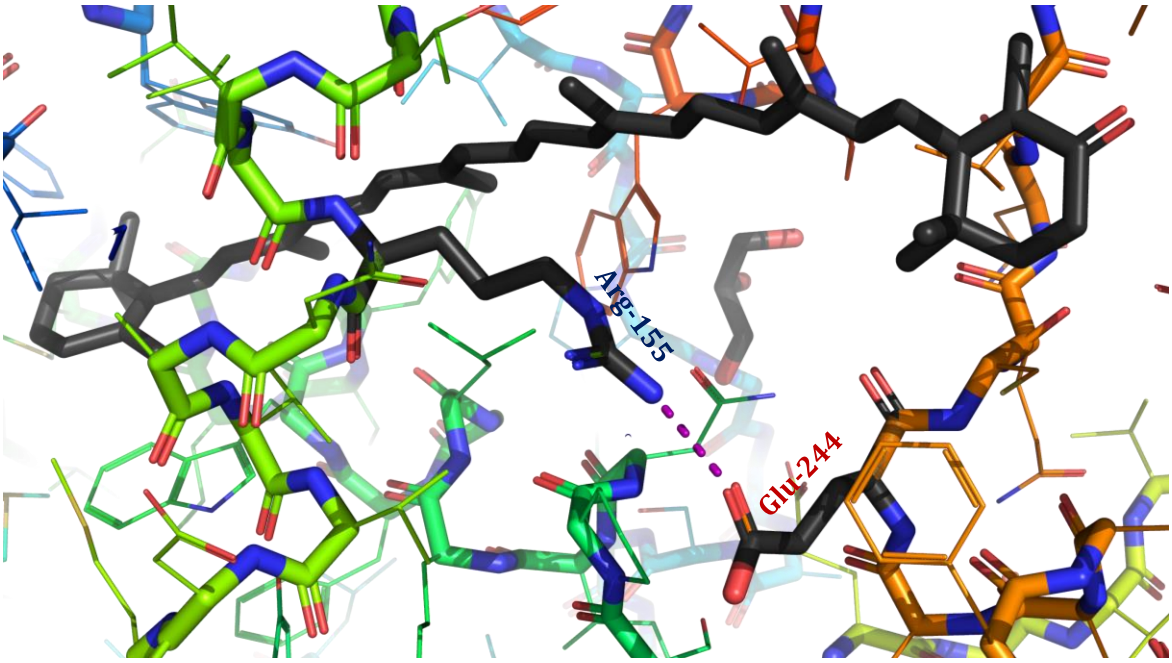

Figure 42. A salt bridge between Arg-155 and Glu-244 in Orange Carotenoid Protein from *Synechocystis* (3MG1 dimeric structure from RCSB database).[237]

The salt bridge between these residues is broken, when NTD and CTD domains separate during photoconversion, exposing the interface, and enabling the OCP to bind to the PBS. It has been demonstrated that positively charged Arg-155 is important in binding to PBS.[42] Another factor important to keep the dark-adapted OCP compact is the α-helix in the N-terminal extension (NTE).[27, 237, 261] It is attached to the CTD β-sheet in the OCP^O form (see in Figure 36), and detaches after illumination, allowing the domains to separate.[27, 261]

It has been found that dark-adapted OCP^O in sufficient concentration can form a homodimer in the solution phase, like it has been found in the crystal structure.[274-275] In low concentrations, most of the OCPs are in the monomeric state, with a minor contribution of the homodimers.[276-277] The ratio of the homodimer versus monomer populations increases with concentration. Even higher-order oligomers can be formed in very high concentrations (>10μM).[277]

Carotenoid conformation in OCP^O

hECN length in *Synechocystis* OCP is 26Å, it is in all-*trans* configuration and it is bent out of its equilibrium shape and distorted around C-C bonds (recall Figure 41).[15, 236, 278] Carotenoid binding pocket forces specific conformation of the carotenoid, which differ from the one found in the solution, where both terminal rings are in *s-cis* configuration.[279] In OCP, the ring with carbonyl group possesses conformation close to *s-trans*, which leads to an increase in the conjugation length of the polyene chain, which further causes red-shifts of the $S_0 \rightarrow S_2$ absorption band (compared to carotenoid in solution).[279] The dominant OCP^O subpopulation (more details about OCP heterogeneity are given later) has a much more pronounced vibrational pattern compared to the solution phase, presumably due to the constrained geometry of the carotenoid imposed by the protein cage.[279-280] Raman spectrum of the OCP^O indicates highly distorted carotenoid structure, which is the effect of the interaction with the protein cage.[278]

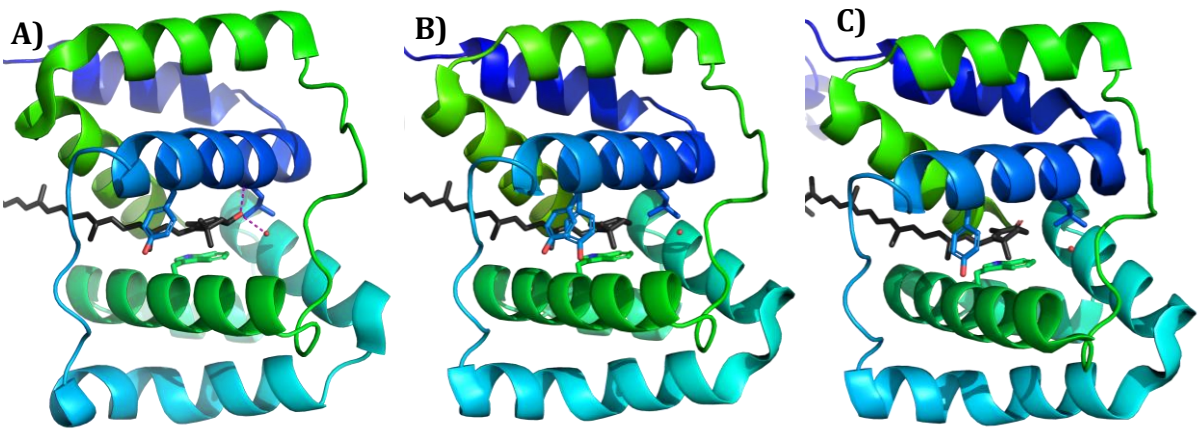

Figure 43. Conformation of the carotenoid β2 ring in the NTD. A) hECN in the OCP from *Arthrospira maxima* (5UI2 structure from RCSB database[236]), B) ECN in the OCP from *Synechocystis* (3MG1 structure from RCSB database[237], note that there are two alternate Tyr-44 conformations), C) CAN in the OCP from *Synechocystis* (4XB5 structure from RCSB database[40]).

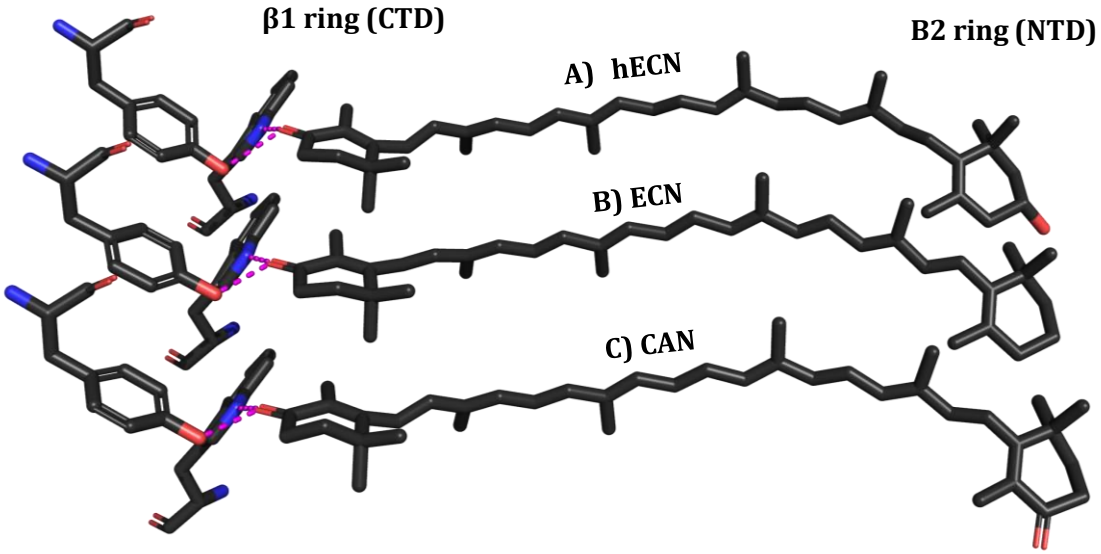

Figure 44. hECN, ECN and CAN carotenoids in the OCP^O form. Taken from A) 5UI2 RCSB structure (*Arthrospira maxima*),[236] B) 3MG1 RCSB structure (*Synechocystis*),[237] C) 4XB5 RCSB (*Synechocystis*)[40].

The carotenoid carbonyl group forms a hydrogen bond with Trp-290 and Tyr-203 residues of the protein in CTD (see Figure 44 and Figure 41).[236] Carotenoid terminal ring on the other side (β2 ring in the NTD) is stabilized by Tyr-44 and Trp-110, by a π-π stacking interaction.[15, 65, 237] Figure 43 shows these residues as well as hECN, ECN and CAN in the OCP^O. In the case of ECN carotenoid, there is no proper group on the β2 ring to form hydrogen bonds with the protein residues. However, in hECN there is a hydroxyl group at the β2 ring, which can form a hydrogen bond with a carbonyl group in the Leu-37 residue in the NTD, constraining the position of the carotenoid.[281] In case of CAN carotenoid, the carbonyl group on the β2 ring collides with the carbonyl group of Leu-37, forcing the β2 ring out of the carotenoid plane, decreasing its coupling to the conjugated polyene chain.[281] Therefore, there are more available conformational degrees of freedom for the CAN, compared to hECN, increasing contribution of nonradiative deactivation

pathways from the S_2 state and promoting the formation of distorted ground state geometries through excited state relaxation.[281] It is possible, that some of these geometries are quite prone to OCP photoconversion, which could explain a high photoconversion efficiency of OCPs functionalized with CAN.

Note that OCPs functionalized by carotenoids without carbonyl group[139] or with mutations at Trp-290 and Tyr-203 residues which disable the formation of both hydrogen bonds with the carotenoid,[65] do not undergo the $OCP^O \rightarrow OCP^R$ photoconversion. Some of them are locked permanently in the photoactive red state.

Heterogeneity of the OCP^O

Based on Raman scattering studies of the carotenoid in the OCP, it has been established, that there are at least two dark-adapted OCP subpopulations in the ground state.[278, 282] Usually they are referred to as "normal" or the "red-shifted" ones.[278, 282] Decomposition of the stationary absorption spectrum reveals, that "normal" subpopulation has structurized, broad absorption spectrum covering most of the whole absorption band.[282-283] On the other hand, "red-shifted" one has homogenous absorption spectrum covering only longer wavelengths, and it constitutes around 20% of the whole OCP population.[282-283] The origin of these subpopulations is unclear. The simplest hypothesis, that the "red-shifted" subpopulation might be ascribed to the OCP^R form partially populated in the dark (due to spectral similarity) was excluded.[282] It was found, that even in OCP containing zeaxanthin, which lacks photoactivity, significant heterogeneity is present.[282]

At low temperature, only one ("normal") population can be observed.[279] Therefore it was proposed, that the "red-shifted" subpopulation may be due to the fraction of carotenoids without hydrogen bonding between the carbonyl group and Trp-290 or Tyr-203 residues of the protein. So, in this case both subpopulations (with and without the hydrogen bond) are in thermal equilibrium at room temperature, but only the one with lower energy remains at low temperature.[279] Recent comparison between OCP1 and OCP2 from *Tolypothrix* confirmed this hypothesis.[23] It was found that heterogeneity in the OCP^O form may stem from carotenoid-protein interactions such as the H-bonding pattern rather than from some differences in carotenoid conformation.[23] It was confirmed by a Trp fluorescence study, using specially designed mutant with only one Trp residue left (the one near the carotenoid carbonyl group, equivalent of Trp-290).[24] Therefore heterogeneity stems from spontaneous disruption of the hydrogen bonds between protein (Trp/Tyr) and the carotenoid carbonyl group.[24] In another study, a mutant with two Tryptophans instead of Tryptophan/Tyrosine pair (equivalent to Trp-290/Tyr-203) bound to the carotenoid carbonyl group was investigated.[21] Only one hydrogen bond with carotenoid carbonyl group was found, due to increased distance between carbonyl group and mutated Trp residue. The determined amount of redshifted OCP^O subpopulation was negligible. Similar effects were observed for mutant, where Tryptophan was replaced with Alanine. It suggests, that in WT OCP, both hydrogen bonds formed between the carotenoid carbonyl group and protein (Trp and Tyr) are in competition. By disabling the formation of one of these bonds, very high homogeneity of the dark-adapted OCP form is obtained. This result supports the hypothesis, that the competition between both hydrogen bonds is a source of OCP^O heterogeneity.[21]

Based on femtosecond transient absorption data, it was found that excitation in the red edge of the stationary absorption band of OCP^O (about 540nm and above) allows to excite the "red-shifted" subpopulation selectively.[282] With the help of the structural data, β_1 angles (defined in Figure 45) of carbonyl terminal ring were proposed for "normal" and "red-shifted" forms.[282]

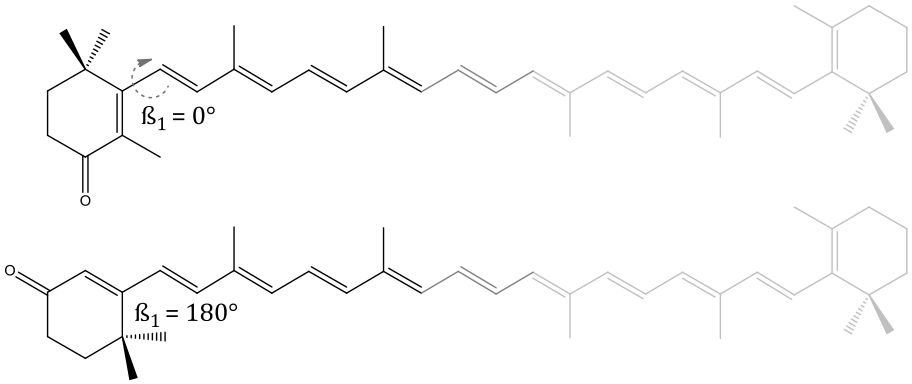

Figure 45. Exemplary β_1 angles of the carbonyl terminal ring of the ECN. β_1=0° represents fully *s-cis* configuration. β_1=180° represents fully *s-trans* configuration, where the carbonyl group is coupled with the conjugated bond system.

For echinenone OCP it was inferred that in the "normal" form β_1=146° (not in the plane), and the "red" form was proposed to have an angle close to β_1=180° (in the plane, results in strong ICT contribution in the femtosecond transient absorption spectrum).[282] QM/MM simulations suggested, that various red-shifted forms in the OCP^O can be populated without breaking any of the Tyr/Trp – carotenoid carbonyl group bonds.[25] The carotenoid binding pocket was found to be loose enough to allow a temporary population of the more planar carotenoid conformations, leading to the red-shifted absorption spectrum due to longer effective conjugation length.[25]

4.3 OCP photoconversion and photoactivity

Upon photoconversion, the UV-vis absorption spectrum of the carotenoid undergoes significant redshift, it loses vibrational structure, becoming almost completely uniform (see Figure 38). Computational chemistry calculations suggest, that the presence of strong inhomogeneous broadening in the OCP^R form stems from conformational disorder, especially associated with rotation of the terminal carotenoid β-ionone rings about single bonds (β_1, see arrow in Figure 45).[30]

OCP^R population formed in the photoconversion process has a very large inhomogeneous distribution due to conformational heterogeneity, presumably caused by carotenoid exposure to the water molecules.[280] It is a huge difference, compared to dark-adapted OCP^O form, where the carotenoid is highly constrained by the protein cage (at least in "normal" subpopulation).[280] Moreover, it seems that only one broad subpopulation exists in the OCP^R form, indicating that photoconversion of any of two OCP^O subpopulations leads to the same OCP^R population.[278]

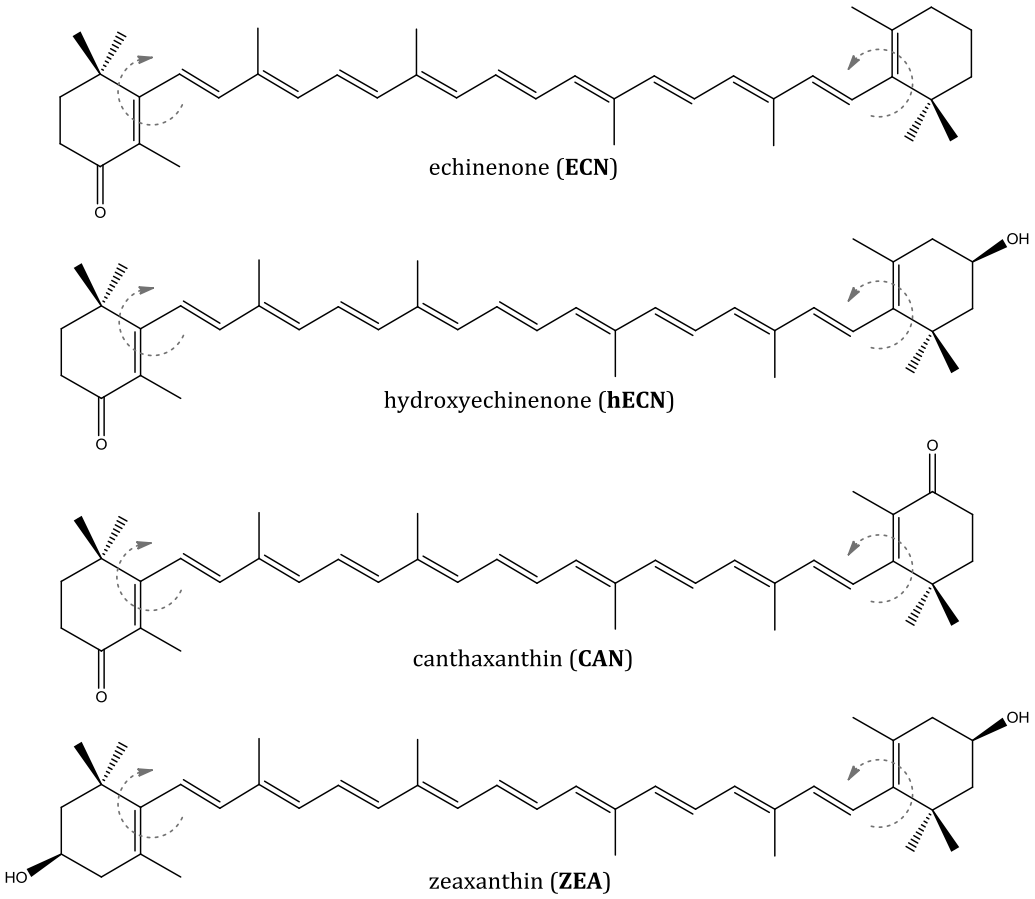

Figure 46. Carbonyl carotenoids found in OCP and zeaxanthin. Terminal β-ionone rings are in *s-cis* conformation in solution phase. In OCP^O, the geometry is bent and β-ionone rings may rotate to *s-trans* configuration (as indicated by arrows), thus increasing conjugation length of the polyene double bond system.

It was found that only carbonyl carotenoids, like echinenone (**ECN**), hydroxyechinenone (**hECN**) or canthaxanthin (**CAN**) allow OCP to function properly (Figure 46). OCP functionalized with zeaxanthin (**ZEA**), which has a similar structure compared to **hECN**, but the only carbonyl group is replaced with a hydroxyl group, shows no OCP^O→OCP^R photoconversion upon irradiation.[139] **ZEA**-functionalized OCP does not quench PBS fluorescence nor exhibit photoprotective properties.[139] Similar effect has been observed in some mutants, where Trp-290 and Tyr-203 were replaced with amino acids that do not form the hydrogen bond with the carotenoid.[65]

OCP with embedded carbonyl carotenoid acts as a molecular switch, activated by blue/green light and deactivated in the dark. The OCP^R - active "red" form of OCP shows a much more pronounced intramolecular charge transfer (ICT) character during the carotenoid excited state decay, and it has been proposed that this state acts as an energy acceptor, which consequently allows to dissipate excess of energy, if it is required.[284-285]

The efficiency of the OCP^O→OCP^R photoconversion is usually very small, about 0.3% in the OCP from *Synechocystis*.[15, 43-45] The mechanism leading to OCP^R formation and back conversion is still unclear, however, various working hypotheses exist. They will be discussed in chapter 5.

Surprisingly, the light is not the only way to photoconvert the OCP. It has been observed, that functional OCP^R can also be formed in the dark, using high concentration (above 1M) of sodium salts, like sodium thiocyanate or sodium iodide.[275] On the other hand, it has been found that the presence of Cu^{2+} ions locks the OCP in the OCP^R form, blocking the recovery.[286] Moreover, not all OCP mutants which can photoconvert to OCP^R can actually quench phycobilisome excited states.[65, 237] It has been demonstrated, that specific mutations of Arg-155, Trp-110 still allow the OCP to undergo $OCP^O \rightarrow OCP^R$ transition, but fluorescence quenching property is no longer exhibited. Therefore, the ability to photoconvert does not guarantee photoactivity, defined as the ability to quench phycobilisomes.[65, 237]

4.4 OCP^R structure

OCP^R-like structures

Since the OCP^R form is metastable, it is not possible to obtain its crystal structure in a straightforward way. It is possible to irradiate OCP crystals and register light minus dark X-ray diffraction pattern, but the OCP^R structure obtained this way is not the same as in a solution phase.[287] Therefore it is necessary to use other stable structures, which exhibit properties similar to the OCP^R and can be crystalized, so they can be used to understand OCP^R.[40]

16kDa Red Carotenoid Protein (RCP) can be isolated from cyanobacteria together with OCP.[234] It is a product of proteolysis of OCP, where the CTD is removed. It can be achieved using acidification.[236] RCP is stable (do not revert to some other form like the OCP^R to OCP^O), exhibits similar activity as OCP^R (performs NPQ) and its UV-vis absorption spectrum closely resembles the OCP^R.[40] Moreover, Raman optical activity spectra calculated using the crystal structure of RCP closely agree with spectra measured for OCP^R.[288] Therefore, RCP can be used to understand better structure of the NTD domain in the OCP^R state.[40] Figure 47A shows the crystal structure of RCP, where canthaxanthin is translocated by about 12 Å with respect to the OCP^O crystal structure.[40]

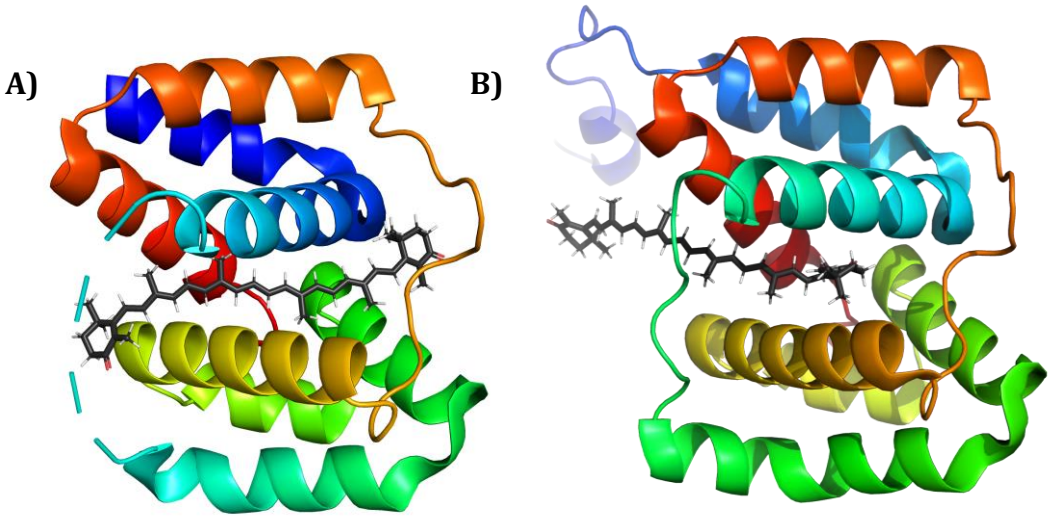

Figure 47. A) RCP monomer with canthaxanthin from *Synechocystis* (4XB4 from RCSB database)[40], B) NTD domain of the OCP^O with canthaxanthin from *Synechocystis* (4XB5 from RCSB database).[40]

Note that NTD in the OCP^O form (pictured in Figure 47B) and RCP structures are similar, but the location and geometry of the CAN is completely different.[40]

Another model, which can be utilized as an approximation of the OCP^R is W228A mutant.[57] Due to the replacement of the Tryptophan (W) with an Alanine (A) residue (comparison in Figure 48), the hydrogen bond between the carotenoid carbonyl group and the removed Tryptophan is absent.[57]

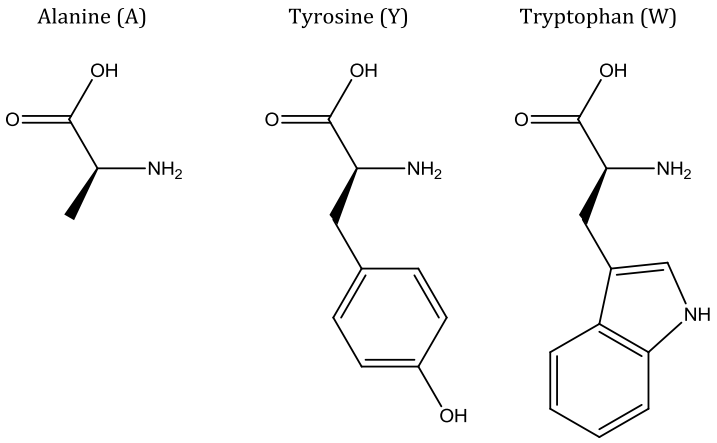

Figure 48. Alanine, Tyrosine and Tryptophan structures.

It has been demonstrated, that the behavior of this mutant resembles OCP^R in many aspects. It binds to the PBS and quenches its fluorescence. It interacts with the FRP similarly compared to OCP^R and possesses a similar UV-vis absorption spectrum. It has increased volume, indicating that domains are separated.[57]

In 2022, cryogenic electron microscopy measurements resolved a structure of the OCP^R-PBS complex from *Synechocystis*, where carotenoid is ECN.[19] In this structure, the NTD and CTD are separated, CTD center of mass is translated by ≈ 60 Å. CTD is rotated around the NTD by 220° (Figure 49).

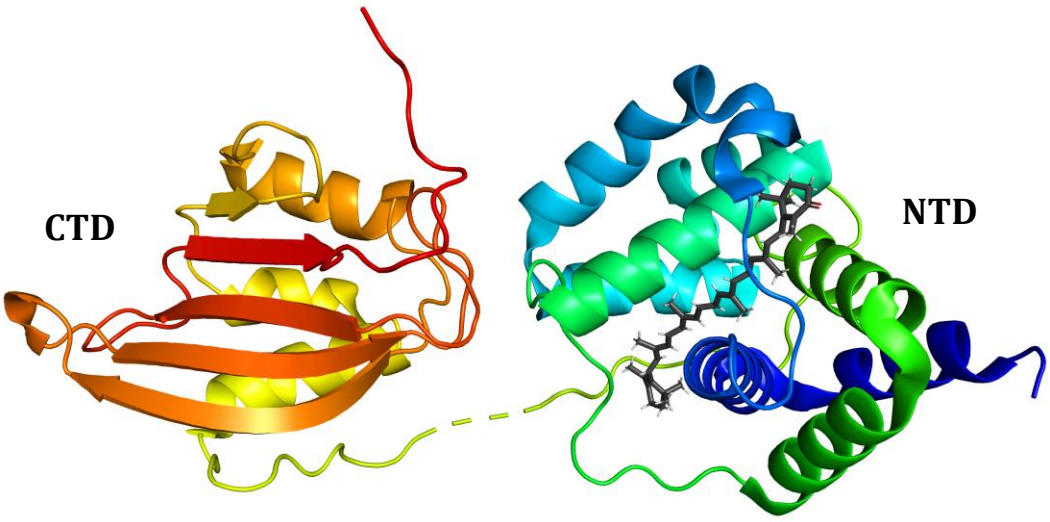

Figure 49. OCP^R geometry when attached to the *Synechocystis* PBS (7SCC structure from RCSB database).[19]

Moreover, it has been found that charge distribution around the carotenoid is asymmetrical, with negative around the β2 carotenoid ring and positive around the β1 ring. In this crystal structure OCP^Rs are in a dimer state, interacting through CTD domains.[19]

Properties of carotenoid-NTD (RCP)

Transient absorption data shows no ICT character in RCP (contrary to OCP^R).[289] Because there is no CTD domain in RCP, a hydrogen bond with the carbonyl group is absent, and the carbonyl side of the carotenoid is exposed.[289] RCP absorption band is red-shifted with respect to the dark-adapted OCP, and possesses no vibrational structure, similarly to light-adapted OCP^R. It is prone to aggregation, which allows it to cover the hydrophobic part from being exposed to the water.[289] Both the OCP^R and RCP have broad absorption spectra resembling all-*trans*-β-carotene in solution.[41]

Based on X-ray crystallography data, it was found that carotenoid is translocated by a 12Å in RCP towards the NTD, compared to the OCP^O (see Figure 50).[40]

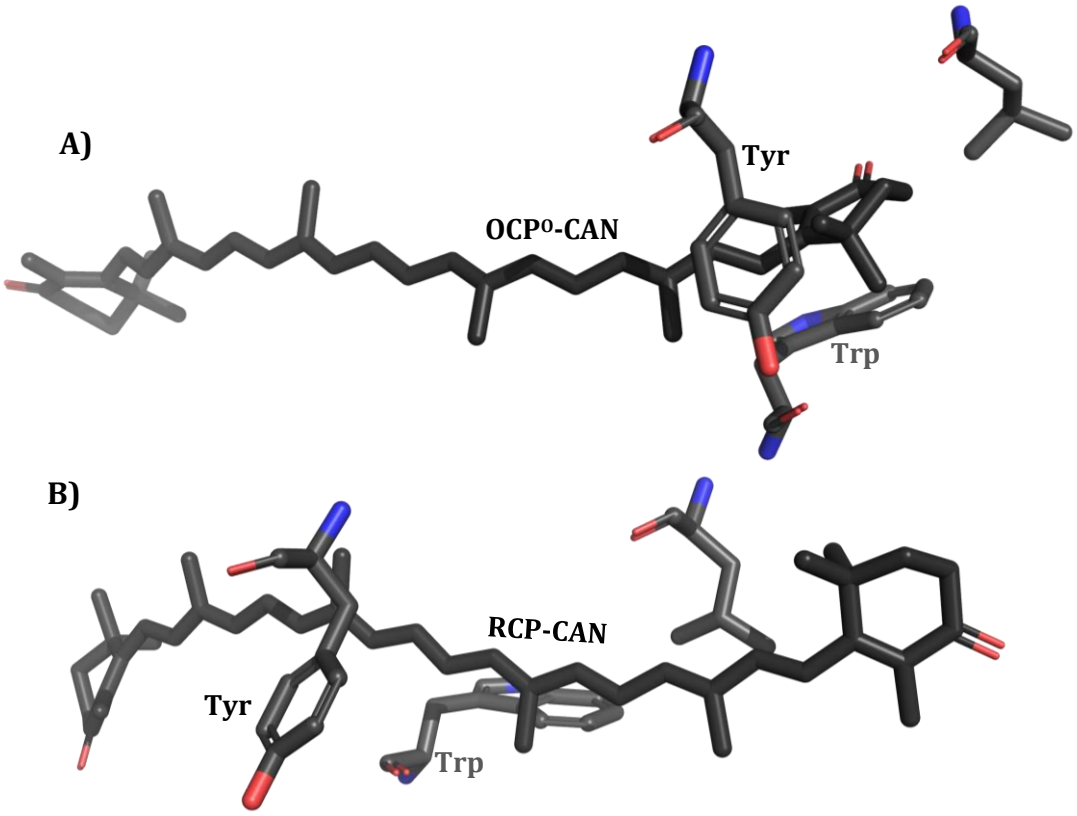

Figure 50. A) Canthaxanthin in the OCP^O from *Synechocystis* (4XB5 from RCSB database[40]), B) canthaxanthin in the RCP from *Synechocystis* (4XB4 from RCSB database[40]).

Approximately 8% of the carotenoid surface is exposed to the solvent around both terminal rings. In RCP, carotenoid is much more planar compared to OCP^O, which explains increased effective conjugation length and red-shift of the UV-vis absorption band. Moreover, end rings keep the configuration close to *s-trans*.[40]

QM/MM calculations show that both terminal rings of the carotenoid in the RCP have a lot of rotational mobility compared to the OCP^O.[30] Computations demonstrated, that a broad

distribution of conformations exists and can interconvert in the μs timescale. Moreover, the conjugation length in the carotenoid is much longer in the RCP. These observations explain the redshift and inhomogeneous broadening of the RCP compared to OCP^O. The carotenoid in RCP is almost planar and stabilized by various charged protein residues.[30]

Protein structure of the OCP^R

A large part of the structural information about OCP^R is based on the assumption, that the NTD and carotenoid have similar properties in the OCP^R form and the RCP protein. Due to the lack of a fully resolved crystal structure of free, noninteracting OCP^R, one must resort to optical spectroscopy methods.

FT-IR spectra recorded for OCP under illumination indicate large rearrangements in the protein structure.[15] The rigidity of the helical structures is decreased (elongation of NH---OC hydrogen bonds that connect the turns). β-sheet of the CTD is being compacted during photoconversion (shortening of NH---OC hydrogen bonds between β-strands).[15]

Mass spectroscopy data indicate, that the OCP^R exists in a monomeric state, contrary to OCP^O, which seems to have a dimeric form (like the OCP crystals used to obtain structural data).[274] Based on mass spectroscopy results, it has been proposed that dark-adapted OCP^O is in a dimer state, and photoconversion is associated with its dissociation into monomers.[274] Note, that according to the recently published report, OCP^R form *in vitro* can also form oligomers in sufficiently high concentration.[290]

During photoconversion to the OCP^R, the global tertiary structure is strongly affected, while the secondary structure stays virtually the same.[41, 45] The CTD structure does not seem to be strongly affected by the photoconversion, except that the carotenoid binding pocket becomes empty due to carotenoid translocation.[40, 262] The NTE, which is normally located on CTD is detached and moved away from the CTD, unlocking both domains.[262] Arg-155 to Glu-244 salt bridge located between domains (Figure 42) breaks so they dissociate and the OCP opens, allowing water molecules to interact with the carotenoid.[40-41, 280] NTD and CTD domains become completely separated, linker part between them and NTD surface becomes more solvent accessible.[40-41, 262] Carotenoid becomes also exposed to the solvent, and hydrogen bonds between the carbonyl group and Tyr-203, Trp-290 are broken.[41] Finally, OCP^R has a significantly more expanded structure compared to OCP^O, which is a result of domain dissociation.[41, 276] Maksimov et al. proposed, that the OCP^R is a molten globule-like protein, where the tertiary structure is lost and the protein structure exhibits increased flexibility (while the secondary structure is still preserved).[45, 276]

Carotenoid conformation in OCP^R

Based on the analogy with RCP, it is clear that in the OCP^R carotenoid is also translocated into the NTD domain, which radically alters carotenoid geometry and environment.[40] Effective conjugation length of the carotenoid increases by approximately one bond length under illumination (the C=C stretching mode shifts to a slightly lower frequency).[15] The evolution of the Raman spectra indicates a less distorted, more planar carotenoid structure in the OCP^R form compared to OCP^O.[15, 278] UV-vis absorption spectra of the OCP^R possess an additional *cis*-peak

located at about 320nm. This peak is usually associated with *trans* to *cis* isomerization in carotenoids in solution.[45] On the other hand, mid-IR anisotropy spectra indicate that OCP^R possesses the same all-*trans* conformation as the OCP^O, so the carbonyl end ring of the carotenoid does not isomerize upon photoconversion.[28]

UV-vis transient absorption spectroscopy shows, that OCP^R exhibits increased ICT character after the femtosecond excitation compared to the OCP^O.[282, 284] The exception is OCP functionalized by CAN, where the contribution of the ICT state is similarly low for both OCP^O and OCP^R state.[23] In CAN, the carbonyl groups are located symmetrically on both terminal rings (see Figure 46).[23] As it was described in the previous chapter, asymmetry is one of the requirements for the ICT character.

Both excited states observed after the excitation of OCP^O (ICT/S_1 and S_1/ICT) have very distinct characters, like they were almost pure ICT and S_1 states.[282, 284-285, 291] Still the S_1 state of OCP^R lives shorter than the carotenoid in solution. It suggests that the terminal ring with carbonyl group still has an *s-trans* configuration, like in OCP^O.[282, 284-285, 291]

5. *Photoconversion dynamics of OCP^O to OCP^R form*

The following chapter introduces all the intermediate products proposed so far, formed after the excitation of the OCP^O. In the first section, the evolution of the carotenoid excited states is described, which ends with the formation of a P_1 – photoproduct considered as the first one starting the rearrangements in the protein structure, which ends in the formation of the OCP^R form. Section 5.2 gathers all the intermediate products observed in timescales longer than 1 ns. Because various authors proposed different labels, which correspond to the same state, they are grouped to avoid confusion. Section 5.3 discusses the process of photoconversion observed upon continuous irradiation conditions. The last section describes the issues, which have not been resolved by the current state of knowledge and formed a clear goal for this thesis.

5.1 Relaxation of the carotenoid excited states

There is still a disagreement about the mechanism describing the first events of the photoconversion process. There seems to be a consensus, that the structural rearrangements in the protein structure are preceded by the cleavage of the *carotenoid – Trp/Tyr* hydrogen bonds. It was proposed that hydrogen bond cleavage may be caused by light-induced keto-enol tautomerization of the keto group in the carotenoid β-ionone end-ring, thus destabilizing the hydrogen bond.[287] Other proposition is that rotation of the β-ionone end-ring causes cleavage of the hydrogen bond due to increased distance between Trp/Tyr residues and the carbonyl oxygen.[45] More recent time-resolved mid-infrared anisotropy experiments do not support the β-ionone rotation hypothesis.[28] It was proposed instead, that structurally distorted S* state formed after the decay of the S_2 state is responsible for the rupture of the hydrogen bond.[28] However this interpretation is questioned within this thesis.[166] Another hypothesis is that the ICT state may trigger the photoconversion by inducing the proton transfer from Tyr or Trp residues to the carotenoid carbonyl group, forming an oxocarbenium ion.[21] A lifetime of oxocarbenium ion is presumably very short, but long enough to alter the geometry sufficiently to prevent the carotenoid from returning to the conformation where a recreation of the hydrogen bonds is still possible.[21] The most recent report, published in 2022, found that the photoconversion process is accompanied by simultaneous isomerization about two single bonds (C6'-C7' and C8'-C9', atom numbering in Figure 28) close to the β2 ring.[20]

Excitation of the carotenoid in OCP

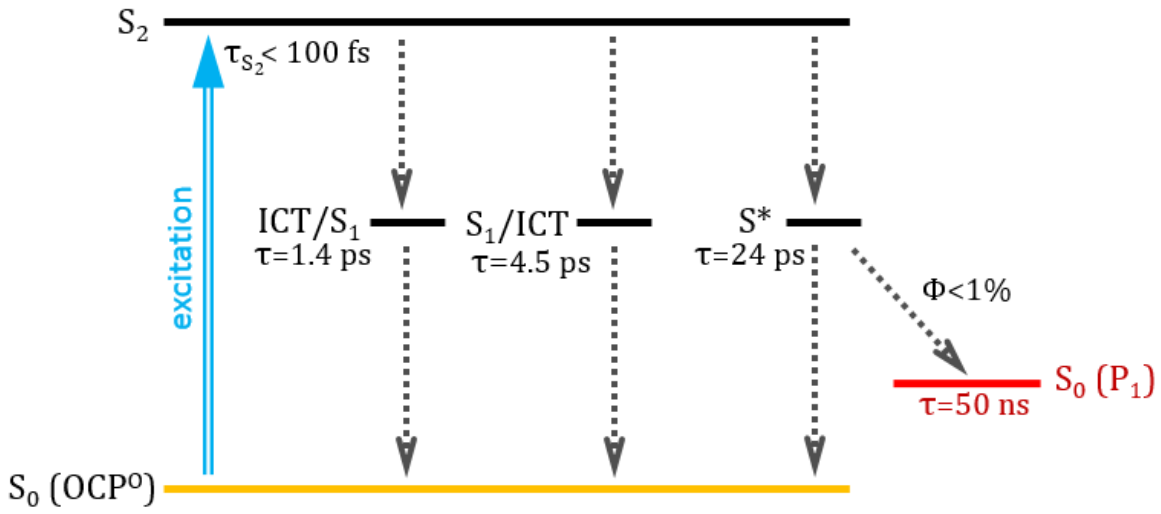

Figure 51. Excitation of the OCP° and populated states in ECN-containing OCP from *Synechocystis*, including S* state as proposed by Konold et al.[28]

After excitation, both dark-adapted OCP subpopulations ("normal" and "red-shifted") are promoted to symmetry-allowed electronic S_2 state (Figure 51).[279] The S_2 state has a lifetime below 100 fs, however usually it is too fast to be well resolved by ultrafast UV-vis spectroscopy.[21, 282] The S_2 state is characterized by a maximum of the ESA band of about 1200 nm, and $S_2 \rightarrow S_0$ stimulated emission spectrally located at the red edge of OCP° ground state absorption band.[283]

The S_2 state population decays into two excited state populations, which are both superpositions of ICT and S_1 state.[279, 285] They are denoted as ICT/S_1 (with a major contribution of ICT) and S_1/ICT (properties closer to pure S_1 state).[279, 285] The third path populates S* state, which was found in OCP in 2019.[28] Excitation wavelength affects the selection of ground state subpopulations, which are consequently promoted to the S_2 state.[279, 282] Excitation wavelengths over 500nm select mostly the "red-shifted" subpopulation with a more pronounced ICT character. It results in a more pronounced ESA band around 740 nm, and a red-shifted GSB band as well.[279, 282] Early studies suggested that the presence of two states (ICT/S_1 and S_1/ICT) stems from two ground state subpopulations.[279, 283] However, latter reports found that each subpopulation is characterized by both ICT/S_1 and S_1/ICT states, so they are not subpopulation-specific.[282, 285] In 2021, so-called "mixed state" was resolved, with a lifetime of about 130 fs.[21] It is populated directly from the S_2 state, and decays to longer-living excited states. Its interpretation is unclear, it may be associated with a hot S_1, ICT, S* populations.[21]

The excited states in OCP have shorter lifetimes, than expected for the same carotenoid in the solution phase.[279] This shortening is attributed to the configuration of the carbonyl end-ring being closer to *s-trans*, caused by the interaction with the protein binding pocket. It results in a longer effective conjugation length of carotenoids in the OCP. It also couples the carbonyl group to the polyene chain, "switching on" the ICT state.[279]

Various reports provide diverse and not always consistent lifetimes for the carotenoid excited states, because the fitting model changed over the years. Moreover, the number of

necessary components is relatively large. The decomposition of the transient absorption spectra into contributions from each state is fundamentally ambiguous, therefore obtained spectra and lifetimes differ significantly in literature.

S_1 state of carotenoid in OCP

In most OCP variants, the S_1 state has a lifetime close to 3 ps, shorter than that of carotenoid in the solution phase.[283] The maximum of the S_1 ESA band is located at about 660nm.[285] Usage of longer excitation wavelength results in slightly shorter S_1 lifetime, and decreased contribution of this state.[282]

In the NIR region, there is an $S_1 \rightarrow S_2$ ESA band located above 1400nm, with a maximum of about 1800nm.[283] This band is redshifted with respect to pure carotenoid in the solution phase, where it figures below 1600nm. The vibrational pattern of this $S_1 \rightarrow S_2$ band is comparable to stationary $S_0 \rightarrow S_2$.[283]

ICT state of carotenoid in OCP

Carbonyl carotenoids in OCP (and also in some light-harvesting complexes) usually show a strong contribution of ICT band, despite the lack of such band in solution.[279, 292] The contribution of ICT depends strongly on the selection of excitation wavelength, due to the selection of different ground state subpopulations.[282] Excitation at the red edge of the stationary OCP^O absorption band result in much more pronounced ICT character.[279, 282-283, 285] Contrary to ECN and hECN, CAN functionalized OCP exhibits almost no ICT state.[282] However, it was found, that UV excitation enhances the ICT character in canthaxanthin.[22, 293]

ICT state in OCP usually has a lifetime slightly below 1 ps.[283, 285] $S_{ICT} \rightarrow S_n$, ESA band of the ICT state spans wavelengths from 650 nm up to 1100 nm, with a maximum around 740 nm.[283, 285] There is a negative stimulated emission band from the ICT state located at about 1200nm, however, it is usually hard to observe in transient absorption data due to overlap with positive ESA bands.[283]

S state of carotenoid in OCP*

Most of the early OCP studies have not considered the S* state. As a consequence, comparison between results in various reports is problematic, due to a different number of components (intermediates) taken into account. Therefore ICT and S_1 lifetimes given in older studies may be overestimated, because they possess a fraction of S* contribution not taken into account. Note, that the S* lifetime is longer than that of ICT and S_1 states.[28] The first report about the S* state in OCP functionalized with hECN observed a 24 ps lifetime (upon excitation with 100 fs, 400 nJ pump), however the usage of stretched, low energy excitation pulse (2 ps, 150 nJ) resulted in a shorter S* lifetime of 15 ps.[28] A UV pump pulse results in an increased contribution of the S* state compared to a visible excitation.[22, 183] A more recent study found a shorter S* lifetime of about 5 ps for wild type OCP and 9 ps for a mutant OCP, where Tyr-203 (equivalent numbering) is replaced with tryptophan (both functionalized with ECN).[21] Replacement of Tyr with Trp results also in approximately a fivefold increase in S* state yield.[21]

It was proposed, that the S* state is a precursor of the P_1 form.[28] In 2020, fluorescence of the Trp-290 (equivalent numbering) was investigated and it was concluded that the breaking of the hydrogen bond between Trp-290 (equivalent numbering) and carotenoid occurs with a time constant of 23 ps.[24] This time constant agrees very well with the lifetime of the S* state, suggesting that indeed it triggers the photoconversion process.[24]

P1 - first ground state intermediate of the OCP

Accordingly to the results of ultrafast spectroscopy, after the decay of all excited states, one can observe a weak signature resembling OCP^R, but slightly redshifted (λ_{max}≈565nm) with respect to the carotenoid S_0 state absorption band in the OCP^R form.[28] It constitutes less than 1% of the initially excited OCP^O population.[15, 28] The hydrogen bond in this intermediate, coined as P_1, is broken.[28] It was proposed, that bent, distorted structure of the carotenoid in the OCP^O state resembles a spring under tension, fixed in place by the carbonyl hydrogen bond.[44, 287] When the P_1 state is formed, and the carbonyl bond no longer exists, the potential energy stored in the bent carotenoid can be released resulting in various rearrangements of the protein structure.[44, 287] This view has been undermined by the recent theoretical results, which proposed that carotenoid resembles a latch, which moves to the NTD releasing all the binding interactions which keep both domains together, allowing them to dissociate (Figure 52).[26]

5.2 Protein structural rearrangements in the ns-ms timescale

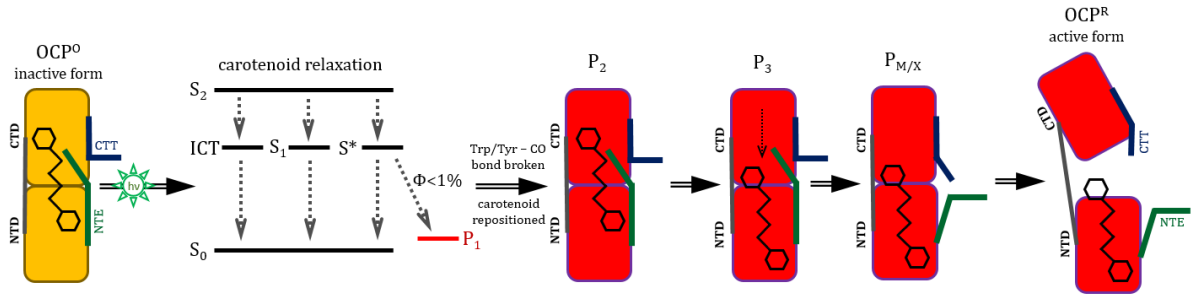

Figure 52. Simplified scheme of the OCP^O→OCP^R photoconversion.

After the decay of carotenoid excited states on the tens of picoseconds timescale, one can observe the signature of the protein intermediate – P_1, which absorption band is redshifted with respect to the OCP^O.[28] There is no significant signal evolution up to a few nanoseconds, which is usually the end of the femtosecond transient absorption time window. After the excitation with the pulse of ns Nd:YAG laser (usually ≈ 10 ns FWHM), one can already observe a red OCP intermediate, spectrally resembling the OCP^R.[44]

Konold et al. proposed a cascade of P_1 (50 ns), P_2 (500 ns – 1.1 µs), P_2' (10 µs) and P_3 (> 1 ms) intermediate forms (see Figure 52), representing different stages of the photoconversion process (up to 1 ms), associated with sequential changes of the protein structure and carotenoid geometry within this structure (while carotenoid stays in the electronic ground state).[28]

Nanosecond transient absorption studies of the OCP from *Synechocystis* at 36 °C revealed 300 µs and 18 ms time constants (plus the third one, representing OCP^R → OCP^O back conversion).

18 ms component has a low amplitude (≈10%) and disappears upon the addition of salt or FRP.[44] It was proposed that the 300 μs time constant represents the decay of the OCP^{RI} intermediate form, where the protein structure still resembles OCP^{O}, except NTE location which is probably already detached from the CTD.[44]

Note that later studies sometimes introduced different nomenclature, therefore the equivalent intermediates proposed by other authors, which are discussed in the following subsections are grouped together.

P_1 intermediate

The P_1 form can be described as the first intermediate of the protein, formed after the decay of the carotenoid excited states. In P_1 the carotenoid – protein hydrogen bond is broken and the absorption spectrum is redshifted.[28] Moreover, it was proposed that the carotenoid in P_1 is planar, but not translocated yet.[28] P_1 decays with a 50 ns time constant at room temperature. It was estimated that around 40% of the P_1 population continues the journey towards the OCP^{R} form, while the remaining 60% recreates hydrogen bond and returns to the OCP^{O} form.[28]

P_2/T_1 and P_2' intermediates

The P_2 form possesses a maximum of difference transient absorption band at about 555 nm and a lifetime of 10 μs.[28] It was proposed, that in this state the carotenoid is repositioned, in the quasi-equilibrium geometry, after being released from the strain caused by the carbonyl group - protein hydrogen bond. Interactions between the β2 carotenoid terminal ring and Tyr-44 and Trp-110 in the NTD are also violated.[28]

The T_1 intermediate resembling P_2 was proposed based on theoretical studies.[26] It is described as a first minimum along the arbitrary reaction coordinate (selected as the distance between the carotenoid and the NTD) after the OCP^{O}, where the carotenoid is not significantly translocated yet, but far enough to break carbonyl group - protein hydrogen bonds.[26] Other theoretical QM/MM study described P_2 state, where a planar carotenoid is already in the halfway of the translocation.[25]

The P_2' form was proposed exclusively based on time-resolved IR spectroscopy results, and it is not visible in the transient UV-vis spectra.[28] P_2' manifests itself as a negative ΔA signal at 1654 cm^{-1} and 1581 cm^{-1} and exhibits evolution on the 0.5 – 1.1 μs timescale (during the decay of the P_2 state). It is associated with structural changes in the helices of NTD, which are triggered in the P_2 form and required to make space for the carotenoid.[28]

$P_3/T_2/P_N/OCP^{RI}$ intermediate

The P_3 form is equivalent to the OCP^{RI} form proposed by Maksimov et al.[44] The shape of the absorption spectrum of P_3 closely resembles OCP^{R}. It was proposed, that in this state carotenoid is translocated towards the NTD, however, NTE and CTT are still not affected and domains are not separated.[27-28] Therefore the 10 μs (P_2 decay) is associated with the carotenoid translocation process.[27-28] P_3 decays with the time constant of 10 ms at 20 °C.[24]

A carotenoid translocation ($P_2 \rightarrow P_3$ process) energy barrier was estimated at approximately 10 kcal/mol, based on QM/MM calculations.[25] It is associated with a transition

bottleneck, where the carotenoid must be highly geometrically distorted to go through, and reach a fully translocated state (P_3). In the P_3 state, the carotenoid restores its planarity.[25] A recent theoretical study confirmed, that indeed carotenoid translocation must occur before domain separation.[26] It was proposed, that carotenoid interacts strongly with both CTD and NTD domains, keeping them together. After the carotenoid is translocated to the NTD, domains are no longer held together – they must dissociate.[26] T_2 intermediate was proposed, which is a P_3 analog. It is described as a second minimum along the arbitrary reaction coordinate after the OCP^O (next one after T_1/P_2).[26] In the T_2 intermediate, the carotenoid is almost completely translocated and resembles geometry found in the RCP.[25-26] However, domains are not separated yet, but the interactions keeping them together are broken.[26]

P_M, P_X intermediates – opening of the protein

The knowledge about the dynamics of the domain dissociation process is very recent and still incomplete. In a recent study by Maksimov et al., a special mutant was designed with only one Tryptophan: Trp-290 (equivalent numbering).[24] It allowed to directly track the state of hydrogen bond with the carotenoid carbonyl group. Based on Trp-290 (equivalent numbering) fluorescence, two additional P_M (τ=35 ms) and P_X (τ=100 ms) forms were proposed.[24] The nature of the P_M and P_X states is not clear, they are likely associated with conformational changes in the NTE and CTT. In the P_X state the NTE and CTT are unfolded, enabling the final step which is the NTD and CTD separation, and subsequent formation of the final OCP^R form.[24]

5.3 OCP^R accumulation and decay

Tracking the absorption spectrum of the OCP *in vivo* is rather challenging, because they constitute less than 1% of all carotenoids in the cyanobacteria cells.[233] Therefore most of the initial studies, which have probed the photoactivity of this protein have been based on PBS fluorescence measurements in the dark and after illumination.[16, 244-246] Later, after the isolation of purified OCP, it became possible to track the absorption of the carotenoid in the OCP directly.[15, 17]

Due to a very low $OCP^O \rightarrow OCP^R$ photoconversion quantum yield, observation of the latter intermediates present after the pulse excitation is challenging. Caution must be taken to distinguish real photoconversion intermediates from artifacts, when low-intensity transient absorption signals are analyzed. Moreover, observed processes extend even beyond one second, so the experiment repetition must be slowed down accordingly, making the task of obtaining a decent signal even harder. Therefore sometimes it is much more convenient to use continuous irradiation light, and observe the accumulation of the redshifted products. Most of the initial studies of OCP were done this way, firstly tracking the fluorescence of phycobilisome *in vivo*, and later, tracking photoinduced changes in the absorbance of pure OCP solutions *in vitro*.

OCP^R accumulation in long timescales

In order to observe how fast the OCP^R population is accumulated, a source of constant light intensity is usually employed. After switching on the irradiation light, the red species start accumulating, which is reflected by a change in the sample's absorption spectrum (*in vitro*), or

fluorescence (*in vivo*). The maximum of the ΔA band of the OCP^R population accumulated by application of the continuous light is close to 550nm.[28]

In modeling of the photoconversion upon continuous irradiation, it has been usually assumed that only one intermediate state exists with a lifetime long enough to be successfully recorded in this experiment (around 7 s *in vivo* and below instrument response time *in vitro*).[43, 45] This intermediate probably describes the process of attaching the OCP^R to PBS.[43, 45]

An experiment done with tracking the gradual FT-IR spectrum changes under continuous illumination revealed, that two asynchronous steps are visible in the seconds time scale at 4 °C (which can be extrapolated to hundreds of milliseconds at room temperature).[32] Both steps are associated with *α*-helices reorganization, and the second step is influenced by the solvent.[32]

Back conversion to the OCP^O form

In the beginning, it was observed that decay of the OCP^R population, observed after the accumulation with intense continuous light is single exponential.[15] Moreover illumination of OCP^R does not speed up back conversion, meaning that there is no light-induced pathway from OCP^R to OCP^O.[15] Back conversion $OCP^R \rightarrow OCP^O$ process is highly temperature dependent.[44] A lifetime of the OCP^R form is about 3 s at 36 °C after pulse excitation.[44] After accumulation with continuous light, OCP^R lifetime equals 43 s at 32 °C and more than one hour at 11°C.[15]

Maksimov et al. first observed double exponential decay of OCP^R formed by continuous illumination (13 s and 66 s at 15°C).[45] Both exponential terms had a constant amplitude ratio 2:1, regardless of temperature.[45] The decay rate constant was found to depend on the irradiation intensity used to populate OCP^R.[45] Based on Trp-fluorescence measurements, it was proposed that $OCP^R \rightarrow OCP^O$ back conversion proceeds through an intermediate orange-like OCP^{OI} form.[44] In order to decay, OCP^R form undergoes back translocation of the carotenoid, followed by repositioning of the NTD with respect to the CTD, so the carotenoid arrives in close proximity of the Tyr-203 residue, forming the hydrogen bond and populating orange-like OCP^{OI} intermediate form. To reach the stable OCP^O form, final readjustments of the protein structure are required and the carotenoid must be properly bent in the binding pocket.[44]

5.4 Questions to be answered

The reading of available OCP literature has opened to us a variety of new questions about photoconversion dynamics. We attempted to answer some of them in the following publications. The most important questions are:

1) Which excited state of the carotenoid initiates the photoconversion process leading to the OCP^R form? Although the S* state was put forward as a candidate, this hypothesis still requires verification.
2) In the publication of Konold *et al.,* the authors found that S* lifetime depends on excitation pulse density. Therefore, for future experiments, it is important to investigate this effect and determine the maximum pump energy, for which observed photophysics is not influenced by nonlinear effects.

3) There are many OCP variants, one can extract them from various strains of cyanobacteria, replace the originally occurring carotenoid (in wild type OCP it is usually hECN) with a different one, or change the site of tagging (which is usually required for the purification purposes, however, it may also influence OCP function). These variants behave differently during photoactivation, therefore investigating how structural properties affect photoactivation may be interesting and allow to understand better the photoconversion process itself.
4) The photoconversion process in longer timescales (above 1ms) is still quite obscured and various intermediates of unclear nature have been proposed (P_M, P_X). The questions remain, when the $OCP^O \rightarrow OCP^R$ photoconversion is fully completed, and what is the mechanism of the final steps of this process.
5) Despite the formation quantum yield of the OCP^R form has been estimated in a few reports, there are still discrepancies. It may be interesting to check if the quantum yield calculated upon continuous irradiation agrees with the quantum yield calculated using nanosecond transient absorption spectroscopy, and check how irradiation intensity affects these yields.
6) Determined crystal structures of the OCP are in the dimeric state, and OCP^O dimers also form in the solution phase at concentrations, which are utilized in transient absorption experiments. Therefore, it may be important to investigate the effect of dimerization on observed kinetics, especially in long time windows where this effect may be more significant.

6. Overview of the included publications

The main purpose of this thesis is to characterize intermediates linking inactive OCP^O form and active OCP^R form, determine their quantum yields and build a scheme describing the photoconversion process. Within this thesis, various new observations about the photoconversion process have been found. Results are presented in 4 published papers.[166, 290, 294-295] In the following sections, each paper is preceded by a short abstract, which summarizes the conclusions with emphasis on work done within this thesis. This overview focuses on work done by the author of this thesis, rather than parts of the publications which have been done by other authors.

6.1 Unifying perspective of the ultrafast photodynamics of orange carotenoid proteins from Synechocystis: Peril of high-power excitation, existence of different S* states, and influence of tagging

In this publication, femtosecond transient absorption vis-NIR spectroscopy was applied to investigate the decay of the excited states of the ECN carotenoid and the formation of the first protein intermediate state P_1 in OCP from *Synechocystis*. Two slightly different OCP samples, C-tagged and N-tagged, were compared using two excitation wavelengths, namely 470 nm and 540 nm, and the influence of excitation laser pulse energy was studied. As a result of the collective interpretation of the multiset dataset, the following conclusions were obtained:

1) All excited states observed for C-tagged OCP decay faster than the N-tagged OCP. The quantum yield of the P_1 form visible at 1 ns is similar regardless of the tagging site (≈0.5%). Despite that, the efficiency of $OCP^O \rightarrow OCP^R$ photoconversion observed upon continuous irradiation light is considerably higher for the N-tagged OCP. Therefore the step which limits the photoconversion efficiency must be located in the nanosecond – millisecond regime.
2) If the excessive pump energy is applied, then radical cation is formed, through a multiphoton excitation channel. Its absorption band can be observed at about 950 nm. Safe and optimal pump energy was defined: 0.4 μJ for 470 nm (peak power density of ≈5 GW/cm^2) and 0.8 μJ for 540 nm (peak power density of ≈10 GW/cm^2). These values are high enough to obtain a visible P_1 band and avoid forming biologically irrelevant species.
3) In order to obtain a consistent and meaningful interpretation, one has to add an extra $S^{\sim}$ component to the fitting scheme of the 470 nm excited data. It is due to the presence of an additional signal after 470 nm excitation, living much longer (≈ 80 ps lifetime) than other states (S_2, S_1, ICT, S*). This state (resembling the $S^{\ddagger}$ state observed in a different study[296]) is likely a result of the presence of different, shorter-chain carotenoids, being a relic of the standard purification process. In order to avoid this contribution, one should use a long-wavelength excitation pulse.

4) Using a comparison between datasets, it was found that the S_1 state is the most likely precursor of the P_1 form, contrary to the hypothesis that the S* leads to the P_1 form.
5) Finally, a scheme describing the OCP deactivation process up to 1 ns was proposed.

This work is important from the experimental perspective, since the data were collected in various conditions. The most optimal pump energy density and excitation wavelength were defined, establishing the standard for the following experiments. However, this work does not explore photoconversion events after 1ns, and focuses mostly on electronic excited states and the formation of the first photoproduct – P_1.

In this publication, I was responsible for femtosecond transient absorption measurements and UV-vis absorption measurements in the dark and upon continuous irradiation, as well as data preprocessing, analysis, fitting and plotting. I wrote the initial version of the manuscript and took part in the development of the final version. Moreover, I contributed to the development of the custom package *Ultrapyfit*[52], which was used to process femtosecond transient absorption data in this and other publications included in this thesis. I also performed preliminary experiments required to determine conditions used in the final experiments (excitation energy, wavelength, optical filtering, accumulation times, etc.).

6.2 Structure-function-dynamics relationships in the peculiar Planktothrix PCC7805 OCP1: Impact of his-tagging and carotenoid type

In this paper, the effect of the functionalizing carotenoid (CAN and ECN) was investigated, moreover, the OCP from *Synechocystis* and *Planktothrix* cyanobacteria were compared. The experiments done within this thesis covered 100 fs to 1 s temporal regime using transient absorption spectroscopy methods, extending greatly the time regime explored in the first paper. The goal was to determine at which timescale the differences between OCP types are manifested, and assign them to the structural events. The results of these experiments are the following:

1) CAN-functionalized OCP photoactivates much more efficiently, but recovers slower than ECN-functionalized OCP.
2) P_1 quantum yields are similar for all the OCP types (≈0.5%), therefore the observed differences in $OCP^O \rightarrow OCP^R$ photoconversion efficiency must occur in longer timescales. Some differences in the excited state dynamics were observed, especially for CAN-functionalized OCPs, the ICT state contribution is much less pronounced, due to the symmetry of the CAN carotenoid.
3) The amount of red-absorbing OCP species at 50 ns (where the time window of the nanosecond experiment starts) is slightly higher for *Planktothrix* compared to *Synechocystis* OCPs. It suggests that some recovery to OCP^O form occurs for *Synechocystis* OCP in the 1 ns – 50 ns time range, during the P_1 state decay ($\tau_{P_1} \approx 50$ ns).
4) A large difference between *Planktothrix* and *Synechocystis* OCPs can be observed in the 50 ns – 10 μs timescale, where the P_2/P_2' forms revert much more efficiently to the

OCP^O in the *Planktothrix* case. It suggests that carotenoid translocation is more efficient in OCPs from *Synechocystis* compared to *Planktothrix*.

5) A large difference between CAN and ECN functionalized OCPs can be observed in the 1 ms -1 s timescale, where the domain dissociation takes place. CAN-functionalized OCPs exhibit much more efficient domain separation, without back conversion to the OCP^O form during this process. At 1 s, the quantum yield of the red species is the highest for CAN-functionalized OCP from *Planktothrix* (≈ 0.2 %). In addition, for this OCP the ΔA(550nm) increases between 0.1 ms and 100 ms, indicating that a band shift or similar effect may occur in this time regime.
6) These results, together with the X-ray scattering data collected by French collaborators allowed to propose an updated scheme describing $OCP^O \rightarrow OCP^R$ photoconversion.

This work provides an important insight into the OCP photoactivation process, which is based on a comparison of time-resolved dynamics between various OCP types. However, this work does not consider dimerization effects, focusing mostly on the comparison between different OCP variants.

In this publication, I was responsible for femtosecond and nanosecond transient absorption measurements and preprocessing, analysis, fitting and graphical presentation of data collected in these experiments. I was also responsible for modifications of the nanosecond transient absorption setup, in order to meet specific requirements associated with the OCP sample (customized probing beam, decreased laser repetition frequency). I also developed a custom method to merge kinetic data registered using various temporal windows.

6.3 Oligomerization processes limit photoactivation and recovery of the orange carotenoid protein

In this publication, dimerization influence on $OCP^O \rightarrow OCP^R$ photoconversion was investigated. Three OCP types were compared - the N-tagged and C-tagged OCP from *Synechocystis* functionalized with ECN, and the so-called "monomeric mutant". In the monomeric mutant, the R27 residue is modified, disabling the OCP^O-OCP^O dimerization interface. The transient absorption data collected within this thesis in a function of temperature and concentration, cover the 100 ns – 1s time window. Two probing wavelengths were applied, namely 440 nm and 565 nm, with excitation at 470 nm. They probe the OCP^O form depletion (440 nm) and the formation of the red-shifted species (565 nm), respectively. It was found, that:

1) The P_2 state, visible at the beginning of the time window is formed with a quantum yield close to 0.7% (estimated from the 440 nm kinetics), regardless of the temperature. Surprisingly, the ΔA at 565 nm decreases with the temperature, suggesting some counterproductive pathway being opened in the higher temperatures.

2) The observed decay kinetics show three steps. The first one ($\tau_1 \approx 2$ µs) shows adiabatic behavior and a decrease in entropy. The remaining ones ($\tau_2 \approx 1$ ms and τ_3 between 40 ms and 200 ms) have activation enthalpies comparable to each other (approximately 20 kcal/mol) and positive change in entropy. Most of the OCP^O recovery occurs during the τ_2 and τ_3 decays.
3) As expected, kinetics registered for monomeric mutant are independent of the concentration, indicating no oligomerization in the OCP^O form. However, the longest time constant (τ_3) of C-tagged OCP doubles its value, when the concentration is increased from 12 µM to 250 µM. It indicates a slower recovery to the OCP^O form, when the dimer is excited, compared to the monomer.
4) The red-shifted species visible 1 s after a single pump pulse are likely not the OCP^R form. The quantum yield of the red-shifted species at 1 s decreases with the temperature, and above 22 °C such intermediates were not observed. The $OCP^O \rightarrow OCP^R$ quantum yield is also higher for N-tagged OCP.
5) The τ_1 time constant is likely associated with the carotenoid translocation from the CTD to the NTD (P_2/P_2' to P_3 transition).
6) The τ_2 and τ_3 time constants are likely associated with recovery of the OCP^O form (reversed carotenoid translocation back to the CTD). The presence of two similar time constants is presumably due to the existence of two ground state subpopulations (normal and red-shifted). Only τ_3 is significantly affected by dimerization.
7) All collected data suggest, that in order to produce a fully developed OCP^R form, both OCPs in the dimer must be photoconverted to the P_3 intermediate. Only then, the P_3/P_3 dimer can separate into monomers, where CTD and NTD domains in both of them can also dissociate, forming two OCP^Rs. The partially photoconverted OCP_O/P_3 dimer formed by a laser pulse is unlikely to reach the OCP^R form. Therefore continuous light is required to accumulate the photoactive OCP^R forms.

These results are based on optical and X-ray spectroscopy time-resolved methods applied synergistically in order to investigate structural events occurring in OCP after the absorption of a photon and the presence of the oligomerization.

In this publication, I was responsible for femtosecond and nanosecond transient absorption measurements, preprocessing, analysis, fitting and graphical presentation of data collected in these experiments. I wrote the initial version of the section about the performed femtosecond transient absorption measurements and nanosecond transient absorption measurements. I participated in the later development of this section. I customized the nanosecond transient absorption setup in order to perform measurement with a low repetition frequency and weak probing beam, in various geometries (to accommodate for specific sample concentration and minimize laser light scattering).

6.4Is orange carotenoid protein photoactivation a single-photon process?

In this article, the process of OCP^R accumulation upon continuous irradiation was investigated in detail. Because very small pulse-induced formation of the OCP^R was observed in the previously published paper, it opened a box full of questions, especially the one asking if pulse-excitation and continuous irradiation lead to the same OCP^R form. Therefore in this paper, a dependence on photoconversion from the irradiation intensity was analyzed more closely. It has been found, that the rate of photoconversion observed after switching on the irradiation light does not increase linearly with the increase of irradiation intensity, as one would expect in a single-photon process scenario. Instead, the determined OCP^R formation quantum yields increase with the irradiation intensity (in the 10 – 200 μmol m^{-2} s^{-1} range). It has been proposed, that absorption of more than one photon is necessary to photoconvert one OCP species efficiently. Comparison with the transient absorption data in the millisecond scale revealed that ≈ 100 ms living intermediate is probably decaying to the OCP^O, unless it absorbs a (second) photon, necessary to reach the final OCP^R form. In other words, two subsequent photon absorption events must occur in order to reach the OCP^R form. In the case of C-tagged OCP, almost no single-photon photoconversion can be observed after a nanosecond pulse excitation. On the other hand, N-tagged OCP may possess both single-photon and two-photon photoconversion pathways.

In this publication, I was responsible for all of the experiments (transient absorption measurements, UV-vis absorption measurements in the dark and upon continuous irradiation and transient absorption measurements with additional continuous irradiation), preprocessing and analysis of the transient absorption data, plotting of the graphs. I modified a stationary UV-vis spectrometer in order to register spectra upon external continuous irradiation light. I performed simulations of the OCP^R accumulation kinetics based on various hypothetical photoconversion models using my custom Python package.[63] I wrote the initial version of the manuscript and participated in the development of the final version of the manuscript. I proposed two-photon mechanism based on analogy to other systems, naphthopyrans.[297-298]

7. Concluding remarks

All four published papers leave us with a very complex picture of the OCP photoconversion mechanism. However, some of the observations may turn out to be important milestones required to understand the process in the future.

Firstly, it is clear that the low quantum yield of the OCP photoconversion is already determined within the first tens of picoseconds after the excitation. The quantum yield of the P_1 is comparably low for all investigated OCP variants (and those studied but not yet published). It opens the question, whether it is practically possible to turn the OCP into an efficient photoswitching system? Maybe it is already so well optimized to perform a photoprotective function with a low yield, so it cannot be significantly altered with a single mutation? On the other hand, maybe it is necessary to modify a chromophore (carotenoid), instead of an amino acid sequence? Since the low yield of the photoconversion is decided presumably even before the relaxation of the carotenoid excited states is completed, it seems reasonable to expect that the carotenoid itself may have a deciding effect on the process of P_1 formation. All the carotenoids encountered in the OCP so far are similar. It may be tempting to examine, for example, a set of carotenoids with various conjugated chain lengths or even something completely different, like 4-ketoretinal, a derivative of the chromophore from bacteriorhodopsin? These molecules possessing various geometries and the nature of excited states could provide us with some interesting information about protein-chromophore interaction in the OCP.

Another important finding is that the most significant differences in the photoconversion process between OCP variants occur 1 ms after the excitation and later. At these timescales, the carotenoid translocation is already completed, and domain separation is the remaining step to reach the final OCP^R form. It seems that some of the OCP variants are more willing to perform this step than others. Nevertheless, designing new mutants which are more prone to complete this last step will not solve the problem of low OCP^R quantum yield (which is decided much earlier).

It has been found that the OCP variant with the most efficient photoconversion is N-tagged CAN-functionalized OCP from *Planktothrix*. This OCP variant is probably the best starting point for further yield-enhancing modifications. The nanosecond transient absorption data suggest that OCPs from Synechocystis undergo slightly more effective carotenoid translocation than OCP from *Planktothrix*, while CAN-functionalized OCP can undergo domain separation more effectively than ECN-functionalized OCP. However, the data suggest also that some band-shifts may occur, so measurements with probing at various wavelengths are required to obtain a better insight into these processes and the full spectra of the intermediates.

In the last paper, we observed a very interesting effect. The C-tagged OCP from *Synechosystis* (with ECN) is not able to reach the final OCP^R form after excitation with a single excitation pulse of the nanosecond laser. This is quite surprising, since one can observe a photoconversion of the same OCP variant upon continuous irradiation. It can be explained that only a consecutive absorption of two photons can push the OCP^O form to convert into OCP^R form. This observation opens numerous questions. What is the efficiency of both photoconversion steps? Is this a general property of all OCPs, or just of this specific variant? Maybe the differences

between variants stem from the presence or lack of a single-photon photoconversion pathway? There is a possibility that two-photon behavior stems from the inability of the OCP^O to complete its photoconversion in one step (so a second "push" is needed). The second possibility is that the presence of two-photon photoconversion is always a dominant mechanism in high light conditions and a symptom of adaptation to the natural conditions (to achieve a high sensitivity in strong sunlight and a low sensitivity in weak sunlight).

Another question concerns the mechanism underlying the two-photon photoconversion. What exactly is an $OCP^{1h\nu}$ species proposed as an intermediate state? Does it decay directly to the OCP^O in the dark or populate some not-fully relaxed form, which is more prone to photoactivation than the OCP^O? These are open questions, and answering them may require the development of completely new experiments. An experiment utilizing two excitation pulses with a variable delay between them is especially promising, because it may provide more direct information about $OCP^{1h\nu}$ lifetime.

Another important issue is the effect of dimerization and its connection with a two-photon behavior. It is clear, that after the nanosecond excitation, the ≈100 ms lifetime increases together with OCP^O concentration. It suggests higher stability of this intermediate in the dimeric OCP^O form compared to the equivalent intermediate in the monomeric OCP^O. It indicates that an OCP dimer where only one half is in the intermediate state (domains aren't separated yet) is more stable than a single monomer in the same intermediate state. Structural insight strongly suggests that the same type of dimer as in the OCP^O form cannot be retained in the OCP^R form, because the OCP^O dimerization sites prevent the domains from separating. Therefore, the OCP^O dimer should dissociate in order to allow for domain separation in one of the monomers and its conversion into the OCP^R form. Due to the complexity of this process, more experiments are needed to understand all the details.

At this point, it is clear that much more data is required to fully describe the photoconversion process. Especially the μs and ms regime must be further investigated. Measurements in these timescales are very challenging due to the influence of the probing light intensity and low repetition rate. Due to these issues, collecting only one kinetics of sufficient quality is very time-consuming.

The state of the literature introduced in the initial chapters of this work provided us with quite a rich understanding of dark-adapted (OCP^O) form and photoactive (OCP^R) form, even with detailed structural information. Despite a well-defined starting point of the study, the remaining questions about the nature of intermediate forms are not trivial. Time-resolved X-ray scattering, especially the SFX method, may shed some light on the protein structure during the early moments of photoconversion. Still, understanding the events in the longer timescales is a challenge due to a very low formation quantum yield of the OCP^R, which disqualifies the straightforward application of these methods. In long timescales, transient-absorption spectroscopy still has the advantage of tracking intermediates with low instantaneous concentrations. However, care must be taken in future studies in order to obtain reliable datasets.

8. References

1. Niziński, S. *Badanie właściwości fotofizycznych miraksantyny V w ekstraktach roślinnych. Bachelor thesis.* Poznań, 2015.
2. Ke, B. Photosynthesis: An Overview. In *Photosynthesis: Photobiochemistry and Photobiophysics*, Govindjee, Ed. Kluwer Academic Publishers: 2001; Vol. 10.
3. Hamilton, T. L.; Bryant, D. A.; Macalady, J. L. The role of biology in planetary evolution: cyanobacterial primary production in low-oxygen Proterozoic oceans. *Environ. Microbiol.* **2016,** *18* (2), 325–340.
4. Larkum, A. W. D. Light-harvesting in cyanobacteria and eukaryotic algae: An overview. In *Photosynthesis in algae: Biochemical and physiological mechanisms*, Larkum, A. W. D.; Grossmann, A. R.; Raven, J. A., Eds. Springer: 2020; Vol. 45.
5. Papageorgiou, G. C.; Govindjee. The non-photochemical quenching of the electronically excited state of chlorophyll a in plants: Definitions, timelines, viewpoints, open questions. In *Non-photochemical quenching and energy dissipation in plants, algae and cyanobacteria*, Demmig-Adams, B.; Garab, G.; Adams III, W.; Govindjee, Eds. Springer: 2014; Vol. 40.
6. Croce, R.; Van Amerongen, H. Natural strategies for photosynthetic light harvesting. *Nat. Chem. Biol.* **2014,** *10* (7), 492–501.
7. Liu, H.; Zhang, H.; Niedzwiedzki, D. M.; Prado, M.; He, G.; Gross, M. L.; Blankenship, R. E. Phycobilisomes supply excitations to both photosystems in a megacomplex in cyanobacteria. *Science* **2013,** *342* (6162), 1104-1107.
8. Kirilovsky, D.; Kaňa, R.; Prášil, O. Mechanisms modulating energy arriving at reaction centers in cyanobacteria. In *Non-photochemical quenching and energy dissipation in plants, algae and cyanobacteria*, Demmig-Adams, B.; Garab, G.; Adams III, W.; Govindjee, Eds. Springer: 2014; Vol. 40.
9. Kirilovsky, D. Modulating energy transfer from phycobilisomes to photosystems: State transitions and OCP-related non-photochemical quenching. In *Photosynthesis in algae: Biochemical and physiological mechanisms*, Larkum, A. W. D.; Grossmann, A. R.; Raven, J. A., Eds. Springer: 2020; Vol. 45.
10. Niedzwiedzki, D. M.; Blankenship, R. E. Singlet and triplet excited state properties of natural chlorophylls and bacteriochlorophylls. *Photosynth Res.* **2010,** *106*, 227–238.
11. Krieger-Liszkay, A.; Fufezan, C.; Trebst, A. Singlet oxygen production in photosystem II and related protection mechanism. *Photosynth Res.* **2008,** *98* (1-3), 551–564.
12. Khorobrykh, S.; Havurinne, V.; Mattila, H.; Tyystjärvi, E. Oxygen and ROS in photosynthesis. *Plants* **2020,** *9* (1), 91.
13. Demmig-Adams, B.; Garab, G.; Adams III, W.; Govindjee. *Non-photochemical quenching and energy dissipation in plants, algae and cyanobacteria*. Springer: 2014; Vol. 40.
14. Ruban, A. V. Nonphotochemical chlorophyll fluorescence quenching: Mechanism and effectiveness in protecting plants from photodamage. *Plant Physiol.* **2016,** *170* (4), 1903–1916.
15. Wilson, A.; Punginelli, C.; Gall, A.; Bonetti, C.; Alexandre, M.; Routaboul, J.; Kerfeld, C. A.; Grondelle, R.; Robert, B.; Kennis, J. T. M.; Kirilovsky, D. A photoactive carotenoid protein acting as light intensity sensor. *Proc. Natl. Acad. Sci. U.S.A.* **2008,** *105* (33), 12075–12080.
16. Wilson, A.; Ajlani, G.; Verbavatz, G. M.; Vass, I.; Kerfeld, C. A.; Kirilovsky, D. A soluble carotenoid protein involved in phycobilisome-related energy dissipation in cyanobacteria. *The Plant Cell* **2006,** *18* (4), 992–1007.
17. Gwizdala, M.; Wilson, A.; Kirilovsky, D. In vitro reconstitution of the cyanobacterial photoprotective mechanism mediated by the Orange Carotenoid Protein in Synechocystis PCC 6803. *The Plant Cell* **2011,** *23* (7), 2631-2643.
18. Kirilovsky, D.; Kerfeld, C. A. Cyanobacterial photoprotection by the orange carotenoid protein. *Nat. Plants 2* **2016,** *2*, 1-7.

19. Domínguez-Martín, M. A.; Sauer, P. V.; Kirst, H.; Sutter, M.; Bína, D.; Greber, B. J.; Nogales, E.; Polívka, T.; Kerfeld, C. A. Structures of a phycobilisome in light-harvesting and photoprotected states. *Nature* **2022,** *609*, 835–845.
20. Chukhutsina, V. U.; Baxter, J. M.; Fadini, A.; Morgan, R. M.; Pope, M. A.; Maghlaoui, K.; Orr, C. M.; Wagner, A.; Van Thor, J. J. Light activation of Orange Carotenoid Protein reveals bicycle-pedal single-bond isomerization. *Nat. Comm.* **2022,** *13* (6420).
21. Yaroshevich, I. A.; Maksimov, E. G.; Sluchanko, N. N.; Zlenko, D. V.; Stepanov, A. V.; Slutskaya, E. A.; Slonimskiy, Y. B.; Botnarevskii, V. S.; Remeeva, A.; Gushchin, I.; Kovalev, K.; Gordeliy, V. I.; Shelaev, I. V.; Gostev, F. E.; Khakhulin, D.; Poddubnyy, V. V.; Gostev, T. S.; Cherepanov, D. A.; Polívka, T.; Kloz, M.; Friedrich, T.; Paschenko, V. Z.; Nadtochenko, V. A.; Rubin, A. B.; Kirpichnikov, M. P. Role of hydrogen bond alternation and charge transfer states in photoactivation of the Orange Carotenoid Protein. *Commun. Biol.* **2021,** *4* (539), 1-13.
22. Khan, T.; Kuznetsova, V.; Dominguez-Martin, M. A.; Kerfeld, C. A.; Polivka, T. UV excitation of carotenoid binding proteins OCP and HCP: excited-state dynamics and product formation. *ChemPhotoChem* **2021,** *5*, 1-11.
23. Kuznetsova, V.; Dominguez-Martin, M. A.; Bao, H.; Gupta, S.; Sutter, M.; Kloz, M.; Rebarz, M.; Přeček, M.; Chen, Y.; Petzold, C. J.; Ralston, C. Y.; Kerfeld, C. A.; Polívka, T. Comparative ultrafast spectroscopy and structural analysis of OCP1 and OCP2 from Tolypothrix. *Biochim Biophys Acta* **2020,** *1861* (2), 1-11.
24. Maksimov, E. G.; Protasova, E. A.; Tsoraev, G. V.; Yaroshevich, I. A.; Maydykovskiy, A. I.; Shirshin, E. A.; Gostev, T. S.; Jelzow, A.; Moldenhauer, M.; Slonimskiy, Y. B.; Sluchanko, N. N.; Friedrich, T. Probing of carotenoid-tryptophan hydrogen bonding dynamics in the single-tryptophan photoactive Orange Carotenoid Protein. *Sci. Rep.* **2020,** *10* (11729), 1-12.
25. Pigni, N. B.; Clark, K. L.; Beck, W. F.; Gascón, J. A. Spectral signatures of canthaxanthin translocation in the Orange Carotenoid Protein. *J. Phys. Chem. B* **2020,** *124* (50), 11387–11395.
26. Bondanza, M.; Cupellini, L.; Faccioli, P.; Mennucci, B. Molecular mechanisms of activation in the Orange Carotenoid Protein revealed by molecular dynamics. *J. Am. Chem. Soc.* **2020,** *142* (52), 21829–21841.
27. Slonimskiy, Y. B.; Maksimov, E. G.; Lukashev, E. P.; Moldenhauer, M.; Friedrich, T.; Sluchanko, N. N. Engineering the photoactive Orange Carotenoid Protein with redox-controllable structural dynamics and photoprotective function. *Biochim. Biophys. Acta - Bioenerg.* **2020,** *1861* (5-6), 148174.
28. Konold, P. E.; van Stokkum, I. H. M.; Muzzopappa, F.; Wilson, A.; Groot, M. L.; Kirilovsky, D.; Kennis, J. T. M. Photoactivation mechanism, timing of protein secondary structure dynamics and carotenoid translocation in the Orange Carotenoid Protein. *J. Am. Chem. Soc.* **2019,** *141* (1), 520−530.
29. Wei, T.; Balevičius, V.; Polívka, T.; Ruban, A. V.; Duffy, C. D. P. How carotenoid distortions may determine optical properties: lessons from the Orange Carotenoid Protein. *Phys. Chem. Chem. Phys.* **2019,** *21* (41), 23187-23197.
30. Bondanza, M.; Cupellini, L.; Lipparini, F.; Mennucci, B. The multiple roles of the protein in the photoactivation of Orange Carotenoid Protein. *Chem* **2019,** *6* (1), 187-203.
31. Squires, A. H.; Dahlberg, P. D.; Liu, H.; Magdaong, N. C. M.; Blankenship, R. E.; Moerner, W. E. Single-molecule trapping and spectroscopy reveals photophysical heterogeneity of phycobilisomes quenched by Orange Carotenoid Protein. *Nature Comm.* **2019,** *1172*, 1-12.
32. Mezzetti, A.; Alexandre, M.; Thurotte, A.; Wilson, A.; Gwizdala, M.; Kirilovsky, D. Two-step structural changes in Orange Carotenoid Protein photoactivation revealed by Time-Resolved Fourier Transform Infrared Spectroscopy. *J. Phys. Chem. B* **2019,** *123* (15), 3259–3266.
33. Gupta, S.; Sutter, M.; Remesh, S. G.; Dominguez-Martin, M. A.; Bao, H.; Feng, X. A.; Chan, L.-J. G.; Petzold, C. J.; Kerfeld, C. A.; Ralston, C. X-ray radiolytic labeling reveals the molecular basis of Orange Carotenoid Protein photoprotection and its interactions with Fluorescence Recovery Protein. *J. Biol. Chem.* **2019,** *294* (22), 8848-8860.
34. Tsoraev, G. V.; Bukhanko, A.; Budylin, G. S.; Shirshin, E. A.; Slonimskiy, Y. B.; Sluchanko, N. N.; Kloz, M.; Cherepanov, D. A.; Shakina, Y. V.; Ge, B.; Moldenhauer, M.; Friedrich, T.; Golub, M.; Pieper,

J.; Maksimov, E. G.; Rubin, A. B. Stages of OCP-FRP interactions in the regulation of photoprotection in cyanobacteria, part 1: Time-resolved spectroscopy. *J. Phys. Chem. B* **2023,** *127* (9), 1890-1900.
35. Leccese, S.; Wilson, A.; Kirilovsky, D.; Spezia, R.; Jolivalt, C.; Mezzetti, A. Light-induced infrared difference spectroscopy on three different forms of orange carotenoid protein: focus on carotenoid vibrations. *Photochem. Photobiol. Sci.* **2023**, doi.org/10.1007/s43630-023-00384-7.
36. Moldenhauer, M.; Tseng, H.-W.; Kraskov, A.; Tavraz, N. N.; Yaroshevich, I. A.; Hildebrandt, P.; Sluchanko, N. N.; Hochberg, G. A.; Essen, L. O.; Budisa, N.; Korf, L.; Maksimov, E. G.; Friedrich, T. Parameterization of a single H-bond in Orange Carotenoid Protein by atomic mutation reveals principles of evolutionary design of complex chemical photosystems. *Front. Mol. Biosci.* **2023,** *10* (1072606).
37. Golub, M.; Moldenhauer, M.; Matsarskaia, O.; Martel, A.; Grudinin, S.; Soloviov, D.; Kuklin, A.; Maksimov, E. G.; Friedrich, T.; Pieper, J. Stages of OCP–FRP interactions in the regulation of photoprotection in cyanobacteria, part 2: Small-angle neutron scattering with partial deuteration. *J. Phys. Chem. B* **2023,** *127* (9), 1901–1913.
38. Mathes, T. Natural resources for optogenetic tools. *Methods Mol Biol.* **2016,** *1408*, 19–36.
39. Lechno-Yossef, S.; Melnicki, M. R.; Bao, H.; Montgomery, B. L.; Kerfeld, C. A. Synthetic OCP heterodimers are photoactive and recapitulate the fusion of two primitive carotenoproteins in the evolution of cyanobacterial photoprotection. *Plant J.* **2017,** *91* (4), 646–656.
40. Leverenz, R. L.; Sutter, M.; Wilson, A.; Gupta, S.; Thurotte, A.; Bourcier de Carbon, C.; Petzold, C. J.; Ralston, C.; Perreau, F.; Kirilovsky, D.; Kerfeld, C. A. A 12 Å carotenoid translocation in a photoswitch associated with cyanobacterial photoprotection. *Science* **2015,** *348* (6242), 1463-6.
41. Leverenz, R. L.; Jallet, D.; Li, M.-D.; Mathies, R. A.; Kirilovsky, D.; Kerfeld, C. A. Structural and functional modularity of the Orange Carotenoid Protein: Distinct roles for the N- and C—terminal domains in cyanobacterial photoprotection. *Plant Cell* **2014,** *26* (1), 426-437.
42. Wilson, A.; Gwizdala, M.; Mezzetti, A.; Alexandre, M.; Kerfeld, C. A.; Kirilovsky, D. The essential role of the N-terminal domain of the orange carotenoid protein in cyanobacterial photoprotection: importance of a positive charge for phycobilisome binding. *Plant Cell* **2012,** *24* (5), 1972–1983.
43. Gorbunov, M. Y.; Kuzminov, F. I.; Fadeev, V. V.; Kim, J. D.; Falkowski, P. G. A kinetic model of non-photochemical quenching in cyanobacteria. *Biochim Biophys Acta Bioenerg* **2011,** *1807* (12), 1591-1599.
44. Maksimov, E. G.; Sluchanko, N. N.; Slonimskiy, Y. B.; Slutskaya, E. A.; Stepanov, A. V.; Argentova-Stevens, A. M.; Shirshin, E. A.; Tsoraev, G. V.; Klementiev, K. E.; Slatinskaya, O. V.; Lukashev, E. P.; Friedrich, T.; Paschenko, V. Z.; Rubin, A. B. The photocycle of orange carotenoid protein conceals distinct intermediates and asynchronous changes in the carotenoid and protein components. *Sci. Rep.* **2017,** *7* (15548), 1-12.
45. Maksimov, E. G.; Shirshin, E. A.; Sluchanko, N. N.; Zlenko, D. V.; Parshina, E. Y.; Tsoraev, G. V.; Klementiev, K. E.; Budylin, G. S.; Schmitt, F. J.; Friedrich, T.; Fadeev, V. V.; Paschenko, V. Z.; Rubin, A. B. The signaling state of Orange Carotenoid Protein. *Biophys J.* **2015,** *109* (3), 595-607.
46. Blanchet, L.; Réhault, J.; Ruckebusch, C.; Huvenne, J. P.; Tauler, R.; de Juan, A. Chemometrics description of measurement error structure: Study of an ultrafast absorption spectroscopy experiment. *Anal. Chim. Acta* **2009,** *642* (1-2), 19-26.
47. Ha-Thi, M.-H.; Changenet, P.; Burdzinski, G.; Pino, T. Transient absorption spectroscopy in inorganic systems. In *Springer Handbook of Inorganic Photochemistry*, Bahnemann, D. W.; Patrocinio, A. O. T., Eds. Springer: 2022.
48. Beckwith, J. S.; Rumble, C. A.; Vauthey, E. Data analysis in transient electronic spectroscopy – an experimentalist's view. *Int. Rev. Phys. Chem.* **2020,** *39* (2), 135-216.
49. Ruckebusch, C.; Sliwa, M.; Pernot, P.; de Juan, A.; Tauler, R. Comprehensive data analysis of femtosecond transient absorption spectra: A review. *J. Photochem. Photobiol. C* **2012,** *13* (1), 1-27.
50. Istratov, A. A.; Vyvenko, O. F. Exponential analysis in physical phenomena. *Rev. Sci. Instrum.* **1999,** *70* (2), 1233-1257.
51. van Stokkum, I. H. N.; Larsen, D. S.; Grondelle, R. Global and target analysis of time-resolved spectra. *Biochim Biophys Acta Bioenerg* **2004,** *1657* (2-3), 82-104.

52. Uriarte, L. M.; Niziński, S.; Labarrière, L. *Ultrapyfit a python package for time resolved data.*, Zenodo: https://doi.org/10.5281/zenodo.5797895, 2021.
53. Lorenc, M.; Ziolek, M.; Naskrecki, R.; Karolczak, J.; Kubicki, J.; Maciejewski, A. Artifacts in femtosecond transient absorption spectroscopy. *Appl. Phys. B* **2002,** *74*, 19–27.
54. Müller, P.; Brettel, K. $[Ru(bpy)_3]^{2+}$ as a reference in transient absorption spectroscopy: differential absorption coefficients for formation of the long-lived ^{3}MLCT excited state. *Photochem. Photobiol. Sci.* **2012,** *11* (4), 632–636.
55. Tarnovsky, A. N.; Gawelda, W.; Johnson, M.; Bressler, C.; Chergui, M. Photexcitation of aqueous ruthenium(II)-tris-(2,2 '-bipyridine) with high-intensity femtosecond laser pulses. *J. Phys. Chem. B* **2006,** *110* (51), 26497-26505.
56. Yoshimura, A.; Hoffman, M. Z.; Sun, H. An evaluation of the excited state absorption spectrum of $Ru(bpy)_3^{2+}$ in aqueous and acetonitrile solutions. *J. Photochem. Photobiol. A* **1993,** *70* (1), 29-33.
57. Sluchanko, N. N.; Klementiev, K. E.; Shirshin, E. A.; Tsoraev, G. V.; Friedrich, T.; Maksimov, E. G. The purple Trp288Ala mutant of Synechocystis OCP persistently quenches phycobilisome fluorescence and tightly interacts with FRP. *Biochim Biophys Acta* **2017,** *1858* (1), 1-11.
58. Kuhn, H. J.; Braslavsky, S. E.; Schmidt, R. Chemical actinometry. *Pure Appl. Chem.* **2009,** *76* (12), 2105-2146.
59. Montalti, M.; Credi, A.; Prodi, L.; Gandolfi, M. 12. Chemical actinometry. In *Handbook of photochemistry*, CRC Press: Boca Raton, 2006.
60. Hatchard, C. G.; Parker, C. A. A new sensitive chemical actinometer. II. Potassium ferrioxalate as a standard chemical actinometer *Proc. R. Soc. Lond.* **1956,** *235* (1203), 518-536.
61. Ritchie, R. J. Modelling photosynthetic photon flux density and maximum potential gross photosynthesis. *Photosynthetica* **2010,** *48* (4), 596-609.
62. Deniel, M. H.; Lavabre, D.; Micheau, J. C. Photokinetics under continuous irradiation. In *Organic photochromic and thermochromic compounds volume 2: physicochemical studies, biological applications, and thermochromism*, Crano, J. C.; Guglielmetti, R. J., Eds. Kluwer Academic Publishers: New York, Boston, Dordrecht, London, Moscow, 2002; pp 167-182.
63. Niziński, S. *ContinuousIrradiation package*, Zenodo: https://doi.org/10.5281/zenodo.6639706, 2022.
64. Bourcier de Carbon, C.; Thurotte, A.; Wilson, A.; Perreau, F.; Kirilovsky, D. Biosynthesis of soluble carotenoid holoproteins in Escherichia coli. *Sci. Rep.* **2015,** *5* (9085), 1-8.
65. Wilson, A.; Punginelli, C.; Couturier, M.; Perreau, F.; Kirilovsky, D. Essential role of two tyrosines and two tryptophans on the photoprotection activity of the Orange Carotenoid Protein. *Biochim. Biophys. Acta - Bioenerg.* **2011,** *1807* (3), 293-301.
66. Son, M.; Hart, S. M.; Schlau-Cohen, G. S. Investigating carotenoid photophysics in photosynthesis with 2D electronic spectroscopy. *Trends Chem.* **2021,** *3* (9), 733-746.
67. Ritz, T.; Damjanović, A.; Schulten, K. The quantum physics of photosynthesis. *ChemPhysChem* **2002,** *3* (3), 243-248.
68. Domonkos, I.; Kis, M.; Gombos, Z.; Ughy, B. Carotenoids, versatile components of oxygenic photosynthesis. *Prog. Lipid Res.* **2013,** *52* (4), 539-561.
69. Andersson, P. O.; Bachilo, S. M.; Chen, R. L.; Gillbro, T. Solvent and temperature effects on dual fluorescence in a series of carotenes. Energy gap dependence of the internal conversion rate. *J. Phys. Chem.* **1995,** *99* (44), 16199–16209.
70. Frank, H. A.; Desamero, R. Z. B.; Chynwat, V.; Gebhard, R.; van der Hoef, I.; Jansen, F. J.; Lugtenburg, J.; Gosztola, D.; Wasielewski, M. R. Spectroscopic properties of spheroidene analogs having different extents of π-electron conjugation. *J. Phys. Chem. A* **1997,** *101* (2), 149–157.
71. Kruk, J.; Szymańska, R. Singlet oxygen oxidation products of carotenoids, fatty acids and phenolic prenyllipids. *J. Photochem. Photobiol. B* **2021,** *216* (112148).
72. Widomska, J.; Welc, R.; Gruszecki, W. I. The effect of carotenoids on the concentration of singlet oxygen in lipid membranes. *Biochim. Biophys. Acta - Biomembr.* **2019,** *1861* (4), 845-851.
73. Foyer, C. H. Reactive oxygen species, oxidative signaling and the regulation of photosynthesis. *Environ. Exp. Bot.* **2018,** *154*, 134-142.

74. Koyama, Y. New trends in photobiology: Structures and functions of carotenoids in photosynthetic systems. *J. Photochem. Photobiol. B* **1991,** *9* (3-4), 265-280.
75. Janik, E.; Bednarska, J.; Zubik, M.; Sowinski, K.; Luchowski, R.; Grudzinski, W.; Matosiuk, D.; Gruszecki, W. I. The xanthophyll cycle pigments, violaxanthin and zeaxanthin, modulate molecular organization of the photosynthetic antenna complex LHCII. *Arch. Biochem. Biophys.* **2016,** *592*, 1-9.
76. Gruszecki, W. I.; Strzałka, K. Does the xanthophyll cycle take part in the regulation of fluidity of the thylakoid membrane? *Biochim. Biophys. Acta - Bioenerg.* **1991,** *1060* (3), 310-314.
77. Gruszecki, W. I.; Grudzinski, W.; Gospodarek, M.; Patyra, M.; Maksymiec, W. Xanthophyll-induced aggregation of LHCII as a switch between light-harvesting and energy dissipation systems. *Biochim. Biophys. Acta - Bioenerg.* **2006,** *1757* (11), 1504-1511.
78. Gruszecki, W. I.; Zubik, M.; Luchowski, R.; Janik, E.; Grudzinski, W.; Gospodarek, M.; Goc, J.; Fiedor, J.; Gryczynski, Z.; Gryczynski, I. Photoprotective role of the xanthophyll cycle studied by means of modeling of xanthophyll–LHCII interactions. *Chem. Phys.* **2010,** *373* (1-2), 122-128.
79. Griffiths, D. J. *Introduction to Quantum Mechanics*. Prentice Hall: 1995.
80. Zimmerman, H. E. *Quantum mechanics for organic chemists*. Academic Press: 1975.
81. Tavan, P.; Schulten, K. Electronic excitations in finite and infinite polyenes. *Phys. Rev. B* **1987,** *36* (8), 4337-4358.
82. Tavan, P.; Schulten, K. The low-lying electronic excitations in long polyenes: A PPP-MRD-CI study. *J. Chem. Phys.* **1986,** *85* (11), 6602-6609.
83. Šebelík, V.; Kloz, M.; Rebarz, M.; Přeček, M.; Kang, E. H.; Choi, T. L.; Christensen, R. L.; Polívka, T. Spectroscopy and excited state dynamics of nearly infinite polyenes. *Phys. Chem. Chem. Phys.* **2020,** *22* (32), 17867-17879.
84. Vincent, A. *Molecular symmetry and group theory*. John Wiley & Sons Ltd: 2001.
85. Hudson, B. S.; Kohler, B. E.; Schulten, K. Linear polyene electronic structure and potential surfaces. *Excited States* **1982,** *6*, 1-95.
86. Hudson, B. S.; Kohler, B. E. A low-lying weak transition in the polyene α,ω-diphenyloctatetraene. *Chem. Phys. Lett.* **1972,** *14* (3), 299-304.
87. Chadwick, R. R.; Gerrity, D. P.; Hudson, B. S. Resonance Raman spectroscopy of butadiene: Demonstration of a 2 ^1A_g state below the 1 ^1B_u V state. *Chem. Phys. Lett.* **1985,** *115* (1), 24-28.
88. Hudson, B. S.; Kohler, B. E. Polyene spectroscopy: The lowest energy excited singlet state of diphenyloctatetraene and other linear polyenes. *J. Chem. Phys* **1973,** *59* (9), 4984-5002.
89. Christensen, R. L.; Kohler, B. E. Vibronic coupling in polyenes: High resolution optical spectroscopy of 2,10-dimethylundecapentaene. *J. Chem. Phys.* **1975,** *63* (5), 1837-1846.
90. Fujii, R.; Onaka, K.; Nagae, H.; Koyama, Y.; Watanabe, Y. Fluorescence spectroscopy of all-*trans*-lycopene: comparison of the energy and the potential displacements of its $2A_g^-$ state with those of neurosporene and spheroidene. *J. Lumin.* **2001,** *92* (3), 213-222.
91. Sashima, T.; Koyama, Y.; Yamada, T.; Hashimoto, H. The $1B_u^+$, $1B_u^-$, and $2A_g^-$ energies of crystalline lycopene, β-carotene, and mini-9-β-carotene as determined by resonance-Raman excitation profiles: dependence of the $1B_u^-$ state energy on the conjugation length. *J. Phys. Chem. B* **2000,** *104* (20), 5011–5019.
92. Sashima, T.; Shiba, M.; Hashimoto, H.; Nagae, H.; Koyama, Y. The $2A_g^-$ energy of crystalline all-trans-spheroidene as determined by resonance-Raman excitation profiles. *Chem. Phys. Lett.* **1998,** *290* (1-3), 36-42.
93. Polívka, T.; Zigmantas, D.; Frank, H. A.; Bautista, J. A.; Herek, J. L.; Koyama, Y.; Fujii, R.; Sundström, V. Near-infrared time-resolved study of the S_1 state dynamics of the carotenoid spheroidene. *J. Phys. Chem. B* **2001,** *105* (5), 1072–1080.
94. Birge, R. R.; Schulten, K.; Karplus, M. Possible influence of a low-lying "covalent" excited state on the absorption spectrum and photoisomerization of 11-*cis* retinal. *Chem. Phys. Lett.* **1975,** *31* (3), 451-454.
95. Schulten, K.; Karplus, M. On the origin of a low-lying forbidden transition in polyenes and related molecules. *Chem. Phys. Lett.* **1972,** *14* (3), 305-309.

96. Christensen, R. L.; Kohler, B. E. Low resolution optical spectroscopy of retinyl polyenes - low-lying electronic levels and spectral broadness. *Photochem. Photobiol.* **1973,** *18* (4), 293-301.
97. Hudson, B. S.; Kohler, B. E. Linear polyene electronic structure and spectroscopy. *Ann. Rev. Phys. Chem.* **1974,** *25*, 437-460.
98. Birge, R. R.; Pierce, B. M. A theoretical analysis of the two-photon properties of linear polyenes and the visual chromophores. *J. Chem. Phys.* **1979,** *70* (1), 165-178.
99. Horbatenko, Y.; Lee, S.; Filatov, M.; Choi, C. H. How beneficial is the explicit account of doubly-excited configurations in linear response theory? *J. Chem. Theory Comput.* **2021,** *17* (2), 975–984.
100. Tavan, P.; Schulten, K. The 2 ^1A_g–1 ^1B_u energy gap in the polyenes: An extended configuration interaction study. *J. Chem. Phys.* **1979,** *70* (12), 5407-5413.
101. Frank, H. A.; Bautista, J. A.; Josue, J.; Pendon, Z.; Hiller, R. G.; Sharples, F. P.; Gosztola, D.; Wasielewski, M. R. Effect of the solvent environment on the spectroscopic properties and dynamics of the lowest excited states of carotenoids. *J. Phys. Chem. B* **2000,** *104* (18), 4557-4569.
102. Čížek, J.; Paldus, J.; Hubač, I. Correlation effects in the low–lying excited states of the PPP models of alternant hydrocarbons. I. Qualitative rules for the effect of limited configuration interaction. *Int. J. Quantum Chem.* **1974,** *8* (6), 951-970.
103. Paldus, J.; Čížek, J.; Hubač, I. Correlation effects in low-lying excited-states of PPP models of alternant hydrocarbons. 2. State correlation diagrams. *Int. J. Quantum Chem.* **1974,** *8*, 293-303.
104. Pariser, R. Theory of the electronic spectra and structure of the polyacenes and of alternant hydrocarbons. *J. Chem. Phys.* **1956,** *24* (2), 250-268.
105. Koutecký, J.; Paldus, J.; Čížek, J. Alternancy symmetry: A unified viewpoint. *J. Chem. Phys.* **1985,** *83* (4), 1722-1735.
106. Fiedor, L.; Heriyanto; Fiedor, J.; Pilch, M. Effects of molecular symmetry on the electronic transitions in carotenoids. *J. Phys. Chem. Lett.* **2016,** *7* (10), 1821-1829.
107. Fujii, R.; Ishikawa, T.; Koyama, Y.; Taguchi, M.; Isobe, Y.; Nagae, H.; Watanabe, Y. Fluorescence spectroscopy of all-*trans*-anhydrorhodovibrin and spirilloxanthin: detection of the $1B_u^-$ fluorescence. *J. Phys. Chem. A* **2001,** *105* (22), 5348–5355.
108. Sashima, T.; Nagae, H.; Kuki, M.; Koyama, Y. A new singlet-excited state of all-*trans*-spheroidene as detected by resonance-Raman excitation profiles. *Chem. Phys. Lett.* **1999,** *299* (2), 187-194.
109. Nagae, H.; Kuki, M.; Zhang, J. P.; Sashima, T.; Mukai, Y.; Koyama, Y. Vibronic coupling through the in-phase, C=C stretching mode plays a major role in the $2A_g^-$ to $1A_g^-$ internal conversion of all-*trans*-β-carotene. *J. Phys. Chem. A* **2000,** *104* (18), 4155–4166.
110. Zhang, J. P.; Inaba, T.; Watanabe, Y.; Koyama, Y. Excited-state dynamics among the $1B_u^+$, $1B_u^-$ and $2A_g^-$ states of all-*trans*-neurosporene as revealed by near-infrared time-resolved absorption spectroscopy. *Chem. Phys. Lett.* **2000,** *332* (3-4), 351-358.
111. Rondonuwu, F. S.; Watanabe, Y.; Zhang, J. P.; Furuichi, K.; Koyama, Y. Internal-conversion and radiative-transition processes among the $1B_u^+$, $1B_u^-$ and $2A_g^-$ states of all-*trans*-neurosporene as revealed by subpicosecond time-resolved Raman spectroscopy. *Chem. Phys. Lett.* **2002,** *357* (5-6), 376-384.
112. Cerullo, G.; Polli, D.; Lanzani, G.; De Silvestri, S.; Hashimoto, H.; Cogdell, R. J. Photosynthetic light harvesting by carotenoids: Detection of an intermediate excited state. *Science* **2002,** *298* (5602), 2395-2398.
113. Yoshizawa, M.; Aoki, H.; Hashimoto, H. Vibrational relaxation of the $2A_g^-$ excited state in all-*trans*-β-carotene obtained by femtosecond time-resolved Raman spectroscopy. *Phys. Rev. B* **2001,** *63* (18), 180301.
114. Rondonuwu, F. S.; Watanabe, Y.; Fujii, R.; Koyama, Y. A first detection of singlet to triplet conversion from the $1^1B_u^-$ to the 1^3A_g state and triplet internal conversion from the 1^3A_g to the 1^3B_u state in carotenoids: dependence on the conjugation length. *Chem. Phys. Lett.* **2003,** *376* (3-4), 292-301.

115. Fujii, R.; Inaba, T.; Watanabe, Y.; Koyama, Y.; Zhang, J. P. Two different pathways of internal conversion in carotenoids depending on the length of the conjugated chain. *Chem. Phys. Lett.* **2003,** *369* (1-2), 165-172.
116. Maiuri, M.; Polli, D.; Brida, D.; Lüer, L.; LaFountain, A. M.; Fuciman, M.; Cogdell, R. J.; Frank, H. A.; Cerullo, G. Solvent-dependent activation of intermediate excited states in the energy relaxation pathways of spheroidene. *Phys. Chem. Chem. Phys.* **2012,** *14* (18), 6312-6319.
117. Ostroumov, E. E.; Mulvaney, R. M.; Cogdell, R. J.; Scholes, G. D. Broadband 2D electronic spectroscopy reveals a carotenoid dark state in purple bacteria. *Science* **2013,** *340* (6128), 52-56.
118. Accomasso, D.; Arslancan, S.; Cupellini, L.; Granucci, G.; Mennucci, B. Ultrafast excited-state dynamics of carotenoids and the role of the S_X state. *J. Phys. Chem. Lett.* **2022,** *13* (29), 6762–6769.
119. Polívka, T.; Sundström, V. Dark excited states of carotenoids: Consensus and controversy. *Chem. Phys. Lett.* **2009,** *477* (1-3), 1-11.
120. Miki, T.; Buckup, T.; Krause, M. S.; Southall, J.; Cogdell, R. J.; Motzkus, M. Vibronic coupling in the excited-states of carotenoids. *Phys. Chem. Chem. Phys.* **2016,** *18* (16), 11443-11453.
121. Noguchi, T.; Hayashi, H.; Tasumi, M.; Atkinson, G. H. Frequencies of the Franck-Condon active a_g C=C stretching mode in the 2 $^1A^{-g}$ excited state of carotenoids. *Chem. Phys. Lett.* **1990,** *175* (3), 163-169.
122. IUPAC. Nomenclature of carotenoids. *Pure Appl. Chem.* **1974,** *41* (3), 405-431.
123. He, Z.; Gosztola, D.; Deng, Y.; Gao, G.; Wasielewski, M. R.; Kispert, L. D. Effect of terminal groups, polyene chain length, and solvent on the first excited singlet states of carotenoids. *J. Phys. Chem. B* **2000,** *104* (28), 6668–6673.
124. Wasielewski, M. R.; Kispert, L. D. Direct measurement of the lowest excited singlet state lifetime of all-*trans*-β-carotene and related carotenoids. *Chem. Phys. Lett.* **1986,** *128* (3), 238-243.
125. Mimuro, M. N., U.; Nagaoka, S.; Takaichi, S.; Yamazaki, I.; Nishimura, Y.; Katoh, T. Direct measurement of the low-lying singlet excited (2 ^1A_g) state of a linear carotenoid, neurosporene, in solution. *Chem. Phys. Lett.* **1993,** *204* (1-2), 101-105.
126. Thrash, R. J.; Fang, H. L. B.; Leroi, G. E. The Raman excitation profile spectrum of β-carotene in the preresonance region: Evidence for a low-lying singlet state. *J. Chem. Phys.* **1977,** *67* (12), 5930-5933.
127. Mimuro, M.; Akimoto, S.; Takaichi, S.; Yamazaki, I. Effect of molecular structures and solvents on the excited state dynamics of the S_2 state of carotenoids analyzed by the femtosecond up-conversion method. *J. Am. Chem. Soc.* **1997,** *119* (6), 1452–1453.
128. LeRosen, A. L.; Reid, C. E. An investigation of certain solvent effect in absorption spectra. *J. Chem. Phys.* **1952,** *20* (2), 233-236.
129. Basu, S. Theory of solvent effects on molecular electronic spectra. *Adv. Quantum Chem.* **1964,** *1*, 145-169.
130. Andersson, P. O.; Gillbro, T.; Ferguson, L.; Cogdell, R. J. Absorption spectral shifts of carotenoids related to medium polarizability. *Photochem. Photobiol.* **1991,** *54* (3), 353-360.
131. Nagae, H.; Kuki, M.; Cogdell, R. J.; Koyama, Y. Shifts of the 1Ag- → 1Bu+ electronic absorption of carotenoids in nonpolar and polar-solvents. *J. Chem. Phys* **1994,** *101* (8), 6750-6765.
132. Bouwman, W. G.; Jones, A. C.; Phillips, D.; Thibodeau, P.; Friel, C.; Christensen, R. L. Fluorescence of gaseous tetraenes and pentaenes. *J. Phys. Chem.* **1990,** *94* (19), 7429–7434.
133. Christensen, R. L. The electronic states of carotenoids. In *The Photochemistry of Carotenoids*, Frank, H. A.; Young, A. J.; Britton, G.; Cogdell, R. J., Eds. Kluwer Academic Publishers: 2004; Vol. 8.
134. Hu, Y.; Hashimoto, H.; Moine, G.; Hengartner, U.; Koyama, Y. Unique properties of the 11-*cis* and 11,11'-di-*cis* isomers of β-carotene as revealed by electronic absorption, resonance Raman and ^1H and ^{13}C NMR spectroscopy and by HPLC analysis of their thermal isomerization. *J . Chem. Soc. Perkin Trans. 2* **1997,** (12), 2699-2710.
135. Niedzwiedzki, D. M.; Sandberg, D. J.; Cong, H.; Sandberg, M. N.; Gibson, G. N.; Birge, R. R.; Frank, H. A. Ultrafast time-resolved absorption spectroscopy of geometric isomers of carotenoids. *Chem. Phys.* **2009,** *357* (1-3), 4-16.

136. Saito, S.; Tasumi, M.; Eugster, C. H. Resonance Raman spectra (5800–40 cm^{-1}) of all-*trans* and 15-*cis* isomers of β-carotene in the solid state and in solution. Measurements with various laser lines from ultraviolet to red. *J. Raman Spectrosc.* **1983,** *14* (5), 299-309.
137. Guo, W.-H.; Tu, C.-Y.; Hu, C.-H. *Cis–trans* isomerizations of β-carotene and lycopene: A theoretical study. *J. Phys. Chem. B* **2008,** *112* (38), 12158–12167.
138. Bautista, J. A.; Connors, R. E.; Raju, B. B.; Hiller, R. G.; Sharples, F. P.; Gosztola, D.; Wasielewski, M. R.; Frank, H. A. Excited state properties of peridinin: observation of a solvent dependence of the lowest excited singlet state lifetime and spectral behavior unique among carotenoids. *J. Phys. Chem. B* **1999,** *103* (41), 8751–8758.
139. Punginelli, C.; Wilson, A.; Routaboul, J. M.; Kirilovsky, D. Influence of zeaxanthin and echinenone binding on the activity of the Orange Carotenoid Protein. *Biochim. Biophys. Acta - Bioenerg.* **2009,** *1787* (4), 280-288.
140. Zigmantas, D.; Hiller, R. G.; Sharples, F. P.; Frank, H. A.; Sundström, V.; Polívka, T. Effect of a conjugated carbonyl group on the photophysical properties of carotenoids. *Phys. Chem. Chem. Phys.* **2004,** *6* (11), 3009-3016.
141. Zigmantas, D.; Polívka, T.; Hiller, R. G.; Yartsev, A.; Sundström, V. Spectroscopic and dynamic properties of the peridinin lowest singlet excited states. *J. Phys. Chem. A* **2001,** *105* (45), 10296–10306.
142. Stalke, S.; Wild, D. A.; Lenzer, T.; Kopczynski, M.; Lohse, P. W.; Oum, K. Solvent-dependent ultrafast internal conversion dynamics of *n*'-apo-β-carotenoic-*n*'-acids (n = 8, 10, 12). *Phys. Chem. Chem. Phys.* **2008,** *10* (16), 2180-2188.
143. Wild, D. A.; Winkler, K.; Stalke, S.; Oum, K.; Lenzer, T. Extremely strong solvent dependence of the $S_1 \rightarrow S_0$ internal conversion lifetime of 12'-apo-β-caroten-12'-al. *Phys. Chem. Chem. Phys.* **2006,** *8* (21), 2499-2505.
144. Kosumi, D.; Kusumoto, T.; Fujii, R.; Sugisaki, M.; Iinuma, Y.; Oka, N.; Takaesu, Y.; Taira, T.; Iha, M.; Frank, H. A.; Hashimoto, H. One- and two-photon pump–probe optical spectroscopic measurements reveal the S_1 and intramolecular charge transfer states are distinct in fucoxanthin. *Chem. Phys. Lett.* **2009,** *483* (1-3), 95-100.
145. Enriquez, M. M.; Fuciman, M.; LaFountain, A. M.; Wagner, N. L.; Birge, R. R.; Frank, H. A. The intramolecular charge transfer state in carbonyl-containing polyenes and carotenoids. *J. Phys. Chem. B* **2010,** *114* (38), 12416–12426.
146. Niedzwiedzki, D. M.; Chatterjee, N.; Enriquez, M. M.; Kajikawa, T.; Hasegawa, S.; Katsumura, S.; Frank, H. A. Spectroscopic investigation of peridinin analogues having different π-electron conjugated chain lengths: exploring the nature of the intramolecular charge transfer state. *J. Phys. Chem. B* **2009,** *113* (41), 13604–13612.
147. Ehlers, F.; Wild, D. A.; Lenzer, T.; Oum, K. Investigation of the S_1/ICT $\rightarrow S_0$ internal conversion lifetime of 4'-apo-β-caroten-4'-al and 8'-apo-β-caroten-8'-al: dependence on conjugation length and solvent polarity. *J. Phys. Chem. A* **2007,** *111* (12), 2257–2265.
148. Zigmantas, D.; Hiller, R. G.; Yartsev, A.; Sundström, V.; Polívka, T. Dynamics of excited states of the carotenoid peridinin in polar solvents: dependence on excitation wavelength, viscosity, and temperature. *J. Phys. Chem. B* **2003,** *107* (22), 5339–5348.
149. Chábera, P.; Fuciman, M.; Naqvi, K. R.; Polívka, T. Ultrafast dynamics of hydrophilic carbonyl carotenoids – Relation between structure and excited-state properties in polar solvents. *Chem. Phys.* **2010,** *373* (1-2), 56-64.
150. Durchan, M.; Fuciman, M.; Šlouf, V.; Keşan, G.; Polívka, T. Excited-state dynamics of monomeric and aggregated carotenoid 8'-apo-β-carotenal. *J. Phys. Chem. A* **2012,** *116* (50), 12330–12338.
151. Polívka, T.; Frank, H. A.; Enriquez, M. M.; Niedzwiedzki, D. M.; Liaaen-Jensen, S.; Hemming, J.; Helliwell, J. R.; Helliwell, M. X-ray crystal structure and time-resolved spectroscopy of the blue carotenoid violerythrin. *J. Phys. Chem. B* **2010,** *114* (26), 8760–8769.
152. Chábera, P.; Fuciman, M.; Hríbek, P.; Polívka, T. Effect of carotenoid structure on excited-state dynamics of carbonyl carotenoids. *Phys. Chem. Chem. Phys.* **2009,** *11* (39), 8795-8803.

153. Takaya, T.; Anan, M.; Iwata, K. Vibrational relaxation dynamics of β-carotene and its derivatives with substituents on terminal rings in electronically excited states as studied by femtosecond time-resolved stimulated Raman spectroscopy in the near-IR region. *Phys. Chem. Chem. Phys.* **2018,** *20* (5), 3320-3327.
154. Mimuro, M.; Nishimura, Y.; Takaichi, S.; Yamano, Y.; Ito, M.; Nagaoka, S.; Yamazaki, I.; Katoh, T.; Nagashima, U. The effect of molecular structure on the relaxation processes of carotenoids containing a carbonyl group. *Chem. Phys. Lett.* **1993,** *213* (5-6), 576-580.
155. Kosumi, D.; Kajikawa, T.; Okumura, S.; Sugisaki, M.; Sakaguchi, K.; Katsumura, S.; Hashimoto, H. Elucidation and control of an intramolecular charge transfer property of fucoxanthin by a modification of its polyene chain length. *J. Phys. Chem. Lett.* **2014,** *5* (5), 792-797.
156. Chatterjee, N.; Niedzwiedzki, D. M.; Aoki, K.; Kajikawa, T.; Katsumura, S.; Hashimoto, H.; Frank, H. A. Effect of structural modifications on the spectroscopic properties and dynamics of the excited states of peridinin. *Arch. Biochem. Biophys.* **2009,** *483* (2), 146-155.
157. Chatterjee, N.; Niedzwiedzki, D. M.; Kajikawa, T.; Hasegawa, S.; Katsumura, S.; Frank, H. A. Effect of π-electron conjugation length on the solvent-dependent S_1 lifetime of peridinin. *Chem. Phys. Lett.* **2008,** *463* (1-3), 219-224.
158. Papagiannakis, E.; Larsen, D. S.; van Stokkum, I. H. M.; Vengris, M.; Hiller, R. G.; Grondelle, R. Resolving the excited state equilibrium of peridinin in solution. *Biochemistry* **2004,** *43* (49), 15303-15309.
159. Redeckas, K.; Voiciuk, V.; Vengris, M. Investigation of the S_1/ICT equilibrium in fucoxanthin by ultrafast pump-dump-probe and femtosecond stimulated Raman scattering spectroscopy. *Photosynth Res.* **2016,** *128* (2), 169-181.
160. Shima, S.; Ilagan, R. P.; Gillespie, N.; Sommer, B. J.; Hiller, R. G.; Sharples, F. P.; Frank, H. A.; Birge, R. R. Two-photon and fluorescence spectroscopy and the effect of environment on the photochemical properties of peridinin in solution and in the peridinin-chlorophyll-protein from *Amphidinium carterae*. *J. Phys. Chem. A* **2003,** *107* (40), 8052–8066.
161. Vaswani, H. M.; Hsu, C. P.; Head-Gordon, M.; Fleming, G. R. Quantum chemical evidence for an intramolecular charge-transfer state in the carotenoid peridinin of peridinin-chlorophyll-protein. *J. Phys. Chem. B* **2003,** *107* (31), 7940–7946.
162. Enriquez, M. M.; Hananoki, S.; Hasegawa, S.; Kajikawa, T.; Katsumura, S.; Wagner, N. L.; Birge, R. R.; Frank, H. A. Effect of molecular symmetry on the spectra and dynamics of the intramolecular charge transfer (ICT) state of peridinin. *J. Phys. Chem. B* **2012,** *116* (35), 10748-10756.
163. Wagner, N. L.; Greco, J. A.; Enriquez, M. M.; Frank, H. A.; Birge, R. R. The nature of the intramolecular charge transfer state in peridinin. *Biophys J.* **2013,** *104* (6), 1314-1325.
164. Spezia, R.; Knecht, S.; Mennucci, B. Excited state characterization of carbonyl containing carotenoids: a comparison between single and multireference descriptions. *Phys. Chem. Chem. Phys.* **2017,** *19* (26), 17156-17166.
165. Kopczynski, M.; Lenzer, T.; Oum, K.; Seehusen, J.; Seidel, M. T.; Ushakov, V. G. Ultrafast transient lens spectroscopy of various C_{40} carotenoids: lycopene, β-carotene, (3R,3'R)-zeaxanthin, (3R,3'R,6'R)-lutein, echinenone, canthaxanthin, and astaxanthin. *Phys. Chem. Chem. Phys.* **2005,** *7* (14), 2793-2803.
166. Nizinski, S.; Wilson, A.; Uriarte, L. M.; Ruckebusch, C.; Andreeva, E. A.; Schlichting, I.; Colletier, J. P.; Kirilovsky, D.; Burdzinski, G.; Sliwa, M. A unifying perspective of the ultrafast photo-dynamics of Orange Carotenoid Protein from *Synechocystis*: Peril of high-power excitation, existence of different S* states and influence of tagging. *JACS Au* **2022,** *2* (5), 1084–1095.
167. Andersson, P. O.; Gillbro, T. Photophysics and dynamics of the lowest excited singlet state in long substituted polyenes with implications to the very longchain limit. *J. Chem. Phys.* **1995,** *103* (7), 2509-2519.
168. Billsten, H. H.; Zigmantas, D.; Sundström, V.; Polívka, T. Dynamics of vibrational relaxation in the S_1 state of carotenoids having 11 conjugated C=C bonds. *Chem. Phys. Lett.* **2002,** *355* (5-6), 465-470.

169. Lenzer, T.; Ehlers, F.; Scholz, M.; Oswald, R.; Oum, K. Assignment of carotene S* state features to the vibrationally hot ground electronic state. *Phys. Chem. Chem. Phys.* **2010,** *12* (31), 8832–8839.
170. Hayashi, H.; Brack, T. L.; Noguchi, T.; Tasumi, M.; Atkinson, G. H. Vibrational relaxation in carotenoids *in vivo* and *in vitro*: picosecond time-resolved anti-Stokes resonance Raman spectroscopy. *J. Phys. Chem.* **1991,** *95* (18), 6797–6802.
171. Noguchi, T.; Hayashi, H.; Tasumi, M.; Atkinson, G. H. Solvent effects on the a_g carbon-carbon double bond stretching mode in the $2^1A_g^-$ excited state of β-carotene and two derivatives: picosecond time-resolved resonance Raman spectroscopy. *J. Phys. Chem.* **1991,** *95* (8), 3167–3172.
172. Gradinaru, C. C.; Kennis, J. T. M.; Papagiannakis, E.; van Stokkum, I. H. M.; Cogdell, R. J.; Fleming, G. R.; Niederman, R. A.; van Grondelle, R. An unusual pathway of excitation energy deactivation in carotenoids: Singlet-to-triplet conversion on an ultrafast timescale in a photosynthetic antenna. *Proc. Natl. Acad. Sci. U. S. A.* **2001,** *98* (5), 2364-2369.
173. Papagiannakis, E.; Kennis, J. T. M.; van Stokkum, I. H. M.; Cogdell, R. J.; Grondelle, R. An alternative carotenoid-to-bacteriochlorophyll energy transfer pathway in photosynthetic light harvesting. *Proc. Natl. Acad. Sci. U. S. A.* **2002,** *99* (9), 6017-6022.
174. Wohlleben, W.; Buckup, T.; Herek, J. L.; Cogdell, R. J.; Motzkus, M. Multichannel carotenoid deactivation in photosynthetic light harvesting as identified by an evolutionary target analysis. *Biophys J.* **2003,** *85* (1), 442-450.
175. Papagiannakis, E.; Das, S. K.; Gall, A.; van Stokkum, I. H. M.; Robert, B.; van Grondelle, R.; Frank, H. A.; Kennis, J. T. M. Light harvesting by carotenoids incorporated into the B850 light-harvesting complex from *Rhodobacter sphaeroides* R-26.1: Excited-state relaxation, ultrafast triplet formation, and energy transfer to bacteriochlorophyll. *J. Phys. Chem. B* **2003,** *107* (23), 5642–5649.
176. Buckup, T.; Savolainen, J.; Wohlleben, W.; Herek, J. L.; Hashimoto, H.; Correra, T. C.; Motzkus, M. Pump-probe and pump-deplete-probe spectroscopies on carotenoids with N = 9 – 15 conjugated bonds. *J. Chem. Phys.* **2006,** *125* (194505).
177. Wohlleben, W.; Buckup, T.; Hashimoto, H.; Cogdell, R. J.; Herek, J. L.; Motzkus, M. Pump-deplete-probe spectroscopy and the puzzle of carotenoid dark states. *J. Phys. Chem. B* **2004,** *108* (10), 3320-3325.
178. Papagiannakis, E.; van Stokkum, I. H. M.; Vengris, M.; Cogdell, R. J.; van Grondelle, R.; Larsen, D. S. Excited-state dynamics of carotenoids in light-harvesting complexes. 1. Exploring the relationship between the S_1 and S* states. *J. Phys. Chem. B* **2006,** *110* (11), 5727–5736.
179. Savolainen, J.; Buckup, T.; Hauer, J.; Jafarpour, A.; Serrat, C.; Motzkus, M.; Herek, J. L. Carotenoid deactivation in an artificial light-harvesting complex via a vibrationally hot ground state. *Chem. Phys.* **2009,** *357* (1-3), 181-187.
180. Ostroumov, E. E.; Müller, M. G.; Reus, M.; Holzwarth, A. R. On the nature of the "Dark S*" excited state of β-carotene. *J. Phys. Chem. A* **2011,** *115* (16), 3698–3712.
181. Ehlers, F.; Scholz, M.; Schimpfhauser, J.; Bienert, J.; Oum, K.; Lenzer, T. Collisional relaxation of apocarotenals: identifying the S* state with vibrationally excited molecules in the ground electronic state S_0*. *Phys. Chem. Chem. Phys.* **2015,** *17* (16), 10478-10488.
182. Staleva, H.; Zeeshan, M.; Chábera, P.; Partali, V.; Sliwka, H. R.; Polívka, T. Ultrafast dynamics of long homologues of carotenoid zeaxanthin. *J. Phys. Chem. A* **2013,** *119* (46), 11304–11312.
183. Khan, T.; Litvín, R.; Šebelík, V.; Polívka, T. Excited-state evolution of keto-carotenoids after excess energy excitation in the UV region. *ChemPhysChem* **2021,** *22* (5), 471-480.
184. Balevičius, V.; Abramavicius, D.; Polívka, T.; Pour, A. G.; Hauer, J. A unified picture of S* in carotenoids. *J. Phys. Chem. Lett.* **2016,** *7* (17), 3347–3352.
185. Ehlers, F.; Scholz, M.; Oum, K.; Lenzer, T. Excited-state dynamics of 3,3'-dihydroxyisorenieratene and (3R,3'R)-zeaxanthin: Observation of vibrationally hot S_0 species. *Arch. Biochem. Biophys.* **2018,** *646*, 137-144.
186. Balevičius, V.; Wei, T.; Tommaso, D. D.; Abramavicius, D.; Hauer, J.; Polívka, T.; Duffy, C. D. P. The full dynamics of energy relaxation in large organic molecules: from photo-excitation to solvent heating. *Chem. Sci.* **2019,** *10* (18), 4792-4804.

187. Christensen, R. L.; Milota, F.; Nemeth, A.; Sperling, J.; Kauffmann, H. F.; Pullerits, T.; Hauer, J. Two-dimensional electronic spectroscopy of β-carotene. *J. Phys. Chem. B* **2009,** *113* (51), 16409-16419.
188. Kloz, M.; Weißenborn, J.; Polívka, T.; Frank, H. A.; Kennis, J. T. M. Spectral watermarking in femtosecond stimulated Raman spectroscopy: resolving the nature of the carotenoid S* state. *Phys. Chem. Chem. Phys.* **2016,** *18* (21), 14619-14628.
189. Jailaubekov, A. E.; Song, S. H.; Vengris, M.; Cogdell, R. J.; Larsen, D. S. Using narrowband excitation to confirm that the S* state in carotenoids is not a vibrationally-excited ground state species. *Chem. Phys. Lett.* **2010,** *487* (1-3), 101-107.
190. Jailaubekov, A. E.; Vengris, M.; Song, S. H.; Kusumoto, T.; Hashimoto, H.; Larsen, D. S. Deconstructing the excited-state dynamics of β-carotene in solution. *J. Phys. Chem. A* **2011,** *115* (16), 3905-3916.
191. de Weerd, F. L.; van Stokkum, I. H. M.; van Grondelle, R. Subpicosecond dynamics in the excited state absorption of all-*trans*-β-carotene. *Chem. Phys. Lett.* **2002,** *354* (1-2), 38-43.
192. Niedzwiedzki, D. M.; Sullivan, J. O.; Polívka, T.; Birge, R. R.; Frank, H. A. Femtosecond time-resolved transient absorption spectroscopy of xanthophylls. *J. Phys. Chem. B* **2006,** *110* (45), 22872-22885.
193. Niedzwiedzki, D. M.; Koscielecki, J. F.; Cong, H.; Sullivan, J. O.; Gibson, G. N.; Birge, R. R.; Frank, H. A. Ultrafast dynamics and excited state spectra of open-chain carotenoids at room and low temperatures. *J. Phys. Chem. B* **2007,** *111* (21), 5984–5998.
194. Hauer, J.; Maiuri, M.; Viola, D.; Lukes, V.; Henry, S.; Carey, A. M.; Cogdell, R. J.; Cerullo, G.; Polli, D. Explaining the temperature dependence of spirilloxanthin's S* signal by an inhomogeneous ground state model. *J. Phys. Chem. A* **2013,** *117* (29), 6303–6310.
195. Lukeš, V.; Christensson, N.; Milota, F.; Kauffmann, H. F.; Hauer, J. Electronic ground state conformers of β-carotene and their role in ultrafast spectroscopy. *Chem. Phys. Lett.* **2011,** *506* (1-3), 122-127.
196. Šebelík, V.; Fuciman, M.; West, R. G.; Polívka, T. Time-resolved two-photon spectroscopy of carotenoids. *Chem. Phys.* **2019,** *522* (171-177).
197. Kuznetsova, V.; Southall, J.; Cogdell, R. J.; Fuciman, M.; Polívka, T. Spectroscopic properties of the S_1 state of linear carotenoids after excess energy excitation. *Chem. Phys. Lett.* **2017,** *683*, 448-453.
198. Niedzwiedzki, D. M.; Hunter, C. N.; Blankenship, R. E. Evaluating the nature of so-called S*-state feature in transient absorption of carotenoids in light-harvesting complex 2 (LH2) from purple photosynthetic bacteria. *J. Phys. Chem. B* **2016,** *120* (43), 11123–11131.
199. Niedzwiedzki, D. M.; Swainsbury, D. J. K.; Martin, E. C.; Hunter, C. N.; Blankenship, R. E. Origin of the S* excited state feature of carotenoids in light-harvesting complex 1 from purple photosynthetic bacteria. *J. Phys. Chem. B* **2017,** *121* (32), 7571–7585.
200. Šebelík, V.; Duffy, C. D. P.; Keil, E.; Polívka, T.; Hauer, J. Understanding carotenoid dynamics via the vibronic energy relaxation approach. *J. Phys. Chem. B* **2022,** *126* (22), 3985-3994.
201. Hashimoto, H.; Uragami, C.; Yukihira, N.; Gardiner, A. T.; Cogdell, R. J. Understanding/unravelling carotenoid excited singlet states. *J. R. Soc. Interface* **2018,** *15* (141), 1-15.
202. Conn, P. F.; Schalch, W.; Truscott, T. G. The singlet oxygen and carotenoid interaction. *J. Photochem. Photobiol. B* **1991,** *11* (1), 41-47.
203. Foote, C. S.; Denny, R. W. Chemistry of singlet oxygen. VII. Quenching by β-carotene. *J. Am. Chem. Soc.* **1968,** *90* (22), 6233–6235.
204. Farmilo, A.; Wilkinson, F. Mechanism of quenching of singlet oxygen in solution. *Photochem. Photobiol.* **1973,** *18* (6), 447-450.
205. Zbyradowski, M.; Duda, M.; Wisniewska-Becker, A.; Heriyanto; Rajwa, W.; Fiedor, J.; Cvetkovic, D.; Pilch, M.; Fiedor, L. Triplet-driven chemical reactivity of β-carotene and its biological implications. *Nature Comm.* **2022,** *13* (2474).
206. Ashikawa, I.; Miyata, A.; Koike, H.; Inoue, Y.; Koyama, Y. Light-induced structural change of β-carotene in thylakoid membranes. *Biochemistry* **1986,** *25* (20), 6154–6160.

207. Billsten, H. H.; Pan, J.; Sinha, S.; Pascher, T.; Sundström, V.; Polívka, T. Excited-state processes in the carotenoid zeaxanthin after excess energy excitation. *J. Phys. Chem. A* **2005,** *109* (31), 6852–6859.
208. Polívka, T.; Balashov, S. P.; Chábera, P.; Imasheva, E. S.; Yartsev, A.; Sundström, V.; Lanyi, J. K. Femtosecond carotenoid to retinal energy transfer in xanthorhodopsin. *Biophys. J.* **2009,** *96* (6), 2268-2277.
209. Nielsen, B. R.; Jørgensen, K.; Skibsted, L. H. Triplet—triplet extinction coefficients, rate constants of triplet decay and rate constant of anthracene triplet sensitization by laser flash photolysis of astaxanthin, β-carotene, canthaxanthin and zeaxanthin in deaerated toluene at 298 K. *J. Photochem. Photobiol. A* **1998,** *112* (2-3), 127-133.
210. Burke, M.; Land, E. J.; McGarvey, D. J.; Truscott, T. G. Carotenoid triplet state lifetimes. *J. Photochem. Photobiol. B* **2000,** *59* (1-3), 132-138.
211. Bachilo, S. M. β-carotene triplet state absorption in the near-IR range. *J. Photochem. Photobiol. A* **1995,** *91* (2), 111-115.
212. Niedzwiedzki, D. M.; Kajikawa, T.; Aoki, K.; Katsumura, S.; Frank, H. A. Excited states energies and dynamics of peridinin analogues and the nature of the intramolecular charge transfer state in carbonyl-containing carotenoids. *J. Phys. Chem. B* **2013,** *117* (23), 6874-6887.
213. Fuciman, M.; Enriquez, M. M.; Kaligotla, S.; Niedzwiedzki, D. M.; Kajikawa, T.; Aoki, K.; Katsumura, S.; Frank, H. A. Singlet and triplet state spectra and dynamics of structurally modified peridinins. *J. Phys. Chem. B* **2011,** *115* (15), 4436–4445.
214. Niedzwiedzki, D. M.; Kobayashi, M.; Blankenship, R. E. Triplet excited state spectra and dynamics of carotenoids from the thermophilic purple photosynthetic bacterium *Thermochromatium tepidum*. *Photosynth Res.* **2011,** *107*, 177–186.
215. Packer, J. E.; Mahood, J. S.; Mora-Arellano, V. O.; Slater, T. F.; Willson, R. L.; Wolfenden, B. S. Free radicals and singlet oxygen scavengers: Reaction of a peroxy-radical with β-carotene, diphenyl furan and 1,4-diazobicyclo(2,2,2)-octane. *Biochem. Biophys. Res. Comm.* **1981,** *98* (4), 901-906.
216. Mortensen, A.; Skibsted, L. H. Importance of carotenoid structure in radical-scavenging reactions. *J. Agric. Food Chem.* **1997,** *45* (8), 2970–2977.
217. Böhm, F.; Tinkler, J. H.; Truscott, T. G. Carotenoids protect against cell membrane damage by the nitrogen dioxide radical. *Nat. Med.* **1995,** *1* (2), 98–99.
218. Hill, T. J.; Land, E. J.; McGarvey, D. J.; Schalch, W.; Tinkler, J. H.; Truscott, T. G. Interactions between carotenoids and the $CCl_3O_2\cdot$ radical *J. Am. Chem. Soc.* **1995,** *117* (32), 8322–8326.
219. Avenson, T. J.; Ahn, T. K.; Zigmantas, D.; Niyogi, K. K.; Li, Z.; Ballottari, M.; Bassi, R.; Fleming, G. R. Zeaxanthin radical cation formation in minor light-harvesting complexes of higher plant antenna. *J. Biol. Chem.* **2008,** *283* (6), 3550-3558.
220. Holt, N. E.; Zigmantas, D.; Valkunas, L.; Li, X.-P.; Niyogi, K. K.; Fleming, G. R. Carotenoid cation formation and the regulation of photosynthetic light harvesting. *Science* **2005,** *307* (5708), 433-436.
221. Cong, H.; Niedzwiedzki, D. M.; Gibson, G. N.; LaFountain, A. M.; Kelsh, R. M.; Gardiner, A. T.; Cogdell, R. J.; Frank, H. A. Ultrafast time-resolved carotenoid to-bacteriochlorophyll energy transfer in LH2 complexes from photosynthetic bacteria. *J. Phys. Chem. B* **2008,** *112* (34), 10689–10703.
222. Polívka, T.; Zigmantas, D.; Herek, J. L.; He, Z.; Pascher, T.; Pullerits, T.; Cogdell, R. J.; Frank, H. A.; Sundström, V. The carotenoid S_1 state in LH2 complexes from purple bacteria *Rhodobacter sphaeroides* and *Rhodopseudomonas acidophila*: S_1 energies, dynamics, and carotenoid radical formation. *J. Phys. Chem. B* **2002,** *106* (42), 11016–11025.
223. Polívka, T.; Pullerits, T.; Frank, H. A.; Cogdell, R. J.; Sundström, V. Ultrafast formation of a carotenoid radical in LH2 antenna complexes of Purple Bacteria. *J. Phys. Chem. B* **2004,** *108* (39), 15398-15407.
224. Polívka, T.; Niedzwiedzki, D. M.; Fuciman, M.; Sundström, V.; Frank, H. A. Role of B800 in carotenoid−bacteriochlorophyll energy and electron transfer in LH2 complexes from the purple bacterium *Rhodobacter sphaeroides*. *J. Phys. Chem. B* **2007,** *111* (25), 7422–7431.
225. Jørgensen, K.; Skibsted, L. H. Carotenoid scavenging of radicals. *Z. Lebensm. Unters. Forsch.* **1993,** *196* (5), 423–429.

226. Zhang, J. P.; Fujii, R.; Koyama, Y.; Rondonuwu, F. S.; Watanabe, Y.; Mortensen, A.; Skibsted, L. H. The $1B_u$-type singlet state of β-carotene as a precursor of the radical cation found in chloroform solution by sub-picosecond time-resolved absorption spectroscopy. *Chem. Phys. Lett.* **2001,** *348* (3-4), 235-241.
227. Jeevarajan, J. A.; Wei, C. C.; Jeevarajan, A. S.; Kispert, L. D. Optical absorption spectra of dications of carotenoids. *J. Phys. Chem.* **1996,** *100* (14), 5637-5641.
228. Gao, G.; Wei, C. C.; Jeevarajan, A. S.; Kispert, L. D. Geometrical isomerization of carotenoids mediated by cation radical/dication formation. *J. Phys. Chem.* **1996,** *100* (13), 5362-5366.
229. Jeevarajan, A. S.; Khaled, M.; Kispert, L. D. Simultaneous electrochemical and electron paramagnetic resonance studies of keto and hydroxy carotenoids. *Chem. Phys. Lett.* **1994,** *225* (4-6), 340-345.
230. Jeevarajan, A. S.; Khaled, M.; Kispert, L. D. Simultaneous electrochemical and electron paramagnetic resonance studies of carotenoids: Effect of electron donating and accepting substituents. *J. Phys. Chem.* **1994,** *98* (32), 7777-7781.
231. Wei, C.-C.; Gao, G.; Kispert, L. D. Selected *cis/trans* isomers of carotenoids formed by bulk electrolysis and iron(III) chloride oxidation. *J. Chem. Soc. Perkin Trans. 2* **1997,** *2* (4), 783-786.
232. Llansola-Portoles, M. J.; Pascal, A. A.; Robert, B. Electronic and vibrational properties of carotenoids: from *in vitro* to *in vivo*. *J. R. Soc. Interface* **2017,** *14* (135), 20170504.
233. Holt, T. K.; Krogmann, D. W. A carotenoid-protein from cyanobacteria. *Biochim Biophys Acta* **1981,** *637* (3), 408-414.
234. Wu, Y. P.; Krogmann, D. W. The orange carotenoid protein of *Synechocystis* PCC 6803. *Biochim Biophys Acta* **1997,** *1322* (1), 1-7.
235. Kerfeld, C. A.; Wu, Y. P.; Chan, C.; Krogmann, D. W.; Yeates, T. O. Crystals of the carotenoid protein from Arthrospira maxima containing uniformly oriented pigment molecules. *Acta Cryst.* **1997,** *53* (6), 720-723.
236. Kerfeld, C. A.; Sawaya, M. R.; Brahmandam, V.; Cascio, D.; Ho, K. K.; Trevithick-Sutton, C. C.; Krogmann, D. W.; Yeates, T. O. The crystal structure of a cyanobacterial water-soluble carotenoid binding protein. *Structure* **2003,** *11*, 55-65.
237. Wilson, A.; Kinney, J. N.; Zwart, P. H.; Punginelli, C.; D'Haene, S.; Perreau, F.; Klein, M. G.; Kirilovsky, D.; Kerfeld, C. A. Structural determinants underlying photoprotection in the photoactive Orange Carotenoid Protein of cyanobacteria. *J Biol Chem.* **2010,** *285* (24), 18364-18375.
238. Kerfeld, C. A.; Melnicki, M. R.; Sutter, M.; Dominguez-Martin, M. A. Structure, function and evolution of the cyanobacterial Orange Carotenoid Protein and its homologs. *New Phytol.* **2017,** *215* (3), 937-951.
239. Bao, H.; Melnicki, M. R.; Pawlowski, E. G.; Sutter, M.; Agostoni, M.; Lechno-Yossef, S.; Cai, F.; Montgomery, B. L.; Kerfeld, C. A. Additional families of Orange Carotenoid Proteins in the photoprotective system of cyanobacteria. *Nat. Plants* **2017,** *3* (17089).
240. Hihara, Y.; Kamei, A.; Kanehisa, M.; Kaplan, A.; Ikeuchi, M. DNA microarray analysis of cyanobacterial gene expression during acclimation to high light. *Plant Cell* **2001,** *13* (4), 793-806.
241. Huang, L.; McCluskey, M. P.; Ni, H.; LaRossa, R. A. Global gene expression profiles of the cyanobacterium *Synechocystis* sp strain PCC 6803 in response to irradiation with UV-B and white light. *J. Bacteriol.* **2002,** *184* (24), 6845-6858.
242. Kerfeld, C. A. Water-soluble carotenoid proteins of cyanobacteria. *Arch. Biochem. Biophys.* **2004,** *430* (1), 2-9.
243. Kerfeld, C. A. Structure and function of the water-soluble carotenoid-binding proteins of cyanobacteria. *Photosynth Res.* **2004,** *81* (3), 215-225.
244. El Bissati, K.; Delphin, E.; Murata, N.; Etienne, A.-L.; Kirilovsky, D. Photosystem II fluorescence quenching in the cyanobacterium *Synechocystis* PCC 6803: involvement of two different mechanisms. *Biochim. Biophys. Acta - Bioenerg.* **2000,** *1457* (3), 229-242.
245. Rakhimberdieva, M. G.; Stadnichuk, I. N.; Elanskaya, I. V.; Karapetyan, N. V. Carotenoid-induced quenching of the phycobilisome fluorescence in photosystem II-deficient mutant of *Synechocystis* sp. *FEBS Lett.* **2004,** *574* (1-3), 85-88.

246. Wilson, A.; Boulay, C.; Wilde, A.; Kerfeld, C. A.; Kirilovsky, D. Light-induced energy dissipation in iron-starved cyanobacteria: roles of OCP and IsiA proteins. *The Plant Cell* **2007,** *19* (2), 656–672.
247. Karapetyan, N. V. Non-photochemical quenching of fluorescence in cyanobacteria. *Biochem. (Mosc.)* **2007,** *72* (10), 1127-1135.
248. Kanesaki, Y.; Suzuki, I.; Allakhverdiev, S. I.; Mikami, K.; Murata, N. Salt stress and hyperosmotic stress regulate the expression of different sets of genes in *Synechocystis* sp. PCC 6803. *Biochem. Biophys. Res. Comm.* **2002,** *290* (1), 339-348.
249. Maksimov, E. G.; Schmidt, F.-J.; Shirshin, E. A.; Svirin, M. D.; Elanskaya, I. V.; Friedrich, T.; Fadeev, V. V.; Paschenko, V. Z.; Rubin, A. B. The time course of non-photochemical quenching in phycobilisomes of *Synechocystis* sp. PCC6803 as revealed by picosecond time-resolved fluorimetry. *Biochim Biophys Acta Bioenerg* **2014,** *1837* (9), 1540-1547.
250. Tian, L.; Gwizdala, M.; van Stokkum, I. H. M.; Koehorst, R. B. M.; Kirilovsky, D.; van Amerongen, H. Picosecond kinetics of light harvesting and photoprotective quenching in wild-type and mutant phycobilisomes isolated from the cyanobacterium *Synechocystis* PCC 6803. *Biophys J.* **2012,** *102* (7), 1692-1700.
251. Tian, L.; van Stokkum, I. H. M.; Koehorst, R. B. M.; Jongerius, A.; Kirilovsky, D.; van Amerongen, H. Site, rate, and mechanism of photoprotective quenching in cyanobacteria. *J. Am. Chem. Soc.* **2011,** *133*, 18304–18311.
252. Harris, D.; Tal, O.; Jallet, D.; Wilson, A.; Kirilovsky, D.; Adir , N. Orange Carotenoid Protein burrows into the phycobilisome to provide photoprotection. *Proc. Natl. Acad. Sci. U. S. A.* **2016,** *113* (12), E1655-E1662.
253. van Stokkum, I. H. M.; Gwizdala, M.; Tian, L.; Snellenburg, J. J.; van Grondelle, R.; van Amerongen, H.; Berera, R. A functional compartmental model of the Synechocystis PCC 6803 phycobilisome. *Photosynth Res.* **2018,** *135* (1), 87–102.
254. Gwizdala, M.; Botha, J. L.; Wilson, A.; Kirilovsky, D.; van Grondelle, R.; Kruger, T. P. J. Switching an individual phycobilisome off and on. *J. Phys. Chem. Lett.* **2018,** *9* (9), 2426-2432.
255. Jallet, D.; Gwizdala, M.; Kirilovsky, D. ApcD, ApcF and ApcE are not required for the Orange Carotenoid Protein related phycobilisome fluorescence quenching in the cyanobacterium *Synechocystis* PCC 6803. *Biochim. Biophys. Acta - Bioenerg.* **2012,** *1817* (8), 1418-1427.
256. Kuzminov, F. I.; Karapetyan, N. V.; Rakhimberdieva, M. G.; Elanskaya, I. V.; Gorbunov, M. Y.; Fadeev, V. V. Investigation of OCP-triggered dissipation of excitation energy in PSI/PSII-less *Synechocystis* sp. PCC 6803 mutant using non-linear laser fluorimetry. *Biochim. Biophys. Acta - Bioenerg.* **2012,** *1817* (7), 1012-1021.
257. Stadnichuk, I. N.; Yanyushin, M. F.; Maksimov, E. G.; Lukashev, E. P.; Zharmukhamedov, S. K.; Elanskaya, I. V.; Paschenko, V. Z. Site of non-photochemical quenching of the phycobilisome by Orange Carotenoid Protein in the cyanobacterium *Synechocystis* sp. PCC 6803. *Biochim. Biophys. Acta - Bioenerg.* **2012,** *1817* (8), 1436-1445.
258. Jallet, D.; Thurotte, A.; Leverenz, R. L.; Perreau, F.; Kerfeld, C. A.; Kirilovsky, D. Specificity of the cyanobacterial Orange Carotenoid Protein: Influences of Orange Carotenoid Protein and phycobilisome structures. *Plant Physiol.* **2014,** *164* (2), 790–804.
259. Boulay, C.; Wilson, A.; D'Haene, S.; Kirilovsky, D. Identification of a protein required for recovery of full antenna capacity in OCP-related photoprotective mechanism in cyanobacteria. *Proc. Natl. Acad. Sci. U. S. A.* **2010,** *107* (25), 11620-11625.
260. Sutter, M.; Wilson, A.; Leverenz, R. L.; Lopez-Igual, R.; Thurotte, A.; Salmeen, A. E.; Kirilovsky, D.; Kerfeld, C. A. Crystal structure of the FRP and identification of the active site for modulation of OCP-mediated photoprotection in cyanobacteria. *Proc. Natl. Acad. Sci. U. S. A.* **2013,** *110* (24), 10022-10027.
261. Liu, H.; Zhang, H.; King, J. D.; Wolf, N. R.; Prado, M.; Gross, M. L.; Blankenship, R. E. Mass spectrometry footprinting reveals the structural rearrangements of cyanobacterial Orange Carotenoid Protein upon light activation. *Biochim. Biophys. Acta - Bioenerg.* **2014,** *1837* (12), 1955-1963.
262. Gupta, S.; Guttman, M.; Leverenz, R. L.; Zhumadilova, K.; Pawlowski, E. G.; Petzold, C. J.; Lee, K. K.; Ralston, C. Y.; Kerfeld, C. A. Local and global structural drivers for the photoactivation of the Orange Carotenoid Protein. *Proc. Natl. Acad. Sci. USA* **2015,** *112* (41), E5567–E5574.

263. Sluchanko, N. N.; Slonimskiy, Y. B.; Moldenhauer, M.; Friedrich, T.; Maksimov, E. G. Deletion of the short N-terminal extension in OCP reveals the main site for FRP binding. *FEBS Lett.* **2017,** *591* (12), 1667-1676.
264. Sluchanko, N. N.; Slonimskiy, Y. B.; Shirshin, E. A.; Moldenhauer, M.; Friedrich, T.; Maksimov, E. G. OCP–FRP protein complex topologies suggest a mechanism for controlling high light tolerance in cyanobacteria. *Nat. Comm.* **2018,** *9* (3869).
265. Harris, D.; Wilson, A.; Muzzopappa, F.; Sluchanko, N. N.; Friedrich, T.; Maksimov, E. G.; Kirilovsky, D.; Adir, N. Structural rearrangements in the C-terminal domain homolog of Orange Carotenoid Protein are crucial for carotenoid transfer. *Nat. Comm. Biol.* **2018,** *1* (125), 1-11.
266. Mohamad, S. B. B.; Yousef, Y. A.; Melø, T.-B.; Jávorfi, T.; Partali, V.; Sliwka, H.-R.; Naqvi, K. R. Singlet oxygen quenching by thione analogues of canthaxanthin, echinenone and rhodoxanthin. *J. Photochem. Photobiol. B* **2006,** *84* (2), 135-140.
267. Sedoud, A.; López-Igual, R.; ur Rehman, A.; Wilson, A.; Perreau, F.; Boulay, C.; Vass, I.; Krieger-Liszkay, A.; Kirilovsky, D. The cyanobacterial photoactive Orange Carotenoid Protein is an excellent singlet oxygen quencher. *Plant Cell* **2014,** *26* (4), 1781–1791.
268. Kirilovsky, D.; Kerfeld, C. A. The Orange Carotenoid Protein: a blue-green light photoactive protein. *Photochem. Photobiol. Sci.* **2013,** *12* (7), 1135–1143.
269. Chukhutsina, V. U.; van Thor, J. J. Molecular activation mechanism and structural dynamics of Orange Carotenoid Protein. *Physchem* **2022,** *2* (3), 235-252.
270. Muzzopappa, F.; Kirilovsky, D. Changing color for photoprotection: The Orange Carotenoid Protein. *Trends Plant Sci.* **2020,** *25* (1), 92-104.
271. Bullock, T. L.; Clarkson, W. D.; Kent, H. M.; Stewart, M. The 1.6 angstrom resolution crystal structure of nuclear transport factor 2 (NTF2). *J. Mol. Biol.* **1996,** *260* (3), 422-431.
272. Christie, M.; Chang, C. W.; Rona, G.; Smith, K. M.; Stewart, A. G.; Takeda, A. A. S.; Fontes, M. R. M.; Stewart, M.; Vertessy, B. G.; Forwood, J. K.; Kobe, B. Structural biology and regulation of protein import into the nucleus. *J Mol. Biol.* **2016,** *428* (10), 2060-2090.
273. Eberhardt, R. Y.; Chang, Y. Y.; Bateman, A.; Murzin, A. G.; Axelrod, H. L.; Hwang, W. C.; Aravind, L. Filling out the structural map of the NTF2-like superfamily. *BMC Bioinform.* **2013,** *14* (327), 1-11.
274. Zhang, H.; Liu, H.; Niedzwiedzki, D. M.; Prado, M.; Jiang, J.; Gross, M. L.; Blankenship, R. E. Molecular mechanism of photoactivation and structural location of the cyanobacterial Orange Carotenoid Protein. *Biochemistry* **2014,** *53* (1), 13–19.
275. King, J. D.; Liu, H.; He, G.; Orf, G. S.; Blankenship, R. E. Chemical activation of the cyanobacterial orange carotenoid protein. *FEBS Lett.* **2014,** *588* (24), 4561-4565.
276. Maksimov, E. G.; Moldenhauer, M.; Shirshin, E. A.; Parshina, E. Y.; Sluchanko, N. N.; Klementiev, K. E.; Tsoraev, G. V.; Tavraz, N. N.; Willoweit, M.; Schmidt, F.-J.; Breitenbach, J.; Sandmann, G.; Paschenko, V. Z.; Friedrich, T.; Rubin, A. B. A comparative study of three signaling forms of the Orange Carotenoid Protein. *Photosynth Res.* **2016,** *130*, 389–401.
277. Lu, Y.; Liu, H.; Saer, R. G.; Zhang, H.; Meyer, C. M.; Li, V. L.; Shi, L.; King, J. D.; Gross, M. L.; Blankenship, R. E. Native mass spectrometry analysis of oligomerization states of Fluorescence Recovery Protein and Orange Carotenoid Protein: Two proteins involved in the cyanobacterial photoprotection cycle. *Biochemistry* **2017,** *56* (1), 160–166.
278. Kish, E.; Pinto, M. M.; Kirilovsky, D.; Spezia, R.; Robert, B. Echinenone vibrational properties: From solvents to the Orange Carotenoid Protein. *Biochim Biophys Acta* **2015,** *1847* (10), 1044-1054.
279. Polivka, T.; Kerfeld, C. A.; Pascher, T.; Sundstrom, V. Spectroscopic properties of the carotenoid 3'-hydroxyechinenone in the Orange Carotenoid Protein from the cyanobacterium *Arthrospira maxima*. *Biochemistry* **2005,** *44* (10), 3994–4003.
280. De Re, E.; Schlau-Cohen, G. S.; Leverenz, R. L.; Huxter, V. M.; Oliver, T. A. A.; Mathies, R. A.; Fleming, G. R. Insights into the structural changes occurring upon photoconversion in the Orange Carotenoid Protein from broadband two-dimensional electronic spectroscopy. *J. Phys. Chem. B* **2014,** *118* (20), 5382-5389.

281. Gurchiek, J. K.; Bao, H.; Domínguez-Martín, M. A.; McGovern, S. E.; Marquardt, C. E.; Roscioli, J. D.; Ghosh, S.; Kerfeld, C. A.; Beck, W. F. Fluorescence and excited-state conformational dynamics of the Orange Carotenoid Protein. *J. Phys. Chem. B* **2018,** *122* (6), 1792–1800.
282. Šlouf, V.; Kuznetsova, V.; Fuciman, M.; Bourcier de Carbon, C.; Wilson, A.; Kirilovsky, D.; Polívka, T. Ultrafast spectroscopy tracks carotenoid configurations in the orange and red carotenoid proteins from cyanobacteria. *Photosynth. Res.* **2017,** *131* (1), 105–117.
283. Polívka, T.; Chábera, P.; Kerfeld, C. A. Carotenoid–protein interaction alters the S_1 energy of hydroxyechinenone in the Orange Carotenoid Protein. *Biochim Biophys Acta* **2013,** *1827* (3), 248–254.
284. Berera, R.; van Stokkum, I. H. M.; Gwizdala, M.; Wilson, A.; Kirilovsky, D.; van Grondelle, R. The photophysics of the Orange Carotenoid Protein, a light-powered molecular switch. *J. Phys. Chem. B* **2012,** *116*, 2568−2574.
285. Berera, R.; Gwizdala, M.; van Stokkum, I. H. M.; Kirilovsky, D.; van Grondelle, R. Excited states of the inactive and active forms of the Orange Carotenoid Protein. *J. Phys. Chem. B* **2013,** *117* (31), 9121-9128.
286. Liu, H.; Lu, Y.; Wolf, B.; Saer, R.; King, J. D.; Blankenship, R. E. Photoactivation and relaxation studies on the cyanobacterial Orange Carotenoid Protein in the presence of copper ion. *Photosynth Res.* **2018,** *135*, 143–147.
287. Bandara, S.; Ren, Z.; Lu, L.; Zeng, X.; Shin, H.; Zhao, K.-H.; Yang, X. Photoactivation mechanism of a carotenoid-based photoreceptor. *Proc. Natl. Acad. Sci. U. S. A.* **2017,** *114* (24), 6286-6291.
288. Fujisawa, T.; Leverenz, R. L.; Nagamine, M.; Kerfeld, C. A.; Unno, M. Raman optical activity reveals carotenoid photoactivation events in the Orange Carotenoid Protein in solution. *J. Am. Chem. Soc.* **2017,** *139* (30), 10456–10460.
289. Chábera, P.; Durchan, M.; Shih, P. M.; Kerfeld, C. A.; Polívka, T. Excited-state properties of the 16 kDa red carotenoid protein from *Arthrospira maxima*. *Biochim Biophys Acta* **2011,** *1807* (1), 30–35.
290. Andreeva, E. A.; Nizinski, S.; Wilson, A.; Levantino, M.; De Zitter, E.; Munro, R.; Muzzopappa, F.; Thureau, A.; Zala, N.; Burdzinski, G.; Sliwa, M.; Kirilovsky, D.; Schirò, G.; Colletier, J. P. Oligomerization processes limit photoactivation and recovery of the Orange Carotenoid Protein. *Biophys J.* **2022,** *121* (15), 2849-2872.
291. Niedzwiedzki, D. M.; Liu, H.; Blankenship, R. E. Excited state properties of 3'-hydroxyechinenone in solvents and in the Orange Carotenoid Protein from *Synechocystis* sp. PCC 6803. *J. Phys. Chem. B* **2014,** *118* (23), 6141–6149.
292. Šlouf, V.; Chábera, P.; Olsen, J. D.; Martin, E. C.; Qian, P.; Hunter, C. N.; Polívka, T. Photoprotection in a purple phototrophic bacterium mediated by oxygen-dependent alteration of carotenoid excited-state properties. *Proc. Natl. Acad. Sci. U. S. A.* **2012,** *109* (22), 8570-8575.
293. Khan, T.; Dominguez-Martin, M. A.; Šímová, I.; Fuciman, M.; Kerfeld, C. A.; Polívka, T. Excited-state properties of canthaxanthin in cyanobacterial carotenoid-binding proteins HCP2 and HCP3. *J. Phys. Chem. B* **2020,** *124* (24), 4896−4905.
294. Wilson, A.; Andreeva, E. A.; Nizinski, S. J.; Talbot, L.; Hartmann, E.; Schlichting, I.; Burdzinski, G.; Sliwa, M.; Kirilovsky, D.; Colletier, J. P. Structure-function-dynamics relationships in the peculiar *Planktothrix* PCC7805 OCP1: Impact of his-tagging and carotenoid type. *Biochim Biophys Acta Bioenerg* **2022,** *1863* (7), 148584.
295. Niziński, S.; Schlichting, I.; Colletier, J. P.; Kirilovsky, D.; Burdziński, G.; Sliwa, M. Is Orange Carotenoid Protein photoactivation a single-photon process? *Biophys. Rep.* **2022,** *2* (3), 100072.
296. Larsen, D. S.; Papagiannakis, E.; van Stokkum, I. H. M.; Vengris, M.; Kennis, J. T. M.; Grondelle, R. Excited state dynamics of β-carotene explored with dispersed multi-pulse transient absorption. *Chem. Phys. Lett.* **2003,** *381* (5-6), 733-742.
297. Brazevic, S.; Nizinski, S.; Sliwa, M.; Abe, J.; Rode, M. F.; Burdzinski, G. Control of the photo-isomerization mechanism in 3H-naphthopyrans to prevent formation of unwanted long-lived photoproducts *Int. J. Mol. Sci.* **2020,** *21* (21), 7825.
298. Brazevic, S.; Nizinski, S.; Szabla, R.; Rode, M. F.; Burdzinski, G. Photochromic reaction in 3H-naphthopyrans studied by vibrational spectroscopy and quantum chemical calculations. *Phys. Chem. Chem. Phys.* **2019,** *21*, 11861-11870.

9. Publications constituting this thesis and authorship statements

JACS Au
AN OPEN ACCESS JOURNAL OF THE AMERICAN CHEMICAL SOCIETY

pubs.acs.org/jacsau

Article

Unifying Perspective of the Ultrafast Photodynamics of Orange Carotenoid Proteins from *Synechocystis*: Peril of High-Power Excitation, Existence of Different S* States, and Influence of Tagging

Stanisław Niziński, Adjéle Wilson, Lucas M. Uriarte, Cyril Ruckebusch, Elena A. Andreeva, Ilme Schlichting, Jacques-Philippe Colletier, Diana Kirilovsky,* Gotard Burdzinski,* and Michel Sliwa*

Cite This: *JACS Au* 2022, 2, 1084−1095

Read Online

ACCESS | Metrics & More | Article Recommendations | Supporting Information

ABSTRACT: A substantial number of Orange Carotenoid Protein (OCP) studies have aimed to describe the evolution of singlet excited states leading to the formation of a photoactivated form, OCP^R. The most recent one suggests that 3 ps-lived excited states are formed after the sub-100 fs decay of the initial S_2 state. The S* state, which has the longest reported lifetime of a few to tens of picoseconds, is considered to be the precursor of the first red photoproduct P_1. Here, we report the ultrafast photodynamics of the OCP from *Synechocystis* PCC 6803 carried out using visible−near infrared femtosecond time-resolved absorption spectroscopy as a function of the excitation pulse power and wavelength. We found that a carotenoid radical cation can form even at relatively low excitation power, obscuring the determination of photoactivation yields for P_1. Moreover, the comparison of green (540 nm) and blue (470 nm) excitations revealed the existence of an hitherto uncharacterized excited state, denoted as S~, living a few tens of picoseconds and formed only upon 470 nm excitation. Because neither the P_1 quantum yield nor the photoactivation speed over hundreds of seconds vary under green and blue continuous irradiation, this S~ species is unlikely to be involved in the photoactivation mechanism leading to OCP^R. We also addressed the effect of His-tagging at the N- or C-termini on the excited-state photophysical properties. Differences in spectral signatures and lifetimes of the different excited states were observed at a variance with the usual assumption that His-tagging hardly influences protein dynamics and function. Altogether our results advocate for the careful consideration of the excitation power and His-tag position when comparing the photoactivation of different OCP variants and beg to revisit the notion that S* is the precursor of photoactivated OCP^R.

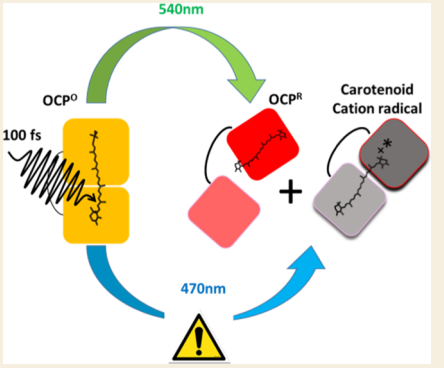

KEYWORDS: *orange carotenoid protein, photodynamics, ultrafast spectroscopy, multiphoton absorption, cation radical, echinenone, quantum yield, His-tag*

INTRODUCTION

The Orange Carotenoid Protein (OCP) is a 35 kDa water-soluble photoactive protein capable of quenching the excess light energy harvested by cyanobacteria.[1−4] In order to perform its energy-quenching function, dark-adapted OCP (abbreviated as OCP^O due to its orange color) must be photoactivated by strong blue-green light illumination, yielding the OCP^R species capable of quenching excited phycobilisomes.[5] The protein is structured as a two-domain protein, where the N-terminal (NTD) domain is the effector, and the C-terminal (CTD) domain is the regulator.[6,7] The functionalizing ketocarotenoid chromophore is embedded at the interface between the NTD and CTD.[8] The main function of OCP is to quench the fluorescence of the cyanobacterial light-harvesting antennas, a.k.a., phycobilisomes. Only the OCP^R state can interact with the latter and perform the quenching function.

The photoactivation of OCP^O starts with the evolution of the chromophore excited-state levels resulting in the formation of P_1. This state is the first red photoproduct with broken H bonds between the carotenoid and the protein.[9] The 12 Å migration of the ketocarotenoid in the NTD[10] and structural changes in the protein, respectively, occurring in the microsecond and millisecond time scales, ultimately[9,11,12] lead to the separation of the two domains (Scheme 1a), yielding OCP^R. The photoconversion quantum yield of OCP^R is very low (0.2% or less),[5,9,11,12] reflecting the functional requirement that OCP remains inactive in low irradiance

Received: October 22, 2021
Revised: February 2, 2022
Accepted: February 3, 2022
Published: April 25, 2022

Scheme 1. (a) General Photodynamical Scheme of OCP Photoactivation Mechanism[a]

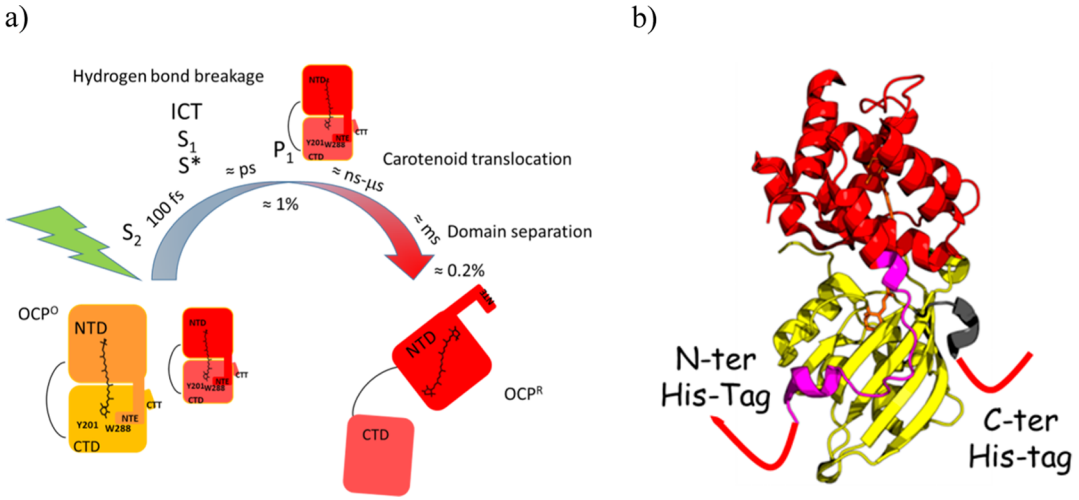

[a]In the dark, two sub-populations of the closed OCP^O are present, a "normal" one and a red-shifted one (the size represents their contribution, Figure S2 in Supporting Information). (b) OCP structure (reproduced from PDB ID 3MG1) comprises a fully α-helical NTD, featuring a fold that is unique to cyanobacteria, whereas the CTD has a mixed α/β architecture and belongs to the NTF-2 family.[8] His-tags can be attached to the N-terminal extension or to the C-terminal tail

conditions, that is, when maximum energy transfer to photochemical centers is needed. The low OCP photoconversion quantum yield is determined during excited-state deactivation, with about 99% of the ketocarotenoid relaxing back to the initial S_0 state within tens of picoseconds.[5,9,12,13] The ultrafast photodynamics of different OCPs and carotenoids [hydroxyechinenone, echinenone (ECN), canthaxanthin, and zeaxanthin] have been studied by femtosecond transient absorption spectroscopy using various excitation wavelengths in the visible range.[5,9,14−18] The most recent studies consider that upon the relaxation of the initial S_2 state, 3 ps-lived excited states are formed: a sub-picosecond-lived intramolecular charge-transfer (ICT) state, a picosecond-lived mixed S_1/ICT state called usually S_1, and an excited state S* characterized by a lifetime in the range of few picoseconds[13] to few tens of picoseconds,[9] depending on the source. There is a longstanding debate regarding the ground *versus* excited-state nature of the carotenoid S* state but no agreement has been reached thus far.[19−22] Carotenoid S* was first postulated to be a hot ground state,[19] then redefined as an electronically excited state,[20] but some publications questioned this hypothesis and pointed out different properties, featuring a vibrationally hot electronic ground state.[21−24] Regardless, the ICT, S_1, and S* populations are all known to decay within few tens of picoseconds, while the first red photoproduct P_1 appears with a yield of about 1.5%.[9] Despite this already vast knowledge, the low magnitude of the P_1 signal implies that a high error intrinsically exists on the determined quantum yield. Furthermore, it remains unclear, which of the excited states, are the precursor of P_1. Recent studies have considered S*, on the basis that S* would have a distorted geometry, which favors the breaking of the hydrogen bond and formation of P_1.[9] However, the issues concerning the genuine nature of S* render any firm conclusion difficult.

Kennis and co-workers were the first to report that the formation yield and lifetime of the S* state depend on the excitation peak power.[9] Such results could be explained by the existence of additional pathways and extra species, possessing similar spectra but different lifetimes and generated by multiphotonic processes caused by femtosecond pulse excitation—as reported for other photoactive proteins.[25,26] Multiphotonic processes are usually accompanied by off-pathway species, such as radical cations and solvated electrons, which are avoided when the excitation pulse is stretched or the excitation energy reduced.[25,26] The Polivka group showed an increase of the S* population and the existence of a long-lived radical signal peaking at 900 nm, when probing the effect of UV excitation on canthaxantin-functionalized OCP.[27] A functional role of an oxocarbenium cation was even suggested in the photoactivation of OCP^O.[13] Surprisingly, despite the fact that the low energy keto-carotenoid absorption band is associated with the $S_0 \rightarrow S_2$ transition, no studies have investigated the power dependence of excitation using femtosecond pulses thus far. Clearly, knowledge of the photoexcitation power dependence and characterization of radical cations is crucial for the interpretation of OCP ultrafast dynamics. Also, two excitation wavelengths have been used depending on studies, *viz.*, 470 and 540 nm,[14,16,28] due to the existence of at least two ground-state populations in the dark form (referred to as "normal" and "red-shifted"[14,29]). The 540 nm excitation presumably selects only the red-shifted sub-population, while 470 nm excites both of them. Last, studies have been performed on the C-tagged or N-tagged OCPs,[5,9,14−18] yet the (admittedly unlikely) hypothesis that tagging could influence ultrafast photodynamics was never investigated, despite both tags being located on helices attached to the sensory domain, that is, the CTD (Scheme 1). It could thus be that tagging affects the equilibrium between the normal and red-shifted dark-adapted OCP^O (Scheme 1) and/or their excited-state dynamics, which could in turn influence the photoconversion yield.

Here, we report a detailed photophysical study on OCP from *Synechocystis* PCC 6803 complexed with the ketocarotenoid ECN. The use of visible−near infrared (NIR) femtosecond transient absorption spectroscopy allowed to identify all species involved in the OCP excited-state deactivation. With an aim to afford a comparison with all previously published transient spectroscopy studies,[5,9,14−18] we

https://doi.org/10.1021/jacsau.1c00472
JACS Au 2022, 2, 1084−1095

investigated light-induced excited-state dynamics upon excitation by either 470 or 540 nm light. Stationary irradiation experiments were also performed at the two excitation wavelengths. Both on the C-tagged or N-tagged variants of OCP were studied, to test the effect of the tag and its position on ultrafast photodynamics. On each construct and at the two wavelengths, we furthermore probed the effect of the excitation power on excited-state dynamics. We show how the picosecond dynamics that determines the formation of P_1, the first crucial intermediate controlling the formation quantum yield of OCP^R, are influenced by the excitation energy and wavelength. The combination of transient absorption and stationary irradiation experiments upon 470 and 540 nm excitation allows us to identify which of the picosecond-lived states correlates with the final photoactivation quantum yield and is thus the most likely candidate to be the precursor of P_1. We show that the use of high excitation power leads to the formation of a carotenoid radical cation, whose presence may result in an erroneous extraction of P_1 yield from OCP bleach kinetics. Finally, we demonstrate that upon 470 nm excitation the photodynamics of OCP feature a yet unidentified S~ state whose existence may compromise the estimation of the S* lifetime and P_1 yield. Taking into account all the above-mentioned aspects of OCP photoexcitation will prove crucial, not only to understand the basis for the biological function of OCP but also to design OCPs with a higher photoactivation quantum yield.

MATERIALS AND METHODS

Protein Expression and Purification

The plasmid pCDF-NtagOCPSyn used for the expression of OCP from *Synechocystis* PCC 6803 carries a sequence coding for a His-tag in the N terminus and was characterized in de Carbon *et al.*[30] The expression of the *OCP* genes in *Escherichia coli* cells containing the genes for the synthesis of ECN and the isolation of ECN-OCP was also described.[30] The expression of the *OCP* genes in *Synechocystis* was reported by Gwizdala *et al.*[31] N-tagged OCP was expressed in *E. coli*, while C-tagged OCP was expressed in the ΔcrtR *Synechocystis* mutant lacking zeaxanthin and hydroxyechinenone. Exactly the same N-tagged OCP was used in Konold *et al.* (same protein expression and purification procedure).[9] The protein concentration used in the experiments described in this work was close to 1 mg/mL (calculated using absorbance at 496 nm) and 40 mM Tris−HCl 25 mM NaCl pH 8.0 buffer was used.

Steady-State UV−Vis Absorption Spectra and Photoconversion under Steady-State Irradiation

Steady-state UV−vis absorption spectra were recorded with a Jasco V-550 spectrophotometer, using 2 nm spectral bandwidth. The cuvette optical path was 10 mm for stationary LED irradiation spectroscopy experiments. The photoconversion kinetics set up is described elsewhere.[32] Here, the photoactivation was induced by green LED irradiation [λ_{max} = 528 nm, full width at half maximum (FWHM) = 28 nm, standard 3 W emitter], and blue LED irradiation (λ_{max} = 470 nm, FWHM = 18 nm, standard 3 W emitter). The probing and irradiation beams were at 90°. The optical irradiation path of the solution was 4 mm and the probing path was 10 mm. The absorbances at 470 and 528 nm were the same for C-tagged and N-tagged OCP (0.53 and 0.28 for 470 and 528 nm, respectively). The irradiation power was 3.4 mW/cm^2 for the blue LED and 3.0 mW/cm^2 for the green LED, therefore the photon flux is the same in both cases.

Femtosecond Vis−NIR Transient Absorption

Femtosecond vis−NIR transient absorption spectra were collected using a commercially available system (Ultrafast Systems, Helios) described previously[33] that consists of a short-pulse titanium-sapphire oscillator (Mai-Tai, Spectra Physics, 70 fs) followed by a high-energy titanium-sapphire regenerative amplifier (Spitfire Ace, Spectra Physics, 100 fs, 1 kHz). The 800 nm beam was split into two beams to generate as follows: (1) the pump (λ_{exc} = 540 or 470 nm) in the optical parametric amplifier (Topas Prime with a NirUVVis frequency mixer) and (2) probe pulses—white light continuum in the vis−NIR range generated by focusing the fundamental beam into a sapphire (430−780 nm) or YAG (820−1390 nm) crystal. The remaining 800 nm probe pulse photons were filtered. The instrument response function (IRF) was determined by fitting the kinetics of the coherent artefact signal from the solvent and was estimated to be ≈ 110 fs (FWHM). The experiments were performed with different pulse energies ranging from 0.2 μJ (3.3×10^{14} photons per cm^2 at FWHM) up to 1.6 μJ upon 470 nm excitation and from 0.4 μJ (6.6×10^{14} photons per cm^2 at FWHM) up to 3.2 μJ upon 540 nm excitation using variable neutral density filters. The pump diameter (FWHM) at the sample was ≈250 μm. Numbers of photons and fluence per pulse are given in the Supporting Information (Figures S5 and S6). In all transient absorption experiments, the absorbance was close to 0.7 at the excitation wavelength in a 2 mm optical path. The sample solution was stirred to keep fresh OCP solution in the probed volume. The transient spectra were registered with 1 nm per pixel and by averaging 500 supercontinuum spectra with and without excitation, respectively. The entire set of the pump−probe time delay points was repeated four times to ensure data reproducibility, then the data were inspected and averaged. Moreover, to ensure that all data sets are comparable to each other, they were measured in one experimental session, in identical conditions except for varied parameters (like pump energy, explicitly given). The pump beam was depolarized to avoid anisotropy effects. The sample temperature was set to 22 °C. The stability of the sample was checked by comparing the stationary UV−vis absorption spectra measured before and after the experiments.

Data Analysis

The transient absorption data were corrected for the chirp of white light continuum based on the given amount of sapphire, water, and BK7 glass, which the probe pulse had to pass through. Afterward, visible and NIR data were merged using a custom procedure.[33] Low intensity of the probing pulse and presence of a relatively strong residual 800 nm beam (even after filtering) resulted in minor artefacts visible in recorded data around 800 nm. For all data sets, the difference absorbance value obtained at the bleaching extremum (in both spectral and temporal dimension) was normalized to −1. Transient spectra were projected onto a 5 nm-spaced grid to get kinetic traces. The comparison of pre-exponential factors at 490 nm (bleaching band) allowed us to estimate the formation quantum yield of the various intermediates. Data processing to determine time constants and decay-associated difference spectra (DADS or DAS) was based on our custom fitting procedure.[34] It consists of two steps. (i) First, it fits globally (time constants are shared) kinetics at representative wavelengths (480, 490, 500, 570, 590, 610, 655, 740, 960, and 1100 nm) with convolution (IRF 110 fs FWHM) and weights (to increase the contribution of the long delays, which are our main interest, to the χ^2 error term). The following weights were used: 1.0 under 0.25 ps, 2.5 between 0.25 and 8 ps, 7.5 between 8 and 12 ps, and 12.5 after 12 ps. (ii) In the second step, time constants extracted from the first step are fixed and used to fit all kinetics separately (again with the same weights and convoluted with IRF), and finally DAS are built from obtained pre-exponential factors. The spectral and temporal ranges of the fit (the same for both steps) are 430 to 1380 nm and −1 ps to 1 ns, respectively. Bootstrapping analysis was also performed to estimate errors (see the Supporting Information for more details). We also tested our results against other procedures, like the one implemented in the Glotaran package.[35] To fit data sets with 540 nm excitation, we used a sum of four exponential terms plus an offset (representing long-lived photoproducts, > 10 ns, namely, P_1 and carotenoid radical). For data sets excited with a 470 nm pulse, it was required to apply an additional component, so in this case there were five exponential terms plus the offset.

https://doi.org/10.1021/jacsau.1c00472
JACS Au 2022, 2, 1084−1095

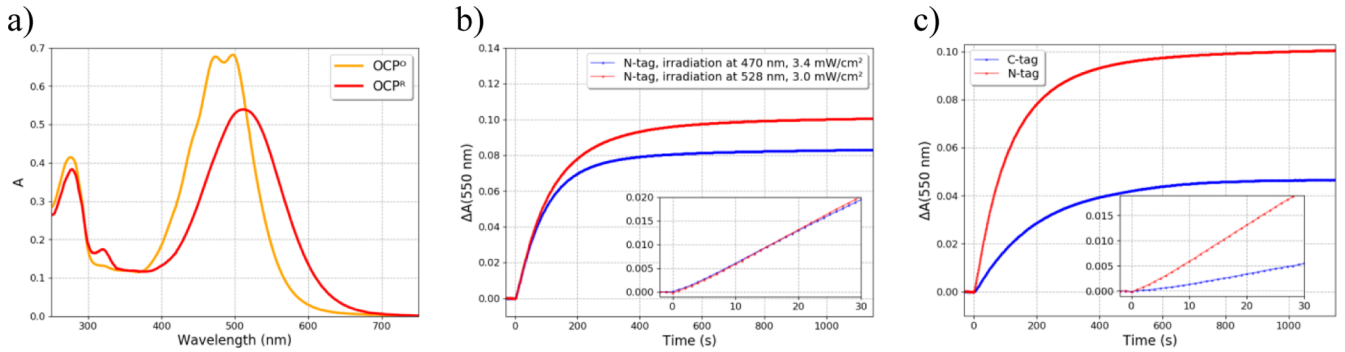

Figure 1. (a) UV−vis stationary spectra of OCP^O (recorded in the dark) and OCP^R (under 452 nm irradiation, 3.2 mW/cm^2), 1 cm path length, 11 °C. (b) Evolution of ΔA at 550 nm (22 °C) for N-tagged OCP (N-tag) upon 528 nm (FWHM = 28 nm, 3.0 mW/cm^2) and 470 nm (FWHM = 18 nm, 3.4 mW/cm^2) LED irradiation and (c) comparison of C-tagged (C-tag) and N-tagged (N-tag) OCP upon 528 nm LED irradiation. Initial slopes are shown in the insets.

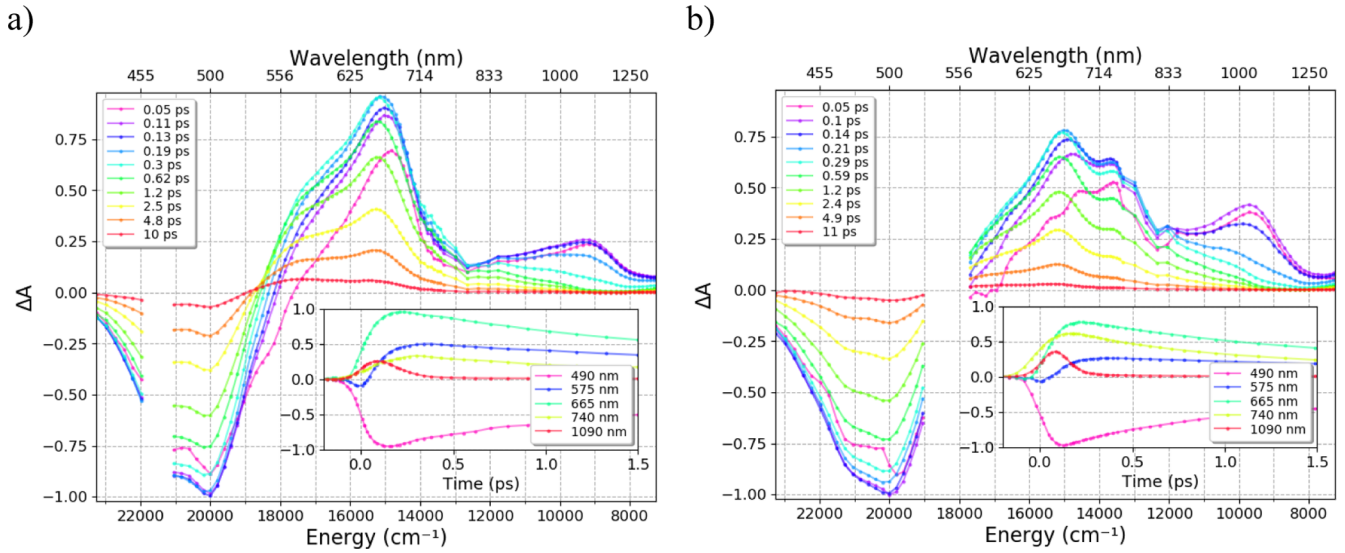

Figure 2. Transient absorption spectra between 0.05 and 10 ps of N-tagged OCP excited at (a) 470 nm (0.4 μJ) and (b) 540 nm (0.8 μJ). All data sets were normalized to −1 at the bleaching extremum (in both spectral and temporal dimensions). To obtain the original signal, multiply plotted values by (a) 0.077 and (b) 0.088. Insets show evolution of the signal in the 1.5 ps time window.

RESULTS

Steady-State Properties

In the OCP^O (dark-adapted) state, UV−visible absorption spectra of N-tagged and C-tagged OCP show almost no difference, both display a broad absorption band, characteristic of the S_0−S_2 transition, with two maxima at 472 and 496 nm and a tail until 650 nm (Figures 1a, S1 in Supporting Information).[29,36] The "red-shifted" population was estimated by Gaussian decomposition to be around 20% for both N-tagged and C-tagged OCPs (Figure S2), in line with previous reports.[14] To determine if a difference in the ability to photoactivate exists between the two dark-adapted sub-populations, N-tagged and C-tagged OCP solutions (same absorbance) were irradiated with blue (470 nm LED) and green (528 nm LED) light, thereby selecting either the "normal" or the "red-shifted" sub-populations of OCP^O. The initial slope of the evolution of the absorbance at 550 nm (Figure 1b), which probes the formation of OCP^R, shows that both sub-populations of N-tagged OCPs photoactivate with the same efficiency when using different irradiation wavelengths. There is a slight difference in the photostationary state (achieved approximately after 600 s of LED irradiation), suggesting that 528 nm irradiation ultimately generates quantitatively more OCP^R. This result can be explained by a deviation from dark-adapted equilibrium between sub-populations in the OCP^O state, caused by an extended period of irradiation (e.g., 528 nm selects one sub-population, but photoactivated OCPs may repopulate both sub-populations after back-conversion). Unexpectedly, the comparison of the evolution of the absorbance traces at 550 nm for the different tags (Figure 1c) reveals a much faster photoactivation of N-tagged OCP than C-tagged OCP (the initial slope is 3.5 times larger for the N-tagged OCP). This difference in OCP^R yield could stem either from different excited-state dynamics, leading to different P_1 formation quantum yield, or from changes in the yield of subsequent ground-state species forming in the ns−ms time scale (Scheme 1, carotenoid translocation and domain separation dynamics).[9,11,12] To split a difference between the two hypotheses, a more detailed analysis of the early stages of the photoinduced processes is needed.

https://doi.org/10.1021/jacsau.1c00472
JACS Au 2022, 2, 1084−1095

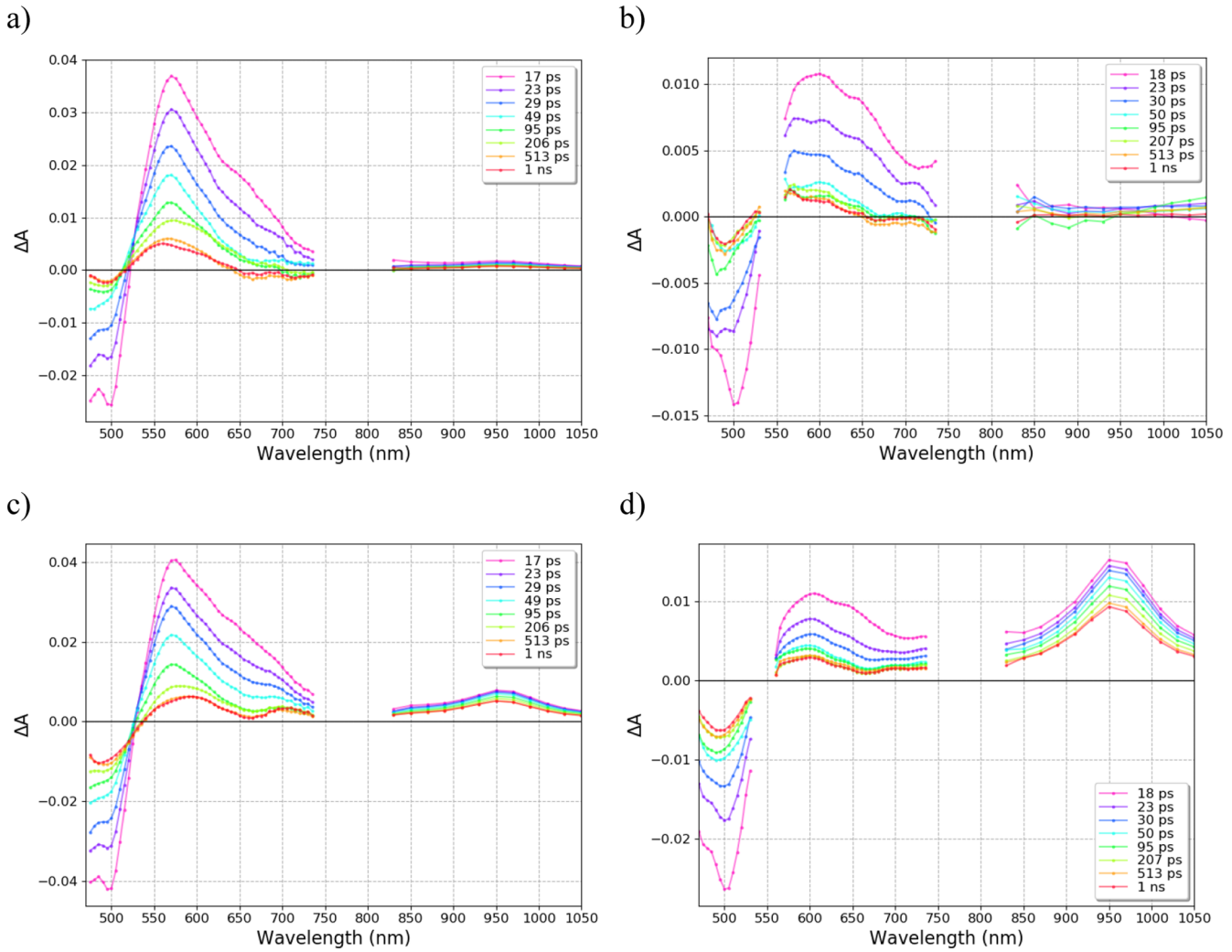

Figure 3. Transient absorption spectra between 17 ps and 1 ns for N-tagged OCP excited at (a) 470 nm (0.4 μJ), (b) 540 nm (0.8 μJ), (c) 470 nm (1.6 μJ), and (d) 540 nm (3.2 μJ). All data sets were normalized to −1 at the bleaching extremum [in both spectral and temporal dimensions, multiply by (a) 0.077, (b) 0.088, (c) 0.163, and (d) 0.234 to get original signal].

Femtosecond Transient Absorption Spectroscopy of N-Tagged OCP

The ultrafast photodynamics of N-tagged OCP was studied upon 470 and 540 nm excitation wavelengths. The excitation pulse energy was initially set to 0.4 μJ at 470 nm and to 0.8 μJ at 540 nm, which ensures being in the linear photoexcitation range (Figure 4), while getting enough S/N to characterize P_1 and keeping the data free of additional signals arising when higher energy is used (detailed discussion in the next section). Figure 2 shows femtosecond transient absorption data recorded with 470 and 540 nm excitation, respectively. Just after 540 nm excitation, at 0.05 ps, a primary positive absorption band peaking at 1050 nm is observed. This band is assigned to the S_2 excited-state population ($S_2 \rightarrow S_n$ transition).[17] The band is broader upon 470 nm excitation and its maximum is shifted to 1100 nm, indicating the presence of an excess of vibrational energy and pointing to the excitation of a larger range of OCP^O sub-populations. Concomitant with the formation of the S_2 state within 50 fs, a ground-state bleaching (GSB; indicative of OCP^O depopulation) signal is observed in the visible region (see Figure S3, which is zooming into the visible region), with a maximum at about 500 nm, as well as the appearance of two main excited-state absorption (ESA) bands, at about 663 and 740 nm (Figures 2, S3). These two ESA can be assigned to the S_1 and ICT states.[14,15] In addition to the ICT and S_1 states, the shoulder around 570 nm can be assigned to the S* state in agreement with the recent literature.[9,13] After 50 femtoseconds, the first signal evolution is the decay of the S_2 state within a few hundreds of femtoseconds. During this time, the ESA bands attributed to S_1 and S* states continue to grow slightly until 0.2 ps. The amplitudes of the bands around 570−585 nm (S* contribution) and 663 nm (S_1 contribution) are higher for the 470 nm excitation. Conversely, and in agreement with previous results,[14,15,28] the ICT character is more pronounced when 540 nm excitation is used, resulting in higher amplitude signals around 740 nm and a long tail up to 1100 nm. This increase in the amplitude of the ICT character is at the expense of the amplitudes of the bands at 663 and 570 nm. After 10 picoseconds, the S_1 and ICT states decay concomitant to recovery of 97% of the GSB band (Figure 2). At 23 ps time delay, the remaining signal is characterized by the broad positive absorption band usually assigned to the S* state, with a maximum at 570 nm and a shoulder around 655 nm (Figure 3).[9] The comparison of the transient spectra at 23 ps recorded after 470 and 540 nm excitations, respectively (Figure 3a,b,

https://doi.org/10.1021/jacsau.1c00472
JACS Au 2022, 2, 1084−1095

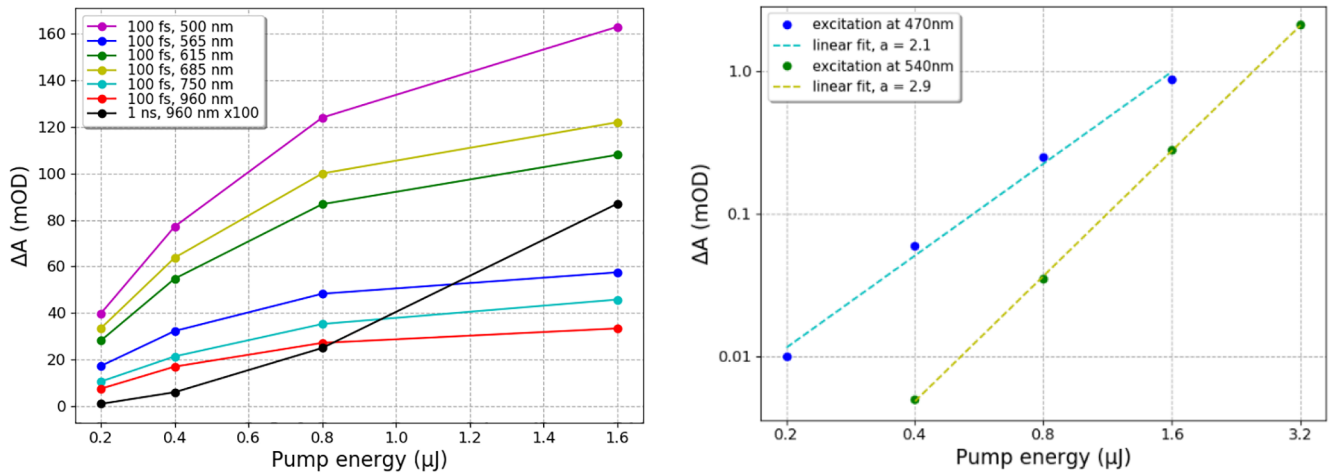

Figure 4. (a) Difference absorbance value at different wavelengths *versus* pump energy for 470 nm excitation (the value at 500 nm was multiplied by −1) and (b) log−log plots of cation radical absorbance (960 nm) at 1 ns time delay *versus* excitation energy upon 470 and 540 nm excitation.

purple spectrum), reveals major differences, the most notable one being that the GSB band is two times smaller for 540 nm excitation (about 0.008 *vs* 0.016 for 540 and 470 nm excitations; values estimated from the GSB signal at 490 nm). Moreover, while the transient absorption band observed upon 470 nm excitation peaks at 570 nm, that observed upon 540 nm excitation has a much broader shape, with the maximum shifted to ≈585 nm and a much higher amplitude of the shoulder around 655 nm. Thus, both excitations lead to different S*-type species. The S* state decays within 50 ps; however, upon 470 nm excitation there is an extra time evolution of the 570 nm band within 500 ps (Figure 3a). This is assigned to the existence of an additional species S˜, forming only upon 470 nm excitation and characterized by a positive absorption band with a maximum located at 570 nm and a lifetime of *ca.* 80 ps. Finally, irrespective of the excitation wavelength, the transient absorption spectrum at 1 ns is characterized by a GSB of OCP^O of similar intensity yet a broad positive band also remains, with a maximum at ≈565 nm, which is broader and two times higher in amplitude when a 470 nm pump is used. This band is assigned to P_1; however, only the GSB band, corresponding to OCP molecules that have not relaxed to the initial OCP^O state, can afford the estimation of the P_1 yield. Thus, using the GSB band of OCP^O at 490 nm and taking into account the positive absorbance contribution from P_1 at 490 nm (see Supporting Information, Figure S4), P_1 formation quantum yields are estimated to be ≈0.5% for both excitations. These results are also in accordance with the photoactivation efficiency being independent of the irradiation wavelength (470 or 528 nm, Figure 1a).

Effect of High Energy Pump Pulse Excitation

Power dependence measurements were done in the energy range of 0.2−1.6 μJ for 470 nm and 0.4−3.2 μJ for 540 nm excitation. Transient absorption spectra for 1.6 μJ (470 nm) and 3.2 μJ (540 nm) are shown for short time delays in the Supporting Information (Figure S7) and presented in Figure 3c,d for time delays between 17 ps and 1 ns. It should be noted that higher energies were also explored; however, fast sample degradation was observed as well as an increase in the scattering of the excitation beam. For the highest pulse energy, the number of photons absorbed per chromophore in the center of the beam was close to 0.8 (Figures S5 and S6). Figure 3 shows that at 1 ns time delay (Figure 3a,b) only P_1 is present for low excitation energies (positive band with a maximum at 565 nm), while additional positive absorption bands at 700 and 960 nm (Figure 3c,d), characteristic of the radical cation species of the carotenoid,[37,38] are observed for high excitation energies. A minor contribution is also present at 600 nm, overlapping with the P_1 absorption band (compare Figure 3a,c at 1 ns time delay). The presence of a radical cation is characterized by an increase in the depopulation (GSB) band extremum value *versus* pulse excitation energy (band at 500 nm), while the maximum value of absorbance for S*, S_1, and ICT states (565/685/750 nm) reaches a plateau for excitation energies exceeding 0.8 μJ for 470 nm and 1.6 μJ for 540 nm (Figure 4a). The radical cation signal also affects the P_1 positive absorption band, although to a lesser extent than the GSB band, which peaks to 1% depopulation of OCP^O when excitation energy reaches 1.6 μJ upon 470 nm excitation (Figure 3c). The thresholds for the observation of the radical cation are 0.4 and 0.8 μJ at 470 and 540 nm, respectively, with the signal at 960 nm being negligible at these excitation energies (Figure 4). These were therefore selected to characterize the photodynamics of OCP with the best possible S/N ratio, while avoiding contribution of biologically irrelevant species. Figures 4b shows a log−log plot of absorbance at 960 nm and 1 ns time delay *versus* excitation energy, underlining the multiphotonic nature of the process leading to the formation of the radical cation. Indeed two photons are involved in the formation of the radical for 470 nm excitation (a slope of two points to a purely biphotonic character, doubling pump pulse power causes fourfold increase in a radical signal) and three photons for 540 nm excitation (Figure 4b). The detailed effects of multiphoton excitation on the different excited states (formation quantum yield and lifetime) can be assessed by multi-exponential analysis, discussed in the next section.

Global Analysis of Transient Absorption Data in the Linear and Nonlinear Excitation Regime

For the 540 nm data sets, four exponential components convoluted with a Gaussian-shaped pulse of 110 fs (FWHM) and an offset for long-lived photoproducts (>10 ns) are required to obtain a quality fit of all kinetic traces. These

https://doi.org/10.1021/jacsau.1c00472
JACS Au 2022, 2, 1084−1095

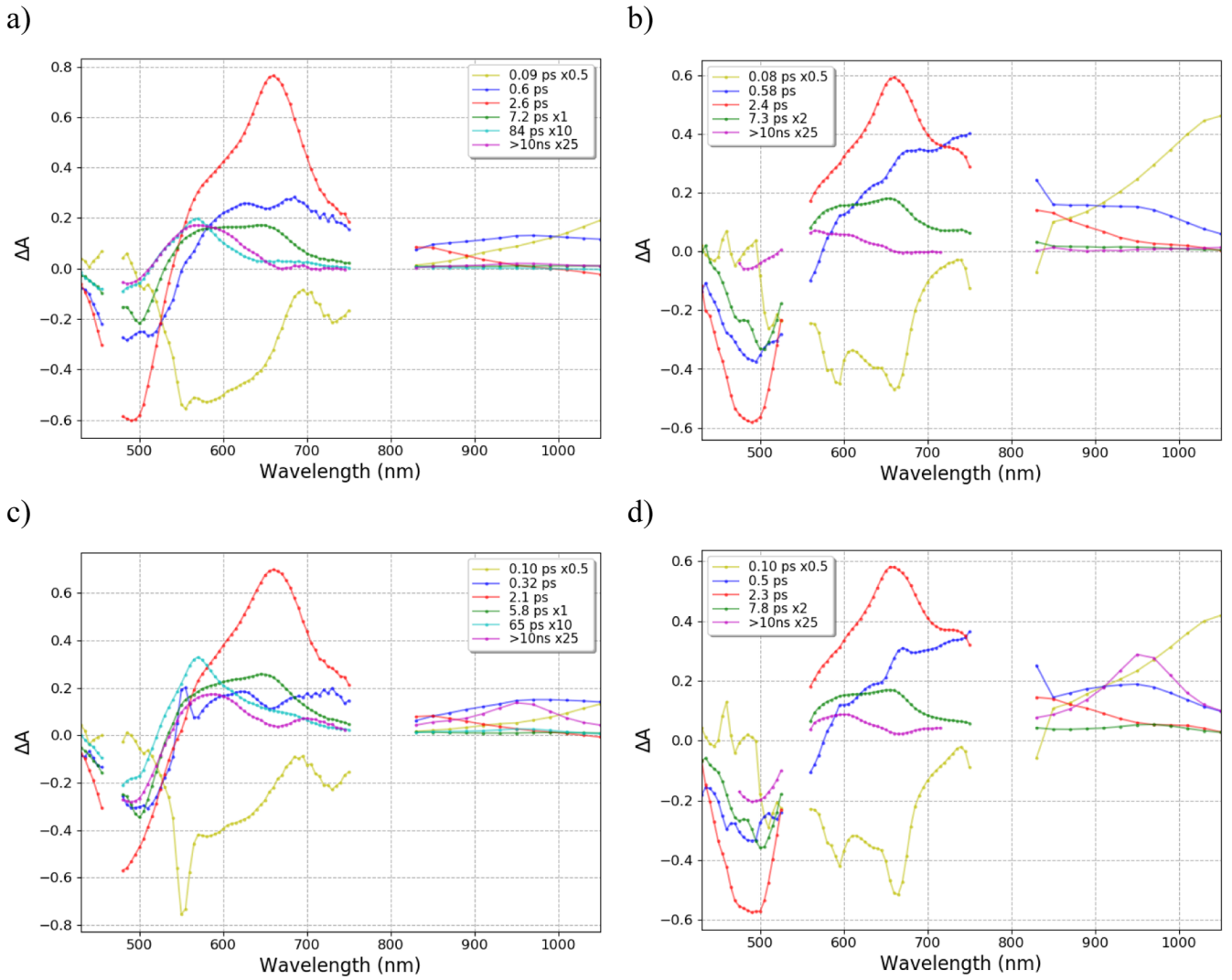

Figure 5. DAS obtained from the global fit of transient absorption data recorded for N-tagged OCP with excitation at (a) 470 nm, 0.4 μJ, (b) 540 nm, 0.8 μJ, (c) 470 nm, 1.6 μJ, and (d) 540 nm, 3.2 μJ. DAS shown in green are multiplied by 2 for 540 nm excitation and DAS shown in yellow and in magenta are multiplied by 0.5 and 25 for both excitations.

components provide four characteristic time constants that can be used to describe the behavior of the different excited states (S_2, ICT, S_1, and S*) and the long-lived photoproduct P_1, populated in the end of our time window (1 ns). As already mentioned, for 470 nm excitation, one additional component is needed, which is denoted as S˜ (see Figure S8). For all data sets, the first component around 100 fs is associated with the S_2 state, and also includes the growth of S_1, ICT, and S*, overlapped with artefacts such as stimulated Raman and eventually any ultrafast intramolecular vibrational relaxation.

The decay associated spectra (5 exponential components for 470 nm and 4 exponential components for 540 nm excitation) for low energy excitation, 0.4 μJ at 470 nm and 0.8 μJ at 540 nm, are shown in Figure 5a,b. Kinetic traces of the representative wavelengths with their fits and residuals are given in Figures S9 and S11 (Figure S16 zooms in on the −0.25 to 1 ps time delay window). The decay associated spectra for both excitations represent S_2 (yellow), ICT (blue), S_1 (red), S* (green), S˜ (cyan, only for 470 nm excitation), and P_1 (magenta) species (Figure 5) with associated time constants around 0.6 ± 0.08, 2.5 ± 0.36, 7.0 ± 2.3, and 80 ± 30 ps (retrieved time constants are provided in Table 1, standard errors calculated from bootstrapping distributions in Tables S2 and S3). For both excitations, the S* state has a lifetime of about 7 ps with a spectrum characterized by a maximum at 655 nm and a shoulder at 585 nm. The S˜ state, which has a longer lifetime of about 80 ps, has its absorption maximum at 570 nm and is similar in shape to the S* state reported by Konold *et al.*[9] (λ_{exc} = 475 nm). This component is not observed for 540 nm excitation. Global analysis with four exponential components (Figures S14 and S15) was also performed for the 470 nm excitation data sets (see the comparison of DAS for four and five exponential components in Figure S15); however, a structure in residuals appears between 10 and 100 ps (Figure S14), and the resulting DAS of the S* state has significantly different properties compared to the ones obtained after 540 nm excitation. In other words, the addition of the S˜ component for the 470 nm data set is indispensable to obtain a consistent description of the results recorded with both excitations. Note that time constants retrieved from four exponential fits of the 470 nm excited data set are in agreement with those reported earlier by Konold *et al.*,[9] suggesting that this component was already present, but

https://doi.org/10.1021/jacsau.1c00472
JACS Au 2022, 2, 1084−1095

Table 1. Lifetimes and Estimated Formation Quantum Yields from Pre-exponential Factors at 490 nm for ICT/S_1/S*/S~/P_1 States (See Supporting Information for Details and Table S1)[a]

	ICT	S_1	S*	S~	P_1[b]
N-tag 470 nm/0.4 μJ	25.8%	57.1%	16.5%	0.7%	0.5%
	0.60 ps	2.6 ps	7 ps	80 ps	
N-tag 470 nm/1.6 μJ	26.5%	46.4%	25.5%	1.6%	2.4%
	0.32 ps	2.1 ps	6 ps	70 ps	
N-tag 540 nm/0.8 μJ	34.1%	53.7%	12.2%		0.5%
	0.58 ps	2.5 ps	7 ps		
N-tag 540 nm/3.2 μJ	31.6%	54.4%	14%		1.7%
	0.50 ps	2.4 ps	8 ps		
C-tag 540 nm/0.8 μJ	34.8%	53.9%	11.3%		0.6%
	0.44 ps	1.9 ps	6 ps		

[a]The following standard errors were estimated (see Supporting Information for details, Table S2 and S3).: τ_{ICT} ± 80 fs, τ_{S1} ± 0.36 ps, τ_{S*} ± 2.3 ps, $\tau_{S\sim}$ ± 30 ps, A_{ICT} ± 5%, A_{S1} ± 1.9%, A_{S*} ± 5%, $A_{S\sim}$ ± 1%, and A_{P1} ± 0.1%. *Note that for P_1 yield is corrected for its positive absorbance contribution at 490 nm (Figure S4) but not for interfering radical species at high power. [b]This P_1 yield represents a fraction of initially populated excited states, which reach P_1 state at 1 ns. The sum of ICT, S_1, S*, and S~ formation yields without P_1 equals 100% (because they represent branching from the S_2 precursor). More details can be found in the Supporting Information.

not identified, in their experiments carried out on the N-tagged protein using 475 nm excitation at 0.4 μJ excitation energy.

The detailed analysis of the DAS extracted from data collected at low excitation energies (0.4 μJ at 470 nm and 0.8 μJ at 540 nm) reflects the differences in amplitude and shape that were already observed in the raw data. (i) For ICT and S_1 states, the value of absorbance above 700 nm is higher for 540 nm excitation. These results were already reported in the literature[14,15,28] and can be explained by a more pronounced charge-transfer character of the S_1 and ICT states formed after 540 nm excitation (which is clearly visible in Figure 2). (ii) The absorbance of the S* state at 655 nm is about two times higher for λ_{exc} = 470 nm. (iii) The absorbance at 663 nm for the S_1 state is substantially higher for λ_{exc} = 470 nm, while for the bleaching extremum (490 nm) it is almost the same for both excitations. (iv) A similar remark can be made for the maximum absorbance of P_1 (>10 ns DAS) at 565 nm, higher for 470 nm excitation, while at 490 nm the amplitude is similar for both excitations, pointing to a similar depletion of the OCP^O state. However, it needs to be noted that the comparison of the magnitude of the P_1 positive absorption bands is difficult due to the scattered laser contribution in the 540 nm excitation data set.

As pointed above, P_1 formation quantum yields can be determined by using the GSB of OCP^O depopulation band at 490 nm. A similar method can be used to determine yields of the excited states, which can be estimated from pre-exponential factors at 490 nm (associated with OCP^O recovery, Table S1), divided by the sum of these excluding P_1 and S_2 (see Supporting Information for details and Table S1), with results shown in Table 1. It should be underlined here that such approximation assumes that (i) S_1, ICT, and S* (and S~ in case of 470 nm excitation) are formed from S_2 in parallel paths ((see discussion section)), (ii) these states decay mainly to S_0 without any interconversion, and (iii) their ESA is small at 490 nm. A comparison of 470 nm excitation (0.4 μJ) and 540 nm excitation (0.8 μJ) indicates a higher and lower contribution of the ICT (34% *vs* 26%) and S* state (12% *vs* 17%), upon excitation at 540 nm excitation. Meanwhile, the S_1 and P_1 formation quantum yields are independent of the excitation wavelength.

For the high excitation energy data sets, DAS for 1.6 μJ at 470 nm and 3.2 μJ at 540 nm are shown in Figure 5c,d, respectively (kinetic traces for representative wavelengths with their fit and residues are given in the Supporting Information, Figures S10 and S12). While the time constants for the S_1/S*/S~ states do not change with increasing excitation energy, the lifetime of the ICT state slightly decreases with a more pronounced effect observed for 470 nm excitation. The absorbance of positive contribution for excited states does not evolve significantly with an increase of the excitation energy. The most relevant feature is that the use of high energy

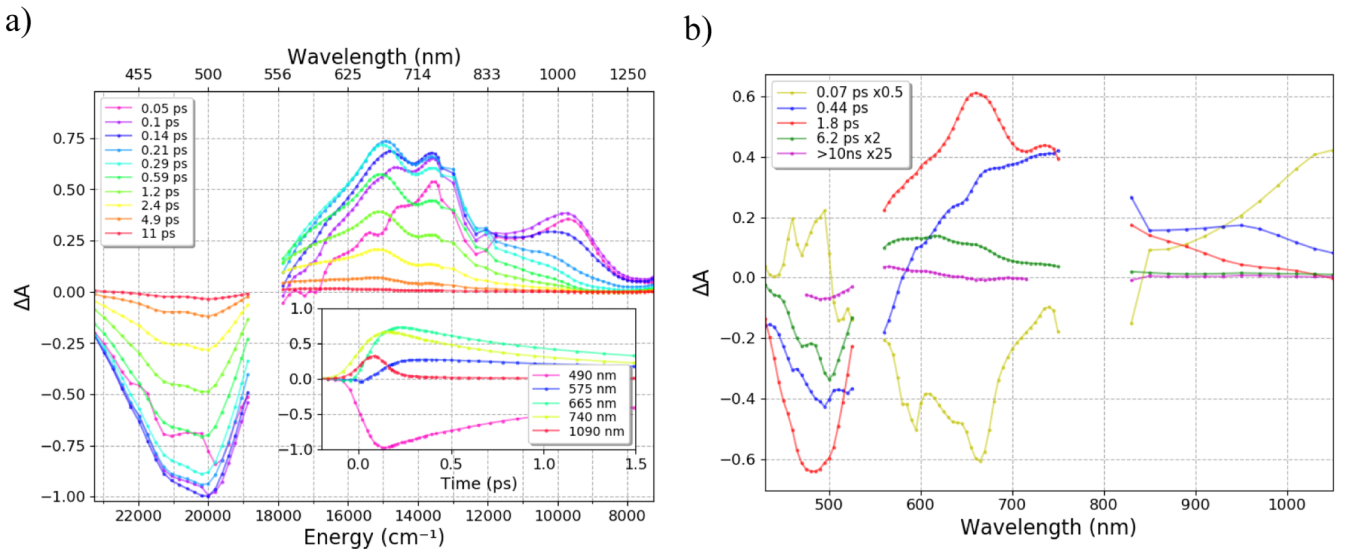

Figure 6. (a) Transient absorption spectra between 0.05 and 11 ps for C-tagged OCP excited at 540 nm (0.8 μJ). (b) DAS obtained from the global fit of transient absorption data. All data sets were normalized to −1 at bleaching extremum (in both spectral and temporal dimensions, multiply by 0.095 to get original signal). Inset shows the evolution of the signal in 1.5 ps time window.

https://doi.org/10.1021/jacsau.1c00472
JACS Au 2022, 2, 1084−1095

severely increases the negative contribution caused by photoproducts (>10 ns, DAS), which is a mixture of P_1 and radical cation.

Influence of Tagging on OCP Photophysics

The above results point to simpler photoinduced dynamics upon 540 nm excitation (no S˜) than 470 nm excitation. Therefore, to study the influence of the His tag, only 540 nm excitation experiments at low energy (0.8 μJ) were performed. Transient spectra for C-tagged OCP-ECN after 540 nm excitation are shown in Figure 6 with DAS (four exponential components; representative kinetic traces with their fits and residuals are shown in Figure S13). The comparison with N-tagged transient spectra (Figure 2b) shows an increase in the initial absorbance at 740 nm together with a decrease in that at 663 nm (0.2 ps time delay, Figure 6a). Moreover, if one compares the transient spectra at specific time delays after 0.5 ps or the raw kinetic profiles of C-tagged *versus* N-tagged OCP (Figure S18), it appears that excited states decay significantly faster in C-tagged OCP. This observation is confirmed by the extraction of DAS (see Table 1). Examination of the DAS (Figure 6b) furthermore suggests that C-tagged OCP is characterized by (i) a higher contribution at 740 nm in the S_1 state, (ii) a different spectral signature of the S* state, with a smaller peak at 655 nm, and (iii) a lower positive signal of P_1 (Figure S17). Nevertheless, the ratios between intermediate states are quite similar for N-tagged and C-tagged OCP. Despite these differences, the P_1 formation quantum yield (Table 1) seems to be roughly similar for both N-tagged and C-tagged OCP and at worst slightly higher for C-tagged OCP. The lower contribution of P_1 absorbance at 490 nm (Figure S17) can explain the slight increase in GSB amplitude and thus formation quantum yield for C-tagged OCP.

DISCUSSION

In the present paper, we undertook a detailed photophysical study on ECN-functionalized *Synechocystis* PCC 6803 OCP with an aim to investigate its effect on photoinduced excited-state dynamics and overall activation yield of (i) excitation at either 470 nm or 540 nm, (ii) His-tagging at the N- (N-tagged) or C- (C-tagged) terminus, and (iii) excitation power. Our results show that all three factors largely influence OCP excited-state dynamics and/or photoactivation yield. Our data also question whether or not the hypothesis that S* is the precursor of P_1 (and therefore OCP^R) is correct. Indeed, we offer demonstration that an additional excited state exists upon excitation at 470 nm and that a radical cation forms upon excitation at high energies—two points that were largely overlooked in the first study which proposed a link between S* and P_1.[9] The present work should thus allow a finer understanding of OCP-embedded keto-carotenoid excited-state dynamics and may thereby open avenues toward the generation of more efficient OCP.

The most unexpected finding was that his-tagging at the N- or C- terminus influences the photoactivation speed and excited-state dynamics. Proteins are nowadays often expressed recombinantly, with N- or C-terminal extensions that facilitate their purification by affinity chromatography, and OCP is no exception. In nearly all recent studies, a His-tag was accordingly added at the N- or C-terminus, aiding purification, and avoiding degradation of the protein.[1,8] It should be noted that in the case of OCP, both the N-terminal and C-terminal helices appose on the same face of the CTD β-sheet, which serves as the regulatory domain (Scheme 1b). Here, we show that the location of the His-tag affects (i) the photoactivation speed, as derived from initial slopes of OCP^R formation (monitored using ΔA at 550 nm) upon continuous irradiation (slower for C-tag, Figure 1c) and (ii) the lifetime of excited states (shorter for C-tag). The population ratio between ps-lived excited states and the P_1 yield is yet unaffected by the change in the position of the six-histidine tag (Table 1). It is unclear how the presence of the latter alters the lifetime and spectral signature of the excited states; however, the most likely hypothesis seems to be that these are affected by different ground-state populations of dark-adapted OCP, which each leads to different spectral signatures (notably for S*) and lifetimes of excited states. Regardless, the most important information is probably that the presence of the tag does not influence the P_1 formation quantum yield (Table 1). Therefore, in line with our results about the influence of the carotenoid (ECN, canthaxanthin) on the photoactivation quantum yield of *Synechocystis* OCP^R,[39] we attribute the effect of the tag on the photoactivation speed to molecular events occurring on the nano- and millisecond time scales, that is, related to carotenoid translocation and/or domain separation (P_1 to OCP^R, Scheme 1a).[10,11] Studies are ongoing to better confirm this hypothesis by determining the influence of his-tagging and its location on the outcome of nanosecond flash photolysis experiments.

Because his-tagging slightly modifies the ultrafast dynamics of the OCP, comparison with earlier studies is only valid if the investigated proteins were tagged at the same location and ideally with the same tag. Ours results can thus be compared to those obtained by Konold *et al.*[9] who studied exactly the same N-tagged OCP-ECN (identical expression in *E. coli* and purification procedure, see materials and methods section) with 475 nm excitation and were the first to characterize and link the S* and P_1 states of OCP. To fit their excited-state transient spectra, they employed a three time constant multiexponential model accounting for three ps-lived excited-state species, *viz.* S_1, ICT, and S*. Analogous analysis of the data set obtained upon 470 nm excitation provides similar results, including a species characterized by a DAS with a maximum at 570 nm and a time constant close to 29 ps (Figure S15). This species was assigned to S* by Konold *et al.* (24 ps in the article[9]). However, these results cannot be easily compared with those we obtained upon 540 nm excitation, where S* is characterized by a DAS peaking at 655 nm and a time constant of 7 ps. In contrast, a recent publication from Yaroshevich *et al.*[13] reports an S* lifetime of 5.13 ps, in a reasonable agreement with a 7 ps lifetime derived from our data collected upon 540 nm excitation. The use of an additional time constant (extra S˜ component) to fit data collected upon 470 nm excitation results in an S* signature that is nearly identical to that obtained after 540 nm excitation (maximum of DAS at 655 nm and lifetime of about 7 ps, Figure S15). The S˜ state is characterized by a DAS peaking at 570 nm and a decay time around 80 ps (Figure 5a). While accounting for only 1% of the excited-state signal upon excitation at 470 nm (Tables 1 and S1), the addition of S˜ to the fitting scheme leads to a higher consistency of determined DAS and time constants for the 470 and 540 nm data sets (Figure S15).

The nature and origin of the extra S˜ species is not straightforward to understand. S˜ lives longer than the usually observed excited states (slightly shorter than 10 ps) and it is

https://doi.org/10.1021/jacsau.1c00472
JACS Au 2022, 2, 1084−1095

absent upon 540 nm excitation. A similar state denoted as $S^{\ddagger}$ has been observed in β-carotene, which is characterized by the presence of a 65 ps-lived component located at the high energy edge of ESA. The $S^{\ddagger}$ state was found to not form upon excitation at the red edge of a β-carotene stationary absorption spectrum, which makes it similar to $S^{\sim}$.[40] The origin of this state was clarified in a later study where it was shown that this component disappears after extensive sample purification.[41] It was concluded that it must originate from minor impurities of blue-absorbing shorter chain carotenoids. Because our data clearly show that the 80 ps component does not lead to the formation of P_1, we believe that $S^{\sim}$ in OCP is likely associated with traces of a non-photoactive carotenoid in OCP. Indeed, it was observed that ECN-OCPs produced in *E. coli* contains 1−2% of an unknown carotenoid of MW 548 and in rare cases also traces of β-carotene.[30] These OCP binding different carotenoids cannot be separated during the purification.

We also addressed the identity of the precursor of P_1 and the interplay between the S*, ICT, and S_1 excited states. A comparison of the formation quantum yields of ICT and S* for 470 and 540 nm excitations shows an anti-correlation (Table 1), suggesting that paths leading to these states compete. Most recently, S* was assigned to a distorted carotenoid geometry and proposed to precede P_1.[9] We found using N-tagged OCP that more S* is produced upon excitation at 470 nm than at 540 nm, despite the P_1 formation quantum yield being the same value of about 0.5% at both excitation wavelengths (Table 1). Surely, the error on P_1 formation quantum yield is large due its low value. Experiments aimed at exploring excitation power dependency showed that 470 nm excitation could involve additional long-lived photoproducts ($S^{\sim}$ and radical). Hence, it is difficult to determine the quantum yield of P_1 upon 470 nm excitation with high precision. It can also explain the difference with Konold *et al.* who reported a value of 1.5%.[9] Furthermore our value (0.5%) is consistent with the OCP^R formation quantum yield estimated by Maksimov *et al.* to be about 0.2% at 200 ns using nanosecond flash photolysis studies.[12] Indeed Konold *et al.* showed that at 200 ns only 40% of the population of P_1 remained, that is, P_1 yield should be about 0.5%.[9] In addition, as photoactivation with continuous irradiation at either 470 or 528 nm yields the same initial slopes, we posit that the absorbance at 490 nm provides a correct estimation for the P_1 formation quantum yield (Table 1). Considering that the S* and ICT states have different yields (Table 1) at both excitation wavelengths, our data thus do not support that S* is the main precursor of P_1. Rather, they suggest that S_1 is the most probable P_1 precursor with a formation quantum yield, which is similar for blue and green excitation (Table 1).

CONCLUSIONS

In this work, the effects of excitation energy and wavelength on OCP photoactivation and excited-state dynamics were investigated in detail, as well as that of his-tagging at the N- and C-termini. Covering the NIR range (800−1400 nm) in addition to the visible spectrum, we were able to uncover the existence of a carotenoid cation radical, characterized by positive absorbance bands at 960 nm and 700 nm, and whose formation also contributes to the negative depopulation band of OCP^O. This radical cation is the dominant photoproduct at 1 ns for energies exceeding the linear photoexcitation range, calling for a careful consideration of excitation energies in future transient spectroscopy studies on OCP. Excitation at 540 nm compared to 470 nm is better suited to reduce the formation of this off-pathway radical species, as a three-photonic regime requires a much higher photon density in the pump pulse. This finding is of importance for the determination of the P_1 formation quantum yield using the OCP^O depopulation band. The formation quantum yield of P_1 is close to 0.5% when the excitation power is low enough to avoid the formation of the cation radical (0.3 mJ/cm^2 or less for λ_{exc} = 470 nm, 0.6 mJ/cm^2 or less for λ_{exc} = 540 nm, Figures S5 and S6), consistent with previous estimates from nanosecond flash photolysis studies.[12] Another important result regarding 470 nm excitation is the existence of a previously unnoticed $S^{\sim}$ species (≈80 ps lifetime), which does not form upon excitation at 540 nm and display similar spectral features as P_1. Most likely, this $S^{\sim}$ species originates from the presence of an unknown carotenoid in the *E. coli* cells that is not completely transformed into ECN or a secondary product that also binds OCP and cannot be removed by purifications.[30] Accounting for this additional species observed upon 470 nm excitation, global fitting of the data sets for the two excitation wavelengths gives similar DAS and lifetime for ICT/S_1/S* regardless of the excitation wavelength (470 *vs* 540 nm). Our analysis shows that the S* lifetime is about 7 ps for 470 nm and 540 nm excitations. Because the $S^{\sim}$ component most likely originates from a chromophore not involved in the photoactivation of OCP, modeling the dynamics using data obtained with green excitation is more relevant for the photodynamics of OCP, particularly because photoactivation experiments using continuous irradiation do not show dependence on the excitation wavelength. An important result is that the formation quantum yield for S* and ICT differs for both excitations (Table 1), while the P_1 and S_1 formation quantum yield do not change. This strongly supports the hypothesis that S_1, but not S*, is the main precursor of P_1. We thus suggest a new path for the picosecond photodynamics, leading to the P_1—photoactivation of OCP (from *Synechocystis* N-tagged with ECN), using results upon 540 nm excitation, and assuming parallel formation and decay of picosecond states (ICT, S_1, and S*) with yields estimated from an OCP^O depopulation band (Scheme 2, Table 1).

Scheme 2. Picosecond Photodynamics of *Synechocystis* N-Tagged ECN-OCP upon 540 nm Excitation (Yields Are Estimated from GSB Recovery of OCP^O at 490 nm and P_1 Represents Overall Formation Yield from S_2, Table 1)

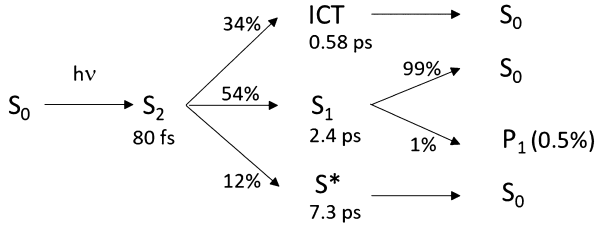

Finally, the comparison of ps dynamics in C-tagged *versus* N-tagged OCP revealed significant differences in the DAS and formation quantum yields of S*, and an overall faster relaxation of excited states in C-tagged OCP. Also, the photoactivation speed observed under continuous irradiation was found to differ significantly. However, the P_1 yield was unchanged. Hence, similar to our results of the influence of carotenoid (ECN, canthaxanthine) on the photoactivation quantum yield

https://doi.org/10.1021/jacsau.1c00472
JACS Au 2022, 2, 1084−1095

of *Synechocystis* OCP^R,[39] we propose that the tagging of OCP influences molecular events occurring past 1ns, that is, carotenoid translocation and/or structural changes (Scheme 1a). Further studies conducted on the nanosecond-millisecond range are ongoing to verify this hypothesis.

■ ASSOCIATED CONTENT

Supporting Information

The Supporting Information is available free of charge at https://pubs.acs.org/doi/10.1021/jacsau.1c00472.

> "Normal" and "red-shifted" sub-populations existing in the dark-adapted state, pump pulse excitation, time resolved spectra at high excitation energy, analysis of kinetics traces, and comparison of P_1 spectra upon different excitation *versus* His-tag and evaluation of error using bootstrapping method (PDF)

■ AUTHOR INFORMATION

Corresponding Authors

Diana Kirilovsky − *Université Paris-Saclay, CEA, CNRS, Institute for Integrative Biology of the Cell (I2BC), Gif-sur-Yvette 91198, France*; Email: Diana.KIRILOVSKY@cea.fr

Gotard Burdzinski − *Quantum Electronics Laboratory, Faculty of Physics, Adam Mickiewicz University in Poznań, Poznan 61-614, Poland*; orcid.org/0000-0002-2947-1602; Email: gotardb@amu.edu.pl

Michel Sliwa − *Univ. Lille, CNRS, UMR 8516, LASIRE, LAboratoire de Spectroscopie pour les Interactions, la Réactivité et l'Environnement, Lille 59000, France*; orcid.org/0000-0002-5073-8180; Email: michel.sliwa@univ-lille.fr

Authors

Stanisław Niziński − *Quantum Electronics Laboratory, Faculty of Physics, Adam Mickiewicz University in Poznań, Poznan 61-614, Poland; Univ. Lille, CNRS, UMR 8516, LASIRE, LAboratoire de Spectroscopie pour les Interactions, la Réactivité et l'Environnement, Lille 59000, France*

Adjéle Wilson − *Université Paris-Saclay, CEA, CNRS, Institute for Integrative Biology of the Cell (I2BC), Gif-sur-Yvette 91198, France*

Lucas M. Uriarte − *Univ. Lille, CNRS, UMR 8516, LASIRE, LAboratoire de Spectroscopie pour les Interactions, la Réactivité et l'Environnement, Lille 59000, France*

Cyril Ruckebusch − *Univ. Lille, CNRS, UMR 8516, LASIRE, LAboratoire de Spectroscopie pour les Interactions, la Réactivité et l'Environnement, Lille 59000, France*; orcid.org/0000-0001-8120-4133

Elena A. Andreeva − *Univ. Grenoble Alpes, CEA, CNRS, Institut de Biologie Structurale, Grenoble 38000, France; Max-Planck-Institut für Medizinische Forschung, Heidelberg 69120, Germany*

Ilme Schlichting − *Max-Planck-Institut für Medizinische Forschung, Heidelberg 69120, Germany*

Jacques-Philippe Colletier − *Univ. Grenoble Alpes, CEA, CNRS, Institut de Biologie Structurale, Grenoble 38000, France*

Complete contact information is available at: https://pubs.acs.org/10.1021/jacsau.1c00472

Notes

The authors declare no competing financial interest.

■ ACKNOWLEDGMENTS

This work was performed with the financial support from the Polish National Science Centre (NCN), project 2018/31/N/ST4/03983, and the French National Research Agency (grant ANR-18-CE11-0005 to M.S., D.K., I.S., and J.P.C.).

■ REFERENCES

(1) Holt, T. K.; Krogmann, D. W. A carotenoid-protein from cyanobacteria. *Biochim. Biophys. Acta* **1981**, *637*, 408−414.

(2) Kirilovsky, D.; Kerfeld, C. A. Cyanobacterial photoprotection by the orange carotenoid protein. *Nat. Plants* **2016**, *2*, 16180.

(3) Sluchanko, N. N.; Slonimskiy, Y. B.; Maksimov, E. G. Features of protein−protein interactions in the cyanobacterial photoprotection mechanism. *Biochemistry* **2017**, *82*, 1592−1614.

(4) Muzzopappa, F.; Kirilovsky, D. Changing color for photoprotection: The Orange Carotenoid Protein. *Trends Plant Sci.* **2020**, *25*, 92−104.

(5) Wilson, A.; Punginelli, C.; Gall, A.; Bonetti, C.; Alexandre, M.; Routaboul, J.-M.; Kerfeld, C. A.; van Grondelle, R.; Robert, B.; Kennis, J. T. M.; Kirilovsky, D. A photoactive carotenoid protein acting as light intensity sensor. *Proc. Natl. Acad. Sci. U.S.A.* **2008**, *105*, 12075−12080.

(6) Wilson, A.; Gwizdala, M.; Mezzetti, A.; Alexandre, M.; Kerfeld, C. A.; Kirilovsky, D. The essential role of the N-terminal domain of the orange carotenoid protein in cyanobacterial photoprotection: importance of a positive charge for phycobilisome binding. *Plant Cell* **2012**, *24*, 1972−1983.

(7) Leverenz, R. L.; Jallet, D.; Li, M.-D.; Mathies, R. A.; Kirilovsky, D.; Kerfeld, C. A. Structural and Functional Modularity of the Orange Carotenoid Protein: Distinct Roles for the N- and C-Terminal Domains in Cyanobacterial Photoprotection. *Plant Cell* **2014**, *26*, 426−437.

(8) Kerfeld, C. A.; Sawaya, M. R.; Brahmandam, V.; Cascio, D.; Ho, K. K.; Trevithick-Sutton, C. C.; Krogmann, D. W.; Yeates, T. O. The crystal structure of a cyanobacterial water-soluble carotenoid binding protein. *Structure* **2003**, *11*, 55−65.

(9) Konold, P. E.; van Stokkum, I. H. M.; Muzzopappa, F.; Wilson, A.; Groot, M.-L.; Kirilovsky, D.; Kennis, J. T. M. Photoactivation mechanism, timing of protein secondary structure dynamics and carotenoid translocation in the Orange Carotenoid Protein. *J. Am. Chem. Soc.* **2019**, *141*, 520−530.

(10) Leverenz, R. L.; Sutter, M.; Wilson, A.; Gupta, S.; Thurotte, A.; Bourcier de Carbon, C.; Petzold, C. J.; Ralston, C.; Perreau, F.; Kirilovsky, D.; Kerfeld, C. A. A 12 Å carotenoid translocation in a photoswitch associated with cyanobacterial photoprotection. *Science* **2015**, *348*, 1463−1466.

(11) Maksimov, E. G.; Protasova, E. A.; Tsoraev, G. V.; Yaroshevich, I. A.; Maydykovskiy, A. I.; Shirshin, E. A.; Gostev, T. S.; Jelzow, A.; Moldenhauer, M.; Slonimskiy, Y. B.; Sluchanko, N. N.; Friedrich, T. Probing of carotenoid-tryptophan hydrogen bonding dynamics in the single-tryptophan photoactive Orange Carotenoid Protein. *Sci. Rep.* **2020**, *10*, 11729.

(12) Maksimov, E. G.; Sluchanko, N. N.; Slonimskiy, Y. B.; Slutskaya, E. A.; Stepanov, A. V.; Argentova-Stevens, A. M.; Shirshin, E. A.; Tsoraev, G. V.; Klementiev, K. E.; Slatinskaya, O. V.; Lukashev, E. P.; Friedrich, T.; Paschenko, V. Z.; Rubin, A. B. The photocycle of orange carotenoid protein conceals distinct intermediates and asynchronous changes in the carotenoid and protein components. *Sci. Rep.* **2017**, *7*, 15548.

(13) Yaroshevich, I. A.; Maksimov, E. G.; Sluchanko, N. N.; Zlenko, D. V.; Stepanov, A. V.; Slutskaya, E. A.; Slonimskiy, Y. B.; Botnarevskii, V. S.; Remeeva, A.; Gushchin, I.; Kovalev, K.; Gordeliy, V. I.; Shelaev, I. V.; Gostev, F. E.; Khakhulin, D.; Poddubnyy, V. V.; Gostev, T. S.; Cherepanov, D. A.; Polívka, T.; Kloz, M.; Friedrich, T.; Paschenko, V. Z.; Nadtochenko, V. A.; Rubin,

A. B.; Kirpichnikov, M. P. Role of hydrogen bond alternation and charge transfer states in photoactivation of the Orange Carotenoid Protein. *Commun. Biol.* **2021**, *4*, 539.
(14) Šlouf, V.; Kuznetsova, V.; Fuciman, M.; de Carbon, C. B.; Wilson, A.; Kirilovsky, D.; Polívka, T. Ultrafast spectroscopy tracks carotenoid configurations in the orange and red carotenoid proteins from cyanobacteria. *Photosynth. Res.* **2017**, *131*, 105−117.
(15) Berera, R.; Gwizdala, M.; van Stokkum, I. H. M.; Kirilovsky, D.; van Grondelle, R. Excited states of the inactive and active forms of the Orange Carotenoid Protein. *J. Phys. Chem. B* **2013**, *117*, 9121−9128.
(16) Berera, R.; van Stokkum, I. H. M.; Gwizdala, M.; Wilson, A.; Kirilovsky, D.; van Grondelle, R. The photophysics of the orange carotenoid protein, a light-powered molecular switch. *J. Phys. Chem. B* **2012**, *116*, 2568−2574.
(17) Polívka, T.; Chábera, P.; Kerfeld, C. A. Carotenoid−protein interaction alters the S1 energy of hydroxyechinenone in the Orange Carotenoid Protein. *Biochim. Biophys. Acta* **2013**, *1827*, 248−254.
(18) Chábera, P.; Durchan, M.; Shih, P. M.; Kerfeld, C. A.; Polívka, T. Excited-state properties of the 16kDa red carotenoid protein from Arthrospira maxima. *Biochim. Biophys. Acta* **2011**, *1807*, 30−35.
(19) Andersson, P. O.; Gillbro, T. Photophysics and dynamics of the lowest excited singlet state in long substituted polyenes with implications to the very long-chain limit. *J. Chem. Phys.* **1995**, *103*, 2509−2519.
(20) Gradinaru, C. C.; Kennis, J. T. M.; Papagiannakis, E.; van Stokkum, I. H. M.; Cogdell, R. J.; Fleming, G. R.; Niederman, R. A.; van Grondelle, R. An unusual pathway of excitation energy deactivation in carotenoids: Singlet-to-triplet conversion on an ultrafast timescale in a photosynthetic antenna. *Proc. Natl. Acad. Sci. U.S.A.* **2001**, *98*, 2364−2369.
(21) Lenzer, T.; Ehlers, F.; Scholz, M.; Oswald, R.; Oum, K. Assignment of carotene S* state features to the vibrationally hot ground electronic state. *Phys. Chem. Chem. Phys.* **2010**, *12*, 8832−8839.
(22) Balevičius, V.; Abramavicius, D.; Polívka, T.; Galestian Pour, A.; Hauer, J. A unified picture of S* in carotenoids. *J. Phys. Chem. Lett.* **2016**, *7*, 3347−3352.
(23) Khan, T.; Dominguez-Martin, M. A.; Šímová, I.; Fuciman, M.; Kerfeld, C. A.; Polívka, T. Excited-state properties of canthaxanthin in cyanobacterial carotenoid-binding proteins HCP2 and HCP3. *J. Phys. Chem. B* **2020**, *124*, 4896−4905.
(24) Kuznetsova, V.; Dominguez-Martin, M. A.; Bao, H.; Gupta, S.; Sutter, M.; Kloz, M.; Rebarz, M.; Přeček, M.; Chen, Y.; Petzold, C. J.; Ralston, C. Y.; Kerfeld, C. A.; Polívka, T. Comparative ultrafast spectroscopy and structural analysis of OCP1 and OCP2 from Tolypothrix. *Biochim. Biophys. Acta* **2020**, *1861*, 148120.
(25) Lincoln, C. N.; Fitzpatrick, A. E.; Thor, J. J. v. Photoisomerisation quantum yield and non-linear cross-sections with femtosecond excitation of the photoactive yellow protein. *Phys. Chem. Chem. Phys.* **2012**, *14*, 15752−15764.
(26) van Stokkum, I. H. N.; Larsen, D. S.; Grondelle, R. Global and target analysis of time-resolved spectra. *Biochim. Biophys. Acta, Bioenerg.* **2004**, *1657*, 82−104.
(27) Khan, T.; Kuznetsova, V.; Dominguez-Martin, M. A.; Kerfeld, C. A.; Polivka, T. UV excitation of carotenoid binding proteins OCP and HCP: excited-state dynamics and product formation. *ChemPhotoChem* **2022**, *6*, No. e202100194.
(28) Polívka, T.; Kerfeld, C. A.; Pascher, T.; Sundström, V. Spectroscopic Properties of the Carotenoid 3'-Hydroxyechinenone in the Orange Carotenoid Protein from the Cyanobacterium Arthrospira maxima. *Biochemistry* **2005**, *44*, 3994−4003.
(29) Kish, E.; Pinto, M. M. M.; Kirilovsky, D.; Spezia, R.; Robert, B. Echinenone vibrational properties: From solvents to the orange carotenoid protein. *Biochim. Biophys. Acta* **2015**, *1847*, 1044−1054.
(30) de Carbon, C. B.; Thurotte, A.; Wilson, A.; Perreau, F.; Kirilovsky, D. Biosynthesis of soluble carotenoid holoproteins in Escherichia coli. *Sci. Rep.* **2015**, *5*, 9085.
(31) Gwizdala, M.; Wilson, A.; Kirilovsky, D. In vitro reconstitution of the cyanobacterial photoprotective mechanism mediated by the Orange Carotenoid Protein in Synechocystis PCC 6803. *Plant Cell* **2011**, *23*, 2631−2643.
(32) Brazevic, S.; Nizinski, S.; Sliwa, M.; Abe, J.; Rode, M. F.; Burdzinski, G. Control of the photo-isomerization mechanism in 3H-naphthopyrans to prevent formation of unwanted long-lived photoproducts. *Int. J. Mol. Sci.* **2020**, *21*, 7825.
(33) Wendel, M.; Nizinski, S.; Tuwalska, D.; Starzak, K.; Szot, D.; Prukala, D.; Sikorski, M.; Wybraniec, S.; Burdzinski, G. Time-resolved spectroscopy of the singlet excited state of betanin in aqueous and alcoholic solutions. *Phys. Chem. Chem. Phys.* **2015**, *17*, 18152−18158.
(34) Uriarte, L. M.; Niziński, S.; Labarrière, L. *Ultrapyfit a python package for time resolved data*; Zenodo, 2021.
(35) Snellenburg, J. J.; Laptenok, S. P.; Seger, R.; Mullen, K. M.; van Stokkum, I. H. M. Glotaran: A Java-based graphical user interface for the R package TIMP. *J. Stat. Softw.* **2012**, *49*, 1−22.
(36) Pigni, N. B.; Clark, K. L.; Beck, W. F.; Gascón, J. A. Spectral signatures of canthaxanthin translocation in the Orange Carotenoid Protein. *J. Phys. Chem. B* **2020**, *124*, 11387−11395.
(37) Jeevarajan, J. A.; Wei, C. C.; Jeevarajan, A. S.; Kispert, L. D. Optical absorption spectra of dications of carotenoids. *J. Phys. Chem.* **1996**, *100*, 5637−5641.
(38) Gao, G.; Wei, C. C.; Jeevarajan, A. S.; Kispert, L. D. Geometrical isomerization of carotenoids mediated by cation radical/dication formation. *J. Phys. Chem.* **1996**, *100*, 5362−5366.
(39) Wilson, A.; Andreeva, E. A.; Nizinski, S.; Talbot, L.; Hartmann, E.; Schlichting, I.; Burdzinski, G.; Sliwa, M.; Kirilovsky, D.; Colletier, J.-P. Structure-function-dynamics relationships in the peculiar Planktothrix PCC7805 OCP1: impact of his-tagging and carotenoid type. *Biorxiv* **2022**, DOI: 10.1101/2022.01.04.474796.
(40) Larsen, D. S.; Papagiannakis, E.; van Stokkum, I. H. M.; Vengris, M.; Kennis, J. T. M.; Grondelle, R. Excited state dynamics of β-carotene explored with dispersed multi-pulse transient absorption. *Chem. Phys. Lett.* **2003**, *381*, 733−742.
(41) Ostroumov, E. E.; Reus, M. G. M. M.; Holzwarth, A. R.; Holzwarth, A. R. On the nature of the "Dark S*" excited state of β-Carotene. *J. Phys. Chem. A* **2011**, *115*, 3698−3712.

https://doi.org/10.1021/jacsau.1c00472
JACS Au 2022, 2, 1084−1095

Title : Unifying perspective of the Ultrafast Photodynamics of Orange Carotenoid Proteins from *Synechocystis*: Peril of High-Power Excitation, Existence of Different S* states, and Influence of Tagging

Authors : Stanisław Niziński,[a, b] Adjéle Wilson,[c] Lucas M. Uriarte,[b] Cyril Ruckebusch,[b] Elena A. Andreeva,[d,e] Ilme Schlichting,[e] Jacques-Philippe Colletier,[d] Diana Kirilovsky,[c *] Gotard Burdzinski,[a *] Michel Sliwa[b *].

Affiliations:

[a] Quantum Electronics Laboratory, Faculty of Physics, Adam Mickiewicz University in Poznań, Uniwersytetu Poznańskiego 2, Poznan 61-614, Poland

[b] Univ. Lille, CNRS, UMR 8516, LASIRE, LAboratoire de Spectroscopie pour les Interactions, la Réactivité et l'Environnement, Lille 59000, France

[c] Université Paris-Saclay, CEA, CNRS, Institute for Integrative Biology of the Cell (I2BC), 91198 Gif-sur-Yvette, France.

[d] Univ. Grenoble Alpes, CEA, CNRS, Institut de Biologie Structurale, 38000 Grenoble, France.

[e] Max-Planck-Institut für medizinische Forschung, Jahnstrasse 29, 69120 Heidelberg, Germany.

Correspondance to: Diana.KIRILOVSKY@cea.fr; gotardb@amu.edu.pl; michel.sliwa@univ-lille.fr

Contents

1) Steady state UV-vis absorption spectra

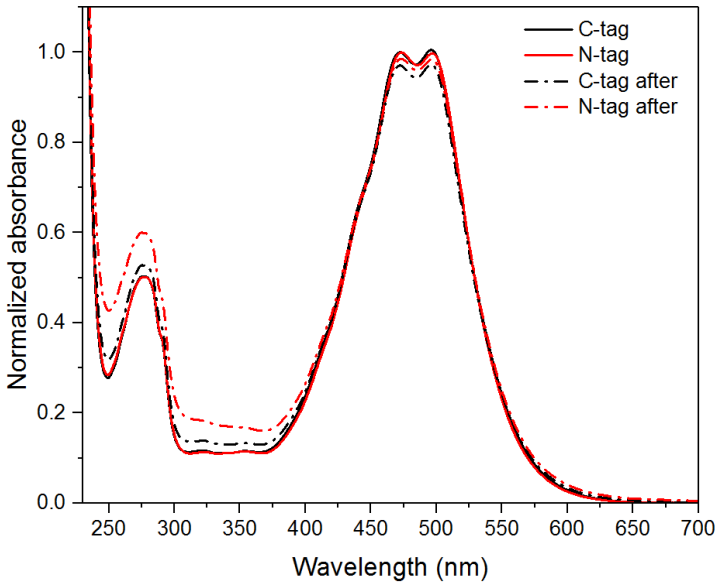

Fig. S1 Absorption spectra of dark-adapted state (OCP^O) for N-tagged and C-tagged OCP, with spectra recorded after one of the femtosecond transient absorption experiments.

a)

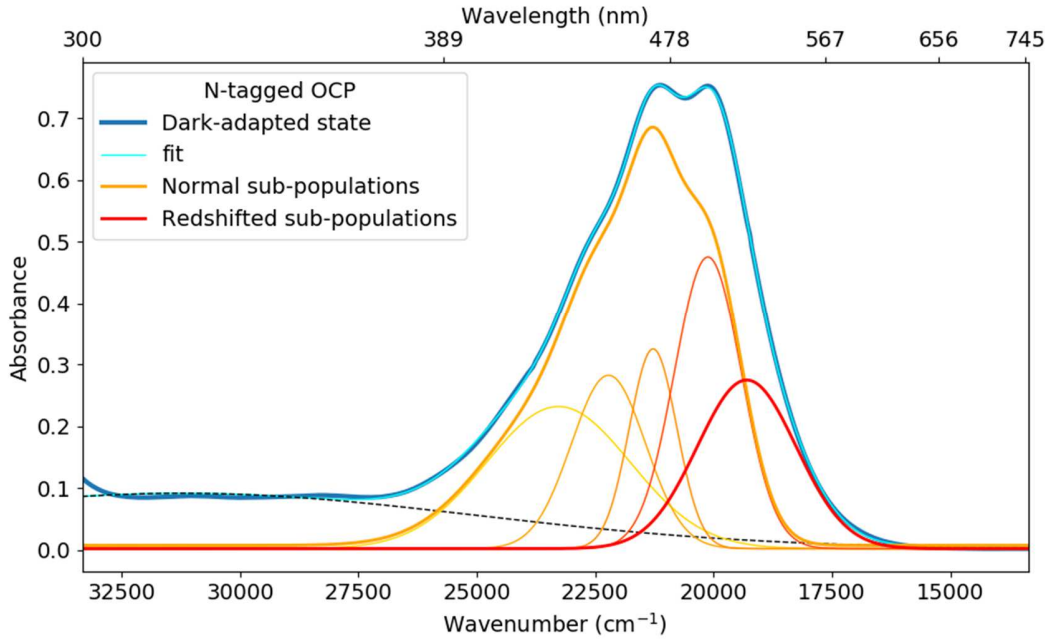

b)

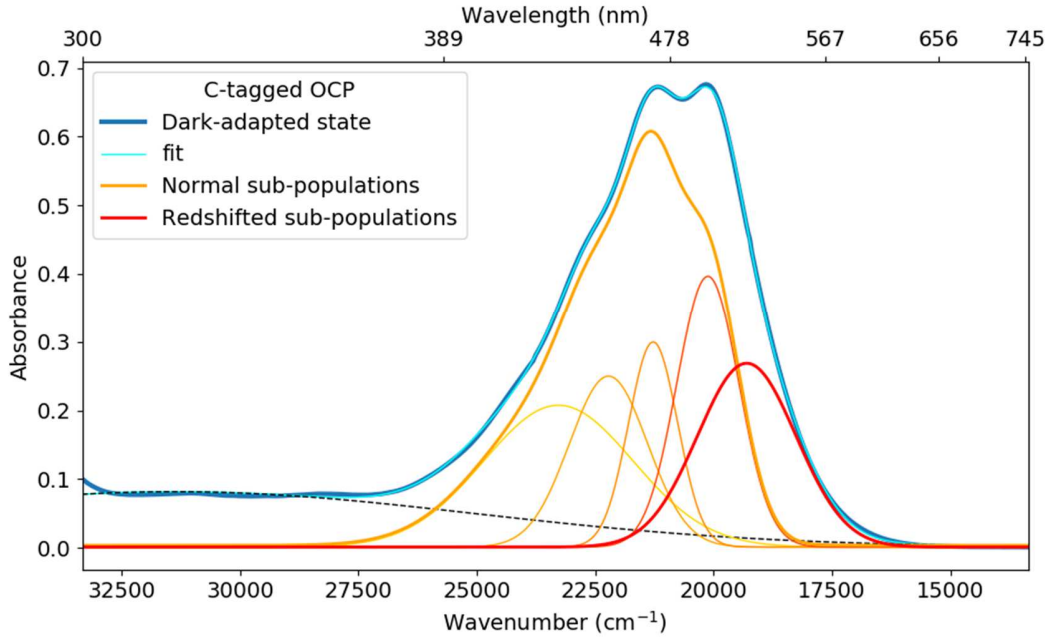

Fig. S2 Gaussian-sum decomposition of the absorption spectra of a) C-tagged OCP b) N-tagged OCP into "normal" and "red-shifted" sub-populations existing in equilibrium in the dark-adapted state (OCP^O).

2) Transient absorption spectra of N-tagged OCP in the visible range

a) b)

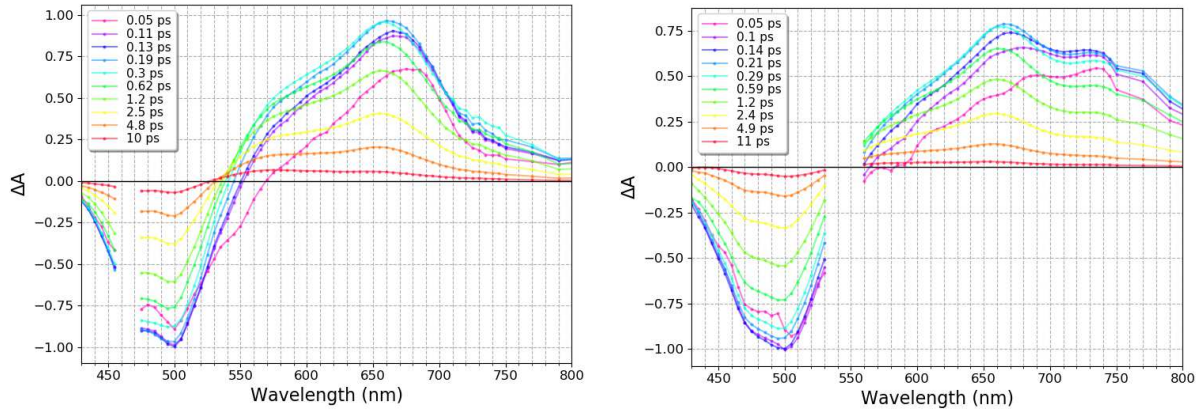

Fig. S3 Visible region of the transient absorption spectra between 0.05 and 10 ps for N-tagged OCP-ECN excited at a) 470 nm (0.4 µJ), and b) 540 nm (0.8 µJ). All datasets were normalized to -1 at the bleaching extremum (in both spectral and temporal dimensions).

3) Determination of P_1 formation quantum yield

Formation quantum yield of P_1 was estimated from the comparison of initial bleached OCP population and final P_1 ΔA(490nm) signal extracted from DAS decomposition. To estimate concentration of the initially excited population, transient spectrum at 0.1 ps time delay was used and -63 000 $M^{-1}cm^{-1}$ extinction coefficient was assumed at the extremum of the depopulation band at 490 nm [1] (normalized to -1). In order to calculate concentration of the P_1 state, amplitude of the DAS for P_1 at 490 nm (Figure 5) was used with an extinction coefficient at 490nm of -29 500$M^{-1}cm^{-1}$. This coefficient was estimated by firstly calculating OCP^R minus OCP^O differential spectrum (Figure 1a), assuming an extinction coefficient of 63 000 $M^{-1}cm^{-1}$ for OCP^O at 490 nm (Figure S4). Konold et al. used these spectra to compensate for induced absorbance of P_1 at 490 nm [2]. However, despite having similar spectral signatures, OCP^R difference absorption has a maximum at 550nm, while P_1 one is peaking around 565 nm (Figure S4). Therefore we shifted stationary OCP^R spectrum to the red by 30nm and then calculated difference spectrum, in a such a way to get a maximum at 565nm for positive signal and a zero crossing point similar to the one of P_1 DAS. Difference spectrum of the OCP^R state (measured data, red curve) and calculated one for P_1 (redshifted before subtraction, black curve) is shown in the Figure S4, in comparison with P_1 DAS obtained with both used excitations.

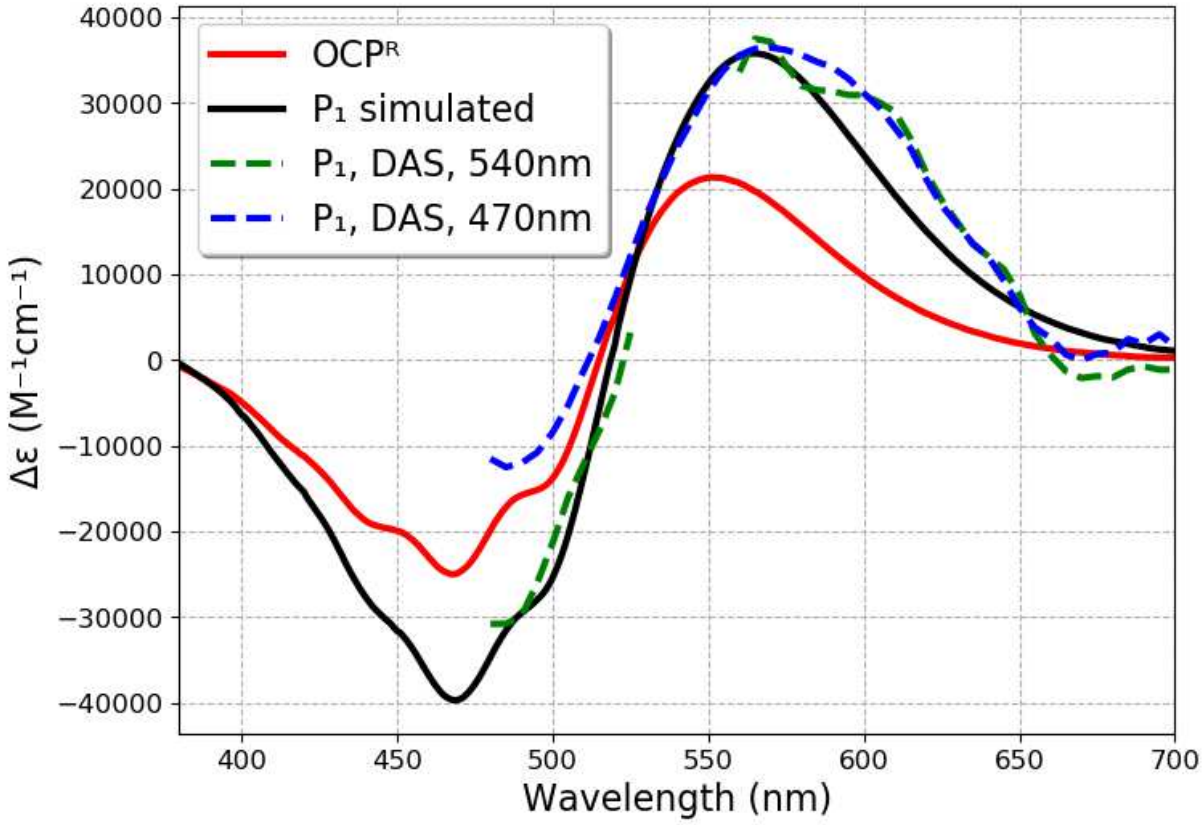

Fig. S4 Difference spectrum of OCP^R state minus OCP^O (measured data, red curve, Figure 1a), difference spectrum calculated one for P_1 by red-shifting OCP^R stationary spectrum (black curve), DAS for P_1 (Figure 5) upon 540 nm excitation (0.8 μJ, green dashed line) and upon 470 nm excitation (0.4 μJ, blue dashed line)

4) Pump pulse characterization

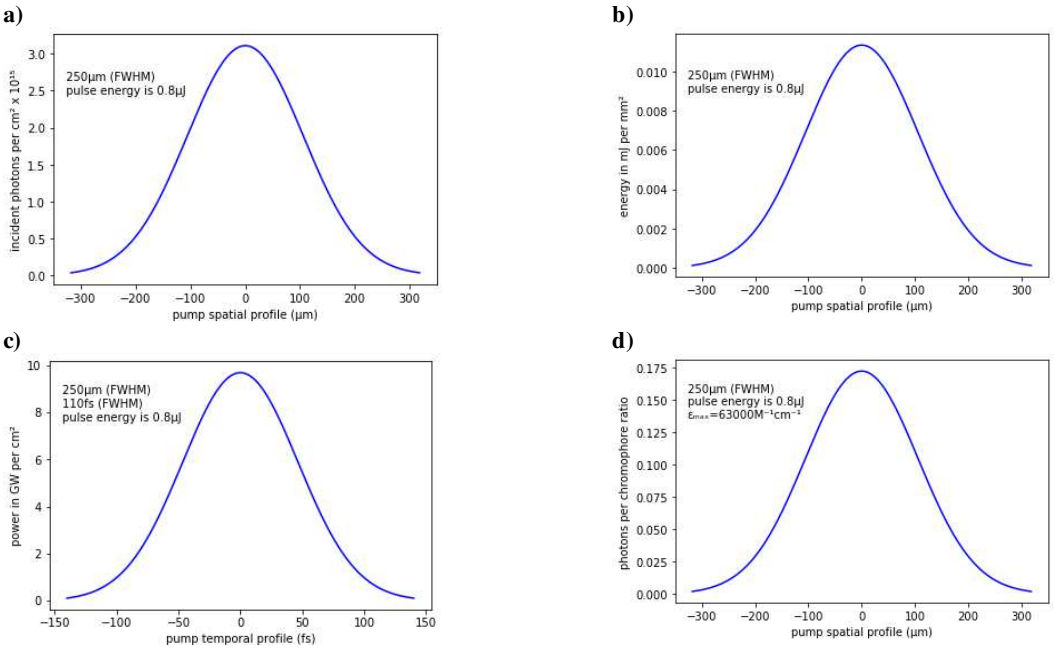

Fig. S5 Simulations showing the energy distribution (a) photons per cm^2, b) $mJ.mm^{-2}$, c) $GW.cm^{-2}$, d) photons absorbed per chromophore) of the pump pulse for N-tagged OCP experiments, excitation 540 nm, energy 0.8 µJ, sample absorption A(540 nm, 2 mm thickness) = 0.19

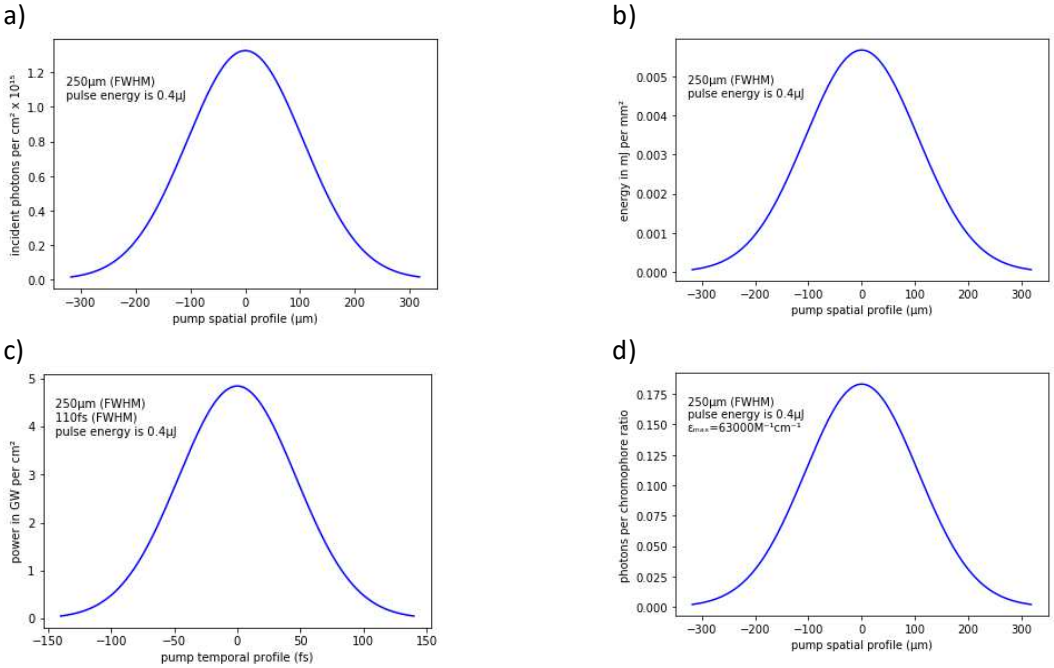

Fig. S6 Simulations showing the energy distribution (a) photon per cm^2, b) $mJ.mm^{-2}$, c) $GW.cm^{-2}$, d) photon absorbed per chromophore) of the pump pulse for N-tagged OCP experiments, excitation 470nm, energy 0.4uJ, sample absorption A(470 nm, 2 mm thickness) = 0.49

Method to determine number of photons absorbed per pulse and ratio of echinenone excited in the excited volume: the number of photons in the pump pulse per unit surface of the plane perpendicular to the pump beam was calculated from the measured pump energy divided by the energy of a photon at the excitation energy. Next a 2D Gaussian distribution defined on the cuvette (cylinder of a 2D Gaussian base and 2 mm length) was assumed at this point, with measured FWHM (250 µm), the same on both axes. The derived distribution was multiplied by $(1 - 10^{-A_{exc}})$ to obtain the number of absorbed photons per unit surface in the excited volume. The OCP concentration was calculated using a molar absorption coefficient of ϵ = 63 000 $M^{-1}cm^{-1}$ at the absorption maximum accordingly to Sluchanko et al. [1] Then number of OCP molecules excited in the illuminated volume was calculated as concentration multiplied by the Avogadro constant and the cuvette internal thickness. Finally the ratio of OCP excited per pulse in the pump volume was found from number of absorbed photons divided by the number of OCP molecules.

5) Transient absorption spectra at high excitation energy

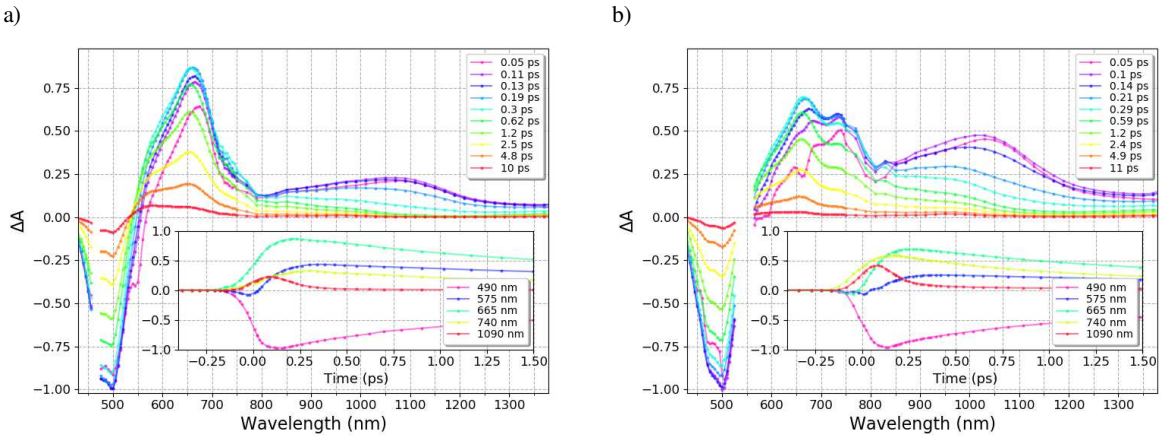

Fig. S7 Transient absorption spectra between 0.05 and 10 ps of N-tagged OCP-ECN excited at a) 470 nm (1.6 µJ, 110 fs FWHM, 250 µm FWHM), and b) 540 nm (3.2 µJ, 110 fs, 250 µm FWHM). All datasets were normalized to -1 at bleaching extremum (in both spectral and temporal dimensions). Insets show the growth of the signal.

6) Analysis of kinetic trace analysis

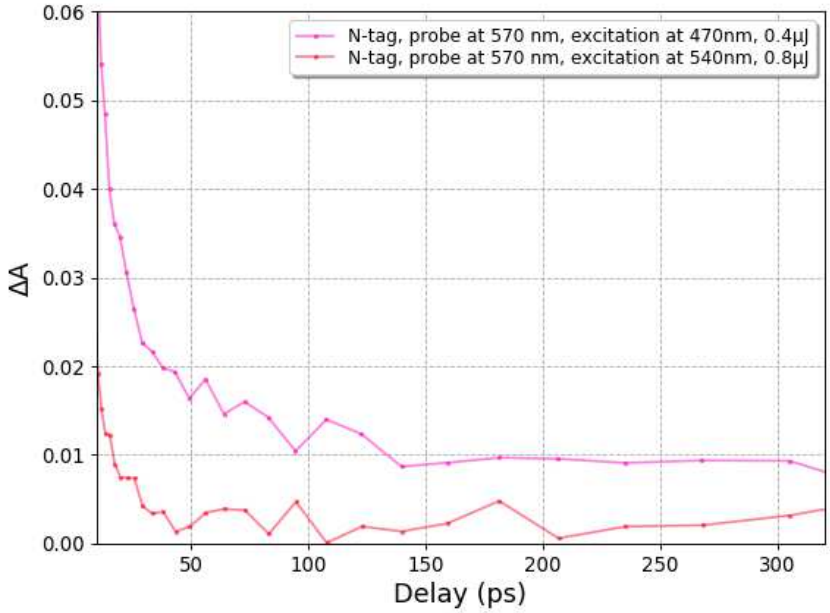

Fig. S8: Kinetics at 570 nm for excitation at 470 nm and 540 nm, respectively.

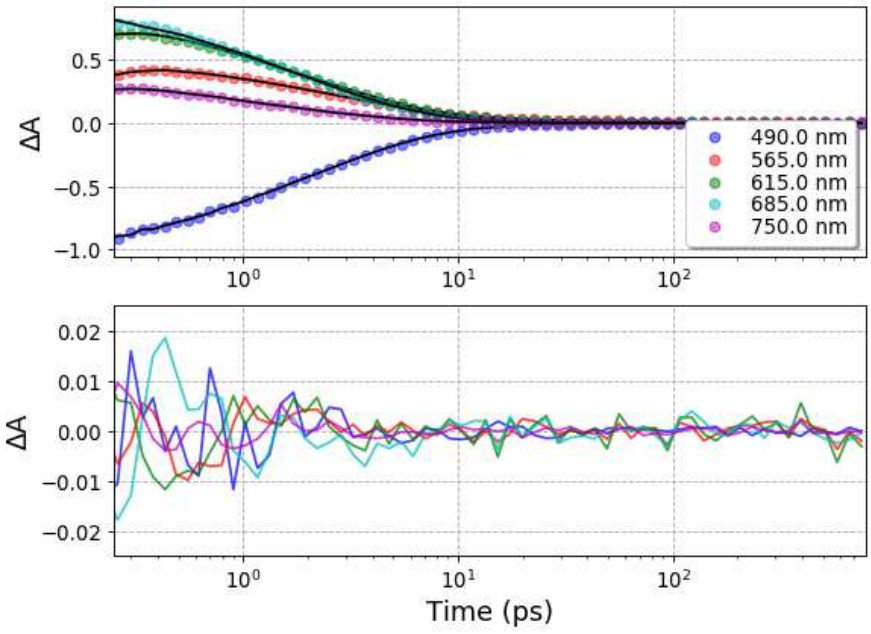

Fig. S9 Representative kinetic traces with their fit and residuals of global fit analysis done on N-tagged OCP (5 exponential components convoluted with a Gaussian-shaped pulse of 110 fs (FWHM) and an offset for long lived photoproducts (> 10 ns)), excitation at 470 nm, 0.4 µJ

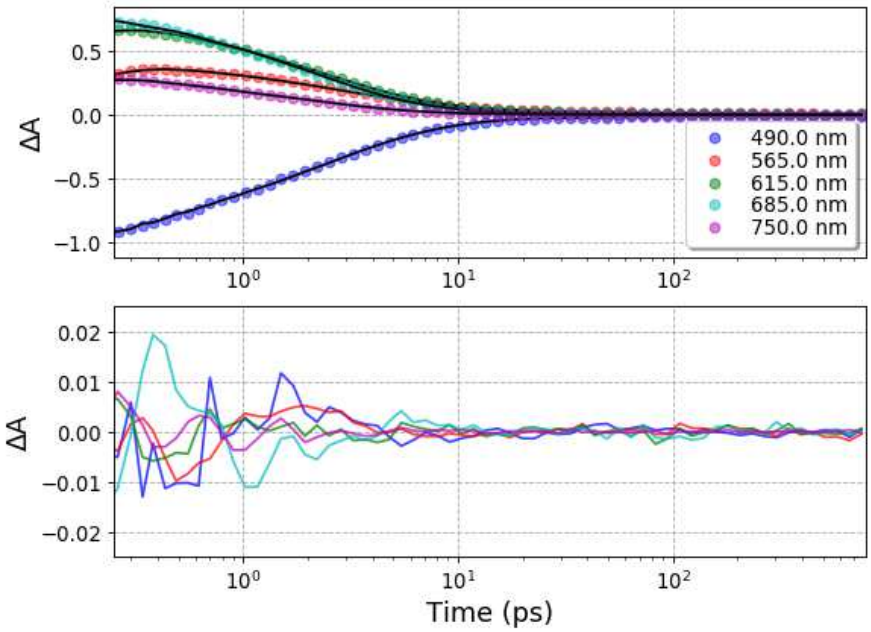

Fig. S10 Representative kinetic traces with their fit and residuals of global fit analysis done on N-tagged OCP (5 exponential components convoluted with a Gaussian-shaped pulse of 110 fs (FWHM) and an offset for long lived photoproducts (> 10 ns)), excitation at 470 nm, 1.6µJ

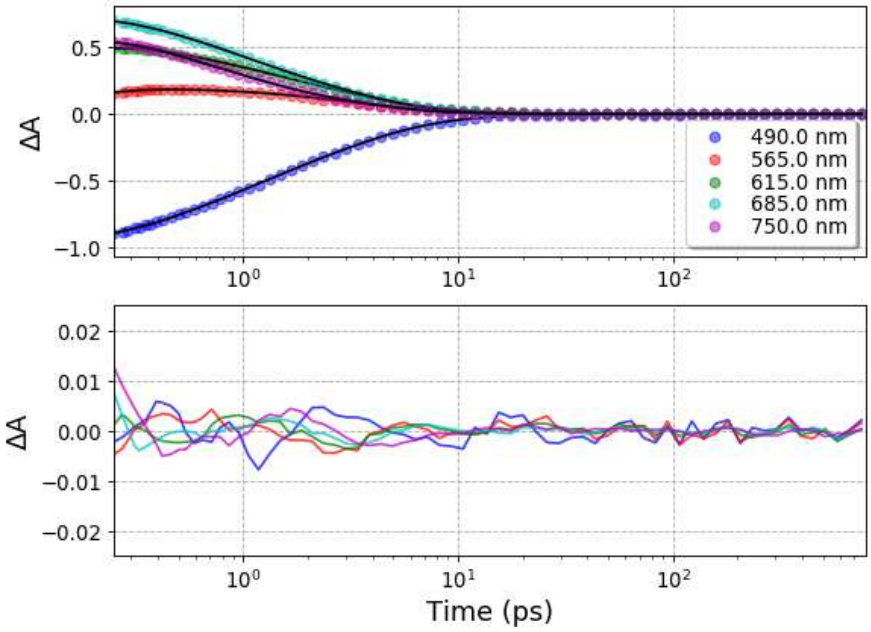

Fig. S11 Representative kinetic traces with their fit and residuals of global fit analysis done on N-tagged OCP (4 exponential components convoluted with a Gaussian-shaped pulse of 110 fs (FWHM) and an offset for long lived photoproducts (> 10 ns)), excitation at 540 nm, 0.8 µJ

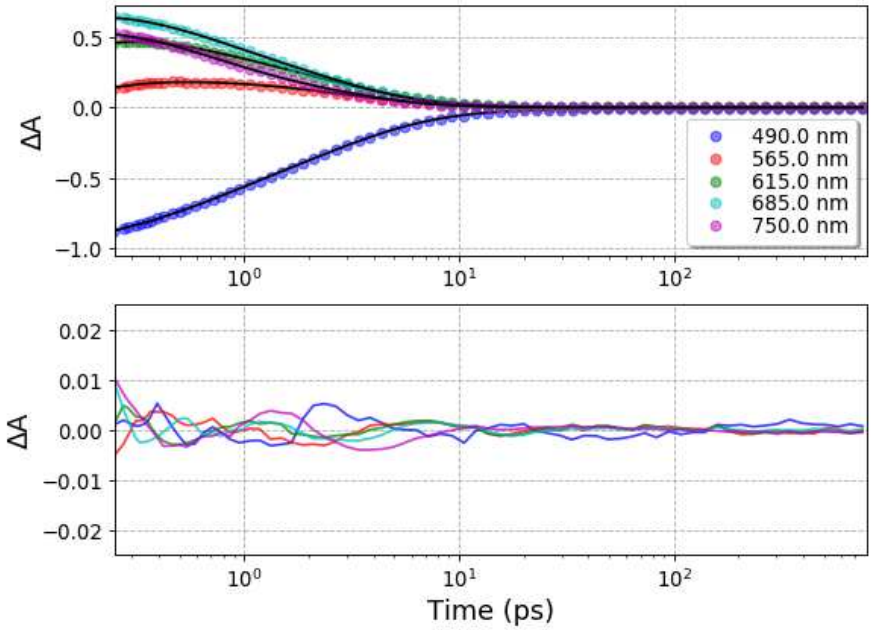

Fig. S12 Representative kinetic traces with their fit and residuals of global fit analysis done on N-tagged OCP (4 exponential components convoluted with a Gaussian-shaped pulse of 110 fs (FWHM) and an offset for long lived photoproducts (> 10 ns)), excitation at 540nm, 3.2µJ

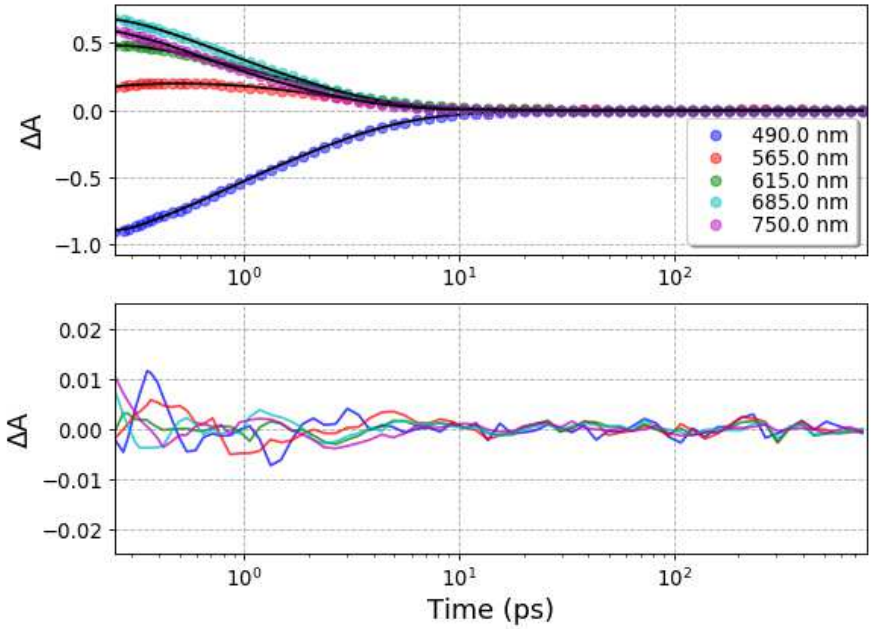

Fig. S13 Representative kinetic traces with their fit and residuals of global fit analysis done on C-tagged OCP (4 exponential components convoluted with a Gaussian-shaped pulse of 110 fs (FWHM) and an offset for long lived photoproducts (> 10 ns)), excitation at 540 nm, 0.8 µJ

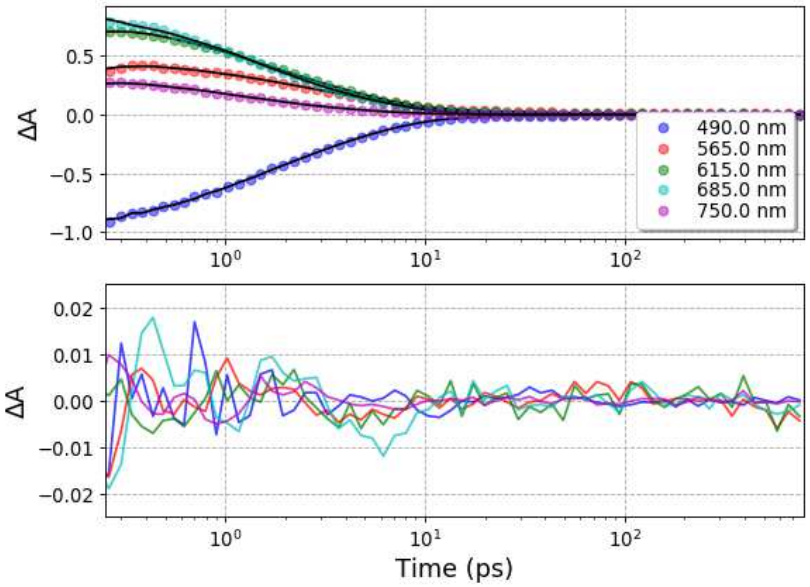

Fig. S14 Representative kinetic traces with their fit and residuals of global fit analysis done on N-tagged OCP (4 exponential components convoluted with a Gaussian-shaped pulse of 110 fs (FWHM) and an offset for long lived photoproducts (> 10 ns)), excitation at 470 nm, 0.4 µJ

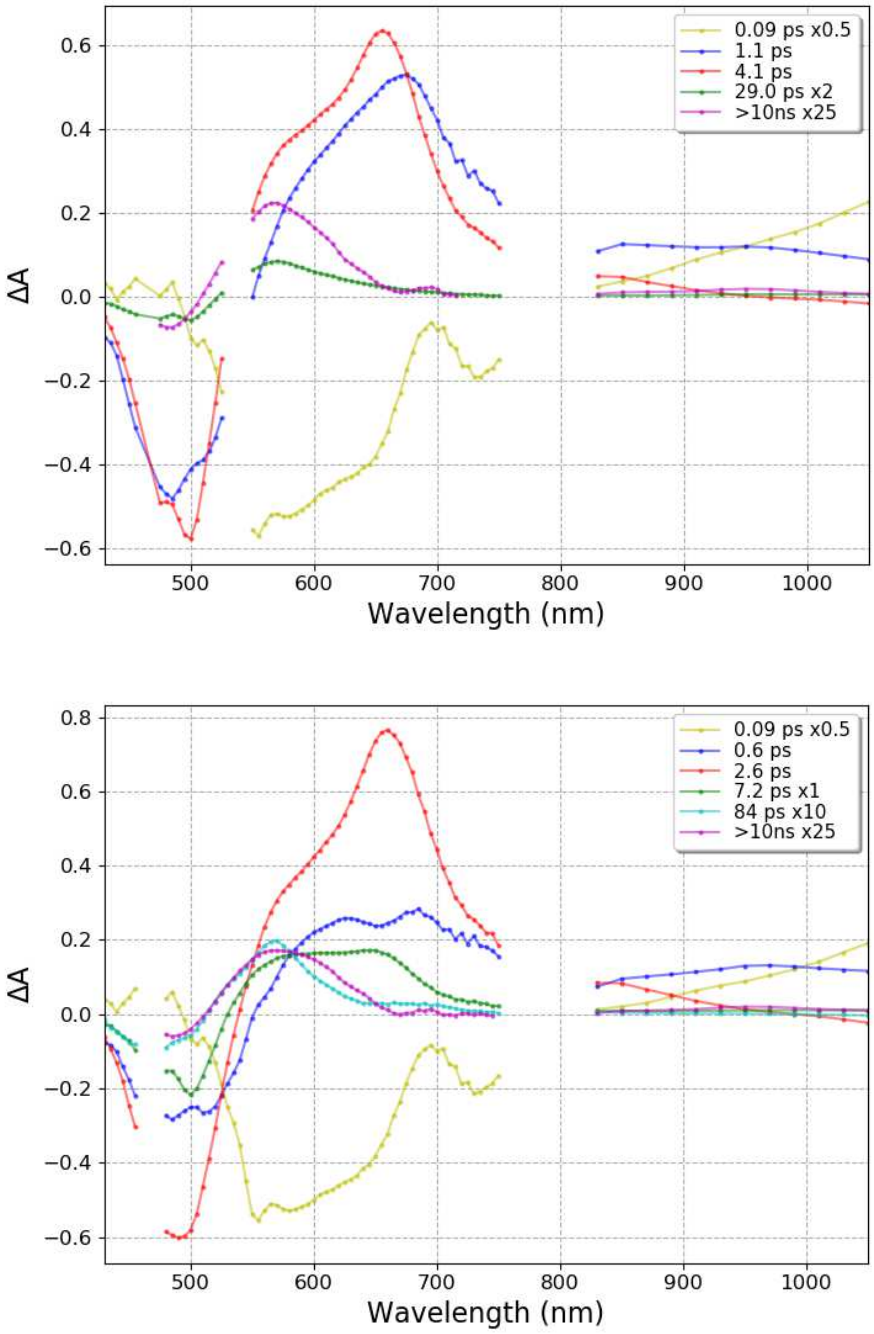

Fig. S15 Decay Associated Spectra (DAS) obtained from the global fit (top panel 4 exponential components convoluted with a Gaussian-shaped pulse of 110 fs (FWHM) and an offset for long lived photoproducts (> 10 ns), bottom panel 5 exponential components convoluted with a Gaussian-shaped pulse of 110 fs (FWHM) and an offset for long lived photoproducts (> 10 ns)) of transient absorption data recorded of N-tagged OCP with excitation at 470 nm (0.4 µJ).

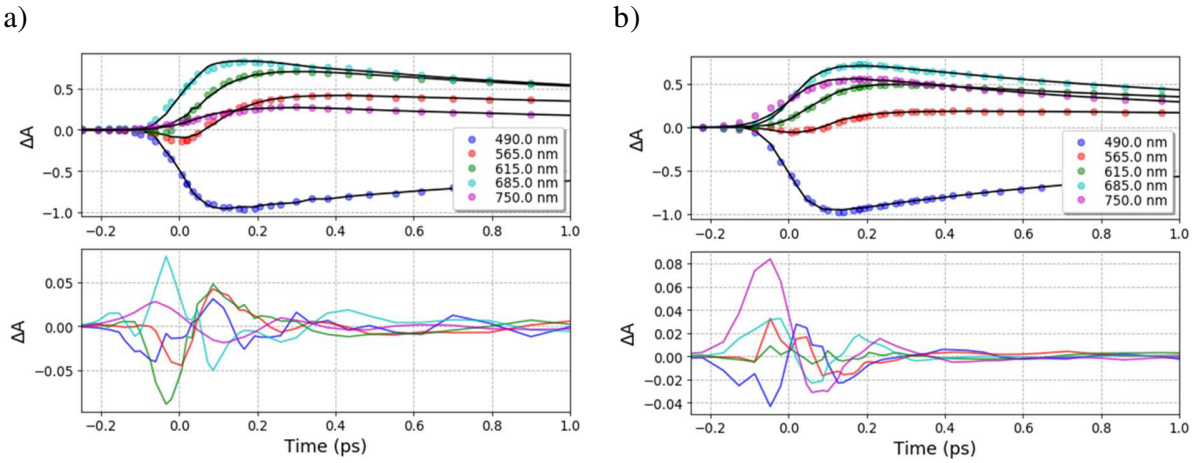

Fig. S16 Representative kinetic traces with their fit and residuals of global fit analysis (zoomed on -0.25ps to 1ps range) done on N-tagged OCP with a) 470nm, 0.4µJ excitation (5 exponential components + offset), b) 540nm, 0.8µJ excitation (4 exponential components + offset), convoluted with a Gaussian-shaped pulse of 110 fs (FWHM).

7) P_1 signature

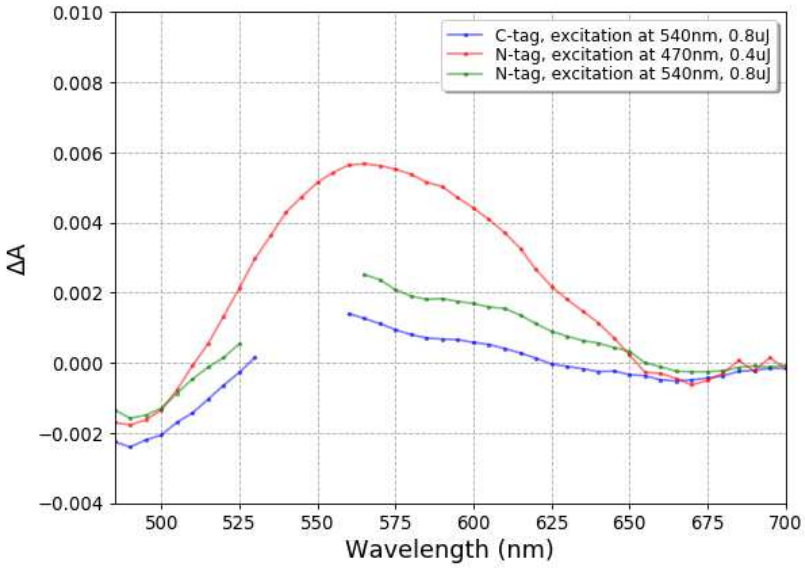

Fig. S17 Transient absorption spectra averaged around 1 ns (P_1 state) of N-tagged and C-tagged OCP.

8) Estimation of formation quantum yields from pre-exponential factors at probe 490 nm

The formation quantum yield of S_1, ICT or S* are estimated from pre-exponential factors at probe 490 nm, i.e. their DAS value at 490 nm (Figure 5, Figure 6, Table S1), divided by sum of S_1, ICT and S* amplitudes excluding P_1 and S_2 (see equations below), with results shown in Table 1 and Scheme 2. It should be underlined here that such approximation assumes that (i) S_1, ICT and S* are formed from S_2 in parallel

paths, (ii) these states decay mainly to S_0 without any interconversion and (iii) their excited state absorption is small at 490 nm. For the P_1 formation quantum yield its positive absorbance contribution at 490 nm is estimated and taken into account (Figure S4).

Table S1: DAS value at 490 nm for ICT, S1, S*, S~ and P_1.

	ICT	S_1	S*	S~	P_1
N-tag 470 nm / 0.4 µJ	0.27	0.60	0.17	0.0070	0.0023
N-tag 470 nm / 1.6 µJ	0.30	0.53	0.29	0.018	0.011
N-tag 540 nm / 0.8 µJ	0.37	0.58	0.13	-	0.0023
N-tag 540 nm / 3.2 µJ	0.33	0.57	0.15	-	0.0082
C-tag 540 nm / 0.8 µJ	0.41	0.63	0.13	-	0.0028

Equations to calculate formation quantum yield for ICT/S_1/S*/S~/P_1:

$$\Phi_{ICT} = DAS_{ICT}(490nm)/\left(DAS_{ICT}(490nm) + DAS_{S_1}(490nm) + DAS_{S*}(490nm) + DAS_{S\sim}(490nm)\right)$$

$$\Phi_{S_1} = DAS_{S_1}(490nm)/\left(DAS_{ICT}(490nm) + DAS_{S_1}(490nm) + DAS_{S*}(490nm) + DAS_{S\sim}(490nm)\right)$$

$$\Phi_{S*} = DAS_{S*}(490nm)/\left(DAS_{ICT}(490nm) + DAS_{S_1}(490nm) + DAS_{S*}(490nm) + DAS_{S\sim}(490nm)\right)$$

$$\Phi_{S\sim} = DAS_{S\sim}(490nm)/\left(DAS_{ICT}(490nm) + DAS_{S_1}(490nm) + DAS_{S*}(490nm) + DAS_{S\sim}(490nm)\right)$$

$$\Phi_{P_1} = DAS_{P_1}(490nm) \cdot 63000/29500$$

where $DAS_X(490nm)$ is DAS value of X state at 490nm, extracted from data normalized to -1 at the bleaching extremum (Figure 5 and Figure 6). $DAS_{S\sim}(490nm)$ value is equal to zero when using 540nm excitation.

9) Estimation of the error on time constants and pre-exponential factors

To assess the error of the extracted time constants and quantum yields (Table 1 in the main text), bootstrap analysis was employed. For the sake of simplicity, we used one dataset. We selected N-tagged OCP, done with excitation at 540 nm, 0.8 µJ, as the most representative one for this study.

Our bootstrap procedure consists of the following steps:

a) Dataset was fitted using a procedure described in Materials and Methods.
b) Residuals from the obtained fit were used to calculate the standard deviation (estimation of the noise in the data) for each kinetics separately (noise levels are different depending on spectral region).

Delays below 0.3 ps were excluded due to strong contribution of artifact signals such as Stimulated Raman Amplification (where residuals don't reflect noise, but they have shape of the artifacts).

c) Sampled datasets were generated, where additional random noise was simulated from standard deviations obtained in previous step, using Gaussian distribution, and added to the original data. 6473 sample datasets were generated in total.

d) Each generated sample dataset was fitted using the same procedure as for the original fit. It allowed to build a distribution of each fit parameter, and calculate a standard errors.

Described procedure yields errors and distributions shown in tables S2 and S3 (below). Obtained sets of errors are expected to be similar between datasets. These tables do not contain information about error of the S˜ state, because 540 nm excited dataset do not contain S˜ state. Nevertheless, it is clear that errors for quantum yield and lifetime of the S˜ state are huge, due to very small contribution. Our fitting procedure on 470 nm excited dataset usually returned something between 50 ps and 110 ps for the S˜, depending on initial fit conditions and tuning of the fitting procedure itself. So we assume that error of the S˜ is better than +/- 30 ps.

Table S2: Distributions of parameters obtained from bootstrap procedure of N-tagged OCP (excitation 540 nm, 0.8 µJ, 6473 samples). Note that amplitudes are calculated as preexponential factor divided by sum of preexponential factors excluding S_2 state.

	ICT	S_1	S*	P_1
τ /ps	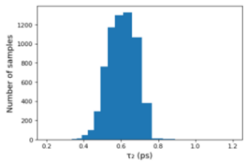	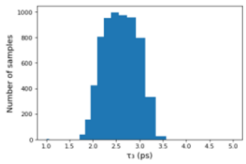	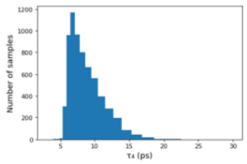	
$A_{490\ nm}$	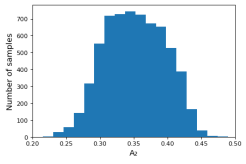	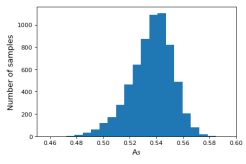	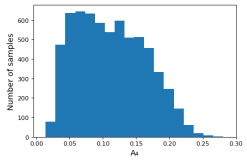	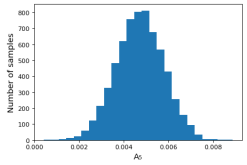

Table S3: Standard errors calculated from bootstrapping distributions of N-tag (exc. 540 nm, 0.8 µJ, Table S1)

	ICT	S_1	S*	P_1
σ(τ) / ps	0.076	0.36	2.3	-
$\sigma(A_{490\ nm})$	0.046	0.019	0.052	0.0011

10) Comparison of kinetic profiles of C-tagged and N-tagged OCP

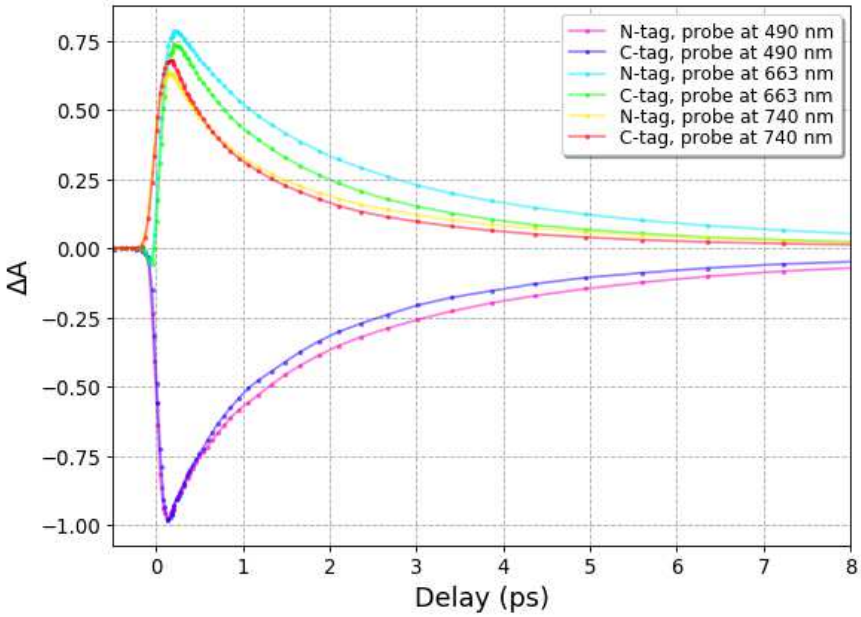

Fig. S18 Comparison of kinetic profiles of C-tag and for N-tag (540 nm, 0.8 μJ)

References:

1. Sluchanko, N.N.; Klementiev, K.E.; Shirshin, E.A.; Tsoraev, G.V.; Friedrich, T.; Maksimov, E.G. The purple Trp288Ala mutant of Synechocystis OCP persistently quenches phycobilisome fluorescence and tightly interacts with FRP. *Biochim Biophys Acta* **2017**, *1858*, 1-11, doi:10.1016/j.bbabio.2016.10.005.
2. Konold, P.E.; van Stokkum, I.H.M.; Muzzopappa, F.; Wilson, A.; Groot, M.L.; Kirilovsky, D.; Kennis, J.T.M. Photoactivation mechanism, timing of protein secondary structure dynamics and carotenoid translocation in the Orange Carotenoid Protein. *J. Am. Chem. Soc.* **2019**, *141*, 520−530, doi:10.1021/jacs.8b11373.

BBA - Bioenergetics 1863 (2022) 148584

Contents lists available at ScienceDirect

BBA - Bioenergetics

journal homepage: www.elsevier.com/locate/bbabio

Structure-function-dynamics relationships in the peculiar *Planktothrix* PCC7805 OCP1: Impact of his-tagging and carotenoid type

Adjélé Wilson [a,1], Elena A. Andreeva [b,c,1], Stanisław Niziński [d,e,1], Léa Talbot [a], Elisabeth Hartmann [c], Ilme Schlichting [c], Gotard Burdzinski [e], Michel Sliwa [d,*], Diana Kirilovsky [a,*], Jacques-Philippe Colletier [b,*]

[a] Université Paris-Saclay, CEA, CNRS, Institute for Integrative Biology of the Cell (I2BC), 91198 Gif-sur-Yvette, France
[b] Univ. Grenoble Alpes, CEA, CNRS, Institut de Biologie Structurale, 38000 Grenoble, France
[c] Max-Planck-Institut für medizinische Forschung, Jahnstrasse 29, 69120 Heidelberg, Germany
[d] Univ. Lille, CNRS, UMR 8516, LASIRE, LAboratoire de Spectroscopie pour les Interactions, la Réactivité et l'Environnement, Lille 59000, France
[e] Quantum Electronics Laboratory, Faculty of Physics, Adam Mickiewicz University in Poznań, Uniwersytetu Poznańskiego 2, Poznan 61-614, Poland

ARTICLE INFO

Keywords:
Cyanobacteria
Flash photolysis
Photosynthetic pigments
Structure function relationships
X-ray diffraction

ABSTRACT

The orange carotenoid protein (OCP) is a photoactive protein involved in cyanobacterial photoprotection. Here, we report on the functional, spectral and structural characteristics of the peculiar *Planktothrix* PCC7805 OCP (Plankto-OCP). We show that this OCP variant is characterized by higher photoactivation and recovery rates, and a stronger energy-quenching activity, compared to other OCP studied thus far. We characterize the effect of the functionalizing carotenoid and of his-tagging on these reactions, and identify the time scales on which these modifications affect photoactivation. The presence of a his-tag at the C-terminus has a large influence on photoactivation, thermal recovery and PBS-fluorescence quenching, and likewise for the nature of the carotenoid that additionally affects the yield and characteristics of excited states and the ns-s dynamics of photoactivated OCP. By solving the structures of Plankto-OCP in the ECN- and CAN-functionalized states, each in two closely-related crystal forms, we further unveil the molecular breathing motions that animate Plankto-OCP at the monomer and dimer levels. We finally discuss the structural changes that could explain the peculiar properties of Plankto-OCP.

1. Introduction

Photosynthetic organisms have evolved to make use of nearly all photons absorbed by their light-harvesting antennas. Under light stress conditions, however, the photosynthetic electron transport chain becomes saturated leading to the formation of harmful reactive oxygen species (ROS), e.g., singlet oxygen ($^1O_2$) [1,2], that can damage the photosystems and other cellular machineries, eventually leading to cell death. Accordingly, photosynthetic organisms have developed a variety of mechanisms, altogether referred-to as non-photochemical quenching (NPQ), that are aimed at reducing the amount of energy reaching the photochemical reactions centers thereby avoiding accumulation of ROS [3]. In a vast majority of cyanobacterial strains, the main light-harvesting antenna is a large soluble complex, the phycobilisome (PBS), and the soluble 35 kDa photoactive Orange Carotenoid Protein (OCP) is at the center of the NPQ mechanism (for review: [4–6]). OCP is capable both of dissipating the excess energy harvested by the PBS [7], and of quenching the produced harmful singlet-oxygen [8,9]. For the energy quenching mechanism to be elicited, OCP must be photoactivated, which triggers the changes in protein structure and pigment position required for PBS binding and discharge of its excessive energy [10,11]. Specifically, upon absorption of a blue-green photon, OCP converts from an inactive dark-adapted state (denoted as OCP^O, due to its orange color) into an active light-adapted state (denoted OCP^R, due to its red color). OCP^O is characterized by two absorption maxima at 475 and 495 nm (vibronic structure), while OCP^R displays a single broader absorption peak between 510 and 530 nm [11]. The photoactivation quantum yield of the protein is notoriously low, viz. 0.2 % [12], meaning that the OCP-supported photoprotective mechanism is at play only under high light conditions and that the concentration of OCP^R is

* Corresponding authors.
E-mail addresses: michel.sliwa@univ-lille.fr (M. Sliwa), diana.kirilovsky@cea.fr (D. Kirilovsky), colletier@ibs.fr (J.-P. Colletier).
[1] These authors contributed equally to this work.

https://doi.org/10.1016/j.bbabio.2022.148584
Received 4 January 2022; Received in revised form 31 May 2022; Accepted 7 June 2022
Available online 23 June 2022

null, or very low, in darkness and under low light conditions [11,13]. Phylogenic studies of OCP sequences allowed their classification into three distinct clades, viz. OCP1, OCP2 and OCPX [14]. Members of the OCP1 clade are characterized by a slow OCP^R to OCP^O thermal recovery (at 8 °C) that is accelerated by the presence of the fluorescence recovery protein (FRP), whereas OCP2 and OCPX exhibit a faster thermal recovery (even at 8 °C) that is not affected by the presence of FRP [15,16].

The best characterized OCP are OCP1 from *Arthrospira maxima* and *Synechocystis* PCC 6803, hereafter referred to as *Arthrospira* and *Synechocystis* OCP, respectively. For both, the dark-adapted structure was solved by X-ray crystallography [8,17], revealing a conserved two-domain modular architecture. The fully α-helical N-terminal domain (NTD, residues 1–165), unique to cyanobacteria, and the C-terminal domain (CTD, residues 187–320), structurally belonging to the nuclear transport factor-2 superfamily (NTF2), encase at their interface a ketocarotenoid pigment, e.g., 3′-hydroxyechineone (3′-hECN) [8] or ECN [17]. Notwithstanding the presence of a linker that covalently attaches the NTD and CTD, the dark-adapted state is stabilized by two main protein interfaces, viz. (i) the central interdomain interface, which features two highly-conserved H-bond (N104-W277) and salt-bridge (R155-E244); and (ii) the interface between the N-terminal helix (also coined, N-terminal extension or NTE) and the CTD β-sheet [8], which features six to seven H-bonds depending on species. Additionally, the ketocarotenoid pigment buries ≈95 % of its highly hydrophobic surface into the binding tunnel spanning the two domains (buried surface area (BSA) of 786 $Å^2$, with a surface complementarity of ~83 %), thereby contributing to the stabilization of the OCP^O. The sole polar interactions between the ketocarotenoid and the protein scaffold are the H-bonds established between the carbonyl oxygen of its β1 ring and the side chain hydroxyl and amine of CTD residues Y201 and W288 (*Synechocystis* OCP residue numbering), respectively [8,17]. Rupture of these H-bonds is the first event along a photo-activation cascade that involves several 'red' intermediate states spanning the ps to second time scale [12,18–20] and culminates with dissociation of the two domains following the 12 Å translocation of the carotenoid into the NTD [21]. Dissociation of the two domains is essential for the energy-quenching function, as only OCP^R is capable of binding to the PBS [10,11]. The energy-quenching activity is measured as the quenching of PBS fluorescence, itself induced by exposure to blue-light.

Despite the considerable knowledge acquired on OCP in the last two decades, the photoactivation mechanism is still under debate. Notably, the very first instants of the photoactivation mechanism remain elusive. Numerous computational and time-resolved spectroscopic studies have recently sought to shed light on the structure, formation and decay of the carotenoid excited states associated with OCP photoactivation ([19,22–24]; Fig. 1). Notably, it was demonstrated that upon photoexcitation, three ps-lived intermediate states are formed following the sub-ps decay of the initial S_2 state, viz. an S_1 and an intra-molecular charge

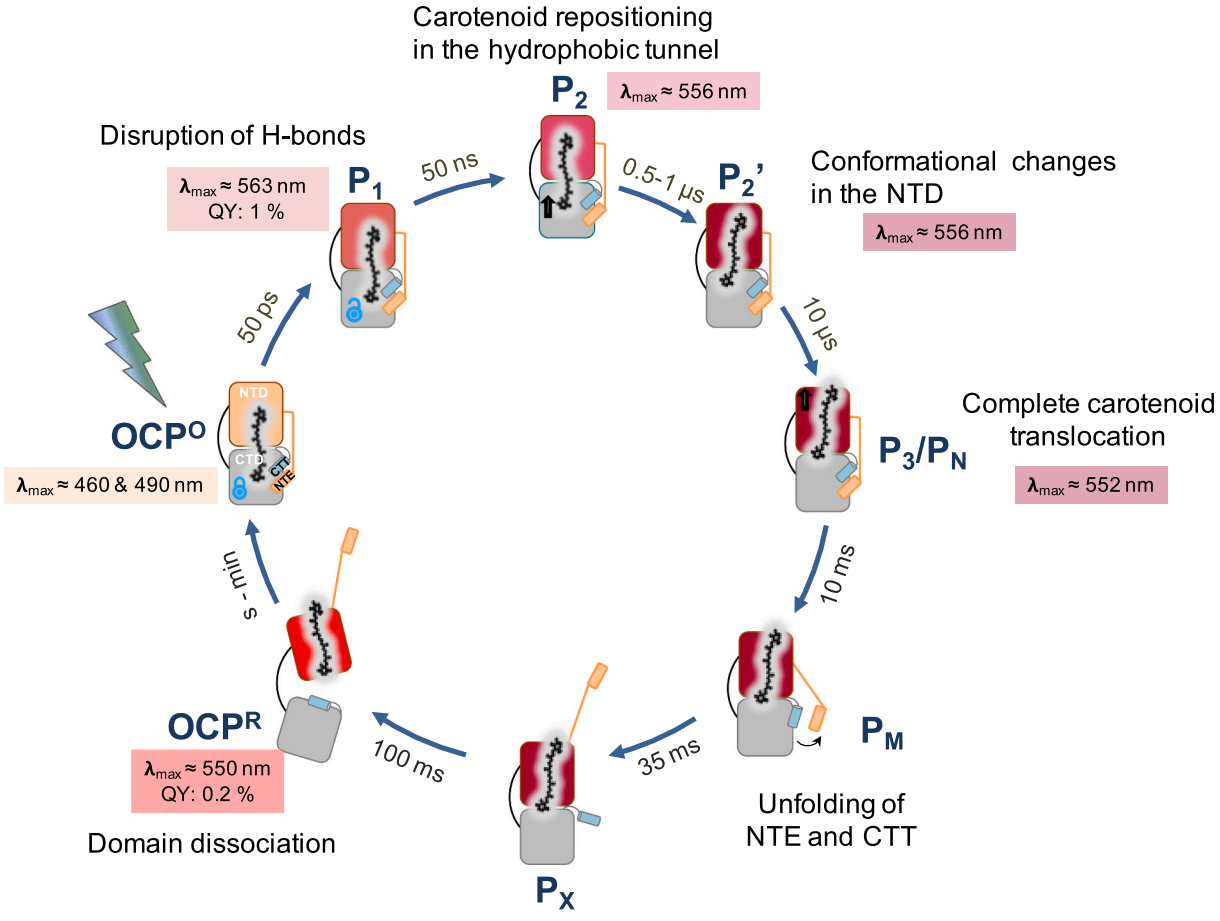

Fig. 1. Formation of OCP^R is a multi-step reaction that spans twelve decades in time. The presented model for OCP photoactivation summarizes findings from multiple studies [12,19,23,32]. The wavelength of maximum difference-absorbance (after subtraction of the OCP^O signal) is indicated for all intermediate states characterized to date. The P_1, P_2, P_2' and P_3 were observed by Konold et al. 2019 in transient absorption UV–Vis experiments upon excitation at 470 nm of Ntag-Syn-OCP_{ECN} [19]. Of important note, P_2' was only observed in transient IR experiments, suggesting that it is characterized by a conformational change in the protein scaffold that does not influence the carotenoid electronic properties. P_N/P_M and P_X were observed by Maksimov et al. in time-resolved fluorimetry experiments conducted on the ECN-functionalized OCP-3FH mutant (W41F, W101F, W110F and W277H) featuring a single tryptophan at position W288, following excitation at 262 nm [23].

transfer (ICT) excited states [25,26], and an S* state [19] that was initially proposed to correspond to a vibrationally hot ground-state (S_0) population [27]. Recently, however, it was proposed that the S* state, characterized by a longer lifetime than the S_1 and ICT states [19,28], is also an excited state which serves as the precursor of the first photoproduct, P_1, in which the H-bonds between the carotenoid and the protein are broken and the protein is, therefore, already 'red' (difference absorption spectrum peaking at 565 nm) [19]. The debate however remains open concerning the nature of the S* state [29–31] and its putative role as the precursor of P_1. Indeed, recent results from our laboratories show that while the photoactivation speed of OCP^R is independent of irradiation light (470 nm versus 540 nm), the concentration of S* decreases by ≈30 % when 540 nm light is used to trigger photoactivation [32]. Hence, S* cannot be the sole precursor of P_1. Evolution of P_1 (50 ns lifetime), wherein the carotenoid is likely untethered from its H-bonding partners in the CTD, leads to a repositioning of the carotenoid in the tunnel, in close vicinity of the dark-state position (P_2; 0.5–1 μs) [19]. After a first partial movement into the NTD (P_2') [19], the ketocarotenoid completes its translocation in around 10 μs, reaching the position that it occupies in the final OCP^R (P_3) [19,23]. Conformational changes in the NTE and CTT ensue (P_M and P_X ~10 ms and 35 ms), followed by an opening of the protein upon dissociation of the two domains (~100 ms) [23]. Thus, the formation of the photoactive OCP^R is a multi-step reaction spanning at least twelve decades in times [12,19,23]. All steps, including the P_2' to P_3 and P_3 to P_M transitions, are accompanied by recovery to the initial OCP^O state, explaining the low quantum yield [12,19,23]. About 1 and 0.2 % of molecules reach the P_1 state [19] and the final OCP^R state [12,19,23,32] (Fig. 1), respectively.

In all recent studies on OCP, the protein was expressed recombinantly [33] and a six-histidine tag (his-tag) was introduced at the N-terminus (OCP produced in *Escherichia coli* cells) or C- terminus (OCP produced in *Synechocystis* and *E. coli* cells) to accelerate purification. It yet remains unclear whether or not presence of a his-tag at either the N- or C-terminal extremity of the protein influences the kinetics of photoactivation, PBS quenching and thermal recovery, respectively. Indeed, after migration of the carotenoid from the NTD/CTD interface into the NTD (≈0.5 μs), formation of OCP^R will require, prior to domain separation, the detachment from the CTD β-sheet of the N-terminal helix αA (or NTE) [19,34,35] and the C-terminal helix αN (or CTT) [35–37], respectively. The hypothesis that his-tagging could affect OCP function is supported by our recent report that the his-tag position affects i) the photoactivation efficiency, with OCP^R accumulation being slower when the his-tag is present at the C-terminus (C-tagged OCP); ii) the lifetimes ofexcited states, which are shorter-lived in C-tagged OCP; and iii) the spectral signatures of the S_1 and S* states. It was also found that the position of the tag does not influence the P_1 formation quantum yield (QY), suggesting that the more efficient photoactivation of the N-tagged protein is related to molecular events occurring on the ns to ms timescales [32].

The influence of the carotenoid type on the various facets of OCP function is also uncharacterized. It has been shown that while the naturally-occurring pigment in *Synechocystis* and *Arthrospira* OCP is 3′-hydroxyechinenone (3′-hECN), the protein may also be functionalized by other similarly-length ketocarotenoids, the palette of which depends on species. Indeed, upon knock-out of the gene coding for the hydrolase converting ECN into hECN, *Synechocystis* OCP binds ECN [38], and likewise when the protein is overexpressed in *Synechocystis* cells, due to the low amount of hECN (≈1 % of all ketocarotenoids) [11,39]. When expressed recombinantly in *E. coli* cells [33], *Synechocystis* OCP can be complexed with ECN, canthaxanthin (CAN) or zeaxanthin (ZEA), depending on the set of carotenoid-producing genes that are co-transformed with the gene coding for the OCP. This feature holds true for all OCP variants produced recombinantly in carotenoid-producing *E. coli* cells, including OCP1 from *Synechocystis*, *Arthrospira* and *Tolypothrix* [15,33], OCP2 from *Tolypothrix* and *Synechocystis* 7508 [15,16], and OCPX from *Scytonema* and *Synechocystis* 7508 [16]. To date, only *Tolypothrix* OCP was found to bind canthaxanthin (CAN) in the natural context, when overexpressed in *Tolypothrix* cells [30]. It is tantalizing to envision that functionalization of OCP by different types of carotenoids could enable regulation of its activity. Early studies showed that the relative populations of the carotenoid S_1 and ICT excited-states depend on the carotenoid that functionalizes OCP, with virtually no ICT in *Synechocystis* OCP functionalized with the fully symmetric CAN (identical β-ionone rings at the two extremities), but up to 50 % ICT in OCP functionalized with the non-symmetric ECN [30,40]. It was then proposed that the absence of the ICT state is a consequence of the fully symmetric nature of the CAN pigment, which is absent in ECN [30,40]. However, the P_1 state was not identified at the time, so that it remains elusive whether or not the change in functionalizing carotenoid also affects the yield of this photoproductive intermediate. Moreover, it is unknown if the rate of OCP^R accumulation and recovery, and the yield of intermediary photoproducts are influenced by the nature of the functionalizing carotenoid. Clearly, a thorough structure-function-dynamics study must be conducted to provide answers to all of the questions introduced above. Ideally, this study should be conducted on OCP variants from different cyanobacterial strains to understand how subtle changes in the structure may affect the function, its regulation or both. For example, it was recently reported that despite a lower intracellular OCP concentration and a quasi-strict conservation of the amino acids lining the OCP carotenoid tunnel, the amplitude of the OCP-related PBS-fluorescence quenching is larger in the cyanobacterium *Planktothrix* PCC 7805 than in *Synechocystis* PCC 6803 [41], and likewise for the PBS-fluorescence recovery.

Here, we address these gaps in knowledge by performing a comparative structure-function study on the OCP1 from two different strains, viz. *Synechocystis* PCC 6803 (Syn-OCP), and *Planktothrix* PCC 7805 (Plankto-OCP). For both OCP1 variants, the kinetics of photoactivation, thermal recovery and PBS-fluorescence quenching were assessed in the native (non-tagged), N-tagged and C-tagged states, and with ECN or CAN as the functionalizing carotenoid. We observed that the presence of the his-tag at the C-terminus has a larger influence on photoactivation, thermal recovery and PBS-fluorescence quenching than its presence at the N-terminus. We found that the nature of the carotenoid influences the yield and characteristics of excited states, the ns-s dynamics of photoactivated OCP and the thermal recovery, leading to different rates of OCP^R accumulation, and of PBS-fluorescence quenching. As only the structures of ECN- and CAN-functionalized Syn-OCP [17,21] were available, we solved the Plankto-OCP structure in both the ECN- and CAN-functionalized states. At 1.4–1.8 Å resolution, these structures shed light on the molecular breathing motions that animate Plankto-OCP monomers and dimers, and point to subtle changes outside of the carotenoid tunnel explaining the peculiar properties of Plankto-OCP.

2. Materials and methods

2.1. Construction of plasmids for ocp gene expression in E. coli cells

The plasmids pCDF-OCPSynCtag and pCDF-NtagOCPSyn featuring the *Synechocystis ocp* gene and coding for C-tagged Syn-OCP and N-tagged Syn-OCP, respectively, were described in [33]. To construct the plasmid *pCDF*-OCPSyn, needed to express the native (non-tagged) *Synechocystis ocp* (*srl963*) gene in *E. coli* cells, the nucleotides coding for the N-terminal his-tag in the plasmid pCDF-NtagOCPSyn were excised by mutagenesis using F-ocpSynNative (5′-ATAAGGAGATATACCATGCCATTCACCATTGACTCT-3′) and R-Duet (5′-CATGGTATATCTCCTTATTAAAGTTAAACAAAATTA-3′) as forward and reverse primers, respectively. To construct the plasmid containing the *Planktothrix agardhii* PCC *7805 ocp* (*PLAM_2315*) gene, a PCR was performed using the genomic DNA of *Planktothrix agardhii str. 7805* as a template, and F-OCPPlank EcoR1 (5′-CGATGCGAATTCTTCATTTACAGTCGATTCAGCCC-3′) and R-OCPPlank Not1 (5′-

CATTATGCGGCCGCCTTCCCCCTTAAATCACAAG-3′), as forward and reverse primers, respectively. Then, the PCR products were cloned into a pCDFDuet-1 plasmid featuring the nucleotides encoding for a six-histidine tag at the N-terminus, after digestion of the plasmid by *Eco*RI and *Not*I. The resultant plasmid, named pCDF-NtagOCPPx, enabled expression of *Planktothrix* OCP with a his-tag at the N-terminus.

To synthesize non-tagged *Planktothrix* OCP, the nucleotides coding for the six-histidine tag in the pCDF-NtagOCPPx plasmid were suppressed using F-OCPPxNoTag (5′-TTAATAAGGAGATATACCATGTCATTTACAGTCGATTCAGCCCGTGGG-3′) and R-Duet (see above) as forward and reverse primers, respectively, enabling to create the plasmid pCDF-OCPPx suited to express the native (non-tagged) *Planktothrix* OCP. Then, a nucleotide sequence encoding a 6-histidine residues was added at the 3′end by mutagenesis using the pCDF-OCPPx plasmid as template and F-DuetOCPPx Ctag (5′-CACCACCACCACCACCACTAATTAATAAACGAATCTAATTTGATATAGC-3′) and R-DuetOCPPx Ctag (5′-GTGGTGGTGGTGGTGGTGACGAACTAAATTTAACAACTCTTTAGGTG-3′) as forward and reverse primers, respectively. Thereby, we obtained the plasmid pCDF-CtagOCPPx, which was used to express *Planktothrix* OCP his-tagged at the C-terminus.

2.2. Construction of plasmids for frp gene expression in E. coli cells

The plasmid used to express the *Synechocystis frp* gene in *E. coli* was described in [10]. To express the *Planktothrix agardhii* PCC *7805 frp* (*PLAM_2314*) gene in *E. coli*, the *frp* gene was amplified by PCR using forward (F-FRPPlank EcoR1: 5′-CGATGCGAATTCTCAAGTAAATGAGATTGAATG-3′) and reverse (R-FRPPlank Not1: 5′-TGCTTAGCGGCCGCAACTCAAATTGTTTTAAGAATCCCCG-3′) primers. The resulting fragment was cloned between the *Eco*RI and *Not*I sites of the pCDFDuet-1 plasmid which contains the nucleotides encoding for a six-histidine tag.

2.3. Holo-OCP and FRP production, isolation and purification

The production and isolation of holo-OCP were previously described [33]. FRP isolation was described in [10]. To isolate non-tagged OCP, *E. coli* cells were resuspended in lysis buffer (40 mM Tris-HCl pH 8, 1 mM EDTA, 1 mM PMSF, 1 mM caproic acid, 1 mM benzamidic acid, 50 μg mL^{-1} DNAse) and broken using a French Press. Membranes were pelleted and the supernatant was loaded on a Whatman DE-52 cellulose column. The OCP was eluted using a gradient of 60–80 mM NaCl in 40 mM Tris-HCl pH 8. A second purification step was performed by hydrophobic interaction chromatography (HiTrap Phenyl HP column, GE Healthcare), where OCP was eluted in 40 mM Tris-HCl pH 8, 0.5 M NaCl. The eluate was dialyzed overnight against 40 mM Tris-HCl pH 8 at 4 °C (2 Liters).

2.4. Absorbance measurements and kinetic analysis

Absorbance spectra of PBS and OCP and kinetics of OCP photoactivation (illumination with 5000 μmol photons·m^{-2}·s^{-1} of white light) and dark recovery were measured with a Specord S600 spectrophotometer (Analytic Jena) using 1 cm path-length cuvette. Experiments were performed at an OCP concentration of ~4.8 μM, corresponding to an OD of 0.3 at 496 nm (calculated using an epsilon equal to 63,000 M^{-1}·cm^{-1} [42]). Spectra were acquired in the 250–700 nm range for each time point. OCP^O photoactivation and OCP^R recovery were both monitored by measuring the increase and decrease in absorbance at 550 nm, respectively.

2.5. Isolation of PBS and fluorescence measurements

The purification of PBS from *Synechocystis* PCC 6803 and *Planktothrix agardhii* PCC 7805 was performed as previously described [43]. The PBS-fluorescence quenching yield was monitored using a pulse amplitude-modulated fluorimeter (101/102/103-PAM, Walz). All measurements were made in a 1 cm path-length stirred cuvette. PBS quenching induced by holo-OCP was measured in 0.5 potassium phosphate buffer (pH 7.5) at 23 °C, under strong blue–green light exposure (900 μmol photons m^{-2} s^{-1}). The PBS concentration used was 0.012 μM and the ratio of OCP to PBS was 40:1. OCP samples were pre-illuminated with 5000 μmol photons m^{-2} s^{-1} of white light at 4 °C. Samples in Pasteur pipettes were quickly frozen by immersion in liquid nitrogen. Fluorescence emission spectra at 77 K were recorded using a CARY Eclipse fluorescence spectrophotometer fluorometer (Varian).

2.6. Protein separation

Proteins were analyzed by SDS-PAGE on 15 % polyacrylamide gels in a Tris-MES buffer [44]. PBS samples were concentrated by precipitation with 10 % (v/v) TCA prior to loading (equal protein quantities in each lane). 10 μL at a PBS concentration of 0.5 μM were deposited per well. The gels were stained by Coomassie Brilliant Blue.

2.7. Femtosecond transient absorption spectroscopy (100 fs - 1 ns timescale)

Transient absorption measurements were performed using a Helios system from Ultrafast Systems. A short-pulse titanium sapphire oscillator (Mai Tai, Spectra Physics, 70 fs pulse length) followed by a high-energy titanium sapphire regenerative amplifier (Spitfire Ace, Spectra Physics, 100 fs, 1 kHz) provided the 800 nm beam, which was further split to generate: (1) a 532 nm pump pulse in the optical parametric amplifier (Topas Prime with a NirUVVis frequency mixer) and (2) a white light continuum (WLC) probe pulse in a sapphire crystal (430–780 nm). The remaining photons of the 800 nm probe-pulse were filtered just after white light continuum generation. The instrument response function (IRF) was estimated to be around 110 fs (FWHM). The pump-pulse diameter (FWHM) at the sample position was approximately 250 μm, for a pulse energy of 0.8 μJ. Absorbance over a 2 mm optical path was close to 0.7 at the excitation wavelength, corresponding to a concentration of 55 μM (or 1.9 mg/mL). The sample solution was stirred to keep the OCP solution fresh in the probed volume. The pump beam was depolarized to avoid anisotropy effects. To ensure that datasets are comparable to each other, they were all measured under identical conditions (at 22 °C) on similarly-aged proteins during a single experimental session. The transient absorption data were corrected for the chirp of white light continuum by aligning kinetics according to a delay introduced by given amount of the material between the OCP sample and the sapphire crystal (used for WLC generation of the probe). For all datasets, the difference absorbance (ΔA) value obtained at the bleaching extremum (in both spectral and temporal dimension) was normalized to −1. Transient spectra were projected onto a 5 nm-spaced grid to get kinetic traces. The comparison of pre-exponential factors at 490 nm (bleaching band) allowed us to estimate the quantum yield of the formation of the various intermediates. For interpretation, we used the most recent proposed model [32], whereby S_1, ICT and S* are formed from S_2 in parallel paths and decay mainly to S_0 without any interconversion and with only small contribution of excited-state absorption at 490 nm. For P_1 formation quantum yield, the positive absorbance contribution was taken into account [32]. Time constants determination and calculation of Decay Associated Difference Spectra (DADS or DAS) were achieved by global analysis using our custom-Python package [32] and the Glotaran software (https://glotaran.org). For the global analyses, a sum of four exponentials (S_2, ICT, S_1, S*) and an offset (representing long-lived photo-products with lifetime >50 ns, namely P_1) convolved by a Gaussian IRF (fixed to 110 fs) was used. Fitted results are reported in Table 1.

Table 1
Time constants and quantum yields obtained from fs and ns transient absorption spectroscopy experiments. (A) Lifetimes of ICT/S_1/S*/P_1 states derived from femtosecond transient absorption measurements (from data in Figs. 5 and S2), and estimated formation quantum yields derived from pre-exponential factors at 490 nm (the magnitude of the bleaching band of each DAS was extracted from the fitting procedure; for more details, see the Materials and methods section and [32]). The standard error is 10 %. P_1 yields are corrected for its positive absorbance contribution at 490 nm. (B) Time constants and yields (percentages in brackets) derived from ns-s transient absorption measurements for P_1, P_2/P_2' and $P_3/P_{N\text{-}M\text{-}X}$. Only in the case of P_1 are the values in brackets actual formation quantum yields; for P_2/P_2' and $P_3/P_{N\text{-}M\text{-}X}$, they indicate the relative contribution of the corresponding exponential term to the overall kinetic. Growing components are indicated in bold. Percentages in the OCP^R column are formation quantum yields of the red intermediates remaining at 10 ms (determined by a comparative actinometry method with ruthenium complex; for details, see Material and methods section and [46]).

Table 1A	ICT	S_1	S*	P_1
Syn-OCP_{CAN}	0.50 ps (25 %)	3.2 ps (59 %)	7.6 ps (16 %)	>1 ns (0.4 %)
Syn-OCP_{ECN}	0.66 ps (36 %)	2.8 ps (56 %)	10.1 ps (8 %)	>1 ns (0.6 %)
Plankto-OCP_{CAN}	0.43 ps (28 %)	2.8 ps (56 %)	7.1 ps (16 %)	>1 ns (0.4 %)
Plankto-OCP_{ECN}	0.30 ps (44 %)	1.7 ps (40 %)	5.4 ps (16 %)	>1 ns (0.4 %)

Table 1B	P_1	P_2/P_2'	$P_3/P_{N\text{-}M\text{-}X}$	OCP^R
Syn-OCP_{CAN}	45 ns (60 %)	830 ns (15 %) 22 µs (6 %)	380 µs (19 %)	0.11 %
Syn-OCP_{ECN}	46 ns (48 %)	400 ns (14 %)	890 µs (22 %) 83 ms (16 %)	0.08 %
Plankto-OCP_{CAN}	52 ns (65 %)	1.3 µs (35 %)	**1.1 ms (33 %)** **24 ms (67 %)**	0.17 %
Plankto-OCP_{ECN}	41 ns (35 %)	410 ns (31 %) 1.9 µs (19 %)	3.0 ms (15 %)	0.05 %

2.8. Nanosecond transient absorption spectroscopy (50 ns – 1 s timescale)

Measurements were performed with our custom apparatus described previously [45]. 532 nm nanosecond excitation pump pulses of 5 mJ energy were used (one pulse every 20 s for < 100 ms kinetics, one pulse every 40 s for kinetics over 100 ms). The probe light from the Xenon lamp was filtered using a 550 nm interference filter (10 nm FWHM) placed before the sample. Scattered pump light was removed by a notch filter placed after the sample. For each experiment, a solution of OCP with absorbance close to 0.7 at the excitation wavelength (1 cm pathlength, *i.e.* a concentration of 11 µM or 0.39 mg/mL) was placed in a 10 × 10 mm cuvette and thermalized at 22 °C. No stirring of the sample was applied, enabling to stretch the time window covered by the experiments. Each set of measurements included 100 replicates of each of the five time-windows, together covering the 50 ns – 1 s time range. Recorded data were merged and projected onto a logarithmic grid. Stability of the protein was checked by its steady-state absorbance after each experiment. The formation quantum yield of OCP^R was determined using ruthenium as an actinometer [46]. The difference molar absorption coefficient at 550 nm for OCP^R was estimated using the molar absorption coefficient (ε) of OCP^O at 490 nm = (63,000 $cm^{-1}{\cdot}M^{-1}$) [42] and that determined for OCP^R after 100 % photo-conversion at 8 °C $\varepsilon(OCP^R, _{550\ nm} \approx$ 48,000, 41,000, 47,000 and 40,000 $cm^{-1}{\cdot}M^{-1}$ for Syn-OCP^R_{CAN}, Syn-OCP^R_{ECN}, Plankto-OCP^R_{CAN} and Plankto-OCP^R_{ECN}, respectively). For each sample, data were fitted globally over the five time-windows using a three-exponential model accounting for three different intermediate states and an offset. The latter is attributed to OCP^R and therefore can be used to estimate the yield. Fitted results are shown in Table 1.

2.9. Crystallization

The N-tagged ECN-functionalized OCP from *Planktothrix agardhii* (Plankto-OCP_{ECN}), purified on Ni-NTA and phenyl-sepharose columns, was further subjected to size exclusion chromatography under dim red light (HiLoad 16/600 Superdex 75 pg, GE Healthcare). The protein eluted as a unique peak in 50 mM Tris-HCl buffer pH 7.4, 150 mM NaCl. Crystallization conditions were screened manually, using as starting conditions those that afforded crystallization of Syn-OCP [17] and *Arthrospira maxima* OCP [8]. The gel-filtrated Plankto-OCP_{ECN} sample was concentrated to 5.2, 6.6 and 7.0 mg/mL (the protein concentration was determined based on the absorption at 495 nm, using an extinction coefficient of 63,000 M^{-1} cm^{-1} [42]) and crystallization trials were performed in 24-well Limbro plates using the vapor diffusion method in the hanging-drop geometry. Crystallization drops were set at 4 °C by mixing 1 µL from the well solution with 1 µL of protein solution. The well solution, of 1 mL volume, was composed of 0.1 M or 0.2 M Bis-Tris pH 5.5 and increasing PEG 3550 concentrations (from 18 % to 25 %) were tested. Crystals appeared within 3 to 5 months in 0.2 M Bis-Tris pH 5.5, 20 %–25 % PEG 3550. Following this success, crystallization trials were optimized enabling growth of crystals in a few hours to few days at room-temperature (~20 °C). Crystallization of Plankto-OCP_{CAN} was achieved using a protein concentration of 1.5–2 mg/mL in 50 mM Tris-HCl pH 7.4, 150 mM NaCl, a well solution composed of 0.1 M sodium acetate, pH 5 and 20–25 % PEG4000, and by mixing these at 1:1 ratio in the crystallization drops.

2.10. X-ray data collection and processing and structure determination

X-ray data were collected at 100 K from crystals cryoprotected by a short soak in the mother liquor complemented with 18–20 % glycerol and directly frozen in the nitrogen gas stream at the European Synchrotron Radiation Facility (ESRF, Grenoble, France), at the Swiss Light Source (SLS, Villigen, Switzerland) or on the MicroMax-007 HF diffractometer (Rigaku) installed at the Max Planck Institute in Heidelberg (MPI-HD). Specifically, we used: (i) ESRF-ID23EH1, for collection of the Plankto-OCP_{ECN} structure in the $P2_1$ space group (1.7 Å resolution; λ = 0.979 Å; beamsize: 30 (h) × 30 (v) $µm^2$); (ii) ESRF-ID29, for collection of the Plankto-OCP_{ECN} in the *C*2 space group (1.7 Å resolution; λ = 0.976 Å; beamsize: 30 (h) × 30 (v) $µm^2$); (iii) SLS-X10SA (PXII), for collection of the Plankto-OCP_{CAN} structures in the $P2_1$ space group (1.4 resolution; λ = 0.99 Å; beamsize: 50 (h) × 10 (v) $µm^2$); and (iv) the MPI-HD diffractometer, for collection of the Plankto-OCP_{CAN} structure in the C2 space group (1.85 Å resolution; λ = 0.99 Å; beamsize: 50 (h) × 10 (v) $µm^2$). Data were collected with an oscillation range of 0.1 (ID29 and ID23-EH1), 0.2 (SLS-X10SA (PXII) or 0.25 degree (MPI-HD). All data were indexed using XDS [47], and scaled and merged using XSCALE [48].

2.11. Molecular replacement and structure refinement

Phaser [49] was used to phase by molecular replacement (MR) the data collected on crystalline Plankto-OCP_{ECN} in the *C*2 space group, using as a starting model chain A from the Syn-OCP_{ECN} structure (PDB id: 3mg1, [17]). We used the CCP4 [50] buccaneer pipeline, based on Buccaneer [51], Parrot [52] and Refmac5 [53] for the initial *in silico* rebuilding of the *C*2 Plankto-OCP_{ECN} structure (76.2 % and 92.8 % identity and similarity with respect to Syn-OCP), resulting in a model characterized by Rfree and Rwork values of 29.63 and 26.17, respectively, and wherein 306 residues had been placed in sequence in two fragments corresponding to the NTD and CTD. Examination of this model revealed imperfections in loop building, which were corrected manually using the molecular graphics program Coot [54]. The *C*2 Plankto-OCP_{ECN} structure was thereafter refined by iterative cycles of reciprocal-space refinement using Refmac5 and manual model-building in real-space using Coot. Therefrom, phasing of the *C*2 Plankto-OCP_{CAN}

data was achieved by rigid-body refinement with Refmac5, while that of the $P2_1$ Plankto-OCP_{ECN} and Plankto-OCP_{CAN} structures was achieved by molecular replacement with Phaser, using as a starting model the refined *C*2 Plankto-OCP_{ECN} structure devoid of the carotenoid, waters and protein alternate conformations. Refinement again consisted of iterative cycles of reciprocal-space refinement using Refmac5 and manual model-building in real-space using Coot. Using *C*2 Plankto-OCP_{CAN} as the reference structure, Cα-Cα distance difference matrices were prepared using a custom-written script, and the hinge motions of domains within monomers, and of monomers within dimers were evaluated using the hinge_find.py script available at https://github.com/gawells/hingefind, inspired from the hinge_find.tcl script [55] available at http://biomachina.org/disseminate/hingefind/hingefind.html. The presence of tunnels in OCP, and notably the extent and volume of the carotenoid binding tunnel, was examined using Caver3 [56] and the dedicated PyMOL [57] plugin available at https://pymolwiki.org/index.php/Caver3). Porcupine plots, showing for each structure the direction and distance travelled by Cα atoms with respect to the *C*2 Plankto-OCP_{CAN} structure, were prepared using the modevectors.py PyMOL script available at https://pymolwiki.org/index.php/Modevectors. Figures were prepared with PyMOL unless stated otherwise. Data processing and refinement statistics are shown in Table 2. *Planktothrix* OCP structures have been deposited in the wwPDB under accession codes 7qd0, 7qcZ, 7qd1 and 7qd2.

3. Results

3.1. Comparison of native (non-tagged) OCP from Planktothrix agardhii and Synechocystis PCC6803

The *Synechocystis* and *Planktothrix* species share the feature that only one *ocp* gene, classified in the OCP1 clade [16], and one *frp* gene are found in their genomes. The two OCP genes display 76.2 % and 92.8 % identity and similarity, respectively, with nearly all residues lining the carotenoid tunnel being conserved. We investigated whether or not the functionalizing carotenoid and his-tagging have an effect on the photoactivation and recovery kinetics of these two OCP, by expressing recombinantly the native (non-tagged), N-tagged and C-tagged *Planktothrix* and *Synechocystis ocp* genes in CAN or ECN producing *E. coli* cells (for details on constructs and on their expression and purification, see Materials and methods section).

We first compared the spectral properties at 9.5 °C of the native (non-tagged) CAN-functionalized Syn-OCP and Plankto-OCP (Fig. 2), viz. Syn-OCP_{CAN} and Plankto-OCP_{CAN}. The two proteins display identical absorption spectra in the dark-adapted (orange) inactive state (OCP^O), however slight differences are seen for the light-adapted (red) active state (OCP^R) (Fig. 2A, D and Supplementary Fig. 1). Both OCP^R_{CAN} spectra present an absorption maximum at 530 nm with a shoulder at 560 nm, which is slightly more pronounced in Syn-OCP^R_{CAN} (Fig. 2A and D). A difference positive absorbance maximum at 560 nm is observed in both OCP (Fig. 2B and E). The normalization of the difference spectra time series on the 470 nm peak shows that the ΔA (560 nm) to ΔA (470 nm) ratio is higher in Syn-OCP^R_{CAN} than in Plankto-OCP^R_{CAN} (Fig. 2C and F), pointing to a stronger absorption of the Syn-OCP^R state. This normalization also evidences a red shift in the spectra of the two OCP^R (from 545 to 550 to 560 nm) as they accumulate (Fig. 2C and F), suggesting that a conformational change could occur that stabilizes the OCP^R state upon increase of its concentration by prolonged illumination.

We then assayed photoactivation and thermal recovery kinetics of Syn-OCP_{CAN} and Plankto-OCP_{CAN} (Fig. 2G and H). Experiments were performed at 9.5 °C, to minimize the negative contribution of thermal recovery to the steady-state accumulation of OCP^R – i.e., to maximize OCP^R concentration in the photostationary equilibrium. Accumulation of OCP^R and recovery of the OCP^O state were monitored by following the rise and decrease in absorbance at 550 nm upon intense white-light illumination and subsequent transfer to darkness, respectively. Results in Fig. 2 show that Plankto-OCP^R_{CAN} not only accumulates faster than Syn-OCP^R_{CAN} (initial slope is twice as high), but it also recovers faster the dark OCP^O state. Indeed, Plankto-OCP^R_{CAN} recovers fully within the 20 min lapse of our experiment (Fig. 2H), whereas only 30 % of Syn-OCP^R has reconverted to OCP^O. The slow recovery kinetics at low temperature of Syn-OCP^R_{CAN} is known, and shared by other OCP1 from *Arthrospira* and *Tolypothrix* [15,16,43], whereas the fast recovery kinetics of Plankto-

Table 2
Data collection and refinement statistics. Statistics for the highest-resolution shell are shown in parentheses.

	Plankto-OCP_{ECN} *C*2	Plankto-OCP_{CAN} *C*2	Plankto-OCP_{ECN} $P2_1$	Plankto-OCP_{CAN} $P2_1$
PDB id.	7QD0	7QCZ	7QD1	7QD2
Wavelength	0.95	1.54	0.98	0.99
Resolution range	32.44–1.7 (1.76–1.7)	18.26–1.85 (1.92–1.85)	75.58–1.71 (1.75–1.71)	43.6–1.4 (1.45–1.4)
Space group	*C* 1 2 1	*C* 1 2 1	*P* 1 2_1 1	*P* 1 2_1 1
Unit cell	81.4 64.87 61.69 90 117.911 90	82.01 67.5 61.94 90 117.821 90	63.36 65.90 77.37 90 102.354 90	63.46 65.94 77.28 90 102.262 90
Total reflections	100,512 (10,488)	57,189 (4493)	214,925 (6579)	272,526 (27,565)
Unique reflections	30,920 (3104)	23,822 (1963)	60,669 (2735)	115,206 (11,285)
Multiplicity	3.3 (3.4)	2.4 (2.3)	3.5 (2.4)	2.4 (2.4)
Completeness (%)	98.61 (99.42)	92.59 (76.47)	90.0 (54.8)	93.90 (92.54)
Mean I/sigma(I)	13.78 (1.84)	11.96 (1.81)	11.16 (1.21)	11.47 (1.90)
Wilson B-factor	25.57	26.48	27.75	21.13
R-merge	0.046 (0.6095)	0.052 (0.5806)	0.063 (0.685)	0.036 (0.3938)
R-meas	0.055 (0.7256)	0.066 (0.7384)	0.074 (0.877)	0.046 (0.5066)
R-pim	0.030 (0.3894)	0.040 (0.4513)	0.038 (0.547)	0.028 (0.3153)
CC1/2	0.999 (0.843)	0.997 (0.682)	0.997 (0.426)	0.998 (0.852)
Reflections used in refinement	30,858 (3097)	23,803 (1963)	60,658 (1519)	115,047 (11,285)
Reflections used for R-free	1545 (154)	1190 (98)	3015 (81)	5753 (564)
R-work	0.1785 (0.3045)	0.1761 (0.3740)	0.1806 (0.4771)	0.2002 (0.2804)
R-free	0.2231 (0.3397)	0.2450 (0.4107)	0.2159 (0.5757)	0.2309 (0.2942)
CC(work)	0.967 (0.901)	0.968 (0.771)	0.942 (0.671)	0.956 (0.626)
CC(free)	0.957 (0.811)	0.937 (0.709)	0.923 (0.470)	0.942 (0.563)
Number of non-hydrogen atoms	3042	3017	5885	5819
Macromolecules	2698	2542	5099	5120
Ligands	85	42	82	100
Solvent	259	433	704	599
Protein residues	308	309	621	614
RMS(bonds)	0.030	0.005	0.05	0.007
RMS(angles)	1.44	0.86	1.34	0.94
Ramachandran favored (%)	98.36	97.70	98.86	98.68
Ramachandran allowed (%)	0.66	1.64	0.98	0.99
Ramachandran outliers (%)	0.99	0.66	0.16	0.33
Rotamer outliers (%)	3.44	2.91	2.76	2.18
Molprobity score	1.84	1.79	1.72	1.51
Clashscore	7.46	6.65	5.68	5.02
Average B-factor	34.30	30.31	32.37	30.40
Macromolecules	32.93	28.56	31.03	29.61
Ligands	37.47	23.55	24.54	24.16
Solvent	47.50	41.26	43.00	38.15

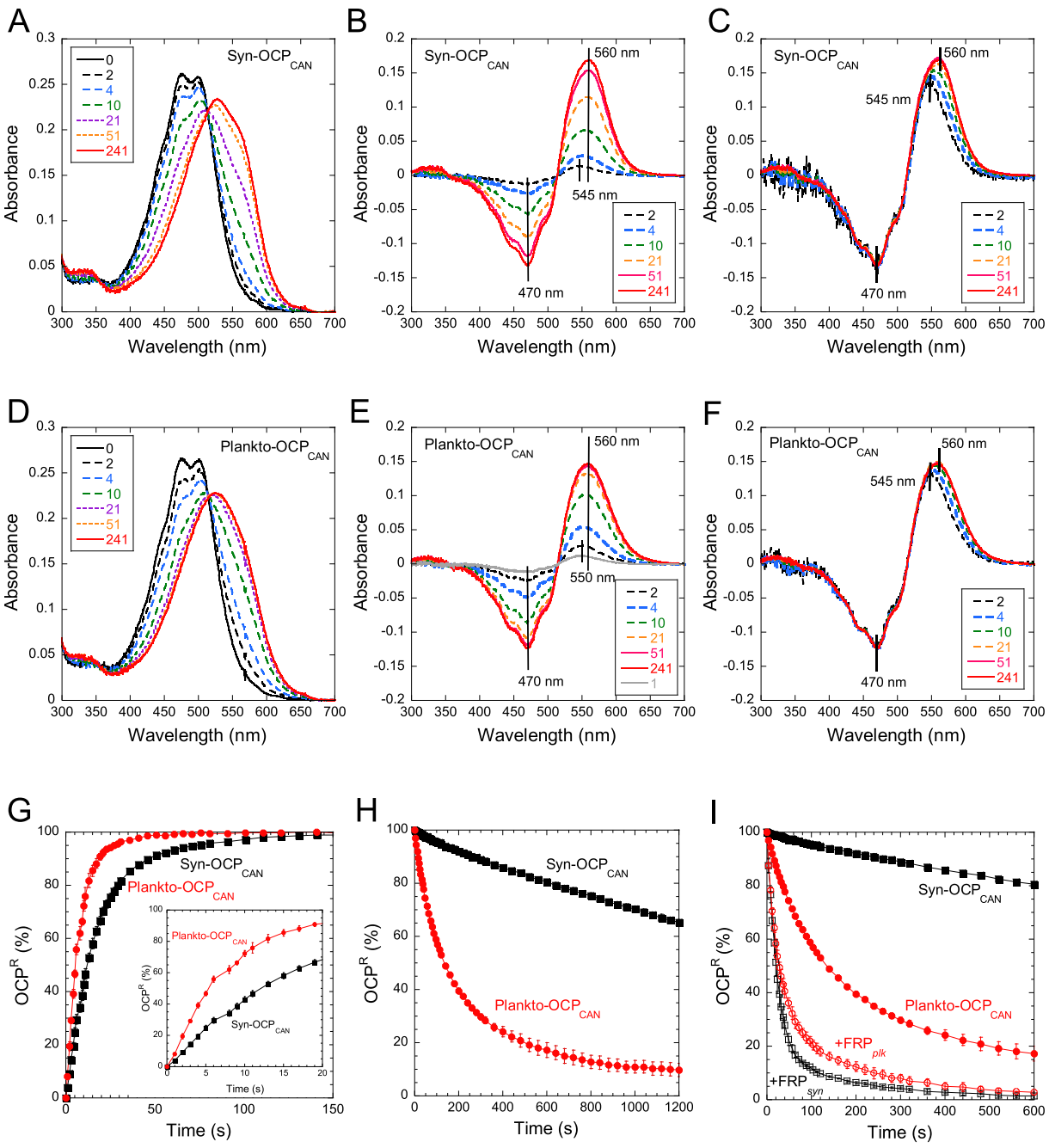

Fig. 2. Photoactivation and recovery of native (non-tagged) CAN-functionalized *Synechocystis* and *Planktothrix* OCP. (A and D) Absorbance spectra of Syn-OCP$_{CAN}$ (A) and Plankto-OCP$_{CAN}$ (D) at different times of illumination. (B and E) Difference absorbance spectra derived from A and D respectively. (C and F) Difference absorbance spectra normalized at 470 nm derived from A and D. (G–I) Kinetics of photoactivation (G) and recovery (H–I) of CAN-functionalized Syn-OCP (black) and Plankto-OCP (red). The inset in G shows a close-up view on the first 30 s of illumination. In (I), the effect of the presence of FRP is shown. The FRP to OCP ratio was 1:1. The accumulation of OCP^R and its thermal deactivation were followed by increase and decrease of absorbance at 550 nm under illumination and in the dark, respectively. Illumination was performed with white light (5000 μmol photons $m^{-2}{\cdot}s^{-1}$) at 9.5 °C. Error bars: standard deviation. Each curve represents the mean of three independent measurements, respectively. (For interpretation of the references to color in this figure legend, the reader is referred to the web version of this article.)

OCP$^R_{CAN}$ is unprecedented for a member of the OCP1 clade and reminisces those displayed by members of the OCP2 [14,16] and OCPX [16] clades. In these clades, the faster OCP^R-to-OCP^O recovery rate coincides with the inability to interact with FRP [15,16]. Therefore, we challenged a possible misclassification of Plankto-OCP as a member of the OCP1 clade by investigating whether or not its recovery is accelerated by the presence of FRP. For this purpose, *Synechocystis* and *Planktothrix* FRPs were expressed and purified, and assayed for their species-specific effect on the CAN-functionalized native OCP (non-tagged). Fig. 2I shows that the presence of Plankto-FRP accelerates the recovery rate of Plankto-OCP$_{CAN}$ (~2.5 fold increase in the initial rate) although the observed acceleration is smaller than for Syn-OCP$_{CAN}$ in presence of Syn-FRP (~20 fold increase in the initial rate). These results confirm the correct assignment of Plankto-OCP to the OCP1 clade. They also show that the species-specific acceleration of OCP recovery by FRP is independent of the rate of the reaction in the absence of FRP.

3.2. Influence of the his-tag on OCP photoactivation and recovery kinetics

We have recently shown that the location of the his-tag influences the photoactivation speed (initial rate) in *Synechocystis* OCP [32]. In particular, by using intermediary light intensity (~100 μmol photons·m^{-2}·s^{-1}) we observed a more efficient accumulation of OCP^R in Ntag-Syn-OCP$_{ECN}$ than in Ctag-Syn-OCP$_{ECN}$ despite a comparable P1 formation quantum yield. Hence, we here asked whether or not presence of a his-tag, and its location at the N- or C-terminus, would influence the photoactivation and thermal recovery of Plankto-OCP and Syn-OCP. We compared results obtained from the N-tagged (Ntag-Syn-OCP$_{CAN}$ and Ntag-Plankto-OCP$_{CAN}$) and C-tagged (Ctag-Syn-OCP$_{CAN}$ and Ctag-Plankto-OCP$_{CAN}$) variants of these OCP to those of the native counterparts. It was consistently observed that the native proteins photoactivate faster than the his-tagged proteins, and that N-tagged OCP photoactivate faster than their C-tagged counterparts (Fig. 3A and B). Nevertheless, when triggered with 5000 μmol photons m^{-2}·s^{-1} white light, the effect of his-tagging on the photoactivation rate was not severe. Focusing next on the thermal OCP^R to OCP^O recovery, we found that it is delayed by presence of a his-tag in all tested OCP (Fig. 3C and D), although the effect is more pronounced in Plankto-OCP$_{CAN}$, which recovers faster than Syn-OCP$_{CAN}$. Introduction of a his-tag at the N-terminus hardly affects the recovery of Plankto-OCP, whereas that at the C-terminus slows down the recovery by a factor of ~6 (Fig. 3D). In contrast, in Syn-OCP, his-tagging only has a slight effect on recovery.

3.3. Influence of the functionalizing carotenoid on OCP photoactivation and recovery kinetics

We then investigated the extent to which photoactivation and thermal recovery are affected by the type of functionalizing carotenoid. As it was found above that N-tagged and native OCP are the most similar in terms of photoactivation and recovery rates, we used N-tagged Syn-OCP and Plankto-OCP in the following assays. Irrespective of the species, OCP^R accumulation was found to be slower in ECN-functionalized than CAN-functionalized OCP (Fig. 4A and B), while recovery was faster (Fig. 4C and D). Indeed, the initial rate of OCP^R accumulation is twice as high in Ntag-Syn-OCP$_{CAN}$ and Ntag-Plankto-OCP$_{CAN}$ than in their ECN-functionalized counterparts (Fig. 4A and B). The most straightforward explanation for these observations is that CAN stabilizes OCP^R and/or facilitates carotenoid translocation during photoactivation. Alike their CAN-functionalized counterparts (Fig. 2A, D), the photoactivated Syn-OCP$^R_{ECN}$ and Plankto-OCP$^R_{ECN}$ are spectrally similar, both presenting a maximum absorption at 510 nm (Fig. 4E and H). In difference absorption spectra, the positive maximum is yet at 550.5 nm, i.e., slightly blue shifted compared to the OCP$_{CAN}$ counterparts (Figs. 2 and 4F, I), due to a

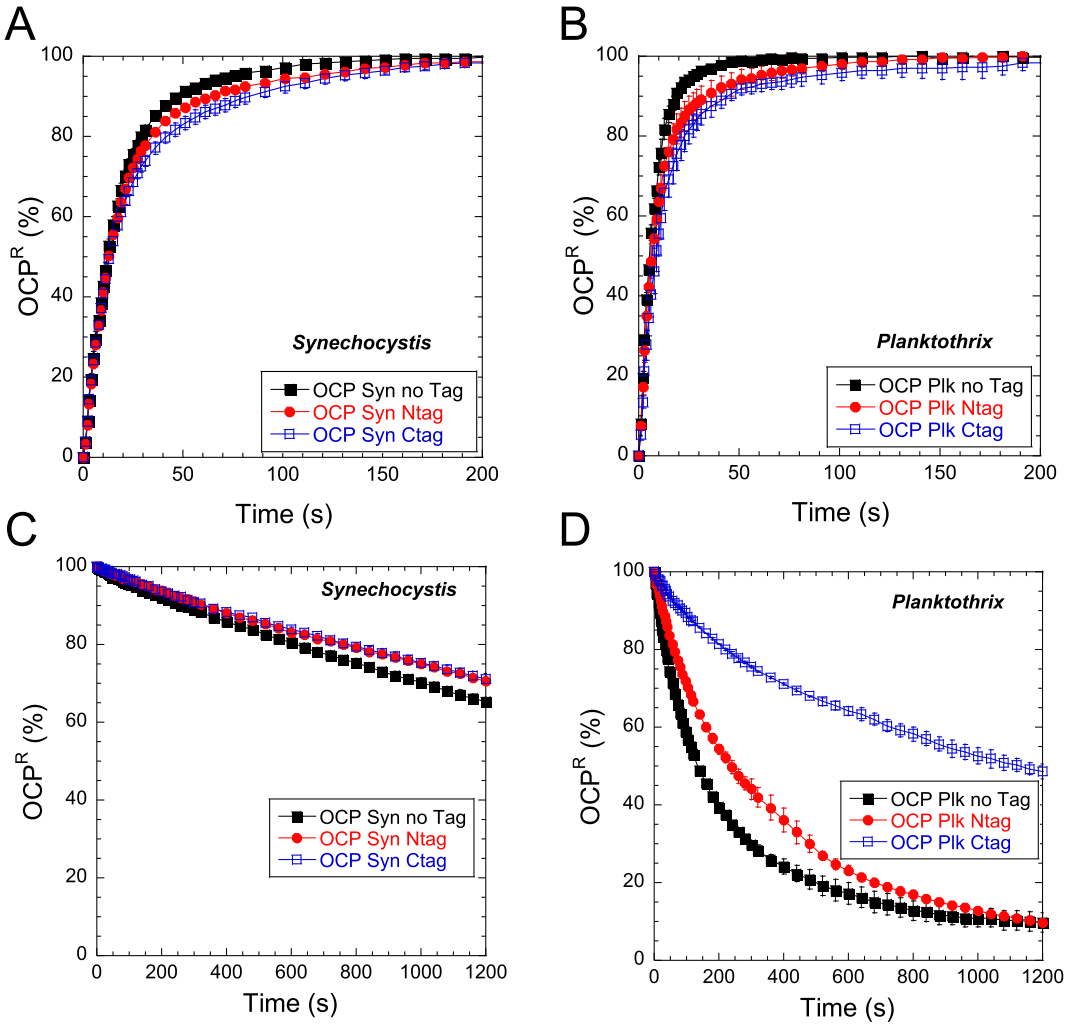

Fig. 3. Presence of a his-tag has an impact on photoactivation and recovery. Effect of presence and position of a his-tag on photoactivation (A–B) and recovery (C–D) of CAN-functionalized *Synechocystis* and *Planktothrix* OCP. The accumulation of OCP^R and its thermal deactivation were followed by increase and decrease of absorbance at 550 nm under illumination and in the dark, respectively. The OCP were illuminated with white light (5000 μmol photons m^{-2}·s^{-1}) at 9.5 °C. Error bars: standard deviation. Each curve represents the mean of three independent measurements.

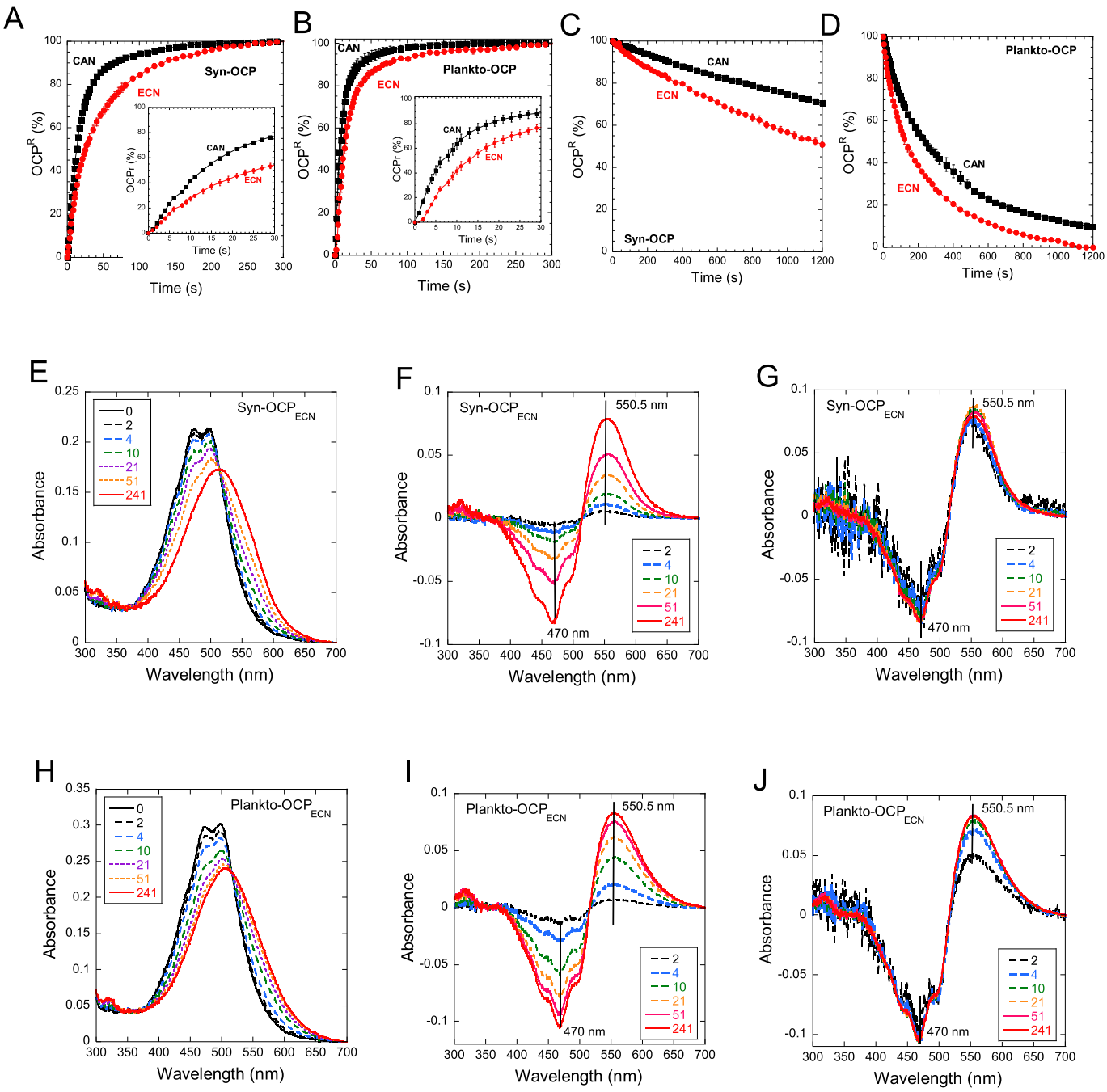

Fig. 4. Effect of the nature of the functionalizing ketocarotenoid on photoactivation and recovery of N-terminally his-tagged *Synechocystis* and *Planktothrix* OCP. (A–B) Kinetics of photoactivation of Syn-OCP (A) and Plankto-OCP (B) functionalized with ECN (red) or CAN (black). The insets in A and B show a close-up view on the first 30 s of illumination. The OCP were illuminated with white light (5000 μmol photons $m^{-2}{\cdot}s^{-1}$) at 9.5 °C. (C and D) Thermal recovery in darkness of ECN- (red) and CAN-functionalized Syn-OCP^R (C) and Plankto-OCP^R (D). The accumulation of OCP^R and its thermal recovery were monitored by following the increase and decrease of absorbance at 550 nm under illumination and in the dark, respectively. Error bars: standard deviation. Each curve represents the mean of three independent measurements, respectively. (E and H) Absorbance spectra of ECN-functionalized Syn-OCP (E) and Plankto-OCP (H) at different times of illumination. (F and I) Raw difference absorbance spectra derived from E and H, respectively. (G and J) Difference absorbance spectra derived from E and H, respectively, after normalization on the 470 nm band. (For interpretation of the references to color in this figure legend, the reader is referred to the web version of this article.)

reduced shoulder at 560 nm. It is notable that an increase in the ΔA (550 nm) to ΔA (470 nm) ratio is observed in the first 10 s of illumination of Plankto-OCP_{ECN} (Fig. 4J); such an effect is not seen with Syn-OCP_{ECN} (Fig. 4G).

We inquired whether or not the increased photoactivation rate of CAN-functionalized Plankto-and Syn-OCP stems from changes in the carotenoid excited state dynamics. By carrying out fs-ns timescale transient absorption spectroscopy on the four OCP variants, we could estimate the primary quantum yields for the formation of the five intermediates occurring during the initial 100 fs-100 ps of the photoactivation cascade, i.e., the S_2, S_1 and ICT excited-states, the S* state, and the first photoproduct P_1 (see Material and methods section and [32]). The formation and decay of these states in CAN- and ECN-functionalized Plankto-OCP (Fig. 5) and Syn-OCP (Supplementary Fig. 2) were monitored by recording and globally-fitting femtosecond transient spectra collected at different time delays following a 110-fs pulse

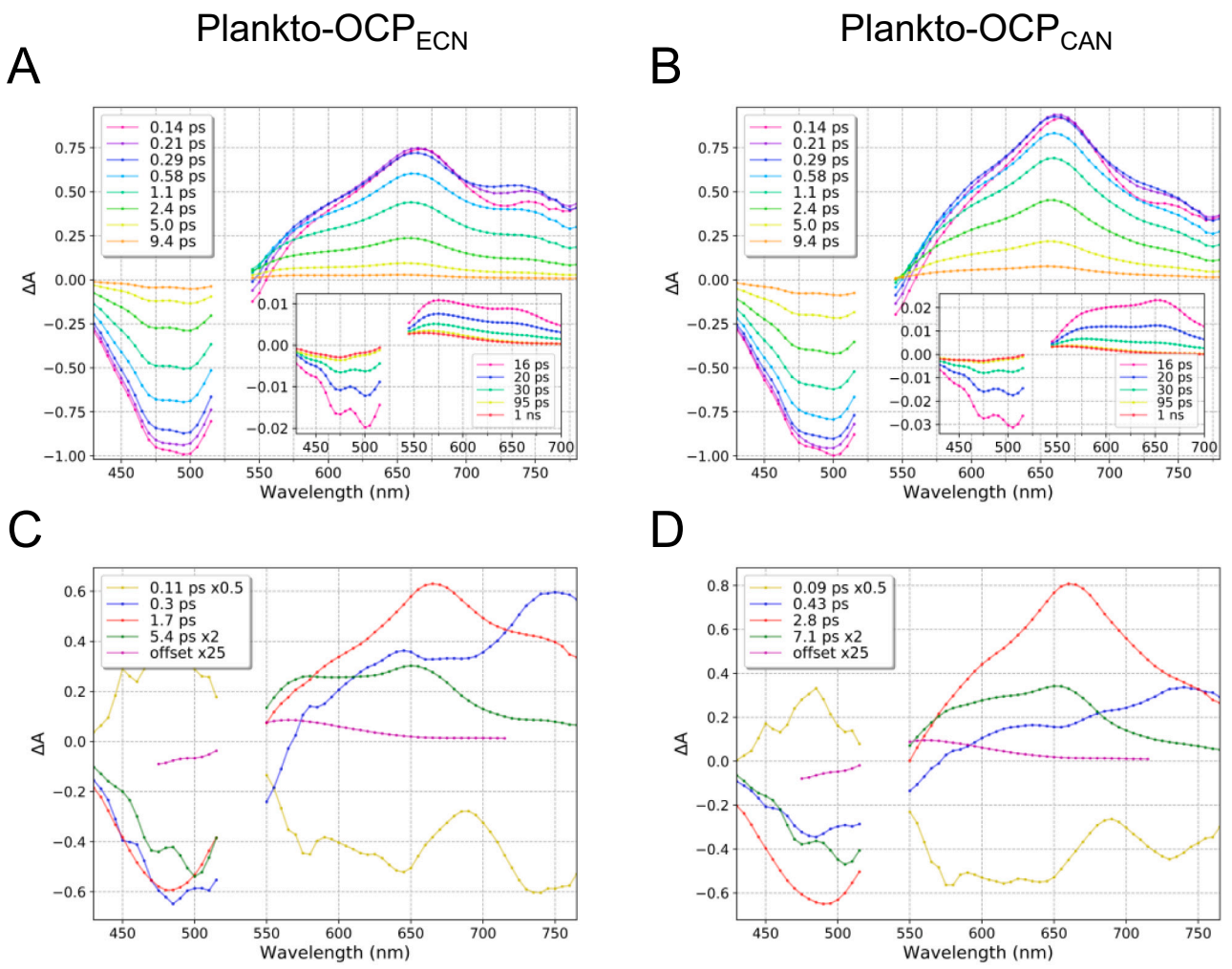

Fig. 5. Femtosecond transient absorption data collected on the Ntag-Plankto-OCP. (A, B) Transient absorption spectra measured after excitation at 532 nm are shown for time delays ranging between 0.14 ps and 1 ns for (A) Ntag-Plankto-OCP$_{ECN}$ and (B) Ntag-Plankto-OCP$_{CAN}$. All datasets were normalized to −1 at the bleaching extremum (*i.e.,* ~490 nm), in both spectral and temporal dimensions. (C, D) Decay Associated Spectra (DAS) obtained from the global fit of the transient absorption spectra shown in (A) and (B), respectively. Data were fitted using four exponentials (S_2, ICT, S_1, S*) and an offset (representing long-lived photo-products with lifetime > 50 ns, namely P_1) convolved by a Gaussian IRF (fixed to 110 fs).

excitation at 532 nm (see the Materials and methods section for further details).

In agreement with previous reports, we found that 0.15 ps after excitation, the S_2 excited state has already started to decay. Transient absorption spectra are characterized by a negative ground state bleaching (GSB) band with an extremum at ≈500 nm, indicative of OCP^O depopulation, and by positive absorption (ESA) bands for the S_1, ICT and S* states peaking at ≈660 nm, ≈750 nm and ≈575 nm (shoulder), respectively. All electronically and vibrationally excited states decay by the 30 ps delay, and only a broad positive band centered at ≈560 nm, previously assigned to the photoproduct P_1 [19,32], can be seen at the 95 ps time delay. P_1 shows no spectral evolution in our experimental time window, i.e., up to 1 ns time delay.

Four exponential components (S_2, ICT, S_1 and S*) and an offset (P_1) were accounted for in the global decay analysis, enabling to extract the decay associated spectra (DAS) and lifetimes of the S_2, ICT, S_1, S* and P_1 states in ECN- and CAN- functionalized Plankto-OCP (Fig. 5C and 5D) and Syn-OCP (Supplementary Fig. 2C and D). Note that as our resolution is about 110 fs, the DAS of the short-lived S2 state is greatly distorted by convolution with IRF. The difference spectrum obtained 30 ps after the excitation (offset value in the sum of exponentials) is attributed to the P_1 intermediate state. Using the GSB kinetics, and assuming that the S_1, ICT and S* states all form from S_2 and parallelly decay to the ground state S_0, we could estimate the quantum yields (QY) of each state, including the P_1 state. In agreement with previous reports, the ps excited-state dynamics and yields are similar for the four tested OCP variants, with similar DAS observed for the ICT (blue), S_1 (red), S* (green) and P_1 (magenta) states, respectively (Fig. 5C and D). However, a careful comparison of the DAS of CAN- and ECN-functionalized OCP reveals that the absorbance amplitudes above 700 nm of the S_1 and ICT states are higher in the ECN-functionalized OCP, reflecting a more pronounced ICT character in these states. The lifetimes derived from the global fitting of our data are also in agreement with previous reports [58], viz. ~0.10 ps (± 0.01 ps), ~0.5 ps (± 0.2 ps), ~2.6 ps (± 0.9 ps) and ~7.5 ps (± 2.5 ps) for the S_2, ICT, S_1 and S* states of the four OCP, respectively (Fig. 5 and Table 1). We note that differences are seen for the lifetimes of the S_1 and S* states in the ECN and CAN-functionalized OCP, which are mostly pronounced in Plankto-OCP. As expected from the DAS and the literature [40], and irrespective of the considered OCP variants, the formation QY for the ICT and S* states are lower and higher in CAN-functionalized OCP, respectively. The observed P_1 yield is yet similar in the four tested OCP (≈0.5 ± 0. 1 %), in agreement with recent results from us [32], and others [19,23].

The above-described fs-ns transient spectroscopy data exclude the

hypothesis that the type of carotenoid or OCP variant significantly influences the yield of P_1. Hence, we next examined the ns-s dynamics by performing nanosecond transient absorption experiments, whereby a nanosecond laser pulse was used to trigger excitation and the photoactivation outcome was probed in the 50 ns – 1 s time window by monitoring changes in the absorbance at 550 nm (Fig. 6). Indeed, on these timescales, the maximum difference-absorbance varies between 563 nm, characteristic of the P_1 state, and 550 nm, signing for the nascent OCP^R state. Intermediate states were assigned on the basis of earlier reports, with the P_1, P_2-P_2' and $P_3(P_N)/P_M/P_X$ states displaying lifetimes of ~50 ns, ~0.5–10 μs, and ~1–100 ms, respectively. Please recall that these states were proposed to be associated with (i) rupture of H-bonds between the carotenoid and the protein scaffold (P_1); (ii) rearrangement of the carotenoid at the NTD/CTD interface (P_2/P_2') and translocation of the carotenoid from the NTD/CTD interface into the NTD (P_3); and (iii) NTE and CTT detachment (P_M) followed by dissociation of the two domains (P_X), respectively. A last conformational change thence occurs, yielding the metastable OCP^R from P_x (Fig. 1). This last step could correspond to the repositioning of the CTT on the CTD-half of the carotenoid tunnel [34]. Note that partial recovery of the OCP^O state occurs at all steps (see Fig. 1), explaining the decrease in absorbance at 550 nm over the probed time window.

Clear differences are seen between the four tested OCP variants in these experiments. First, irrespective of the carotenoid, the starting difference absorbance signal (at 50 ns) is higher for Plankto-OCP (~0.002) than for Syn-OCP (~0.0015), suggesting a higher P_1 yield (Fig. 6). This observation contradicts the above assumption that the P_1 yield is the same for all investigated OCP, but can be rationalized by recalling that (i) in the fs-ns experiments, the GSB band at 490 nm is used to estimate the P_1 yield, instead of the characteristic positive absorption band at 563 nm, in the ns-s experiments; and, most importantly, (ii) a large fraction of P_1 reverts to the dark-adapted OCP^O state. Thus, the higher P_1 yield observed for Plankto-OCP at the start of ns-s transient absorption experiments (50 ns) could be related to a reduced recovery from P_1 of the Plankto-OCP^O state, rather than from an increased P_1 yield. Also irrespective of the functionalizing carotenoid, the difference absorption of Plankto-OCP and Syn-OCP drop by about 60 % and 40 % on the ns - μs time scale, respectively, with a larger drop in the Plankto-OCP signal that could underlie sub-optimal translocation of the carotenoid into the Plankto-NTD, compared to the Syn-NTD. The most important differences between Plankto-OCP and Syn-OCP are visible in the μs to ms timescale, whereas differences between CAN- and ECN-functionalized OCP concentrate in the ms-s time window. Thus, both carotenoid translocation and NTE/CTT detachments seem to be affected by the change in protein scaffold, but it is domain dissociation that is most affected by a change in the functionalizing carotenoid. This step appears to be faster and more efficient in CAN-functionalized OCP, with a slight increase in ΔA (550 nm) being visible after 1 ms, whereas recovery to the initial state is higher for ECN-functionalized OCP, as evidenced by the decrease of ΔA (550 nm). The observation of this decline being present only in ECN-functionalized OCP is in line with the observation that CAN-functionalized OCP can be photoactivated more efficiently (Fig. 4). In the case of Plankto-OCP_{CAN}, we observe faster domain separation and no recovery to OCP^O on the μs-s timescale, suggesting 100 % conversion efficiency from P_3 to final OCP^R. The larger difference absorption signal observed for Plankto-OCP (most notably Plankto-OCP_{CAN}) on the 10 ms - 1 s time window mirrors the difference in photoactivation efficiency observed in stationary irradiation experiments.

Multiscale exponential fitting was carried out to extract the lifetimes of the ns-s intermediate states (Table 1). The lifetime of the P_1 state was found to be almost independent of the OCP variant, i.e., ~50 ns. For the P_2-P_2' states (i.e., on the 50 ns to 10 μs time scale), data were fitted by one or two exponentials, depending on the case, yielding lifetimes in the order of 0.5–2 μs. Likewise, for the $P_3/P_N/P_X$ states (i.e., on the 0.1–10 ms time scale), either one or two exponentials were required to fit the data, yielding lifetimes in the order of 0.1–1 ms. Note that these lifetimes are in good agreement with those reported earlier based on experiments carried out on the C-tagged Syn-OCP_{ECN} [19,23]. Regardless, our data establish that the OCP^R yield is higher for CAN-functionalized OCP, and that Plankto-OCP photoactivates more efficiently. Thus, the differences observed in the photoactivation efficiency of CAN- and ECN-functionalized Plankto- and Syn-OCP stem from evolutions observed during the (comparatively-slow) carotenoid translocation, NTE/CTT detachment and domain dissociation steps – but not from changes in the excited-state dynamics of the OCP-embedded carotenoid. The experimental setup did not allow evaluating a lifetime for OCP^R, but previous reports have pointed to the second timescale [23].

3.4. Interaction between OCP and the phycobilisome

We inquired the energy-quenching performance of the various ECN- and CAN-functionalized OCP, focusing on OCP and PBS from *Synechocystis* and *Planktothrix*. The PBS from *Synechocystis* has been well

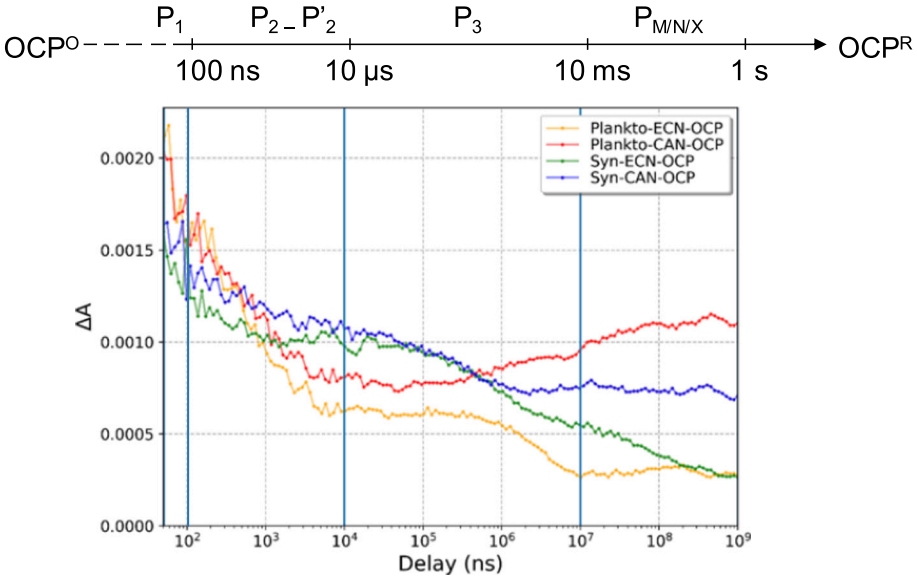

Fig. 6. Nanosecond-second dynamics in CAN- and ECN-functionalized Plankto-OCP and Syn-OCP. Time evolution (50 ns to 1 s) of the difference absorption signals at 550 nm recorded after excitation by a 532 nm ns-pulse of Plankto-OCP_{ECN} (yellow), Plankto-OCP_{CAN} (red), Syn-OCP_{ECN} (green) and Syn-OCP_{CAN} (blue). The intermediate states proposed [12,19,23] to underlie the observed absorption changes are indicated at the top of the figure. Measurements were carried out at 22° C. Each set of measurements included 100 replicates of each of the five merged time-windows, together covering the 50 ns – 1 s time range. (For interpretation of the references to color in this figure legend, the reader is referred to the web version of this article.)

characterized in several laboratories, including ours [43,59], yet no information was available regarding the *Planktothrix* PBS. Hence, a prerequisite was to characterize it biochemically and spectroscopically (Supplementary Fig. 3). We found that similar to *Synechocystis* PBS, *Planktothrix* PBS consists of a core (formed by three cylinders containing four allophycocyanin (APC) trimers) from which radiate six rods constituted of three phycocyanin (PC) hexamers.

With this characterization in hand, we pursued the investigation of native Syn-OCP and Plankto-OCP energy-quenching activities, focusing first on the effect of the functionalizing-carotenoid (Fig. 7) in species-specific OCP/PBS complexes. The decrease of PBS fluorescence was followed using a PAM fluorimeter during incubation of PBS under strong blue-green light and in presence of pre-photoactivated OCP. Under these conditions, a faster and larger decrease of fluorescence is suggestive of a stronger OCP-PBS interaction. We found that native Syn-OCP$_{CAN}$ and Syn-OCP$_{ECN}$ induce similar Syn-PBS fluorescence quenching (~75 % of PBS fluorescence is quenched after 300 s), despite a slightly lower initial rate for native-Syn-OCP$_{CAN}$ suggesting a weaker binding to the PBS (Fig. 7A). This hypothesis was confirmed by the eight times faster PBS fluorescence recovery observed for native-Syn-OCP$_{CAN}$, compared to native-Syn-OCP$_{ECN}$ (Fig. 7B). The nature of the functionalizing-carotenoid also had an effect on native-Plankto-OCP quenching efficiency and on the Plankto-PBS fluorescence recovery rate. PBS fluorescence quenching was twice more efficient with native-Plankto-OCP$_{ECN}$ than with native-Plankto-OCP$_{CAN}$ (75 and 40 % of fluorescence quenching after 300 s incubation, respectively) and fluorescence recovery was nearly three times faster for native-Plankto-OCP$_{CAN}$ than native-Plankto-OCP$_{ECN}$ (Fig. 7C, D). These results support the hypothesis that CAN-functionalized OCP displays a reduced affinity for the PBS.

We also investigated the effect of a his-tag, present either at the N- or C-terminus, on the species-specific PBS-fluorescence quenching efficiency and recovery rate (Fig. 8). We found that irrespective of the species (i.e., for both Syn-OCP + Syn-PBS and Plankto-OCP + Plankto-PBS), his-tagged OCP are more efficient at inducing PBS-fluorescence quenching, with C-tagged OCP further surpassing the N-tagged variants (Fig. 8A and B). This effect is most clear when considering the native, N-tagged and C-tagged Plankto-OCP/PBS complexes (Fig. 8B). A possible rationalization could come from the higher stabilization of the OCP^R state upon his-tagging at the C-terminus. However, this stabilization is not sufficient to explain the observed drastic difference in PBS fluorescence-recovery rates. Indeed, only up to 20 % of the initial PBS fluorescence is recovered after 20 min incubation in the dark with the C-tagged Plankto-OCP, which is at variance with the full recoveries observed when native or N-tagged Plankto-OCP and Syn-OCP are used (Fig. 8D, E). Thus, we favor the hypothesis that atop of stabilizing OCP^R, the C-terminal his-tag also stabilizes the OCP^R/PBS complex, explaining both the faster quenching and slower recovery.

In the past, we demonstrated that *Synechocystis*, *Arthrospira* and *Anabaena* OCP bind more strongly to the *Synechocystis* PBS than to the *Anabaena* or *Arthrospira* PBS [43], while Syn-OCP binds weakly to the PBS from other species [43]. Hence, we asked whether or not these conclusions would hold for Plankto-OCP and Plankto-PBS as well. We found that irrespective of the presence and position of the his-tag, Plankto-OCP binds more strongly to Syn-PBS than to Plankto-PBS, with all Plankto-OCP variants inducing a faster and more efficient fluorescence quenching of Syn-PBS (Fig. 8C) compared to Plankto-PBS (Fig. 8B). Furthermore, the Syn-PBS fluorescence recovery was virtually null, indicating that the complex formed by Plankto-OCP and Syn-PBS is highly-stable at 0.5 M phosphate (Fig. 8F). Contrastingly, Syn-OCP was unable to induce Plankto-PBS fluorescence quenching even at higher phosphate concentrations (up to 1.4 M phosphate), suggesting that it is able to interact only with Syn-PBS.

3.5. Structures of CAN- and ECN-functionalized Planktothrix OCP reveal new features

The crystal structures of *Anabaena* PCC 7120 (PDB id: 5hgr; also referred to as *Nostoc*) and *Tolypothrix* PCC 7601 (PDB id: 6pq1; also referred to as *Fremyella diplosiphon*) OCP have been solved in the CAN-functionalized states, while that of *Arthrospira maxima* (PDB id: 5ui2; also referred to as *Limnospira*) was determined in hECN functionalized states. Only the structure of *Synechocystis* PCC 6803 OCP was solved in both the CAN- and the ECN-functionalized states (PDB ids: 4xb5 and 3mg1, respectively), offering a first basis to rationalize the more efficient photoactivation observed for CAN-functionalized OCP in transient absorption (Fig. 6) and photostationary experiments (Fig. 4). Structural information on Plankto-OCP was yet absent, preventing identification of the structural features that could underlie its functional characteristics – notably, the thwarted translocation of carotenoids into the NTD, revealed by transient absorption spectroscopy, and the increased photoactivation rate and lower stability of its OCP^R state, revealed by photostationary experiments (Figs. 4 and 6).

Hence, we set to characterize the structure of Ntag-Plankto-OCP in the CAN- and ECN-functionalized states. The structure was solved, for each of these, in two space groups, viz. *C*2 and *P*2$_1$, revealing a remarkable conservation of the secondary structure (Fig. 9A) (Table 2). In the *P*2$_1$ space group, the asymmetric unit features the dimer that has been observed in previous structures [8,17,21,30,58,60,61]. Note that in the case of Syn-OCP$_{CAN}$ (4xb5) and *Tolypothrix*-OCP$_{CAN}$ (6pq1), the dimer is crystallographic, i.e., the dimerization interface perfectly aligns with a crystallographic axis; hence, the asymmetric unit confusingly features a monomer and application of symmetry operations are needed

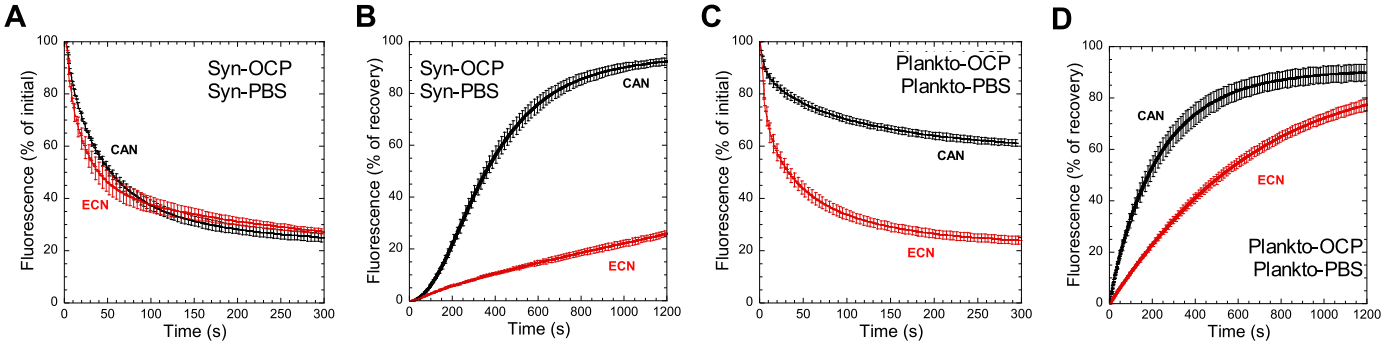

Fig. 7. Effect of ketocarotenoid on OCP-PBS interaction. (A, C) Syn-PBS (A) and Plankto-PBS (C) fluorescence-quenching induced at 23 °C in 0.5 M phosphate buffer by non-tagged (native) CAN- (black) and ECN- (red) functionalized Syn-OCP (A) and Plankto-OCP (C). For these experiments, OCP was pre-photoactivated by illumination with a strong white light (5000 μmol photons $m^{-2}{\cdot}s^{-1}$) at 4 °C, then mixed with Syn-PBS or Plankto-PBS at a 40:1 ratio, and kept under illumination by strong blue-green light (900 μmol photons $m^{-2}{\cdot}s^{-1}$) during the lapse of the measurement. (B, D) Dark recovery of fluorescence in Syn-PBS (B) and Plankto-PBS (D). In all graphs, 100 % of fluorescence corresponds to the initial fluorescence of PBS without quenching. Error bars: standard deviation. Each curve represents the mean of three independent measurements. (For interpretation of the references to color in this figure legend, the reader is referred to the web version of this article.)

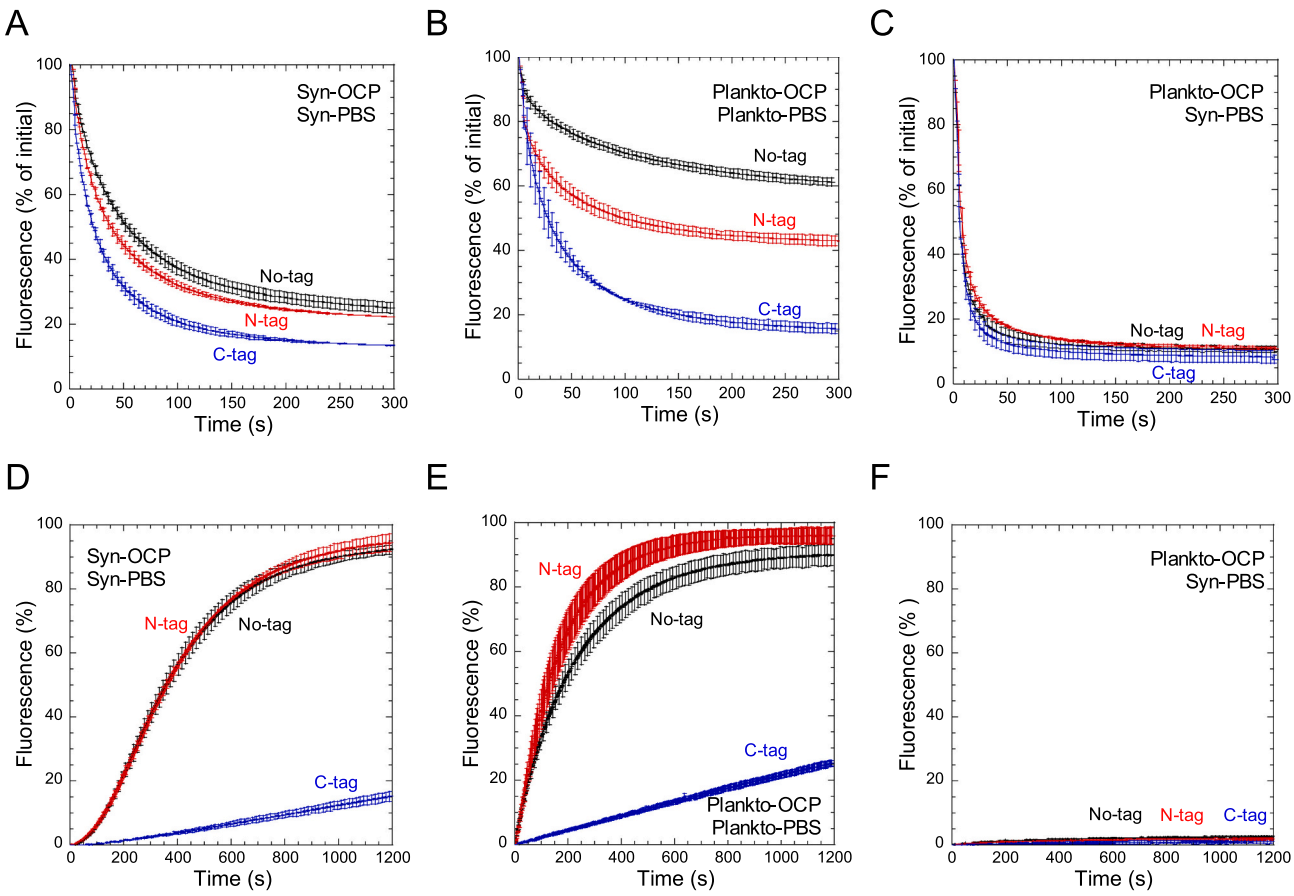

Fig. 8. Effect of the presence and position of a his-tag on OCP-PBS interaction. (A-C) *Synechocystis* (A, C) and *Planktothrix* (B) PBS fluorescence quenching induced at 23 °C in 0.5 M phosphate buffer by native (non-tagged; black), N-tagged (red) and C- tagged (blue) CAN-functionalized Syn-OCP (A) and Plankto-OCP (B, C). For these experiments, OCP was pre-photoactivated by illumination with a strong white light (5000 μmol photons $m^{-2}{\cdot}s^{-1}$) at 4 °C, then mixed with Syn-PBS or Plankto-PBS at a 40:1 ratio, and kept under illumination by strong blue-green light (900 μmol photons $m^{-2}{\cdot}s^{-1}$) during the lapse of the measurement. (D–F) Dark recovery of fluorescence in Syn-PBS (D, F) and Plankto-PBS (E). In all graphs, 100 % of fluorescence corresponds to the initial fluorescence of PBS without quenching. Error bars: standard deviation. Each curve represents the mean of three independent measurements. (For interpretation of the references to color in this figure legend, the reader is referred to the web version of this article.)

to reveal the dimer. In Syn-OCP_{ECN} (3mg1), Anabaena OCP_{CAN} (5hgr) and Arthrospira-OCP_{ECN} (5ui2), however, the asymmetric unit features a dimer. In the case of Syn-OCP, this dimer was recently shown to naturally occur in vitro [62,63] with a dissociation constant in the order of 14–17 μM, depending on reports [16,63]. The large dimerization interface (1046.7 and 1084.7 $Å^2$ of buried surface area (BSA) in the $P2_1$ structures of Plankto-OCP_{CAN} and Plankto-OCP_{ECN}) is mainly supported by N-terminal helices αA (NTE) and αB, which contribute ~70 % of the BSA, with minor contributions from helix αH (~20 % of the BSA) and the αE-αF and β2-β3 loops (~10 % of the BSA) (Fig. 9B, C and Supplementary Table S1). Interestingly, the relative contributions of αA and αB to the BSA at the dimerization interface vary depending on the functionalizing carotenoid, amounting to 37 and 33 % in Plankto-OCP_{CAN}, and 27 and 40 %, in Plankto-OCP_{ECN}, respectively. Additionally, two H-bonds fixing αA and αB from facing monomers in the Plankto-OCP_{CAN} dimer (viz. R9(NH2)–Q30(O) and R9(NH1)–L31(O)) are suppressed in the Plankto-OCP_{ECN} dimer (Fig. 9D and Supplementary Table S1). Thus, the NTE (αA) is less constrained (BSA decreases by 25 %) at the dimerization interface in the $P2_1$ Plankto-OCP_{ECN} structure than in the $P2_1$ Plankto-OCP_{CAN} structure, but the dimer is more tightly packed, with 25, 41 and 52 % increase in the BSA contributed by αB (largest contributor to the dimerization interface in all structures), and the αE-αF and β2-β3 loops, respectively (Supplementary Table S1). The rest of the H-bonding network at the dimerization interface is overall conserved in the $P2_1$ structures, with 3 H-bonds between αB and the facing αH (N14 (OD1)–A133(N), T15(O)–N134(ND2), T17(OG1)–N134(ND2)), one H-bond between αA and the facing αEF loop (either D6(OD2)–T90(OG1) or D6(OD2)–N88(ND2) in the Plankto-OCP_{CAN} and Plankto-OCP_{ECN} structures, respectively) and a salt-bridge between facing αB residues (D19 (OD2)-R27(NE)) (Supplementary Figs. 4 and 5). The latter salt-bridge is preserved among all OCP structures reported thus far, suggesting that it is a defining interaction in the naturally-occurring OCP dimer. Indeed, it was shown that mutation into a leucine of the highly-conserved R27 yields a constitutively monomeric OCP [16].

In the *C*2 structures, the dimerization interface is crystallographic (−x, y, −z) and at the origin of the two-fold symmetry of the crystals. The BSA at the dimerization interface amounts to 1061 and 1023 $Å^2$ in the Plankto-OCP_{CAN} and Plankto-OCP_{ECN} structures, respectively (Supplementary Table S1). We note that in the *C*2 structures, the relative contributions of αA and αB to the BSA at the dimerization interface hardly vary depending on the functionalizing carotenoid, amounting to respectively 32 and 40 % in Plankto-OCP_{CAN}, and 30 and 42 %, in Plankto-OCP_{ECN} (Supplementary Table S1). Nonetheless, alike in the $P2_1$ structures, the two H-bonds affixing αA and αB from facing monomers in the *C*2 Plankto-OCP_{CAN} dimer, i.e., R9(NH2)-Q30(O) and R9(NH1)-L31 (O), are absent in the *C*2 Plankto-OCP_{ECN} dimer. Thus, these H-bonds are present in both the $P2_1$ and *C*2 Plankto-OCP_{CAN} structures, but in neither of the Plankto-OCP_{ECN} structures. The rest of the H-bonding network at the dimerization interface is yet overall preserved in the two *C*2 structures, with two to three H-bonds between αA and the facing αH (T15(O)-

N134(ND2) and T17(OG1)-N134(ND2) in the two structures, and N14 (OD1)-A133(N) in the Plankto-OCP$_{CAN}$ structure only), one H-bond between αA and the facing αE-αF loop (D6(OD2)-T90(OG1) and the salt-bridge between facing αB residues (D19(OD2)-R27(NE)) (Fig. 9D). The extent of the biological dimerization interface is accordingly overall preserved among all available OCP structures including ours, with a mean BSA of 1051 ± 90 Å^2 (viz. 6pq1, 5ui2, 5hgr, 3 mg1, 4xb5, and 7qd0, 7qcZ, 7qd1 and 7qd2). In this context, two structures stand out, viz. the *Tolypothrix* OCP$_{CAN}$ and *Arthrospira* OCP$_{hECN}$ structures, with BSA of 857.9 and 1186.1 Å^2, respectively (Supplementary Tables S1 and S2).

Further analysis of the crystalline interfaces reveals that differences between the *P*2$_1$ and *C*2 crystals originate at a second large interface, absent in previously characterized OCP structures (Fig. 10). This additional interface, coined interface X, matches the extent of the dimerization interface in the *P*2$_1$ crystals (BSA of 1001.6 and 1054.6 Å^2 in the Ntag-Plankto-OCP$_{CAN}$ and Ntag-Plankto-OCP$_{ECN}$ structures, respectively) but largely exceeds it in the *C*2 crystals (BSA of 1650.3 and 1548.7 Å^2 in the Plankto-OCP$_{CAN}$ and Plankto-OCP$_{ECN}$ structures) (Supplementary Table S3). Interface X involves multiple secondary structure elements, including the αC-αD loop (~20 and 36 % of the overall BSA in *C*2 and *P*2$_1$ crystals, respectively), αD (~20 and 10 %, respectively), αE (~10 and 5 %, respectively), αG and the αG-αH loop (20 and 30 %, respectively), the linker (20 and 10 %), and the αM-β4 (~5 and 4 %, respectively) and β5-β6 (~2 and 5 %, respectively) loops (Supplementary Table S3). Only the first two structural elements contribute H-bonds at interface X in the *P*2$_1$ crystals, whereas all of them do in the *C*2 crystals (Supplementary Table S3). Conformational changes in αG and in the αC-αD and αG-αH loops result in changes in the BSA contributed by the αC-αD loop (+8 and +24 % in the Ntag-Plankto-OCP$_{CAN}$ and Ntag-Plankto-OCP$_{ECN}$ structures, respectively), αD (−64 and −68 %, respectively), αE (−70 and −66 %, respectively) and the linker (−74 and −68 %, respectively), explaining the shrunken interface X in the *P*2$_1$ crystals, compared to the *C*2 crystals (Supplementary Table S3). These changes in conformation and packing translate to changes in the opening-angles at the dimerization (Fig. 9E, F, G) and NTD/CTD interfaces (Fig. 11), offering a glimpse into the molecular breathing motions that animate OCP, at both the monomer and the dimer levels (Fig. 10). Briefly, monomers come closer to one another in the *P*2$_1$ (asymmetric unit) dimer than in the *C*2 (crystallographic) dimer (change in opening-angle and distance between chains: −5.6° and +1.1 Å for Ntag-Plankto-OCP$_{CAN}$; −6.8° and +1.2 Å for Ntag-Plankto-OCP$_{ECN}$).

Nonetheless, the *P*2$_1$ monomers are characterized by an increased opening angle between the NTD and the CTD (Figs. 9G, 10 and 11). Chain A shows a larger deviation with respect to the unique chain in *C*2 crystals (change in opening-angle and distance between the NTD and CTD: +3.1° and +1.0 Å for Ntag-Plankto-OCP$_{CAN}$; +4.6° and +1.0 Å for Ntag-Plankto-OCP$_{ECN}$) than chain B (change in opening-angle and distance between the NTD and CTD: +1.3° and +0.4 Å for Ntag-Plankto-OCP$_{CAN}$; +1.4° and +0.3 Å for Ntag-Plankto-OCP$_{ECN}$) (Fig. 9G). As a result, the predicted radii of gyration (Rg) for the *P*2$_1$ asymmetric unit dimers (26.16 and 26.12 Å for Ntag-Plankto-OCP$_{CAN}$ and Ntag-Plankto-OCP$_{ECN}$, respectively) are larger than those predicted for the *C*2 crystallographic dimers (26.01 and 25.90 Å for Ntag-Plankto-OCP$_{CAN}$ and Ntag-Plankto-OCP$_{ECN}$, respectively) (Supplementary Table S2). Consistently, *P*2$_1$ chain B features a structure that is intermediate between *P*2$_1$ chain A and the unique C2 chain (change in opening-angle and distance between the NTD and CTD in *P*2$_1$ chain A with respect to *P*2$_1$ chain B: +3.3° and +0.9 Å for Ntag-Plankto-OCP$_{CAN}$; +4.0° and +0.7 Å for Ntag-Plankto-OCP$_{ECN}$) (Fig. 11A). This is visible also in the predicted Rg for the various chains (20.81, 20.67 and 20.52 Å for Ntag- *P*2$_1$ chain A, *P*2$_1$ chain B and *C*2 Plankto-OCP$_{CAN}$, respectively; and 20.73, 20.50 and 20.48 Å for the Ntag-Plankto-OCP$_{ECN}$ counterparts, respectively) (Supplementary Table S2). Altogether, these changes affect the positioning of the carotenoid which tilts towards Y44 in the *P*2$_1$ structures, despite preservation of H-bonds from its carbonyl oxygen to Y203(OH) (2.5–2.8 Å distance between non-hydrogen atoms) and W290(NH1) (2.8–3.0 Å distance between non-hydrogen atoms) and a quasi-perfect alignment of its β1-ring in the CTD (Fig. 11B). With respect to the *C*2 Ntag-Plankto-OCP$_{CAN}$ structure, the tilt angles of the carotenoid are 3.8 and 1.8° in chains A and B of the *P*2$_1$ Ntag-Plankto-OCP$_{ECN}$ structure, 3.2 and 2.9° in chains A and B of the *P*2$_1$ Ntag-Plankto-OCP$_{CAN}$ structure, and 0.8° in the *C*2 Ntag-Plankto-OCP$_{ECN}$ structure. Thus, crystal packing traps different conformations of the Ntag-Plankto-OCP monomers, which differ in (i) the positioning of the carotenoid (Figs. 9–12); (ii) the conformation displayed, at interface X, by αG and the αC-αD and αG-αH loops, (iii) the opening angle between domains, at the NTD/CTD interface; and (iv) in the opening angle between monomers, in the biological dimer. It is of important note that despite these changes, and the presence of two alternate side-chain conformations for R155 in the Ntag-Plankto-OCP$_{ECN}$ structures, the R155-E246 salt-bridge and N104-W279 H-bond, which support the NTD/CTD interface, are preserved in all structures (distance between non-hydrogen atoms 2.8–3.2 Å) (Supplementary Figs. 4 and 5). We also note that previously determined structures of *Synechocystis*, *Anabaena*, *Tolypothrix* and *Arthrospira* OCP align best with the *C*2 Ntag-Plankto-OCP$_{CAN}$ and Ntag-Plankto-OCP$_{ECN}$ structures, suggesting that these should be used for comparisons, rather than the *P*2$_1$ structures (Supplementary Table S2). In this context, it must be stated that differences in the opening angle between the NTD and the CTD can also be seen from the comparison of the two chains constituting the asymmetric unit dimer in the *Anabaena* OCP structure (PDB id: 5hgr), with chain A aligning best with the *C*2 Ntag-Plankto-OCP conformers. We last note that ECN-functionalized OCP monomers and dimers are more compact than the CAN-functionalized counterparts (Supplementary Table S2), and that a similar trend is visible in the comparison of the Ntag-Syn-OCP structures functionalized by CAN (PDB id: 4xb5; one chain with a predicted radius of gyration of 20.49 Å) and ECN (PDB id: 3mg1; two chains with predicted radii of gyration of 20.34 and 20.33 Å). In the case of the Plankto-OCP structure, conformational changes again concentrate in the NTD (Fig. 12).

Conformational changes at the Cα level are best visualized in Cα-Cα distance difference matrices (DDM). Calculated using the *C*2 Ntag-Plankto-OCP$_{CAN}$ structure as a reference, these confirm that the main difference between the *P*2$_1$ chain A, *P*2$_1$ chain B and *C*2 structures is a change in the orientation of the NTD vs. the CTD, accompanied (or triggered) by a change in the conformation of αA and the αC-αD and αG-αH loops. As a result, the two loops draw away from the CTD, pulling with them αC, αD, αE, αF and αG (Fig. 13A). Conformational changes are far less pronounced in the CTD, where only β5 slightly changes position, moving away from αJ, β2 and αM (Fig. 13A). In this context, it should be recalled that aside αA, the NTD consists of two 4-helix bundles contributed by helices αB-αC-αH-αI and αD-αE-αF-αG, respectively, which appose one onto the other leaving a central void that constitutes the carotenoid tunnel in the NTD. Our structural comparison indicates that regions most affected by the change in space group are those linking the two bundles, with conformational changes affecting the position – but not the internal structure – of the second bundle with respect to the CTD. Interestingly, the αC-αD and αG-αH loops are also the secondary structure elements most affected by the change in functionalizing carotenoid. From the comparison of the *C*2 structures, it is visible that these changes result in a modification of the distance between helices αD and αF, on the one hand, and the CTD, on the other hand. Thus, the structural dynamics at the basis of the change in space group and those resulting from the change in functionalizing carotenoid are localized in the same regions of the protein. This suggests that they could reflect a functional role. In line with this hypothesis, calculation of a DDM between the isolated NTD of Syn-OCP$_{CAN}$, considered as a surrogate for the structure of the NTD in OCP^R, and the NTD in the dark-adapted Syn-OCP$^O_{CAN}$ reveals major changes in the αC-αD and αG-αH loops (Fig. 13B), which result in a dramatic rearrangement of the first αB-αC-αH-αI bundle while leaving unperturbed the internal conformation of the αD-αE-αF-αG bundle. Thus, like changes in space group and functionalizing

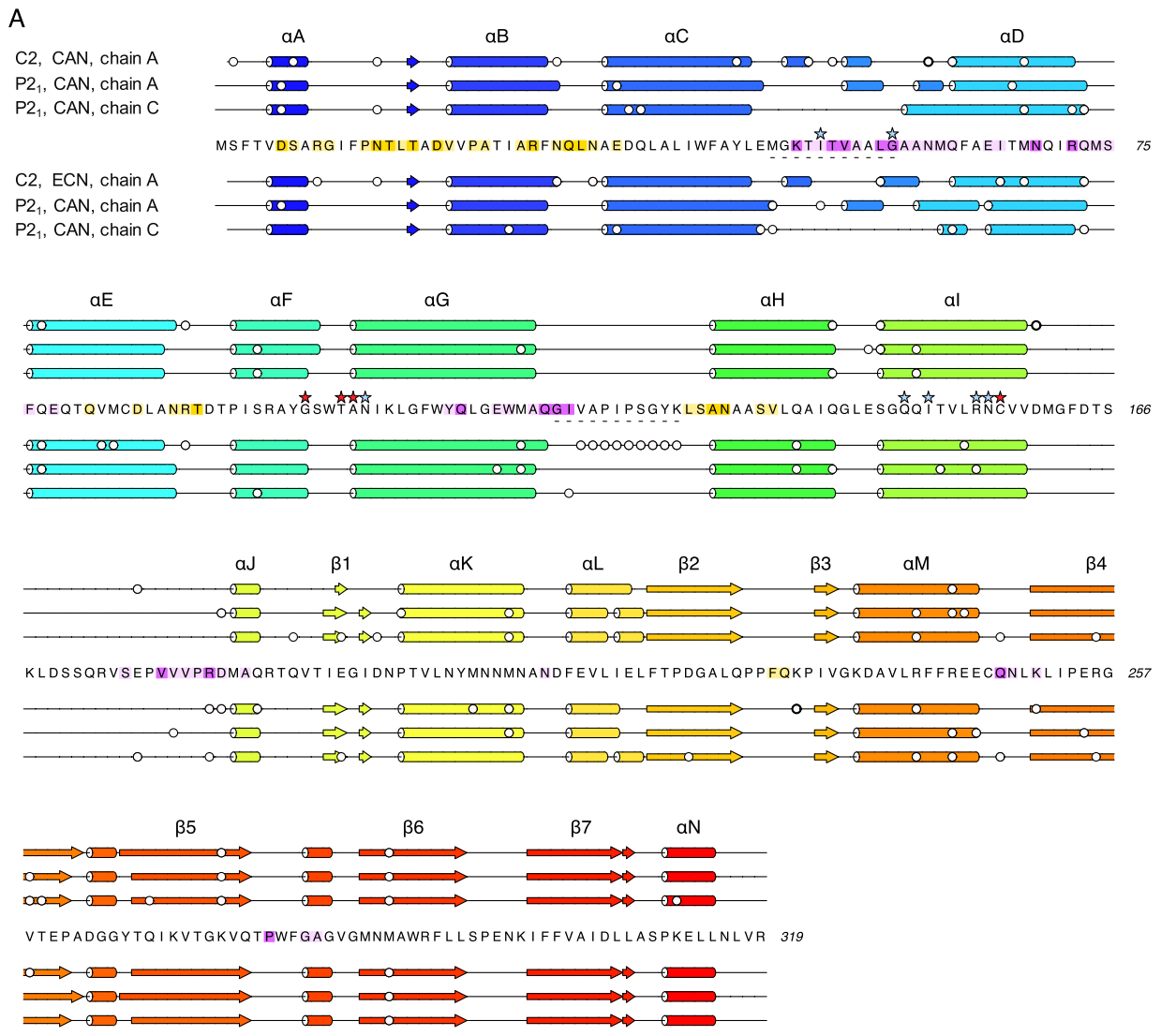

(caption on next page)

Fig. 9. All OCP structures feature a dimer, including those of Plankto-OCP. (A) The secondary structure of OCP is overall well conserved among Plankto-OCP structures obtained in different space groups and with different pigments. Residues involved in the dimerization are highlighted in yellow, whereas residues involved in the formation of interface X are highlighted in purple. Dark and light colouring indicate residues involved in polar and van der Walls interactions, respectively. White dots highlight residues which are observed in alternate conformations. Blue stars indicate residues which have been shown to play a role in the OCP-PBS interaction, and red stars point to residues that could be at the origin of the stronger attachment of Plankto-OCP to the Syn-PBS. (B–C). The asymmetric unit of the $P2_1$ crystals features a dimer (here shown as a ribbon with the two facing monomers colored sequence-wise, from cold (N-ter) to hot (C-ter) colors), whereas in *C*2 crystals, the dimer is crystallographic, hence only a single monomer is found in the asymmetric unit. (D) Polar contacts at the dimerization interface involve a conserved salt-bridge between D19 and R27, as well as conserved H-bonds between facing D6 and T90, and between facing N134 and N14, T15, and T17. (E, F, G) The *C*2 structures display a more compact conformation than the $P2_1$ structures, at both the dimer (E, F) and the monomer levels (G). The figure illustrates the trajectory followed by Plankto-OCP Cα atoms as we interpolate from the *C*2-CAN to the $P2_1$-CAN structure, highlighting the secondary structure elements which diverge most upon packing in the two crystal types. Arrows show the overall direction travelled by domains, revealing compaction of the OCP monomer. (For interpretation of the references to color in this figure legend, the reader is referred to the web version of this article.)

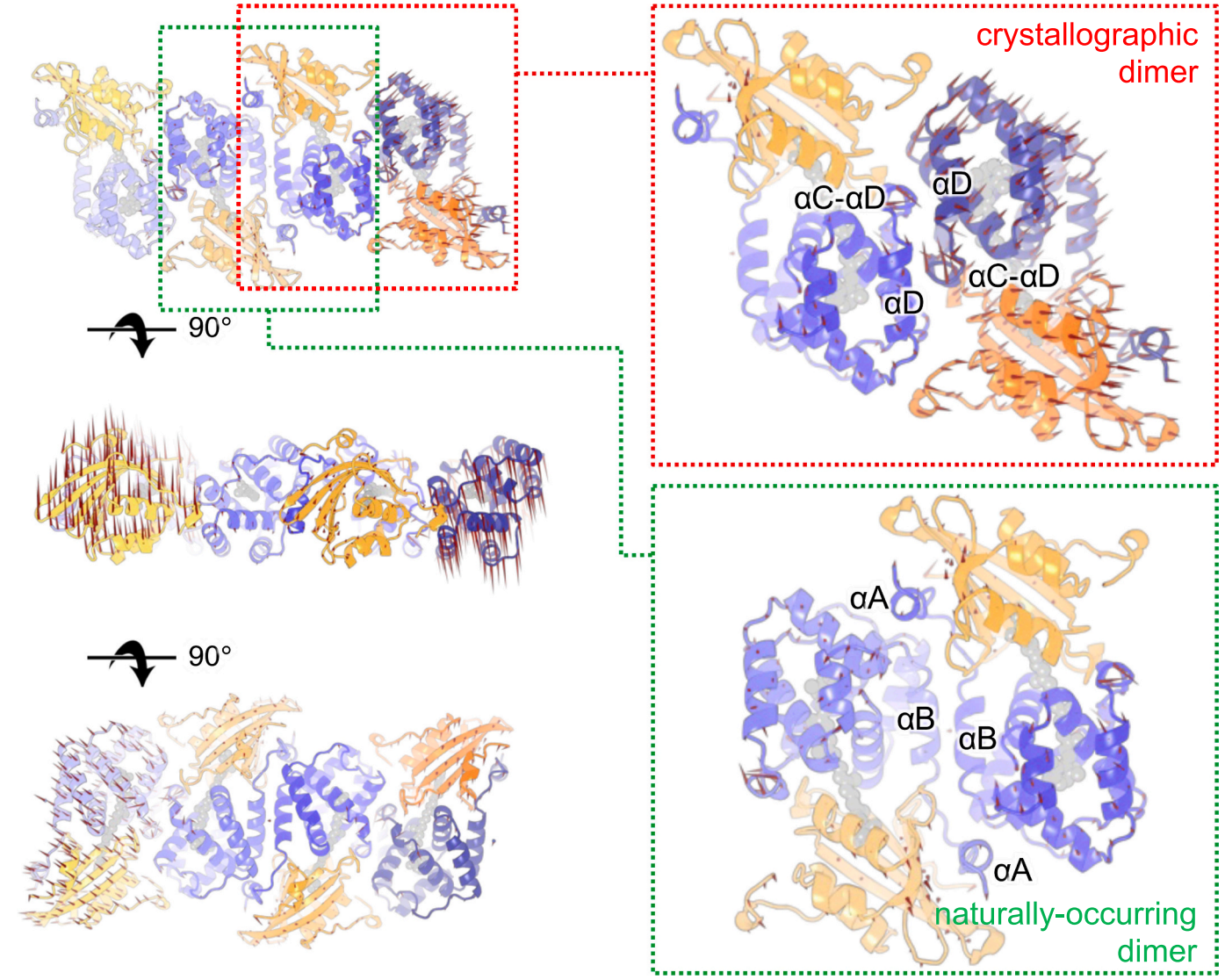

Fig. 10. The *Planktothrix* OCP features two similarly large packing interfaces in crystals. In Plankto-OCP crystals, a large interface, additional to the dimerization interface (Table S1), is found which we coined interface X (Table S3). This interface, mainly contributed by helices αD, αE and αG, and by the αC-αD and αG-αH loops, matches the extent of the dimerization interface, in $P2_1$ crystals (BSA of ~1050 Å^2), but largely exceeds it, in the *C*2 crystals (BSA of ~1600 Å^2). Changes in the extent of interface X result in a reorientation of domains in each monomer forming the naturally-occurring dimer, and in an increase in the opening angle between monomers, in the dimer. Arrows indicate the direction and distance along which Cα atoms travel as we interpolate from the $P2_1$ to the *C*2 crystals.

carotenoid in Ntag-Plankto-OCP, photoactivation affects the internal structure and relative positioning of the Syn-OCP αB-αC-αH-αI bundle through conformational changes in the αC-αD and αG-αH loops, while the second αD-αE-αF-αG bundle appears stable and acts as a base. This observation is surprising given that the interface between the first bundle and the CTD is larger (BSA of 643.2 Å^2; four H-bonds and a salt bridge) than that between the second bundle and the CTD (BSA of 189.3 Å^2; 1 H-bond). Regardless, our results show that the two most mobile regions across the NTD – and therefore, across the whole Plankto-OCP – are the αC-αD and αG-αH loops, making these the first candidates to explain the increased photoactivation efficiency of Plankto-OCP.

The αC-αD loop conformation differs in the $P2_1$ chain A, $P2_1$ chain B

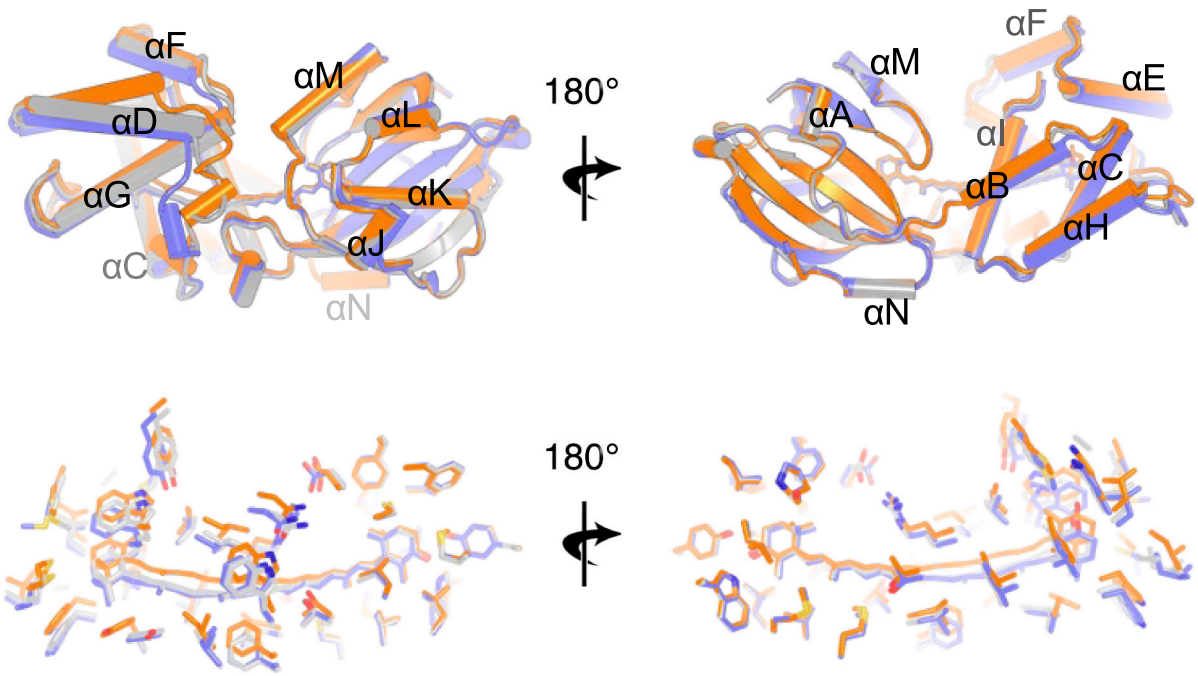

Fig. 11. Plankto-OCP structures differ in the compaction of the monomer as well as in the internal structure of the NTD. (A) The *C*2 (orange), and $P2_1$ chain A (slate) and chain B (grey) structures are overlaid as ribbons. Structural alignment, performed using the CTD atoms, highlights the change in opening angle between the CTD and the NTD. Indeed, the CTD structure is highly conserved with hardly no conformational changes observed among structures. Large differences are yet seen in the NTD, notably in the αC-αD and αG-αH loops, but as well in the relative positioning of the αC and αD helices. Here, the Plankto-OCP_{CAN} structures are shown, but the same observations can be made by comparing the Plankto-OCP_{ECN} structures. (B) Close up view on CAN and on the residues lining the carotenoid tunnel. A change in the orientation of the carotenoid is seen upon compaction of the OCP structure due to change in space group.

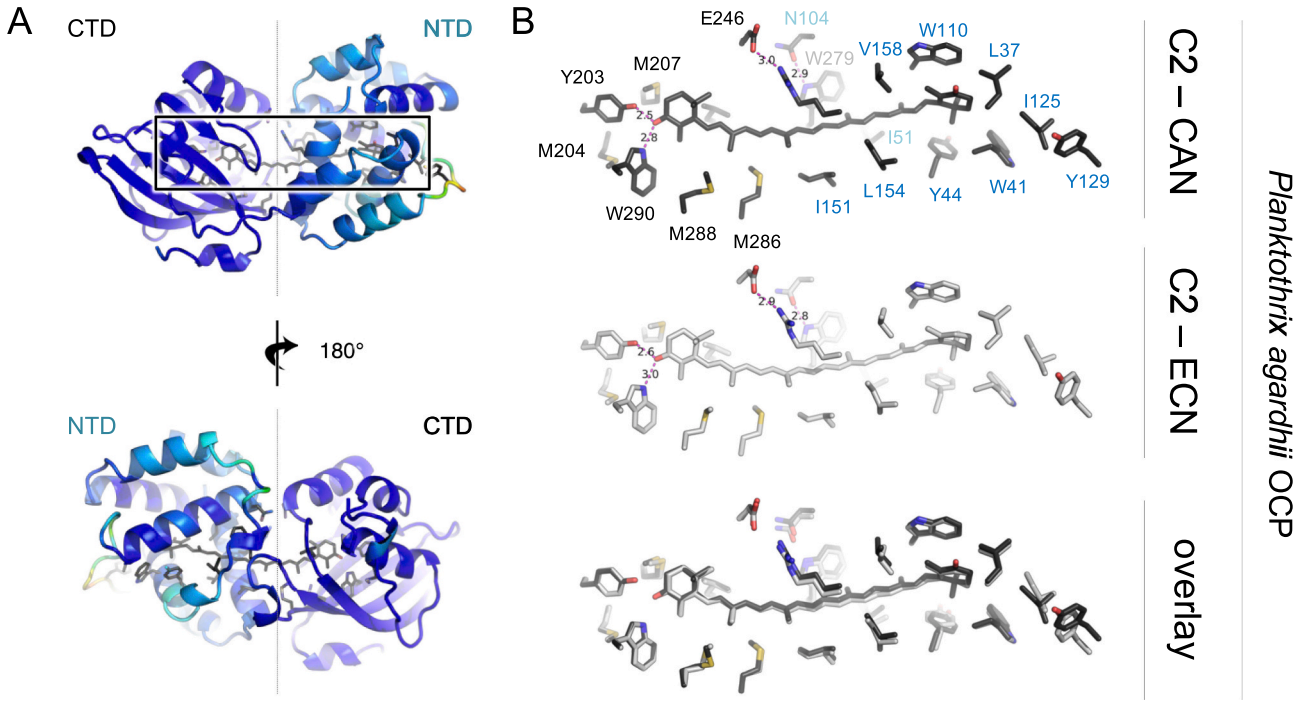

Fig. 12. Conformational changes observed upon change of the functionalizing carotenoid are limited to the NTD. (A) The structure of Plankto-OCP_{CAN} is shown as a ribbon colored from cold to hot colors as a function of the RMSD to the Plankto-OCP_{ECN} structure. (B) Close-up view on the carotenoid and residues lining the homonymous tunnel. The orientation in (B) is similar to that in the upper panel of (A).

and *C*2 structures, but is overall preserved in each pair of ECN- and CAN-functionalized structures – notwithstanding the presence of multiple residues in alternate conformations in the C2 Ntag-Plankto-OCP_{ECN} structure (Fig. 13 and Supplementary Table S2). The αG-αH loop conformation is also overall preserved among $P2_1$ structures, with only a slight displacement of αH observed between the $P2_1$ chains A and B, as a result of changes in the αC conformation concomitant to those in the αC-αD loop (Figs. 11 and 13). The αG-αH loop conformation is yet more

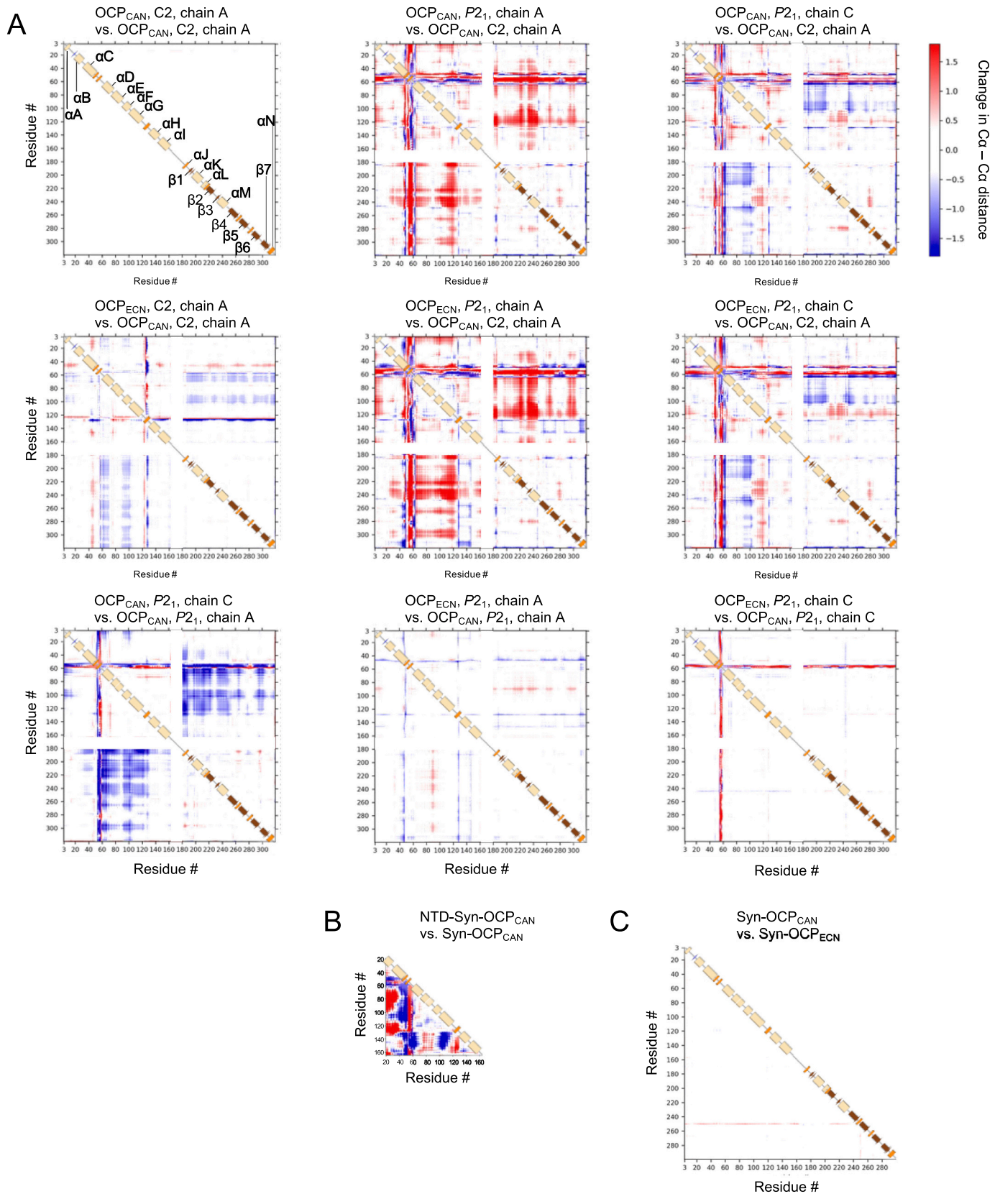

(caption on next page)

Fig. 13. Crystal packing traps different conformations of the Ntag-Plankto-OCP monomers. (A) Changes in Cα-Cα distances in the various ECN- and CAN-functionalized *C*2 and $P2_1$ chains were monitored by computing Cα-Cα difference-distance matrices (DDM). As a reference structure, we used the *C*2 Plankto-OCP_{CAN} (2 first rows), or either chain A or C of the $P2_1$ Plankto-OCP_{CAN} structure (third line). In each DDM, the lower and upper panels (separated by a sketch of the secondary structure) show the changes in Cα-Cα distances for alternate conformers A and B with respect to the reference structure. Indeed, alternate conformations are seen in all Plankto-OCP structures. The overall similarity between upper and lower panels indicates that alternate conformations hardly affect the protein backbone. (Upper row) In the $P2_1$ crystals, two chains are found, which either display a more expanded (chain A) or a more compact (chain B) structure, due to changes in the opening angle between the NTD and the CTD. The DDM further indicates that these changes stem from helix αD, and the αC-αD and αG-αH loops, either drawing away (chain A) or coming closer (chain B) to the CTD, respectively. (Middle row) Comparison of the *C*2-CAN and *C*2-ECN structures suggests that the presence of CAN results in a more compact protein, but support to this hypothesis could not be obtained from comparison of the $P2_1$ chain A or $P2_1$ chain B structures. (Lower row) Nonetheless, we observe a similar trend when comparing, either in the CAN-functionalized or the ECN-functionalized states, $P2_1$ chain C and $P2_1$ chain A. Thus, changes in functionalizing carotenoid have a lesser influence on the OCP conformation than changes in space group. (B) DDM calculated for the isolated NTD of Syn-OCP_{CAN} vs. corresponding residues in the dark-adapted Syn-OCP_{CAN}. This DDM suggests that upon photoactivation, large scale conformational changes occur in the NTD that mainly result in helix αB drawing away from helices αD to αG, while the αC-αD loop comes closer to these and to helices αH to αI. Also, αG edges closer to helices αH to αI, while the αG-αH loop draws farther. (C) DDM calculated for Syn-OCP_{CAN} vs. Syn-OCP_{ECN}. Hardly no change in the Syn-OCP structure is seen upon change in the functionalizing carotenoid.

divergent among the *C*2 structures, with the *C*2 Ntag-Plankto-OCP_{ECN} structure displaying two alternate main-chain conformations for the highly-conserved residues 122-VAPIPSGYKL-130, of which none overlaps with the conformations observed in *C*2 Ntag-Plankto-OCP_{CAN} and in the $P2_1$ chains (Supplementary Figs. 6 and 7 and Supplementary Table S2). Interestingly, these changes in the conformations of the αC-αD and αG-αH loops result in the opening/closing of water-channels from the protein surface to the carotenoid tunnel in the NTD. Briefly, four main channels (#1, #2, #3 and #4) can be identified on the basis of our structures (Supplementary Figs. 6, 7 and 8). The first one (#1), which is colinear with the carotenoid axis and adjacent to the β2-ring, features at its bottleneck the fully conserved L37, M83, M117 and I125 (Supplementary Figs. 6, 7 and 8) and encompasses the binding site of the carotenoid in the structure of the isolated NTD of Syn-OCP_{CAN} (Supplementary Tables S2 and S4). Channel #1 is opened in all Ntag-Plankto-OCP structures, and as well in all previously determined OCP structures. In the *C*2 Ntag-Plankto-OCP_{ECN} structure, however, the presence of two alternate main-chain conformations for αG-αH loop residues 120-GIAPIPSGYKL-131 (Supplementary Fig. 7) results in two configurations of the channel (see Supplementary Table S4) characterized by either a wider or narrower opening (Supplementary Figs. 6, 7 and 8). The enlargement of channel #1 is compulsory for the carotenoid to translocate fully across the NTD, as illustrated by the observation that the αG-αH loop displays a large conformational change in the structure of the isolated NTD of Syn-OCP_{CAN}, compared to the NTD in the dark-adapted Syn-OCP^{O}_{CAN} (Fig. 13B) [21]. Hence the two *C*2 Ntag-Plankto-OCP_{ECN} conformers offer an illustration of how structural dynamics in the αG-αH loop may participate in the regulation of photoactivation.

The second (#2), third (#3) and fourth channel (#4) are all perpendicular to the carotenoid tunnel, and open on either side of Y44 side chain, ending up just above the β2-ring of the carotenoid (#2) or its second terpene unit (#3, #4) (Supplementary Figs. 6, 7 and 8). Channel #2 features W41 and Y44 at its bottleneck, whereas channel #3 is lined by Y44, M47, I51, I151 and F280, and channel #4 by Y44, Y111 and αG (Supplementary Figs. 6, 7 and 8). Residues W41, M47, I151 and M280 are strictly conserved, whereas V53 and I53 fill the structural position of Plankto-OCP I51 in *Anabaena* OCP and Syn-OCP, respectively, and Y44 and Y111 are replaced by a phenylalanine (F44) and an asparagine (N111), respectively, in *Anabaena* OCP. We find that channel #2 is opened towards the bulk in all $P2_1$ structures, albeit a much wider opening is observed in chain A of the $P2_1$ Ntag-Plankto-OCP_{ECN} structure, due to a large swing of Y44 towards Y111 (Supplementary Figs. 7 and 8) – i.e., away from W41. Of note, Y44 is found in alternate side-chain conformations in the *C*2 Ntag-Plankto-OCP_{CAN} structure, and as well in the previously determined Syn-OCP_{ECN} structure (Supplementary Figs. 6, 7 and 8). Additionally, channel #3 is opened in chain A of the $P2_1$ Ntag-Plankto-OCP_{CAN} and Ntag-Plankto-OCP_{ECN} structures, although in only one alternate conformer due to alternate conformations in M47. In both *C*2 structures, channel #2 and #3 are closed. Nonetheless, in one of the two alternate conformers of the C2 Ntag-Plankto-OCP_{CAN} structure, channel #4 is opened (Supplementary Figs. 6 and 8). We note that all previously determined OCP structures feature similar openings of the carotenoid tunnel towards the bulk that are perpendicular to the carotenoid axis. For example, channels #3 and #4 are opened in the Syn-OCP structures (PDB ids: 3mg1 and 4xb5), while channels #2 and channel #3 are opened in the *Tolypothrix* OCP structure (PDB id: 6pq1) and in the two chains of the asymmetric unit dimer from the *Arthrospira* structure (PDB id: 5ui2; also referred to as *Limnospira*). In *Tolypothrix* OCP, a supplementary channel (#5) is observed, ~180° apart from channel #2, which is lined by the highly conserved F28, I40, S157 and M161 (Supplementary Fig. 9). The opening of channel #5, which alike channel #2 ends up above the β2-ring of the carotenoid albeit from the other side of the tunnel, mainly depends on the side chain conformation of M161 in the *Tolypothrix* OCP structure. Channel #5 is also opened in the two chains of the asymmetric unit dimer from the *Anabaena* OCP structure (PDB id: 5hgr), where its opening if facilitated by the substitution of I40 (in Plankto-OCP, Syn-OCP, *Arthrospira* and *Tolypothrix* OCP) for a valine – of the conformational change in M161. Channel #3 is additionally opened in chain B of *Anabaena* OCP, but closed in chain A due to change in the conformation of M47. Thus, the Ntag-Plankto-OCP structures recapitulate most previously observed conformational dynamics in the carotenoid tunnel residues and illustrate that the opening of channel #1–4 mainly depends on the conformations displayed by residues in αC (A33-E46) and in the αC-αD (M47-G57) and αG-αH (G120-L131) loops. The *Tolypothrix* and *Anabaena* OCP structures additionally reveal the existence of another channel (#5), which ends up on the side of the carotenoid β2 ring where the methyl or carbonyl oxygen atom of ECN and CAN are exposed, respectively. Given that the *Tolypothrix* OCP features the same residue distribution as Plankto-OCP, Syn-OCP and *Arthrospira* OCP along the five channels, it is possible that channel #5 would open in these as well.

We noted earlier that the positioning of the carotenoid differs in the various Ntag-Plankto-OCP structures, due to changes in the opening angle between domains, i.e. at the NTD/CTD interface. Besides this point, the most notable dissimilarity in the carotenoid tunnel of Plankto-OCP is the presence of a methionine at position 207, instead of a leucine in other OCP (L205 in Syn-OCP, and L207 in *Anabaena, Arthrospira* and *Tolypothrix* OCP) (Supplementary Figs. 4, 5 and 9). At position 288, a methionine is found in Plankto-OCP, Ana-OCP (PDB id: 5hgr) and *Tolypothrix* (PDB id: 6pq1)) OCP (PDB id: 4xb5), which is substituted for an isoleucine in Syn-OCP (I286) and *Arthrospira* OCP (I288) (Supplementary Figs. 4, 5 and 9). Thus, Plankto-OCP is particularly enriched in methionine residues. Of these two additional methionines, we speculate that only the former may be related to the higher photoactivation rate of Plankto-OCP, given that the slower *Tolypothrix* and *Anabaena* OCP also feature a methionine at position 288. The only other structural difference between the carotenoid tunnels of Plankto-OCP and Syn-OCP is the placement of Plankto-OCP I51 at the position occupied by Syn-OCP I53, due to changes in the sequence of the αC-αD loop (47-MGKTITVAAL-GAA-59 in Plankto-OCP vs. 47-MGKTLTIAAPGAA-59 in Syn-OCP).

Again, we speculate that these changes could be involved in the higher photoactivation and recovery rates of Plankto-OCP, given that the αC-αD loop exhibits varying conformations in the various Ntag-Plankto-OCP structures (Figs. 11 and 13, and Supplementary Fig. 9) but adopts the same conformation in the *Synechocystis* (Syn-OCP), *Anabaena*, *Arthrospira* and *Tolypothrix* OCP structures. Since the αC-αD loop in Ana-OCP (47-MGKTITVAAPGAA-59) differs from that in Plankto-OCP only by the substitution of L56 for a proline – found as well in *Synechocystis* (Syn-OCP), *Arthrospira* and *Tolypothrix* OCP – it is most probable that the increased dynamics of this loop in Plankto-OCP originate from the replacement of this residue (Supplementary Fig. 9). P56 fits into a groove at the surface of the NTD (formed by S60, M61, G108, Y111 and W277 in Syn-OCP; S60, M61, G108, N111 and W279 in *Anabaena* OCP; and N60, M61, G108, Y111 and W279 in *Arthrospira* and *Tolypothrix* OCP) in all previously described OCP structures but is solvent exposed in Plankto-OCP. This unfavorable feature could be at the basis of the increased conformational variability of the αC-αD loop in Plankto-OCP.

4. Discussion

Here, we reported results from a comparative analysis of structure-function-dynamics relationships in various OCP1 from different cyanobacterial species, including the previously uncharacterized Plankto-OCP and the most studied Syn-OCP. All OCP-related functional properties – photoactivation, thermal recovery, interaction of the OCP^R state with the PBS and consequential fluorescence quenching and recovery – were examined for their dependence on the functionalizing carotenoid (ECN vs. CAN). We also investigated the influence of his-tagging at either the N or C-terminus, which afforded information on the role of the NTE (αA) and the CTT (αN) in the various molecular processes. In an attempt to rationalize functional observations, we solved the *hitherto* uncharacterized structures of Plankto-OCP in the ECN- and CAN-functionalized states, each in two space groups, and compared them to the available structures of ECN- and CAN-functionalized Syn-OCP [17,21]. When useful, we also included in our structural comparison the structures of CAN-functionalized *Anabaena* OCP [61], hECN-functionalized *Arthrospira* OCP [8] and of CAN-functionalized *Tolypothrix* OCP [30].

Initially, our interest in Plankto-OCP was sparked by the recent observation that the OCP-related NPQ-mechanism is more efficient in *Planktothrix* cells than in *Synechocystis* cells [41]. The functional characterization of Plankto-OCP properties afforded rationalization of this phenotype, showing that it not only photoactivates faster than Syn-OCP, but also recovers faster (especially at 9 °C). Such a fast thermal recovery had thus far been observed only for OCP2 and OCPX variants, but not for members of the OCP1 clade. Indeed, *Synechocystis*, *Arthrospira* and *Tolypothrix* OCP1 are all characterized by a slow recovery at 9 °C. The recovery of Plankto-OCP can be further accelerated by addition of FRP, confirming its belonging to the OCP1 clade, but the degree of acceleration is reduced by at least 8-fold, compared to Syn-OCP. In previous studies, it was found that slow recovery and the ability to bind to FRP coincide in the OCP1 clade, as opposed to OCP2 and OCPX [16] which recover faster thermally, but are unable to bind FRP. Based on sequence alignments, it was further suggested that the defining feature of the OCP1 clade is the presence of residues R229 and D262 (*Synechocystis* numbering), which are absent in OCP2 and OCPX [16]. Our data confirm that presence of R229 and D262 correlates with the ability to bind FRP, but indicate that the slow recovery rate of *Synechocystis*, *Arthrospira* and *Tolypothrix* OCP1 is unrelated to their presence.

The faster photoactivation and recovery of Plankto-OCP could stem from its higher protein flexibility, illustrated by our Plankto-OCP crystalline structures. Indeed, crystal packing traps different conformations of the Ntag-Plankto-OCP monomers, which differ in (i) in the positioning of the carotenoid (Figs. 9–13); (ii) the conformation displayed by αG and the αC-αD and αG-αH loops; (iii) the opening angle between domains at the NTD/CTD interface; and (iv) the opening angle between monomers in the naturally-occurring dark-adapted dimer. Hence, the Plankto-OCP structures offer a peek into the molecular breathing motions that animate OCP, at the monomer and the dimer levels. The $P2_1$ structures demonstrate that the two monomers in a dimer can adopt slightly different structures, differing in the opening angle at the NTD/CTD interface, and consequently, in the orientation of the carotenoid in the tunnel. These differences could account for the spectroscopic observation that two states of dark-adapted OCP coexist in vitro [40]. The conformations present in the *C*2 structures match best those displayed by chain B in the $P2_1$ structures but they are not equivalent, differing in the opening angle at the NTD/CTD interface, in the exact positioning of helices around the carotenoid, and in the conformation displayed by the αC-αD and αG-αH loops. These two loops show the highest diversity among the various structures reported herein, whereas they adopt the same conformation in all previously-determined *Synechocystis* (Syn-OCP), *Anabaena*, *Arthrospira* and *Tolypothrix* OCP structures. Hence, conformational diversity in these loops could be at the basis of the peculiar functional properties of Plankto-OCP. Below, we further detail how our observations could be linked to function.

The $P2_1$ chain A and $P2_1$ chain B structures feature a "porous wall", traversed by channels perpendicular to the carotenoid tunnel, whereas the *C*2 structures feature a carotenoid tunnel that is insulated from the bulk, except at its extremities (Supplementary Figs. 6, 7 and 8, and Supplementary Tables S2 and S4). Together, the six Plankto-OCP chains illustrate that the opening of channels #1–4 mainly depends on the conformations displayed by residues in αC (A33-E46; channels 1–2) and in the αC-αD (M47-G57; channels 2–4) and αG-αH (G120-L131; channel 1) loops, and question the possible role of bulk-water access to the carotenoid tunnel in the photoactivation mechanism. The enlargement of channel #1 is compulsory for the carotenoid to fully translocate across the NTD, and accordingly, a large conformational change was seen in the αG-αH loop in the structure of the isolated NTD of Syn-OCP_{CAN}, compared to the NTD in the dark-adapted Syn-OCP^O_{CAN} structure [21] (Fig. 13B). Two alternate conformations are observed for this loop in the *C*2 Ntag-Plankto-OCP_{ECN} structure, offering further illustration of how structural dynamics could participate in the regulation of photoactivation. We yet note that none of the conformations observed in our various Ntag-Plankto-OCP structures, nor in any of the previously determined OCP structures, matches that found in the structure of the isolated NTD of Syn-OCP_{CAN} [21], indicating that full translocation of the carotenoid into the NTD must occur for this conformation of the αG-αH loop to become favorable.

We also investigated if the presence of multiple alternate conformations could underlie the higher photoactivity of Plankto-OCP. Plotting these against the secondary (Fig. 9A and Supplementary Table S2) or tertiary structure, we identify the αC-αD (M47-G57) loop, αM and β4 as clusters. Indeed, these secondary-structure elements or epitopes appear prone to display alternate conformations, irrespective of the space group or functionalizing carotenoid (Fig. 9A). For example, W288, at the CTD end of the carotenoid tunnel, is present in alternate conformations in all structures. Additionally, D6, N14, Q73, Q77, M117, M207, R241, R244, V258, K275 are present in alternate conformations in three of the six structurally-analyzed Plankto-OCP chains. In conclusion, we propose that the structural traits which explain the higher photoactivation rate of Plankto-OCP are (i) the increased flexibility in the αC-αD (M47-G57) and αG-αH (G120-L131) loops, which results in opening of water channels to the carotenoid tunnel; and (ii) the increased molecular breathing motions at the levels of the dimer, the NTD/CTD interface, and the NTD helix core. As to the increased recovery rate, a possible hypothesis is that it originates from a decreased stabilization of the Plankto-OCP^R state. Comparing residues distribution along the carotenoid tunnel in the NTD, we found that the only structural difference between the NTD tunnels of Plankto-OCP and Syn-OCP is the placement of Plankto-OCP I51 at the position occupied by Syn-OCP I53, due to changes in the sequence of the αC-αD loop (47-MGKTITVAALGAA-59 in Plankto-OCP vs. 47-MGKTLTIAAPGAA-59 in Syn-OCP) (Supplementary Fig. 9), suggesting a role for this residue in

the stabilization of OCP^R. Another, more hypothetical means by which the Plankto-OCP^R state would be rendered less stable could be through a decrease in the affinity of the CTT for the empty CTD tunnel. Syn-OCP is indeed unique among the variants discussed herein in that it features a 314-NFAR-317 sequence at its C-terminus instead of 316-NLVR-319 in the other OCP (Supplementary Fig. 9). The combined substitution of a leucine for a phenylalanine, and of a valine for an alanine, could account for a higher affinity of the Syn-OCP CTT for the empty CTD tunnel. Reversely, the replacement of Syn-OCP I286 by a methionine in Plankto-OCP (M288) could decrease the affinity of the CTT for the empty CTD tunnel.

We also examined the effect of his-tagging at the N- or C-terminus on the various functional properties of OCP (Figs. 3 and 8). Indeed, both the NTE and the CTT have been proposed to play important roles in the OCP photoactivation and recovery mechanisms. We found that irrespective of the variant, the N-tagged protein displays the best match to the native protein, both in terms of photoactivation rate and thermal recovery rate. Native Syn-OCP and Plankto-OCP display the fastest photoactivation rate, indicating that increased disorder in their NTE and/or a weaker interaction between the NTE and the CTD does not benefit photoactivation as was previously suggested [64]. Recovery was also found to be faster in native Syn-OCP and Plankto-OCP than in their his-tagged counterparts. Notably, a dramatic drop in the recovery rate was observed for the C-tagged Plankto-OCP, which could stem either from a higher stability of the OCP^R state in presence of a C-terminal his-tag, or from a frustrated recovery of the OCP^O state due to hindered rebinding of the CTT to the CTD β-sheet. Regardless, these results point to an important role played by the CTT in the stabilization of OCP^R and thermal recovery of the OCP^O state. Little is known regarding the configuration of the CTT residues in the OCP^R state and its role in OCP photoactivation and recovery. However, it was shown that in the *Synechocystis* C-terminal domain homolog (CTDH), which belongs to a family of carotenoid-transporting proteins structurally homologous to the OCP CTD [36,37], the CTT can exchange between a closed conformation, whereby it covers the empty carotenoid tunnel, and an opened conformation, similar to that observed in OCP^O. By analogy, it was therefore proposed that the last step of OCP photoactivation is the repositioning of the CTT on the empty CTD-half of the carotenoid tunnel, preventing exposure to the bulk of its highly hydrophobic residues. Presence of a six-histidine tag in the CTT could hinder this movement, leading to slower kinetics of photoactivation and recovery. The position of the his-tag also influences the PBS quenching, with again a more pronounced effect of C-terminal his-tagging. It was earlier suggested that the presence of a six-histidine tag upstream the NTE could destabilize the interaction with the PBS [64], yet the present data invalidate the hypothesis, demonstrating that N-tagged and native OCP detach as swiftly from the PBS. Contrastingly, introduction of the six-histidine tag downstream the CTT results in increased PBS-fluorescence quenching and slower fluorescence recovery. This result can be rationalized by envisioning that the C-terminal his-tag strongly stabilizes the PBS-bound OCP^R structure, possibly through interaction of the tag with PBS amino acids. In conclusion, our investigation of the effect of his-tagging on the functional properties of OCP suggests that rebinding of the CTT and (to a lesser extent) the NTE to the CTD β-sheet are rate limiting steps in the thermal recovery of the OCP^O state. Completion of these steps is inhibited by presence of a his-tag at either the C- or N-terminal extremities, but C-terminal his-tagging furthermore stabilizes the OCP^R/PBS complex.

A cross-species characterization of OCP/PBS complexes was also conducted, which revealed that irrespective of his-tagging, Plankto-OCP binds stronger to Syn-PBS than does Syn-OCP, and binds stronger to Syn-PBS than to Plankto-PBS. These findings echo the previous observation that both *Arthrospira* and *Anabaena* OCP bind stronger to Syn-PBS than to *Arthrospira* and *Anabaena* PBS, respectively [43]. Recent studies on Syn-OCP have shown that besides R155, early demonstrated as compulsory for binding to the PBS [65], residues L51, P56, G57, A58, N104, I151, and N156 play important roles in the OCP/PBS interaction [66]. In all OCP, N104 and R155 are involved in the stabilization of the OCP^O state by contributing H-bonds to the NTD/CTD interface (N104 (OD1) to W277(Syn)-/W279(Plankto)-(NE1); R155(NH2) to E244 (Syn)-/E246(Plankto)-(OE1)) and in addition, N104 contributes to the stabilization of the linker by establishing a H-bond to E174(OE1) in all structures but the Plankto-OCP structures. As G57, N104, I151, R155 and N156 are structurally conserved in Plankto-OCP, one can eliminate the hypothesis that the observed differences in Syn-PBS quenching would stem from these. As to Syn-OCP L51, it is replaced by an isoleucine in the *Anabaena*, *Limnospira* and *Tolypothrix* proteins, but the side chain of this residue occupies the same position in all structures, fitting in a groove contributed by M47, I151, F280 and V284, at the NTD-CTD interface. In Plankto-OCP, L51 is conserved but it is found at the position occupied by I53 in all previously-determined OCP structures due to changes in the sequence of the αC-αD loop (47-MGKTITVAALGAA-59 in Plankto-OCP vs. 47-MGKTLTIAAPGAA-59 in Syn-OCP). Contrastingly Syn-OCP P56 is replaced by a leucine in Plankto-OCP, while being conserved in the other OCP. Hence, the difference in PBS binding-affinity and fluorescence-quenching observed between Syn-OCP and Plankto-OCP could stem from this specific change in the sequence and structure of the αC-αD loop. Within 4 Å of R155, supposedly central to the interaction, we find four additional candidate positions at which residue substitutions could explain the higher affinity of Plankto-OCP as compared to Syn-OCP: G99, T102, A103 and C157, respectively. These residues are substituted by A99, S102, P103 and A157 in Syn-OCP, and by A99, S102, P103 and S157 in Ana-OCP. Future mutagenesis work concentrated on these residues could unveil the molecular basis for this unexpected cross-species preference of all tested OCP for the Syn-PBS. Specific to the lower affinity of Plankto-OCP for Plankto-PBS than for Syn-PBS, it must be recalled that OCP binding to the PBS is very sensitive to the structural intactness of the PBS core. Although 77 K fluorescence spectra of both isolated PBS suggested an as efficient energy transfer from PC to the last core emitters, we cannot discard the hypothesis that a slightly different interaction between the APC trimers could be at the origin of the weaker OCP-PBS binding observed for *Arthrospira* and *Planktothrix* species-specific complexes. As it was also observed that the Plankto-Lcm protein is more sensitive to proteolysis than Syn-Lcm (Supplementary Fig. 3), another (not necessarily exclusive) hypothesis could be that the reduced affinity of Plankto-OCP for the Plankto-PBS originates in the partial degradation of the Lcm component.

We last examined the influence of the functionalizing carotenoid on OCP excited and intermediate states dynamics, following the observation that CAN-functionalized OCP photoactivates faster and recovers slower than ECN-functionalized OCP. Using fs-ns and ns-s transient absorption spectroscopy on ECN- and CAN-functionalized Plankto-OCP and Syn-OCP, we inquired the time scale(s) on which the gain in photoactivation efficiency occurs for the CAN-functionalized proteins. We observed differences in the respective yields of the S_1, ICT and S* states, but nearly no change in their characteristic lifetimes nor in the P_1 yield (Table 1). Hence, the difference in photoactivation rate of ECN- and CAN-functionalized OCP does not stem from changes in their excited state dynamics nor in the P1 formation quantum yield. Interestingly, the increased S* yield observed for CAN-functionalized Plankto-OCP and Syn-OCP is not mirrored by an increase in the P_1 yield, suggesting that the former is not its only precursor. Contrastingly, clear differences between the four tested OCP were observed in the ns-s time scale. The most striking differences between Plankto-OCP and Syn-OCP are visible in the ns-ms time window, while those between CAN- and ECN-functionalized OCP concentrate in the ms-s timescale. Thus, our results suggest that both carotenoid translocation (ns-μs) and NTE/CTT detachments (μs-ms) are affected by the change in protein scaffold, whereas it is domain dissociation that is most affected by a change in the functionalizing carotenoid (ms-s). Our data support that domain dissociation is faster and more efficient in CAN-functionalized OCP, with no decline observed in the difference absorption at 550 nm. Specific to

Plankto-OCP$_{CAN}$, a faster domain separation is observed with virtually no recovery to OCP^O on the μs-s timescale (100 % efficiency from P_3 to final OCP^R). The increased photoactivation rate of Plankto-CAN is likely grounded in this property. Thus, the differences observed in the photoactivation speed of CAN- and ECN-functionalized Plankto-OCP and Syn-OCP stem from changes in the (comparatively-slow) carotenoid translocation, NTE/CTT detachment and domain dissociation steps – rather than from changes in the excited-state dynamics or P1 formation quantum yield. We yet must note that a larger drop in difference absorption at 563 nm is seen on the ns-μs time scale, which could sign for a higher barrier for carotenoid translocation into the Plankto-NTD than the Syn-NTD.

It remains unclear whether or not canthaxanthin is used as a functionalizing carotenoid for OCP in the natural context. When expressed in their parent strain, *Arthrospira* and *Synechocystis* OCP [8,11,17] bind hECN, while *Tolypothrix* OCP1 binds CAN [30]. Recombinant expression of *Arthrospira* and *Anabaena* OCP in *Synechocystis* cells also yield an hECN-functionalized proteins [33,43]. Yet, when overexpressed and isolated from CAN-producing *E. coli* cells, all these OCP bind CAN, suggesting that OCP may alternatively bind hECN or CAN depending on the carotenoid presents in the cells. We earlier reported the partial inability of *Anabaena* and *Tolypothrix* OCP to fully convert to OCP^R, when functionalized by ECN [8,11,17]. Here, thermal recovery kinetics were found to be slower in the CAN-functionalized Syn- and Plankto-OCP, possibly due to a reduced stabilization of the OCP^R state by ECN, compared to CAN. Assuming that the β-rings of the carotenoid are exposed to the bulk in the OCP^R state, as suggested by the structure of the CAN-functionalized isolated NTD of Syn-OCP (PDB id: 4xb4; [21]), the higher stability of the CAN-functionalized OCP^R could result from the presence of an oxygen on its β2 ring, favoring interaction with the bulk. A similar stability would thus be expected for hECN, which features a hydroxyl group in the β2-ring. Hence, the possibility remains that all OCP bind hECN in their parent strain.

Supporting this hypothesis is the observation that quenching by *Plankto*-OCP of the *Plankto*-PBS fluorescence is efficient only when ECN is used as the functionalizing carotenoid (or when the protein is tagged at the C-terminus). It is difficult to rationalize the observation that PBS interaction with CAN-OCP is weaker than that with ECN-OCP (Figs. 7 and 8, and Supplementary Fig. 10), because these results are at variance with the observation that CAN stabilizes the OCP^R state, and suggest that the isolated OCP^R and the PBS-bound OCP^R structures could differ. The sole difference between CAN- and ECN-functionalized OCP^R is the presence of a carbonyl oxygen on the β2-ring, but this difference should not affect binding to the PBS, since its epitope has been mapped at the opposite end of the carotenoid tunnel in the NTD, proximate to R155. Thus, it is presumably the β1-ring, identical in CAN and ECN, which will be in contact with the PBS. A possible explanation could be that upon OCP binding to PBS, the carotenoid migrates into to the PBS, enabling a better interaction with the bilin pigments, as proposed earlier [21,67]. If the β1-ring plunges into the PBS – i.e., the carotenoid moves backwards with respect to the OCP^O to OCP^R transition – then the β2-ring will be repositioned inside the highly hydrophobic carotenoid tunnel, possibly past its original position in the OCP^O structure, which would explain the reduced stability of the CAN-functionalized OCP-PBS complexes, due to replacement of a methyl in ECN by a carbonyl oxygen in CAN. If true, OCP-related quenching of PBS-fluorescence would be a two-step reaction (at the very least), with first the binding of OCP^R to PBS, and then a change in the OCP^R structure – as initially proposed by [21,67].

5. Conclusion

Here, we have reported on a comparative structure-function-dynamics study on two OCP from the OCP1 clade, i.e., Syn-OCP and Plankto-OCP. Our structures reveal that Plankto-OCP is more flexible and we speculate that this increase in flexibility explains its faster photoactivation and recovery. Specifically, our Plankto-OCP structures evidence increased structural dynamics in the αC-αD loop, shown to play a central role in the interaction between OCP^R and PBS [65–67]. Increased dynamics in this loop could be at the origin of the stronger binding of Plankto-OCP (compared to Syn-OCP) to Syn-PBS. Irrespectively, our data point to more efficient carotenoid translocation and NTE/CTT detachment in Plankto-OCP. We also show that presence of a his-tag influences both the photocycle of OCP [32] and its interaction with the PBS. Most impacting is introduction of the his-tag at the C-terminus, which results both in large damping of the photoactivation and recovery, and in stronger binding to the PBS, suggesting an important role for the CTT in these molecular processes. Finally, our work uncovers the strong influence of the nature of the functionalizing carotenoid on all aspects of OCP function. The mere substitution on ring β2 of a dimethyl in ECN by a carbonyl in CAN results in increased photoactivation efficiency, which our ns-s spectroscopic data suggest to be due to faster domain dissociation. Nonetheless, CAN-functionalized OCP display reduced recovery, reduced binding to PBS and reduced energy-quenching activity. These features could result from thwarted back-migration of CAN, compared to ECN, as required for recovery and, presumably, PBS quenching and stabilization of the OCP-PBS complex. Additionally, the observation that quenching of Plankto-PBS is efficient only when Plankto-OCP is functionalized by ECN suggests that likely, the carotenoid functionalizing OCP in the *Planktothrix* cells is not CAN.

Supplementary data to this article can be found online at https://doi.org/10.1016/j.bbabio.2022.148584.

Declaration of competing interest

Authors declare no competing interests.

Acknowledgments

We are grateful to Giorgio Schirò and Martin Weik for continued support of the project. We thank Sandrine Cot for technical assistance. We thank the ESRF and SLS synchrotron radiation facilities for beamtime allocation under long-term projects MX1992 and MX2329 (IBS BAG at ESRF), and acknowledge financial support by CEA, CNRS, Université Grenoble Alpes and Université Paris-Saclay. IBS acknowledges integration into the Interdisciplinary Research Institute of Grenoble (IRIG, CEA). This work was supported by the Agence Nationale de la Recherche (grants ANR-17-CE11-0018-01 to J.-P.C. and ANR-2018-CE11-0005-02 to the three French laboratories), the Polish National Science Centre (NCN project 2018/31/N/ST4/03983), and used the platforms of the Grenoble Instruct-ERIC center (ISBG; UMS 3518 CNRS-CEA-UGA-EMBL) within the Grenoble Partnership for Structural Biology (PSB). Platform access was supported by FRISBI (ANR-10-INBS-05-02) and GRAL, a project of the University Grenoble Alpes graduate school (Écoles Universitaires de Recherche) CBH-EUR-GS (ANR-17-EURE-0003).

Data and materials availability

Atomic coordinates and structure factors have been deposited in the Protein Data Bank under the following accession codes: 7qd0, 7qcZ, 7qd1 and 7qd2. All other data are available in the main text or the supplementary materials.

References

[1] N. Adir, H. Zer, S. Shochat, I. Ohad, Photoinhibition – a historical perspective, Photosynth. Res. 76 (2003) 343, https://doi.org/10.1023/A:1024969518145.
[2] A. Krieger-Liszkay, C. Fufezan, A. Trebst, Singlet oxygen production in photosystem II and related protection mechanism, Photosyn. Res. 98 (2008) 551–564, https://doi.org/10.1007/s11120-008-9349-3.
[3] K.K. Niyogi, T.B. Truong, Evolution of flexible non-photochemical quenching mechanisms that regulate light harvesting in oxygenic photosynthesis, Curr. Opin. Plant Biol. 16 (2013) 307–314, https://doi.org/10.1016/j.pbi.2013.03.011.

[4] D. Kirilovsky, C.A. Kerfeld, Cyanobacterial photoprotection by the orange carotenoid protein, Nat. Plants 2 (2016) 16180, https://doi.org/10.1038/nplants.2016.180.
[5] D. Kirilovsky, C.A. Kerfeld, The orange carotenoid protein in photoprotection of photosystem II in cyanobacteria, Biochim. Biophys. Acta 2012 (1817) 158–166, https://doi.org/10.1016/j.bbabio.2011.04.013.
[6] F. Muzzopappa, D. Kirilovsky, Changing color for photoprotection: the Orange carotenoid protein, Trends Plant Sci. 25 (2020) 92–104, https://doi.org/10.1016/j.tplants.2019.09.013.
[7] A. Wilson, G. Ajlani, J.-M. Verbavatz, I. Vass, C.A. Kerfeld, D. Kirilovsky, A soluble carotenoid protein involved in phycobilisome-related energy dissipation in cyanobacteria, Plant Cell 18 (2006) 992–1007, https://doi.org/10.1105/tpc.105.040121.
[8] C.A. Kerfeld, M.R. Sawaya, V. Brahmandam, D. Cascio, K.K. Ho, C.C. Trevithick-Sutton, D.W. Krogmann, T.O. Yeates, The crystal structure of a cyanobacterial water-soluble carotenoid binding protein, Structure 11 (2003) 55–65, https://doi.org/10.1016/S0969-2126(02)00936-X.
[9] A. Sedoud, R. López-Igual, A. Wilson, F. Perreau, C. Boulay, I. Vass, A. Krieger-Liszkay, D. Kirilovsky, A. ur Rehman, The cyanobacterial photoactive orange carotenoid protein is an excellent singlet oxygen quencher, Plant Cell. 26 (2014) 1781–1791, https://doi.org/10.1105/tpc.114.123802.
[10] M. Gwizdala, A. Wilson, D. Kirilovsky, In vitro reconstitution of the cyanobacterial photoprotective mechanism mediated by the Orange carotenoid protein in synechocystis PCC 6803, Plant Cell 23 (2011) 2631–2643, https://doi.org/10.1105/tpc.111.086884.
[11] A. Wilson, C. Punginelli, A. Gall, C. Bonetti, M. Alexandre, J.-M. Routaboul, C. A. Kerfeld, R. van Grondelle, B. Robert, J.T.M. Kennis, D. Kirilovsky, A photoactive carotenoid protein acting as light intensity sensor, Proc. Natl. Acad. Sci. U. S. A. 105 (2008) 12075–12080, https://doi.org/10.1073/pnas.0804636105.
[12] E.G. Maksimov, N.N. Sluchanko, Y.B. Slonimskiy, E.A. Slutskaya, A.V. Stepanov, A. M. Argentova-Stevens, E.A. Shirshin, G.V. Tsoraev, K.E. Klementiev, O. V. Slatinskaya, E.P. Lukashev, T. Friedrich, V.Z. Paschenko, A.B. Rubin, The photocycle of orange carotenoid protein conceals distinct intermediates and asynchronous changes in the carotenoid and protein components, Sci. Rep. 7 (2017) 15548, https://doi.org/10.1038/s41598-017-15520-4.
[13] M.Y. Gorbunov, F.I. Kuzminov, V.V. Fadeev, J.D. Kim, P.G. Falkowski, A kinetic model of non-photochemical quenching in cyanobacteria, Biochim. Biophys. Acta 2011 (1807) 1591–1599, https://doi.org/10.1016/j.bbabio.2011.08.009.
[14] H. Bao, M.R. Melnicki, E.G. Pawlowski, M. Sutter, M. Agostoni, S. Lechno-Yossef, F. Cai, B.L. Montgomery, C.A. Kerfeld, Additional families of orange carotenoid proteins in the photoprotective system of cyanobacteria, Nat. Plants 3 (2017) 17089, https://doi.org/10.1038/nplants.2017.89.
[15] S. Lechno-Yossef, M.R. Melnicki, H. Bao, B.L. Montgomery, C.A. Kerfeld, Synthetic OCP heterodimers are photoactive and recapitulate the fusion of two primitive carotenoproteins in the evolution of cyanobacterial photoprotection, Plant J. 91 (2017) 646–656, https://doi.org/10.1111/tpj.13593.
[16] F. Muzzopappa, A. Wilson, D. Kirilovsky, Interdomain interactions reveal the molecular evolution of the orange carotenoid protein, Nat. Plants 5 (2019) 1076–1086, https://doi.org/10.1038/s41477-019-0514-9.
[17] A. Wilson, J.N. Kinney, P.H. Zwart, C. Punginelli, S. D'Haene, F. Perreau, M. G. Klein, D. Kirilovsky, C.A. Kerfeld, Structural determinants underlying photoprotection in the photoactive orange carotenoid protein of cyanobacteria, J. Biol. Chem. 285 (2010) 18364–18375, https://doi.org/10.1074/jbc.M110.115709.
[18] S. Gupta, M. Sutter, S.G. Remesh, M.A. Dominguez-Martin, H. Bao, X.A. Feng, L.-J. G. Chan, C.J. Petzold, C.A. Kerfeld, C.Y. Ralston, X-ray radiolytic labeling reveals the molecular basis of orange carotenoid protein photoprotection and its interactions with fluorescence recovery protein, J. Biol. Chem. 294 (2019) 8848–8860, https://doi.org/10.1074/jbc.RA119.007592.
[19] P.E. Konold, I.H.M. van Stokkum, F. Muzzopappa, A. Wilson, M.L. Groot, D. Kirilovsky, J.T.M. Kennis, Photoactivation mechanism, timing of protein secondary structure dynamics and carotenoid translocation in the Orange carotenoid protein, J. Am. Chem. Soc. (2018), https://doi.org/10.1021/jacs.8b11373.
[20] Y.B. Slonimskiy, E.G. Maksimov, E.P. Lukashev, M. Moldenhauer, T. Friedrich, N. N. Sluchanko, Engineering the photoactive orange carotenoid protein with redox-controllable structural dynamics and photoprotective function, Biochim. Biophys. Acta, Bioenerg. 1861 (2020), 148174, https://doi.org/10.1016/j.bbabio.2020.148174.
[21] R.L. Leverenz, M. Sutter, A. Wilson, S. Gupta, A. Thurotte, C.B. de Carbon, C. J. Petzold, C. Ralston, F. Perreau, D. Kirilovsky, C.A. Kerfeld, A 12 Å carotenoid translocation in a photoswitch associated with cyanobacterial photoprotection, Science 348 (2015) 1463–1466, https://doi.org/10.1126/science.aaa7234.
[22] M. Bondanza, L. Cupellini, P. Faccioli, B. Mennucci, Molecular mechanisms of activation in the Orange carotenoid protein revealed by molecular dynamics, J. Am. Chem. Soc. 142 (2020) 21829–21841, https://doi.org/10.1021/jacs.0c10461.
[23] E.G. Maksimov, E.A. Protasova, G.V. Tsoraev, I.A. Yaroshevich, A.I. Maydykovskiy, E.A. Shirshin, T.S. Gostev, A. Jelzow, M. Moldenhauer, Y.B. Slonimskiy, N. N. Sluchanko, T. Friedrich, Probing of carotenoid-tryptophan hydrogen bonding dynamics in the single-tryptophan photoactive Orange carotenoid protein, Sci. Rep. 10 (2020) 11729, https://doi.org/10.1038/s41598-020-68463-8.
[24] N.B. Pigni, K.L. Clark, W.F. Beck, J.A. Gascón, Spectral signatures of canthaxanthin translocation in the Orange carotenoid protein, J. Phys. Chem. B 124 (2020) 11387–11395, https://doi.org/10.1021/acs.jpcb.0c08756.
[25] R. Berera, I.H.M. van Stokkum, S. d'Haene, J.T.M. Kennis, R. van Grondelle, J. P. Dekker, A mechanism of energy dissipation in cyanobacteria, Biophys. J. 96 (2009) 2261–2267, https://doi.org/10.1016/j.bpj.2008.12.3905.
[26] R. Berera, I.H.M. van Stokkum, M. Gwizdala, A. Wilson, D. Kirilovsky, R. van Grondelle, The photophysics of the orange carotenoid protein, a light-powered molecular switch, J. Phys. Chem. B 116 (2012) 2568–2574, https://doi.org/10.1021/jp2108329.
[27] P.O. Andersson, T. Gillbro, Photophysics and dynamics of the lowest excited singlet state in long substituted polyenes with implications to the very long-chain limit, J. Chem. Phys. 103 (1995) 2509–2519, https://doi.org/10.1063/1.469672.
[28] C.C. Gradinaru, J.T.M. Kennis, E. Papagiannakis, I.H.M. van Stokkum, R.J. Cogdell, G.R. Fleming, R.A. Niederman, R. van Grondelle, An unusual pathway of excitation energy deactivation in carotenoids: singlet-to-triplet conversion on an ultrafast timescale in a photosynthetic antenna, Proc. Natl. Acad. Sci. U. S. A. 98 (2001) 2364–2369, https://doi.org/10.1073/pnas.051501298.
[29] V. Balevičius, D. Abramavicius, T. Polívka, A. GalestianPour, J. Hauer, A unified picture of S* in carotenoids, J. Phys. Chem. Lett. 7 (2016) 3347–3352, https://doi.org/10.1021/acs.jpclett.6b01455.
[30] V. Kuznetsova, M.A. Dominguez-Martin, H. Bao, S. Gupta, M. Sutter, M. Kloz, M. Rebarz, M. Přeček, Y. Chen, C.J. Petzold, C.Y. Ralston, C.A. Kerfeld, T. Polívka, Ultrafast spectroscopy and structural analysis explain differences between the photoactivation mechanism of OCP1 and OCP2, Biochim. Biophys. Acta Bioenerg. 1861 (2020), 148120, https://doi.org/10.1016/j.bbabio.2019.148120.
[31] T. Lenzer, F. Ehlers, M. Scholz, R. Oswald, K. Oum, Assignment of carotene S* state features to the vibrationally hot ground electronic state, Phys. Chem. Chem. Phys. 12 (2010) 8832–8839, https://doi.org/10.1039/B925071A.
[32] S. Niziński, A. Wilson, L.M. Uriarte, C. Ruckebusch, E.A. Andreeva, I. Schlichting, J.-P. Colletier, D. Kirilovsky, G. Burdzinski, M. Sliwa, Unifying Perspective of the ultrafast photodynamics of orange carotenoid proteins from synechocystis: peril of high-power excitation, existence of different S* States, and influence of tagging, JACS Au. 2 (2022) 1084–1095, https://doi.org/10.1021/jacsau.1c00472.
[33] C.B. de Carbon, A. Thurotte, A. Wilson, F. Perreau, D. Kirilovsky, Biosynthesis of soluble carotenoid holoproteins in Escherichia coli, Sci. Rep. 5 (2015), https://doi.org/10.1038/srep09085.
[34] S. Gupta, M. Guttman, R.L. Leverenz, K. Zhumadilova, E.G. Pawlowski, C. J. Petzold, K.K. Lee, C.Y. Ralston, C.A. Kerfeld, Local and global structural drivers for the photoactivation of the orange carotenoid protein, PNAS 112 (2015) E5567–E5574, https://doi.org/10.1073/pnas.1512240112.
[35] A. Mezzetti, M. Alexandre, A. Thurotte, A. Wilson, M. Gwizdala, D. Kirilovsky, Two-step structural changes in Orange carotenoid protein photoactivation revealed by time-resolved Fourier transform infrared spectroscopy, J. Phys. Chem. B 123 (2019) 3259–3266, https://doi.org/10.1021/acs.jpcb.9b01242.
[36] D. Harris, F. Muzzopappa, F. Glaser, A. Wilson, D. Kirilovsky, N. Adir, Structural dynamics in the C terminal domain homolog of orange carotenoid protein reveals residues critical for carotenoid uptake, Biochim. Biophys. Acta Bioenerg. 1861 (2020), 148214, https://doi.org/10.1016/j.bbabio.2020.148214.
[37] D. Harris, A. Wilson, F. Muzzopappa, N.N. Sluchanko, T. Friedrich, E.G. Maksimov, D. Kirilovsky, N. Adir, Structural rearrangements in the C-terminal domain homolog of Orange carotenoid protein are crucial for carotenoid transfer, Commun. Biol. 1 (2018) 125, https://doi.org/10.1038/s42003-018-0132-5.
[38] A. Wilson, C. Punginelli, M. Couturier, F. Perreau, D. Kirilovsky, Essential role of two tyrosines and two tryptophans on the photoprotection activity of the Orange carotenoid protein, Biochim. Biophys. Acta 2011 (1807) 293–301, https://doi.org/10.1016/j.bbabio.2010.12.009.
[39] C. Punginelli, A. Wilson, J.-M. Routaboul, D. Kirilovsky, Influence of zeaxanthin and echinenone binding on the activity of the orange carotenoid protein, Biochim. Biophys. Acta 1787 (2009) 280–288, https://doi.org/10.1016/j.bbabio.2009.01.011.
[40] V. Šlouf, V. Kuznetsova, M. Fuciman, C.B. de Carbon, A. Wilson, D. Kirilovsky, T. Polívka, Ultrafast spectroscopy tracks carotenoid configurations in the orange and red carotenoid proteins from cyanobacteria, Photosyn. Res. 131 (2017) 105–117, https://doi.org/10.1007/s11120-016-0302-6.
[41] C. Djediat, K. Feilke, A. Brochard, L. Caramelle, S. Kim Tiam, P. Sétif, T. Gauvrit, C. Yéprémian, A. Wilson, L. Talbot, B. Marie, D. Kirilovsky, C. Bernard, Light stress in green and red planktothrix strains: the orange carotenoid protein and its related photoprotective mechanism, Biochim. Biophys. Acta Bioenerg. 1861 (2020), 148037, https://doi.org/10.1016/j.bbabio.2019.06.009.
[42] N.N. Sluchanko, K.E. Klementiev, E.A. Shirshin, G.V. Tsoraev, T. Friedrich, E. G. Maksimov, The purple Trp288Ala mutant of synechocystis OCP persistently quenches phycobilisome fluorescence and tightly interacts with FRP, Biochim. Biophys. Acta Bioenerg. 2017 (1858) 1–11, https://doi.org/10.1016/j.bbabio.2016.10.005.
[43] D. Jallet, A. Thurotte, R.L. Leverenz, F. Perreau, C.A. Kerfeld, D. Kirilovsky, Specificity of the cyanobacterial orange carotenoid protein: influences of orange carotenoid protein and phycobilisome structures, Plant Physiol. 164 (2014) 790–804, https://doi.org/10.1104/pp.113.229997.
[44] Y. Kashino, H. Koike, K. Satoh, An improved sodium dodecyl sulfate-polyacrylamide gel electrophoresis system for the analysis of membrane protein complexes, Electrophoresis 22 (2001) 1004–1007, doi:10.1002/1522-268322:6<1004::AID-ELPS1004>3.0.CO;2-Y.
[45] G. Burdzinski, M. Bayda, G.L. Hug, M. Majchrzak, B. Marciniec, B. Marciniak, Time-resolved studies on the photoisomerization of a phenylene–silylene–vinylene type compound in its first singlet excited state, J. Lumin. 131 (2011) 577–580, https://doi.org/10.1016/j.jlumin.2010.10.031.
[46] P. Müller, K. Brettel, [Ru(bpy)3]2+ as a reference in transient absorption spectroscopy: differential absorption coefficients for formation of the long-lived

3MLCT excited state, Photochem. Photobiol. Sci. 11 (2012) 632–636, https://doi.org/10.1039/C2PP05333K.
[47] W. Kabsch, XDS, Acta Crystallogr. D Biol. Crystallogr. 66 (2010) 125–132, https://doi.org/10.1107/S0907444909047337.
[48] W. Kabsch, Integration, scaling, space-group assignment and post-refinement, Acta Cryst. D 66 (2010) 133–144, https://doi.org/10.1107/S0907444909047374.
[49] A.J. McCoy, R.W. Grosse-Kunstleve, P.D. Adams, M.D. Winn, L.C. Storoni, R. J. Read, Phaser crystallographic software, J. Appl. Crystallogr. 40 (2007) 658–674, https://doi.org/10.1107/S0021889807021206.
[50] M.D. Winn, C.C. Ballard, K.D. Cowtan, E.J. Dodson, P. Emsley, P.R. Evans, R. M. Keegan, E.B. Krissinel, A.G.W. Leslie, A. McCoy, S.J. McNicholas, G. N. Murshudov, N.S. Pannu, E.A. Potterton, H.R. Powell, R.J. Read, A. Vagin, K. S. Wilson, Overview of the CCP4 suite and current developments, Acta Crystallogr. D Biol. Crystallogr. 67 (2011) 235–242, https://doi.org/10.1107/S0907444910045749.
[51] K. Cowtan, Fitting molecular fragments into electron density, Acta Crystallogr. D Biol. Crystallogr. 64 (2008) 83–89, https://doi.org/10.1107/S0907444907033938.
[52] K. Cowtan, Recent developments in classical density modification, Acta Crystallogr D Biol Crystallogr. 66 (2010) 470–478, https://doi.org/10.1107/S090744490903947X.
[53] G.N. Murshudov, P. Skubák, A.A. Lebedev, N.S. Pannu, R.A. Steiner, R.A. Nicholls, M.D. Winn, F. Long, A.A. Vagin, REFMAC5 for the refinement of macromolecular crystal structures, Acta Crystallogr. D Biol. Crystallogr. 67 (2011) 355–367, https://doi.org/10.1107/S0907444911001314.
[54] P. Emsley, B. Lohkamp, W.G. Scott, K. Cowtan, Features and development of coot, Acta Crystallogr. D Biol. Crystallogr. 66 (2010) 486–501, https://doi.org/10.1107/S0907444910007493.
[55] W. Wriggers, K. Schulten, Protein domain movements: detection of rigid domains and visualization of hinges in comparisons of atomic coordinates, Proteins 29 (1997) 1–14.
[56] E. Chovancova, A. Pavelka, P. Benes, O. Strnad, J. Brezovsky, B. Kozlikova, A. Gora, V. Sustr, M. Klvana, P. Medek, L. Biedermannova, J. Sochor, J. Damborsky, CAVER 3.0: a tool for the analysis of transport pathways in dynamic protein structures, PLoS Comput Biol. 8 (2012), e1002708, https://doi.org/10.1371/journal.pcbi.1002708.
[57] L.L.C. Schrödinger, The PyMOL Molecular Graphics System, Version 1.8, 2015.
[58] I.A. Yaroshevich, E.G. Maksimov, N.N. Sluchanko, D.V. Zlenko, A.V. Stepanov, E. A. Slutskaya, Y.B. Slonimskiy, V.S. Botnarevskii, A. Remeeva, I. Gushchin, K. Kovalev, V.I. Gordeliy, I.V. Shelaev, F.E. Gostev, D. Khakhulin, V.V. Poddubnyy, T.S. Gostev, D.A. Cherepanov, T. Polívka, M. Kloz, T. Friedrich, V.Z. Paschenko, V. A. Nadtochenko, A.B. Rubin, M.P. Kirpichnikov, Role of hydrogen bond alternation and charge transfer states in photoactivation of the Orange carotenoid protein, Commun. Biol. 4 (2021) 539, https://doi.org/10.1038/s42003-021-02022-3.
[59] A.A. Arteni, G. Ajlani, E.J. Boekema, Structural organisation of phycobilisomes from Synechocystis sp. strain PCC6803 and their interaction with the membrane, Biochim. Biophys. Acta 1787 (2009) 272–279, https://doi.org/10.1016/j.bbabio.2009.01.009.
[60] S. Bandara, Z. Ren, L. Lu, X. Zeng, H. Shin, K.-H. Zhao, X. Yang, Photoactivation mechanism of a carotenoid-based photoreceptor, PNAS 114 (2017) 6286–6291, https://doi.org/10.1073/pnas.1700956114.
[61] R. López-Igual, A. Wilson, R.L. Leverenz, M.R. Melnicki, C.B. de Carbon, M. Sutter, A. Turmo, F. Perreau, C.A. Kerfeld, D. Kirilovsky, Different functions of the paralogs to the N-terminal domain of the Orange carotenoid protein in the Cyanobacterium Anabaena sp. PCC 7120, Plant Physiol. 171 (2016) 1852–1866, https://doi.org/10.1104/pp.16.00502.
[62] M. Golub, M. Moldenhauer, F.-J. Schmitt, W. Lohstroh, E.G. Maksimov, T. Friedrich, J. Pieper, Solution structure and conformational flexibility in the active state of the orange carotenoid protein. Part II: quasielastic neutron scattering, J. Phys. Chem. B 123 (2019) 9536–9545, https://doi.org/10.1021/acs.jpcb.9b05073.
[63] E.A. Andreeva, S. Nizinski, A. Wilson, M. Levantino, E.D. Zitter, R. Munro, F. Muzzopappa, A. Thureau, N. Zala, G. Burdzinski, M. Sliwa, D. Kirilovsky, G. Schirò, J.-P. Colletier, Oligomerization Processes Limit Photoactivation and Recovery of the Orange Carotenoid Protein, 2022, https://doi.org/10.1101/2022.02.04.479168.
[64] A. Thurotte, R. Lopez-Igual, A. Wilson, L. Comolet, C. Bourcier de Carbon, F. Xiao, D. Kirilovsky, Regulation of Orange carotenoid protein activity in cyanobacterial Photoprotection1[OPEN], Plant Physiol. 169 (2015) 737–747, https://doi.org/10.1104/pp.15.00843.
[65] A. Wilson, M. Gwizdala, A. Mezzetti, M. Alexandre, C.A. Kerfeld, D. Kirilovsky, The essential role of the N-terminal domain of the Orange carotenoid protein in cyanobacterial photoprotection: importance of a positive charge for phycobilisome Binding[C][W], Plant Cell 24 (2012) 1972–1983, https://doi.org/10.1105/tpc.112.096909.
[66] A. Wilson, F. Muzzopappa, D. Kirilovsky, Elucidation of the essential amino acids involved in the binding of the cyanobacterial Orange carotenoid protein to the phycobilisome, Biochim. Biophys. Acta, Bioenerg. 1863 (2022), 148504, https://doi.org/10.1016/j.bbabio.2021.148504.
[67] W. Lou, D.M. Niedzwiedzki, R.J. Jiang, R.E. Blankenship, H. Liu, Binding of red form of Orange Carotenoid Protein (OCP) to phycobilisome is not sufficient for quenching, Biochim. Biophys. Acta Bioenerg. 1861 (2020), 148155, https://doi.org/10.1016/j.bbabio.2020.148155.

Biophysical Journal
Article

Biophysical Society

Oligomerization processes limit photoactivation and recovery of the orange carotenoid protein

Elena A. Andreeva,[1,2] Stanisław Niziński,[3,7] Adjélé Wilson,[4] Matteo Levantino,[5] Elke De Zitter,[1] Rory Munro,[1] Fernando Muzzopappa,[4] Aurélien Thureau,[6] Ninon Zala,[1] Gotard Burdzinski,[3] Michel Sliwa,[7] Diana Kirilovsky,[4] Giorgio Schirò,[1] and Jacques-Philippe Colletier[1,*]

[1]Institut de Biologie Structurale (IBS), Université Grenoble Alpes, CEA, CNRS, Grenoble, France; [2]Max-Planck-Institut für medizinische Forschung, Heidelberg, Germany; [3]Quantum Electronics Laboratory, Faculty of Physics, Adam Mickiewicz University in Poznan, Poznan, Poland; [4]Institute for Integrative Biology of the Cell (I2BC), CEA, CNRS, Université Paris-Sud, Université Paris-Saclay, Gif-sur-Yvette, France; [5]European Synchrotron Radiation Facility (ESRF), Grenoble, France; [6]Synchrotron SOLEIL, 91190, Saint Aubin, France; and [7]Univ. Lille, CNRS, UMR 8516 - LASIRe - Laboratoire de Spectroscopie pour les Interactions la Réactivité et l'Environnement, F-59000 Lille, France

ABSTRACT The orange carotenoid protein (OCP) is a photoactive protein involved in cyanobacterial photoprotection by quenching of the excess of light-harvested energy. The photoactivation mechanism remains elusive, in part due to absence of data pertaining to the timescales over which protein structural changes take place. It also remains unclear whether or not oligomerization of the dark-adapted and light-adapted OCP could play a role in the regulation of its energy-quenching activity. Here, we probed photoinduced structural changes in OCP by a combination of static and time-resolved X-ray scattering and steady-state and transient optical spectroscopy in the visible range. Our results suggest that oligomerization partakes in regulation of the OCP photocycle, with different oligomers slowing down the overall thermal recovery of the dark-adapted state of OCP. They furthermore reveal that upon non-photoproductive excitation a numbed state forms, which remains in a non-photoexcitable structural state for at least $\approx 0.5\ \mu$s after absorption of a first photon.

SIGNIFICANCE The orange carotenoid protein (OCP) is a photoactivatable protein involved in cyanobacterial photoprotection. Upon photoactivation, OCP becomes able to quench the excess of energy taken up by the light-harvesting antennae, thereby evading damage to the cells. However, the exact OCP photoactivation mechanism, and whether or not oligomerization partakes in the regulation of the OCP function, remains unclear. Here, we investigated these issues by combining static and time-resolved X-ray scattering and optical spectroscopy. Our results show that OCP oligomerizes in both the dark-adapted inactive and light-adapted active states, suggesting a functional role for oligomerization. Time-resolved scattering data furthermore reveal that the first large-scale conformational changes associated with OCP photoactivation take place on the microsecond timescale.

INTRODUCTION

Photosynthetic organisms have evolved to make use of up to 99% of light-harvested energy (1). In most cyanobacteria, the main light-harvesting antenna is the phycobilisome (PBS), a soluble complex capable of directly funneling its harvested photon energy into thylakoid-membrane-embedded reaction centers. In the event of an energy overflow into photosystem II reaction center, charge recombination can occur that will lead to the production of $^1O_2$, which in turn may damage the photosynthetic apparatus (2,3). The main function of the soluble two-domain photoactive orange carotenoid protein (OCP) is to quench the excessive energy absorbed by the PBS, enabling the dissipation of this energy into heat. This is accompanied by a decrease in the PBS fluorescence. For its energy-quenching function to be elicited, OCP needs to be photoactivated by the absorption of a blue-green photon, which triggers the transition from the dark inactive orange state (OCP^O) to the active red state (OCP^R) (4–11) capable of quenching up to 80% of the PBS fluorescence (12). As the photoactivation yield of OCP is extremely low (0.2%) (13,14), the interaction between

Submitted February 4, 2022, and accepted for publication July 1, 2022.

*Correspondence: colletier@ibs.fr

Fernando Muzzopappa's present address is Center for Integrative Biology (CBI), University of Toulouse, CNRS, Toulouse, France.

Editor: Wendy Shaw.

https://doi.org/10.1016/j.bpj.2022.07.004

PBS and OCP^R only occurs when irradiance threatens cell survival. Additionally, OCP can also quench $^1O_2$ and is thus one of the central players in cyanobacterial photoprotection (15,16). Phylogenetic investigations have allowed classification of OCP sequences into three clades, namely OCP1, OCP2, and OCPX (17).

Most research endeavors on OCP (including the present work) have been conducted on the *Synechocystis* PCC 6803 OCP1 variant featuring echinenone (ECN) as the functionalizing carotenoid (18,19). Nonetheless, the first crystallographic structure of a dark-adapted OCP^O was from the cyanobacteria *Limnospira* (*Arthrospira*) *maxima*, and featured 3′-hydroxy-ECN as the natural pigment (15). The structure revealed that OCP crystallizes as a dimer (Fig. 1, *A* and *B*) wherein each monomer folds into two domains separated by a ≈20-residue linker (Fig. 1 *C*). The N-terminal domain (NTD), comprising residues 1–165, is the effector domain binding to PBS, while the C-terminal domain (CTD) is composed of residues 190–317 and serves as the regulator of OCP energy-quenching activity (20). The ketocarotenoid pigment binds in a ≈35-Å-long hydrophobic tunnel that spans the two domains. The NTD is fully α-helical (αA to αJ), featuring a fold unique to cyanobacteria, whereas the CTD is a seven-stranded β-sheet (β1 to β7) sandwiched between two sets of α-helices, namely αK, αL, and αM, on one side (referred to as the F-side) (21), and the terminal αA (residues 1–19; also referred to as the N-terminal extension or NTE) and αN (residues 304–317; also referred to as the C-terminal tail or CTT), on the opposite side (referred to as the A-side) (21). The αA and αN helices have been shown to play important roles in the regulation of OCP photoactivation and recovery. Stabilization of the OCP^O state is achieved at two main interfaces, namely the NTD/CTD interface, burying 677 $Å^2$ of surface area and featuring two strictly conserved H bonds (i.e., R155 to E244, N104 to W277; Fig. 1 *C*), and the αA/CTD interface, burying 790 $Å^2$ and featuring six H bonds (buried surface areas calculated from the *Synechocystis* OCP structure) two of which to the C-terminal αN (L16(O)–A308(N) and A18(N)–L307(O)). Thus, the αA helix is one of the main secondary structure elements supporting the stabilization of the OCP^O structure. Additionally, the carotenoid buries ≈990 $Å^2$ of surface area across the two domains (≈545 and 445 $Å^2$ in the NTD and the CTD, respectively), establishing two H bonds with Y201(OH) and W288(Nε1) in the CTD (Fig. 1 *C*). The pigment is therefore also essential in stabilizing OCP^O.

All available crystal structures of OCP^O feature a dimer, wherein monomers are associated through contacts between facing αA, αB, and αH helices, burying ≈1090 $Å^2$ at the dimerization interface (Fig. 1, *A* and *B*). Due to the high concentration of OCP^O within crystals (20–30 mM, depending on the crystal structure considered), the prevalence of OCP^O in its dimeric form was, until recently, regarded as a crystallization artifact and therefore overlooked (18). Recent results obtained using native mass spectrometry have since shown that OCP^O dimers can form in solution at concentrations as low as 3 μM (0.1 mg/mL) (22). The presence of OCP^O dimers was also observed by size-exclusion chromatography (SEC) and in small-angle X-ray/neutron scattering (SAXS/SANS) experiments (23,24), which furthermore identified the crystallographic dimer as that which naturally occurs. Also supporting the hypothesis that OCP^O dimers could form in vivo is the report that the mutation of a single (R27) of the three most-conserved residues (D19, R27, S134) among the 22 making up the dimerization interface (18) results in a constitutively monomeric mutant (10). Further adding to this complexity is the question as to whether or not the light-adapted OCP^R can also oligomerize, which has been supported by recent SAXS/SANS data (21,22) but not by native mass spectrometry (10,22,25,26). Altogether these results raise cogent questions as to whether and how oligomerization participates in the regulation of OCP function.

The exact photoactivation mechanism of OCP—meaning accumulation of OCP^R, not the mere appearance of a red spectrum already achieved 50 ps after excitation—remains elusive. Indeed, despite the use of different experimental approaches to probe the OCP^O-to-OCP^R transition with a high resolution in either time (27–29) or space (19,30–32), uncertainties remain regarding the exact sequence of events leading to photoactivation, in part because data are lacking that pertain to the (long) timescales over which (large-scale) structural changes take place. All investigators agree on the fact that upon photon absorption, the carotenoid transitions to an excited S_2 state, which decays within ≈0.1 ps into multiple picosecond-lived excited states (S_1, ICT, S*). Only one of these presumably leads to the minute-lived OCP^R state (S* in (27), S_1 in (14)) after the formation of at least four different intermediates (photoproducts P_1, P_2, $P_{2'}$, P_3) over the picosecond-microsecond timescale (27). Thus, the formation of OCP^R is mainly limited by picosecond-timescale excited-state dynamics, with ≈99% of carotenoids relaxing back to the ground state along non-productive pathways. It was suggested that photoproduct P_1 is characterized by rupture of the H bonds between the carotenoid and the protein, P_2 by a repositioning of the β1-ring in the CTD, and P_3 by the translocation (12 Å) of the carotenoid into the NTD. The dissociation of helices αA and αN from the A-side of the CTD was suggested to await the millisecond timescale (25) and to be followed by dissociation of the two domains, yielding the photoactive OCP^R. This hypothesis has since been supported by SEC and SAXS (30). By specific labeling of accessible carboxylate groups, mass spectrometry further pointed to a signal transduction mechanism whereby disorder is propagated across the CTD β-sheet, upon photoactivation and rupture of H bonds between the carotenoid and the CTD, resulting in a detachment of helix αA and subsequent dissociation of the dimer through destabilization of helix αB. Direct structural evidence for the existence of these steps is still lacking. Most recently, experiments carried out on an OCP mutant wherein

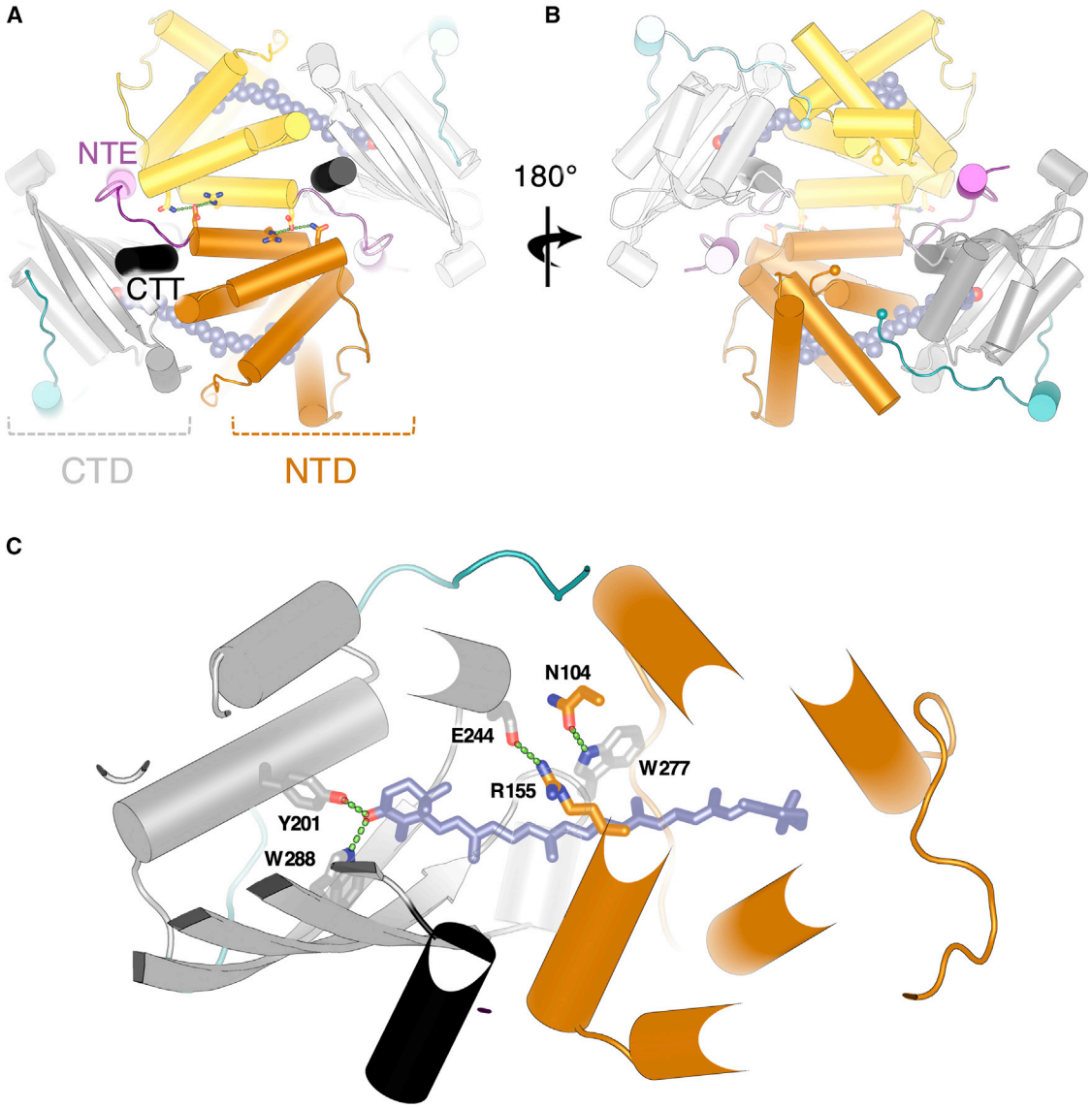

FIGURE 1 OCP crystallizes as a dimer. (*A* and *B*) Structure of dark-adapted OCP (OCP^O) dimer from the cyanobacteria *Synechocystis* PCC 6703 (PDB: 3MG1). Within the dimer, each OCP monomer features two domains: 1) an N-terminal domain (NTD; colored *orange*) comprising residues 1–165; 2) a C-terminal domain (CTD; colored *gray*) comprising residues 193–317. The N-terminal extension (NTE) and the C-terminal tail (CTT) are shown in pink and black, respectively. The two domains are attached by a ≈20-residue linker (colored *cyan*). The keto-carotenoid pigment, e.g., echinenone (ECN; colored *slate* and shown as *spheres*), binds in a ≈35-Å-long hydrophobic tunnel spanning the two domains and H bonds to Y201 and W288 in the CTD. The dimerization interface is supported by conserved H bonds between D19, R27, and N134 (shown as *sticks*). (*C*) Close-up view of dark-adapted OCP (OCP^O) monomer in the dimer (*A* and *B*). The interaction between the NTD and the CTD within the OCP^O monomer is supported by two strictly conserved interactions, i.e., a salt bridge between R155 and E244, and H bonds between N104 and W277 (shown as *sticks*). The two H bonds of the carotenoid to Y201 and W288 (shown as *sticks*) are also shown (*green dashes*). To see this figure in color, go online.

stabilization of the carotenoid to the NTD is modified (mutation into phenylalanine of W101, W110, and W277) supported the existence of two additional intermediate states between P_3 and OCP^R, namely P_M and P_X, proposed to be characterized by dissociation of the αA and αN helices, respectively (29). It yet remains unclear whether these states also exist in the wild-type protein.

In the present work, we used a combination of mutagenesis, transient spectroscopy in the visible range, and static and time-resolved X-ray solution scattering to clarify 1) the oligomerization states of OCP^O and OCP^R in solution, 2) the timescale over which large-scale structural changes associated with photoactivation take place, and 3) whether or not pulsed illumination permits the formation of OCP^R. By conducting static SAXS experiments on the wild-type OCP and on a stable monomeric R27L mutant (10), wherein the conserved R27-D19 salt bridge at the dimerization interface is suppressed, we obtained confirmation that both OCP^O

and OCP^R can oligomerize in solution, suggesting that oligomerization could play a role in the regulation of OCP activity. Using time-resolved (TR)-SAXS, we obtained evidence that the "red"-shifted state generated by pulsed illumination, which forms and decays within ≈10 μs and ≈10–200 ms (depending on the His-tag location), respectively, differs from the OCP^R state accumulated under stationary illumination conditions, which forms and decays within ≈1 ms and ≈1–30 min (depending on concentration), respectively. Our data furthermore reveal that upon a non-productive pulsed photoexcitation—i.e., in the 99.7% of the cases where OCP^R does not form—OCP remains in a non-photoexcitable structural state for at least ≈0.5 μs, despite the carotenoid returning back to the electronic ground state within tens of picoseconds and the protein featuring a spectrum characteristic of the OCP^O state (27).

MATERIALS AND METHODS

Protein expression and sample preparation

OCP expression and extraction were carried out as described in Gwizdala et al. (8) and Bourcier de Carbon et al. (33). In brief, expression in the holo form of the N-terminally His-tagged wild-type OCP ($OCP_{wt\text{-}Ntag}$) and the N-terminally His-tagged monomeric mutant ($OCP_{R27L\text{-}Ntag}$) was achieved by respective transformation of the *pCDF-NtagOCPSyn* or *pCDF-NtagOCPSynR27L* plasmids into ECN-producing BL21 (DE3) *Escherichia coli* cells, i.e., cells previously transformed with the pAC-BETA and pBAD-CrtO plasmids described in Bourcier de Carbon et al. (31). Expression in *Synechocystis* cells of the holo form of C-terminally His-tagged wild-type OCP ($OCP_{wt\text{-}Ctag}$) was achieved using the protocol described in Gwizdala et al. (8). The proteins were purified in three steps including affinity chromatography on an Ni-NTA column (Ni-Probond resin; Invitrogen, Waltham, MA), hydrophobic chromatography on a phenyl-Sepharose column (HiTrap Phenyl HP; GE Healthcare, Chicago, IL), and SEC on an analytical HiLoad 16/60 Superdex 75 (HiLoad 16/600 Superdex 75 pg; Sigma-Aldrich, St. Louis, MO). Proteins were eluted from the latter at a flow rate of 1 mL/min using a 50 mM Tris-HCl (pH 7.4) and 150 mM NaCl buffer. To assert the molecular weight of eluted species, the column was calibrated beforehand using the following standard proteins: γ-globulin (158 kDa), ovalbumin (44 kDa), myoglobin (17 kDa), and vitamin B12 (1.35 kDa). The purity of both OCP variants was assessed by 12% SDS-PAGE electrophoresis (Fig. S11). OCP concentrations were estimated from the absorbance signal at 490 nm, using the extinction coefficient of 63,000 $M^{-1}\cdot cm^{-1}$ proposed by Sluchanko et al. (34). We note that an uncertainty remains as to the exact extinction coefficient that should be used to derive OCP concentration from absorbance measurement. Protein concentration is nowadays generally estimated using the absorbance signal at 280 nm and a calculated extinction coefficient (e.g., obtained from https://web.expasy.org/cgi-bin/protparam/protparam (35,36)), which in the case of *Synechocystis* OCP amounts to 34,659 $M^{-1}\cdot cm^{-1}$. This value agrees well with the extinction coefficient at 490 nm proposed by Sluchanko et al., as the ratio between the 490 and 280 nm peaks is ≈2 for the pure protein, but it neglects the potential absorption of the keto-carotenoid pigment at 280 nm. Thus far, most of the papers published on OCP have accordingly used an extinction coefficient of 110,000 $M^{-1}\cdot cm^{-1}$ at 490 nm, based on the debatable assumption that the keto-carotenoid pigment has a similar absorption spectrum when bound to OCP or dissolved in organic solvents. Indeed, if there is no absorbance of the carotenoid at 280 nm, then one expects a ratio of ≈3 between the absorbance peaks at 490 nm and 280 nm. But if we consider absorption of the carotenoid at 280 nm and assume the same extinction coefficient when bound to the protein scaffold or dissolved in organic solvents—i.e., roughly 15% of the absorption peak at 490 nm (measured by us as well as others)—then the measured ratio of ≈2 between the absorbance at 490 and 280 nm can be rationalized since $A_{280\ nm} = (0.33 + 0.15) \times A_{490\ nm} = 0.48 \times A_{490\ nm}$. At present, we cannot favor either hypothesis. However, as our current aim is to report on oligomerization processes, we believe it is preferable that we underestimate rather than overestimate dissociation constants. Hence, the concentrations reported in the present paper were estimated using the conservative extinction coefficient of 63,000 $M^{-1}\cdot cm^{-1}$ (34). The actual concentrations and dissociation constants could yet be 1.7-times lower if the keto-carotenoid absorbs at 280 nm and the real extinction coefficient of OCP at 490 nm is 110,000 $M^{-1}\cdot cm^{-1}$.

Static SAXS measurements

Static X-ray scattering data were collected at 21°C on an EigerX-4M detector at the SWING beamline of the SOLEIL Synchrotron (Saint-Aubin, France). X-ray solution scattering signals in the SAXS region (q = 0.02–0.5 $Å^{-1}$) were collected for $OCP_{wt\text{-}Ctag}$ and $OCP_{R27L\text{-}Ntag}$ at various concentrations using a monochromatic (double Si(111) monochromator) X-ray beam centered at 12 keV and an EigerX-4M (Dectris) detector. Two sets of measurements were carried out, before and after 30-min irradiation of OCP solutions with a 430 nm LED source (≈500 mW/cm^2), allowing collection of X-ray scattering signals in the dark-adapted (OCP^O) and light-adapted (OCP^R) states, respectively. For $OCP_{wt\text{-}Ctag}$, data were acquired at 0.7, 3.5, 10.5, and 23 mg/mL for the OCP^O state and at 0.7, 3.5, and 10.5 mg/mL for the OCP^R state, while for $OCP_{R27L\ -Ntag}$, data were recorded at 0.7, 3.5, 10.5, and 14 mg/mL for the OCP^O state and at 0.7, 3.5, and 10.5 mg/mL for the OCP^R state. For each concentration, 30 X-ray scattering signals (each registered after 990 ms of X-ray exposure) were collected with 30 analogous signals of the buffer before and after each protein measurement. Each two-dimensional signal was converted to a one-dimensional scattering profile by azimuthal integration using the Foxtrot-3.5.2 software available at the SWING beamline. Corresponding scattering profiles were averaged and protein signals were obtained by subtraction of buffer scattering. The distance distribution functions were computed using GNOM (37), and the data collection parameters reported in Table S1 were determined from the reduced data using relevant programs from the ATSAS suite (37,38). Data were also examined using RAW (39), which enabled extraction of Porod (V_p) and correlation volumes (V_c), and an independent estimate of the molecular weight of scattering (Tables S2 and S3). Low-resolution molecular envelopes were computed using the ATSAS reconstitution tool DAMMIF (37) (Fig. S1 and Table S4). To construct models for OCP^R dimer and higher-order oligomers, we used the published structures of paralogs of the isolated N-terminal and C-terminal OCP domains, namely the crystal structures of *Anabaena Nostoc* PCC 7120 and *Fremyella diplosiphon* helical carotenoid protein (Protein Data Bank accession PDB: 6MCJ and 5FCX, respectively) (40,41), and of *Anabaena Nostoc* PCC 7120 CTD homolog (PDB: 5FEJ) (21). Our modeling strategy is presented in the results section. The presence of oligomers larger than dimers was inferred from the superimposition of OCP^R models to the DAMMIF envelopes (Fig. S1) and validated by SREFLEX (42) normal mode analysis (Fig. S2 and Table S5). The final data and models for each OCP variant were deposited in the Small-Angle Scattering Biological Data Bank (SASBDB: https://www.sasbdb.org) (43). The accession IDs are available in Table S5.

Spectroscopic monitoring of the OCP^R-to-OCP^O thermal recovery after accumulation of OCP^R by a prolonged continuous illumination

Thermal recovery was investigated as a function of concentration on the three OCP variants, using a JASCO (Easton, MD) V-630 UV-visible spectrophotometer. Purified proteins in $OCP_{R27L\text{-}Ntag}$ and $OCP_{wt\text{-}Ctag}$ were assayed at 0.1, 1.7, 3, and 16 mg/mL, and $OCP_{wt\text{-}Ntag}$ at 0.1, 3, 10, and 16 mg/mL. Specifically, the absorption at 467 nm was monitored at room

temperature (21°C) in the dark following 30 min of continuous blue light irradiation with a 430 nm LED light collimated to 1 cm (≈500 mW/cm^2) to maximize accumulation of OCP^R and reproduce the conditions used in the static SAXS experiments. Measurements at 0.1 mg/mL were carried out in a polymethyl methacrylate cuvette with 1 cm pathlength; those at 1.7, 3, and 10 mg/mL in a quartz cuvette with 0.1 cm pathlength; and that at 16 mg/mL in an Infrasil cuvette with 0.005 cm pathlength. Stability of the proteins over the course of experiments was verified by comparison of their steady-state absorbance spectra before illumination and after illumination and recovery, respectively (Fig. S6).

To facilitate comparison of data collected at various concentrations, the absorption difference at 467 nm was normalized using $A_{Norm} = [A(t) - A(t_0)]/[A(t_{max}) - A(t_0)]$, where $A(t)$, $A(t_0)$, and $A(t_{max})$ are the absorption values measured at a generic time t after switching off the 430 nm light; at time t_0 (i.e., just after illumination at 430 nm was switched off, when the concentration of OCP^O is at its minimum); and at the time t_{max} when the starting OCP^O state has recovered. The non-linear least-squares optimization and parameter extraction were performed using LMFIT (44). After individual fits of each curve data pointed to the necessity to use at least three exponential components to fit the recovery data, we opted for a per-OCP variant global-fitting of the normalized absorption data. For each sample, the recovery data measured at four concentrations were jointly fitted using either a triple or a quadruple exponential function,

$$A(t) = a_{ci-1} \times \left[1 - \exp\left(\frac{-t}{\tau_{ci-1}}\right)\right] + a_{ci-2} \times \left[1 - \exp\left(\frac{-t}{\tau_{ci-2}}\right)\right] + a_{ci-3} \times \left[1 - \exp\left(\frac{-t}{\tau_{ci-3}}\right)\right] + a_{ci-4} \times \left[1 - \exp\left(\frac{-t}{\tau_{ci-4}}\right)\right],$$

where $a_{ci\text{-}1}$, $a_{ci\text{-}2}$, $a_{ci\text{-}3}$, and $a_{ci\text{-}4}$ are concentration-dependent pre-exponential factors, $\tau_{ci\text{-}1}$, $\tau_{ci\text{-}2}$, $\tau_{ci\text{-}3}$, and $\tau_{ci\text{-}4}$ are process-dependent lifetimes, and $a_{ci\text{-}4}$ is fixed to zero in the case of a triple exponential fit. A better fit was obtained with four exponential components for the OCP$_{wt\text{-}Ctag}$ recovery data, but improvements were marginal for the data collected on OCP$_{wt\text{-}Ntag}$ and OCP$_{R27L\text{-}Ntag}$, with amplitudes for the fourth component consistently inferior to 0.1 (see Tables S2 and S3). Hence, we retained results from the four-exponential fit for OCP$_{wt\text{-}Ctag}$, but from the three-exponential fit for the two N-tagged variants. We nonetheless present results for both types of fits in Figs. 4, S7, and S8, and in Tables S6 and S7.

Spectroscopic monitoring of the spectral evolution after nanosecond-pulsed excitation at 470 nm

Measurements were performed using the custom apparatus described previously (45). OCP^O photoexcitation was achieved using a 470 nm nanosecond laser delivering 5 mJ energy per 8 ns pulse at a repetition rate of 0.05 Hz. The probing beam was filtered using a bandpass filter, so that only 440 nm (full width at half maximum (FWHM): 9 nm) or 565 nm (FWHM: 12 nm) light passed through the sample, avoiding putative probe-induced effects from the white spectrum of the xenon lamp. Scattered pump light was reduced by a notch filter set installed upstream of the monochromator which precedes the photomultiplier tube. All measurements were carried out at a sample absorbance of ≈0.7 at 470 nm. For the lowest concentration, a 10 × 10 mm cuvette was used, which was set with a right-angle configuration between the pump and the probe beams. For higher concentrations, 2 mm and 500 μm flat cuvettes were used, affording to increase the concentration while keeping the absorbance within the optimal range. Use of these cuvettes required a quasi-collinear (≈5° angle) configuration between the pump and probe beams. Measurements were performed at different temperatures ranging from 8°C to 36°C. Stirring was not applied to avoid sample displacement from the probed volume at longer time delays. All experiments were repeated 100 times on each of four partially overlapping time windows, altogether covering the 50 ns to 1 s time range. Recorded data were then merged and projected on a logarithmic grid. Stability of the protein was checked by its steady-state absorbance after each experiment. The quantum yield formation of photoproducts was determined using ruthenium as actinometer (34,46) and molar absorption coefficient of OCP^O at 490 nm = 63,000 $M^{-1}\cdot cm^{-1}$ (34).

Time-resolved X-ray scattering

TR-SAXS/wide-angle X-ray scattering (WAXS) experiments were performed at the ID09 beamline of the European Synchrotron Radiation Facility (ESRF, Grenoble, France) (47). X-ray solution scattering signals in the WAXS region (q = 0.03–2.5 Å^{-1}) were collected at 23 mg/mL (620 μM) for OCP$_{wt\text{-}Ntag}$ and OCP$_{wt\text{-}Ctag}$, using a pink polychromatic X-ray beam centered at 15 keV (≈0.3 keV bandwidth, achieved using a multilayer monochromator) and a Rayonix MX170-HS detector placed 350 mm from the sample. The protein samples, OCP$_{wt\text{-}Ntag}$ and OCP$_{wt\text{-}Ctag}$, were photoactivated with laser pulses from two different laser systems: either an EKSPLA (Vilnius, Lithuania) NT342B laser or a Coherent (Santa Clara, CA) Evolution laser. While the first laser is a tunable laser generating 5 ns duration pulses (FWHM) at a maximum repetition rate of 10 Hz, the second laser runs at 1 kHz, has a fixed wavelength (527 nm), and has a pulse duration that can be modulated by changing the current of its diode pump. The use of the Evolution laser allowed us to perform a set of experiments with pulse durations longer than those of the EKSPLA laser (in particular, experiments with 300- or 450-ns-long pulses were performed); moreover, it allowed us to excite the protein sample with either a single laser pulse or a burst of several laser pulses (up to 30) at 1 kHz. For each experiment, the required number of photoexcitation laser pulses was extracted from the train of pulses generated by the Evolution laser by means of a pair of synchronized fast mechanical shutters (Lambda SC; Sutter, Novato, CA). By changing the relative delay of the first shutter opening and of the last shutter closing, it was possible to cleanly select either a single laser pulse or several. In all experiments, the laser beam was focused with cylindrical lenses to an elliptical spot approximately 2.5 × 0.25 mm^2 (FWHM) and the energy was regulated so as to have an energy density of ≈3 mJ/mm^2 at the sample position, corresponding to ≈75 absorbed photons per chromophore.

To maximize the overlap between the pump- and probe-illuminated volumes an orthogonal pump-probe geometry was employed, with the X-ray beam (0.06 × 0.1 mm^2, FWHM) hitting the sample capillary 0.3 mm from its edge. To both minimize X-ray radiation damage and allow the recovery of the OCP^O state, the protein solution (≈5 mL) was circulated with a peristaltic pump (Minipuls 3; Gilson, Middleton, WI) through a 2 mm X-ray quartz capillary in a closed loop. During the flow, most of the sample was contained in a small reservoir kept in the experimental hutch, thermalized at 22°C. The flow speed was set according to both the optical-laser pump X-ray probe time delay and the repetition rate, allowing the sample to be kept in the pump-probe intersection area during a pump-probe sequence while refreshing it between two consecutive pump pulses. Single X-ray pulses (5, 10, or 30 μs depending on the time delay) were selected from the synchrotron pulse train by means of a high-speed chopper and a millisecond shutter. It was verified that the scattering signal obtained with 5–30 μs X-ray pulses is qualitatively similar. Laser-off (dark) signals were also acquired with the X-ray pulse arriving 50 ms before the laser pulse and used as a reference to compute the difference profiles after normalization to the water peak (2–2.2 Å^{-1}) (47). Signals were azimuthally

integrated, and the peak of the undulator spectrum ($\approx$0.83 Å^{-1}) was used as the reference to convert the scattering angle to the momentum transfer q. Up to 30 scattering profiles per time delay were acquired and averaged to improve the signal/noise ratio. Independent TR-WAXS measurements on a solution of 4-amino-1,1′-azobenzene-3,4′-disulfonic acid monosodium salt with an optical density comparable with that of the OCP sample were used to correct the water-heating scattering signal of the collected OCP data (48). TR-WAXS was also used to follow the OCP^R to OCP^O thermal recovery with a direct structurally sensitive technique. In particular, X-ray scattering profiles were collected over 30 min from a sample of $OCP_{wt\text{-}Ctag}$ that had been exposed for 30 min to continuous illumination by a 430 nm LED light.

The TR X-ray scattering data set was analyzed by a singular value decomposition (SVD) (49) using a custom-written Python script (Fig. S12). The time-dependent difference profiles form a j $\times$ k matrix, with j the number of q-values and k the number of time delays. The SVD algorithm calculates the matrices U and V and the vector S, so that A = U $\times$ S $\times$ V^T. The columns of matrix U are called left singular vectors, or basis patterns, the rows of V^T are called right singular vectors, or amplitude vectors, and the elements of S are called singular values. The basis patterns are ordered following the high-to-low sorting of singular values. The SVD analysis of kinetic data provides a subset of time-independent patterns containing the relevant information derived from the random noise. The data set can then be reproduced as a linear combination of such time-independent patterns. Inspection of the shape of basis patterns, amplitude vectors, and singular values together with the autocorrelation analysis of both basis patterns and amplitude vectors (50) indicates that only one component contains significant information. Hence, a two-step model (with growing and decaying exponentials) was used to fit the evolution of the integrated TR X-ray scattering profile.

RESULTS

Soluble OCP^O can form dimers in solution

We used SAXS to investigate the oligomerization state of dark-adapted OCP (OCP^O) in solution. For this purpose, we worked on two proteins: 1) a wild-type OCP, functionalized by ECN and featuring a six-histidine tag (6xHis-tag) at the C-terminus ($OCP_{wt\text{-}Ctag}$); and 2) a R27L monomeric mutant, functionalized by ECN and featuring a 6xHis-tag at the N-terminus ($OCP_{R27L\text{-}Ntag}$) (10).

Data were collected on dark-adapted $OCP_{wt\text{-}Ctag}$ and $OCP_{R27L\text{-}Ntag}$ at increasing protein concentrations, informing on the OCP^O state. The buffer-subtracted scattering profiles of dark-adapted $OCP_{wt\text{-}Ctag}$ and $OCP_{R27L\text{-}Ntag}$ are shown in Fig. 2, *A* and *B*. For $OCP_{R27L\text{-}Ntag}$ at all concentrations, the I(0)/c and the radii of gyration (Rg) derived from the Guinier region are similar (Fig. 3, *A* and *B*), and the derived pairwise distance distribution functions P(r) overlay (Fig. 2 *C*). Accordingly, the low-resolution molecular envelopes calculated from the dark-adapted $OCP_{R27L\text{-}Ntag}$ data collected at 0.7, 3.5, and 10.5 mg/mL (Fig. S1) are comparable, both matching the crystallographic OCP^O monomer. Hence the $OCP^O{}_{R27L\text{-}Ntag}$ sample, wherein the conserved D19-R27 salt bridge is suppressed, remains in the same monomeric state at all tested concentrations and therefore offers a good control for monomeric OCP^O. Contrastingly, examination of the P(r) for dark-adapted $OCP_{wt\text{-}Ctag}$ samples (Fig. 2 *C*) reveals an increase in pairwise distances when the concentration exceeds 3.5 mg/mL. Accordingly, an increase is observed in the I(0)/c (Fig. 3 *A*) and the radii of gyration derived from the Guinier region (Fig. 3 *B*). These three observations indicate that the average size of dark-adapted $OCP_{wt\text{-}Ctag}$ increases with concentration. The low-resolution molecular envelopes calculated by DAMMIF (37) from the dark-adapted $OCP_{wt\text{-}Ctag}$ data are consistent with the presence of a predominant OCP^O dimer (Fig. S1) at concentrations $\geq$3.5 mg/mL, and a mixture of monomers and dimers at 0.7 mg/mL. It is important to note that the above assignments of molecular envelopes to monomers and dimers agree with the molecular weight estimates from I(0) (i.e., the intensity extrapolated at $q = 0$), and Porod (Vp) and correlation (Vc) volumes (see Table S2).

We used the program OLIGOMER (38) to estimate the relative abundance of monomers and dimers in the dark-adapted $OCP_{wt\text{-}Ctag}$ samples prepared at different concentrations (Fig. 3 *C*). Calculated X-ray scattering curves for dimeric and monomeric OCP^O were generated from the crystal structure of *Synechocystis* PCC 6803 OCP (PDB: 3MG1) (18) (Fig. 1) and used for deconvolution of the experimental scattering profiles measured at increasing concentrations (see materials and methods). The fit suggests that at 0.7 mg/mL ($\approx$20 μM), dark-adapted $OCP_{wt\text{-}Ctag}$ is present as a 1:1 mixture of monomers and dimers. The latter attain dominance at $\approx$3.5 mg/mL ($\approx$100 μM) with a dissociation constant of ca. 0.5 mg/mL ($\approx$14 μM). Of course, the accuracy of this value is limited given the low resolution of method used and the coarseness of the titration data.

Illumination induces a dissociation of the dark OCP^O dimer and the formation of OCP^R dimers and higher-order oligomers

To provide details of the large-scale conformational changes accompanying the OCP^O-to-OCP^R transition, including possible change(s) in oligomeric state, we also collected X-ray scattering data on light-adapted $OCP_{wt\text{-}Ctag}$ and $OCP_{R27LNtag}$ at 0.7, 3.5, and 10.5 mg/mL (Fig. 2, *D* and *E*). To assess the time required for the accumulation of the $OCP^R{}_{wt\text{-}Ctag}$ and $OCP^R{}_{R27L\text{-}Ntag}$ states, we carried out preliminary pre-illumination experiments at ESRF-ID09. A highly concentrated protein solution (30 mg/mL) of $OCP_{wt\text{-}Ctag}$ was used, which was presented to the X-ray beam in a 2-mm-thick glass capillary. Firstly, a reference profile was collected on the dark-adapted protein, after which the protein was illuminated by exposure to a 430 nm LED. The distance between the light source and the sample was such that the diameter of the illumination spot was $\approx$1 cm at sample position. Scattering profiles were collected every 15 s, each with 750 ms X-ray exposure, and two illumination powers were consecutively tested, namely 250 and 500 mW. Only after tens of minutes of illumination at 500 mW was accumulation of OCP^R found to reach a plateau under our experimental conditions

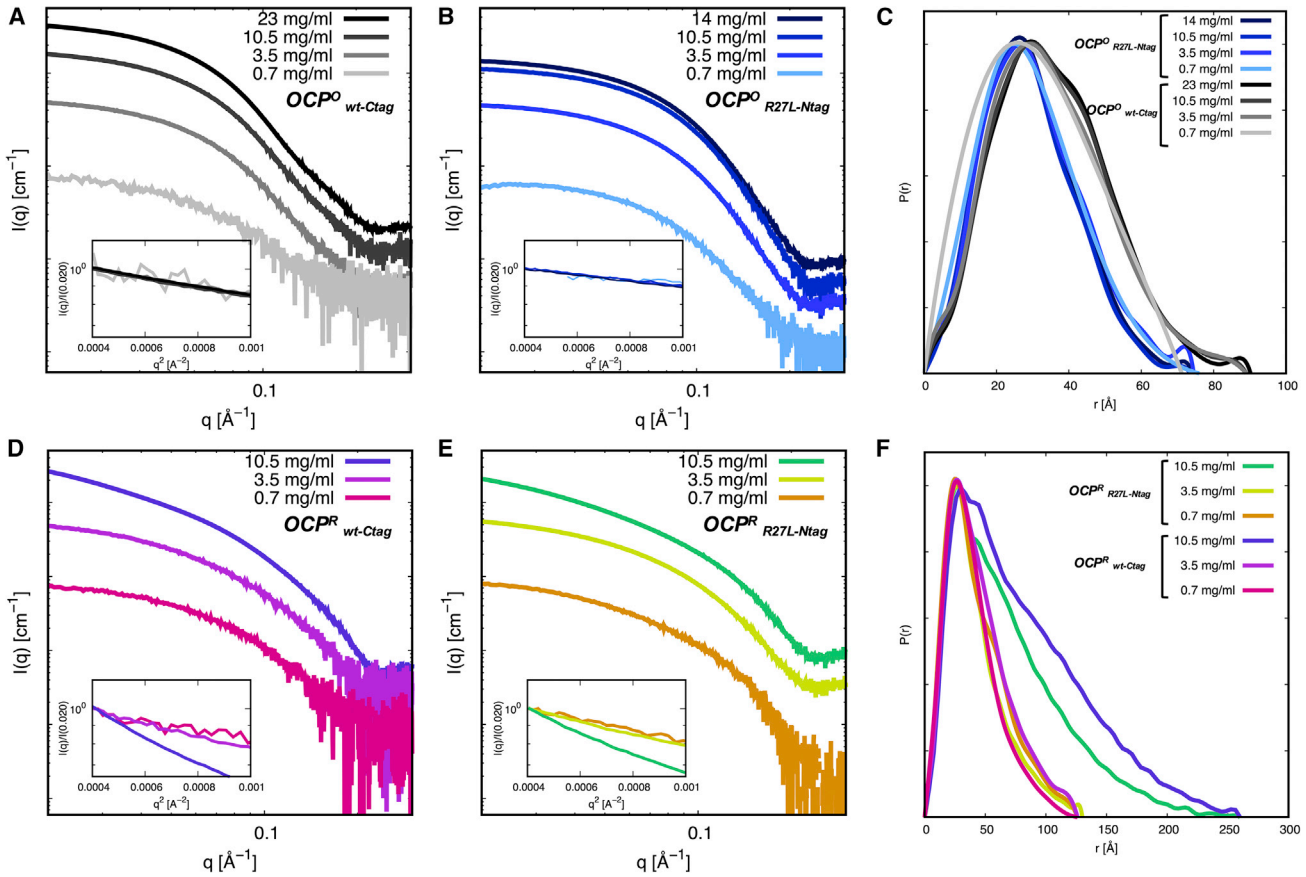

FIGURE 2 Static X-ray scattering reveals changes in the OCP structure and oligomerization state upon illumination and increase of concentration. (*A* and *B*) X-ray scattering profiles of dark-adapted $OCP^{O}_{wt\text{-}Ctag}$ (*A*) and $OCP^{O}_{R27L\text{-}Ntag}$ (*B*) and their corresponding overlays in the Guinier region (*insets*) at various concentrations. (*C*) Normalized pair distance distribution function P(r) of dark-adapted $OCP^{O}_{wt\text{-}Ctag}$ and $OCP^{O}_{R27L\text{-}Ntag}$ at various concentrations. (*D* and *E*) X-ray scattering profiles of light-adapted $OCP^{R}_{wt\text{-}Ctag}$ (*D*) and $OCP^{R}_{R27L\text{-}Ntag}$ (*E*) at various concentrations. (*F*) Normalized pair distance distribution function P(r) of light-adapted $OCP^{R}_{wt\text{-}Ctag}$ and $OCP^{R}_{R27L\text{-}Ntag}$ at various concentrations.

(Fig. S4). Therefore, all subsequent experiments were aimed at characterizing the active OCP^{R} state involved ≈30 min illumination by the 500 mW continuous LED source emitting at 430 nm prior to data collection.

A concentration series was recorded for $OCP_{R27LNtag}$ and $OCP_{wt\text{-}Ctag}$ in their light-adapted states at the SWING bio-SAXS beamline (Synchrotron SOLEIL) (Table S1). Absolute X-ray scattering profiles of light-adapted $OCP^{R}_{wt\text{-}Ctag}$ and $OCP^{R}_{R27L\text{-}Ntag}$ (Fig. 2, *D* and *E*, respectively) strongly differ from those obtained at the same concentrations for the corresponding proteins in their dark state (Fig. 2, *A* and *B*, respectively). The profiles exhibit a dependence on protein concentration, with the low-resolution signal increasing as the latter augments. Accordingly, the Rg of light-adapted $OCP^{R}_{R27L\text{-}Ntag}$ and $OCP^{R}_{wt\text{-}Ctag}$ increase with concentration, starting from 32.5 Å and 29.0 Å at 0.7 mg/mL, respectively, and reaching 44.9 Å and 43.8 Å at 10.5 mg/mL, respectively (Fig. 3 *B* and Table S3). These values are far larger than those observed for the dark-adapted counterparts, but notably similar for the two proteins at each of the three tested concentrations (0.7, 3.5, and 10.5 mg/mL) (Tables S1–S3). The increase in size of $OCP_{R27L\text{-}Ntag}$ and $OCP_{wt\text{-}Ctag}$ upon illumination, the dependence of this size on the concentration, and the similarity between $OCP^{R}_{R27L\text{-}Ntag}$ and $OCP^{R}_{wt\text{-}Ctag}$ at comparable concentrations can also be deduced from the derived P(r) (Fig. 2 *F*), from the I(0)-derived molecular weight, and from Vp and Vc (Table S3). Thus, our results not only indicate an overall expansion of the protein upon illumination, but also a change in the OCP^{R} quaternary structure as a function of concentration. Similar results (notwithstanding a missing data point for 3.5 mg/mL concentration) were obtained with $OCP^{R}_{wt\text{-}Ntag}$ (data not shown). For each protein, a light minus dark difference scattering profile $\Delta I(q)$ was calculated at the highest tested concentration (10.5 mg/mL), offering a signature of the change in scattering signal upon illumination (Fig. 3 *D*). The $\Delta I(q)$ for $OCP_{wt\text{-}Ctag}$ is characterized by the presence of a negative peak at ≈0.05 $Å^{-1}$ and a positive peak at ≈0.12 $Å^{-1}$, whereas for $OCP_{R27L\text{-}Ntag}$ the negative peak is observed at ≈0.07 $Å^{-1}$ and the positive peak at ≈0.14 $Å^{-1}$ (Fig. 3 *D*). Since $OCP^{R}_{R27L\text{-}Ntag}$ and $OCP^{R}_{wt\text{-}Ctag}$ adopt similar states at 10.5 mg/mL, the displacement of negative and positive peaks can be proposed to

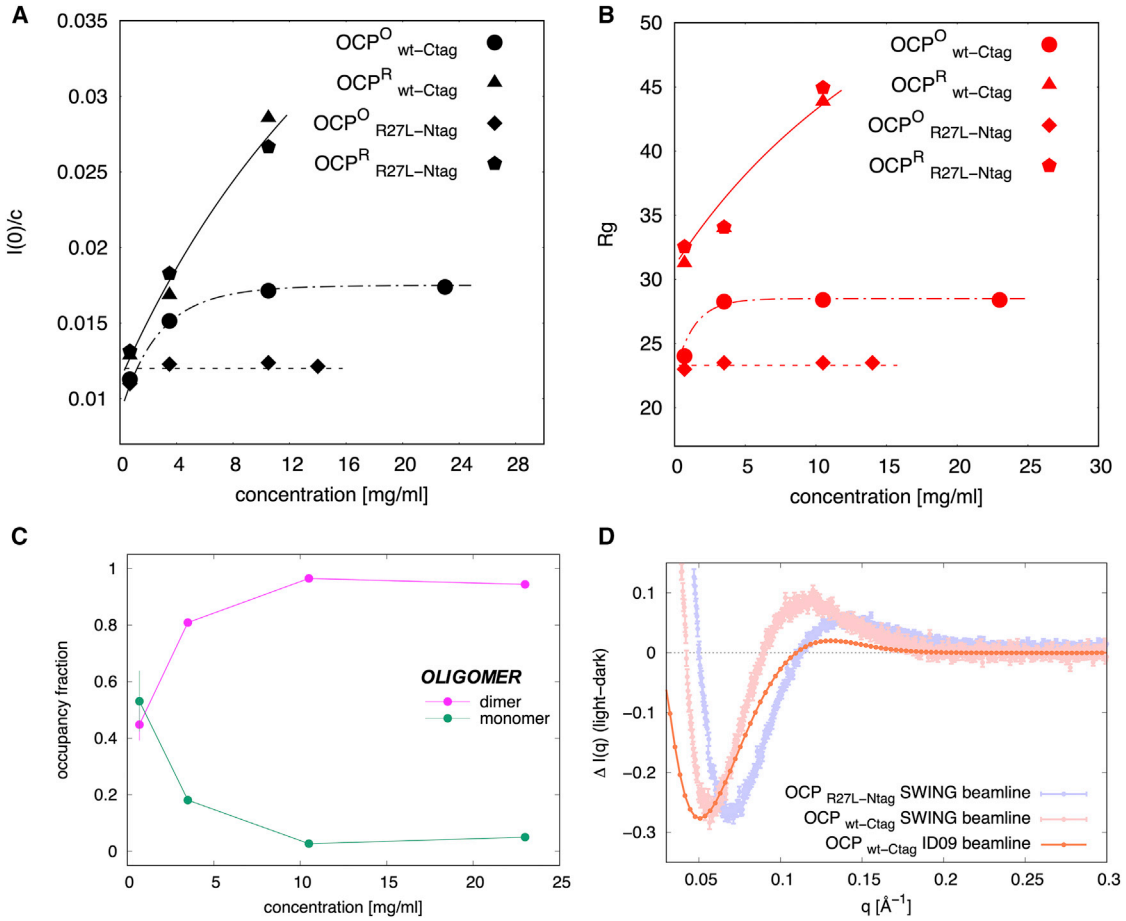

FIGURE 3 Probing OCP oligomerization in the dark- and light-adapted states. (*A*) Evolution of I(0)/c for dark-adapted and light-adapted $OCP_{wt\text{-}Ctag}$ and $OCP_{R27L\text{-}Ntag}$ as a function of concentration (*lines* provide a guide to the eye). (*B*) Evolution of the radii of gyration (Rg, in Å) for dark-adapted and light-adapted $OCP_{wt\text{-}Ctag}$ and $OCP_{R27L\text{-}Ntag}$ as a function of concentration (*lines* provide a guide to the eye). (*C*) Estimation of the relative populations of $OCP^{O}_{wt\text{-}Ctag}$ monomer and dimer as a function of protein concentration using OLIGOMER. Error bars are reported when larger than the symbol size. (*D*) Light minus dark SAXS difference profiles $\Delta I(q)$ for $OCP_{R27L\text{-}Ntag}$ and $OCP_{wt\text{-}Ctag}$ at 10.5 mg/mL (signal recorded on the bio-SAXS SWING beamline, Synchrotron SOLEIL) and for $OCP_{wt\text{-}Ctag}$ at 23 mg/mL (signal recorded at ID09 beamline, ESRF). Error bars are reported when larger than the symbol size. Shifts on the position of the positive and negative peaks are likely due to the different illumination protocols and concentrations of the protein. The larger beamstop and shorter sample to detector distance at ID09 likely also influence the signal at low q-values. Nonetheless, the figure shows that depletion of the $OCP^{O}_{wt\text{-}Ctag}$ state can be achieved in the circulating conditions imposed at ID09, although the smaller positive peak suggests the presence of less OCP^{R}.

emanate solely from the difference between dark-adapted structures, namely $OCP^{O}_{R27L\text{-}Ntag}$ and $OCP^{O}_{wt\text{-}Ctag}$.

We used DAMMIF to compute the low-resolution molecular envelopes of $OCP^{R}_{R27L\text{-}Ntag}$ and $OCP^{R}_{wt\text{-}Ctag}$ at the three tested concentrations (0.7, 3.5, and 10.5 mg/mL). At 0.7 and 3.5 mg/mL (20 and 100 μM), envelopes consistent with the presence of a dimer formed by two elongated OCP molecules are obtained for both $OCP_{wt\text{-}Ctag}$ and $OCP_{R27L\text{-}Ntag}$ (Fig. S1). While at odds with the report of Gupta et al. (30), these results agree with the findings of Golub et al. (23) who earlier reported a similar structure for $OCP^{R}_{wt\text{-}Ctag}$ at 1 and 65 mg/mL (i.e., 28 μM and 1.8 mM) based on SAXS and SANS data. The molecular envelopes computed for $OCP^{R}_{R27L\text{-}Ntag}$ and $OCP^{R}_{wt\text{-}Ctag}$ at 10.5 mg/mL (300 μM), however, are both consistent with the presence of up to four elongated OCP molecules, suggesting that oligomers of higher order than dimers can form at increased concentrations: either OCP^{R} trimers or OCP^{R} tetramers, or a mixture thereof (Fig. S1). The assignment of these molecular envelopes to tetramers is supported by the molecular weights derived from I(0), whereas Porod volumes (Vp) and correlation volumes (Vc) coherently point to OCP^{R} trimers. Given the weight of the Guinier region on I(0) and on the SAXS molecular envelope reconstruction, it is only expected that these would be dominated by the higher molecular weight species (tetramers), even if their population is minor. Meanwhile, the accuracy of molecular weight estimations based on the Vp and Vc methods strongly depends on the exactness of the subtraction of the buffer contribution, leading to possible errors in the estimation. Hence, our data do not allow clear assignment of the nature of our higher-order OCP^{R} oligomers, and it is in fact possible that a mixture of OCP^{R} trimers and tetramers is present under our experimental conditions. What is certain,

however, is that the SAXS data collected on light-adapted OCP^R at concentrations equal to or larger than 10 mg/mL cannot be accounted for by the presence of OCP^R dimers only (Fig. S2; Tables S4 and S5). Differences between our findings and those of Golub et al. (23) could arise from the difference in ionic strength of buffer solutions, as these investigators used 10 mM phosphate buffer at pH 7.4 whereas here we used 50 mM Tris-HCl at pH 7.4 complemented with 150 mM NaCl. Presence of NaCl was intended to reproduce the osmolarity of cyanobacterial cells and could have favored the formation of higher-order oligomers.

We attempted to model the OCP^R structures assuming that:

1) OCP^R dimers and higher-order oligomers are related, i.e., the latter form from the coalescence of two OCP^R dimers;
2) interactions between OCP^R monomers in a dimer and between OCP^R dimers in a higher-order oligomer should be symmetrical, i.e., they should involve the same interface in the two interacting proteins;
3) functional OCP^R dimers should assemble via their CTD so that their two NTDs are exposed and free to interact with PBS via R155 (51); consequently, OCP^R higher-order oligomers would form from an interaction between two NTDs in the OCP^R dimer;
4) the interfaces allowing the assembly of OCP^R dimers and higher-order oligomers should not involve R27 (and, by extension, the dark dimerization interface contributed by helix αB) since the R27L mutant—unable to form OCP^O dimers—is capable of forming OCP^R dimers and higher-order oligomers;
5) rather, the CTD-CTD and NTD-NTD interfaces involved in OCP^R oligomerization should feature residues that are not exposed in the dark OCP^O dimer nor present at symmetrical crystal contacts in the OCP^O structure, otherwise OCP^O higher oligomers would form in the dark-adapted state; presumably, residues involved in OCP^R oligomerization would be present at the NTD-CTD interface in the dark OCP^O, echoing the earlier proposal of Moldenhauer et al. (52) and Muzzopappa et al. (10,52,53) that the interface between CTD domains in an OCP^R dimer should overlap with the CTD residues that interacts with the NTD in OCP^O;
6) the interfaces allowing the assembly of OCP^R dimers and higher-order oligomers may already have been observed in available crystal structures of OCP and isolated OCP domains, e.g., in the structure of the isolated holo-NTD of wild-type OCP (19), or in those of NTD and CTD paralogs, respectively coined helical carotenoid proteins (HCPs) and CTD homologs (CTDH) in the literature (21,40,41).

Indeed, the study of Harris et al. (21) has shown that the apo-*Anabaena* CTDH, a homolog of the CTD of OCP involved in carotenoid transport and wherein the C-terminal helix is not apposed onto the β-sheet, is capable of forming two types of dimers, associating either through back-to-back (A-type) or head-to-head (F-type) interactions between two CTDHs. In the F-type dimer CTDH residues, equivalent to those involved in carotenoid binding in the CTD of OCP^O that face one another reconstituting a carotenoid tunnel, were proposed to be involved in carotenoid uptake (21). In the absence of the carotenoid, however, the A-type interface can form between CTDH molecules, and it was demonstrated by SAXS that the isolated apo-CTD of OCP^O dimerizes by this interface. Golub et al. therefore proposed that the two monomers in a OCP^R dimer interact by this interface (10,24). Like them, we hypothesize that OCP^R dimers form through interaction at this interface, which fulfills our above hypotheses for a sound modeling of OCP^R oligomers. It was further verified that only the A-type interface can fit the extended molecular envelope derived from our data. Indeed, the F-type interface would result in a "Z"-shaped molecular envelope. In the dark OCP^O, interaction by the A-type interface is prevented by the presence of helices αN (CTT, corresponding to residues 304–317) and αA (or NTE, corresponding to residues 1–17), which appose aside on the external face of the β-sheet but detach upon photoactivation. These helices were therefore considered as disordered in OCP^R and not included in our OCP^R dimer model. To further avoid clashes and account for the known exposure, in OCP^R, of the face of the NTD that interacts with the CTD in OCP^O, the NTD was rotated by 180° and translated by 10 Å. The OCP^R dimer was then used as a starting point for modeling a tetramer, by assembly of two NTDs in a fashion reminiscent of that observed in the HCP crystal structures from *Anabaena Nostoc* PCC 7120 and *Fremyella diplosiphon* (PDB: 5FCX and 6MCJ, respectively) (40,41). In these, two molecules are found in the asymmetric unit, forming a dimer assembled through a symmetrical interface that features the residue equivalent to OCP-R155 at its center. Hence, in our model, the two dimers in an OCP^R tetramer would interact by the same face known to bind the PBS, leaving two NTDs available for binding to the latter. This tetramer model fits the ab initio envelopes computed for $OCP^R_{R27L\text{-}Ntag}$ and $OCP^R_{wt\text{-}Ctag}$ at 10.5 mg/mL (300 μM) (Fig. S1), but uncertainties remain as to whether only tetramers, only trimers, or a mixture thereof co-exist in our experiments.

Kinetics of thermal recovery after accumulation of OCP^R by continuous illumination

The recoveries of the OCP scaffold and the carotenoid structure could be uncoupled. Hence, with the aim of splitting a difference between the structural recovery (informing on the protein structure) and the spectral recovery (informing on the electronic structure and environment of the carotenoid pigment), we monitored the kinetics of thermal OCP^R-to-OCP^O recovery using SAXS ($OCP_{wt\text{-}Ctag}$)

and absorption spectroscopy at 467 nm ($OCP_{R27L\text{-}Ntag}$, $OCP_{wt\text{-}Ntag}$, and $OCP_{wt\text{-}Ctag}$). For the structural monitoring, accumulation of the OCP^R state was achieved by illuminating a 23 mg/mL (620 μM) solution of $OCP_{wt\text{-}Ctag}$ for $\approx$30 min at 430 nm with a 500 mW continuous LED source collimated to $\approx$1 cm (i.e., the same illumination protocol used in SAXS experiments described in the previous section), providing the starting point of the kinetics, and scattering data were thereafter recorded every $\approx$12 s. It was established in our static SAXS measurements that formation of $OCP^R{}_{wt\text{-}Ctag}$ state is characterized by the presence, in the $\Delta I(q)$ difference profile, of a negative peak at $\approx$0.05 $Å^{-1}$ and a positive peak at $\approx$0.12 $Å^{-1}$ (Fig. 3 *D*). Hence, we used as a proxy to evaluate the structural recovery of the starting $OCP^O{}_{wt\text{-}Ctag}$ state the $\Delta I = I(q)_t - I(q)_{t0}$ difference signal in the 0.05–0.5 $Å^{-1}$ range, where $I(q)_t$ and $I(q)_{t0}$ are the scattering profiles at a generic time (t) after switching off the 430 nm light and before the 430 nm irradiation procedure, respectively (Fig. S5). These data show that when $OCP^R{}_{wt\text{-}Ctag}$ is accumulated at high concentrations by prolonged illumination, structural recovery of the dimeric $OCP^O{}_{wt\text{-}Ctag}$ state occurs on a timescale of tens of minutes.

The absorbance recovery of $OCP_{R27L\text{-}Ntag}$, $OCP_{wt\text{-}Ntag}$, and $OCP_{wt\text{-}Ctag}$ was monitored in the 0.1–16 mg/mL concentration range, after accumulation of OCP^R by the same illumination protocol used in the static SAXS measurements. Just after switching off the 430 nm light at time t_0 (i.e., when the concentration of OCP^R is at its maximum), the time evolution of the normalized absorption difference $[A(t) - A(t_0)]/[A(t_{max}) - A(t_0)]$ at 467 nm was monitored, where $A(t)$ and $A(t_{max})$ are the absorption values measured at a generic time t during the thermal recovery and at the time t_{max} = 5000 s, where the initial OCP^O state has been 95%–99% recovered (Fig. S5), respectively. The 467 nm wavelength was chosen because it is that at which the difference absorption signal is maximal (highest contrast) between OCP^O and OCP^R. Normalization was performed to enable direct comparison of data (Fig. S7) and of the fits at the various tested concentrations, namely 0.1, 1.7, 3, and 16 mg/mL (Fig. S8). Like the structural recovery, spectroscopic recovery occurs on a timescale of tens of minutes, with recovery slowing down as the protein concentration increases. Regardless of the concentration, however, $OCP_{R27L\text{-}Ntag}$ recovers faster than $OCP_{wt\text{-}Ntag}$, which itself recovers faster than $OCP_{wt\text{-}Ctag}$. As $OCP_{R27L\text{-}Ntag}$ and $OCP_{wt\text{-}Ntag}$ differ only in their capacity to form OCP^O dimers, and $OCP_{wt\text{-}Ntag}$ and $OCP_{wt\text{-}Ctag}$ only in the location of the His-tag, these observations suggest that 1) the reassociation of OCP^O monomers into dimers is the limiting step in the recovery of $OCP_{wt\text{-}Ntag}$, and 2) the presence of a His-tag at the C-terminus negatively impacts dark-state recovery. Based on the results described in the previous sections we can expect that the thermal recovery of $OCP_{wt\text{-}Ctag}$ involves at least the following states: OCP^R higher-order oligomer $\rightarrow$ OCP^R dimer $\rightarrow$ OCP^R monomer $\rightarrow$ OCP^O monomer $\rightarrow$ OCP^O dimer; while that of $OCP_{R27L\text{-}Ntag}$ transitions across OCP^R higher-order oligomers $\rightarrow$ OCP^R dimer $\rightarrow$ OCP^R monomer $\rightarrow$ OCP^O monomer. We attempted fitting the recovery data using constrained (same set of lifetimes for the four concentrations) mono-to-quadruple exponential functions (see materials and methods), where 1) a_{ci}-1, a_{ci}-2, a_{ci}-3, and a_{ci}-4 are pre-exponential factors depending on the protein variant and the concentration, and 2) τ_{ci}-1, τ_{ci}-2, τ_{ci}-3, and τ_{ci}-4 are lifetimes describing up to four separate molecular steps. A minimum of three exponentials are needed to account for the recovery kinetics of the three OCP variants. The lifetimes derived from the $OCP_{R27L\text{-}Ntag}$ data (τ_{ci}-1 = 59.8 $\pm$ 0.3 s; τ_{ci}-2 = 159.1 $\pm$ 0.6 s; τ_{ci}-3 = 641.7 $\pm$ 1.1 s; Table S2) are nearly half of those derived from the $OCP_{wt\text{-}Ntag}$ data (τ_{ci}-1 = 94.5 $\pm$ 0.2 s; τ_{ci}-2 = 356.5 $\pm$ 1.2 s; τ_{ci}-3 = 1327.5 $\pm$ 4.3 s; Table S6), and no better fits are obtained by accounting for a fourth component (similar χ^2 for either data set; Tables S6 and S7), precluding extraction of a lifetime for dimerization of $OCP_{wt\text{-}Ntag}$. A similar three-exponential fitting procedure applied to the $OCP_{wt\text{-}Ctag}$ (Table S3) data yields longer lifetimes (τ_{ci}-1 = 76.7 $\pm$ 0.2 s; τ_{ci}-2 = 593.1 $\pm$ 2.1 s; τ_{ci}-3 = 9517.4 $\pm$ 75 s), in line with the observed slower recovery, yet the data are better fitted

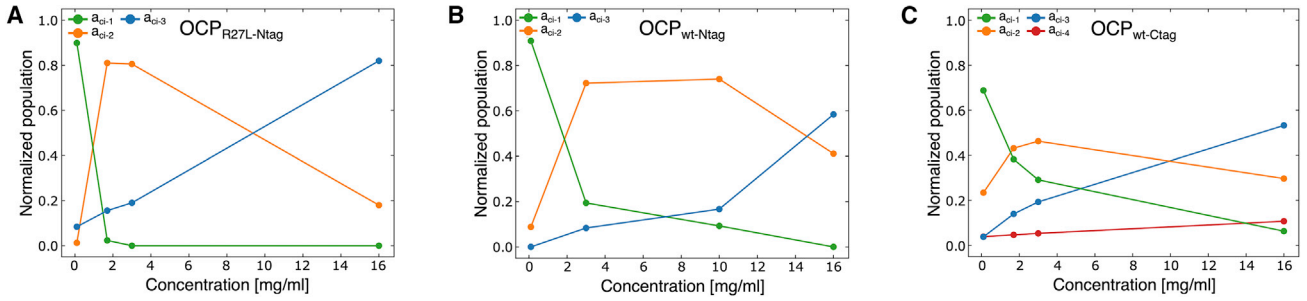

FIGURE 4 Kinetic analysis of OCP thermal recovery data at various concentrations suggests that oligomerized OCP^R reverts more slowly to the dark-adapted state. Plots of the pre-exponential factors retrieved from fits of thermal recovery kinetics monitored by following changes in absorbance at 467 nm (see Figs. S7 and S8; Tables S6 and S7). (*A*) $OCP_{R27L\text{-}Ntag}$, (*B*) $OCP_{wt\text{-}Ntag}$, and (*C*) $OCP_{wt\text{-}Ctag}$. The apparent lifetime of OCP^R state is increased in dimers and higher-order oligomers, suggesting that oligomerization stabilizes the light-adapted state. Residuals are reported in Tables S6 and S7.

(≈4 times smaller χ^2, i.e., a value close to those obtained for $OCP_{R27L\text{-}Ntag}$ and $OCP_{wt\text{-}Ntag}$ regardless of whether three or four exponential components are considered) by a four-exponential model ($\tau_{ci\text{-}1}$ = 51.5 ± 0.2 s; $\tau_{ci\text{-}2}$ = 209.9 ± 1.3 s; $\tau_{ci\text{-}3}$ = 946.0 ± 3.7 s; $\tau_{ci\text{-}4}$ = 14,057.7 ± 68.8 s; Table S6). A global four-exponential fit of the three data sets, whereby the lifetimes for $OCP_{R27L\text{-}Ntag}$, $OCP_{wt\text{-}Ctag}$, and $OCP_{wt\text{-}Ntag}$ were constrained to be identical and the simpler kinetics of $OCP_{R27L\text{-}Ntag}$ (no dimerization of OCP^O) accounted for by constraining to zero the population parameter $a_{ci\text{-}4}$, corresponding to the longest lifetime, was unsuccessful. Our data thus point to at least three, and in the case of $OCP_{wt\text{-}Ctag}$ four, independent molecular steps being involved in the OCP^R-to-OCP^O recovery.

Kinetics of photoactivation and recovery upon formation of OCP^R by pulsed illumination

To investigate short-lived intermediate states which exist along the OCP^O-to-OCP^R and OCP^R-to-OCP^O transitions, we used nanosecond-to-second timescale transient absorption spectroscopy. In brief, 8 ns pulses from a 470 nm laser (5 mJ pulse energy) were employed to trigger photoactivation, and difference absorbance (ΔA) signals at 440 and 565 nm were monitored, respectively. The 440 nm probe wavelength is located at the blue edge of OCP^O absorption spectrum, and therefore informs on the depletion and recovery of this state upon and after excitation by the 470 nm pulse, respectively. Conversely, the 565 nm probe is at the red edge of the OCP^R absorption spectrum and thus serves as an indicator for the formation of the red absorbing states, including the first probed photoproduct P_2 ($\lambda_{\Delta Amax}$ = 565 nm, with occupancy proportional to the ΔA signal), the photoactive OCP^R ($\lambda_{\Delta Amax}$ = 550 nm), and all red intermediate states between these (27).

We first investigated $OCP_{wt\text{-}Ctag}$, $OCP_{R27L\text{-}Ntag}$, and $OCP_{wt\text{-}Ntag}$ at 12 μM concentration, i.e., ≈0.18 mg/mL (Fig. 5 *A*), where nearly as many $OCP^O{}_{wt\text{-}Ctag}$ and $OCP^O{}_{wt\text{-}Ntag}$ are present in the monomeric form (54%, i.e., 6.5 μM) and in the dimeric form (46%, i.e., 2.79 μM (Table S4)), assuming a similar dissociation constant of 14 μM for the two wild-type variants. Given this starting concentration, the pulsed nature of the excitation, and the low quantum yield of photoactivation, OCP^R cannot accumulate in these experiments, hence the formation of OCP^R dimers and higher-order oligomers is extremely unlikely. We examined the temperature dependence (8°C–36°C) of the ΔA signals at 440 nm and 565 nm in $OCP_{wt\text{-}Ctag}$, with the aim of identifying key intermediate states and determining their associated enthalpy and entropy of activation. Experiments revealed that irrespective of temperature, all kinetics recorded at 440 nm start from the same ΔA value, namely, −2 mOD (Fig. S9), indicating that depletion of the initial $OCP^O{}_{wt\text{-}Ctag}$ state (with ≈0.7% yield, as determined by ruthenium actinometer; see materials and methods) hardly depends on the temperature. Notwithstanding, the initial (≈50 ns) ΔA signal at 565 nm decreases with increasing temperature, amounting to 3 mOD at 8°C but only 1.5 mOD at 36°C (Fig. S9, *A* and *E*).

The ΔA signal for $OCP_{wt\text{-}Ctag}$ at 565 nm appears triphasic in the 8°C–36°C range (Fig. S9, *A–F*), and likewise for the 440 nm ΔA signal in the 8°C–22°C range (Fig. S9, *C–F*). Similar lifetimes and activation energies can be derived from the two sets of data (Table S4 and Fig. 5 *E*, respectively), confirming that the two sets of difference absorbance signals at 440 and 565 nm probe the same molecular events. Hence, we opted for a global triexponential fitting of the 440 and 565 nm data. Note that an additional fourth component intrudes into kinetics after 100 ms at 29°C and 36°C (Fig. S9, *D* and *E*), which presumably lives longer than our time window at lower temperatures. Lifetimes were extracted for each step (Table S8) and Eyring plots generated from the measurements carried out at different temperatures (Fig. 5 *E*). The fastest component (≈2 μs) displays an adiabatic behavior and is associated with a negative change in entropy. The two other components, characterized by lifetimes in the 0.2–5 and 10–250 ms range, respectively, are both characterized by increase of the entropy (11–18 cal mol^{-1} K^{-1}), indicating irreversibility, and display similar enthalpies of activation, namely 18 kcal/mol (Fig. 5 *E*).

The extent of recovery of the ΔA signal at 440 nm is slightly higher at increased temperature, with ≈50% of the initially depleted OCP^O state (0.7% at 50 ns) having recovered after 1 s at 8°C, but up to 75% at 36°C (Fig. S9). In brief, overall OCP^R yields of 0.35%, 0.26%, 0.25%, 0.20%, and 0.18% are found at 8°C, 15°C, 22°C, 29°C, and 36°C based on the 440 nm data at 500 ms, respectively. Hence, the recovery of the OCP^O state somehow benefits from increased thermal energy but is not completed after 1 s (i.e., the ΔA signal at 440 nm is not null), regardless of temperature (Fig. S9). Hence, the limiting step in the monomeric $OCP^R{}_{wt\text{-}Ctag}$ to $OCP^O{}_{wt\text{-}Ctag}$ transition occurs on a timescale longer than 1 s (observed in SAXS data (Fig. S3; Tables S2 and S3)). The 565 nm kinetics also decays faster at higher temperatures, confirming the drop in yield for the red states (including $OCP^R{}_{wt\text{-}Ctag}$) as the temperature augments. Surprisingly, however, the ΔA signal at 565 nm is null after 1 s at 29°C (and negative at 36°C), which would suggest that no $OCP^R{}_{wt\text{-}Ctag}$ remains (yields of 0.8%, 0.44%, 0.18%, 0.02%, and −0.16% based on the 565 nm data at 8°C, 15°C, 22°C, 29°C, and 36°C, respectively). These diverging results illustrate the usefulness of probing photoactivation and recovery at the two extremes of OCP^O and OCP^R absorption spectra to obtain meaningful insights into the complex underlying mechanisms.

We repeated the experiments described above on the constitutively monomeric $OCP_{R27L\text{-}Ntag}$ mutant. The 565 nm kinetics, shown in Fig. 5, are overall similar for $OCP_{wt\text{-}Ctag}$ and the $OCP_{R27L\text{-}Ntag}$ mutant. From the multiexponential fits, we accordingly derive comparable lifetimes, with the

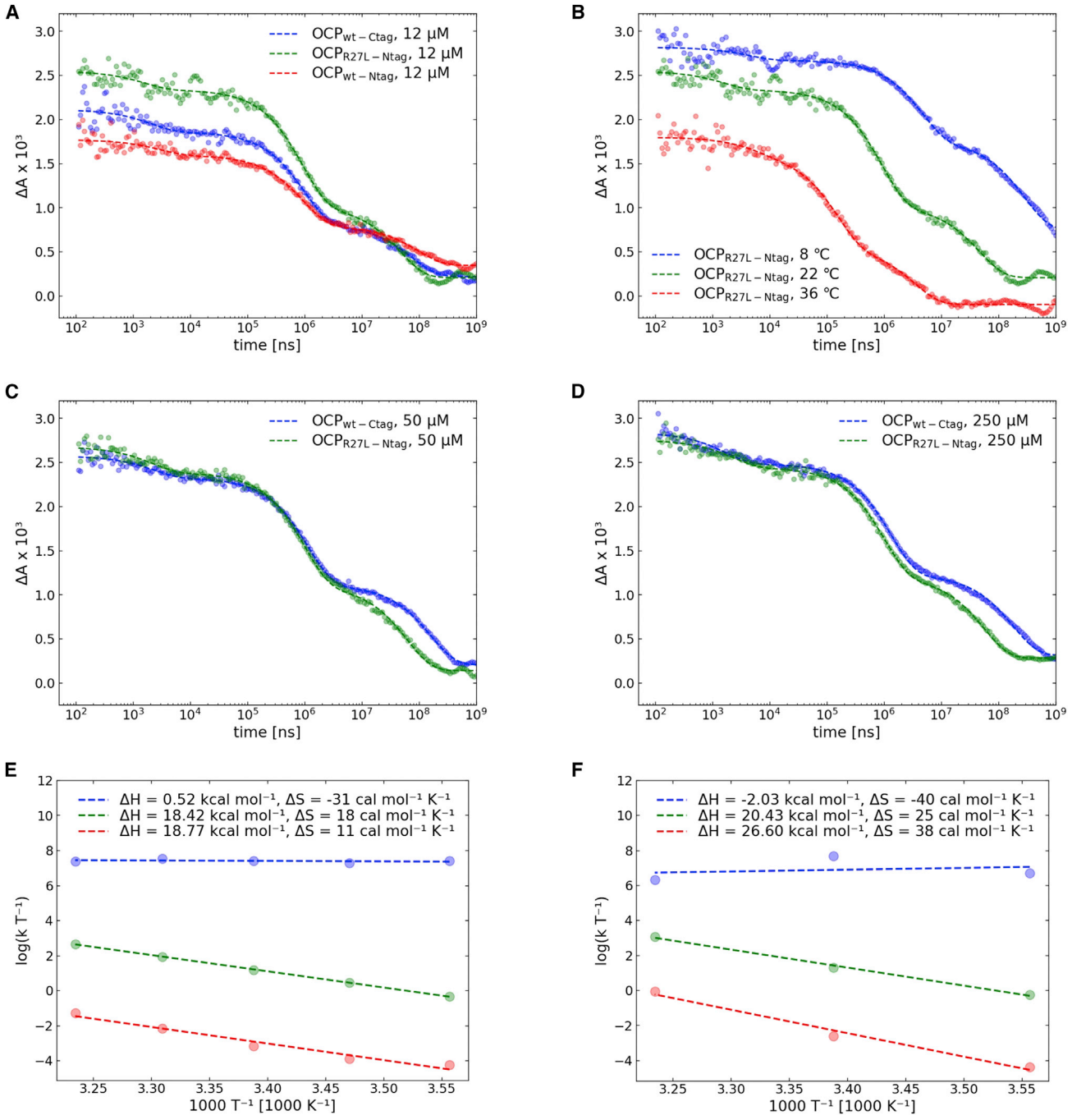

FIGURE 5 Transient absorption spectroscopy enables identification of three intermediate states along the formation of OCP^R and OCP^R-to-OCP^O thermal recovery. Difference absorption (ΔA) signals were monitored at 565 nm. (*A*) Nanosecond transient absorption data for $OCP_{wt\text{-}Ctag}$, $OCP_{wt\text{-}Ntag}$, and $OCP_{R27L\text{-}Ntag}$ at 12 μM. (*B*) Nanosecond transient absorption data for $OCP_{R27L\text{-}Ntag}$ at 12 μM and various temperatures. (*C* and *D*) Comparison of nanosecond transient absorption data between $OCP_{wt\text{-}Ctag}$ and $OCP_{R27L\text{-}Ntag}$ at 50 μM, and $OCP_{wt\text{-}Ctag}$ and $OCP_{R27L\text{-}Ntag}$ at 250 μM, respectively. (*E* and *F*) Eyring plots for $OCP_{wt\text{-}Ctag}$ (*E*) and $OCP_{R27L\text{-}Ntag}$ (*F*). These enable extraction of enthalpy and entropy of activation ($\kappa = 1$ is assumed). See Fig. S9 for complementary data.

main difference between the two proteins being a twofold shorter τ_3 component for $OCP_{R27L\text{-}Ntag}$ as compared with $OCP_{wt\text{-}Ctag}$ (Table S8). Thus, only the last component shows a putative influence of the presence of dimers (recall that 46% of $OCP^O_{wt\text{-}Ctag}$ is present in the form of dimers at 12 μM). Accordingly, the Eyring plots of $OCP_{R27L\text{-}Ntag}$ (Fig. 5 *F*) reveal trends analogous to those of $OCP_{wt\text{-}Ctag}$ for the two first components, while the τ_3 component is characterized by larger activation enthalpy and entropy. To determine whether or not these differences could arise from the position of the His-tag at the N- or C-terminus of the protein, we further investigated $OCP_{wt\text{-}Ntag}$ at 22°C and compared lifetimes with

those characterizing $OCP_{R27L\text{-}Ntag}$ and $OCP_{wt\text{-}Ctag}$ (Table S8). We again observed similar dynamics, with derived lifetimes and relative contributions for the three steps being almost identical in $OCP_{wt\text{-}Ntag}$ and $OCP_{wt\text{-}Ctag}$. An interesting difference is, however, that despite a similar P_2 yield, $OCP_{wt\text{-}Ntag}$ displays a nearly twofold increased OCP^R yield at 500 ms compared with $OCP_{wt\text{-}Ctag}$. This observation suggests that dissociation of the NTE from the CTD, facilitated by adjunction of a His-tag at the N-terminus, is a limiting step in the photoactivation of OCP. This event is still silent in terms of changes in the absorption of the carotenoid, since none of the components identifiable in the 440 nm and 565 nm kinetics are affected by the change in tag position in $OCP_{wt\text{-}Ntag}$ and $OCP_{wt\text{-}Ctag}$.

Transient spectroscopy data presented so far were acquired in conditions where $OCP^O{}_{wt\text{-}Ctag}$ and $OCP^O{}_{wt\text{-}Ntag}$ monomers are slightly prevalent (54%), and differences with the constitutively monomeric $OCP^O{}_{R27L\text{-}Ntag}$ were seen only for the τ_3 component, suggesting that the underlying step was sensitive to the dimerization of the protein. To verify this hypothesis, we repeated experiments on $OCP_{wt\text{-}Ctag}$ and $OCP_{R27L\text{-}Ntag}$ at 50 and 250 μM, where dimers account for 78% and 95% of the OCP^O population, respectively (Fig. 5, *C* and *D*). Only the ΔA signal at 565 nm was probed. Both the initial P_2 yield at 50 ns and the overall OCP^R yield at 0.1 s increase with concentration for $OCP_{wt\text{-}Ctag}$ but not for $OCP_{R27L\text{-}Ntag}$, indicating that stabilization of the closed conformation of OCP^O through dimerization (54) favors the initial steps of photoactivation (Fig. S10 *A* and Table S8). The lifetimes derived for the $OCP_{R27L\text{-}Ntag}$ sample are only marginally affected by the increase in concentration, whereas a nearly twofold increase in τ_3 lifetime is seen for $OCP_{wt\text{-}Ctag}$ at 50 and 250 μM. These experiments confirm that the τ_3 component, although present also in the monomer, is affected by dimerization. Specifically, a plot of τ_3 lifetime as a function of OCP dimer concentration, assuming for zero dimer concentration the average τ_3 lifetime of $OCP_{R27L\text{-}Ntag}$, reveals a logarithmic behavior with half maximum reached at $\approx$10 μM dimer, corresponding to $\approx$25 μM $OCP^O{}_{wt\text{-}Ctag}$ (Fig. S10 *B*). It is interesting to note that regardless of the sample and concentration, the τ_2 component ($\approx$1 ms) has an almost constant value and relative contribution in all kinetics measured at 22°C. The underlying step is therefore affected neither by tagging nor monomerization.

Time-resolved X-ray scattering

TR X-ray scattering measurements were carried out using a pump-probe scheme with a view to investigate the large-scale structural changes occurring in OCP_{wt} upon photoactivation, and the associated timescales. We used two variants of OCP_{wt}, namely $OCP_{wt\text{-}Ntag}$ and $OCP_{wt\text{-}Ctag}$, enabling us to test whether or not the presence of a His-tag at the N- or C-terminus influences pulsed photoactivation kinetics. Indeed, it has been observed that both OCP^R accumulation under prolonged illumination and the subsequent thermal recovery of the OCP^R state are faster for $OCP_{wt\text{-}Ntag}$ than $OCP_{wt\text{-}Ctag}$ (14,54). From our nanosecond-to-second transient absorption characterization of photoactivation and recovery in $OCP_{wt\text{-}Ntag}$ and $OCP_{wt\text{-}Ctag}$ and the derived Eyring plots, it was expected that at 22°C, the two steps involving large-scale motions are characterized by lifetimes of $\approx$1 ms and $\approx$80 ms (Fig. 5). Hence, time delays (Δt) between the pump optical-laser pulse and the probe X-ray pulse ranged from 15 μs to 200 ms. Experiments were performed at 23 mg/mL (620 μM) $OCP_{wt\text{-}Ntag}$ and $OCP_{wt\text{-}Ctag}$, i.e., a concentration at which dimers account for $\approx$98% of the protein.

The experimental setup designed for this experiment, described in materials and methods and illustrated in Fig. 6 *A*, involves the circulation of a large volume of sample across the X-ray beam to minimize cumulative X-ray damage during the experiment. The circulation speed was set so as to ensure that the sample is kept in the pump-probe intersection area during a pump-probe sequence, but refreshed between two consecutive pump pulses. We verified that with this setup, the same difference scattering signal observed in static SAXS experiments could be obtained upon continuous illumination of the sample reservoir by a 500 mW LED source emitting at 430 nm. The LED illumination was prolonged until the photoinduced change in scattering signal was stable. The resulting difference scattering profile is similar to that produced from our static measurements, i.e., it features a negative peak at $\approx$0.05 Å^{-1} and a positive peak at $\approx$0.12 Å^{-1} (Fig. 3 *D*). This control indicates that the use of a different continuous illumination setup at a different beamline does not result in shifts in the difference scattering signal (Fig. 6 *B*).

With the intention to determine the extent to which photoactivation can be increased by successive re-excitations within the pulse, we first measured the "light" (laser-on) minus "dark" (laser-off) difference scattering signal at $\Delta t = 1$ ms, using two different laser pulse durations, namely 5 and 450 ns. This required the use of two different lasers, emitting at 430 and 527 nm, respectively. At these wavelengths, the extinction coefficient of OCP^O is similar ($\approx$35,000 $M^{-1}\cdot cm^{-1}$), suggesting that the OCP^R formation quantum yield should be comparable and that an increase in the difference signal at 527 nm would thus stem from successful re-excitation within the 450 ns pulse. Both pulse durations are indeed longer than the time necessary to recover the electronic ground state ($\approx$20 ps) (27,55). A pulse power density of 3 mJ mm^{-2} was chosen, affording the delivery of $\approx$75 photons per chromophore across the pulse, corresponding to a photon every 0.06 and 5 ns for the 5 and 450 ns pulse durations, respectively. The "light" (laser-on) minus "dark" (laser-off) difference scattering profiles obtained 1 ms post excitation by either laser feature a negative peak in the small-angle region up to $\approx$0.1 Å^{-1}, but the

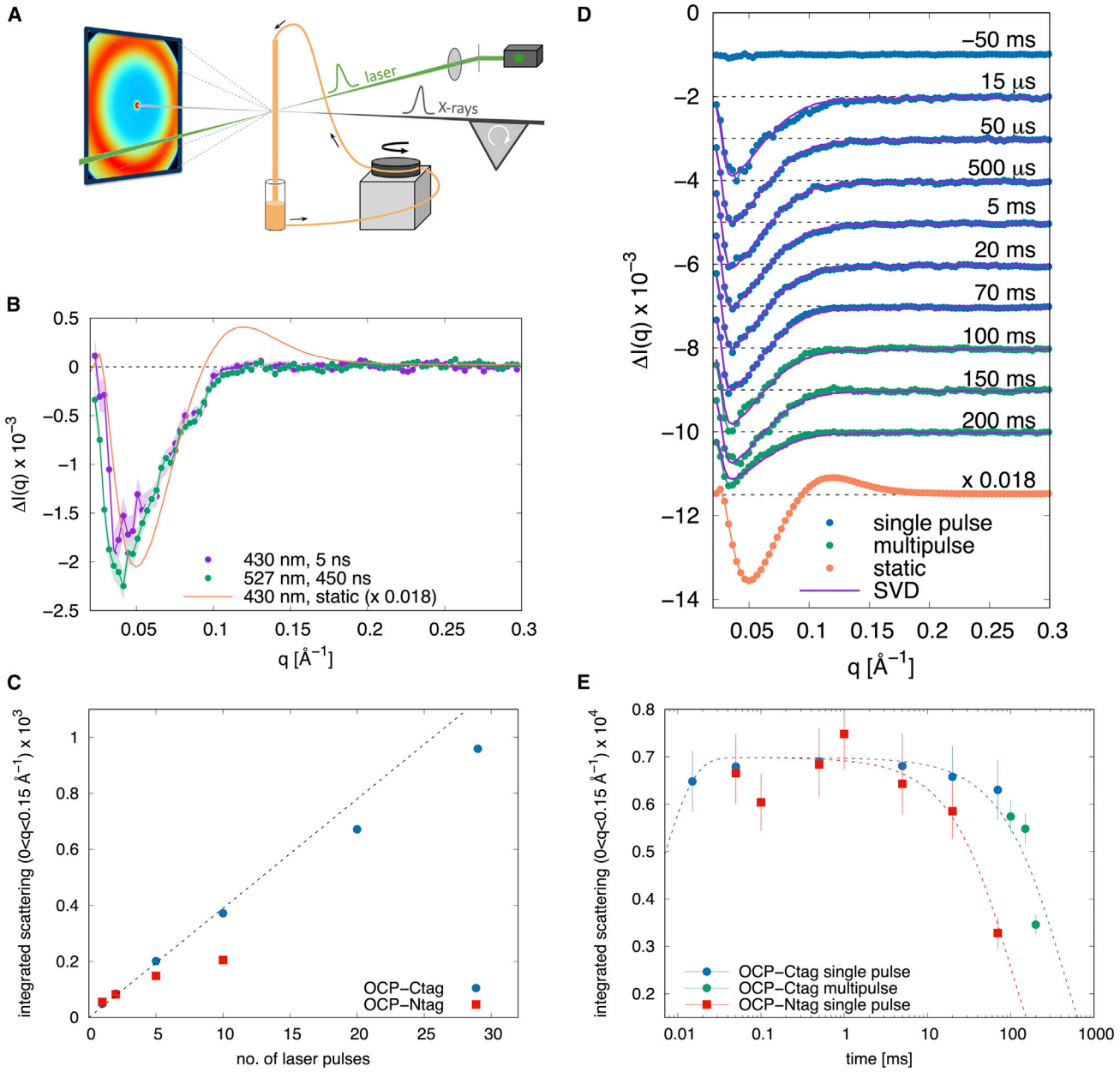

FIGURE 6 Time-resolved X-ray scattering reveals the kinetics of light-induced structural changes in the micro- to millisecond timescale. (*A*) Schematic representation of the experimental setup used for time-resolved SAXS/WAXS experiments at the ID09 beamline of ESRF. The OCP solution (*orange*) flows through a quartz capillary connected to a peristaltic pump. A nanosecond laser pulse (*green*) synchronized with a microsecond X-ray pulse train (*gray*) is used to trigger OCP^O-to-OCP^R photoconversion. Protein structural changes give rise to changes in the X-ray scattering pattern measured on a CCD detector. (*B*) Comparison of the time-resolved laser-on/laser-off X-ray difference profile at $\Delta t = 1$ ms after excitation by both a 5 ns pulse at 430 nm and a 450 ns pulse at 527 nm with the static OCP^R-OCP^O X-ray difference profile (scaled by a factor 0.018) calculated by subtracting the profile of the dark-adapted sample from that illuminated at 430 nm. (*C*) Integrated difference scattering in the region $0 < q < 0.15$ Å^{-1} as a function of the number of laser pulses (527 nm) for $OCP_{wt\text{-}Ctag}$ (*blue circles*) and $OCP_{wt\text{-}Ntag}$ (*red squares*). Pulse energy and duration were 2 mJ and 400 ns, respectively, and the pulses were spaced by 1 ms. (*D*) Light-induced time-resolved X-ray scattering difference profiles for $OCP_{wt\text{-}Ctag}$. The static OCP^R-OCP^O X-ray scattering difference pattern (scaled by a factor 0.018) is also shown for comparison. Data are vertically offset for clarity. (*E*) Time evolution of the integrated difference scattering in the region $0 < q < 0.15$ Å^{-1} after laser excitation at 527 nm for $OCP_{wt\text{-}Ctag}$ (*blue and green circles*) and $OCP_{wt\text{-}Ntag}$ (*red squares*). Dashed lines are fitting curves with a double exponential. To see this figure in color, go online.

amplitude of the peak does not vary significantly, indicating that stretching the pulse up to 450 ns does not improve the photoactivation extent (Fig. 6 *B*). Thus, OCP molecules that have not engaged toward formation of a red state (P_1) and are back to the ground state (27) cannot be re-excited within the 450 ns pulse. Given the fact that these molecules do not show a difference signal in transient absorption spectroscopy experiments—meaning that the carotenoid is back

in the orange state and therefore presumably H-bonded to the protein scaffold—their inability to re-enter a photocycle could be rooted in the fact that some protein residues, which are important for photoactivation but do not influence the spectrum, have not yet returned to their initial conformation after 450 ns. We refer to this hitherto undescribed intermediate state, which accounts for 99.3% of the OCP^{O} population upon pulsed illumination at 22°C, as the OCP "numbed state," abbreviated OCP^{NS}. To estimate an upper boundary for the lifetime of this intermediate, the repetition rate (1 kHz) of the 527 nm laser, coupled with a synchronized chopper/shutter system, was used to measure TR profiles at a time delay of 100 ms post excitation by an increasing number (up to 30 pulses) of consecutive pulses spaced by 1 ms. The scattering difference signal (laser-on minus laser-off) was then integrated in the 0–0.15 $Å^{-1}$ range and plotted as a function of the number of pulses (Fig. 6 *C*). The signal increases linearly with the number of pulses up to 5 pulses for $OCP_{wt\text{-}Ntag}$ and up to 10 pulses for $OCP_{wt\text{-}Ctag}$, after which a plateau is observed, presumably due to concomitant recovery of the dark-state structure (see below). Thus, the lifetime of the non-re-excitable OCP^{NS} can be estimated to lie between 450 ns and 1 ms. Irrespective of this, comparison of the two TR difference signals with the static difference scattering signal shows that the shape of the difference profile generated by pulsed excitation does not coincide with that obtained by stationary illumination. In particular, the position of the negative peak differs, and the positive peak at ≈ 0.12 $Å^{-1}$ is absent (Fig. 6 *C*).

A complete TR data set was measured at time delays between 15 μs and 200 ms. Data for $OCP_{wt\text{-}Ctag}$ are shown in Fig. 6 *D*, while analogous results are obtained for $OCP_{wt\text{-}Ntag}$. Fig. 6 *D* demonstrates that substantial changes in the scattering profiles are 1) already visible after 15 μs, 2) maximized before 1 ms, and 3) substantially damped by 200 ms. To further investigate the kinetics of the scattering signal changes, the TR scattering data set were analyzed by the SVD method (see Fig. S12 and materials and methods), which revealed that the entire data set can be described by a single time-independent basis pattern (*continuous line* in Fig. 6 *D*). In other words, no other intermediate state than that responsible for this basis pattern is visible in our data. It must be noted that the difference between the TR and static difference signals (i.e., the shift in q-value of the negative peak and the absence of a positive peak) is observed for all recorded time delays (15 μs to 200 ms). Notwithstanding, a rough estimation of the photoactivation extent by pulsed nanosecond excitation can be obtained by scaling the amplitude of the TR difference signal to that measured in static experiments, pointing to a photoactivation efficiency of $\approx 1.8\%$ (Fig. 6 *B*). The difference profiles shown in Fig. 6 *D* were integrated in the 0–0.15 $Å^{-1}$ range, and the results are shown as a function of time for both $OCP_{wt\text{-}Ntag}$ and $OCP_{wt\text{-}Ctag}$ in Fig. 6 *E*. The integrated intensity starts decaying between 1 and 10 ms in $OCP_{wt\text{-}Ntag}$ and between 10 and 100 ms in $OCP_{wt\text{-}Ctag}$, indicating a recovery of the dark state in these timescales, in full agreement with the results in Fig. 6 *C*. Thus, large-scale conformational changes start occurring as of ≈ 10 μs, maximize at 1 ms, and revert with apparent lifetimes (i.e., time at half-maximum amplitudes) of 69 $\pm$ 14 and 280 $\pm$ 50 ms for $OCP_{wt\text{-}Ntag}$ and $OCP_{wt\text{-}Ctag}$, respectively.

It is tantalizing, but difficult, to propose an interpretation for our observations. It has been proposed earlier that the first large-scale conformational change (≈ 1 ms timescale) occurring in OCP after excitation is the detachment of the NTE from the CTD β-sheet, either concomitant or prior to a repositioning of the CTT, and that thereafter only dissociation of the two domains may befall (27,29). Given the quantum yield of OCP and the fact that our TR-SAXS experiment was carried out at 23 mg/mL (620 μM), where dimers account for $\approx 98\%$ of the sample, it is extremely unlikely that two monomers in the same dimer would have been photoexcited by the same pulse (probability is the square of the quantum yield, i.e., 0.4×10^{-5}) and that our signal would inform on the formation of the photoactive OCP^{R}. Furthermore, since the NTE is involved in the dimerization interface, the domain dissociation characteristic of the OCP^{R} state would have to await monomerization. Hence, it is most probable that the conformational change probed in our experiment is neither dimer nor domain dissociation, but rather a subtle conformational change occurring in only one of the two monomers in a dimer.

DISCUSSION

In the present work, we used TR visible spectroscopy, as well as static and TR X-ray scattering, to investigate the structural changes—including changes in quaternary structure—accompanying photoactivation of the OCP. It was repeatedly observed that OCP crystallizes as a dimer, yet it had remained elusive whether or not this interface is functional given the high concentration of the protein in crystals, namely ≈ 23 mM. Mutation of a single highly conserved residue at the crystalline dimerization interface results in the loss of the ability of OCP^{O} to dimerize, suggesting that the dark-adapted dimer could be functional (10). Collection and analysis of static X-ray scattering profiles of dark-adapted $OCP_{wt\text{-}Ctag}$ as a function of concentration confirm the in vitro existence, already suggested in the literature (22,23,25,26,30,56), of a dimer that becomes predominant at concentrations ≥ 1 mg/mL (Figs. 3 *C* and S1). Our SAXS titration data ($K_D \approx 14$ μM) is in accordance with: 1) previous results from native mass spectrometry experiments, reporting the presence of OCP^{O} dimers at concentration as low as 3 μM (22); 2) the recent assertion based on SAXS and SANS data that OCP^{O} resides in the same state at 1 and 65 mg/mL (i.e., 28 μM and 1.8 mM) (23,24); and 3) the dissociation constant that can be derived from SEC

results presented in Fig. 3 of Muzzopappa et al. (10), i.e., ≈0.6 mg/mL (17 μM), provided that we use the same extinction coefficient at 490 nm to estimate protein concentrations.

Analogous concentration-dependent analyses of static X-ray scattering profiles collected after accumulation of $OCP^{R}_{wt\text{-}Ctag}$ and $OCP^{R}_{R27L\text{-}Ntag}$ by 30 min irradiation at 430 nm suggest that they are also prone to oligomerization. Indeed, for both proteins, not only is the scattering signal different between the dark-adapted (OCP^{O}) and light-adapted (OCP^{R}) states, but that difference evolves as a function of concentration. Remarkably, $OCP^{R}_{R27L\text{-}Ntag}$ and $OCP^{R}_{wt\text{-}Ctag}$ display similar P(r) (Fig. 2 *F*) and Rg (Fig. 3 *B*) at the various tested concentrations, indicating that they form the same OCP^{R} state(s). The high concentration (10.5 mg/mL) difference scattering profiles between the light- and dark-adapted states, i.e., $\Delta I(q)_{R27L\text{-}Ntag}$ and $\Delta I(q)_{wt\text{-}Ctag}$, are characterized by the presence of a negative peak (at 0.07 and 0.05 $Å^{-1}$, respectively) and a positive peak (at 0.14 and 0.12 $Å^{-1}$, respectively) (Fig. 3 *D*). These peaks respectively signal the loss and gain of interatomic distances in the OCP samples upon illumination-triggered transition from the OCP^{O} to the OCP^{R} state. Given that $OCP^{R}_{R27L\text{-}Ntag}$ and $OCP^{R}_{wt\text{-}Ctag}$ form the same OCP^{R} species, the observation that the negative and positive peaks are found at different q-values in the $\Delta I(q)_{R27L\text{-}Ntag}$ and $\Delta I(q)_{wt\text{-}Ctag}$ difference profiles can be rationalized by the fact that their dark-adapted states differ, $OCP^{O}_{R27L\text{-}Ntag}$ being present as a monomer whereas $OCP^{O}_{wt\text{-}Ctag}$ features as a dimer.

The molecular envelopes reconstructed from the OCP^{R} data suggest that OCP^{R} dimers form as of 0.7 mg/mL (20 μM), while higher-order oligomers form at 10 mg/mL (≈300 μM) (Figs. 3, *A* and *B*; Figs. S1 and S2; Tables S4 and S5). The observation that the R27L mutant also forms OCP^{R} dimers and higher-order oligomers suggests that the dimerization interfaces of OCP^{O} and OCP^{R} do not overlap. Based on this hypothesis and on knowledge from the literature, we were able to build tentative models for OCP^{R} dimers and higher-order oligomers. The models notably assume that: 1) OCP^{R} higher-order oligomers form from the coalescence of either two OCP^{R} dimers (yielding tetramers) or one OCP^{R} monomer and one OCP^{R} dimer (yielding trimers); 2) interactions between OCP^{R} monomers in a dimer and between OCP^{R} dimers and/or monomers in a higher-order oligomer involve the same interface in the two interacting monomers; 3) residues involved in assembly of OCP^{R} into dimers and higher-order oligomers are not exposed in the dark OCP^{O} dimer (51,53); and 4) OCP^{R} dimers assemble via their CTD, so that their two NTDs are exposed and free to interact with PBS via R155 (51), while the OCP^{R} higher-order oligomers form from an interaction between two NTDs using an interface similar to that observed in all three currently available crystal structures of the homologous HCP homologs (PDB: 5FCX and 6MCJ (40,41)). This interface features the residue equivalent to R155 in OCP, and thus corresponds to the face of the NTD that presides to the NTD/CTD interaction in OCP^{O}. Our model for the $OCP^{R}_{wt\text{-}Ctag}$ dimer is in overall agreement with that proposed earlier (23), featuring two monomers associated by their CTD at an interface reminiscent of that observed at the A-type interface in the apo-*Anabaena* CTDH crystal structure. Of note, helices αN (or CTT) and αA (or NTE), which sit aside one another on this side of the β-sheet in the OCP^{O} state but detach upon photoactivation (9), were considered as disordered in OCP^{R} and therefore not included in our OCP^{R} dimer model. To account for the known exposure, in OCP^{R}, of the face of the NTD that interacts with the CTD in OCP^{O}, each NTD was rotated by 180° and further translated by a few angstroms to avoid clashes with the CTD. This face of the NTD features R155, which tethers the NTD to the CTD via H bonding to E244 in OCP^{O} (Fig. 1), but is essential for the interaction of OCP^{R} with the PBS. Our data do not allow us to firmly assign the precise nature of higher-order oligomers. Indeed, the elongated molecular envelope derived from OCP^{R} samples at high concentrations (>10 mg/mL) could either stem from the presence of elongated OCP^{R} trimers (formed by the interaction of an OCP^{R} monomers and an OCP^{R} dimer) or more compact OCP^{R} tetramers (formed by the interaction of two OCP^{R} dimers), or a mixture thereof. Fig. S1 shows the superimposition of a tentative OCP^{R} tetramer model over the molecular envelopes derived from SAXS data collected on $OCP^{R}_{wt\text{-}Ctag}$ and $OCP^{R}_{R27L\text{-}Ntag}$ at ≈10 mg/mL. The molecular envelopes could yet also be explained by elongated OCP^{R} trimers or by a mixture of trimers and tetramers. An important question which remains open is that of the in vivo concentration of OCP, as it would determine whether or not the OCP^{O} and OCP^{R} dimers and OCP^{R} higher-order oligomers are of functional relevance. The in vivo concentration of OCP remains elusive—notably the local concentration in the vicinity of the thylakoid membranes, where OCP localizes—hence, we cannot ascertain that the concentrations used in our study are found in the cell. It must be recalled, however, that the overall mass-concentration of proteins in cells is estimated to lie between 200 and 300 mg/mL (57), corresponding to a molar concentration of ≈5 mM—i.e., nearly the concentration of proteins in crystals—assuming an average molecular weight of 50 kDa. Hence, we may speculate that in cyanobacterial cells, the propensity of OCP to form dimers would be high even in the case where its overall concentration would be lower than the dissociation constant. Furthermore, OCP is localized in the vicinity of the thylakoid membranes, where its local concentration could be higher. Strongly supporting the relevance of OCP^{R} dimers is, in all cases, the recently determined cryo-electron microscopy structure of the OCP-quenched PBS (58), which reveals binding to the PBS of an OCP^{R} dimer. The overall similarity between our model and that presented in the preprint of the manuscript (coordinates are not accessible as yet) is notable.

Given that the dissociation constants of OCP^O and OCP^R dimers are on the same order, it may be proposed that if the latter is functional, the second must also be.

We used a combination of optical spectroscopy and X-ray scattering to investigate OCP^R-to-OCP^O thermal recovery and determine whether or not it is influenced by oligomerization processes. First, we monitored the structural recovery of the $OCP^O_{wt\text{-}Ctag}$ state, following accumulation of the $OCP^R_{wt\text{-}Ctag}$ state by prolonged illumination at 430 nm. The difference scattering profile features a positive and a negative peak (Fig. 3 *D*), which together signal the disappearance of the starting $OCP^O_{wt\text{-}Ctag}$ state and the concomitant appearance of the $OCP^R_{wt\text{-}Ctag}$ states. Hence, the time evolution of the difference signal in the 0.05–0.5 $Å^{-1}$ q-range was used to follow the overall thermal recovery, which after prolonged illumination occurs on the timescale of tens of minutes (Fig. S4).

Further insights into the OCP^R-to-OCP^O thermal recovery were attained by resorting to spectroscopy at various protein concentrations. First, we accumulated OCP^R by prolonged illumination at 430 nm and monitored the recovery of OCP^O by following absorption at 467 nm. Regardless of the sample, we found that the recovery time markedly increases as a function of concentration, in full agreement with the indication from static X-ray scattering data that both OCP^O ($OCP_{R27L\text{-}Ntag}$, $OCP_{wt\text{-}Ntag}$, and $OCP_{wt\text{-}Ctag}$) and OCP^R ($OCP_{R27L\text{-}Ntag}$, $OCP_{wt\text{-}Ntag}$, and $OCP_{wt\text{-}Ctag}$) can oligomerize. Indeed, the more oligomeric OCP^R states are present, the higher the overall energy barrier for a full recovery of the starting dark OCP^O to occur and, therefore, the longer it will take. Irrespective of the assayed concentration, the spectroscopic recovery of $OCP^O_{wt\text{-}Ntag}$ was found to be slower than that of $OCP^O_{R27L\text{-}Ntag}$, indicating that the reassembly into dimers of OCP^O monomers is the step that limits $OCP^O_{wt\text{-}Ntag}$ recovery. Likewise, the recovery of $OCP^O_{wt\text{-}Ctag}$ was slower than that of $OCP^O_{wt\text{-}Ntag}$, indicating that presence of the His-tag at the C-terminus adversely affects recovery of the dark-adapted state. Recovery data could only be fitted with three- or four-exponential functions, suggesting the occurrence of multiple sequential steps. We plotted the pre-exponential factors as a function of concentration to follow the evolution of the associated populations (Fig. 4, *A* and *C*; Fig. S8). Focusing first on results from the three-exponential fits, we observe a similar evolution as a function of concentration in the three samples: 1) the amplitude of the fastest component ($a_{ci\text{-}1}$, $\tau_{ci\text{-}1}$) decreases; 2) the amplitude of the intermediate component ($a_{ci\text{-}2}$, $\tau_{ci\text{-}2}$) initially increases but then decreases; 3) the amplitude of the slowest component ($a_{ci\text{-}3}$, $\tau_{ci\text{-}3}$) steeply increases. The observation of intersections at 0.5 population between amplitudes of rising and declining components is indicative of a balance in their relative populations and therefore is suggestive of sequentiality between the underlying steps (Fig. 4, *A*–*C*). The populations of the first and second components feature such an intersection at concentrations of ≈0.7 and ≈1.8 mg/mL, in $OCP_{R27L\text{-}Ntag}$ (Fig. 4 *A*) and $OCP_{wt\text{-}Ntag}$ (Fig. 4 *C*), and at ≈6 mg/mL in $OCP_{wt\text{-}Ctag}$ (Fig. S8 *C*). Assuming that the first ($a_{ci\text{-}1}$; $\tau_{ci\text{-}1}$) and second ($a_{ci\text{-}2}$; $\tau_{ci\text{-}2}$) components inform on the contribution to recovery of OCP^R monomers and dimers, a possible explanation is that presence of the His-tag at the C-terminus challenges dimerization of OCP^R in $OCP_{wt\text{-}Ctag}$, elevating the apparent dissociation constant. For $OCP_{R27L\text{-}Ntag}$ and $OCP_{wt\text{-}Ntag}$, we furthermore see that the population of third component intersects with those of the first (at ≈1.7 and ≈7 mg/mL, respectively) and second components (at ≈9.5 and ≈14.5 mg/mL, respectively). Assuming that the slowest component informs on the contribution of OCP^R higher-order oligomers to the recovery signal, this observation would be suggestive of a facilitated accumulation of these in $OCP^R_{R27L\text{-}Ntag}$, compared with the $OCP^R_{wt\text{-}Ntag}$—possibly due to elimination of a competition between the dark-adapted dimerization and light-adapted trimerization and/or tetramerization interfaces. Indeed, both are localized in the NTD of $OCP_{wt\text{-}Ntag}$. In the $OCP_{wt\text{-}Ctag}$ sample, we do not see intersections of the slowest component amplitude with those of other components when results of the three-exponential fit are considered. However, a much better agreement is obtained when the $OCP_{wt\text{-}Ctag}$ data are fit with four exponentials (Tables S6 and S7), yielding a χ^2 comparable with that obtained with three exponentials for $OCP_{R27L\text{-}Ntag}$ and $OCP_{wt\text{-}Ntag}$. Plotting the four amplitudes as a function of concentration, the same observations can be made for the $OCP_{wt\text{-}Ctag}$ (Fig. 4 *C*), i.e., intersections at 0.5 population can be seen at ≈1.7 mg/mL for the first and second component, and at ≈10 mg/mL for the second and third component. The population of the additional fourth component, characterized by a lifetime in the order of ≈4 h (14,057.7 ± 68.8 s), varies from ≈0.04 to 0.1 with increasing concentrations, indicating that the contribution of this rate-limiting step to the recovery signal is small. We see two possible explanations for the presence of this additional component. A first hypothesis is that it informs on the dimerization of $OCP^O_{wt\text{-}Ctag}$ monomers, which due to absence of a tag at the N-terminus would reassemble faster than $OCP^O_{wt\text{-}Ntag}$, explaining that a lifetime can be extracted for the former but not for the latter, in our experiments (t_{max} = 5000 s). Another hypothesis is that the additional component informs on a step that is dramatically slowed down in $OCP_{wt\text{-}Ctag}$ compared with $OCP_{wt\text{-}Ntag}$, e.g., the reattachment of the CTT to the F-side of the CTD β-sheet. Indeed, the CTT is longer and presumably more flexible in $OCP_{wt\text{-}Ctag}$ compared with $OCP_{wt\text{-}Ntag}$, and it was accordingly shown that $OCP^O_{wt\text{-}Ctag}$ recovers faster than $OCP^O_{wt\text{-}Ntag}$ (14,54). Our data do not allow us to favor one hypothesis over the other. However, the doubling of the lifetimes extracted for $OCP_{wt\text{-}Ntag}$, compared with $OCP_{R27L\text{-}Ntag}$ provides circumstantial evidence that dimerization of the dark-adapted $OCP^O_{wt\text{-}Ntag}$ is the limiting

step in its recovery. Therefore, we favor the first hypothesis. We accordingly propose that our recovery data inform on four molecular steps (Fig. 7) involved in the concentration-dependent OCP^R-to-OCP^O thermal recovery: 1) the transition from monomeric OCP^R to OCP^O, characterized by a lifetime $\tau_{ci\text{-}1}$ = 50–100 s; 2) the dissociation of OCP^R dimer into OCP^R monomers, characterized by a lifetime $\tau_{ci\text{-}2}$ = 160–600 s and a dissociation constant on the order of 14–30 μM (recovery data point to values of 30–40 μM but the observation that $OCP^R{}_{R27L\text{-}Ntag}$ dimers attain dominance at 0.7 mg/mL, where occupancy of the $OCP^O{}_{wt\text{-}Ctag}$ dimer is partial (0.7 mg/mL), suggests a dissociation constant below 14 μM); 3) the dissociation of OCP^R higher-order oligomers into OCP^R dimers and/or monomers, characterized by a lifetime $\tau_{ci\text{-}3}$ = 640–950 s and an approximately 20-fold higher dissociation constant ($\approx$280 μM), since these oligomers are visible as of 10 mg/mL; 4) the reassociation of OCP^O monomers into OCP^O dimers, characterized by a lifetime $\tau_{ci\text{-}4} > 14{,}057$ s and a dissociation constant on the order of $\approx$0.5 mg/mL ($\approx$14 μM). That OCP^O dimer formation is slowed down in $OCP_{wt\text{-}Ntag}$ compared with $OCP_{wt\text{-}Ctag}$ could result from the presence of the His-tag at the N-terminus, i.e., in the vicinity of the OCP^O dimerization interface.

To obtain additional insights into molecular events occurring on shorter timescales, we used pulsed nanosecond illumination to generate OCP^R (with a yield of $\approx$0.7%), and monitored the nanosecond-to-second timescale evolution of the difference absorption signal (ΔA) at the blue and red edges of the OCP^O (440 nm) and OCP^R (565 nm) absorption spectra, respectively. The use of the two wavelengths was justified by our need to obtain insights into both the recovery of the OCP^O state ($\Delta A_{440\ nm}$) and the formation and disappearance of OCP^R and preceding red intermediates ($\Delta A_{565\ nm}$). The wild-type $OCP_{wt\text{-}Ntag}$ and $OCP_{wt\text{-}Ctag}$ were investigated, as well as the constitutively monomeric $OCP_{R27L\text{-}Ntag}$ mutant. Regardless of the OCP sample, we could identify three intermediate states with lifetimes of $\approx$2 μs, $\approx$1 ms, and $\approx$40–200 ms, respectively, at 22°C. The lifetimes derived from $OCP_{wt\text{-}Ntag}$ and $OCP_{wt\text{-}Ctag}$ data are nearly identical, indicating that the presence of the His-tag does not influence the dynamics probed at the carotenoid level on the nanoseond-to-second timescale. Nonetheless, a higher OCP^R yield was found for $OCP_{wt\text{-}Ntag}$, demonstrating influence of the tag on a step that is not rate-limiting, and whose contribution to photoactivation and recovery is silent from the spectroscopic perspective. In these experiments, carried out at a concentration where the dimeric form accounts for 46% of the wild-type proteins (12 μM), the first and second components were found to not vary as a function of the protein variant, while a twofold reduced lifetime was found for the third component in the constitutively monomeric $OCP_{R27L\text{-}Ntag}$. Additional experiments carried out at 50 and 250 μM concentrations of $OCP_{R27L\text{-}Ntag}$ and $OCP_{wt\text{-}Ctag}$, where the prevalence of $OCP^O{}_{wt\text{-}Ctag}$ dimers is 78% and 95%, respectively, revealed a marginal influence of concentration on the lifetimes determined for $OCP_{R27L\text{-}Ntag}$, but a twofold increase in that of the third component $\tau_{ci\text{-}3}$ for $OCP_{wt\text{-}Ctag}$. This result establishes that the presence of dimers influences component τ_3, but neither τ_1 nor τ_2, in a concentration-dependent fashion. A plot of the τ_3 lifetime as a function of dimer concentration, using for zero concentration the average value from $OCP_{R27L\text{-}Ntag}$ measurements at 12, 50, and 250 μM (i.e., 54.8 $\pm$ 7.7 ms), shows a logarithmic shape, with a dimer concentration of $\approx$10 μM (corresponding to an overall $OCP_{wt\text{-}Ctag}$ concentration of $\approx$20 μM) at half maximum (Fig. S10 *B*). The data also show that the presence of OCP^O dimers does not benefit the overall $OCP^R{}_{wt\text{-}Ctag}$ yield, despite the yield of the initial P_2 intermediate rising with increased $OCP_{wt\text{-}Ctag}$ concentration (Fig. S10 *A*). To obtain further insights into the enthalpic and entropic contributions to the formation of each of the three states, we furthered our analysis by carrying out experiments at various temperatures in the 8°C–36°C range (Figs. 5 *B* and S9). Increased temperatures were associated to a lower yield of the red states, including the final $OCP^R{}_{wt\text{-}Ctag}$, possibly due to non-adiabatic processes occurring earlier than our first data point ($\approx$50 ns), which do not repopulate directly the dark $OCP^O{}_{wt\text{-}Ctag}$ state (monitored at 440 nm). Another interpretation could be that the molar extinction coefficient of the OCP^R-bound carotenoid decreases with increasing temperature. Irrespective of this, we found that in both $OCP_{wt\text{-}Ctag}$ and $OCP_{R27L\text{-}Ntag}$, the first intermediate—whose associated lifetime hardly varies among proteins and concentrations—is adiabatically formed, i.e., with no exchange of heat (Fig. 5, *E* and *F*). Thus, all the energy necessary for the formation of this intermediate is funneled into the protein scaffold before 50 ns, i.e., the first data point in our nanosecond-to-second time span. The fact that no enthalpic contribution is associated with this component indicates that no H bond or salt bridge forms nor breaks upon accumulation of the corresponding intermediate, while the observation of a negative entropic contribution suggests a reduction in the complexity of the system. Hence, component τ_1 could underlie the multistep translocation of the carotenoid from the NTD/CTD interface into the NTD. Regarding the two other components, τ_2 and τ_3, they are associated with similar enthalpies of activation ($\approx$18 kcal mol^{-1}) in $OCP_{wt\text{-}Ctag}$, whereas a slightly larger value is found for τ_3 ($\approx$26 kcal mol^{-1}) compared with τ_2 ($\approx$20 kcal mol^{-1}) in $OCP_{R27L\text{-}Ntag}$. This difference in enthalpy could be rooted in the absence of dimers in the $OCP_{R27L\text{-}Ntag}$ sample, as we have seen that the τ_3 component—but not the τ_2 component—is affected by the presence of these.

TR-SAXS/WAXS on the 15 μs to 200 ms timescale allowed us to shed partial light on the structural changes associated with the OCP photocycle. Pulsed illumination results in a negative peak at $\approx$0.03 $Å^{-1}$ in the "light minus dark" $\Delta I(q)$ profile, with this peak being already present at 15 μs,

maximizing before 1 ms, and starting to decrease as of ≈10 ms and 100 ms in $OCP_{wt\text{-}Ntag}$ (lifetime ≈70 ms) and $OCP_{wt\text{-}Ctag}$ (lifetime ≈280 ms), respectively. Hence, our data demonstrate that the first large-scale conformational changes associated with OCP photoactivation take place on the tens of microseconds timescale (15 μs), and that the localization of the His-tag influences the structural recovery rate. Both transient absorption spectroscopy and TR-SAXS were required to work at comparatively high OCP concentration, with more than 98% dimers at the highest concentration tested in spectroscopy experiments or used in TR-SAXS/WAXS experiments, and a minimum of ≈46% dimers at the lowest concentration tested in spectroscopy experiments. Hence, we probed, with the two techniques, the effect on OCP dimers of nanosecond pulse illumination, from the structural and the spectral perspectives. The TR-SAXS/WAXS data are indeed sensitive to structural changes regardless of where they occur in the protein, but is of too low resolution to afford information on the carotenoid position and on non-predominant species. This is at variance with our spectroscopy data, which may inform on the formation of all red-shifted intermediates—productive (OCP^R, offset at 0.5 s) and unproductive alike (Table S8)—but is blind to structural changes that do not affect the local environment of the carotenoid (e.g., detachment of NTE and CTT) (14,54). As structural and spectroscopic transitions may be asynchronous, they should be considered independently.

Given that the probability that two monomers in a dimer can be activated by the same pulse is the square of the quantum yield, i.e., $<0.4 \times 10^{-5}$, our TR-SAXS could not probe the formation of OCP^R, but only that of the predominant non-productive intermediate state. Keeping this in mind, we can propose the following sequence of events for the OCP photocycle based on ours as well as others' results (Fig. 8). Upon absorption of the actinic photon, an S_2 state forms which decays within picoseconds into at least three states: the S_1 and ICT excited states, and S*, which could either be an excited state (27) or a vibrationally hot ground state (59). Within 20 ps, 99.3% of molecules are back to the ground state and do not progress further toward OCP^R. Our TR-SAXS/WAXS experiment reveals the existence of a "numbed" OCP intermediate, OCP^{NS}, which is formed upon such non-productive laser excitation and remains up to the microsecond timescale in a non-re-excitable structural state (Figs. 6 *C* and 8 *A*). Evidence for the existence of this state was obtained serendipitously, as we attempted to increase the extent of photoactivation by distribution of actinic photons in a longer pulse (5 vs. 450 ns pulses). This attempt was infructuous, indicating that the ground-state OCP^O structure formed after excitation remains non-photoactivatable for at least 0.5 μs, in line with the previous report that increasing the power of nanosecond pulses does not result in a higher photoactivation yield (13). By use of a multipulse approach, whereby re-excitation was triggered every 1 ms for up to 30 pulses, we were able to estimate the lifetime of OCP^{NS} to lie between 450 ns and 1 ms (Fig. 6, *B* and *C*).

Specific to the photoproductive pathway (Fig. 8 *B*), it has been proposed that S* is the precursor of the first red photoproduct P_1, characterized by rupture of the H bonds between the carotenoid and the protein scaffold and a lifetime of ≈50 ns. The carotenoid therefrom debuts its migration from the NTD/CTD interface into the NTD, first forming photoproduct P_2, after repositioning at the NTD/CTD interface, and then $P_{2'}$, after further migration across the NTD. From the structural perspective, and as noted already by Konold et al. (27), this migration of the carotenoid must be accompanied by changes in the relative orientation of helices αC, αE, and αG, which harbor the carotenoid-tunnel bottleneck residues L37, M83, and M117. Eventually, these changes will propagate to the αG-αH loop and to E34, at the kink between αB and αC, resulting in an opening of the carotenoid tunnel across the NTD wall and complete migration of the carotenoid pigment, forming P_3, wherein the β2 ionone ring of the carotenoid is exposed to the solvent, possibly as in the structure of the isolated NTD with canthaxanthin (19). We suppose that the first steps identified in our transient absorption spectroscopy (τ_1 ≈ 2–3 μs) and TR-SAXS/WAXS (<15 μs) experiments correspond to the $P_2/P_{2'}$-to-P_3 transition, in line with Konold et al. (0.5–1 and 10 μs for P_2-to-$P_{2'}$ and $P_{2'}$-to-P_3 transitions, respectively) (27). In the TR-SAXS/WAXS experiments, however, it is clear that this transition can only occur within OCP^O dimers. Hence, a partly activated dimer would form, featuring a P_3 monomer and a dark-adapted monomer (i.e., P_3/OCP^O dimer). Failure to fully migrate across the carotenoid tunnel and form P_3 is presumably sanctioned by rapid back-migration and rebinding to H-bonding partners in the CTD (component τ_1), i.e., partial recovery of OCP^O from $P_2/P_{2'}$, as supported by the fact that the decrease in $\Delta A_{565\ nm}$ is mirrored by an increase in $\Delta A_{440\ nm}$ (Fig. S9). The next spectroscopically visible steps (τ_2, τ_3) occur on the ≈1 ms and ≈50–200 ms timescales, respectively, and they are characterized by a large decrease in $\Delta A_{565\ nm}$ that is not accompanied by a similarly extended increase in $\Delta A_{440\ nm}$. Hence, only limited spectral recovery of the OCP^O state occurs on this timescale. Remarkably, the τ_2 and τ_3 components display the same activation energy, suggesting that they would inform a similar molecular event, but only the latter is influenced by concentration. TR-SAXS data indicate that no structural changes other than reversion to the OCP^O state occurs up to 200 ms, excluding that the τ_2 and τ_3 components would inform on further progression of the P_3/OCP^O dimers toward the OCP^R state—e.g., detachment of NTE from the CTD, which would be a prerequisite to dimer dissociation that itself would precede separation of the two domains. Hence, we propose that the τ_2 and τ_3 components both signal the back-migration of the carotenoid into the carotenoid tunnel

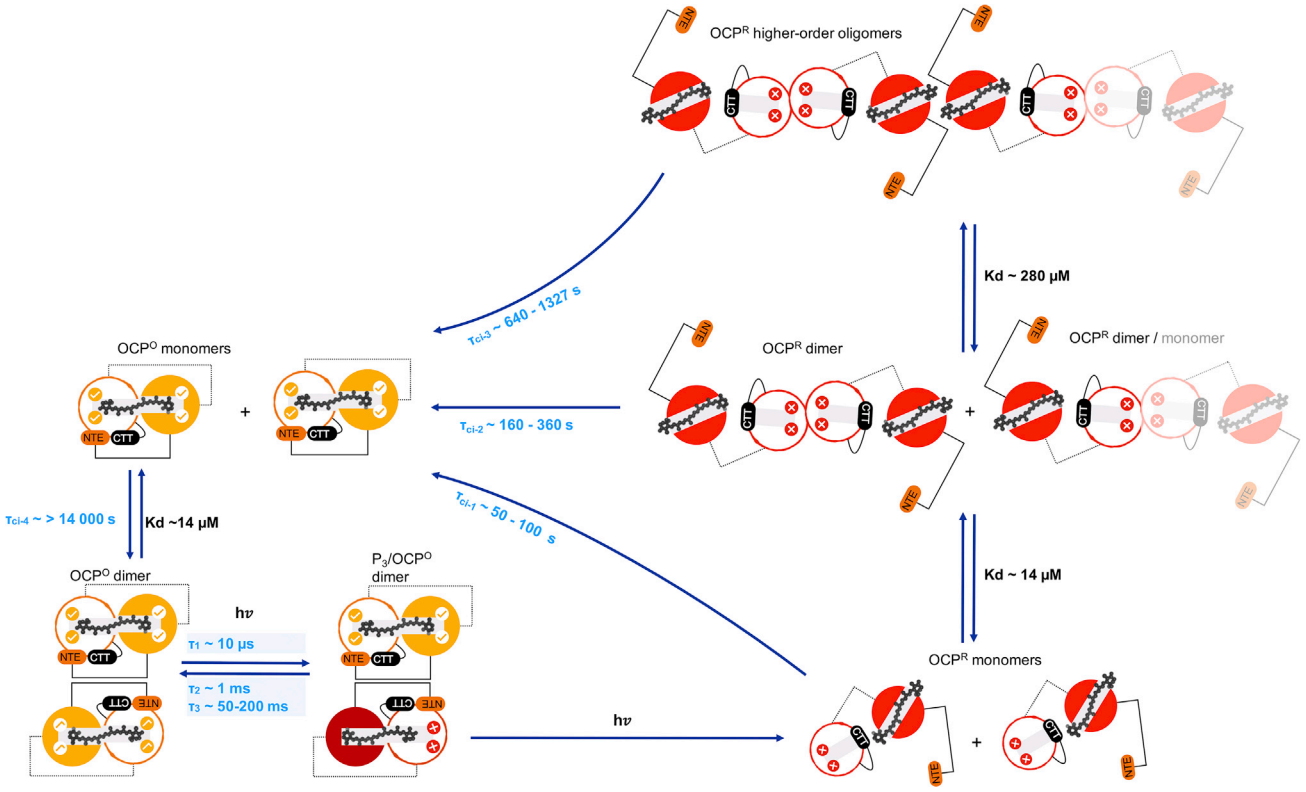

FIGURE 7 Proposed model for OCP photoactivation and recovery upon continuous illumination. OCP monomers and dimers are represented schematically with their N-terminal (colored *orange* and *red* for OCP^O and OCP^R, respectively) and C-terminal (colored *white*) domains. The ground state keto-carotenoid is shown in gray. Ticks and crosses in the CTD indicate presence and absence of H bonds between the carotenoid and CTD residues Tyr201 and Trp288. The presence of ticks in the NTD indicate the presence of π-stacking interactions between the carotenoid and NTD residues Tyr44 and Trp110. Our data show that dark-adapted $OCP^O{}_{wt}$ forms dimers, with a dissociation constant of $\approx 14\ \mu M$. The dimerization interface at play is likely that which has been repeatedly observed in OCP crystal structures. In the event where one of the two monomers in a dimer is activated, it may undergo all photoactivation steps until formation of P_3 but will promptly revert to the dark state unless the second monomer is as well photoactivated, forming a P_3/OCP^O dimer. Indeed, domain dissociation can only occur after dimer disassembly, which itself can only befall after NTE detachment. The latter is in turn dependent on the carotenoid achieving a successful transit across the NTD as required to induce conformational disorder in αC, αB, and consequently αA. In practice, this means that reaching the OCP^R state in a pulsed illumination experiment probing OCP_{wt} dimer is extremely unlikely (probability $= QY^2 = 0.4 \times 10^{-5}$), unless re-excitation can be achieved within the lapse of the excitation pulse. Under continuous illumination, however, the OCP^R state can be accumulated, which first coalesces into dimers, with a dissociation constant similar to that displayed by dark-adapted OCP ($\approx 14\ \mu M$), but may further progress to the formation of higher-order oligomers at higher concentrations (the dissociation constant is at least 20 times higher, i.e., $\approx 286\ \mu M$). Higher stabilization of OCP^R in these oligomers elevates the overall energy barrier for a full recovery of the starting dark OCP^O to occur, and therefore delay the upturn of the OCP^O state. At concentrations where the dark OCP^O dimer may form, it is yet the reassociation of dark monomers into dimers ($\tau_{ci\text{-}4}$) of $\approx 14{,}000$ s that constitute the limiting step in the recovery. Hence, OCP photoactivation and recovery are limited by oligomerization processes. To see this figure in color, go online.

of the P_3 monomer in the P_3/OCP^O dimer, but that each component informs on this process in a structurally different, partly activated dimer. It has indeed been shown that two types of OCP^O exist, i.e., a red-shifted and a blue-shifted OCP^O (13). It is reasonable to propose that OCP dimerization would influence the equilibrium between these two OCP^O states, with the less flexible state being favored in the dimer, thus explaining the longer lifetime before back-migration occurs. The τ_2 and τ_3 components could thus underlie back-migration of the carotenoid in two such OCP^O.

Taken together, our steady-state and TR optical spectroscopy and X-ray scattering data point to the conclusion that formation of P_3 must occur in each of the two monomers, and the P_3/P_3 dimer dissociate into its monomeric counterparts, for OCP^O dimers to yield (monomeric) OCP^R (Fig. 8 *C*). Presumably, the next step in the photoactivation mechanism is the detachment from the CTD of αA and αN (associated with loss of 794 and 394 $Å^2$ of buried surface area in the OCP^O monomer, respectively), which will rapidly be followed by dissociation of the two domains, given that the carotenoid has already fully migrated into the NTD (loss of 345 $Å^2$ of buried surface area in the CTD) and does not contribute any longer to the stabilization of the closed conformation (only 674 $Å^2$ of buried surface area is left at the NTD/CTD interface). The lifetime of monomeric OCP^R is 50–100 s, but it may further associate into dimers or higher-order oligomers upon increase in concentration, and these changes in quaternary structure will extend its lifetime to tens of minutes (lifetimes of 160–360 and 640–1327 s

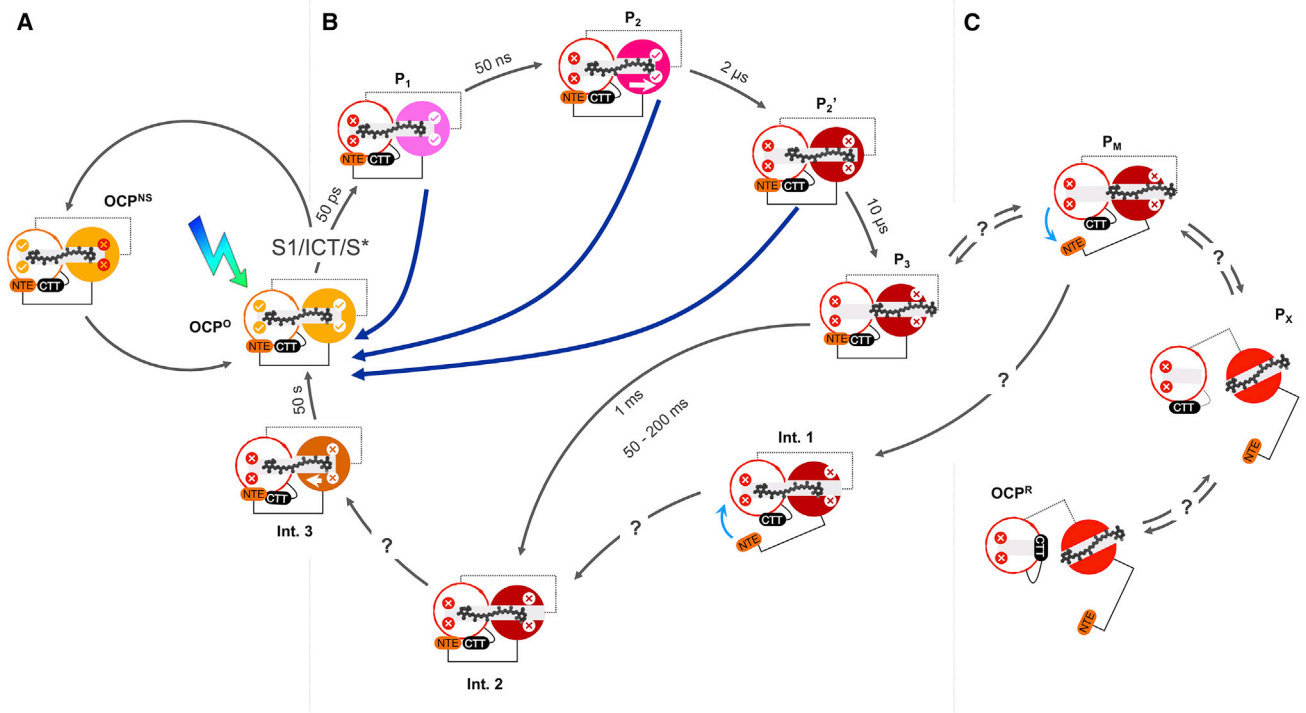

FIGURE 8 Proposed model for OCP photoactivation and recovery upon pulsed excitation. OCP is schematically represented with its N-terminal (colored *orange* for OCP^O, *pink* for P_1, *magenta* for P_2, and *red* for $P_{2'}$, P_3, OCP^R, Int.1, Int.2, and Int.3) and C-terminal domains (colored *white*). The ground state keto-carotenoid is shown in gray. Ticks and crosses in the CTD indicate presence and absence of H bonds between the carotenoid and CTD residues Tyr201 and Trp288. Ticks and crosses in the NTD indicate presence and absence of π-stacking interactions between the carotenoid and NTD residues Tyr44 and Trp110. In the absence of the former, the carotenoid may partially see the bulk solvent, since Tyr44 is a gating residue for a side channel to the carotenoid tunnel (54). Complete migration of the carotenoid across the NTD tunnel requires the unsettling of interactions with Tyr44 and Trp110 and passage of a bottleneck contributed by NTD residues Leu37, Met83, and Met117. (*A*) Non-productive photoexcitation does not allow recovery of a photoexcitable state; instead a numbed state forms, OCP^{NS}, which remains in a non-excitable structural state for at least 0.5 μs. (*B*) Productive photoexcitation yields P_1, after rupture of H bonds to the carotenoid. Past 50 ns, the carotenoid repositions at the NTD/CTD interface (P_2), before bridging a first bottleneck at 2–3 μs ($P_{2'}$; 0.5–1 and 0.4 μs, according to (27) and (54), respectively). Conformational changes occur in the NTD domain, enabling the carotenoid to pass across the NTD wall and its β2 ionone ring to become exposed to the solvent (P_3; 10 μs and 15 μs, according to (27) and our TR-SAXS/WAXS data, respectively). At all steps before P_3, back-migration of the carotenoid to its dark-state position can occur with rapid recovery of the orange state, as the tunnel remains shielded from the bulk (Figs. 5 and S9). After P_3, recovery follows yet another pathway that does not enable rapid recovery of the orange-state spectrum. (*C*) We presume that in the fraction of P_3 that does not recover and further advances toward the OCP^R state, the NTE will detach from the CTD β-sheet, forming P_M. Dissociation of the two domains thereafter becomes possible, yielding P_X. The CTT may next reposition itself on the CTD, enabling to shield residues contributing to the carotenoid tunnel in OCP^O from the bulk, and thereby forming the minute-lived, photoactive OCP^R. Recovery of OCP^O from OCP^R will have to await unbinding of the CTT from the carotenoid tunnel residues and reassociation of the two domains. It yet remains unclear whether the next step will be back-migration of the carotenoid into the tunnel or reattachment to the CTD of the NTE. In the latter case, P_3 would serve as an intermediate along the OCP^R-to-OCP^O recovery. In the former case, another pathway would exist whereby the carotenoid first back-migrates into the carotenoid tunnel (Int. 1) and only then does the NTE reattach to the CTD (Int. 2). The latter intermediate Int. 2 would exist in the two pathways. It seems likely that another intermediate would exist, which we refer to as Int. 3, given that even after 500 ms, the P_3/OCP^O dimer has not reverted to the starting OCP^O state. This state would share all structural features of the OCP^O state albeit H bonding of the carotenoid to CTD residues Y201 and W288. To see this figure in color, go online.

for OCP^R dimers or higher-order oligomers, respectively) (Fig. 7). It is unclear whether recovery of the OCP^O state from the OCP^R monomer channels back through the P_3 intermediate (i.e., the NTD and CTD domains reassociate and αA and αN reattach to the CTD before back-migration of the carotenoid into the tunnel) or follow another pathway, whereby after reassociation of the NTD and the CTD, back-migration of the carotenoid into the tunnel occurs before reattachment of αA and αN to the CTD (Fig. 8 *C*). Reformation of an OCP^O dimer may ensue depending on concentration (Fig. 7). Given the low quantum yield of photoactivation, the existence of OCP^{NS}, the back-migration of the carotenoid on the timescales of 1 and 50–200 ms in partly activated P_3/OCP^O dimers, and our finding that P_3 starts recovering the structural OCP^O state on the timescale of $\approx$70 and $\approx$280 ms in N-tagged and C-tagged partly activated dimers, respectively, the time window for absorption of an actinic photon by the second monomer in a partly activated dimer is 0.5 μs to 200 ms. Any photon that arrives before 0.5 μs is set to be unproductive, while that which arrives after 200 ms will hit a dimer where both monomers are structurally back in the starting state (Figs. 7 and 8). Hence, productive photoactivation of dimers (meaning the accumulation of photoactive OCP^R) is achievable only in

experiments where one photon is delivered per chromophore every few milliseconds. This is, for example, the case in our continuous illumination experiments where we estimate that 1 photon is delivered per chromophore every 10–30 ms upon illumination of a 23 mg/mL (620 μM) OCP solution with a 500 mW LED emitting at 430 nm. In hindsight, it must be acknowledged that a TR-SAXS experiment conducted on the constitutively monomeric $OCP_{R27L\ Ntag}$ mutant would have been more informative on functionally relevant structural dynamics, as progression toward the OCP^R state would not have been impeded by the presence of OCP^O dimers. Our next experiments will focus on this variant and may enable tracking of the photoproductive OCP^R state.

CONCLUSIONS

The emerging picture from our study suggests that oligomerization partakes in the regulation of the OCP photocycle at the level of both OCP^O and OCP^R. Whether or not these findings have implications regarding the biological function depends on the local concentration of OCP in the vicinity of cyanobacterial thylakoid membranes, yet the observation that the mutation of a single conserved amino acid at the OCP^O dimerization interface results in monomerization of the protein is a strong argument in favor of a functional role for OCP^O dimers. The dissociation constant of OCP^O was estimated to be 14 μM, and that of OCP^R dimers was suggested to be similar. Hence, OCP^R dimers could be functional. The dissociation constant of OCP^R higher-order oligomers is likely to fall in the 100–280 μM range, raising doubts as to their relevance for the physiological context. We also found that the first large-scale conformational changes occurring in photoactivated OCP take place on the microsecond timescale, likely corresponding to the P_2-P_3 transition. We note that ours is, to the best of our knowledge, the first study to offer time-resolved structural insights into the OCP photocycle with a non-resonant structural technique, and as well the first TR structural study to be carried out on a protein with such a low quantum yield. We hope that our work attracts the attention of structural biologists on the possibilities offered by TR-SAXS/WAXS.

DATA AND MATERIALS AVAILABILITY

All data are available in the main text or the supporting material. Raw SAXS data have been deposited in the SASBDB under the following accession codes and can be made available upon request. SASBDB: SASDNY9, SASDNZ9, SASDP22, SASDP32, SASDP42, SASDP52, SASDP62, SASDP72, SASDP82, SASDP92, SASDPA2, SASDPB2, SASDPC2, SASDPD2. See Table S5 for details of the corresponding data sets.

SUPPORTING MATERIAL

Supporting material can be found online at https://doi.org/10.1016/j.bpj.2022.07.004.

AUTHOR CONTRIBUTIONS

J.-P.C. coordinated the project. E.A.A., G.S., and A.T. performed static X-ray scattering. E.A.A. analyzed static X-ray scattering data and performed thermal recovery assays. S.N., M.S., and G.B. performed TR spectroscopy. S.N. analyzed TR spectroscopy data. A.W. and D.K. performed protein expression and purification; E.A.A., N.Z., and R.M. prepared protein samples. E.D.Z. performed fitting analysis of thermal recovery data. J.-P.C., G.S., and M.L. designed the TR-SAXS experiment. E.A.A., S.N., M.L., F.M., G.B., M.S., G.S., and J.-P.C. performed the TR-SAXS experiment. G.S. analyzed TR X-ray scattering data. E.A.A. and J.-P.C. wrote the paper with input from other co-authors.

ACKNOWLEDGMENTS

We are grateful to Ilme Schlichting and Martin Weik for continued support of the project. We thank the SOLEIL and ESRF synchrotron radiation facilities for repeated allocation of beamtime on the SWING and ID09 beamlines, where the static and TR-SAXS experiments were performed, respectively. IBS acknowledges integration into the Interdisciplinary Research Institute of Grenoble (IRIG, CEA). This work was supported by the Agence Nationale de la Recherche (grants ANR-17-CE11-0018-01 and ANR-2018-CE11-0005-02 to J.-P.C.) and the Polish National Science Centre (NCN project 2018/31/N/ST4/03983), and used the platforms of the Grenoble Instruct-ERIC center (ISBG; UMS 3518 CNRS-CEA-UGA-EMBL) within the Grenoble Partnership for Structural Biology (PSB). Platform access was supported by FRISBI (ANR-10-INBS-05-02) and GRAL, a project of the Université Grenoble Alpes graduate school (Ecoles Universitaires de Recherche) CBH-EUR-GS (ANR-17-EURE-0003). The access and travel fees of G.B. and S.N. to ESRF were financed by the Polish Ministry of Science and High Education, decision number: DIR/WK/2016/19. R.M. is supported by a GRAL PhD fellowship (7C047GRAL).

DECLARATION OF INTERESTS

The authors declare no competing interests.

REFERENCES

1. Agusti, S., S. Enriquez, …, C. M. Duarte. 1994. Light harvesting among photosynthetic organisms. *Funct. Ecol.* 8:273.
2. Adir, N. 2005. Elucidation of the molecular structures of components of the phycobilisome: reconstructing a giant. *Photosynth. Res.* 85:15–32.
3. Grossman, A. R., M. R. Schaefer, …, J. L. Collier. 1993. The phycobilisome, a light-harvesting complex responsive to environmental conditions. *Microbiol. Rev.* 57:725–749.
4. Wilson, A., G. Ajlani, …, D. Kirilovsky. 2006. A soluble carotenoid protein involved in phycobilisome-related energy dissipation in cyanobacteria. *Plant Cell.* 18:992–1007.
5. Wilson, A., C. Punginelli, …, D. Kirilovsky. 2008. A photoactive carotenoid protein acting as light intensity sensor. *Proc. Natl. Acad. Sci. USA.* 105:12075–12080.
6. Demmig-Adams, B., G. Garab, …, Govindjee. 2014. Non-Photochemical Quenching and Energy Dissipation in Plants, Algae and Cyanobacteria. Springer.
7. Scott, M., C. McCollum, …, D. Bruce. 2006. Mechanism of the down regulation of photosynthesis by blue light in the Cyanobacterium synechocystis sp. PCC 6803. *Biochemistry.* 45:8952–8958.
8. Gwizdala, M., A. Wilson, and D. Kirilovsky. 2011. In vitro reconstitution of the cyanobacterial photoprotective mechanism mediated by the

Orange Carotenoid Protein in Synechocystis PCC 6803. *Plant Cell.* 23:2631–2643.

9. Muzzopappa, F., and D. Kirilovsky. 2020. Changing color for photoprotection: the orange carotenoid protein. *Trends Plant Sci.* 25:92–104.
10. Muzzopappa, F., A. Wilson, and D. Kirilovsky. 2019. Interdomain interactions reveal the molecular evolution of the orange carotenoid protein. *Nat. Plants.* 5:1076–1086.
11. Kirilovsky, D., and C. A. Kerfeld. 2013. The Orange Carotenoid Protein: a blue-green light photoactive protein. *Photochem. Photobiol. Sci.* 12:1135–1143.
12. Tian, L., I. H. M. van Stokkum, …, H. van Amerongen. 2011. Site, rate, and mechanism of photoprotective quenching in cyanobacteria. *J. Am. Chem. Soc.* 133:18304–18311.
13. Maksimov, E. G., N. N. Sluchanko, …, A. B. Rubin. 2017. The photocycle of orange carotenoid protein conceals distinct intermediates and asynchronous changes in the carotenoid and protein components. *Sci. Rep.* 7:15548.
14. Niziński, S., A. Wilson, …, M. Sliwa. 2022. Unifying perspective of the ultrafast photodynamics of orange carotenoid proteins from *Synechocystis*: Peril of high-power excitation, existence of different S* States, and influence of tagging. *JACS Au.* 2:1084–1095.
15. Kerfeld, C. A., M. R. Sawaya, …, T. O. Yeates. 2003. The crystal structure of a cyanobacterial water-soluble carotenoid binding protein. *Structure.* 11:55–65.
16. Sedoud, A., R. López-Igual, …, D. Kirilovsky. 2014. The cyanobacterial photoactive orange carotenoid protein is an excellent singlet oxygen quencher. *Plant Cell.* 26:1781–1791.
17. Bao, H., M. R. Melnicki, …, C. A. Kerfeld. 2017. Additional families of orange carotenoid proteins in the photoprotective system of cyanobacteria. *Nat. Plants.* 3:17089.
18. Wilson, A., J. N. Kinney, …, C. A. Kerfeld. 2010. Structural determinants underlying photoprotection in the photoactive orange carotenoid protein of cyanobacteria. *J. Biol. Chem.* 285:18364–18375.
19. Leverenz, R. L., M. Sutter, …, C. A. Kerfeld. 2015. PHOTOSYNTHESIS. A 12 Å carotenoid translocation in a photoswitch associated with cyanobacterial photoprotection. *Science.* 348:1463–1466.
20. Leverenz, R. L., D. Jallet, …, C. A. Kerfeld. 2014. Structural and functional modularity of the orange carotenoid protein: distinct roles for the N- and C-terminal domains in cyanobacterial photoprotection. *Plant Cell.* 26:426–437.
21. Harris, D., A. Wilson, …, N. Adir. 2018. Structural rearrangements in the C-terminal domain homolog of Orange Carotenoid Protein are crucial for carotenoid transfer. *Commun. Biol.* 1:125.
22. Lu, Y., H. Liu, …, R. E. Blankenship. 2017. Native mass spectrometry analysis of oligomerization states of fluorescence recovery protein and orange carotenoid protein: two proteins involved in the cyanobacterial photoprotection cycle. *Biochemistry.* 56:160–166.
23. Golub, M., M. Moldenhauer, …, J. Pieper. 2019. Solution structure and conformational flexibility in the active state of the orange carotenoid protein: Part I. Small-angle scattering. *J. Phys. Chem. B.* 123:9525–9535.
24. Golub, M., M. Moldenhauer, …, J. Pieper. 2019. Solution structure and conformational flexibility in the active state of the orange carotenoid protein. Part II: quasielastic neutron scattering. *J. Phys. Chem. B.* 123:9536–9545.
25. Zhang, H., H. Liu, …, R. E. Blankenship. 2016. Native mass spectrometry and ion mobility characterize the orange carotenoid protein functional domains. *Biochim. Biophys. Acta.* 1857:734–739.
26. Liu, H., H. Zhang, …, R. E. Blankenship. 2016. Dramatic domain rearrangements of the cyanobacterial orange carotenoid protein upon photoactivation. *Biochemistry.* 55:1003–1009.
27. Konold, P. E., I. H. M. van Stokkum, …, J. T. M. Kennis. 2019. Photoactivation mechanism, timing of protein secondary structure dynamics and carotenoid translocation in the orange carotenoid protein. *J. Am. Chem. Soc.* 141:520–530.
28. Mezzetti, A., M. Alexandre, …, D. Kirilovsky. 2019. Two-step structural changes in orange carotenoid protein photoactivation revealed by time-resolved fourier transform infrared spectroscopy. *J. Phys. Chem. B.* 123:3259–3266.
29. Maksimov, E. G., E. A. Protasova, …, T. Friedrich. 2020. Probing of carotenoid-tryptophan hydrogen bonding dynamics in the single-tryptophan photoactive Orange Carotenoid Protein. *Sci. Rep.* 10:11729.
30. Gupta, S., M. Guttman, …, C. A. Kerfeld. 2015. Local and global structural drivers for the photoactivation of the orange carotenoid protein. *Proc. Natl. Acad. Sci. USA.* 112:E5567–E5574.
31. Gupta, S., M. Sutter, …, C. Y. Ralston. 2019. X-ray radiolytic labeling reveals the molecular basis of orange carotenoid protein photoprotection and its interactions with fluorescence recovery protein. *J. Biol. Chem.* 294:8848–8860.
32. Bandara, S., Z. Ren, …, X. Yang. 2017. Photoactivation mechanism of a carotenoid-based photoreceptor. *Proc. Natl. Acad. Sci. USA.* 114:6286–6291.
33. Bourcier de Carbon, C., A. Thurotte, …, D. Kirilovsky. 2015. Biosynthesis of soluble carotenoid holoproteins in Escherichia coli. *Sci. Rep.* 5:9085.
34. Sluchanko, N. N., K. E. Klementiev, …, E. G. Maksimov. 2017. The purple Trp288Ala mutant of Synechocystis OCP persistently quenches phycobilisome fluorescence and tightly interacts with FRP. *Biochim. Biophys. Acta Bioenerg.* 1858:1–11.
35. Gasteiger, E., C. Hoogland, …, A. Bairoch. 2005. Protein identification and analysis tools on the ExPASy server. *In* The Proteomics Protocols Handbook. Springer, pp. 571–607.
36. Walker, J. M. 2005. The Proteomics Protocols Handbook. Springer Science & Business Media.
37. Franke, D., and D. I. Svergun. 2009. DAMMIF, a program for rapid *ab-initio* shape determination in small-angle scattering. *J. Appl. Crystallogr.* 42:342–346.
38. Konarev, P. V., V. V. Volkov, …, D. I. Svergun. 2003. PRIMUS: a Windows PC-based system for small-angle scattering data analysis. *J. Appl. Crystallogr.* 36:1277–1282.
39. Hopkins, J. B., R. E. Gillilan, and S. Skou. 2017. BioXTAS RAW: improvements to a free open-source program for small-angle X-ray scattering data reduction and analysis. *J. Appl. Crystallogr.* 50:1545–1553.
40. Melnicki, M. R., R. L. Leverenz, …, C. A. Kerfeld. 2016. Structure, diversity, and evolution of a new family of soluble carotenoid-binding proteins in cyanobacteria. *Mol. Plant.* 9:1379–1394.
41. Dominguez-Martin, M. A., T. Polívka, …, C. A. Kerfeld. 2019. Structural and spectroscopic characterization of HCP2. *Biochim. Biophys. Acta Bioenerg.* 1860:414–424.
42. Panjkovich, A., and D. I. Svergun. 2016. Deciphering conformational transitions of proteins by small angle X-ray scattering and normal mode analysis. *Phys. Chem. Chem. Phys.* 18:5707–5719.
43. Kikhney, A. G., C. R. Borges, …, D. I. Svergun. 2020. SASBDB: towards an automatically curated and validated repository for biological scattering data. *Protein Sci.* 29:66–75.
44. Newville, M., T. Stensitzki, B. Daniel, A. Ingargiola…, 2014. LMFIT: Non-Linear Least-Square Minimization and Curve-Fitting for Python (0.8.0). Zenodo. https://zenodo.org/record/11813#.YtUlES0iuck.
45. Burdzinski, G., M. Bayda, …, B. Marciniak. 2011. Time-resolved studies on the photoisomerization of a phenylene-silylene-vinylene type compound in its first singlet excited state. *J. Lumin.* 131:577–580.
46. Müller, P., and K. Brettel. 2012. (2+) as a reference in transient absorption spectroscopy: differential absorption coefficients for formation of the long-lived (3)MLCT excited state. *Photochem. Photobiol. Sci.* 11:632–636.
47. Cammarata, M., M. Levantino, …, H. Ihee. 2008. Tracking the structural dynamics of proteins in solution using time-resolved wide-angle X-ray scattering. *Nat. Methods.* 5:881–886.
48. Cammarata, M., M. Levantino, …, A. Cupane. 2010. Unveiling the timescale of the R-T transition in human hemoglobin. *J. Mol. Biol.* 400:951–962.

49. Henry, E. R., and J. Hofrichter. 1992. Singular value decomposition: application to analysis of experimental data. *Methods Enzymol.* 210:129–192.

50. Svergun, D. I. 1999. Restoring low resolution structure of biological macromolecules from solution scattering using simulated annealing. *Biophys. J.* 76:2879–2886.

51. Wilson, A., M. Gwizdala, …, D. Kirilovsky. 2012. The essential role of the N-terminal domain of the orange carotenoid protein in cyanobacterial photoprotection: importance of a positive charge for phycobilisome binding. *Plant Cell.* 24:1972–1983.

52. Moldenhauer, M., N. N. Sluchanko, …, T. Friedrich. 2017. Assembly of photoactive orange carotenoid protein from its domains unravels a carotenoid shuttle mechanism. *Photosynth. Res.* 133:327–341.

53. Muzzopappa, F., A. Wilson, …, D. Kirilovsky. 2017. Paralogs of the C-terminal domain of the cyanobacterial orange carotenoid protein are carotenoid donors to helical carotenoid proteins. *Plant Physiol.* 175:1283–1303.

54. Wilson, A., E. A. Andreeva, …, J.-P. Colletier. 2022. Structure-function-dynamics relationships in the peculiar Planktothrix PCC7805 OCP1: impact of his-tagging and carotenoid type. Preprint at bioRxiv. https://doi.org/10.1101/2022.01.04.474796.

55. Yaroshevich, I. A., E. G. Maksimov, …, M. P. Kirpichnikov. 2021. Role of hydrogen bond alternation and charge transfer states in photoactivation of the Orange Carotenoid Protein. *Commun. Biol.* 4:539.

56. Zhang, H., H. Liu, …, R. E. Blankenship. 2014. Molecular mechanism of photoactivation and structural location of the cyanobacterial orange carotenoid protein. *Biochemistry.* 53:13–19.

57. Wiśniewski, J. R., M. Y. Hein, …, M. Mann. 2014. A "proteomic ruler" for protein copy number and concentration estimation without spike-in standards. *Mol. Cell. Proteomics.* 13:3497–3506.

58. Dominguez-Martin, M. A., P. V. Sauer, …, C. A. Kerfeld. 2021. Structure of the quenched cyanobacterial OCP-phycobilisome complex. Preprint at bioRxiv. https://doi.org/10.1101/2021.11.15.468719.

59. Balevičius, V., Jr., D. Abramavicius, …, J. Hauer. 2016. A unified picture of S* in carotenoids. *J. Phys. Chem. Lett.* 7:3347–3352.

Biophysical Journal, Volume *121*

Supplemental information

Oligomerization processes limit photoactivation and recovery of the orange carotenoid protein

Elena A. Andreeva, Stanisław Niziński, Adjélé Wilson, Matteo Levantino, Elke De Zitter, Rory Munro, Fernando Muzzopappa, Aurélien Thureau, Ninon Zala, Gotard Burdzinski, Michel Sliwa, Diana Kirilovsky, Giorgio Schirò, and Jacques-Philippe Colletier

Supplementary Information for:

Oligomerization processes limit photoactivation and recovery of the Orange Carotenoid Protein.

by

Elena A. Andreeva, Stanislaw Nizinski, Adjélé Wilson, Matteo Levantino, Elke De Zitter, Rory Munro, Fernando Muzzopappa, Aurélien Thureau, Ninon Zala, Gotard Burdzinski, Michel Sliwa, Diana Kirilovsky, Giorgio Schirò, Jacques-Philippe Colletier

This PDF file contains:

- Supplementary Figures S1-S12
- Supplementary Tables S1-S8

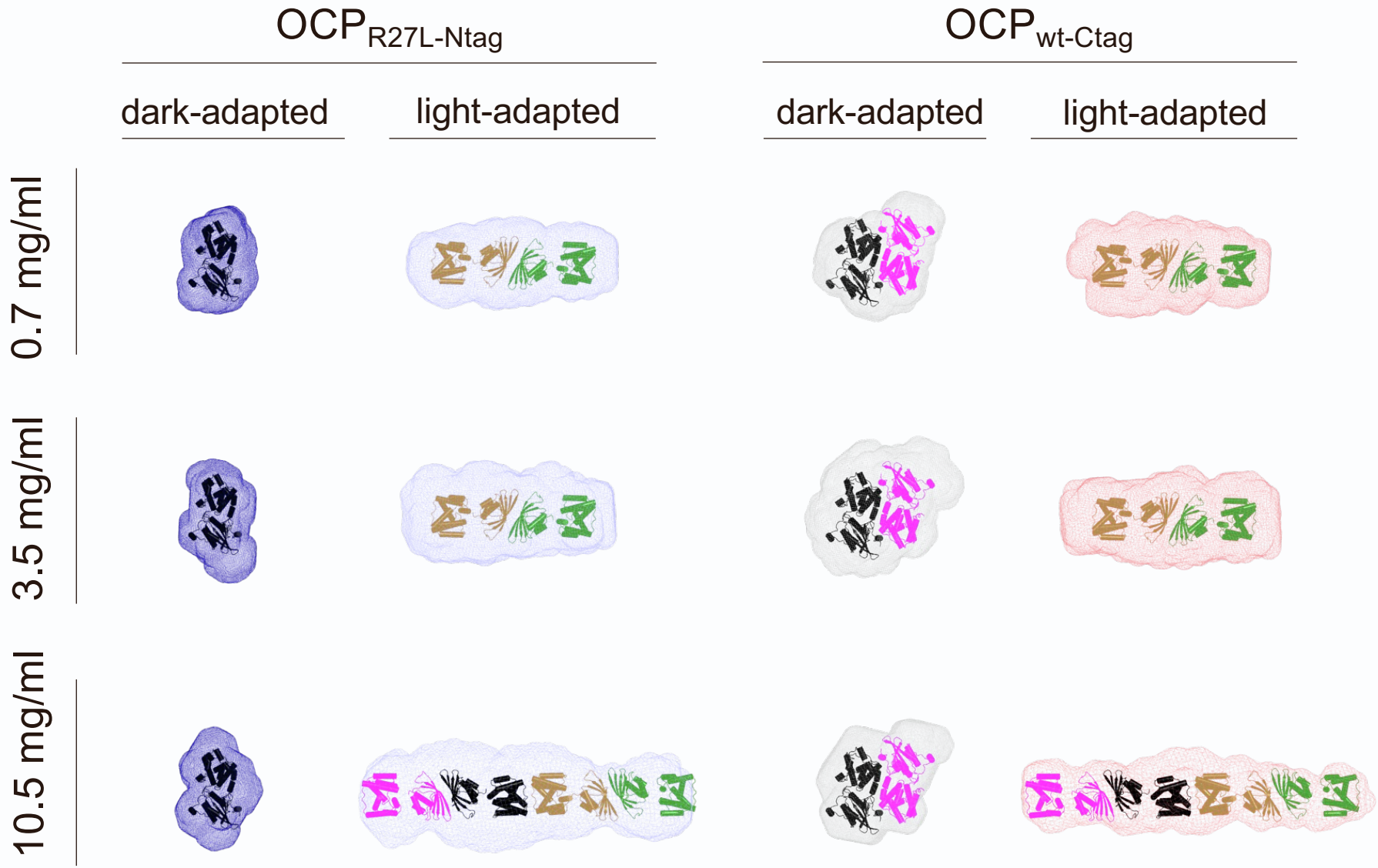

Figure S1. Molecular envelopes and proposed OCP^R models for dark-adapted and light-adapted $OCP_{wt\text{-}Ctag}$ and $OCP_{R27L\text{-}Ntag}$ at different concentrations. The molecular envelopes, determined *ab initio* based on experimental static SAXS data are shown for $OCP_{R27L\text{-}Ntag}$ and $OCP_{wt\text{-}Ctag}$ in their dark-adapted and light-adapted states at three concentrations. The proposed models are overlayed on the molecular envelopes. For the dark-adapted $OCP^O_{R27L\text{-}Ntag}$, the molecular envelopes are consistent with the presence of an OCP^O monomer, whereas for the dark-adapted $OCP^O_{wt\text{-}Ctag}$, the molecular envelopes are better fitted by the crystallographic OCP^O dimer (PDB id: 3MG1). At each concentration, the molecular envelopes determined for light-adapted $OCP^R_{R27L\text{-}Ntag}$ and $OCP^R_{wt\text{-}Ctag}$ are similar, and consistent with the presence of an OCP^R dimer, at 0.7 and 3.5 mg/ml, and a higher-order OCP^R oligomers at 10.5 mg/ml, e.g., a compact tetramer or a more extended trimer, wherein one monomer associated by the NTD interface would be more opened than those associated via the CTD.

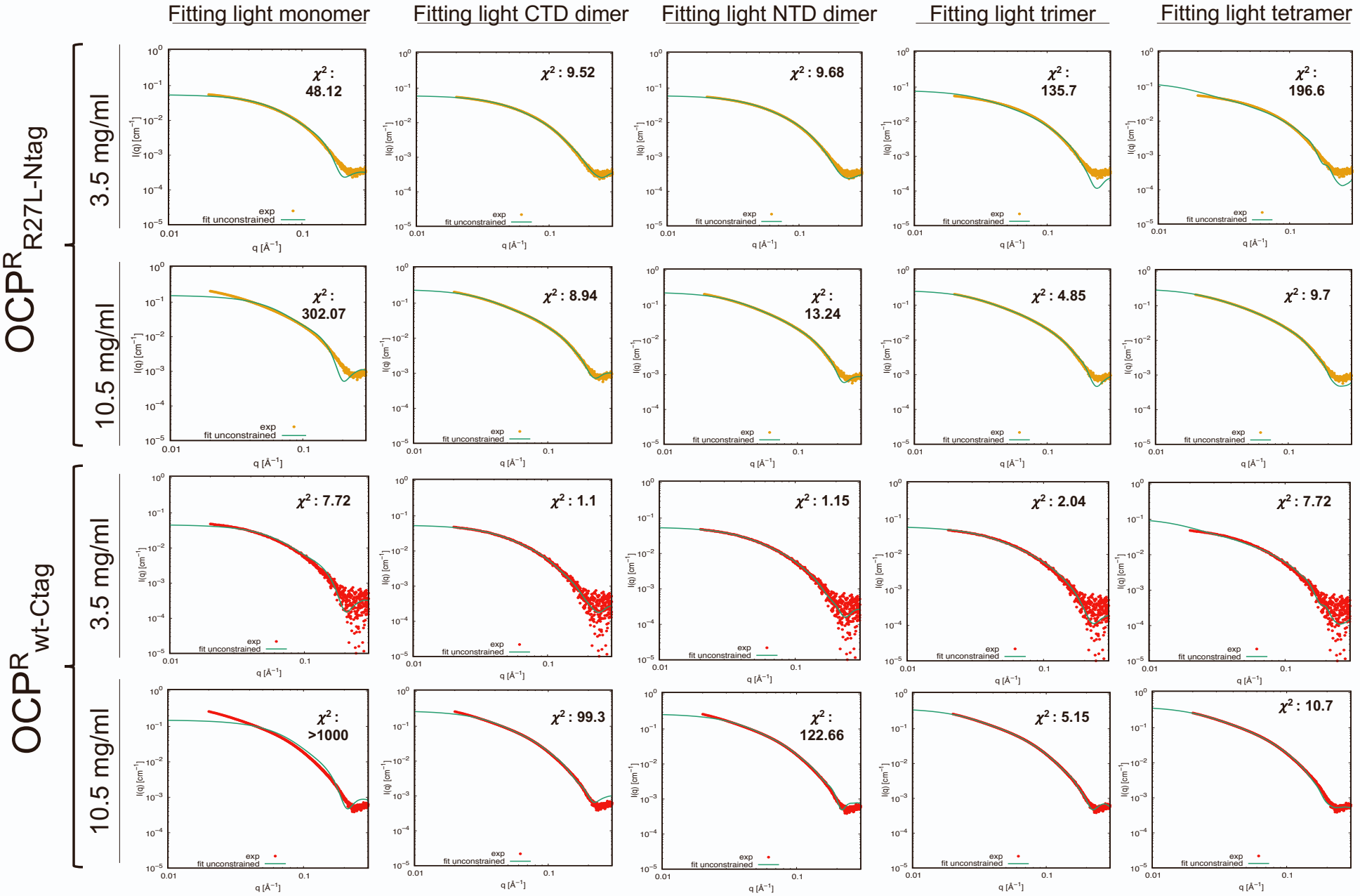

Figure S2. SREFLEX modeling of light-adapted OCP. The red circles show the X-ray scattering profiles of $OCP^{R}_{wt\text{-}Ctag}$ and $OCP^{R}_{R27L\text{-}Ntag}$ at 3.5 and 10.5 mg/ml. Continuous curves (coloured in green) represent calculated profiles using SREFLEX normal mode analysis with different OCP light-adapted oligomeric forms. The resulting chi-squared of SREFLEX analyses are indicated.

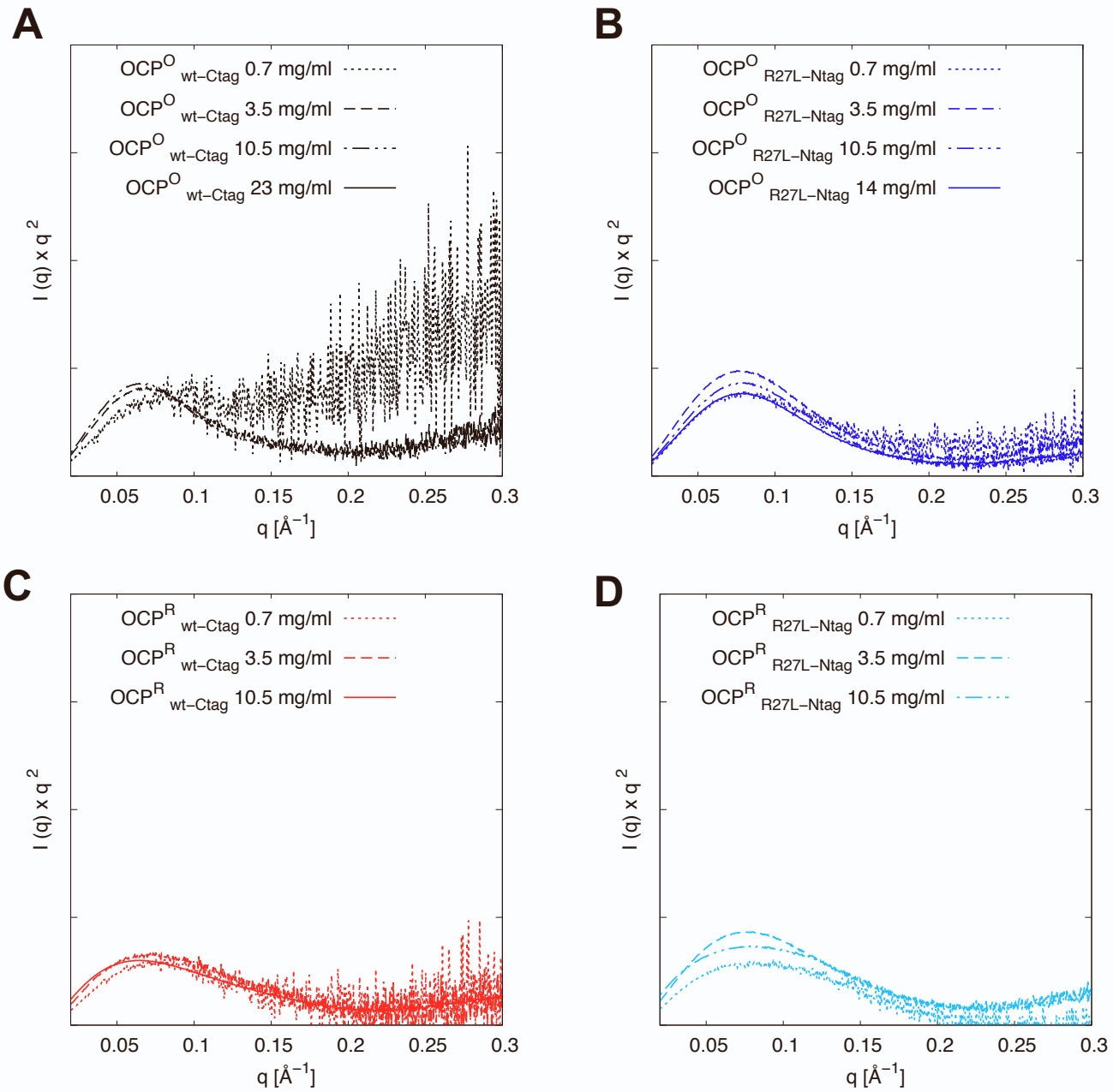

FIGURE S3. Dimensionless Kratky plots for dark-adapted and light-adapted OCP variants. (*A, B)* Normalized Kratky profiles of dark-adapted $OCP^{O}_{wt\text{-}Ctag}$ (*A*) and $OCP^{O}_{R27L\text{-}Ntag}$ (*B*) at various concentrations. (*C, D*) Normalized Kratky profiles of light-adapted $OCP^{R}_{wt\text{-}Ctag}$ (*C*) and $OCP^{R}_{R27L\text{-}Ntag}$ (*D*) at various concentrations. Note that the Kratky plot for $OCP^{O}_{wt\text{-}Ctag}$ at 0.7 mg/ml does not show the expected profile for a folded protein likely due to the poor signal to noise ratio.

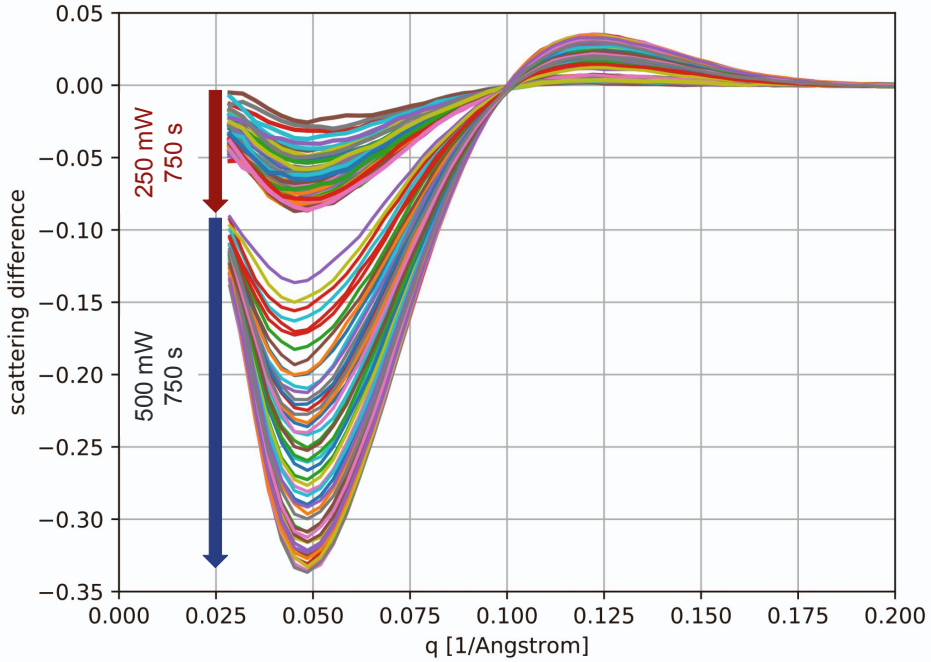

Figure S4. Photoactivation of OCP at 30 mg/ml requires tens of minutes of illumination by a 430 nm LED operating at 500 mW. The figure shows X-ray scattering difference signals collected on $OCP_{wt\text{-}Ctag}$ at 30 mg/ml during continuous illumination by a 430 nm collimated light-source in a 2 mm thick capillary. The LED nominal power was first set at 250 mW, switched to 500 mW after ~750 s and kept on during 750 s after which saturation of the signal change was reached. Data was collected at the ID09 beamline (ESRF, Grenoble). Accumulation of the red state required using a nominal LED power of 500 mW and an illumination time of at least 700 sec. In these conditions, it is estimated that 1 to 3 photons are delivered every 30 ms per chromophore.

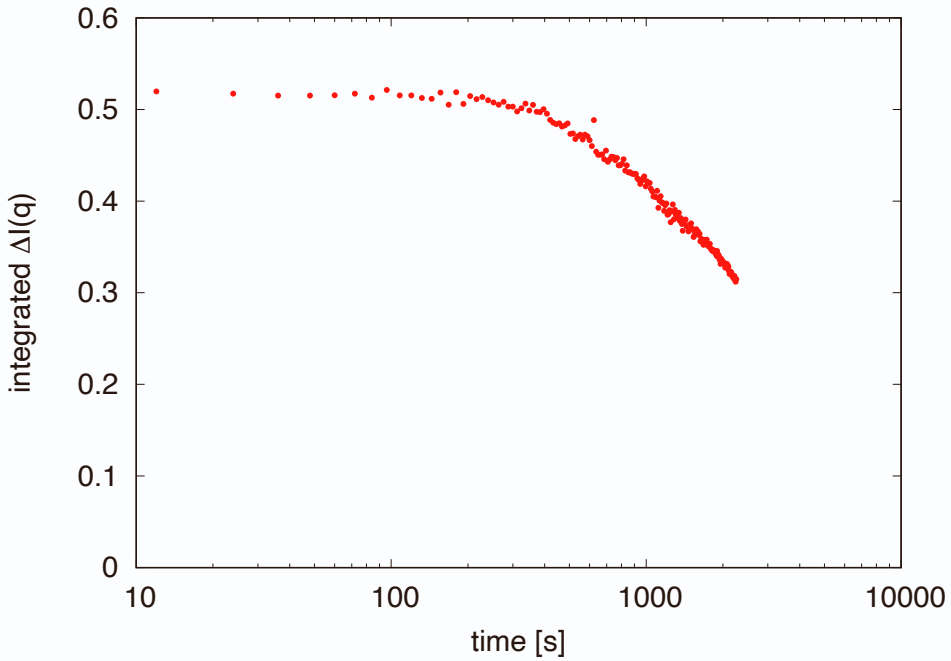

Figure S5. Structural recovery of $OCP^{O}_{wt\text{-}Ctag}$, following accumulation of $OCP^{R}_{wt\text{-}Ctag}$. The plot shows the time evolution of the integrated intensity in the 0.05-0.5 $Å^{-1}$ region of the X-ray difference profile $\Delta I(q) = I(q)_t - I(q)_{t0}$, with $I(q)_t$ and $I(q)_{t0}$ the scattering intensities at a generic time t after switching off the 430 nm light and before the 430 nm irradiation procedure, respectively. The data establish that after accumulation of the OCP^{R} state at 23 mg/ml, recovery of the starting structural state of the $OCP_{wt\text{-}Ctag}$ sample spans a time-scale of at least 2.5 hours.

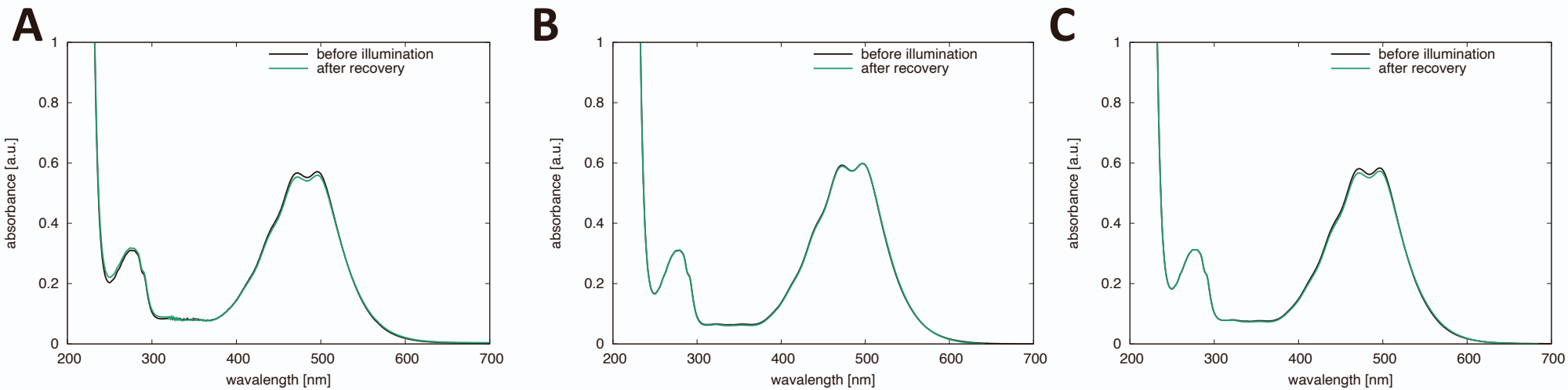

Figure S6. The illumination procedure used to investigate OCP photoactivation and recovery does not significantly damage the protein sample. Absorption spectra recorded before (black) and after (green) 30 minutes illumination plus 16 hours of thermal recovery for (*A)* $OCP_{wt\text{-}Ntag}$ at 3 mg/ml, (*B*) $OCP_{R27L\text{-}Ntag}$ at 1.7 mg/ml and (*D*) $OCP_{wt\text{-}Ctag}$ at 1.7 mg/ml. The OCP concentration and optical pathlength were 3 mg/ml and 0.1 cm, respectively.

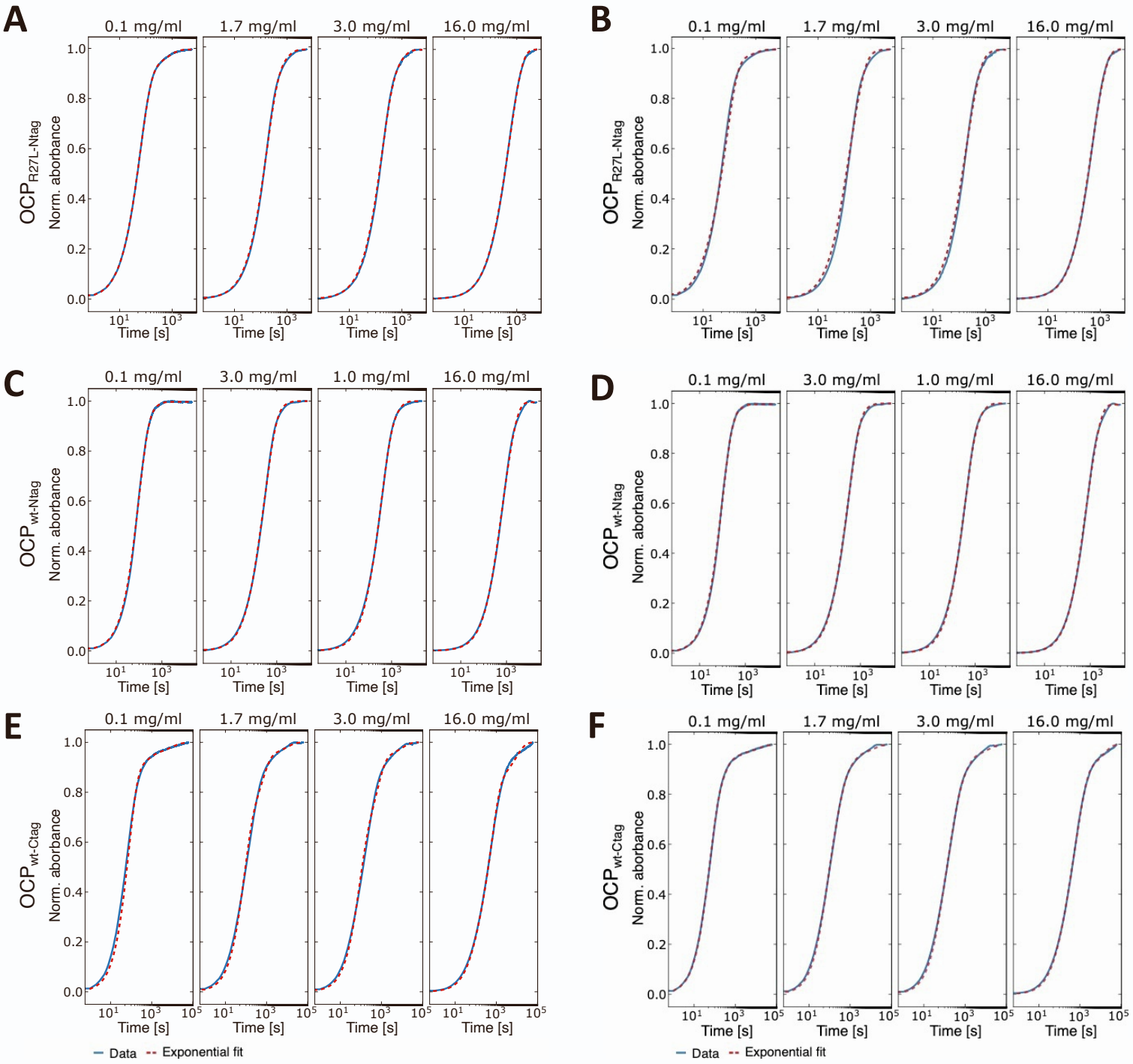

Figure S7. Global fitting of the recovery data recorder for the different OCP variants. (*A*, *B*) Thermal recovery was monitored at four concentrations of $OCP_{R27L-Ntag}$ (*A*, *B*), $OCP_{wt-Ntag}$ (*C*, *D*) and $OCP_{wt-Ctag}$ (*E*, *F*), and data were globally fitted for each variant using a model accounting either for three (*A, C, E*) or four (*B, D, F*) exponential components. Fitting parameters are reported in Table S6 and S7.

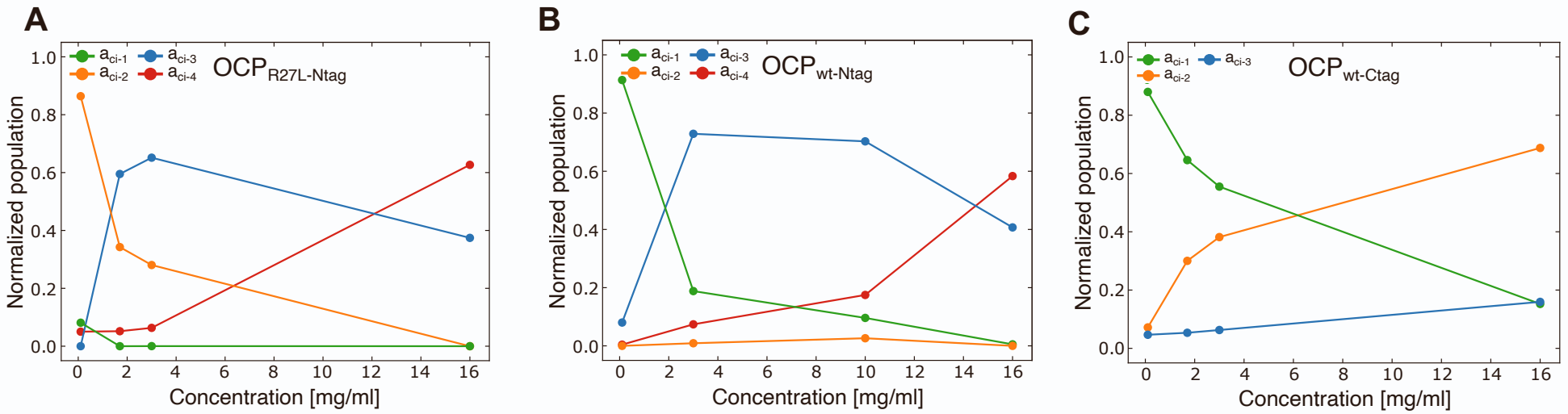

Figure S8. Kinetic analysis of OCP thermal recovery data at various concentrations suggests that oligomerized OCP^R reverts more slowly to the dark-adapted state. Plots of the pre-exponential factors retrieved from fits of thermal recovery kinetics (see also Fig. S7, Table S6 and Table S7) when four exponential components are used to account for the change in absorbance at 467 nm of $OCP_{R27L-Ntag}$ (*A*) and $OCP_{wt-Ntag}$ (*B*) data, and three exponential components for that of $OCP_{wt-Ctag}$ (*C*). The apparent lifetime of OCP^R state is increased in dimers and higher-order oligomers, suggesting that oligomerization stabilizes the light-adapted state.

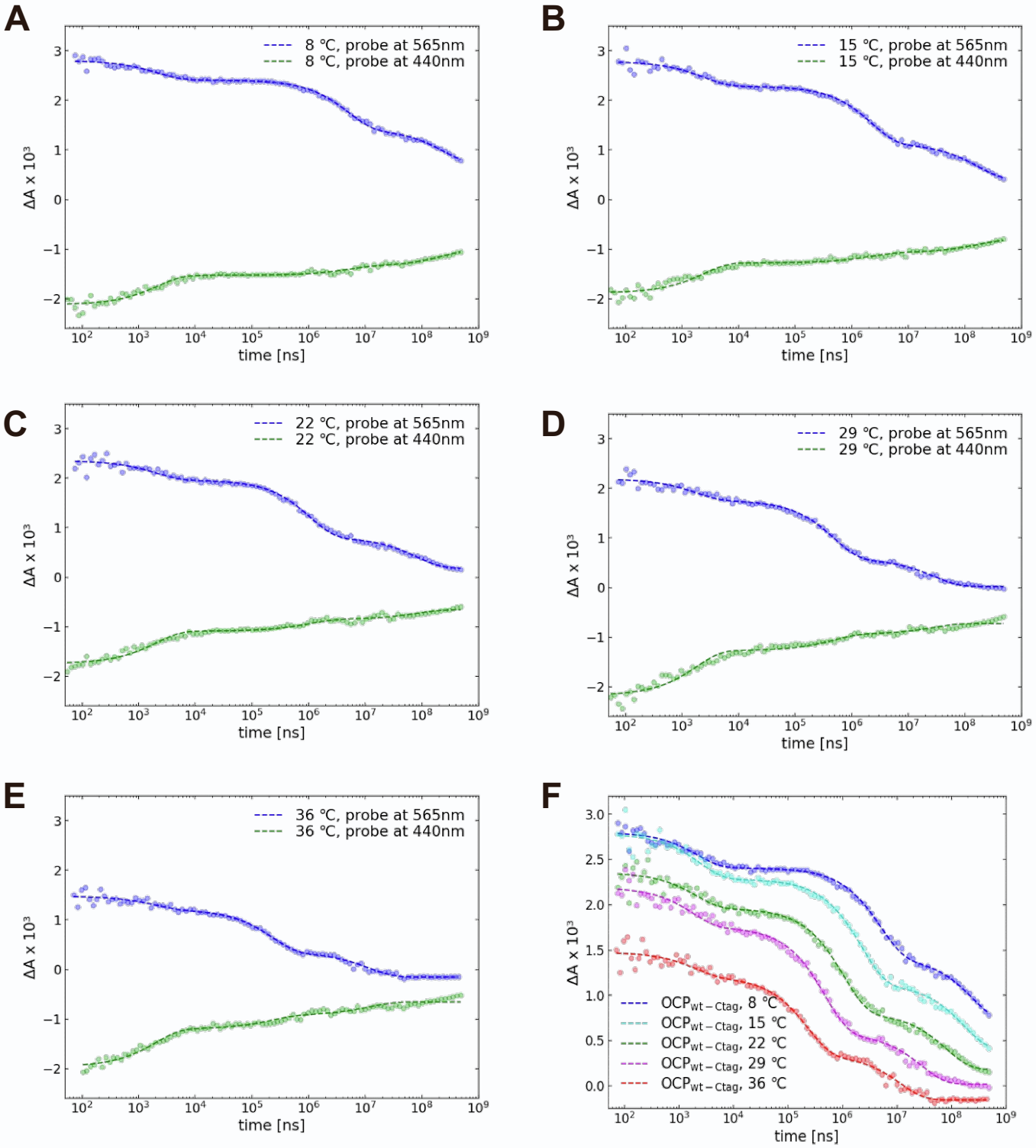

Figure S9. Nanosecond transient absorption kinetics recorded on $OCP_{wt\text{-}Ctag}$ at different temperatures. (*A-E*) Difference absorption was monitored at both 440 and 565 nm, enabling to probe photoactivation and recovery at the blue and red edges of OCP^O and OCP^R absorption spectra, respectively. (*F*) Nanosecond transient absorption data recorded at 565 nm for $OCP_{wt\text{-}Ctag}$ at various temperatures, from 8 to 36 °C. See Table S4 for complementary data.

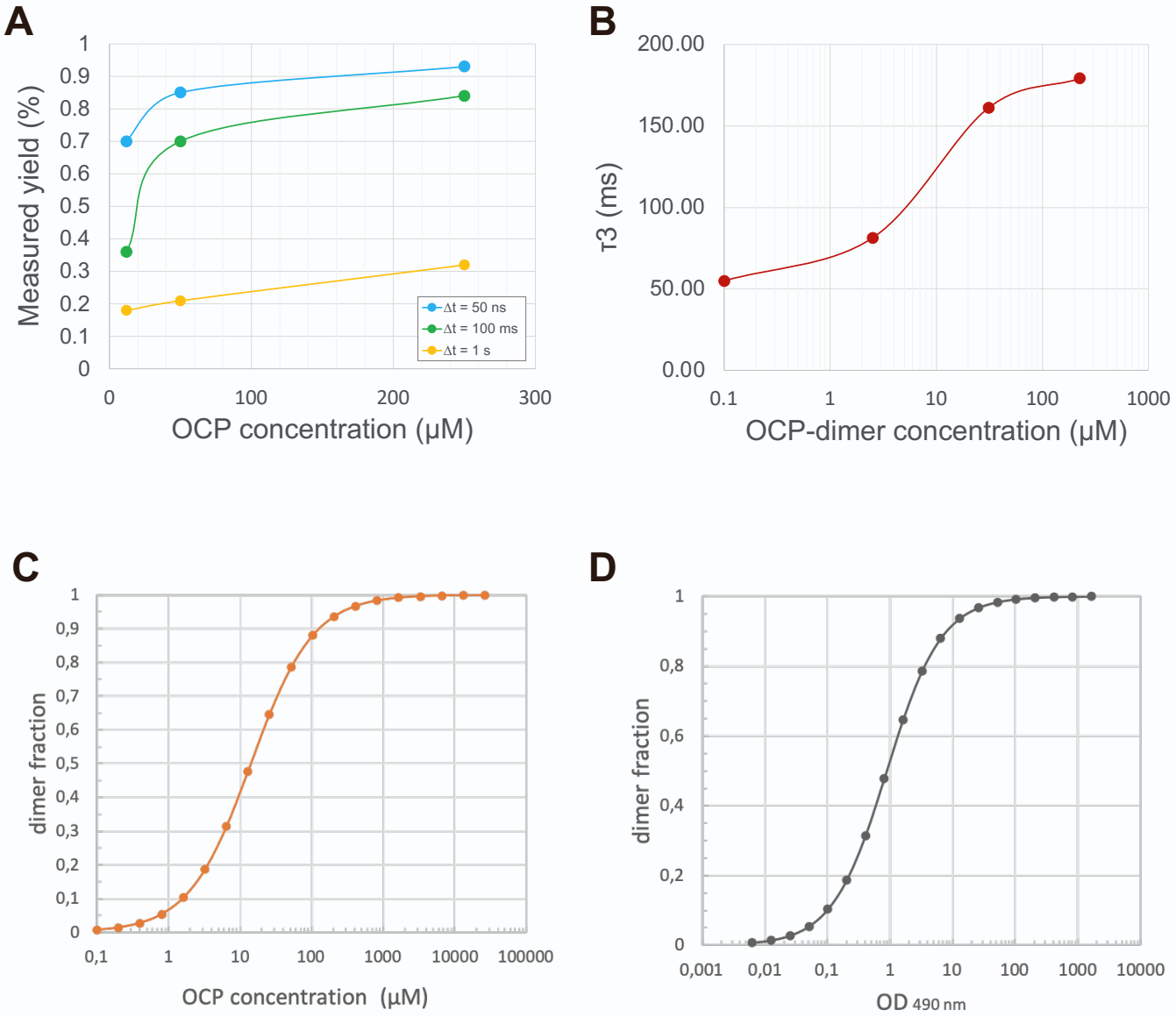

Figure S10. OCP dimerization increases the yields at shorter time delays and delays the occurrence of the last recovery step in the ns-s spectral evolution. (*A*) Estimated yields of $OCP_{wt\text{-}Ctag}$ red-states at various time delays and concentrations. The plot indicates that dimerization benefits the P_1 and P_3 yields. The OCP^R yield, however, only improves slightly. (*B*) The lifetime for the third component used to fit the ns-s spectral evolution of $OCP_{wt\text{-}Ctag}$ increases as a function of OCP-dimer concentration. The average lifetime extracted from fits of the $OCP_{R27L\text{-}Ntag}$ data at various concentrations was used for zero dimer concentration. (*C, D*) Predicted fraction of OCP^O dimers as a function of concentration (*C*) or optical density (OD) at 490 nm (*D*) based on a dissociation constant (K_d) of 14 µM for OCP^O dimers.

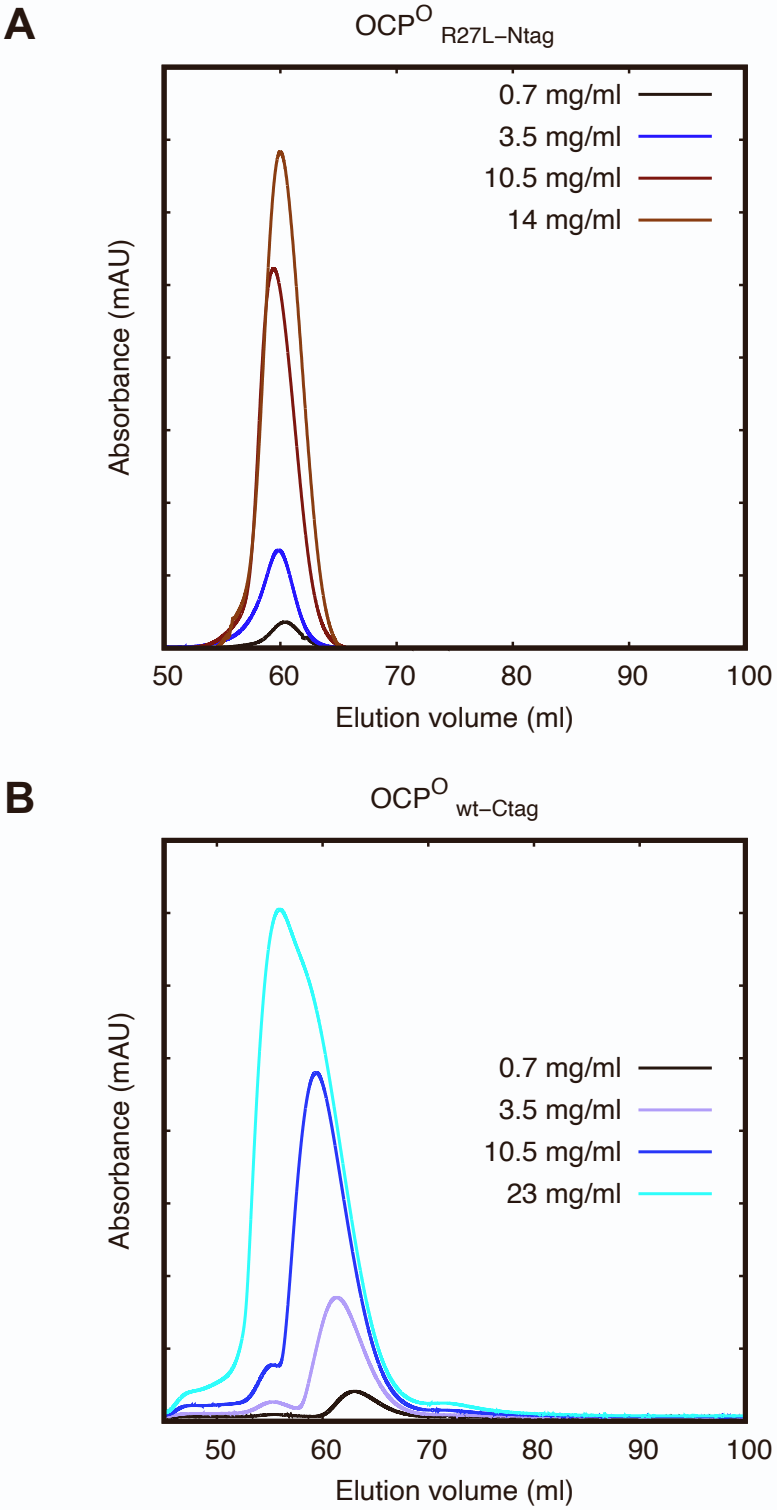

Figure S11. Size exclusion chromatography assesses the purity and dispersity of our OCP samples. (*A*) At all tested concentration, the $OCP^{O}_{R27L\text{-}Ntag}$ sample is monodisperse and features a monomer. (*B*) Contrastingly, the $OCP^{O}_{wt\text{-}Ctag}$ sample features monomers and dimers.

```
import numpy as np
import pylab as plt
from scipy import optimize
import scipy.optimize
from sys import exit

np.set_printoptions(threshold=np.inf)
datafile = ' '
f = open(datafile,"r")
data = f.readlines()
f.close()
time = data[0].split()[1:]
# ---------- read data and calculate SVD
matrix_plot = np.loadtxt(datafile)
q = matrix_plot.T[0]
matrix = np.delete(matrix_plot,[0],1)
rank_full = len(matrix[0])
U,s,V = np.linalg.svd(matrix,0)
S = np.diag(s)
br =  # basis rank to be plotted
# ---------- plot basis patterns
fig1 = plt.figure()
fig1.suptitle("basis patterns amplitude vectors")
for (ind,u) in zip(range(br),np.dot(U,S).T):
 plt.subplot(br,2,2*ind+1)
 plt.plot(q,u)
 plt.grid()
plt.xlabel("q / A^-1")
plt.show(block=False)
open(' ', "w").close()
q_array = np.array([q])
q_basis = np.concatenate((q_array.T,np.dot(U,S)),axis=1)
np.savetxt(' ',q_basis,delimiter="\t",newline="\n")
# ---------- plot amplitude vectors
for (ind,v) in zip(range(br),V):
 plt.subplot(br,2,2*ind+2)
 plt.plot(time,v,"o-")
 plt.xscale('log')
 plt.grid()
plt.xlabel("time / sec")
plt.show(block=False)
# ---------- plot singular values
fig2 = plt.figure()
fig2.suptitle("singular values")
plt.plot(np.arange(1,rank_full+1),s,"o-")
plt.axis([0,20,0,0.1])
plt.grid()
plt.show(block=False)
plt.xlabel("matrix index")
plt.show(block=False)
A1 = np.dot(U,S)
A2 = np.dot(A1,V)
# ---------- calculate and plot U and V autocorrelations
fig3 = plt.figure()
fig3.suptitle("U and V autocorrelations")
u_corr = [np.sum(U.T[i][0:len(U)-1]*U.T[i][1:len(U)]) for i in range(len(U.T))]
plt.subplot(211)
plt.plot(np.arange(1,rank_full+1),u_corr,"o-")
plt.grid()
v_corr = [np.sum(V[i][0:len(V)-1]*V[i][1:len(V)]) for i in range(len(V))]
plt.subplot(212)
plt.plot(np.arange(1,rank_full+1),v_corr,"o-")
plt.xlabel("matrix index")
plt.grid()
plt.show(block=False)
# ---------- reconstruct data with n. #rank basis patterns
data1 = np.loadtxt(datafile)
rank =   #rank
U3 = U[:,0:rank]
S3 = S[0:rank,0:rank]
V3 = V[0:rank,:]
A3a = np.dot(U3,S3)
A3b = np.dot(A3a,V3)
fig4 = plt.figure()
fig4.suptitle("reduced rank representation")
for j in np.arange(rank_full):
 plt.plot(data1.transpose()[0],data1.transpose()[j+1]*data1.transpose()[0] - 0.0001*j,"bo", ms = 5)
 plt.plot(data1.transpose()[0],A3b.transpose()[j]*data1.transpose()[0] - 0.0001*j,"r-", linewidth = 3)
plt.axis([0.02,0.3,-0.0005*rank_full-0.0002,0.0002])
plt.yticks(np.arange(-0.0005*rank_full,0.0002,0.0005),([''] + time[::-1] + ['seconds']))
plt.grid()
plt.xlabel("q / $\AA^{-1}$")
plt.ylabel("$\Delta$S x q / $\AA^{-1}$")
plt.show(block=False)
open(' ', "w").close()
svd_reconstr = np.concatenate((q_array.T,A3b),axis=1)
np.savetxt(' ',svd_reconstr,delimiter="\t",newline="\n")
```

Figure S12. SVD analysis. Python-based script for singular value decomposition (SVD) analysis of time-resolved (TR) difference profiles measured at ID09 (ESRF, Grenoble) in the µs-ms time-scale (See Fig. 6D).

Table S1: Data collection and processing parameters for static SAXS measurements recorded at the BioSAXS SWING beamline (Synchrotron SOLEIL, France)

A) SAXS data collection parameters	
Instrument	SOLEIL Synchrotron SWING beamline with EIGER-4M detector
Wavelength (Å)	1.03319
Beam geometry	200 x 20 to 500 x 200 μm^2
q measurement range ($Å^{-1}$)	0.02 - 0.5
Absolute scaling method	Comparison with scattering from 1 mm pure H2O
Exposure time	990 ms
Sample vial temperature (°C)	21

B) SAXS data collection parameters	
Employed sofware for azimutal integration	Foxtrot-3.2.5 (https://www.synchrotron-soleil.fr/fr/lignes-de-lumiere/swing)
Employed sofware for SAXS data reduction	PRIMUS/qt ATSAS 2.8.2 (Manalastas-Cantos,K. et *al*., 2021)
Calculation of V_c, V_p	RAW 2.1.1. (Hopkins J. B. et *al*., 2017)
Ab initio modeling	DAMMIF (Franke & Svergun, 2009) via PRIMUS/qt ATSAS 2.8.2
Model fit	SREFLEX (Panjkovich, A. et al. 2016)
3D graphics representations	PyMOL v.2.2.0

Table S2: Structural parameters extracted using ATSAS from static SAXS analysis on dark-adapted (OCP^O) $OCP_{wt\text{-}Ctag}$ and $OCP_{R27L\text{-}Ntag}$ at various concentrations.

Structural parameters of dark-adapted OCP (OCP^O)								
Protein variant	$OCP_{wt\text{-}Ctag}$				$OCP_{R27L\text{-}Ntag}$			
Conc. (mg/ml)	0.7	3.5	10.5	23	0.7	3.5	10.5	14
Guinier analysis								
$I(0)$ (cm^{-1})	0.00824 ± 0.0001	0.0533 ± 0.00008	0.1771± 0.0002	0.3552 ± 0.0004	0.00727 ± 0.00002	0.0487 ± 0.00003	0.1183 ± 0.00009	0.1444 ± 0.00007
R_g (Å)	24.35 ± 0.77	28.27 ± 0.16	28.02 ± 0.05	28.13 ± 0.01	22.24 ± 0.19	24.2 ± 0.04	22.93 ± 0.08	23.48 ± 0.02
q min ($Å^{-1}$)	0.02	0.02	0.02	0.02	0.02	0.02	0.02	0.02
q Rg max	1.2931	1.2912	1.2954	1.2984	1.2950	1.2915	1.2943	1.2918
R^2	0.8483	0.9979	0.9986	0.9995	0.9928	0.9995	0.9994	0.9994
P (r) analysis								
$I(0)$ (cm^{-1})	0.00789 ± 0.00006	0.0532 ± 0.00007	0.1765 ± 0.0001	0.3536 ± 0.00006	0.0073 ± 0.00002	0.0484 ± 0.00002	0.1177 ± 0.00008	0.1436 ± 0.00007
R_g (Å)	24.68 ± 0.17	27.9 ± 0.05	28.48 ± 0.03	28.17 ± 0.005	22.58 ± 0.06	24.19 ± 0.01	22.76 ± 0.02	23.29 ± 0.01
d_{max}	71	90.2	93	90	68	76	75.2	76
q range	0.02 – 0.5	0.02 – 0.5	0.02 – 0.5	0.02 – 0.5	0.02 – 0.5	0.02 – 0.5	0.02 – 0.5	0.02 – 0.5
MW (kDa) from $I(0)$	n/a	45.6	58	25	35.1	36.4	36.8	36.5
MW (kDa) from Vp	37.1	56.2	63.4	63.1	34.9	40.8	38.3	39
MW (kDa) from Vc	37	52.9	59.6	57.8	37.1	37	36.5	37
Calculated R_g (Å) monomer	21.72							
Calculated R_g (Å) dimer	27.16							

Table S3: Structural parameters extracted using ATSAS from static SAXS analysis on light-adapted (OCP^R) $OCP_{wt\text{-}Ctag}$ and $OCP_{R27L\text{-}Ntag}$ at various concentrations.

Structural parameters of light-adapted (OCP^R)						
Protein variant	$OCP_{wt\text{-}Ctag}$			$OCP_{R27L\text{-}Ntag}$		
Conc. (mg/ml)	0.7	3.5	10.5	0.7	3.5	10.5
Guinier analysis						
$I(0)$ (cm^{-1})	0.00811 ± 0.000063	0.00549 ± 0.00022	0.4975 ± 0.00204	0.00921 ± 0.00007	0.0605 ± 0.00018	0.2817 ± 0.00100
R_g (Å)	29.11 ± 0.35	34 ± 0.2	43.8 ± 0.04	32.5 ± 0.23	34.15 ± 0.09	48 ± 0.2
q min ($Å^{-1}$)	0.02	0.02	0.02	0.02	0.02	0.02
q Rg max	1.2808	1.2936	1.2870	1.2915	1.2869	1.2918
R^2	0.9674	0.9924	0.9975	0.9949	0.9969	0.9971
P (r) analysis						
$I(0)$ (cm^{-1})	0.00835 ± 0.000063	0.0056 ± 0.0021	0.5571 ± 0.00216	0.00943 ± 0.00005	0.0628 ± 0.0014	0.3192 ± 0.0031
R_g (Å)	31.59 ± 0.6	36.05 ± 0.2	59.48 ± 0.41	35.13 ± 0.3	34.70 ± 0.1	61.56 ± 0.8
d_{max}	127	126	260	126	130	260
q range	0.02 – 0.5	0.02 – 0.5	0.02 – 0.5	0.02 – 0.5	0.02 – 0.5	0.02 – 0.5
MW (kDa) from $I(0)$	62	62.7	169.4	60	62.5	165
MW from Vp	54.2	64.8	99.3	58.2	54.3	76.1
MW from Vc	52.1	56.4	84.2	47.4	46.1	92.8

Table S4: Modeling parameters retrieved from static SAXS analysis on dark-adapted (OCP^O) and light-adapted (OCP^R) $OCP_{wt\text{-}Ctag}$ and $OCP_{R27L\text{-}Ntag}$ at various concentrations.

A) Ab initio modeling of dark-adapted OCP (OCP^O)

Protein variant	$OCP_{wt\text{-}Ctag}$				$OCP_{R27L\text{-}Ntag}$			
Conc. (mg/ml)	0.7	3.5	10.5	23	0.7	3.5	10.5	14
DAMMIF (default parameters, 20 repetitions)								
q range ($Å^{-1}$)	0.02-0.156	0.02-0.135	0.02-0.227	0.02-0.279	0.02-0.357	0.02-0.357	0.02-0.357	0.02-0.357
Symmetry	*P*1	*P*1	*P*1	*P*1	*P*1	*P*1	*P*1	*P*1
Mean value of NSD	1.108	1.062	0.650	0.630	0.719	0.776	0.715	0.699
χ^2	1.1	1.057	1.127	1.517	1.029	1.173	0.956	1.036
constant adjustment	none	none	5.676E-04	1.592E-03	5.336E-05	2.268E-04	3.020E-04	5.026E-04

B) Ab initio modeling of light-adapted (OCP^R)

Protein variant	$OCP_{wt\text{-}Ctag}$			$OCP_{R27L\text{-}Ntag}$		
Conc. (mg/ml)	0.7	3.5	10.5	0.7	3.5	10.5
DAMMIF (default parameters, 20 repetitions)						
q range ($Å^{-1}$)	0.02-0.293	0.02-0.293	0.02-0.293	0.02-0.293	0.02-0.293	0.02-0.293
Symmetry	*P*1	*P*1	*P*1	*P*1	*P*1	*P*1
Mean value of NSD	1.324	0.849	0.718	0.573	0.927	0.765
χ^2	0.995	1.022	1.124	1.035	1.135	1.024
Constant adjustment	4.125E-05	1.270E-04	1.303E-03	none	2.303E-04	5.046E-04

Table S5: Fitting parameters retrieved from static SAXS analysis on dark-adapted (OCP^O) and light-adapted (OCP^R) $OCP_{wt\text{-}Ctag}$ and $OCP_{R27L\text{-}Ntag}$ at various concentrations.

A) SREFLEX fitting parameters of light-adapted (OCP^R)

Protein variant	$OCP_{wt\text{-}Ctag}$		$OCP_{R27L\text{-}Ntag}$	
Conc. (mg/ml)	3.5	10.5	3.5	10.5
Fitχ2 monomer	7.72	> 1000	48.12	302.07
Fitχ2 dimer CTD	1.11	99.3	9.52	8.94
Fitχ2 dimer NTD	1.15	112.66	9.68	13.24
Fitχ2 trimer	2.04	5.15	135.57	4.85
Fitχ2 tetramer	7.72	10.07	196.59	9.71

B) SASBDB IDs

Protein variant	dark-adapted $OCP_{wt\text{-}Ctag}$				dark-adapted $OCP_{R27L\text{-}Ntag}$			
Conc. (mg/ml)	0.7	3.5	10.5	23	0.7	3.5	10.5	14
IDs	SAS3996	SAS3997	SAS3999	SAS4000	SAS4001	SAS4002	SAS4003	SAS4004
Protein variant	light-adapted $OCP_{wt\text{-}Ctag}$				light-adapted $OCP_{R27L\text{-}Ntag}$			
Conc. (mg/ml)	0.7	3.5	10.5		0.7	3.5	10.5	
IDs	SAS4006	SAS4007	SAS4008		SAS4010	SAS4011	SAS4012	

Table S6: Retained fitting parameters for the spectral (absorbance at 467 nm) recovery of $OCP_{wt\text{-}Ctag}$, $OCP_{wt\text{-}Ntag}$ and $OCP_{R27L\text{-}Ntag}$, following accumulation of their OCP^R counterparts.

Spectroscopic recovery	fitting function: $a_{ci-1}\times[1-\exp(-t/\tau_{ci-1})] + a_{ci-2} \times [1-\exp(-t/\tau_{ci-2})] + a_{ci-3} \times [1-\exp(-t/\tau_{ci-3})]$		
	$\tau_{ci\text{-}1}$ [s]	$\tau_{ci\text{-}2}$ [s]	$\tau_{ci\text{-}3}$ [s]
	59.825 ± 0.253	159.132 ± 0.594	641.708 ± 1.147
$OCP_{R27L\text{-}Ctag}$	$a_{ci\text{-}1}$	$a_{ci\text{-}2}$	$a_{ci\text{-}3}$
0.1 mg/ml	0.899 ± 0.004	0.013 ± 0.005	0.084 ± 0.001
1.7 mg/ml	0.023 ± 0.003	0.810 ± 0.003	0.156 ± 0.001
3.0 mg/ml	0.000 ± 0.035	0.805 ± 0.003	0.190 ± 0.037
16.0 mg/ml	0.000 ± 0.022	0.180 ± 0.003	0.820 ± 0.003

§ $a_{ci\text{-}4}$ was constrained to $a_{ci\text{-}3} = (1\text{-}a_{ci\text{-}1}\text{-}a_{ci\text{-}2}\text{-}a_{ci\text{-}3})$
chi^2 = 0.157; reduced chi^2 = 2.242e-05

Spectroscopic recovery	fitting function: $a_{ci-1}\times[1-\exp(-t/\tau_{ci-1})] + a_{ci-2} \times [1-\exp(-t/\tau_{ci-2})] + a_{ci-3} \times [1-\exp(-t/\tau_{ci-3})]$		
	$\tau_{ci\text{-}1}$ [s]	$\tau_{ci\text{-}2}$ [s]	$\tau_{ci\text{-}3}$ [s]
	94.513 ± 0.247	356.523 ± 1.246	1327.486 ± 4.338
$OCP_{wt\text{-}Ntag}$	$a_{ci\text{-}1}$	$a_{ci\text{-}2}$	$a_{ci\text{-}3}$
0.1 mg/ml	0.909 ± 0.001	0.088 ± 0.002	0.000 ± 0.000
3.0 mg/ml	0.194 ± 0.002	0.722 ± 0.002	0.083 ± 0.001
10.0 mg/ml	0.093 ± 0.002	0.740 ± 0.002	0.167 ± 0.001
16.0 mg/ml	0.000 ± 0.004	0.411 ± 0.003	0.584 ± 0.003

§ $a_{ci\text{-}3}$ was constrained to $a_{ci\text{-}3} = (\text{maximum}\text{-}a_{ci\text{-}1}\text{-}a_{ci\text{-}2})$
chi^2 = 0.305; reduced chi^2 = 3.261e-05

Spectroscopic recovery	fitting function: $a_{ci-1}\times[1-\exp(-t/\tau_{ci-1})] + a_{ci-2} \times [1-\exp(-t/\tau_{ci-2})] + a_{ci-3} \times [1-\exp(-t/\tau_{ci-3})] + a_{ci-4} \times [1-\exp(-t/\tau_{ci-4})]$			
	$\tau_{ci\text{-}1}$ [s]	$\tau_{ci\text{-}2}$ [s]	$\tau_{ci\text{-}3}$ [s]	$\tau_{ci\text{-}4}$ [s]
	51.491 ± 0.218	209.893 ± 1.288	945.989 ± 3.703	14057.656 ± 68.830
$OCP_{wt\text{-}Ctag}$	$a_{ci\text{-}1}$ §	$a_{ci\text{-}2}$	$a_{ci\text{-}3}$	$a_{ci\text{-}4}$
0.1 mg/ml	0.688 ± 0.002	0.234 ± 0.003	0.038 ± 0.001	0.039 ± 0.000
1.7 mg/ml	0.382 ± 0.002	0.431 ± 0.002	0.140 ± 0.001	0.047 ± 0.000
3.0 mg/ml	0.291 ± 0.002	0.462 ± 0.002	0.193 ± 0.001	0.053 ± 0.000
16.0 mg/ml	0.063 ± 0.001	0.297 ± 0.002	0.533 ± 0.002	0.107 ± 0.000

Table S7: Alternative Fitting parameters for the spectral (absorbance at 467 nm) recovery of $OCP_{wt\text{-}Ctag}$, $OCP_{wt\text{-}Ntag}$ and $OCP_{R27L\text{-}Ntag}$, following accumulation of their OCP^R counterparts.

Spectroscopic recovery	fitting function: $a_{ci-1} \times [1-\exp(-t/\tau_{ci-1})] + a_{ci-2} \times [1-\exp(-t/\tau_{ci-2})] + a_{ci-3} \times [1-\exp(-t/\tau_{ci-3})] + a_{ci-4} \times [1-\exp(-t/\tau_{ci-4})]$			
	$\tau_{ci\text{-}1}$ [s]	$\tau_{ci\text{-}2}$ [s]	$\tau_{ci\text{-}3}$ [s]	$\tau_{ci\text{-}4}$ [s]
	9.402 ± 1.551	76.390 ± 1.121	257.289 ± 3.199	760.380 ± 8.141
$OCP_{R27L\text{-}Ctag}$	$a_{ci\text{-}1}$ §	$a_{ci\text{-}2}$	$a_{ci\text{-}3}$	$a_{ci\text{-}4}$
0.1 mg/ml	0.081 ± 0.008	0.864 ± 0.007	0.000 ± 0.009	0.050 ± 0.002
1.7 mg/ml	0.000 ± 0.003	0.343 ± 0.009	0.595 ± 0.007	0.052 ± 0.004
3.0 mg/ml	0.000 ± 0.003	0.281 ± 0.009	0.651 ± 0.006	0.063 ± 0.004
16.0 mg/ml	0.000 ± 0.001	0.000 ± 0.004	0.374 ± 0.011	0.627 ± 0.009

§ $a_{ci\text{-}4}$ was constrained to $a_{ci\text{-}4}$ = (maximum-$a_{ci\text{-}1}$-$a_{ci\text{-}2}$-$a_{ci\text{-}3}$)
chi² = 0.824; reduced chi² = 1.180e-04

Spectroscopic recovery	fitting function: $a_{ci-1} \times [1-\exp(-t/\tau_{ci-1})] + a_{ci-2} \times [1-\exp(-t/\tau_{ci-2})] + a_{ci-3} \times [1-\exp(-t/\tau_{ci-3})] + a_{ci-4} \times [1-\exp(-t/\tau_{ci-4})]$			
	$\tau_{ci\text{-}1}$ [s]	$\tau_{ci\text{-}2}$ [s]	$\tau_{ci\text{-}3}$ [s]	$\tau_{ci\text{-}4}$ [s]
	94.786 ± 0.336	225.655 ± 298.575	360.181 ± 10.521	1325.753 ± 7.249
$OCP_{wt\text{-}Ntag}$	$a_{ci\text{-}1}$ §	$a_{ci\text{-}2}$	$a_{ci\text{-}3}$	$a_{ci\text{-}4}$
0.1 mg/ml	0.913 ± 0.003	0.000 ± 0.000	0.080 ± 0.003	0.004 ± 0.001
3.0 mg/ml	0.188 ± 0.005	0.009 ± 0.068	0.729 ± 0.064	0.074 ± 0.002
10.0 mg/ml	0.096 ± 0.010	0.026 ± 0.090	0.703 ± 0.097	0.175 ± 0.002
16.0 mg/ml	0.005 ± 0.004	0.000 ± 0.028	0.407 ± 0.023	0.583 ± 0.005

§ $a_{ci\text{-}4}$ was constrained to $a_{ci\text{-}4}$ = (maximum-$a_{ci\text{-}1}$-$a_{ci\text{-}2}$-$a_{ci\text{-}3}$)
chi² = 0.323; reduced chi² = 3.45e-05

Spectroscopic recovery	fitting function: $a_{ci-1} \times [1-\exp(-t/\tau_{ci-1})] + a_{ci-2} \times [1-\exp(-t/\tau_{ci-2})] + a_{ci-3} \times [1-\exp(-t/\tau_{ci-3})]$		
	$\tau_{ci\text{-}1}$ [s]	$\tau_{ci\text{-}2}$ [s]	$\tau_{ci\text{-}3}$ [s]
	76.669 ± 0.202	593.111 ± 2.088	9517.368 ± 75.252
$OCP_{wt\text{-}Ctag}$	$a_{ci\text{-}1}$ §	$a_{ci\text{-}2}$	$a_{ci\text{-}3}$
0.1 mg/ml	0.880 ± 0.001	0.072 ± 0.001	0.047 ± 0.000
1.7 mg/ml	0.646 ± 0.001	0.300 ± 0.001	0.053 ± 0.000
3.0 mg/ml	0.555 ± 0.001	0.382 ± 0.001	0.063 ± 0.000
16.0 mg/ml	0.152 ± 0.001	0.688 ± 0.001	0.159 ± 0.001

Table S8: Fitted parameters extracted from nanosecond transient absorption data. Percentage contributions in the table are calculated as a given pre-exponential factor divided by a_1+ a_2+ a_3+ a_4. Measurement of C-tag at 22 °C was repeated twice to confirm repeatability (note replicated row in the table).

fitting function: $a_1 \times [\exp(-t/\tau_1)] + a_2 \times [\exp(-t/\tau_2)] + a_3 \times [\exp(-t/\tau_3)] + a_4$							
$OCP_{wt\text{-}Ctag}$ 12 µM	τ_1 [µs]	a_1 (%)	τ_2 [ms]	a_2 (%)	τ_3 [ms]	a_3 (%)	a_4 (%)
8 °C	2.2 ± 0.15	14.0 ± 1.0	4.94 ± 0.29	35.5 ± 2.3	245.0 ± 57.0	25.4 ± 2.9	25.1 ± 3.2
15 °C	2.4 ± 0.18	17.9 ± 1.3	2.25 ± 0.13	41.6 ± 2.6	171.0 ± 30.0	26.2 ± 2.3	14.3 ± 2.1
22 °C	2.1 ± 0.17	16.6 ± 1.5	1.05 ± 0.06	49.4 ± 3.6	81.1 ± 11.0	26.4 ± 2.2	7.7 ± 1.2
29 °C	1.8 ± 0.14	20.0 ± 2.0	0.48 ± 0.03	53.6 ± 4.3	28.6 ± 4.0	25.5 ± 2.4	0.9 ± 0.9
36 °C	2.0 ± 0.18	18.4 ± 2.7	0.23 ± 0.01	58.5 ± 6.9	11.7 ± 1.5	34.0 ± 4.2	-10.9 ± 1.5
$OCP_{R27L\text{-}Ntag}$ 12 µM	τ_1 [µs]	a_1 (%)	τ_2 [ms]	a_2 (%)	τ_3 [ms]	a_3 (%)	a_4 (%)
8 °C	4 ± 1.5	5.3 ± 0.7	4.61 ± 0.28	32.6 ± 2.1	286 ± 28	35.5 ± 2.4	26.6 ± 2.1
22 °C	2 ± 0.4	8.2 ± 1.0	0.91 ± 0.04	51.8 ± 3.5	46.5 ± 3.4	31.8 ± 2.3	8.2 ± 0.7
36 °C	6 ± 2.0	10.6 ± 1.8	0.15 ± 0.01	58.9 ± 6.0	3.44 ± 0.3	36.1 ± 3.8	-5.6 ± 0.7
Ctag vs. Ntag 12 µM 22 °C	τ_1 [µs]	a_1 (%)	τ_2 [ms]	a_2 (%)	τ_3 [ms]	a_3 (%)	a_4 (%)
$OCP_{wt\text{-}Ntag}$	3 ± 0.7	10.0 ± 1.4	0.93 ± 0.05	45.3 ± 5.0	96.8 ± 10	25.3 ± 3.0	19.3 ± 2.3
$OCP_{wt\text{-}Ctag}$	2 ± 0.4	12.2 ± 1.4	0.98 ± 0.05	49.7 ± 4.5	75.2 ± 7.0	28.0 ± 2.6	10.1 ± 1.1
Ctag vs. R27L 50 µM 22 °C	τ_1 [µs]	a_1 (%)	τ_2 [ms]	a_2 (%)	τ_3 [ms]	a_3 (%)	a_4 (%)
$OCP_{wt\text{-}Ctag}$	2 ± 0.29	9.8 ± 0.8	1.14 ± 0.03	47.3 ± 3.1	161 ± 7.0	35.2 ± 2.3	7.8 ± 0.7
$OCP_{R27L\text{-}Ntag}$	2 ± 0.27	10.9 ± 0.8	0.99 ± 0.03	47.9 ± 3.0	61.7 ± 2.5	36.0 ± 3.3	5.2 ± 0.5
Ctag vs. R27L 250 µM 22 °C	τ_1 [µs]	a_1 (%)	τ_2 [ms]	a_2 (%)	τ_3 [ms]	a_3 (%)	a_4 (%)
$OCP_{wt\text{-}Ctag}$	2 ± 0.16	12.7 ± 0.9	1.33 ± 0.03	44.4 ± 2.6	179 ± 8	32.0 ± 2	10.9 ± 0.8
$OCP_{R27L\text{-}Ntag}$	2 ± 0.26	11.3 ± 0.8	1.00 ± 0.03	45.1 ± 2.8	56.2 ± 2.3	33.5 ± 2.1	10.2 ± 0.7

Biophysical Reports

REPORT

Is orange carotenoid protein photoactivation a single-photon process?

Stanisław Niziński,[1,2,*] Ilme Schlichting,[3] Jacques-Philippe Colletier,[4] Diana Kirilovsky,[5] Gotard Burdzinski,[1,*] and Michel Sliwa[2,*]

[1]Quantum Electronics Laboratory, Faculty of Physics, Adam Mickiewicz University in Poznań, Poznan, Poland; [2]Univ. Lille, CNRS, UMR 8516 - LASIRE, Laboratoire Avancé de Spectroscopie pour les Interactions, la Réactivité et l'Environnement, Lille, France; [3]Max-Planck-Institut für medizinische Forschung, Heidelberg, Germany; [4]Université Grenoble Alpes, CEA, CNRS, Institut de Biologie Structurale, Grenoble, France; and [5]Université Paris-Saclay, CEA, CNRS, Institute for Integrative Biology of the Cell (I2BC), Gif-sur-Yvette, France

ABSTRACT In all published photoactivation mechanisms of orange carotenoid protein (OCP), absorption of a single photon by the orange dark state starts a cascade of red-shifted OCP ground-state intermediates that subsequently decay within hundreds of milliseconds, resulting in the formation of the final red form OCP^R, which is the biologically active form that plays a key role in cyanobacteria photoprotection. A major challenge in deducing the photoactivation mechanism is to create a uniform description explaining both single-pulse excitation experiments, involving single-photon absorption, and continuous light irradiation experiments, where the red-shifted OCP intermediate species may undergo re-excitation. We thus investigated photoactivation of *Synechocystis* OCP using stationary irradiation light with a biologically relevant photon flux density coupled with nanosecond laser pulse excitation. The kinetics of photoactivation upon continuous and nanosecond pulse irradiation light show that the OCP^R formation quantum yield increases with photon flux density; thus, a simple single-photon model cannot describe the data recorded for OCP *in vitro*. The results strongly suggest a consecutive absorption of two photons involving a red intermediate with ≈100 millisecond lifetime. This intermediate is required in the photoactivation mechanism and formation of the red active form OCP^R.

WHY IT MATTERS We question whether the $OCP^O \rightarrow OCP^R$ photoconversion can be completed upon absorption of only a single photon, as implicitly assumed in the literature. This quest is important from a biological point of view, as one can expect that the photoactivation mechanism of OCP should be as selective as possible. The proposed two-photon mechanism fulfills this condition perfectly because it allows efficient OCP photoactivation (and quenching excited phycobilisomes) above a light threshold of around 1 mW/cm^2 (≈ 40 $\mu mol\ m^{-2}\ s^{-1}$) but not at low light conditions, where any dissipative mechanism is very unfavorable, because it would reduce photosynthesis efficiency. One should expect a clear evolutionary advantage for cyanobacteria possessing such a two-photon photoprotective mechanism compared with much less selective single-photon mechanism.

INTRODUCTION

Orange carotenoid protein (OCP) (1) is a photoactive protein, acting as a photoprotective factor in cyanobacteria (2,3). The dark-adapted form (OCP^O due to its orange color) can be photoconverted into the active form (OCP^R due to red-shifted absorption spectrum) by blue or green light. OCP^R is capable of quenching excited phycobilisomes (PBSs), protecting reaction centers from energy overload, thus avoiding formation of reactive oxygen species (4). The photoconversion process $OCP^O \rightarrow OCP^R$ starts with absorption of a photon, which triggers hydrogen bond cleavage enabling carotenoid translocation into the N-terminal domain (NTD) (5,6), followed by NTD and C-terminal domain separation on the millisecond timescale (7–9).

The majority of the recent models of OCP photoconversion have been proposed based on the *in vitro* evolution of absorbance induced by a laser pulse excitation spanning temporal regimes from hundreds of femtoseconds to single seconds (5,8,10,11). These

Submitted April 18, 2022, and accepted for publication August 17, 2022.

*Correspondence: nizin@amu.edu.pl or gotardb@amu.edu.pl or michel.sliwa@univ-lille.fr

Twitter: @michelsliwa

Editor: Hagen Hofmann.

https://doi.org/10.1016/j.bpr.2022.100072

techniques are very powerful in tracking short living species, but they have also a major drawback: the observation of the final OCP^R state is very challenging due to a very low formation quantum yield. When seeking biologically relevant information, continuous irradiation is superior to pulse excitation. Experiments with continuous irradiation reflect the biological conditions very well and allow OCP^R to accumulate, overcoming its ultra-low quantum yield (below 0.2%) (8).

Rakhimberdieva et al. (12) studied light-induced fluorescence changes of the PBSs in a PSII-deficient mutant of *Synechocystis*. They measured action spectrum, which is magnitude of fluorescence quenching represented in function of wavelength of irradiation light used to induce the quenching (while keeping fixed fluorescence excitation light at 580 nm). 10 s irradiation was used with photon flux density above 200 μmol m^{-2} s^{-1}. This spectrum has been found to overlap with dark-adapted OCP absorption spectrum (13).

Wilson et al. (3) presented how temperature and irradiation intensity affect the photoactivation speed. They investigated the mechanism of non-photochemical quenching tracking PBS fluorescence *in vivo* and the photoconversion OCP from *Synechocystis* containing hydroxyechinenone using absorption spectroscopy *in vitro*. They used spectrally broad irradiation light in the band from 400 to 550 nm with irradiances between 20 μmol m^{-2} s^{-1} and 1.2 mmol m^{-2} s^{-1}. The most important conclusion was that low temperature and high light intensity facilitate efficient formation of quenching-capable OCP^R. They found that the initial slope of the photoactivation kinetics (dA/dt) correlates with the irradiation intensity and the quantum yield of photoactivation is about 1% when using femtosecond transient absorption spectroscopy. Moreover, variation of the temperature (11°C–32°C) did not affect the initial dA/dt (3).

Gorbunow et al. (14) investigated *in vivo* the quenching of PBS fluorescence with wild-type OCP from *Synechocystis* (and other strains). The OCP photoactivation was triggered by 470 nm light, with various photon flux densities from 10 μmol m^{-2} s^{-1} to 15 mmol m^{-2} s^{-1}. In agreement with Gwizdala et al. (15) and Rakhimberdieva et al. (16), they introduced a three-state model containing an additional non-quenching intermediate (7 s lifetime) before the formation of quenching centers and determined the quantum yield *in vivo* to be 0.1% (14).

The first model for the *in vitro* photoconversion of purified OCP was proposed by Maksimov et al. (17). They measured the kinetics of the absorbance at 550 nm upon 460 nm irradiation (photon flux density up to 4 mmol m^{-2} s^{-1}, only one experiment below 200 μmol m^{-2} s^{-1}), using OCP from *Arthrospira maxima* with the hydroxyechinenone chromophore. They concluded that the rate of photoactivation grows linearly with light intensity (17). They also applied the same three-states scheme proposed for OCP *in vivo*. In purified OCP, the non-quenching intermediate was found to live below instrument resolution (0.1 s) (17). They found that the photoactivation quantum yield is about 0.1%, just like the formation quantum yield of quenching centers *in vivo*. Maksimov et al. (17) reported two more important observations: firstly, the OCP^R decay is not monoexponential, and secondly, its lifetime in the dark depends on the applied photon flux density.

In the following report, Maksimov et al. (9) performed a transient absorption experiment *in vitro* with 532 nm nanosecond pulse excitation in the μs to second temporal range, using N-tagged OCP from *Synechocystis*. They calculated the quantum yield of OCP^R formation to be around 0.2%. A red intermediate OCP^{RI} living around 0.3 ms (at 36 °C) was observed and identified as a precursor of the final long-lived photoactive OCP^R.

In the latest report, Maksimov et al. (8) used a mutant protein that contained only one tryptophan (Trp-288), which forms an H-bond with the carotenoid, to track cleavage of this bond following illumination using tryptophan fluorescence measurements. Using 5 ms and 100 ms flashes of 450 nm light, they found additional intermediate states in the millisecond timescale before the formation of active OCP^R: P_N (τ = 10 ms), P_M (τ = 35 ms), and P_X (τ = 100 ms) at 20°C. The $P_X \rightarrow OCP_R$ process was assigned to C-terminal domain and NTD separation.

Recently, Mezetti et al. identified an interesting two-step evolution in the seconds timescale upon continuous irradiation using Fourier transform infrared probing (at 4 °C), both associated with α-helix reorganization (18).

Thus, the literature about formation of the active form OCP^R is already quite rich. However, several incoherent perspectives exist. Moreover, the studies done so far explored mostly the high intensity irradiation regime, whereas the *in vivo* biological working conditions of OCP are limited by the light intensity of the sun. The total photon flux density of the sun in the 420 to 550 nm wavelength range (which is the OCP sensitivity region) is below 1000 μmol m^{-2} s^{-1} (solar photosynthetic photon flux density equals 2200 μmol m^{-2} s^{-1} for noon at the equator at equinox (19)). Therefore, light intensities exceeding this range do not represent the conditions naturally encountered by the OCP *in vivo*. In fact, OCP should already perform its photoprotective function efficiently much below these light levels, because 1) in most places on Earth, the solar intensity is much weaker than at the equator, 2) usually OCP is not directly exposed to sunlight as it is confined

in cyanobacteria cells, 3) the water surface will reflect part of the incident light, etc.

For all these reasons, we investigate here the photoactivation in the lower irradiation intensity regime of the most studied *Synechocystis* OCP containing the ECN chromophore (echinenone). We used C-tagged and N-tagged OCP variants for which we have reported recently diametrically different photoactivation speeds (20). To ensure that our results reflect the natural working conditions of OCP, we limited our photon flux density range to about 200 μmol m^{-2} s^{-1}, which certainly does not exceed the biological photoexcitation regime of OCP *in vivo*. We designed a nanosecond transient absorption experiment combined with continuous irradiation to investigate the re-excitation of millisecond lifetime intermediates that could participate in the photoactivation process. Our experiment revealed that upon additional continuous irradiation, the laser pulse-induced ΔA signal dramatically increases, which eliminates the hypothesis that OCP^R formation is purely a single-photon process.

Efficiency of the photoactivation: Is the single-photon mechanism valid?

To begin with, we investigated photoactivation using stationary absorption spectroscopy as a function of irradiation photon flux density, with probing done at the OCP^R absorption band (Fig. S1 *a*). Fig. 1 shows the difference absorbance (subtraction of absorbance at time zero; see supporting methods in the supporting material) induced by 452 nm irradiation, probed at 580 nm for C-tagged OCP. A comparison between the N-tagged and C-tagged protein is presented in the supporting material (Fig. S2). In order to quantify the efficiency of photoactivation, one can calculate the derivative dA/dt during the first seconds of irradiation, where the growth of the absorbance is still linear (using linear fits, presented in Fig. S3). The dA/dt value obtained this way is plotted in Fig. 2 *a*, and it represents the speed of photoactivation. If the process is caused by absorption of a single photon, one would expect that doubling the irradiation intensity should result in a doubled rate of OCP^R accumulation (so dA/dt should also double). This can be visualized in a log-log plot, where this dependence should result in a linear fit with slope equal to 1. Linear fits in Fig. 2 *a* (*dashed line*) show that both C-tagged and N-tagged OCPs are characterized by a slope higher than 1 (meaning that doubling light intensity causes more than doubled speed of photoactivation), with a larger slope determined for C-tagged OCP. The C-tagged dataset was measured twice, with 550 (green) and 580 nm (red) probing, to ensure that the slope value is reproducible.

Before going further, it is required that we define the quantum yield of OCP photoactivation, i.e., the quantum yield of OCP^R formation for a simple photochemical one-photon process (pictured in Fig. 2 *c*). It can be formulated as a reaction rate equation (21):

$$\frac{d\left[OCP^R\right]}{dt} = \varphi\, I_0\, F\, \left[OCP^O\right] \epsilon_{OCP^O}\, l_{irr} - k_{OCP^R \rightarrow OCP^O} \left[OCP^R\right] \quad (1)$$

$$F = \left(1 - 10^{-A_{irr}}\right)/A_{irr}, \quad (2)$$

where φ is the quantum yield of OCP^R formation using 452 nm irradiation wavelength. It assumes that all thermal processes occurring after photon absorption lead back to the initial OCP^O state or generate the OCP^R with a probability equal to φ. So, the φ term should be understood as a "black box" that encapsulates various relaxation schemes initialized by absorption of the single photon. F is the so-called photokinetic factor. A_{irr} is the total absorbance of the sample solution at irradiation wavelength and optical path length (l_{irr}). $[OCP^O]$ and $[OCP^R]$ are molar concentrations of OCP^O and OCP^R, respectively. I_0 is the photon flux density measured in moles of photons s^{-1} L^{-1}. $k_{OCP^R \rightarrow OCP^O}$ is associated with the thermal back recovery, i.e., the inverse of the OCP^R decay time constant ($\tau_{OCP^R \rightarrow OCP^O}$; k in Fig. 2 *c*). ϵ_{OCP^O} is the molar absorption coefficient of OCP^O at irradiation wavelength (452 nm).

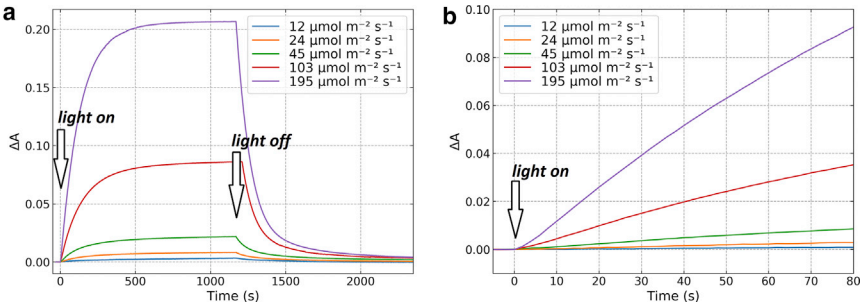

FIGURE 1 (*a*) Difference absorbance kinetics recorded at 580 nm of C-tagged OCP recorded upon 452 nm irradiation. (*b*) Zoom in at the initial rate of photoactivation. To obtain the light intensity in mW cm^{-2}, multiply the value given in μmol m^{-2} s^{-1} by a factor of 0.026.

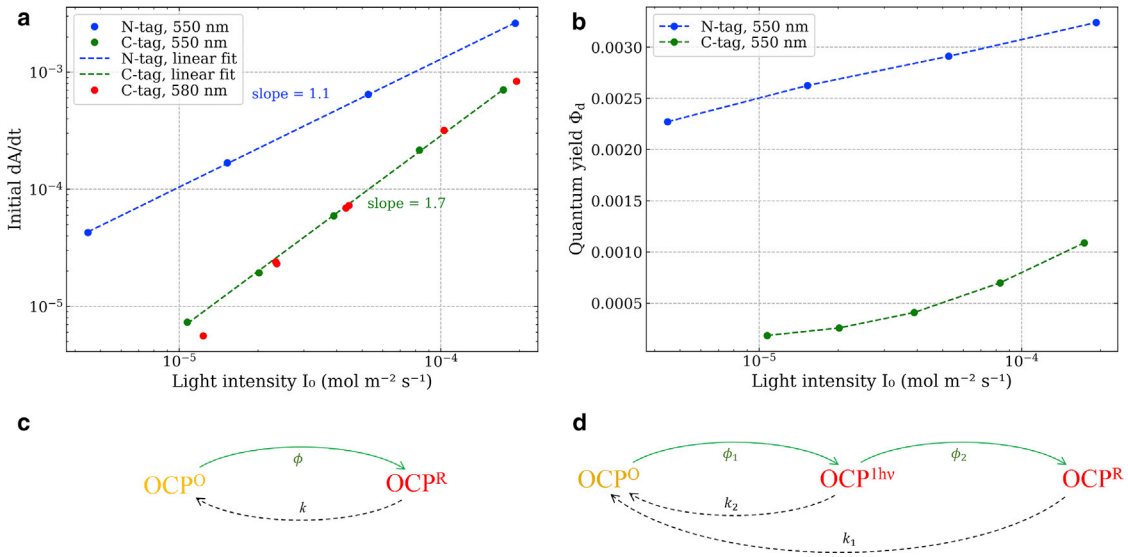

FIGURE 2 (*a*) Initial photoactivation speed dA/dt plotted versus light intensity using log-log graph. (*b*) Differential photoactivation quantum yield formation of OCP^R calculated using Eq. 3 for N-tagged and C-tagged OCPs. (*c*) Single-photon model. (*d*) Example of a two-photon model.

$k_{OCP^R \rightarrow OCP^O}\,[OCP^R]$ term can be understood as decrease in OCP^R concentration per second due to thermal relaxation. $[OCP^O]\,\epsilon_{OCP^O}\,l_{irr}$ represents the absorbance of all OCP^O species, which, when multiplied by F, becomes the probability that a photon of irradiation light is absorbed by the OCP^O species in the sample solution (but not by OCP^R). Going further, this probability multiplied by $\varphi\, I_0$ is linked to the decrease of OCP^O concentration per second, caused by photoconversion of OCP^O into OCP^R. Therefore, overall $d[OCP^R]/dt$ originates from species being photoactivated to OCP^R minus species relaxing back to the OCP^O state.

From Eq. 1, it is clear that in the initial period of the irradiation (much shorter than OCP^R thermal back recovery time constant,), the OCP^R concentration should indeed grow linearly with time. Only when the irradiation timescale approaches $\tau_{OCP^R \rightarrow OCP^O}$ the concentration profile will start to flatten, settling finally in the photostationary state (in which concentrations of OCP^R and OCP^O do not change anymore). Since the OCP^R lifetime is long, in the order of single minutes (Table S1, at room temperature), one can fit the initial seconds of the evolution of the absorbance during irradiation to extract the OCP^R formation quantum yield φ (Fig. S3). At the early stages of irradiation, the depletion of the dark OCP^O state is negligible, and OCP^R is too weakly populated to allow its decay to play any role, so the kinetics can be approximated by a straight line. Note, it has been demonstrated that there is no light-induced back conversion, the $OCP^R + h\nu \rightarrow OCP^O$ pathway is then blocked (3). By neglecting thermal back recovery in Eq. 1, one can obtain a simplified expression and determine the quantum yield of OCP^R formation from initial dA/dt value:

$$\varphi_d = \frac{dA_{probe}}{dt}\,\frac{1}{I_0\, I_{probe}\, \Delta\epsilon_{OCP^R}\, F_{t=0}\, A_{irr,t=0}}. \qquad (3)$$

φ_d is equivalent to a differential quantum yield, defined by IUPAC (22). $\Delta\epsilon_{OCP^R}$ is the OCP^R difference molar absorption coefficient at the probe wavelength ($\epsilon_{OCP^R} - \epsilon_{OCP^O}$; see Fig. S1 *b*). $F_{t=0}\, A_{irr,t=0}$ is the photokinetic factor multiplied by the absorbance of the solution at the irradiation wavelength, at the $t = 0$ time point, when the irradiation light was just switched on. One can obtain Eq. 3 directly from the Eq. 1, using the Beer-Lambert law and substituting molar concentrations. Differential quantum yields of OCP^R formation calculated this way are presented in Fig. 2 *a*.

The results obtained this way are quite unexpected. One can clearly see in Fig. 2 *b* that for experiments performed with a higher irradiation intensity, one obtains a much higher differential quantum yield φ_d. Therefore, it is clear that a single-photon mechanism for the formation of OCP^R (pictured in Fig. 2 *c*) cannot describe the data (the photoactivation quantum yield φ_d should be the same regardless of the irradiation power, which stems from Eq. 1). It is especially striking for C-tagged OCP, where the differential quantum yield increases more than fourfold in the range of used irradiation intensities (Fig. 2 *b*). The obvious inherent contradiction that the quantum yield Φ in a single-photon model must be constant for any light intensity rules out not only the simple $OCP^O + h\nu \rightarrow OCP^R$ model but in fact any model where absorption of a single

photon starts a cascade of intermediates leading to OCP^R. An additional justification of our conclusion is shown in the supporting material, where we present simulated differential quantum yields (Fig. S4) using exemplary single-photon (Φ, Fig. 2 *c*) and two-photon models (Φ_1 x Φ_2, Fig. 2 *d*; see detailed description in supporting material). The curvature observed in Fig. 2 *b* can only be reproduced with a two-photon model (Fig. S4).

Decay absorption kinetics after nanosecond laser pulse excitation are affected by the intensity of auxiliary continuous light

To further solidify our results on the existence of two-photon pathway for the formation of OCP^R, influence of continuous irradiation on laser pulse-induced transient absorption kinetics of OCP was investigated. Red traces in Fig. 3 show the ΔA evolution at 550 nm after a 532 nm nanosecond laser pulse, without additional continuous irradiation. A red-shifted species with roughly one hundred millisecond lifetime is observed (180 ms for C-tagged OCP and 100 ms for N-tagged OCP). According to literature, this time constant could be associated with the decay of P_X species and domain separation process (8). In C-tagged OCP, the signal recorded after 1 s decays almost to zero ($\Delta A(1\ s) \approx 2.5 \times 10^{-5}$; Fig. 3 *a*, *red trace*). It shows that the single-photon channel leading to photoactivated OCP^R is negligible for C-tagged OCP.

In order to directly observe how two-photon process influences the formation of OCP^R, additional 452 nm continuous irradiation with various intensities was applied (see the supporting material for a detailed description of the experimental setup). ΔA represents increase of absorption signal after the ns laser pulse, compared with the reference measurement where no laser pulse is present. Additional continuous irradiation is applied during both laser-pulse and reference cycles. At high continuous irradiation intensity (Fig. 3 *b*, *cyan curve*), some fraction of OCP will be photoconverted to the OCP^R state, reducing the number of available OCP^Os that can contribute to the laser pulse-induced signal. Therefore, additional continuous irradiation should decrease the $\Delta A(t)$ signal unless some type of interplay between both continuous and laser pulse light is present.

If formation of a single OCP^R protein requires absorption of two consecutive photons (like in Fig. 2 *d*), then application of continuous light irradiation generates a steady-state population of intermediate states (denoted as $OCP^{1h\nu}$; Fig. 2 *d*) that can be subsequently transformed into OCP^R after absorption of a second photon (delivered by ns laser pulse), effectively increasing ΔA signal at 1 s. If OCP photoactivation is triggered by a single-photon absorption, then no such effect should be observed.

Fig. 3 shows clearly that red-shifted species are populated more efficiently in the presence of additional continuous light. Indeed, both N-tagged and C-tagged OCPs exhibit increased ΔA at 1 s (OCP^R concentration) at 550 nm when additional LED irradiation is applied (ΔA at 1 s increases from 2.5×10^{-5} to 3.25×10^{-4} for C-tagged and from 2×10^{-4} to 6.25×10^{-4} for N-tagged OCP; see Fig. 3). This indicates that significant two-photon pathways must be present for both investigated OCPs.

For N-tagged OCP, a single-photon pathway leading to OCP^R cannot be excluded completely due to a positive signal when no continuous irradiation is present (Fig. 3 *b*, *red curve*). However, for C-tagged OCP, the one-photon channel seems to be almost completely blocked, so only the two-photon pathway is allowed to reach OCP^R. One can wonder whether a weak (but still significant) 550 nm probe light could generate enough of the intermediate $OCP^{1h\nu}$ population to enable a sequential two-photon mechanism in N-tagged OCP. Nevertheless, it is evident that N-tagged OCP possesses a very efficient two-photon channel: even a very small amount of external continuous light doubles the signal at 1 s, from 0.2 mOD to 0.4 mOD (Fig. 3 *b*, compare *red* and *orange kinetics*). All these observations are direct evidence that both N-tagged and C-tagged OCPs possess a dominant two-photon photoactivation channel.

One remark should be made on the continuous irradiation: it generates not only a stationary population of

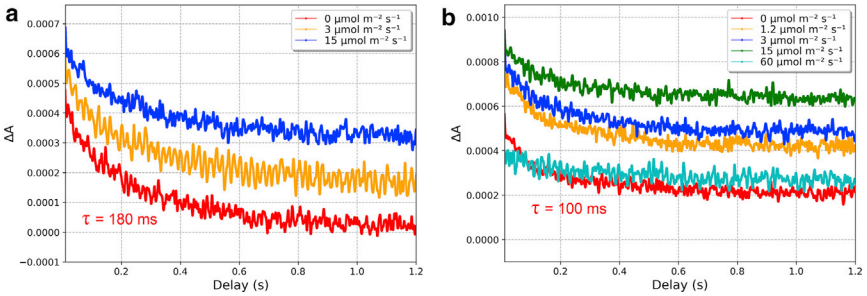

FIGURE 3 (*a* and *b*) Nanosecond laser pulse-induced ΔA kinetics (5 mJ, 532 nm) probed at 550 nm in the presence of various intensities of stationary LED irradiation at 452 nm for (*a*) C-tagged and (*b*) N-tagged OCP. The indicated time constant was retrieved using a monoexponential fit of the red curve (no 452 nm LED irradiation).

the $OCP^{1h\nu}$ intermediate states but also OCP^R at a much larger number. Therefore, at some threshold intensity of continuous irradiation light, ΔA should not increase anymore due to a significant depletion of the dark-adapted OCP^O form. If most of the sample is photoconverted to OCP^R population by the continuous irradiation, the amplitude of ns pulse-induced ΔA signal should decrease. Note that it was demonstrated that OCP^R is a non-photoactive state (3). Indeed, in N-tagged OCP above 15 μmol m^{-2} s^{-1} light intensity, the signal saturates (Fig. 3 *b*, *green kinetic*), and above 60 μmol m^{-2} s^{-1} intensity, the signal drops significantly (Fig. 3 *b*, *cyan kinetic* at 1 s). As expected, only low levels of continuous irradiation allow us to observe two-photon behavior manifested by an increase in ΔA(1 s) because strong irradiation causes significant depletion of OCP^O.

DISCUSSION

Continuous irradiation experiments and nanosecond pulse with continuous irradiation experiments were performed to bridge photoexcitation with laser pulses and continuous light. A sequential two-photon mechanism is feasible for the continuous LED source above certain power threshold, leading to a differential quantum yield φ_d dependence extracted from the irradiation kinetics (Fig. 2 *b*). Fig. 4 attempts to illustrate this effect by showing a millisecond transient absorption signal obtained after nanosecond excitation superimposed with the integrated number of photons to be absorbed by a single $OCP^{1h\nu}$ molecule living during a given period (which equals $I_0\, F\, \epsilon_{OCP^R}\, l_{irr}\, t$, calculated by integration of Eq. 1). As one can see, this number is close to one photon absorbed within 1 s when 200 μmol m^{-2} s^{-1} light is present. The green area between both curves indicates a temporal region where the probability of absorption of a second photon is significant, and there still exist some intermediate $OCP^{1h\nu}$ states that can absorb another photon. This region is almost negligible for a low light intensity illumination (10 μmol m^{-2} s^{-1}; Fig. 4, *below blue line*) but quite significant for high light intensity (200 μmol m^{-2} s^{-1}; Fig. 4, *below red line*).

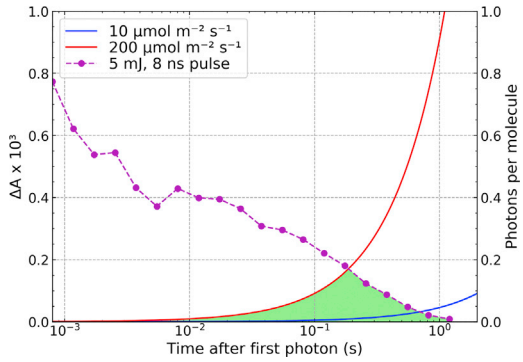

FIGURE 4 ΔA kinetics at 550 nm obtained for C-tagged OCP at 21°C using a nanosecond laser pulse (*red curve* from Fig. 3 *a*) compared with the cumulative number of photons absorbed by $OCP^{1h\nu}$ red intermediate until a given time. For 200 μmol m^{-2} s^{-1} continuous irradiation, the red intermediate formed upon absorption of a single photon and living exactly 1 s will absorb almost 1 photon (which will be its second) on average.

Fig. 4 shows clearly that absorption of a second photon in less than 10 ms after absorption of the first one is very improbable when using biologically relevant light intensities. Therefore, the $OCP^{1h\nu}$ intermediate must live longer than that, otherwise we would not have observed the two-photon absorption characteristics (Fig. 2). One can also exclude that the intermediate lives longer than 1 s because the absorption kinetics grow instantly after switching the light on and ΔA decays instantly after switching the light off (Fig. 1). Therefore, the $OCP^{1h\nu}$ intermediate must be a short-lived state, otherwise one would see an increase in dA/dt (acceleration) at the beginning of the irradiation due to accumulation of the intermediate, which clearly is not the case. The observed ≈100 ms lifetime red-shifted species seems to be a good candidate for $OCP^{1h\nu}$. It seems to be equivalent of P_X state proposed by Maksimov et al. (8) Indeed, the simulation presented in Fig. S4 with the two-photon photochemical scheme of Fig. 2 *d* can reproduce the curvature observed in Fig. 2 *b*. However, it remains an open question whether the decay at 550 nm observed after laser pulse excitation only is really associated with $OCP^{1h\nu}$.

Our results are contradictory to some of the previous reports (3,17) that have concluded a linear dependence of the photon flux density on the initial light-induced dA/dt. However, in previous nanosecond and femtosecond time-revolved absorption experiments, it was shown that only very small fraction of red-shifted OCP species is formed at 1 ns (values between 0.2% and 1.5% are given (5,20)), and almost nothing remains after 1 s (5,7–9,23). We found for C-tagged OCP that upon nanosecond pulse excitation at 532 nm, the absorbance at 550 nm drops to almost zero before 1 s (Fig. 4), indicating that there should not be any long-lived OCP^R species. So, the question arises:how is it possible that upon continuous irradiation, a significant population of OCP^R is formed with a lifetime much longer than 1 s when we clearly see that this species decays much earlier (<1 s) in laser pulse excitation experiments (Fig. 4)? This question leads to the conclusion that a second photon must be required in the mechanism to transform the partially photoactivated "OCP^R-like" ($OCP^{1h\nu}$ from Fig. 2 *d*) intermediate into a long-living OCP^R red form. If a sequential two-photon mechanism is indeed present, then discrepancies between this and various previous studies

may originate from different repetition rates of the experiments. With repetition rates faster than 1 Hz, it is also possible that the observed species are a result of absorption of two consecutive photons (or more). For example, in our nanosecond experiments, we have found that the ΔA kinetics depend on the repetition rate; the usage of a single laser pump pulse per 10–20 s was required to avoid this effect.

CONCLUSIONS

Here, we present compelling evidence that the mechanism of OCP photoactivation cannot be described by single-photon absorption, followed by a chain of thermally decaying intermediates leading to the OCP^R, as described in the currently available literature. We found that absorption of a second photon must be incorporated into the photoactivation mechanism. From our data, it is also clear that the location of His-tag (facilitating protein purification) affects the millisecond kinetics and nature of the photoactivation in a dramatic way, resulting in different photoactivation speeds (20). In C-tagged OCP, the two-photon nature is much more pronounced compared with N-tagged OCP. Nevertheless, the nanosecond laser pulse-induced kinetics points to a two-photon photoactivation mechanism also in N-tagged OCP because the ΔA signal at 1 s triples upon auxiliary continuous irradiation (0.002 to 0.006; Fig. 3 *b*). In C-tagged OCP, our data exclude a single-photon photoactivation channel because almost no ΔA signal is observed at 1 s after nanosecond pulse excitation. The majority of the photoactivation models proposed so far for OCP take the form of different $OCP^O \rightarrow P_1 \rightarrow P_2 \rightarrow \ldots \rightarrow OCP^R$ chains (5,8). We believe that this commonly accepted single-photon mechanism must be reevaluated.

SUPPORTING MATERIAL

Supporting material can be found online at https://doi.org/10.1016/j.bpr.2022.100072.

AUTHOR CONTRIBUTIONS

Conceptualization, S.N., M.S., G.B., D.K., and J.-P.C.; methodology, S.N., M.S., G.B., D.K., and J.-P.C.; simulations, S.N.; experiments and data analysis, S.N.; resources, D.K.; writing, S.N., M.S., G.B., D.K., and I.S.; supervision, M.S., G.B., D.K., J.-P.C., and I.S.

ACKNOWLEDGMENTS

We are grateful to Adjéle Wilson for supplying the purified proteins. This work was performed with financial support from the Polish National Science Centre (NCN), project 2018/31/N/ST4/03983, and the French National Research Agency (grant ANR-18-CE11-0005).

DECLARATION OF INTERESTS

The authors declare no competing interests.

REFERENCES

1. Kay Holt, T., and D. W. Krogmann. 1981. A carotenoid-protein from cyanobacteria. *Biochim. Biophys. Acta Bioenerg.* 637: 408–414.
2. Wilson, A., G. Ajlani, …, D. Kirilovsky. 2006. A soluble carotenoid protein involved in phycobilisome-related energy dissipation in cyanobacteria. *Plant Cell.* 18:992–1007.
3. Wilson, A., C. Punginelli, …, D. Kirilovsky. 2008. A photoactive carotenoid protein acting as light intensity sensor. *Proc. Natl. Acad. Sci. USA.* 105:12075–12080.
4. Kirilovsky, D., and C. A. Kerfeld. 2016. Cyanobacterial photoprotection by the orange carotenoid protein. *Native Plants.* 2:16180–16197.
5. Konold, P. E., I. H. M. van Stokkum, and J. T. M. Kennis. 2019. Photoactivation mechanism, timing of protein secondary structure dynamics and carotenoid translocation in the Orange Carotenoid Protein. *J. Am. Chem. Soc.* 141:520–530.
6. Leverenz, R. L., M. Sutter, and C. A. Kerfeld. 2015. A 12 Å carotenoid translocation in a photoswitch associated with cyanobacterial photoprotection. *Science.* 348:1463–1466.
7. Wilson, A., E. A. Andreeva, J. P. Colletier…, 2022. Structure-function-dynamics relationships in the peculiar Planktothrix PCC7805 OCP1: impact of his-tagging and carotenoid type. *Biochim Biophys Acta Bioenerg.* 1863 (7):148584–148608. https://doi.org/10.1016/j.bbabio.2022.148584.
8. Maksimov, E. G., E. A. Protasova, …, T. Friedrich. 2020. Probing of carotenoid-tryptophan hydrogen bonding dynamics in the single-tryptophan photoactive Orange Carotenoid Protein. *Sci. Rep.* 10. 11729-12.
9. Maksimov, E. G., N. N. Sluchanko, …, A. B. Rubin. 2017. The photocycle of orange carotenoid protein conceals distinct intermediates and asynchronous changes in the carotenoid and protein components. *Sci. Rep.* 7. 15548-12.
10. Yaroshevich, I. A., E. G. Maksimov, …, M. P. Kirpichnikov. 2021. Role of hydrogen bond alternation and charge transfer states in photoactivation of the Orange Carotenoid Protein. *Commun. Biol.* 4:539-13.
11. Kuznetsova, V., M. A. Dominguez-Martin, …, T. Polívka. 2020. Comparative ultrafast spectroscopy and structural analysis of OCP1 and OCP2 from Tolypothrix. *Biochim. Biophys. Acta Bioenerg.* 1861. 148120-11.
12. Rakhimberdieva, M. G., I. N. Stadnichuk, …, N. V. Karapetyan. 2004. Carotenoid-induced quenching of the phycobilisome fluorescence in photosystem II-deficient mutant of Synechocystis sp. *FEBS Lett.* 574:85–88.
13. Karapetyan, N. V. 2007. Non-photochemical quenching of fluorescence in cyanobacteria. *Biochemistry.* 72:1127–1135.
14. Gorbunov, M. Y., F. I. Kuzminov, …, P. G. Falkowski. 2011. A kinetic model of non-photochemical quenching in cyanobacteria. *Biochim. Biophys. Acta.* 1807:1591–1599.
15. Gwizdala, M., A. Wilson, and D. Kirilovsky. 2011. In vitro reconstitution of the cyanobacterial photoprotective mechanism mediated by the Orange Carotenoid Protein in Synechocystis PCC 6803. *Plant Cell.* 23:2631–2643.
16. Rakhimberdieva, M. G., F. I. Kuzminov, …, N. V. Karapetyan. 2011. Synechocystis sp. PCC 6803 mutant lacking both photosystems exhibits strong carotenoid-induced quenching of phycobilisome fluorescence. *FEBS Lett.* 585:585–589.
17. Maksimov, E. G., E. A. Shirshin, …, A. B. Rubin. 2015. The signaling state of Orange Carotenoid Protein. *Biophys. J.* 109:595–607.

18. Mezzetti, A., M. Alexandre, …, D. Kirilovsky. 2019. Two-step structural changes in Orange Carotenoid Protein photoactivation revealed by Time-Resolved Fourier Transform Infrared Spectroscopy. *J. Phys. Chem. B.* 123:3259–3266.

19. Ritchie, R. J. 2010. Modelling photosynthetic photon flux density and maximum potential gross photosynthesis. *Photosynthetica.* 48:596–609.

20. Nizinski, S., A. Wilson, …, M. Sliwa. 2022. A unifying perspective of the ultrafast photo-dynamics of Orange Carotenoid Protein from Synechocystis: peril of high-power excitation, existence of different S* states and influence of tagging. *JACS Au.* 2:1084–1095. https://doi.org/10.1021/jacsau.1c00472.

21. Deniel, M. H., D. Lavabre, and J. C. Micheau. 2002. Photokinetics under continuous irradiation. *In* Organic photochromic and thermochromic compounds volume 2: physicochemical studies, biological applications, and thermochromism. J. C. Crano and R. J. Guglielmetti, eds. Kluwer Academic Publishers, pp. 167–182.

22. Chalk, S. J. 2019. *In* IUPAC. Compendium of Chemical Terminology, Second edition the "Gold Book". https://goldbook.iupac.org/terms/view/Q04991.

23. Andreeva, E. A., S. Nizinski, J. P. Colletier…, 2022. Oligomerization processes limit photoactivation and recovery of the Orange Carotenoid Protein. *Biophys. J.* 121:2849–2872. https://doi.org/10.1016/j.bpj.2022.07.004.

Biophysical Reports, Volume *2*

Supplemental information

Is orange carotenoid protein photoactivation a single-photon process?

Stanisław Niziński, Ilme Schlichting, Jacques-Philippe Colletier, Diana Kirilovsky, Gotard Burdzinski, and Michel Sliwa

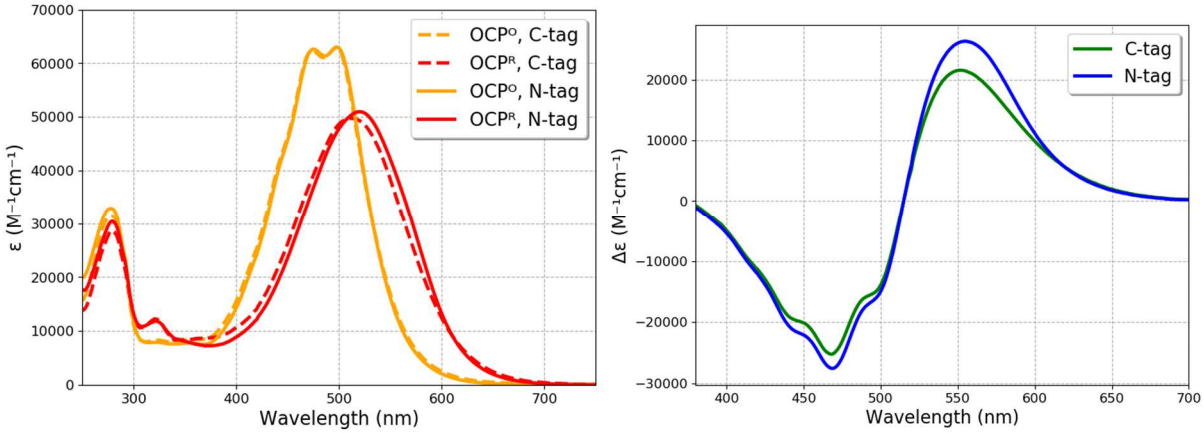

Figure S1. a) Absorption spectra of OCP^O, OCP^R and b) difference OCP^R-OCP^O absorption spectra represented as molar extinction coefficients (452 nm irradiation, 11 °C).

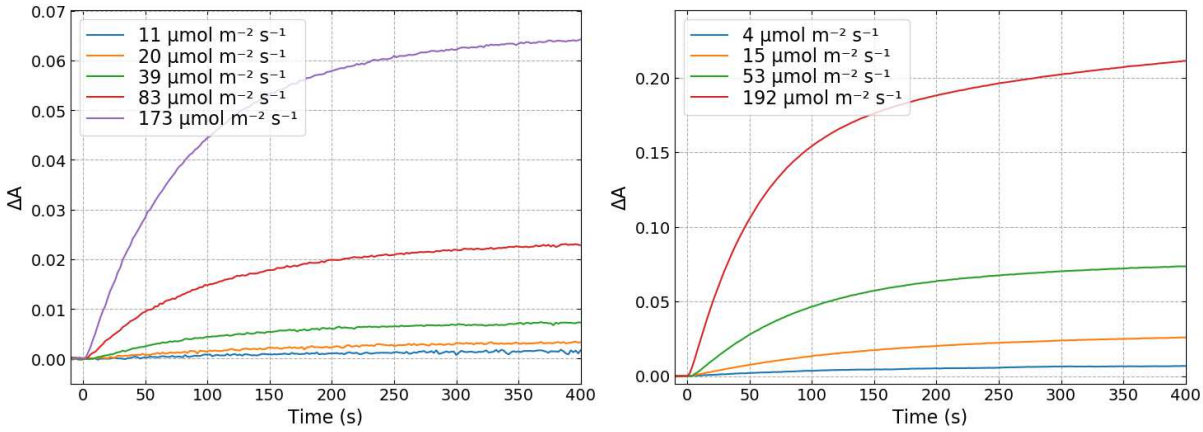

Figure S2. ΔA kinetics measured at 550 nm of a) C-tagged, b) N-tagged OCP upon 452 nm continuous irradiation switched on at 0 s.

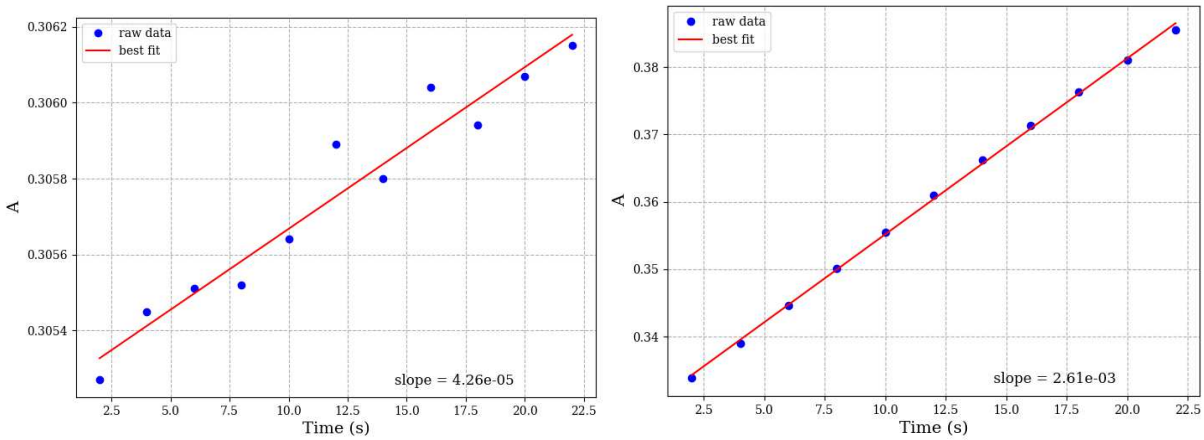

Figure S3. Linear fit of A(550 nm) after start of the 452 nm irradiation to determine initial dA/dt. Done for a) 4 µmol s^{-1} m^{-2}, b) 192 µmol s^{-1} m^{-2} photon flux density, for N-tagged OCP.

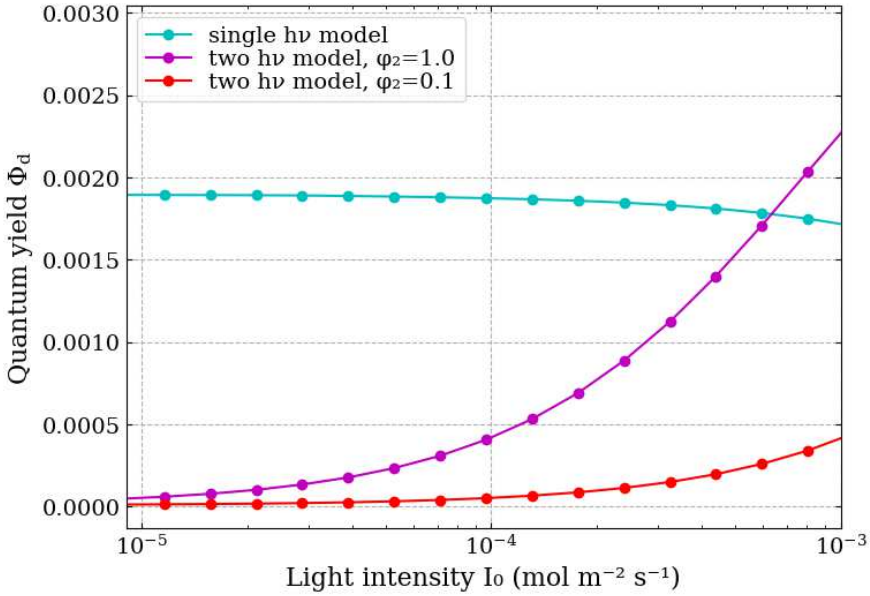

Figure S4. Differential quantum yield ϕ_d extracted from the simulated photoactivation kinetics.

Table S1. Extracted time constants and preexponential factors (normalized to 100%) from the thermal back recovery kinetics of OCP^R (C-tagged, probe at 580 nm). At the highest used photon flux density (≈200 µmol s^{-1} m^{-2}), τ_1 dominates. Therefore, τ_1 value was used as an input for the two photon model.

I_0 (µmol s^{-1} m^{-2})	τ_1 (s)	A_1	τ_2 (s)	A_2
12	23	14	349	86
24	81	49	516	51
45	69	55	394	45
103	75	74	336	26
195	92	89	738	11

Supplemental materials, protein, experiments and simulation details:

Sample preparation

The plasmid pCDF-NtagOCPSyn used for expression of OCP from *Synechocystis* PCC 6803 carries a sequence coding for a His-tag at the N terminus, and has been characterized in Bourcier de Carbon et al.[1] The expression of the *ocp* genes in *E. coli.* cells containing the genes for synthesis of echinenone and the isolation of ECN-OCP was also described in Bourcier de Carbon et al.[1] The expression of the *ocp* genes in *Synechocystis* has been reported by Gwizdala et al.[2] N-tagged OCP was expressed in *E. coli.*, while C-tagged OCP was expressed in the crtR *Synechocystis* mutant lacking zeaxanthin and hydroxyechinenone. The protein concentrations used in the experiments described in this work were between 0.3 – 0.6 mg/ml (0.5 – 1.1 absorbance on 1 cm at absorption maximum and using 63 000 M^{-1}cm^{-1} extinction coefficient at the maximum at 490 nm[3]). Low concentration minimize presence of OCP^O dimers.[4] 40 mM Tris HCl pH 8.0 buffer was used.

Photoactivation of OCP under stationary irradiation

The kinetics upon continuous irradiation were measured in a 2×10 mm quartz cuvette (*Hellma*), where the probing light path is 10 mm and irradiation light path is 2 mm, sample volume 0.3 mL (Scheme S1). In this configuration following conditions can be ensured: i) absorbance of the irradiation light is relatively small (absorbance is below 0.2 at 452 nm) thus there is no gradient of absorbed light along this path (sample is irradiated uniformly over whole volume), ii) absorbance changes visible by the probe are large due to a longer path length, iii) there is efficient sample temperature cooling due to large surface of the internal cuvette cavity. Our experimental setup is shown in Scheme S1. The study of OCP photoactivation was done using a Jasco V-550 spectrophotometer and by following the kinetics of absorbance every 2 s (integration time) at 550 nm or 580 nm probing wavelengths, with longpass filter after the sample to remove scattered irradiation light. This instrument provided a very good S/N ratio, together with a very weak probing light intensity and a long term stability. To irradiate the sample, a 452 nm blue LED (custom made module with standard 3 W emitter) was used, collimated by an aspheric lens. The range of used photon flux densities was 5 - 200 μmol m^{-2} s^{-1}. The light intensity was determined using a power meter and ferrioxalate actinometer, prepared as described previously[5]. Both methods provided similar results, however the one obtained using the actinometer was later used due to higher reliability (the actinometer reflects the true number of absorbed photons). The temperature of the experiments was 21 °C (unless stated otherwise), stabilized using a Quantum Northwest temperature holder. The whole volume of the sample was irradiated uniformly, so no stirring was needed.

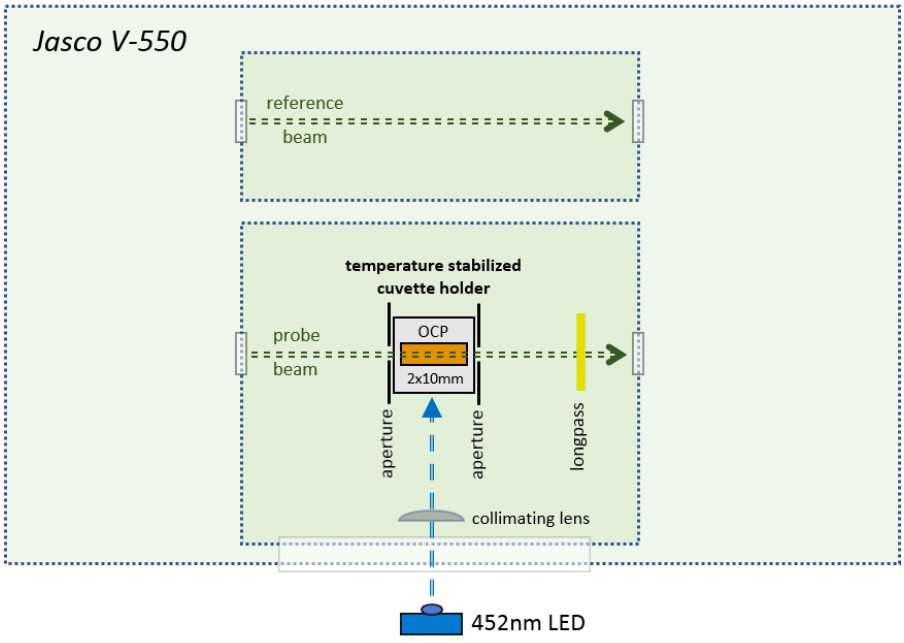

Scheme S1. Scheme of the experiments for the study of OCP photoactivation upon continuous irradiation at 452 nm

Modelling of OCP photoconversion upon stationary irradiation

The modelling of the stationary photoconversion experiment was done using our custom package written in Python. Source of performed simulations can be found as an exemplary code named "differential quantum yield for two vs single photon model.py" in the package repository (doi.org/10.5281/zenodo.6639706). It is designed to build system of equations analogically to eq. 1, based on a model diagram (Schemes S2 and S3 were used). These equations are then solved by the *odeint* procedure from *scipy.integrate*. We used two toy models, with the intent to visualize the differences between two photon and single photon classes of models.

By single photon model we consider any model where the main photoactivation pathway is initialized by absorption of one photon, which decays to the initial (dark OCP^O) state or to the photoactivated (OCP^R) state. Our "exemplary" single photon model (Scheme S2) possess only two species: OCP^O and OCP^R. Absorption of a photon by OCP^O results in formation of OCP^R with 0.002 yield (0.001 – 0.002 is a common quantum yield found in the literature[6-8]). There is only one thermal back recovery process allowing OCP^R to decay to the OCP^O form with a rate constant k = 0.011 s^{-1} (τ = 92 s, like in Table S1 for irradiation 195 µmol s^{-1} m^{-2}). A decay time constant of $\tau \approx 90$ s is commonly encountered when investigating OCP in high irradiation conditions (check Table S1). The molar absorption coefficients for both species are assumed like in ECN containing C-tagged OCP from *Synechocystis* (see Figure S1a). The probing pathlength is 10 mm, irradiation pathlength is 2 mm, like in the experiment. This model is described by eq. 1. Note that this model acknowledges any ensemble of intermediates, which decay faster than the instrument temporal resolution (≈ 1 s), leaving only OCP^O or OCP^R forms.

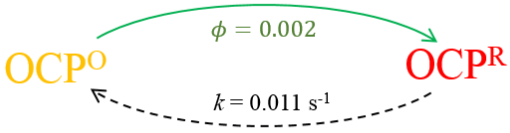

Scheme S2. Single photon model used for the simulations

The class of two photon models is much more diverse because one can implement two subsequent photoinduced electronic transitions in a many different ways depending on the mechanistic scenario. In the specific case of OCP, we considered a photo-active intermediate state which lives longer than a few tens of milliseconds (absorption of two photons within 10ms or less is improbable with sunlight due to its low photon flux density), but shorter than a second (otherwise we would see that during the first seconds of irradiation the process "speeds up" due to accumulation of the intermediate state). In the nanosecond transient absorption experiment, we found that there is some red absorbing species decaying below 1s at room temperature (see Figure 3a). It seems to be a good candidate for the intermediate state. Therefore in our exemplary two photon model (Scheme S3), we added the $OCP^{1h\nu}$ state, for which the same molar absorption coefficient was assumed as for OCP^R. To show the behavior of the two photon models, the following assumptions were made: There are two consecutive photonic transitions: $OCP^O + h\nu \rightarrow OCP^{1h\nu}$ (with a quantum yield $\phi_1 = 0.005$) and $OCP^{1h\nu} + h\nu \rightarrow OCP^R$ (quantum yield is unknown, therefore we presented two cases $\phi_2 = 1.0$ and $\phi_2 = 0.1$). The ϕ_1 value was selected to reflect the yield of the species populated in ns-µs timescale[9-10]. The product of ϕ_1 and ϕ_2 should be of the same order of magnitude as the differential quantum yield ϕ_d extracted from initial dA/dt recorded during the continuous irradiation experiment. There are two thermal processes: $k_1 = 0.011$ s^{-1} ($OCP^R \rightarrow OCP^O$) and $k_2 = 5.6$ s^{-1} ($OCP^{1h\nu} \rightarrow OCP^O$, τ_2 = 180 ms is extracted from the red curve in Figure 3a). k_1 is assumed to be the same as k in the single

photon model, while k_2 reflects approximately the decay of the red spectral feature on the hundreds of millisecond time scale. The model can be solved using following equations:

$$\frac{d[OCP^O]}{dt} = -\phi_1 I_0 F [OCP^O] \epsilon_{OCP^O} l_{irr} + k_2 [OCP^{1hv}] + k_1 [OCP^R] \quad \text{(S1)}$$

$$\frac{d[OCP^{1hv}]}{dt} = \phi_1 I_0 F [OCP^O] \epsilon_{OCP^O} l_{irr} - \phi_2 I_0 F [OCP^{1hv}] \epsilon_{OCP^{1hv}} l_{irr} - k_2 [OCP^{1hv}] \quad \text{(S2)}$$

$$\frac{d[OCP^R]}{dt} = \phi_2 I_0 F [OCP^{1hv}] \epsilon_{OCP^{1hv}} l_{irr} - k_1 [OCP^R] \quad \text{(S3)}$$

Identical molar absorption coefficients for OCP^R and OCP^{1hv} at 452nm were assumed ($\epsilon_{OCP^{1hv}} = \epsilon_{OCP^R}$). Equations above are used to calculate concentration profiles for all three OCP forms (OCP^O, OCP^R and OCP^{1hv}). Then concentrations are converted to absorbance using Beer-Lambert law, and assuming 10 mm probing length and identical molar absorption coefficients at 550nm for OCP^R and OCP^{1hv}. Molar absorption coefficients for OCP^O and OCP^R are given in Figure S1a. Simulation was repeated for various photon flux densities, and initial dA/dt was calculated in the same way as was done for experimental data. The results are presented in Figure S4.

Note, that this model does not reproduce fully the nature of OCP photoactivation. Thermal back recovery of OCP^R isn't monoexponential and extra species could be involved. The parameters used are based on observed experimental features, and they are not free from ambiguity. One can find many sets of parameters reflecting the dependence in Figure 2. Moreover, one can find more complex models that will fit the experimental data, however the scheme S3 is somehow the most simple one that avoid over-parametrization and reproduce the dependence of differential quantum yield with irradiation light and the curvature observed in Figure 2b. The study of all the models that reproduce experimental data (not only the dA/dt but also its dependence of the temperature) is a very complex task and exceeds greatly the scope of this article. Here, the intention is only to present an example of a simple two photon model that reproduces the increase of the differential quantum yield Φ with the photon flux density with the usage of parameters which are observed experimentally.

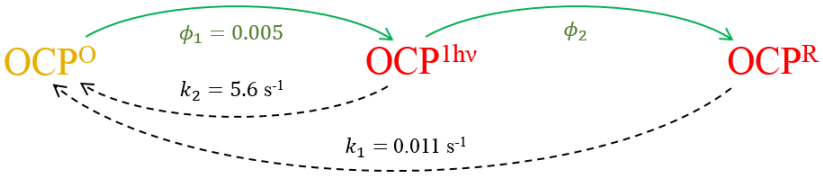

Scheme S3. Two photon model used for the simulations

Nanosecond transient absorption measurements

The nanosecond transient absorption kinetics were recorded with nanosecond pulse excitation at 532 nm, 5 mJ per pulse, as presented in the Scheme S4. The laser pulse is delivered by a Q-switched flashlamp pumped Nd:YAG laser (*Continuum Surelite II*), using its second harmonic; it is characterized by 6 mm spatial and 8 ns temporal widths (FWHM), which yields 12 mJ/cm^2, or 0.5 mmol m^{-2} in the center of the pulse. A right angle configuration was used, with probing light at 550 nm. The probing source was a standard white LED emitter (custom made module), filtered using a 550 nm bandpass filter (FWHM = 10 nm). A 532 nm notch filter (*Thorlabs*) was used to suppress the scattered pump light from the probing beam. The probing light goes through monochromator (*SpectraPro-300i Acton Research* equipped with 300 g/mm grating) and is collected by a *R928 Hamamatsu* PMT (with 5 active dynodes). A *Tektronix TDS 680 C* oscilloscope, triggered by the laser pulse, is used to register the kinetics of ΔA with 15 000 samples in the time range record and 20 MHz lowpass filter, and 5 kΩ input impedance. The experiment repetition was 10 s between each kinetics registered, 100 kinetics in total used for averaging. The additional irradiation was done from the top of the cuvette, with a 452 nm LED (located directly above the sample), therefore the irradiation intensities given in this case are only rough approximates (the light intensity is not uniform over the whole cuvette volume). The intensities were within the range 1.2 - 60 µmol m^{-2} s^{-1}. The probe shutter was opened for a 1.25 s period every 10 s to probe the sample. Only the probed volume of the cuvette was excited by the nanosecond pulse, not the whole sample volume (around 2 mL). No stirring was applied to afford a long probing time window. The experiment consists of two cycles repeating alternately: i) reference kinetic ($I_{ref}(t)$) is done with the probing light only, and then ii) second kinetic is measured after the absorption of the laser pulse ($I_{exc}(t)$). At the end all the $I_{ref}(t)$ and $I_{exc}(t)$ are averaged (separately), and finally the differential absorption is calculated as $\Delta A(t) = -log_{10}\left(I_{exc}(t)/I_{ref}(t)\right)$. Note, that if there is some factor influencing both $I_{exc}(t)$ and $I_{ref}(t)$ kinetics identically, it compensates, and the final $\Delta A(t)$ kinetic will stay unaffected. Therefore, $\Delta A(t)$ tracks exclusively laser pulse-induced evolution.

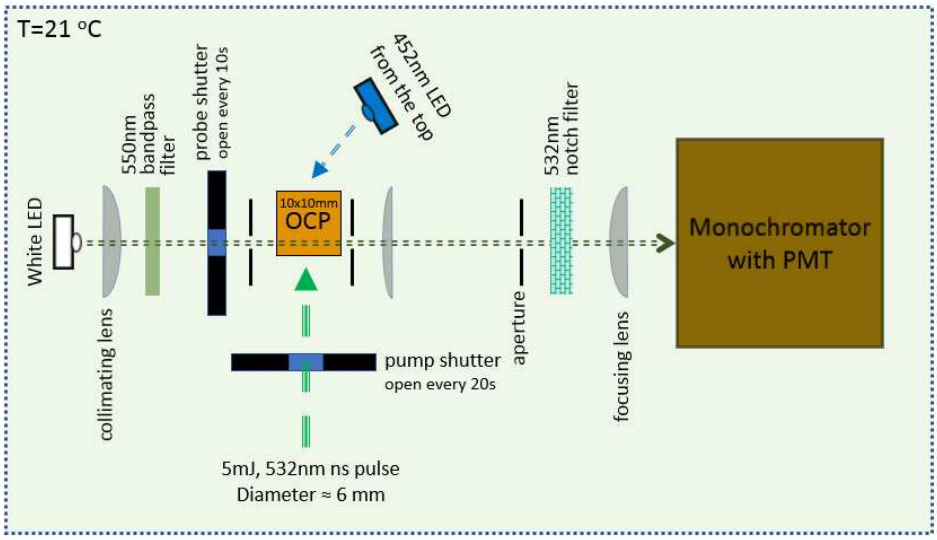

Scheme S4. Setup used to measure laser pulse induced kinetics in the presence of continuous irradiation at 452 nm.

Supplemental References:

1. Bourcier de Carbon, C.; Thurotte, A.; Wilson, A.; Perreau, F.; Kirilovsky, D. Biosynthesis of soluble carotenoid holoproteins in Escherichia coli. *Sci. Rep.* **2015,** *5* (9085), 1-8.
2. Gwizdala, M.; Wilson, A.; Kirilovsky, D. In vitro reconstitution of the cyanobacterial photoprotective mechanism mediated by the Orange Carotenoid Protein in Synechocystis PCC 6803. *The Plant Cell* **2011,** *23* (7), 2631-2643.
3. Sluchanko, N. N.; Klementiev, K. E.; Shirshin, E. A.; Tsoraev, G. V.; Friedrich, T.; Maksimov, E. G. The purple Trp288Ala mutant of Synechocystis OCP persistently quenches phycobilisome fluorescence and tightly interacts with FRP. *Biochim Biophys Acta* **2017,** *1858* (1), 1-11.
4. Andreeva, E. A.; Nizinski, S.; Wilson, A.; Levantino, M.; De Zitter, E.; Munro, R.; Muzzopappa, F.; Thureau, A.; Zala, N.; Burdzinski, G.; Sliwa, M.; Kirilovsky, D.; Schirò, G.; Colletier, J. P. Oligomerization processes limit photoactivation and recovery of the Orange Carotenoid Protein. *Biophys J.* **2022,** *121* (15), 2849-2872.
5. Brazevic, S.; Nizinski, S.; Szabla, R.; Rode, M. F.; Burdzinski, G. Photochromic reaction in 3H-naphthopyrans studied by vibrational spectroscopy and quantum chemical calculations. *Phys. Chem. Chem. Phys.* **2019,** *21*, 11861-11870.
6. Maksimov, E. G.; Sluchanko, N. N.; Slonimskiy, Y. B.; Slutskaya, E. A.; Stepanov, A. V.; Argentova-Stevens, A. M.; Shirshin, E. A.; Tsoraev, G. V.; Klementiev, K. E.; Slatinskaya, O. V.; Lukashev, E. P.; Friedrich, T.; Paschenko, V. Z.; Rubin, A. B. The photocycle of orange carotenoid protein conceals distinct intermediates and asynchronous changes in the carotenoid and protein components. *Sci. Rep.* **2017,** *7* (15548), 1-12.
7. Gorbunov, M. Y.; Kuzminov, F. I.; Fadeev, V. V.; Kim, J. D.; Falkowski, P. G. A kinetic model of non-photochemical quenching in cyanobacteria. *Biochim Biophys Acta Bioenerg* **2011,** *1807* (12), 1591-1599.
8. Maksimov, E. G.; Shirshin, E. A.; Sluchanko, N. N.; Zlenko, D. V.; Parshina, E. Y.; Tsoraev, G. V.; Klementiev, K. E.; Budylin, G. S.; Schmitt, F. J.; Friedrich, T.; Fadeev, V. V.; Paschenko, V. Z.; Rubin, A. B. The signaling state of Orange Carotenoid Protein. *Biophys J.* **2015,** *109* (3), 595-607.
9. Wilson, A.; Andreeva, E. A.; Nizinski, S. J.; Talbot, L.; Hartmann, E.; Schlichting, I.; Burdzinski, G.; Sliwa, M.; Kirilovsky, D.; Colletier, J. P. Structure-function-dynamics relationships in the peculiar Planktothrix PCC7805 OCP1: impact of his-tagging and carotenoid type. *Biochim Biophys Acta Bioenerg* **2022,** *1863* (7), 148584-148608.
10. Maksimov, E. G.; Protasova, E. A.; Tsoraev, G. V.; Yaroshevich, I. A.; Maydykovskiy, A. I.; Shirshin, E. A.; Gostev, T. S.; Jelzow, A.; Moldenhauer, M.; Slonimskiy, Y. B.; Sluchanko, N. N.; Friedrich, T. Probing of carotenoid-tryptophan hydrogen bonding dynamics in the single-tryptophan photoactive Orange Carotenoid Protein. *Sci. Rep.* **2020,** *10* (11729), 1-12.

Poznań, 18.05.2023

Stanisław Niziński
Wydział Fizyki UAM
Ul. Uniwersytetu Poznańskiego 2,
61-614 Poznań

I hereby declare that my contribution to the presented publications have been as follows:

Nizinski, S.; Wilson, A.; Uriarte, L. M.; Ruckebusch, C.; Andreeva, E. A.; Schlichting, I.; Colletier, J. P.; Kirilovsky, D.*; Burdzinski, G.*; Sliwa, M.* A unifying perspective of the ultrafast photo-dynamics of Orange Carotenoid Proteins from Synechocystis: Peril of high-power excitation, existence of different S* states and influence of tagging. *JACS Au* **2022,** 2 (5), 1084–1095.

My contribution to this article:

1) Performing all of the experiments on 2 different proteins (femtosecond vis-NIR transient absorption measurements, UV-vis absorption measurements in the dark and upon continuous irradiation).
2) Preprocessing and analysis of the transient absorption data, fitting of the data and making figures and table.
3) Writing initial version of the manuscript and supporting information, taking part in the finalization of the submitted manuscript with its supporting materials, participating actively in the response process (three revised versions) before the final published version.
4) Participation in the scientific discussion and finalization of the final photodynamical scheme including the excited state that controls the photoconversion, and influence of excitation power on formation quantum yield of the first red species of OCP^R.

Wilson, A.; Andreeva, E. A.; Nizinski, S. J.; Talbot, L.; Hartmann, E.; Schlichting, I.; Burdzinski, G.; Sliwa, M.*; Kirilovsky, D.*; Colletier, J. P.* Structure-function-dynamics relationships in the peculiar Planktothrix PCC7805 OCP1: Impact of his-tagging and carotenoid type. *Biochim Biophys Acta Bioenerg* **2022**, 1863 (7), 148584.

My contribution to this article:

1) Performing visible femtosecond transient absorption measurements and nanosecond transient absorption measurements on 4 different proteins.
2) Preprocessing and analysis of the visible femtosecond transient absorption measurements and nanosecond transient absorption data, fitting of these data and making figures and table related to femtosecond-millisecond time resolved experiments in the manuscript.
3) Determination of the OCP^R formation quantum yield with single laser pulse excitation.
4) Optimization of nanosecond – second transient absorption experiments to measure very low yield photo-activation process.
5) Writing the section related to femtosecond-millisecond time-resolved experiments and OCP^R formation quantum yield in the manuscript (for the submitted version and one revised version with response to reviewer).
6) Reading, participation and comments to the final results of the article, especially about intermediate states that influence the formation quantum yield of OCP^R for investigated proteins.

Andreeva, E. A.; Nizinski, S.; Wilson, A.; Levantino, M.; De Zitter, E.; Munro, R.; Muzzopappa, F.; Thureau, A.; Zala, N.; Burdzinski, G.; Sliwa, M.; Kirilovsky, D.; Schirò, G.; Colletier, J. P.* Oligomerization processes limit photoactivation and recovery of the Orange Carotenoid Protein. *Biophys J.* **2022**, 121 (15), 2849-2872.

My contribution to this article:

1) Performing nanosecond transient absorption measurements for different concentrations (in the collinear and right-angle configurations) and temperature for 2 different proteins.
2) Preprocessing and analysis of nanosecond transient absorption data, fitting of these data for different temperatures, performing thermodynamic analysis, and making figures and table in the manuscript and supporting information.
3) Optimization of nanosecond – millisecond transient absorption experiments to measure very low and very high concentration absorbing species (collinear excitation) for a very low yield photo-activation process.
4) Writing the section related to nanosecond-millisecond time resolved experiments in the manuscript and supporting information (for the submitted version and one revised version with response to reviewer).
5) Reading, participation and comments to the final results of the article, especially on the existence of the oligomers in solution that can influence the kinetics and number of intermediates in the photoconversion scheme.

Niziński, S.*; Schlichting, I.; Colletier, J. P.; Kirilovsky, D.; Burdziński, G.*; Sliwa, M.* Is Orange Carotenoid Protein photoactivation a single-photon process? *Biophys. Rep.* **2022**, 2 (3), 100072.

My contribution to this article:

1) Performing all of the photoconversion experiments upon different irradiation power and different excitation configurations for two different proteins (nanosecond transient absorption measurements, UV–vis absorption measurements in the dark and upon continuous irradiation and transient absorption measurements with additional continuous irradiation).
2) Preprocessing and analysis of the transient absorption data and making figures for the manuscript and supporting information.
3) Performing simulations of the OCP^R accumulation based on various hypothetical photoconversion models and creating a Python package used to analyze the data (https://doi.org/10.5281/zenodo.6639706).
4) Writing the initial version of the manuscript and supporting information, taking part in the finalization of the submitted version of the manuscript with its supporting materials, participating actively in the response process (one revised version) before the final published version.
5) Participation in the scientific discussion, and finalization of the photoconversion scheme with the existence of a two photon mechanism for the formation of the OCP^R form.

Stanisław Niziński

Stanisław Niziński

potwierdza promotor
Gotard Burdziński

prof. dr hab. Gotard Burdziński

Wydział Fizyki Uniwersytetu im. Adama Mickiewicza w Poznaniu

ul. Uniwersytetu Poznańskiego 2, 61-614 Poznań

I declare that I am the co-author of the following publications and my contribution is as follows:

Nizinski, S.; Wilson, A.; Uriarte, L. M.; Ruckebusch, C.; Andreeva, E. A.; Schlichting, I.; Colletier, J. P.; Kirilovsky, D.; Burdzinski, G.*; Sliwa, M.* A unifying perspective of the ultrafast photo-dynamics of Orange Carotenoid Proteins from Synechocystis: Peril of high-power excitation, existence of different S* states and influence of tagging. JACS Au* ***2022,*** *2 (5), 1084–1095.*

My contribution to this article:

1) Supervising the analysis, quality and reproducibility of the experiments (femtosecond vis-NIR transient absorption measurements, UV-vis absorption measurements in the dark and upon continuous irradiation).
2) Review and editing of the different versions of the manuscript and supporting information (submitted version, response letter, revised version, published version).

Wilson, A.; Andreeva, E. A.; Nizinski, S. J.; Talbot, L.; Hartmann, E.; Schlichting, I.; Burdzinski, G.; Sliwa, M.; Kirilovsky, D.*; Colletier, J. P.* Structure-function-dynamics relationships in the peculiar Planktothrix PCC7805 OCP1: Impact of his-tagging and carotenoid type. Biochim Biophys Acta Bioenerg 2022, 1863 (7), 148584.*

My contribution to this article:

1) Supervising the analysis, quality and reproducibility of the femtosecond transient absorption measurements and nanosecond transient absorption measurements in the visible spectral range.
2) Review and editing of the different versions of the manuscript and supporting information (submitted version, response letter, revised version, published version).

Andreeva, E. A.; Nizinski, S.; Wilson, A.; Levantino, M.; De Zitter, E.; Munro, R.; Muzzopappa, F.; Thureau, A.; Zala, N.; Burdzinski, G.; Sliwa, M.; Kirilovsky, D.; Schirò, G.; Colletier, J. P. Oligomerization processes limit photoactivation and recovery of the Orange Carotenoid Protein. Biophys J. 2022, 121 (15), 2849-2872.*

My contribution to this article:

1) Supervising the analysis, quality and reproducibility of nanosecond transient absorption measurements.
2) Review and editing of the different versions of the manuscript and supporting information (submitted version, response letter, revised version, published version).

Niziński, S.; Schlichting, I.; Colletier, J. P.; Kirilovsky, D.; Burdziński, G.*; Sliwa, M.* Is orange carotenoid protein photoactivation a single-photon process? Biophys. Rep. 2022, 2 (3), 100072.*

My contribution to this article:

1) Conceptualization of the research, i.e. the involvement of a second photon to produce the final photo-active product.
2) Supervising the analysis, quality and reproducibility of all the experiments (nanosecond transient absorption measurements, with or without additional continuous irradiation, UV-vis absorption measurements in the dark and upon continuous irradiation).
3) Supervising the quality and reproducibility of the simulations of the OCP^R accumulation based on various hypothetical photoconversion models. Simulations were also tested on 3*H*-naphthopyrans showing a photochromic response.
4) Review and editing of the different versions of the manuscript and supporting information (submitted version, response letter, revised version, published version).

Poznań, May 18th 2023

Gotard Burdziński

Dr. Michel SLIWA
CNRS Director of Research / HDR
Head of Dynamics & Nanoscopy & Chemometrics team
http://lasir.cnrs.fr/dynachem/
Deputy Director of LIA Nanosynergetics
http://www.nanosynergetics.cnrs.fr/
Phone : + 33 (0)6 82 56 97 99
e-mail : michel.sliwa@univ-lille.fr

18th May, 2023 at Lille

Object: Authorship statement for the PhD thesis of Stanislaw Nizinski,

By this letter, I declare that I am the co-author of the following publications and my contribution is as follows:

1) **Nizinski, S.**; Wilson, A.; Uriarte, L. M.; Ruckebusch, C.; Andreeva, E. A.; Schlichting, I.; Colletier, J. P.; Kirilovsky, D.*; Burdzinski, G.*; **Sliwa, M.*** A unifying perspective of the ultrafast photo-dynamics of Orange Carotenoid Proteins from Synechocystis: Peril of high-power excitation, existence of different S* states and influence of tagging. **JACS Au 2022,** 2 (5), 1084–1095.

My contribution to this article:

- Coordination of the research project.
- Supervising the interpretation of the analysis of the transient absorption data, especially the discussion of the quantum formation quantum yield for the first precursor of OCP^R.
- Writing the manuscript and supporting information with the input from other co-authors.
- Submission of the manuscript, response letters and editing the final published version.

2) Wilson, A.; Andreeva, E. A.; **Nizinski, S.**; Talbot, L.; Hartmann, E.; Schlichting, I.; Burdzinski, G.; **Sliwa, M.***; Kirilovsky, D.*; Colletier, J. P.* Structure-function-dynamics relationships in the peculiar Planktothrix PCC7805 OCP1: Impact of his-tagging and carotenoid type. Biochim **Biophys Acta Bioenerg 2022**, 1863 (7), 148584.

My contribution to this article:

- Handling the interpretation of the analysis of the visible femtosecond and nanosecond transient absorption data.
- Writing the initial version of the section about the performed visible femtosecond transient absorption measurements and nanosecond transient absorption measurements.
- Participating in the scientific discussion with the different co-authors to interpret the different results.
- As co-corresponding author, participating to the submission and writing of the different versions of the manuscript and supporting information.

Université de Lille

Université de Lille, CNRS, UMR 8516, LAboratoire de Spectroscopie pour les Interactions, la Réactivité et l'Environnement, CNRS, UMR 8516, bât C5, 59655 Villeneuve d'Ascq Cedex, France

3) Andreeva, E. A.; **Nizinski, S.**; Wilson, A.; Levantino, M.; De Zitter, E.; Munro, R.; Muzzopappa, F.; Thureau, A.; Zala, N.; Burdzinski, G.; **Sliwa, M.**; Kirilovsky, D.; Schirò, G.; Colletier, J. P.* Oligomerization processes limit photoactivation and recovery of the Orange Carotenoid Protein. **Biophys J. 2022**, 121 (15), 2849-2872.

My contribution to this article:

- Supervising the preprocessing and analysis of the nanosecond transient absorption data.
- Participating in the scientific discussion with the different co-authors to interpret the different results.
- Participating in the writing of the different versions of the manuscript and supporting information.

4) **Niziński, S.***; Schlichting, I.; Colletier, J. P.; Kirilovsky, D.; Burdziński, G.*; **Sliwa, M.*** Is Orange Carotenoid Protein photoactivation a single-photon process? **Biophys. Rep. 2022**, 2 (3), 100072.

My contribution to this article:

- Supervising of the preprocessing and analysis of the transient absorption data.
- Discussion with other co-authors on the validity of the simulations of the OCP^R accumulation based on various hypothetical photoconversion models.
- Writing the manuscript and supporting information with the input from other co-authors.
- Submission of the manuscript, the response letter and editing the final published version.

Sincerely yours,

Lille, 18th May 2023

Michel Sliwa

Michel Sliwa
CNRS Research Director

Université de Lille

cnrs

Université de Lille, CNRS, UMR 8516, LAboratoire de Spectroscopie pour les Interactions, la Réactivité et l'Environnement, CNRS, UMR 8516, bât C5, 59655 Villeneuve d'Ascq Cedex, France

Diana Kirilovsky (Research Director Emeritus)
Equipe Photobiology, Photosynthesis, Photocatalysis
B3S Department
Institute for Integrative Biology of the Cell
91198 Gif sur Yvete

Paris, 26/05/2023

I declare that I am the co-author of the following publications and my contribution is as follows:

- Nizinski, S.; Wilson, A.; Uriarte, L. M.; Ruckebusch, C.; Andreeva, E. A.; Schlichting, I.; Colletier, J. P.; Kirilovsky, D.*; Burdzinski, G.*; Sliwa, M.* A unifying perspective of the ultrafast photo-dynamics of Orange Carotenoid Proteins from Synechocystis: Peril of high-power excitation, existence of different S* states and influence of tagging. *JACS Au* **2022,** 2 (5), 1084–1095.

My contribution to this article:

1) Responsible for protein expression and purification.
2) Responsible for the biological interpretation of the results and their comparison with the literature.
3) Reviewing, editing and submission of the final manuscript version as co-corresponding author.

- Wilson, A.; Andreeva, E. A.; Nizinski, S. J.; Talbot, L.; Hartmann, E.; Schlichting, I.; Burdzinski, G.; Sliwa, M.*; Kirilovsky, D.*; Colletier, J. P.* Structure-function-dynamics relationships in the peculiar Planktothrix PCC7805 OCP1: Impact of his-tagging and carotenoid type. *Biochim Biophys Acta Bioenerg* **2022**, 1863 (7), 148584.

My contribution to this article:

1) Conceptualization and supervision of the research project to design an OCP with higher photo-activation quantum yield.
2) Preparation of the new efficient *Planktothrix* OCP, responsible of protein expression and purification.
3) Supervising the experiments, the analysis and interpretation of the photo-activation experiments under continuous irradiation.
4) Writing of the manuscript first version.

5) Review and editing of the progressively developed versions of the manuscript and supporting information.
6) Submission of the manuscript, response letter and final corrections of the accepted manuscript as co-corresponding author.

- Andreeva, E. A.; Nizinski, S.; Wilson, A.; Levantino, M.; De Zitter, E.; Munro, R.; Muzzopappa, F.; Thureau, A.; Zala, N.; Burdzinski, G.; Sliwa, M.; Kirilovsky, D.; Schirò, G.; Colletier, J. P.* Oligomerization processes limit photoactivation and recovery of the Orange Carotenoid Protein. *Biophys J.* **2022**, 121 (15), 2849-2872.

My contribution to this article:

1) Supervising the process of protein preparation and purification.
2) Scientific discussion and advice on the interpretation of the results.
3) Review, editing and corrections of the final manuscript version.

- Niziński, S.*; Schlichting, I.; Colletier, J. P.; Kirilovsky, D.; Burdziński, G.*; Sliwa, M.* Is Orange Carotenoid Protein photoactivation a single-photon process? *Biophys. Rep.* **2022**, 2 (3), 100072.

My contribution to this article:

1) Supervising the process of protein preparation and purification.
2) Advises and participate in the scientific discussion concerning proposed mechanism involving subsequent absorption of two photons.
3) Review, reading and editing of the final version of the manuscript.

Paris, 26th May 2023

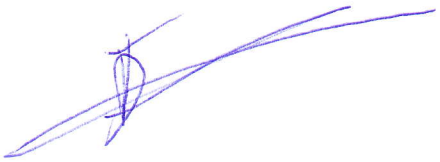

Dr Diana Kirilovsky
Directeur de Recherche (DR Emérite, CNRS)

INSTITUT DE BIOLOGIE INTEGRATIVE DE LA CELLULE (I2BC)
Unité mixte CEA – CNRS – Université Paris-Sud - UMR 9198
iBiTec-S-Bâtiment 532 – CEA Saclay- F91191 Gif-sur-Yvette cedex
Tél : 01 69 08 95 71 - courriel : diana.kirilovsky@cea.fr and diana.kirilovsky@i2bc.paris-saclay.fr
www.i2bc.paris-saclay.fr

Institut de Biologie Structurale
UMR 5075 CNRS-CEA-UJF
71, Avenue des Martyrs
Grenoble, France

Jacques-Philippe Colletier, Ph.D.,
Directeur de Recherche au CNRS (DR2)
Serial Nano-Crystallography (SNaX) team leader
Tel. : +33 457 428 515
E-mail: colletier@ibs.fr

Grenoble, May 23rd, 2022

I hereby declare that I am the co-author of the following publications and that my contributions are as follows:

#1: Nizinski, S.; Wilson, A.; Uriarte, L. M.; Ruckebusch, C.; Andreeva, E. A.; Schlichting, I.; Colletier, J. P.; Kirilovsky, D.*; Burdzinski, G.*; Sliwa, M.* (2022) "A unifying perspective of the ultrafast photo-dynamics of Orange Carotenoid Proteins from Synechocystis: Peril of high-power excitation, existence of different S* states and influence of tagging." *JACS Au*, 2 (5), 1084–1095.

My contributions to this article:

1. Review, editing and corrections of the final version of the manuscript.
2. Participation in the scientific discussion and advices regarding the final photo-dynamical OCP^R formation scheme.

#2: Wilson, A.; Andreeva, E. A.; Nizinski, S. J.; Talbot, L.; Hartmann, E.; Schlichting, I.; Burdzinski, G.; Sliwa, M.*; Kirilovsky, D.*; Colletier, J. P.* (2022) "Structure-function-dynamics relationships in the peculiar Planktothrix PCC7805 OCP1: Impact of his-tagging and carotenoid type". *Biochim Biophys Acta Bioenerg*, 1863 (7), 148584.

My contributions to this article:

1. Conceptualization and coordination of the research.
2. Supervision of all of the X-ray crystallography experiments.
3. Structure determination and interpretation.
4. Writing and editing the final version of article and submission of the article.
5. Submission of the manuscript, response letter and final corrections of the accepted manuscript as co-corresponding author.

#3: Andreeva, E. A.; Nizinski, S.; Wilson, A.; Levantino, M.; De Zitter, E.; Munro, R.; Muzzopappa, F.; Thureau, A.; Zala, N.; Burdzinski, G.; Sliwa, M.; Kirilovsky, D.; Schirò, G.; Colletier, J. P.* (2022) Oligomerization processes limit photoactivation and recovery of the Orange Carotenoid Protein. *Biophys J* 121 (15), 2849-2872.

My contributions to this article:

1. Conceptualization and coordination of the research.
2. Responsible of the performance and supervision of all of the X-ray scattering experiments.
3. Data analysis of all of the X-ray scattering experiments.
4. Supervising the stationary absorption data preprocessing and analysis.
5. Writing of the manuscript initial and final versions.
6. Review and editing of all the versions of the manuscript and supporting information.

7. Submission of the manuscript, response letter and final corrections of the accepted manuscript as co-corresponding author.

#4: Niziński, S.*; Schlichting, I.; Colletier, J. P.; Kirilovsky, D.; Burdziński, G.*; Sliwa, M.* (2022) "Is Orange Carotenoid Protein photoactivation a single-photon process ?" *Biophys Rep* 2 (3), 100072.

My contributions to this article:

1. Review, reading and editing of the final version of the manuscript.
2. Suggestions, advice and participation in the scientific discussion about the existence of the two photon photoconversion mechanism.

Please do not hesitate in contacting me if I can be of any further assistance.

Sincerely,

Jacques-Philippe Colletier